

**SYNTHESIS, CHARACTERIZATION AND
PHOTOLUMINESCENCE SPECTROSCOPY OF
LANTHANIDE ION DOPED OXIDE
MATERIALS**

By

SANTOSH KUMAR GUPTA

CHEM01201104026

Bhabha Atomic Research Centre, Mumbai

*A thesis submitted to the
Board of Studies in Chemical Sciences
In partial fulfillment of requirements
For the Degree of*

DOCTOR OF PHILOSOPHY

of

HOMI BHABHA NATIONAL INSTITUTE



JUNE, 2014

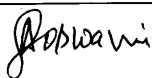
HOMI BHABHA NATIONAL INSTITUTE

Recommendations of the Viva Voce Board

As members of the Viva Voce Board, we certify that we have read the dissertation prepared by **Santosh Kumar Gupta** entitled “**Synthesis, Characterization and Photoluminescence spectroscopy of lanthanide ion doped Oxide Materials**” and recommend that it may be accepted as fulfilling the dissertation requirement for the Degree of Doctor of Philosophy.

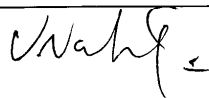
Date: 5.11.2014

Chairman: Dr. A. Goswami



Date:

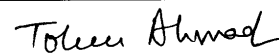
Guide: Dr. V. Natarajan



Date:

5.11.2014

External Examiner: Dr. T. Ahmad



Date:

5/11/14

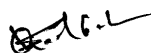
Co-Guide: Dr. R.M. Kadam



Date:

05/11/2014

Member 1: Dr. S.V. Godbole



Date: 5/11/2014

Member 2: Dr. V. Sudarsan



5/11/2014

Final approval and acceptance of this dissertation is contingent upon the candidate's submission of the final copies of the dissertation to HBNI. I hereby certify that I have read this dissertation prepared under my direction and recommend that it may be accepted as fulfilling the dissertation requirement.

Date:

Place:

STATEMENT BY AUTHOR

This dissertation has been submitted in partial fulfillment of requirements for an advanced degree at Homi Bhabha National Institute (HBNI) and is deposited in the Library to be made available to borrowers under rules of the HBNI.

Brief quotations from this dissertation are allowable without special permission, provided that accurate acknowledgement of source is made. Requests for permission for extended quotation from or reproduction of this manuscript in whole or in part may be granted by the Competent Authority of HBNI when in his or her judgment the proposed use of the material is in the interests of scholarship. In all other instances, however, permission must be obtained from the author.



Santosh Kumar Gupta

DECLARATION

I, hereby declare that the investigations presented in the thesis have been carried out by me. The work is original and has not been submitted earlier as a whole or in part for a degree /diploma at this or any other Institution / University.



Santosh Kumar Gupta

Dedicated to

My Parents

List of Publications

REFEREED JOURNALS

1. "Probing Site symmetry around Eu^{3+} in nanocrystalline ThO_2 using time resolved emission spectroscopy" Santosh K. Gupta, M.K. Bhide S.V. Godbole, V. Natarajan, **Journal of American ceramic society**, DOI: 10.1111/jace.13143, 2014
2. "Understanding the local environment of Sm^{3+} in doped SrZrO_3 and energy transfer mechanism using time resolved luminescence: A combined theoretical and experimental approach", Santosh K. Gupta, P. Ghosh, N. Pathak, A. Arya, V. Natarajan, **RSC Advances**, 4 (2014) 29202
3. "A Novel near white light emitting nanocrystalline $\text{Zn}_2\text{P}_2\text{O}_7$: Sm^{3+} derived using citrate precursor route: Photoluminescence spectroscopy", ", Santosh K. Gupta, N. Pathak, M. Sahu, V. Natarajan , **Advanced powder Technology** , 25 (2014) 1388-1393
4. "Evidence for the stabilization of manganese ion as Mn (II) and Mn (IV) in α - $\text{Zn}_2\text{P}_2\text{O}_7$: Probed by EPR, luminescence and electrochemical studies", Santosh K. Gupta, R.M. Kadam, R. Gupta, M. Sahu, V. Natarajan , **Materials chemistry and physics**, 145 (2014) 162-167
5. "Warm white light emitting ThO_2 : Sm^{3+} nanorods: Cationic surfactant assisted reverse micellar synthesis and Photoluminescence properties", Santosh K. Gupta, R. Gupta, V. Natarajan and S.V. Godbole, **Materials Reasearch Bulletin**, 49 (2014) 297-301
6. "Nanoparticles of $\text{Sr}_{0.995}\text{Gd}_{0.005}\text{ZrO}_3$: Gel-combustion Synthesis, Characterization, Fluorescence and EPR spectroscopy", Santosh K. Gupta, R.M. Kadam, V. Natarajan and S.V. Godbole, **Materials Science & Engineering B**, 183 (2014) 6-11
7. "Photophysical Properties of Eu(III) in Zirconia Nanocrystals Derived via Microemulsion Route from Oxalate Precursor", Santosh K. Gupta, R. Phatak, S.K. Thulasidas, V. Natarajan, **Advanced Science Engineering and medicine**, 6 (2014) 1-9
8. "Bluish white Sr_2CeO_4 and Red emitting Sr_2CeO_4 : Eu^{3+} nanoparticles: Optimization of synthesis parameter, characterization, energy transfer and photoluminescence", Santosh K. Gupta, M. Sahu, K. Krishnan, M. Saxena, V. Natarajan and S.V. Godbole, **Journal of Materials Chemistry C**, 1(2013)7054-7063

9. "On the unusual photoluminescence of Eu^{3+} in $\alpha\text{-Zn}_2\text{P}_2\text{O}_7$: a time resolved emission spectrometric and Judd-- Ofelt study", Santosh K. Gupta, M. Mohapatra, V. Natarajan and S.V. Godbole, *RSC Advances*, 3 (2013) 20046-20053
10. "Optical properties of Sol-Gel derived $\text{Sr}_2\text{SiO}_4:\text{Dy}^{3+}$ - Photo & Thermally stimulated luminescence", Santosh K. Gupta, M. Kumar, V. Natarajan and S.V. Godbole, *Optical Material*, 35 (2013) 2320-2328
11. "Structural phase transition in $\text{Zn}_{1.98}\text{Mn}_{0.02}\text{P}_2\text{O}_7$: EPR evidence for enhanced line broadening and large zero field splitting parameter in high temperature phase", Santosh K. Gupta, R.M. Kadam, P. Samui, V. Natarajan, S.V. Godbole, *Journal of Materials Research*, 28 (2013) 3157-3163
12. "Photoluminescence investigations of the near white light emitting perovskite ceramic $\text{SrZrO}_3:\text{Dy}^{3+}$ prepared via gel combustion route.", S.K. Gupta, M. Mohapatra, V. Natarajan and S.V. Godbole, *International Journal of Applied Ceramic Technology*, 10 (2013) 593-602
13. "Nanorods of white light emitting $\text{Sr}_2\text{SiO}_4:\text{Eu}^{2+}$: microemulsion-based synthesis, EPR, photoluminescence, and thermoluminescence studies", Santosh K. Gupta, M.K. Bhide, R.M. Kadam, V. Natarajan and S.V. Godbole, *Journal of experimental Nanoscience*, 2013, DOI:10.1080/17458080.2013.858833,
14. "Site specific luminescence of Eu^{3+} in gel combustion derived strontium zirconate perovskite nanophosphors", S.K. Gupta, M. Mohapatra, V. Natarajan and S.V. Godbole, *Journal of Materials Science*, 47 (2012) 3504-3515
15. "Structure and site selective luminescence of sol-gel derived $\text{Eu}:\text{Sr}_2\text{SiO}_4$ ", S.K. Gupta, M. Mohapatra, S. Kaity, V. Natarajan and S.V. Godbole, *Journal of Luminescence*, 132 (2012) 1329-1338
16. "Probing local site occupancy of various lanthanide ions (Eu^{3+} , Dy^{3+} and Sm^{3+}) in a- Sr_2SiO_4 host: TRFS, EXAFS and Theoretical calculations", Santosh K Gupta, Sandeep Nigam, A. Yadav, M. Mohapatra, S.N. Jha, C. Majumader, D. Bhattacharya, V. Natarajan, Inorganic Chemistry (**Communicated**)

National and International Symposia: 6

1. Structural phase transition in zincpyrophosphate: EPR and HTXRD investigations, Santosh K. Gupta, R.M. Kadam, V. Natarajan and S. V. Godbole, International symposium on materials chemistry, ISMC-2012, Mumbai, Dec-2012

2. Synthesis and Photoluminescence properties of $\text{Eu}^{3+}:\text{Sr}_2\text{SiO}_4$, , **Santosh Kumar Gupta**, M. Mohapatra, V. Natarajan, and S.V.Godbole, International conference on luminescence and its application (ICLA-2012), Hyderabad, Feb-2012(**Best poster award**)
3. Europium doped zinc pyrophosphate: Photo and Thermoluminescence, , **Santosh K. Gupta**, B. Sanyal (FTD), V. Natarajan, and S.V. Godbole, National conference on luminescence and its application (NCLA-2012), Bangalore, Jan-2013
4. Oxidation State Of Manganese in Zinc Pyrophosphate: Probed By Luminescence And EPR Studies, **Santosh K. Gupta**, R.M. Kadam, V. Natarajan and S. V. Godbole, Solid state physics symposium, SSPS-2013, Patiala, Dec-2013
5. Optical and magnetic properties of nanocrystalline SrZrO_3 , **Santosh K. Gupta**, P. Ghosh, N. Pathak, R.M. Kadam, A. Arya, V. Natarajan, ICONSAT-2014, INST, Chandigarh, march-2014
6. Local site symmetry of Sm^{3+} in α' - Sr_2SiO_4 : Probed by emission and fluorescence lifetime spectroscopy, **Santosh K. Gupta**, N. Pathak, S.K. Thulasidas, V. Natarajan, ICL-2014, Wroclaw, Poland, July 2014

ACKNOWLEDGEMENTS

Though only my name appears on the cover of this dissertation, a lot many people have contributed to its production. I owe my gratitude to all those people who have made this dissertation possible and because of whom my doctorate experience has been one that I will cherish forever.

My deepest gratitude is to my advisor, *Dr. V. Natarajan*. I have been amazingly fortunate to have an advisor who gave me the freedom to explore on my own and at the same time the guidance to recover when my steps faltered. He taught me how to question thoughts and express ideas. His patience and support helped me overcome many crisis situations and finish this dissertation.

My co-advisor, *Dr. R.M. Kadam*, has been always there to listen and give advice. I am deeply grateful to him for the long discussions that helped me sort out the technical details of my work. I am also thankful to him for teaching me the intricacies of EPR instrument.

I would like also like to thank members of my doctoral committee; *Dr. A. Goswami, Dr. S.V. Godbole and Dr. V. Sudarsan*, for their time, encouragement, thoughtful ideas and critical evaluation during the course of Ph.D.

In particular *Dr. S.V. Godbole's* insightful comments and constructive criticisms at different stages of my research were thought-provoking and they helped me focus my ideas. I am grateful to him for holding me to a high research standard and enforcing strict validations for each research result, and thus teaching me how to do research.

I would like to express my sincere gratitude to *Dr. Manoj Mohapatra* who has introduced me to this field. His calm demeanor, logical way of guidance, help in crucial experiments, monitoring the progress of work, teachings about the writing of manuscript has helped to bring out the proper shape of this work.

My sincere thanks are due to *Dr. Neelam Goyal* for her precious help and cooperation. She has been the real source of inspiration and the guiding force behind my work ethics.

I would like to thank **Mr. Nimai Pathak** for his help in sample preparation and stimulating discussion and for always motivating me.

I would also like to thank my colleagues *Dr. M.K. Bhide, Dr. S.K.Thulasidas, Dr. Paru Purohit, Dr M. Kumar, Mrs. B. Rajeshwari, Mr. B.A. Dhawale, Mr. N.S.*

Hon, Dr. A.R. Dhobale, Dr. V.C. Adya and all my section mates for their help, encouragement and support during the course of the research work.

I would like also like to thank my collaborator from other division **Santu Kaity (RMD)**, *N. Meshram (IITB) and S. Soni (IITB)* for electron microscopy, *Rohan Phatak and Dr K. Krishnan (FCD)* for X-ray diffraction, **Dr. Sandip Nigam (ChD)**, *Dr C. Mazumdar (ChD) and P. Ghosh (MSD)* for Thoretical studies.

I am blessed to have friends who are constant source of laughter, joy and support. I would like to thank all my friends *Manju, Sukanta, Vinita, Ankur, Sangita, Raj Kishore, Aishwarya, Soumitra, Dhiraj, Renu, Shankar, Chhavi, Debojit, Parfful Abhishek, Naresh, Raja, Indira, Sheleena, Prashant, Shivranjan, Deepti, Gunjan, Kailash, Pankaj, Prashant, Rimpi, Sreenu, Ankit, Avinash, and Rohan* who always stood by me and lend constant encouragement and support.

I take this opportunity to thank all the staff members of RCD for their cooperation.

I would like to thank *my parents* for their unconditional love, support, faith, encouragement and confidence in me. I run short of words in expressing my gratitude towards my wife **Ruma** who always stood by me and encouraged me up at every step of life. I would like to express thanks to my *son Avyaan* who in his own way geared me up to reach the goal.

Perhaps, I forgot someone... so, just in case: thank you to whomever it concerns!.

Santosh Kumar Gupta

LIST OF ACRONYMS:

MD- Magnetic dipole

ED-Electric dipole

EQ- Electric Quadrupole

UC- Up-Conversion

QC-Quantum cutting

MPR- Multiphonon-relaxation

NR- Non-radiative

J-O-Judd-Ofelt

MLCT- metal to ligand charge transfer

LMCT- ligand to metal charge transfer

CT- Charge transfer

CS-combustion synthesis

SCS-solution combustion synthesis

SHS- self-propagating high-temperature synthesis

TEOS-Tetra ethyl orthosilicate

EG-ethylene glycol

CA-citric acid

XRD- X-ray diffraction

TGA-Thermogravimetric analysis

DTA- Differential thermal analysis

DSC-differential scanning calorimetry

SEM- scanning electron microscope

CRT- cathode ray tube

TEM-transmission electron microscope

CCD- charge coupled device

DLS-dynamic light scattering

FTIR-Fourier transform infrared

IR-infrared

PAS-positron annihilation spectroscopy

PALS- positron annihilation lifetime spectroscopy

CDB- coincidence Doppler Broadening

LTS- lifetime spectroscopy

EPR- electron paramagnetic resonance

EMR- electromagnetic radiation

TSL- thermally stimulated luminescence

VB- valence band

CB - conduction band

Eh - trap depth for hole

Ee - trap depth for electron,

L - Luminescent center

A - hole trap

D - Electron trap

PL- Photoluminescence

CIE- Commission Internationale de l'Eclairage

IC = internal conversion,

ISC= intersystem conversion

F= fluorescence

P= phosphorescence

PMT-photomultiplier tube

TCSPC- time correlated single photon counting
CFD- constant fraction discriminator
TAC- time to amplitude convertor
ADC- analog to digital converter
DEL- electrical delays
MEM- digital memory
HTXRD- high temperature x-ray diffraction
AFM- atomic force microscopy
EXAFS- extended x-ray absorption fine structure
VASP-Vienna Ab-initio simulation package
PAW- projected augmented wave
PBE- Perdew–Burke–Ernzerhof

CONTENTS

CONTENTS

Synopsis	I
List of figures	XVI
List of tables	XXVII
Chapter 1-Introduction	1
1.1 General Introduction	2
1.2 Luminescence of trivalent lanthanide ion	3
1.2.1 The 4f energy levels and selection rules	5
1.2.2 Radiative and non-radiative transitions in lanthanides	8
1.2.3 Phosphor Design: Selection of dopant and hosts	14
1.2.4 Lanthanide photophysics	18
1.2.4.1 <i>Absorption spectra</i>	18
1.2.4.2 <i>Emission spectra</i>	22
1.2.5 Information gained from lanthanide luminescence: Structural probing	26
1.2.5.1 <i>Number of metal ion sites: N</i>	27
1.2.5.2 <i>Composition of the first coordination sphere</i>	27
1.2.5.3 <i>Population analysis</i>	27
1.2.5.4 <i>Site symmetry</i>	28
1.2.5.5 <i>Strength of Ln-L bond</i>	30
1.2.5.6 <i>Solvation state of Ln^{III} ion</i>	30
1.2.5.7 <i>Donor-Acceptor distances</i>	31
1.3 Luminescence Quenching	31
1.3.1 Multiphonon emission	35
1.3.2 Energy transfer between lanthanide ions	39
1.3.3 Cross relaxation	40
1.4 Lanthanide doped nanoparticles	41
1.4.1 Significance of lanthanide doped nanoparticles	41
1.4.2 Difference in Luminescent properties of Lanthanide doped nanoparticles w.r.t bulk	43
1.4.2.1 <i>Excitation and emission spectra</i>	43
1.4.2.2 <i>Symmetry of the lanthanide ion</i>	45
1.4.3 Lanthanide ion in semiconductor nanoparticles	45
1.5 Motivation of the present work	46
1.6 Scope of the thesis	49
Chapter 2-Experimental	51
2.1 Synthesis of luminescent materials	52
2.1.1 Conventional solid state route	52
2.1.2 Sol-gel method	53
2.1.3 Gel-combustion method	57
2.1.4 Polymeric precursor method	59

2.1.5	Reverse micellar route	60
2.2	Characterization Techniques	62
2.2.1	X-Ray diffraction	62
2.2.1.1	<i>Principle</i>	62
2.2.1.2	<i>X-ray production</i>	64
2.2.1.3	<i>XRD diffractometer</i>	65
2.2.1.4	<i>XRD applications: Phase purity and crystallite size</i>	66
2.2.2	Thermal Analysis: TGA/DTA/DSC	67
2.2.3	Electron microscopy: SEM/TEM	68
2.2.4	Dynamic light scattering (DLS)	74
2.2.5	Fourier transformed infrared spectroscopy (FTIR)	74
2.2.6	Positron annihilation spectroscopy (PAS)	75
2.2.7	Electron paramagnetic resonance (EPR)	77
2.2.8	Thermally stimulated luminescence (TSL)	82
2.2.9	Photoluminescence spectroscopy (PL)	84

Chapter 3- Lanthanide doped binary oxides (Thoria and zirconia) 92

3.1.	General Introduction	93
3.2.	Synthesis and characterization of ThO ₂ :Sm ³⁺ nanoparticles	94
3.2.1	Synthesis of ThO ₂ :Sm ³⁺ nanorods	95
3.2.2	Characterization of ThO ₂ :Sm ³⁺ nanorods	95
3.2.2.1	<i>Thermal studies of oxalate :TGA/DTA</i>	96
3.2.2.2	<i>Phase purity and structure: XRD</i>	96
3.2.2.3	<i>Morphological studies: TEM</i>	97
3.3	Photoluminescence properties of ThO ₂ :Sm ³⁺ nanorods	98
3.4	Synthesis and characterization of ThO ₂ :Eu ³⁺ nanoparticles	100
3.4.1	Synthesis of ThO ₂ :Eu ³⁺ nanoparticles	100
3.4.2	Characterization of ThO ₂ :Eu ³⁺ nanoparticles	101
3.4.2.1	<i>Thermal studies: TGA/DTA</i>	101
3.4.2.2	<i>Phase purity and structure: XRD</i>	101
3.4.2.3	<i>Morphological studies: TEM</i>	103
3.5.	Photoluminescence properties of ThO ₂ :Eu ³⁺ nanoparticles	104
3.5.1	Effect of annealing temperature on PL properties of ThO ₂ :Eu ³⁺ nanoparticles	104
3.5.2	Excitation and emission spectroscopy ThO ₂ :Eu ³⁺ nanoparticles (900°C annealed)	106
3.5.3	Time resolved emission spectroscopy of ThO ₂ :Eu ³⁺ nanoparticles (900°C annealed)	110
3.6	Synthesis and characterization of ZrO ₂ :Eu ³⁺ nanocubes	113
3.6.1	Synthesis of ZrO ₂ :Eu ³⁺ nanocubes	113
3.6.2	Characterization of ZrO ₂ :Eu ³⁺ nanocubes	114
3.6.2.1	<i>Thermal studies: TGA</i>	114
3.6.2.2	<i>Structural analysis: XRD</i>	115

3.6.2.3	Vibrational spectroscopy: FTIR	116
3.6.2.4	Size and morphology: HRTEM	117
3.7	Photoluminescence properties of ZrO ₂ :Eu ³⁺ nanocubes	118
3.7.1	Emission and lifetime spectroscopy of undoped zirconium oxalate and zirconia	118
3.7.2	Excitation, emission and lifetime spectroscopy of Eu ³⁺ doped zirconium oxalate and zirconia	119
3.8	Summary	123

Chapter 4- Luminescent properties of various lanthanide ions (Sm, Eu and Dy) in α' -Sr₂SiO₄: understanding differences in their local environment

4.1	General introduction	126
4.2	Synthesis and characterization of Sr ₂ SiO ₄ :Ln ³⁺ (Ln=Sm, Eu, Dy)	129
4.2.1	Synthesis of Sr ₂ SiO ₄ :Ln ³⁺ (Ln=Sm, Eu, Dy)	129
4.2.2	Characterization of Sr ₂ SiO ₄ :Ln ³⁺ (Ln=Sm, Eu, Dy)	130
4.2.2.1	Phase purity and structure: XRD	130
4.2.2.1	Morphological studies and particle size distribution: SEM, AFM and DLS	131
4.3	Photoluminescence properties of Sr ₂ SiO ₄ :Eu ³⁺	133
4.4	Reduction of Eu ³⁺ to Eu ²⁺ : EPR spectroscopy	139
4.5	Photoluminescence properties of Sr ₂ SiO ₄ :Eu ²⁺	140
4.6	Photoluminescence properties of Sr ₂ SiO ₄ :Dy ³⁺	142
4.7	Photoluminescence properties of Sr ₂ SiO ₄ :Sm ³⁺	144
4.8	X-ray absorption spectroscopy: EXAFS	147
4.9	Positron annihilation spectroscopy: Probing defects	151
4.10	Theoretical calculations	153
4.11	Evaluation of color coordinates	156
4.12	Summary	156

Chapter 5- Luminescent properties of various lanthanide ions (Sm, Eu, Gd and Dy) in SrZrO₃: A distorted perovskite

5.1	General introduction	159
5.2	Synthesis and characterization of SrZrO ₃ :Ln ³⁺ (Ln=Sm, Eu, Gd, Dy)	162
5.2.1	Synthesis of SrZrO ₃	162
5.2.2	Characterization of SrZrO ₃	162
5.2.2.1	Phase purity and structure: XRD	162
5.2.2.2	Morphological studies: SEM	166

5.2.2.3	<i>Size distribution: DLS</i>	167
5.3	Unique properties of SrZrO ₃ : PL and EPR	167
5.3.1	Emission spectroscopy	167
5.3.2	Theoretical calculations	169
5.3.3	Excitation spectroscopy	172
5.3.4	EPR spectroscopy for probing defects	173
5.3.5	Luminescence decay	173
5.4	Luminescence properties of SrZrO ₃ :Sm ³⁺	174
5.4.1	Excitation and Emission spectroscopy of Sm ³⁺ doped SrZrO ₃	175
5.4.2	Decay Time and TRES studies	177
5.4.3	Energy Transfer from Host to Rare-Earth Ions in SrZrO ₃ :Sm ³⁺	180
5.4.3.1	<i>Luminescence experiment</i>	180
5.4.3.2	<i>Electronic structure</i>	181
5.4.4	Photoluminescence mechanism in Sm ³⁺ doped SrZrO ₃	184
5.4.5	Materials Performance –color coordinate	185
5.4.6	Radiative and non-radiative transition in SrZrO ₃ :Sm ³⁺ compared to pure Sm ₂ O ₃ powder- Photoacoustic spectroscopy	185
5.5	Luminescence properties of SrZrO ₃ :Eu ³⁺	187
5.5.1	Effect of annealing temperature on PL properties	187
5.5.2	Excitation and Emission characteristics	188
5.5.3	Decay Time and TRES studies	191
5.5.4	Evaluation of J-O parameters of the Eu ³⁺ sample	196
5.5.5	Evaluation of colour coordinates:	197
5.6	Luminescence and EPR properties of SrZrO ₃ :Gd ³⁺	198
5.6.1	Emission and Life time	199
5.6.2	EPR studies	201
5.7	Luminescence properties of SrZrO ₃ :Dy ³⁺	202
5.8	Summary	209
 Chapter 6- Luminescent properties of Eu³⁺ ion in Sr₂CeO₄: A low phonon energy host		211
6.1	General Introduction	212
6.2	Synthesis and characterization of Sr ₂ CeO ₄ :Eu ³⁺	213
6.2.1	Synthesis of Sr ₂ CeO ₄ :Eu ³⁺	213
6.2.2	Characterization of Sr ₂ CeO ₄ :Eu ³⁺	214
6.2.2.1	<i>Phase purity and structure: XRD</i>	214
6.2.2.2	<i>Thermal studies: TGA/DTA</i>	214
6.2.2.3	<i>Morphological studies: SEM</i>	217

6.3	Luminescence properties of Sr ₂ CeO ₄	219
6.4	Luminescence properties of Sr ₂ CeO ₄ :Eu ³⁺	221
6.4.1	Emission, excitation and luminescence decay studies on Sr ₂ CeO ₄ :Eu ³⁺	221
6.4.2	Concentration variation effect on Eu ³⁺ photoluminescence	224
6.4.3	Energy transfer mechanism in Sr ₂ CeO ₄ :Eu ³⁺	226
6.4.4	Materials Performance –color coordinate	227
6.4.5	Judd-Ofelt Analysis	228
6.5	Summary	229
Chapter 7- Synthesis, structural characterization and spectroscopic investigations on a new host for lanthanide doping: Zn₂P₂O₇		231
7.1	General introduction	232
7.2	Synthesis and characterization of Zn ₂ P ₂ O ₇	233
7.2.1	Synthesis of Zn ₂ P ₂ O ₇	233
7.2.2	Characterization of Zn ₂ P ₂ O ₇	233
7.2.2.1	Phase purity and structure: XRD	233
7.2.2.2	Compositional characterization: FTIR	234
7.2.2.3	Phase transition: HTXRD, DSC and EPR	236
7.3	Luminescence properties of Zn ₂ P ₂ O ₇ :Eu ³⁺	242
7.3.1	Emission, excitation and luminescence decay studies on Zn ₂ P ₂ O ₇ :Eu ³⁺	242
7.3.2	Life-Time and time resolved fluorescence spectroscopy (TRES)	244
7.3.3	Judd-Ofelt Analysis	247
7.4	Effect of crystal field: Mn doped α-Zn ₂ P ₂ O ₇	248
7.4.1	EPR spectroscopy	248
7.4.2	PL spectroscopy	252
7.5	Exploring α-Zn ₂ P ₂ O ₇ for synthesis of lanthanide ion based White LEDs	255
7.5.1	Effect of synthesis condition (rare earth concentration and annealing temperature) on luminescence properties	253
7.5.2	Excitation and emission spectroscopy of Zn ₂ P ₂ O ₇ : Sm ³⁺	256
7.6	Summary	260
Conclusions and future scope		262
References		266

SYNOPSIS

The subject of this Ph. D. thesis is the “Synthesis, characterization and photoluminescence spectroscopy of lanthanide ion doped oxide materials” of interest in photonics and optoelectronics. Optical materials doped with rare earth elements are of great relevance in science and technology. Modern solid state optical technology is mainly based on lanthanide doped materials, with applications ranging from solid state lighting, field emission diodes, in-vivo fluorescence imaging, white-light-emitting phosphor for UV-LEDs, finger print detection, proton detector, lasers, dosimetry, drug delivery and optical & MRI imaging [1-13]. From the scientific point of view, lanthanide doped materials attract increasing attention due to their particular physical properties. In the context of global energy shortage, energy-saving is an important issue that we are facing on. In the field of lighting, white light emitting diode (WLED), a new generation solid source has been highlighted due to its high luminous efficiency, low energy consumption and great potential in environmental protection. Thereafter there is a present trend to replace the traditional incandescent and fluorescent lamps [14, 15]. There is a tremendous growth in the development of WLED worldwide due to its various applications viz. lighting, motor vehicle and backlight for mobile panel and liquid crystal displays [16-19].

Luminescent dopants are extensively used as local probes for identifying local structures in crystalline material, understanding the effect of chemical and thermal treatment on catalysts and probing the structure of biological molecules. In view of its non-degenerate emissive state, 5D_0 , Eu (III) ion is most appropriate as a luminescent structural probe [20-23] for the determination of the number of metal ion sites in a compound, their symmetry, and their respective population. Other lanthanide ions have transitions that are usually the mixtures of electric dipole transition (EDT) and magnetic dipole transition (MDT) and the effects of symmetry are less pronounced. Because of unique spectroscopic properties and luminescent dynamics of f -electron states, doping luminescent rare earth ions into nano-hosts has been demonstrated as an optimistic approach to develop highly efficient and stable nanophosphors for various applications. Nanotechnology is a major factor in the advancement of luminescence technology—it makes luminescence much brighter, leading to some special applications. Of the numerous publications and reports on nanomaterials, half are related to luminescence in one way or another. More than half of nanoscale materials

Synopsis

exhibit intense luminescence. These include semiconductor nanoparticles or quantum dots, organic nanoparticles, metallic nanoparticles, doped nanoparticles, carbon nanotubes and insulator nanoparticles. Quantum size confinement results in brighter luminescence and easy tunability of the emission color of semiconductor nanoparticles. Along with other advantages, such as small size, water-solubility, good photo-stability, narrow emission bandwidth, and surface functionalities, luminescence nanomaterials have tremendous potential for practical applications. Fortunately, due to the physics of quantum size confinement, nanoscale phosphors provide an avenue for further advancing solid-state luminescence. Compared to bulk materials, nanoparticles exhibit greater electron–hole overlap, thereby yielding greater oscillator strength and enhanced luminescence quantum efficiency. Improved oscillator strength is important because a phosphor’s emission decay lifetime is inversely proportional to its oscillator strength and typically shortens as particle size decreases. Similarly, by overcoming the inherent loss of luminescence efficiency normally associated with smaller size materials, luminescence nanoparticles hold the promise of practical phosphors that are considerably smaller than what can be achieved currently. Among the materials evaluated as hosts for lanthanide ions in this work, our attention was mostly focused on alkaline earth silicate, zirconate and cerate. These materials are characterized by good transmission properties in the visible part of the electromagnetic spectrum and relatively low phonon energies. They can be efficiently doped with lanthanide ions, due the similarity between the ionic radius of the alkaline earth and the lanthanide ions. Therefore these materials are prospective high efficiency luminophors and are attracting increasing interest for photonics and optoelectronics applications. Indeed alkaline earth silicate, zirconate and cerate are resistant to many chemicals and air exposure. They can also be grown with low-cost techniques. They are also thermally, chemically and mechanically stable. Few new oxide hosts were also tried to venture into novel lanthanide doped luminescent materials viz. $\text{Zn}_2\text{P}_2\text{O}_7$, ThO_2 and ZrO_2 .

We have also synthesized some novel white light emitting materials with high CRI index and efficiency. The idea is to synthesize low phonon-energy luminescent materials (micro and nano regime) to minimize non-radiative losses.

Synthesizing nanoparticles of refractory oxides like ThO_2 and ZrO_2 at lower synthesis temperature is a challenge. Hosts like ThO_2 , $\text{Zn}_2\text{P}_2\text{O}_7$ and Sr_2CeO_4 having very low phonon energy are good candidates for luminescent materials; but they are

relatively unexplored. Another novel approach is to use lanthanide ion as a structural probe (structure- properties correlation). Further understanding why different lanthanides (Sm, Eu and Dy) behave differently in same host is an interesting problem. This can be solved by theoretical validation of experimental results.

Although many reports are available on lanthanide doped ZrO_2 nanoparticles, very few reports are there on luminescence properties of lanthanide ion in ThO_2 . Eu^{3+} is used as a structural probe to understand its local site symmetry in nanocrystalline ThO_2 . For the first time, reverse micellar route is used to synthesize ThO_2 . Although reports exist on luminescence properties of lanthanide ion in Sr_2SiO_4 and $SrZrO_3$ (SZ), none of them explain the site occupancy of Ln^{3+} and its related effect on luminescence properties in these matrices. Time resolved emission spectroscopy (TRES) is extensively used as a tool to understand such phenomena. In Sr_2SiO_4 , there are two types of sites for Sr^{2+} . One is a more symmetric 10 coordinated site Sr (1) and the other is a less symmetric 9 coordinated site Sr (2). In $SrZrO_3$ also there is 8-coordinated Sr and 6-coordinated Zr. However, when an active dopant is introduced into this perovskite, the optical and magnetic properties are dramatically changed depending on the distribution of the dopant in the perovskite ceramic. Studies of dopant ion distribution in perovskite have attracted much attention, because they may lead to better understanding of the correlations between structure and properties such as color, magnetic behavior, catalytic activity, and optical properties, *etc.*, which are strongly dependent on the occupation of these two sites by metal ions. None of the available literature explained the site symmetry of Ln^{3+} in $SrZrO_3$ nanocrystals. Considering the relatively wide band gap, high refractive index and lower phonon energy, SZ is a good candidate to be used as the host material in order to excite RE ions efficiently and to yield intense luminescence. Metal ions could be conveniently substituted into the SZ lattice, if their ionic radii are comparable to that of the Sr^{2+}/Zr^{4+} cations. It is thought that these “magic” dopants can choose their site occupancy as a result of the local Sr/Zr ratio and oxygen partial pressure during firing. Such dopants are also termed “amphoteric”, because the site change of a dopant with well defined valence causes a change of the relative charge. We have used PL to investigate a series of lanthanide ions doped in strontium zirconate, with the main aim of determining the site occupancy of the lanthanide.

Different lanthanide ions viz. Eu, Sm and Dy ions have been used as structural probes to understand their site occupancy in Sr_2SiO_4 and $SrZrO_3$. These ions were

Synopsis

found to behave differently in terms of their local site occupancy in these matrices. This aspect has been investigated in detail in the present work. Theoretical modeling and EXAFS studies were carried out to explain such anomaly. Effect of replacing Si (IV) by Ce (IV) in Sr_2SiO_4 is investigated in Sr_2CeO_4 system. Ionic size of silicon 0.40 Å; not ideal for Eu^{3+} substitution- entire Eu is distributed to Sr^{2+} site. Si (IV) is replaced by Ce (IV) whose ionic radius is very close to Eu (III). Also synthesizing Sr_2CeO_4 is a challenge, because it decomposes peritectically to SrO and SrCeO_3 at higher temperatures.

In addition, Judd-Ofelt parameter and other photophysical properties like (radiative transition rate, radiative lifetime, efficiency, and branching ratio) of Eu^{3+} ion in zirconium oxalate and zirconium dioxide was evaluated by adopting standard Judd-Ofelt (J-O) analysis procedures. These J-O parameters reflect the local structure around the metal ion in the host and provide information regarding the nature of the metal-ligand bonding in the matrix.

Luminescence properties of hosts like $\text{Zn}_2\text{P}_2\text{O}_7$ (both undoped and doped) with lanthanide ions have been investigated for the first time with a view to develop new and robust phosphor materials having multifunctional applications. Zinc pyrophosphate is known to undergo structural phase transition at 132°C. We have doped 2.0 mol % Mn^{2+} in zinc pyrophosphate and used electron paramagnetic resonance (EPR) as a probe to understand the mechanism for phase transition. This aspect was also supported by high temperature x-ray diffraction (HTXRD) and differential scanning calorimetry (DSC).

Cost of lanthanide ion is an issue; keeping this in mind, we have synthesized rare earth free visible emitting luminescent materials viz. SrZrO_3 , Sr_2CeO_4 and $\text{Zn}_2\text{P}_2\text{O}_7$. Hence, it is expected that suitable modification in the synthesis procedure as well doping these hosts with lanthanide ions can give efficient luminescent materials, which can have multi colour emission.

Keeping the above mentioned aspects in mind, the luminescence properties of these nanomaterials have been investigated during the course of the present investigation. Effect of various synthesis conditions like concentration of dopant ion and annealing temperature on photoluminescence properties (emission spectra, excitation spectra and luminescence life time) of lanthanide were investigated. Based on critical distance calculations we have proposed mechanism for concentration quenching.

Based on concentration quenching, mechanism for the same is also proposed. SrZrO₃ is an interesting host because of its multicolor emission properties and ferromagnetic behavior. EPR study showed the presence of oxygen vacancy in SrZrO₃ nanocrystals. Emission and EPR studies along with theoretical calculations were carried out to bring out the possible reason for multicolor emission in SrZrO₃ nanocrystals.

Various synthesis techniques were explored to synthesize the nanoparticles viz. Sol-gel, combustion, polymeric precursor, reverse micellar etc. Characterization of the materials is done by various physical and chemical methods. For structure, phase purity and crystallite size, X-Ray Diffraction has been used. For morphology and average particle size electron microscopy has been used. Dynamic light scattering (DLS) has been used for calculating particle size distribution and hydrodynamic radii. Extended X-ray absorption fine structure (EXAFS) is used to understand the local environment around Ln³⁺ ion in various inorganic hosts. Positron annihilation spectroscopy (PAS) is used to understand the nature of defects which arises due to aliovalent substitution. TRES has been extensively used in this work for recording such as emission and excitation spectra and luminescence lifetimes. The thesis is divided into 7 chapters. A brief description of the different chapters is given below.

Chapter 1: Introduction

In this chapter, the fascinating luminescence properties of lanthanide ion and the reason for the same have been discussed. In contrast to the broad band's observed for transition metal ions, the lanthanide f-f electronic transitions exhibit typically very narrow spectra in the luminescence and absorption spectra. Since change in the local environment of the lanthanide ion has a negligible influence on the 4f-electrons, coordination will only affect the fine structure of the absorption and emission bands, rather than resulting in major shift in the peak position. Lanthanide ions can show emission in the near-UV, visible, near-infrared and infrared spectral regions. Each lanthanide ion has a characteristic absorption and emission spectra. It also describes about various selection rules pertaining to f-f transition and energy levels of various lanthanide ions.

This chapter also explains about the choice of host and luminescent dopant to synthesize the phosphor. With respect to the energy gap requirement, it is obvious that Eu (III), Gd (III), and Tb (III) are the best ions, with $\Delta E = 12\,300$ ($^5D_0 \rightarrow ^7F_6$), $32\,200$ ($^6P_{7/2} \rightarrow ^8S_{7/2}$) and $14\,800$ ($^5D_4 \rightarrow ^7F_0$) cm⁻¹, respectively. However, Gd (III) emits in

the UV and is not very useful as luminescent probe for bioanalyses, because its luminescence interferes with either emission or absorption processes in the organic part of the complex molecules. Lanthanide photophysics, Judd-Ofelt Theory, information gained from lanthanide luminescence, luminescence quenching, energy transfer, multiphonon emission, cross relaxation and importance of lanthanide doped nanomaterials are also discussed in this chapter. Difference in Luminescent properties of lanthanide doped nanoparticles w.r.t. bulk has also been discussed in this chapter.

Chapter 2: Experimental

The synthesis techniques adopted in preparation of different nano/micro luminescent materials and the experimental techniques used for characterization of these materials have been presented in Chapter 2. The reverse micellar route has been used for the synthesis of refractory oxide like thoria and zirconia at very low temperature. Different types of surfactant are employed to obtain nanorods and nanocubes. Sol-gel route and combustion method adopted for preparation of Sr_2SiO_4 and SrZrO_3 has been elaborated. Solution-Polymerization method used for synthesis of zinc pyrophosphate and strontium cerate is also discussed in great deal. Thermal analysis (TG/DSC) of the gel precursors / precursor powders has been carried out in order to study the nature of thermal decomposition and determination of calcination temperatures. Phase evolution of synthesized powders was characterized by X-ray diffraction after calcination. Particle size of powder was characterized by laser scattering particle size analyzer. Particle morphologies were observed in scanning electron microscope (SEM) and transmission electron microscope (TEM). Local environment/ site symmetry around lanthanide ion in a particular host is investigated using time resolved fluorescence spectroscopy (TRFS) and extended x-ray absorption fine structure (EXAFS) measurement employing synchrotron. Theoretical calculations were also done to understand the difference in behavior of different lanthanides in terms of their local site occupancy in strontium silicate. Positron annihilation spectroscopy (PAS) has been carried out on lanthanide doped strontium silicate sample to probe the nature of defects, which arise due to aliovalent substitution.

Chapter 3: Lanthanide doped binary oxides (thoria and zirconia)

This chapter discusses about the photoluminescence properties of lanthanide ions in nanocrystalline thoria and zirconia matrices. Here, we had introduced $\text{Sm}^{3+}/\text{Eu}^{3+}$ ions in nanocrystalline ThO_2 and Eu^{3+} in ZrO_2 by means of a versatile microemulsion based synthesis (reverse micellar route) in order to obtain multifunctional materials, which combine the optical properties of the lanthanides with the properties of the host matrix. The main idea behind this work was that by appropriate control of the synthesis parameters, one can use these nanoreactors to produce tailor-made products down to nanoscale level with new and special properties. The aim of this study was to lower the synthesis temperature for preparing thoria nanorods and zirconia nanocubes from their oxalate precursor via the surfactant (Cetyl Trimethyl ammonium bromide, CTAB for thoria and tergitol for zirconia) assisted reverse micellar route and characterize the same with Thermogravimetric analysis (TGA), X-ray diffraction (XRD), High resolution transmission electron microscopy (HRTEM), and Photoluminescence (PL) spectroscopy. Through the present work, we have tried to investigate the emission, excitation and lifetime studies of the samarium/europium ion in thoria matrix. The sites occupied by Sm^{3+} ions and effect of site symmetry were studied using time resolved emission spectrometry. PL spectra of $\text{Eu}^{3+}:\text{ThO}_2$ nanocrystals was studied after annealing at higher temperatures in the range 500-900°C. Eu^{3+} ion occupied two different sites in the host and relaxes at different time intervals. The change in lifetime of Eu^{3+} at two sites with annealing temperature could be related with changes in structure of the host by investigating the changes in intensity of time resolved emission spectra of Eu^{3+} at two different sites. As far as $\text{ZrO}_2:\text{Eu}^{3+}$ is concerned; this is the first report on synthesis of zirconia using non-ionic surfactant in reverse micelle. Through this route, we could stabilize metastable tetragonal phase at 500°C through the addition of 1 mol % Eu^{3+} , which is technologically more important. We have tried to investigate the effect of ligand field (oxalate and oxide) on emission, excitation and lifetime studies of the Europium doped zirconium oxalate (precursor stage) and zirconium dioxide samples. In addition, Judd-Ofelt parameter and other photophysical properties (radiative transition rate, radiative lifetime, efficiency, branching ratio) of Eu^{3+} ion in the zirconium oxalate and zirconium dioxide were evaluated by adopting standard Judd-Ofelt (J-O) analysis procedures. These J-O parameters reflect the local structure around the metal

ion in the host and provide information regarding nature of the metal-ligand bonding in the matrix.

CHAPTER 4: Luminescent properties of various lanthanide ions (Sm, Eu, and Dy) in α' - Sr_2SiO_4 : understanding differences in their local environment

This chapter discusses about the luminescence properties of Eu, Dy and Sm in strontium silicate and their local site occupancy in this matrix. Oxide-based hosts have received considerable attention for use in flat-panel displays due to their luminescent characteristics, stability in high vacuum, and the absence of corrosive gas emission under electron bombardment, as compared to currently used sulfide-based phosphors [23]. Therefore, oxide-based phosphors are likely to emerge as the choice for field emission diodes (FED) green or red phosphors. Among these, strontium silicate is an excellent matrix due its stable crystal structure, good mechanical strength and high thermal stability provided by the tetrahedral silicate (SiO_4)²⁻ group [24]. Sr_2SiO_4 has attracted current interest due to its special structural features and potential application in developing white light-emitting-diodes (LEDs), because GaN (400 nm chip) coated with $\text{Sr}_2\text{SiO}_4 : \text{Eu}^{2+}$ exhibits better luminous efficiency than that of industrially available products such as InGaN (460 nm chip) coated with YAG : Ce [25]. The optical band gaps of alkaline earth silicates range between 4 -7 eV and therefore these materials are characterized by good transmission properties in the visible part of the electromagnetic spectrum. In the structure of Sr_2SiO_4 , there are two different Sr sites: one having coordination number 9 and the other with coordination number 10. The ten coordinated Sr(1) sites form linear three-membered rows of (Si–O–Sr(1)–O–Sr(2)), whereas the nine coordinated Sr(2) sites form zig-zag chains of (Sr(1)–O–Sr(2)–O–Sr(1)) along the b-axis [26]. Sr (1) polyhedron has more symmetric environment with hexagonal pseudo-symmetry along the y-axis [27]. It shares the face and the vertex with the two SiO_4 tetrahedra, which are vertically above and below it and the three edges with three SiO_4 tetrahedra. We have doped 0.5 mol % Eu, Dy and Sm in Sr_2SiO_4 . TRFS studies showed that that Eu(III)/Eu(II) occupy both Sr(1) and Sr(2) sites, whereas Dy and Sm occupy only Sr(2). Theoretical calculations were done to validate the experimental results. Theoretical calculation showed that energetically substitution of Sr in Sr_2SiO_4 at 9-coordinated site is more

favorable than at 10-coordinated site. Due to relatively higher bond strength of Dy-O and Sm-O bonds, the inclusion of these at 10-coordinated site results in shortening of few M-O bonds, which leads to distortion in MO_{10} polyhedra. Such a distortion leads to destabilization of the conformer having Dy/Sm ion at 10-coordinated sites.

CHAPTER 5: Luminescent properties of various lanthanide ions (Sm, Eu, Dy and Gd) in $SrZrO_3$: A distorted perovskite

This chapter discusses about the EPR and luminescence properties of gel-combustion derived undoped $SrZrO_3$ and luminescence properties of Eu, Dy, Sm and Gd in strontium zirconate and their local site occupancy in this particular matrix. Results for optical properties of undoped and Sm doped $SrZrO_3$ is modelled using density function theory (DFT) calculations.

Light emission from lanthanide ions plays an important role in solid state lighting (phosphor-converted light emitting diodes), display (plasma and field emission displays), and bioimaging (fluorescent markers) technologies. Owing to their high thermal and chemical stability and low environmental toxicity, lanthanide-doped alkaline-earth perovskite oxides of formula ABO_3 and their corresponding solid solutions $(A,A')(B,B')O_3$ ($A, A' = Ca, Sr, Ba$; $B, B' = Ti, Zr, Hf$) are attractive candidates for nanostructured phosphors for display and bioimaging technologies. Specifically, they have shown potential as phosphors for field emission [28] and electroluminescent [29] displays, and as fluorescent markers for bioimaging [30]. Recently much attention has been devoted to the photoluminescent (PL) properties of titanates and zirconates with disordered perovskite structure. The main reason is the distinct potential of these materials for electro-optic applications [31, 32]. The optical properties of disordered semiconductors are characterized by the presence of a broad PL band. This phenomenon is attributed to the electronic states inside the band gap, which are the main defects for an intense PL response. According to Longo et al., the displacement of Zr or Sr atoms in disordered perovskite $SrZrO_3$ may induce some vacancies at the axial and planar oxygen sites of the $[ZrO_6]$ octahedral [33]. It is well known that the vacancies defects may play important roles as luminescence centers and thus it is expected that the perovskite $SrZrO_3$ may show host emission. Defect induced violet blue emission from strontium zirconate host has been observed by many workers [33, 34-36].

The perovskite material of ABO_3 type having various crystalline structures shows interesting physiochemical properties and is a potential host for the chemical substitution. Substitution at both A and B sites can lead to change in symmetry and composition and thus create various defects viz. cation or oxygen vacancies, which can drastically influence the band structures and it is the main factor in determining the electronic structures. In particular, these materials can accommodate lanthanide ions on the A-site or B-site. These doped oxides are not only used as probes to investigate local centers and energy, but also to provoke changes in their optical behavior. Moreover, doping foreign elements into a semiconductor with a wide band gap to create a new optical absorption edge is known to be one of the primary strategies for developing materials with optically driven properties. However, the role of the rare earth dopant ion in the perovskite structure is not very clear and is still being discussed.

However, when an active luminescent dopant like Sm, Eu, Gd and Tb is introduced into these perovskites, their optical and magnetic properties are dramatically changed depending on its distribution in the perovskite ceramic. None of the literature available explained the site symmetry of Ln^{3+} in $SrZrO_3$ nanocrystals. Considering the relatively wide band gaps, high refractive indices and lower phonon energy, SZ is a good candidate to be used as the host material for efficient excitation of RE ions and intense luminescence. Metal ions could be conveniently substituted into SZ lattice, if their ionic radii are comparable to that of the Sr^{2+}/Zr^{4+} cations. We have used PL to investigate a series of lanthanide-doped strontium zirconate, with the aim of determining the site occupancy of the lanthanide. Effect of concentration of dopant ion and annealing temperature on the luminescence properties were also studied.

CHAPTER 6: Luminescent properties of Eu^{3+} ion in Sr_2CeO_4 : A low phonon energy host

This chapter discusses the work relating to the synthesis via polymeric precursor route, and photo luminescence (PL) investigations of strontium cerate nanoparticles incorporated with varied concentration of europium. The synthesis conditions for the sample have been optimized. Mechanism for energy transfer and concentration quenching of the observed PL has been proposed. The color coordinates of the system

were evaluated and plotted on a standard CIE index diagram. The polymeric precursors method has been successfully applied for the synthesis of nanosized cerate red phosphors with different europium ion concentrations. Detailed X-ray investigations were done to optimize the parameter w.r.t to calcination temperature and time to get pure phase. Detailed photoluminescence investigations of undoped Sr_2CeO_4 showed bluish white emission with single lifetime of 59 μs .

Danielson et al. [37] have reported a novel blue luminescent material Sr_2CeO_4 prepared by combinatorial material synthesis technique, which exhibits the emission peak at 485 nm. The luminescence was believed to originate from a ligand-to-metal Ce^{4+} charge transfer mechanism. Sr_2CeO_4 phosphor has been confirmed to have an orthorhombic crystal structure with one-dimensional chains of edge-sharing CeO_6 octahedrons linked by strontium ions [38] and was considered to be a potential candidate for blue phosphors [39]. Thus, Sr_2CeO_4 belongs to a small group of crystals, whose luminescence properties are governed by regularly located luminescent elements. The main feature of such luminescent systems is the interaction of its regular optical centers, which promotes spatial delocalization of excitation energy. Such an interaction will facilitate the effective excitation energy transfer from the host to doped centers emitting in another spectral range. In addition, Sr_2CeO_4 was found to emit efficiently under ultraviolet, cathode ray and X-ray excitation [37] and [40]. The emission spectra of europium doped cerate sample showed characteristic peaks corresponding to the ${}^5\text{D}_0 \rightarrow {}^7\text{F}_j$ ($j=1, 2$) transitions of Eu^{3+} ion as well as host emission under CTB. The PL decay time studies showed a bi-exponential decay, which was attributed to presence of europium ion at both Sr^{2+} as well as Ce^{4+} sites. Longer lifetime component (800 μs) arises due to the Eu^{3+} ions sitting at regular centrosymmetric Ce^{4+} sites and the short lifetime component (60 μs) arise due to the Eu^{3+} ion at non-centrosymmetric Sr^{2+} sites. The concentration quenching of the PL signal intensity was observed for dopant ion concentration of more than 5 mol%. From this, the critical energy transfer distance of Eu^{3+} was calculated to be 13 Å and the mechanism of concentration quenching was determined to be the multipole–multipole interaction. It was observed that with increase in Eu^{3+} concentration, PL intensity of europium emission lines increases, whereas that of host emission decreases. This was assigned to energy transfer between host and europium ion. The

J-O parameters and other radiative properties were evaluated for all samples adopting standard procedure and were related with spectral features of europium ion.

CHAPTER 7: Synthesis, structural characterization and spectroscopic investigations on a new host for lanthanide doping: $Zn_2P_2O_7$

This chapter discusses about the synthesis and structural characterization of zincpyrophosphate; a novel inorganic host for lanthanide luminescence.

Luminescence properties of hosts like $Zn_2P_2O_7$ (both undoped and doped) with lanthanide ions (Eu and Sm) are investigated for the first time with a view to develop new and robust phosphor materials having multifunctional applications. Zinc pyrophosphate is known to undergo structural phase transition at 132°C. We have doped 2.0 mol % Mn^{2+} in zinc pyrophosphate and used EPR as a probe to understand the mechanism for phase transition. This aspect was also supported by HTXRD and DSC.

Among the various hosts used as phosphor systems, phosphate based matrices offer a range of compositional and structural possibilities that facilitate the tailoring of chemical and physical properties of interest for specific technological applications. These hosts offer better homogeneity, chemical and thermal stability with lower sintering temperatures [41-44]. Pyrophosphates having general formula $M_2P_2O_7$ (M=Ca, Sr, Ba, Mg, Zn, Mn etc.) are one of the phosphate systems, which are reported to be excellent host materials [45, 46]. Special interest in pyrophosphate arises from the unique spectroscopic behavior of the metal cation polyhedra with well-defined and low symmetry coordination [47, 48]. Among these, the thortveitite-type pyrophosphate α - $Zn_2P_2O_7$ is a promising low temperature co-fired ceramic (LTCC) material [49]. In zinc pyrophosphate, there are two cationic sites in lattice, i.e., five-coordinated Zn^{2+} sites (square pyramidal coordination) and six-coordinated Zn^{2+} sites (octahedral coordination).

Europium was used as a structural probe to understand the local environment. Based on the time resolved emission spectroscopic investigations (TRES), it was inferred that two different types of Eu^{3+} ions were present in the zinc pyrophosphate. The first type was a long lived species ($\sim\tau = 1.77$ ms) present at relatively less symmetric '5-coordinated Zn' sites, while the second was a short lived species ($\sim\tau = 620$ μ s) present

at symmetric '6-coordinated Zn' sites. This unusual behavior of the trivalent rare earth species could be explained with the help of Judd-Ofelt (J-O) calculations. From the calculations, the radiative (τ_R) and non radiative (τ_{NR}) life times were evaluated for both the species. The radiative life time of the Eu^{3+} species present in symmetric environment was found to be higher than that of the species present in asymmetric environment. This is consistent with the selection rules governing the transition. It was observed that, the presence of a very strong non-radiative component at the symmetric site brings down the overall lifetime value. It was found that for short lived species; $\Omega_4 > \Omega_2$, while for the long lived species, the reverse trend was observed further confirming the correlation in between the asymmetry and bonding. Since effect of crystal field can be more prominently seen in transition metal than lanthanide ion; 2.0 mol% MnCO_3 was doped in $\text{Zn}_2\text{P}_2\text{O}_7$. It is very interesting to know that in $\text{Zn}_2\text{P}_2\text{O}_7$, manganese was stabilized as both Mn (II) and Mn (IV). This has been validated using EPR and PL spectroscopy.

References

1. K. G. Sharma, T.P. Singh, N. R. Singh, *J. Alloy Compd.* **602** (2014) 275.
2. R. Cao, X. Yu, X. Sun, C. Cao, J. Qiu, *Spectrochim Acta A*, **128** (2014) 671
3. Z.W. Zhang, A.J. Song, M.Z. Ma, X.Y. Zhang, Y. Yue, R.P. Liu, *J. Alloy Compd.* **601**(2014) 231.
4. R. Dey, A. Pandey, V.K. Rai, *Spectrochim Acta A*, **128** (2014) 508
5. W. Wu, Z. Xia, *RSC Adv.*, **3**, (2013) 6051.
6. Z. Xu, S. Bian, J. Wang, T. Liu, L. Wang, Y. Gao, *RSC Adv.*, **3** (2013) 1410.
7. G. Ajithkumar, B. Yoo, D.E. Goral, P.J. Hornsky, A.L. Lin, U. Ladiwala, U.P. Dravid, D.K. Sarkar, *J. Mat. Chem. B*, **1** (2013) 1561.
8. S.J. Dhobale, I.M. Nagpure, N.S. Dhobale, P. Molina, *J. Mat. Sci*, **46** (2011) 7253.
9. N.O. Nunez, S. Rivera, D. Alcantara, J.M.D.L. Fuente, J.C. Sevillano, M. Olana, *Dalton. Trans.*, 10.1039/C3DT50676B
10. S. Huang, Z. Cheng, P. Ma, X. Kang, Y. Dai, J. Lin, *Dalton. Trans.* **42** (2013) 6523.
11. N. Zhang, C. Guo, H. Jing, *RSC Adv.*, **3**, (2013) 7495.
12. Y. Wang, S. Gai, C. Li, X. Zhang, N. Niu, F. He, M. Zhang, P. Yang, *RSC Adv.*, **3** (2013) 5945.

13. X. Li, Z. Hou, P. Ma, X. Zhang, C. Li, Z. Cheng, Y. Pai, J. Lian, J. Lin, *RSC Adv.*, **3** (2013) 8517.
14. N. Kimura, K. Sakuma, S. Hirafune, K. Asano, N. Hiroski, R.J. Xie, *Applied Physics Letter*. **90** (2007) 051109.
15. E.F. Schubert, J.K. Kim, *Science*, **308** (2005) 1274.
16. R.F. Wang, J.L. Zhang, X.M. Xu, Y.L. Wang, L.Y. Zhou, B. Li, *Materials Letters* , **84** (2012) 24.
17. Z.L. Wang, H.B. Liang, L.Y. Zhou, J. Wang, M.L. Gong, Q.J. Su, **128** (2008) 147.
18. S.D. Jee, J.K. Park, S.H. Lee, *Journal of materials science*, **41** (2006) 3139.
19. H.J. Yang, H.R. Xu, G.S. Zhu, L. Yuan, C. Zhang, F.S. Li, A.B. Yu, *Materials Letter*, **92** (2013) 161.
20. S. K. Gupta, M. Mohapatra, S. Kaity, V. Natarajan and S.V. Godbole, *J .Lumin.* **132** (2012) 1329.
21. S. K. Gupta, M. Mohapatra, V. Natarajan and S.V. Godbole, *J .Mater. Sci.*, **147** (2012) 3504.
22. S. K. Gupta, M. Sahu, K. Krishnan, M. Saxena, V. Natarajan and S.V. Godbole, *J. Mater. Chem. C*, **1** (2013) 7054.
23. S. K. Gupta, M. Mohapatra, V. Natarajan and S.V. Godbole, *RSC Advances*. **3** (2013) 20046.
24. S.C. Prashantha, B.N. Lakshminarasappa,, B.M. Nagabhushana, *J. Alloys Compd.* **2011**, 509, 10185
25. K.A. Denault, J. Brgoch, M.W. Gaultois, A. Mikhailovski, R. Petry, H. Winker, S.P. Denbaars, R. Seshadri, *Chem. Mater.*, **26** (2014) 2275
26. A. Nag, T. R. N. Kutty, *J. Mater. Chem.* **14** (2004) 1598.
27. M. Catti, G. Gazzoni, G. Ivaldi, *Acta Crystallogr. Sect. C.* **39** (1983) 29.
28. A. Vecht, D. Smith, S. S. Chadha, C. S. Gibbons, J. Koh and D. Morton, *J. Vac. Sci. Technol*, **12** (1994), 781.
29. H. Takashima, K. Shimada, N. Miura, T. Katsumata, Y. Inaguma, K. Ueda and M. Itoh, *Adv. Mater.*, **21** (2009) 3699.
30. R. Pazik, R. Tekoriute, S. Hakansson, R. Wiglusz, W. Strek, G. Seisenbaeva, Y. K. Gun'ko and V. G. Kessler, *Chem. Eur. J.*, **15** (2009) 6820.
31. B. Bouma and G. Blasse, *J. Phys. Chem. Solids*, **56** (1995) 261.
32. P. S. Pizani, H. C. Basso, F. Lanciotti, T. M. Baschi, F. M. Pontes, E. Longo and E. R. Leite, *Appl. Phys. Lett.*, **81** (2002) 253.

33. V.M. Longo, L.S. Cavalcante, R. Erlo, V.R. Mastelaro, A.T. De Figueiredo, J. R. Sambrano, S. de Lazaro, A.Z. Freitas, L. Gomes, N.D. Vieira Jr., J.A. Varela and E. Longo, *Acta Mater.*, **56** (2008) 2191.
34. D. J. Lee, D. H. Kim, J. W. Park and Y.S. Lee, *J. Korean Phys. Soc.*, **59** (2011) 2797.
35. J. W. Park , D. J. Lee, D. H. Kim and Y.S. Lee, *J. Korean Phys. Soc.*, **58** (2011) 316.
36. V. M. Longo, L.S. Cavalcante, A.T. De Figueiredo, L. P. S. Santos, E. Longo, J.A. Varela, J.R. Sambrano, and A.C. Hernandez, *Appl. Phys. Lett.*, **90** (2007) 091906.
37. E. Danielson, M. Devenney, D.M. Giaquinta, J.H. Golden, R.C. Haushalter, E.W. McFarland, D.M. Poojary, C.M. Reaves, W.H. Weinberg, X.D. Wu, *Science*, **279** (1998) 837.
38. E. Danielson, M. Devenney, D.M. Giaquinta, J.H. Golden, R.C. Haushalter, E.W. McFarland, D.M. Poojary, C.M. Reaves, W.H. Weinberg, X.D. Wu, *J. Mol. Struct.*, **470** (1998) 229.
39. M. Liu, Y. Luo, J. Lin, *J. Cryst. Growth*, **290** (2006) 266.
40. T. Masui, T. Chiga, N. Imanaka, G. Adachi, *Mater. Res. Bull.*, **38** (2003) 17.
41. M. Zhao, L. Li, J. Zheng, L. Yang, G. Li, *Inorg. Chem.*, **52** (2013) 807.
42. B.S. Naidu, B. Vishwanadh, V. Sudarsan, R. Vatsa, *Dalton Trans.*, **41** (2012) 3194.
43. E. Song, W. Zhao, G. Zhou, X. Dou, H. Ming, C. Yi, *Curr. Appl. Phys.*, 11 (2011)1374
44. D.E. Day, Z. Wu, C.S. Ray, P. Hrma, *J. Non-Cryst. Solids*, 241 (1998) 1.
45. G.K. Marasinghe, M. Karabulut, C.S. Ray, D.E. Day, D.K. Shuh, P.G. Allen, M.L. Saboungi, M. Grimsditch, D. Haefner, *J. Non-Cryst. Solids*, **263-264** (2000) 146.
46. M. Karabulut, G.K. Marasinghe, C.S. Ray, D.E. Day, G.D. Waddill, C.H. Booth, P.G. Allen, J.J. Bucher, D.L. Caulder, D.K. Shuh, *J. Non-Cryst. Solids*, **306** (2002) 182.
47. M. Weil, R. Glaum, *Eur. J. Solid State Inorg. Chem.*, L **35** (1998) 495.
48. J.J. Bian, D.W. Kim, K.S. Hong, *Jpn. J.Appl. Phys.*, **43** (2004) 3521.
49. J.J. Bian, K.S. Hong, *J Mater. Sci.*, **40** (2005)1801.

LIST OF FIGURES:

Chapter 1

Figure 1.1: The periodic table of elements.

Figure 1.2: Splitting of the 4f energy levels of Eu^{3+} as a result of electronic repulsion, spin-orbit coupling, and the ligand field.

Figure 1.3: Energy diagram of the 4f levels responsible for the lanthanide luminescence.

Figure 1.4: Electronic transitions in lanthanide ions: (a) absorption/excitation, (b) excited state absorption, (c) direct excitation into a higher excited state, (d) “conventional” emission from the lowest luminescent state, (e) non-radiative relaxation, (f) radiative transition between excited states, (g) emission from a higher excited state

Figure 1.5: Graphical representation of the number of vibrational quanta of four high frequency oscillators that is required to match the energy gap between the lowest luminescent state and the highest non-luminescent state of the lanthanide ion (the dashed line is merely a guide to the eye).

Figure 1.6: Some of the phosphor applications.

Figure 1.7: Energy of the 4f–5d transitions in $\text{Ln}^{\text{III}}:\text{CaF}_2$ (squares) and of the 2p (O)-4f LMCT transitions (triangles)

Figure 1.8: Absorption spectrum of $[\text{Ce}(\text{H}_2\text{O})_9]^{3+}$ and its assignment (D_{3h} symmetry)

Figure 1.9: Configurational coordinate diagram for emission from (left) an organic chromophore and (right) a lanthanide ion

Figure 1.10: Luminescence decay for an Eu^{III} sample with its bi-exponential analysis; straight lines correspond to the two decay rates and the red line is the calculated fit

Figure 1.11: Ligand-field splitting of the Eu (${}^7\text{F}_1$) sublevel and sign of the B_2^0 parameter and corresponding high resolution ${}^5\text{D}_0 \rightarrow {}^7\text{F}_1$ spectra

Figure 1.12: Stern Volmer plot in case of dynamic quenching

Figure 1.13: Effect of collisional quenching on lifetime of fluorophore

Figure 1.14: Schematic of static quenching

Figure 1.15: Schematic of dynamic versus static (association) quenching

Figure 1.16: Model diagnostic plots to distinguish between dynamic and static quenching

List of figures and tables

Figure 1.17: Stern Volmer plot in case of when both dynamic and static quenching occurs simultaneously

Figure 1.18: Illustration of energy transfer phenomenon

Figure 1.19: Coupled transitions between donor emission and acceptor absorbance in fluorescence resonance energy transfer. The coupled transitions are drawn with dashed lines. The phenomenon of energy transfer is illustrated by a blue arrow

Figure 1.20: Donor emission and quencher absorption spectral overlap

Figure 1.21: Schematic diagram for Forster and Dexter energy transfer

Figure 1.22: Cross-relaxation processes in Eu^{3+} and Pr^{3+} .

Figure 1.23: Schematic excitation spectrum of $\text{Y}_2\text{O}_2\text{S}:\text{Er}$ nanoparticles and bulk $\text{Y}_2\text{O}_2\text{S}:\text{Er}$ at 7 K

Chapter 2

Figure 2.1: Various steps in the sol-gel process to control the final morphology of the product

Figure 2.2: Acid and base catalyzed hydrolysis step

Figure 2.3: Simplified representation of the condensation of TEOS in sol gel process

Figure 2.4: Typical synthesis stages in polymeric precursor route

Figure 2.5: A typical structure of micelle.

Figure 2.6: Scattering of x-rays from atoms and Bragg's law

Figure 2.7: Continuous and characteristic x-rays for copper

Figure 2.8: Using a Nickel filter for Cu X-rays

Figure 2.9: X-ray diffractometer.

Figure 2.10: Typical range of light and electron microscope

Figure 2.11: Schematic of scanning electron microscope

Figure 2.12: Various electron and photon emitted in SEM and information's gathered from them.

Figure 2.13: Schematic of transmission electron microscope.

Figure 2.14: Schematic representation of positron annihilation indicating the basis for the three experimental techniques of positron annihilation spectroscopy (PAS): lifetime, angular correlation, and Doppler broadening.

List of figures and tables

Figure 2.15: The conventional positron lifetime measurement system.

Figure 2.16: Separation between the lower and the upper state for unpaired free electrons in EPR.

Figure 2.17: Photograph of Bruker ESP-300 EPR spectrometer

Figure 2.18: Block diagram of typical EPR spectrometers.

Figure 2.19: Thermally stimulated luminescence

Figure 2.20: Processes involved in radiation induced electron/hole trapping and subsequent recombination on thermal stimulation with associated luminescence emission.

Figure 2.21: A Jablonski diagram shows the possible relaxation processes in a molecule after the molecule has absorbed a photon (A): IC = internal conversion, ISC= intersystem conversion, F= fluorescence, P= phosphorescence.

Figure 2.22: Parameters affecting fluorescence emission.

Figure 2.23: Block diagram of spectrofluorometer.

Figure 2.24: Photograph of the time resolved fluorescence spectrometer.

Figure 2.25: TCSPC - A fast stopwatch with two inputs.

Figure 2.26: The main components for signal processing in TCSPC.

Chapter 3

Figure 3.1: (a) TGA of thorium oxalate hexahydrate powders in air atmosphere (b) DTA of thorium oxalate dihydrate powders

Figure 3.2: PXRD pattern of thorium oxalate hexahydrate and thorium oxide doped. Inset in figure shows the crystal structure of thoria.

Figure 3.3: High resolution TEM micrograph of ThO₂

Figure 3.4: (a) Excitation spectra λ_{em} - 569 nm) (b) Emission spectra λ_{ex} - 245 nm) of the ThO₂: Sm³⁺

Figure 3.5: (a) Luminescence decay time profile of the ThO₂: Sm³⁺ (b) TRES spectra for short and long lived samarium ion in thorium dioxide.

Figure 3.6: CIE index diagram of the ThO₂: Sm³⁺

Figure 3.7: Thermogram for ThO₂: Eu prepared via combustion synthesis route using Urea

List of figures and tables

Figure 3.8: X-ray diffraction patterns for the powder samples obtained via combustion synthesis by annealing at different temperatures. Inset shows the effect of temperature in line broadening of peak at $2\theta=28^\circ$.

Figure 3.9: TEM micrographs of $\text{ThO}_2:\text{Eu}^{3+}$ annealed at 300°C (as prepared samples) under different magnifications

Figure 3.10: SAED micrographs of $\text{ThO}_2:\text{Eu}^{3+}$ annealed at 300°C (as prepared samples)

Figure 3.11: Variation in PL emission intensity with annealing temperature.

Figure 3.12: Variation in asymmetry ratio with annealing temperature

Figure 3.13: Excitation spectra of powder sample of $\text{ThO}_2:\text{Eu}^{3+}$ 1.0 mol% annealed at 900°C .

Figure 3.14: Emission spectra ($\lambda_{\text{ex}}=256$ nm) of $\text{ThO}_2:\text{Eu}^{3+}$ 1.0 mol% annealed at 900°C

Figure 3.15: Emission spectra ($\lambda_{\text{ex}}=256$ nm) of $\text{ThO}_2:\text{Eu}^{3+}$ in different transition region

Figure 3.16: Decay curves for the $^5\text{D}_0$ level of Eu^{3+} in $\text{ThO}_2:\text{Eu}$ samples annealed at different temperatures. Samples were excited at 256 nm and emission was monitored at 592 nm for the as-prepared (300°C) and 500, 700 $^\circ\text{C}$ and 900°C heated samples.

Figure 3.17: Effect of annealing temperature on the fraction of short and long lived species

Figure 3.18: Time resolved emission for long lived component

Figure 3.19: Time resolved emission for short lived component

Figure 3.20: TGA/DTA plot for the decomposition of zirconium oxalate. The black line represents the TGA curve. The red line represents the DTA curve

Figure 3.21: Rietveld- refined X-ray diffraction pattern of (a) ZrO_2 (b) $\text{ZrO}_2:\text{Eu}^{3+}$

Figure 3.22: Structure of (a) monoclinic and (b) tetragonal phases of zirconia

Figure 3.23: FTIR spectra of zirconium oxalate

Figure 3.24: HRTEM image of (a) zirconium oxalate (precursor) (b) zirconia nanoparticles

Figure 3.25: Emission spectra (a) and fluorescence decay profile (b) of zirconium oxalate and zirconium oxide nanoparticles

Figure 3.26 (a): Excitation spectra (b): Emission spectrum powder sample of zirconium oxalate and zirconium oxide nanoparticles

Figure 3.27: Luminescence decay time profile of the Eu doped zirconium oxalate and

zirconium oxide nanoparticles

Chapter 4

Figure 4.1: XRD pattern Sr_2SiO_4 and $\text{Sr}_2\text{SiO}_4:\text{Ln}^{3+}$ (Ln = Eu, Dy, and Sm)

Figure 4.2: (a) Crystal structure of α' - Sr_2SiO_4 (b) Pictorial representation of 9- and 10-coordinated Sr^{2+} in strontium silicate

Figure 4.3: (a) 2D (XY)-AFM topographies ($\sim 50\mu \times 50\mu$) of silicate host matrix (b) Particle size distribution of as prepared sample obtained from AFM topographies.

Figure 4.4: SEM micrographs of as prepared samples at magnification of 3000X.

Figure 4.5: Size distribution plot obtained by dynamic light scattering studies of Sr_2SiO_4 powder after heating at 600°C .

Figure 4.6: Excitation spectrum $\text{Sr}_2\text{SiO}_4:\text{Eu}^{3+}$

Figure 4.7: Emission spectrum of $\text{Sr}_2\text{SiO}_4:\text{Eu}^{3+}$ with $\lambda_{\text{ex}} = 243$ nm. The inset figure shows the $^5\text{D}_0$ to $^7\text{F}_0$ transition at 575 nm.

Figure 4.8: Excitation and emission spectra of the strontium silicate doped Eu sample with $\lambda_{\text{em}} = 575$ nm and $\lambda_{\text{ex}} = 296$ nm.

Figure 4.9: Emission spectra of the two RE ions species obtained after giving suitable delay times following TRES measurements (with 243 nm excitation). The emission spectrum of the species getting selectively excited at 296 nm is also shown.

Figure 4.10: (a) EPR spectra of $\text{Sr}_2\text{SiO}_4:\text{Eu}^{2+}$ (b) EPR showing hfs of Eu^{2+} signal in Sample

Figure 4.11: (a) Excitation spectra ($\lambda_{\text{em}}=485$ nm) and (b) Emission spectra ($\lambda_{\text{ex}}=350$ nm) of 0.5 mol% Eu^{2+} doped Sr_2SiO_4

Figure 4.12: Luminescence decay time profile of Eu^{2+} doped Sr_2SiO_4 with $\lambda_{\text{ex}}=350$ nm under $\lambda_{\text{em}} - 485$ and 600 nm

Figure 4.13: (a) Excitation spectrum and (b) Emission spectrum of the powder sample of $\text{Sr}_2\text{SiO}_4:\text{Dy}^{3+}$ with excitation wavelength 250 nm and 351 nm (0.1 mol % annealed at 600°C)

Figure 4.14: Energy level scheme for $\text{Sr}_2\text{SiO}_4:\text{Dy}^{3+}$ (0.5 mol % annealed at 600°C)

Figure 4.15: Luminescence decay time profile of the D 18 sample ($\lambda_{\text{ex}}=250$ nm and $\lambda_{\text{em}} - 575$ nm)

Figure 4.16: Excitation spectra $\text{SrZrO}_3:\text{Sm}^{3+}$. Inset shows the f-f lines of Sm^{3+}

Figure 4.17: Emission spectra of air sintered $\text{Sr}_2\text{SiO}_4:\text{Sm}^{3+}$ at excitation wavelength

List of figures and tables

(a) 243 nm (CTB) (b) 407 nm (f-f band)

Figure 4.18: Luminescence decay time profile of $\text{Sr}_2\text{SiO}_4:\text{Sm}^{3+}$ at $\lambda_{\text{ex}}=407$ nm under $\lambda_{\text{em}}=597$ nm

Figure 4.19: Normalized EXAFS spectra of blank Sr_2SiO_4 along with Dy and Eu doped Sr_2SiO_4 .

Figure 4.20: Fourier transformed EXAFS spectra at Sr K-edge (Scatter points) and theoretical fit (Solid line) for (a) Sr_2SiO_4 (b) Dy doped Sr_2SiO_4 and (c) Eu doped Sr_2SiO_4 .

Figure 4.21: Ratio curves with respect to Si single crystal from coincidence Doppler broadening measurements on different Sr_2SiO_4 samples

Figure 4.22: Structure of Sr_2SiO_4 showing 9 and 10-coordinated Sr-sites

Figure 4.23: Pictorial representation of various Sr-O bond lengths in SrO_9 polyhedra in Sr_2SiO_4 .

Figure 4.24: Pictorial representation of various Sr-O bond lengths in SrO_{10} polyhedra in Sr_2SiO_4 .

Figure 4.25: CIE index diagram of Sr_2SiO_4 doped with various lanthanides

Chapter 5

Figure 5.1: XRD patterns of the SrZrO_3 samples annealed at different temperatures and the standard JCPDS pattern for file no 44-0161. The peaks corresponding to minor impurity phases are identified by asterisk.

Figure 5.2: EDXRF pattern for SrZrO_3

Figure 5.3: Effect of temperature on broadness of strong diffraction peak (30 degree)

Figure 5.4: Schematic crystal structure of SrZrO_3

Figure 5.5: SEM micrographs of SrZrO_3 sample annealed at (a) 600 (b) 700 (c) 800 and (d) 900°C at similar magnification.

Figure 5.6: Size distribution plot obtained by dynamic light scattering studies strontium SrZrO_3 sample annealed at (a) 600 (b) 700 (c) 800 and (d) 900°C.

Figure 5.7: Emission spectra of air sintered SrZrO_3

Figure 5.8: Schematic of SrZrO_3 unitcell. Arrows indicate direction of atomic displacement for the Zr and Sr network. O_1 and O_2 are the axial and planar oxygen atoms, respectively.

Figure 5.9: Total and orbital angular momentum projected DOS for: (a) o-SZ, (b) f-SZ, (c) m-SZ and fm-SZ models. The vertical lines represent Fermi level.

List of figures and tables

Figure 5.10: Excitation spectra of air sintered SrZrO₃ under different excitation wavelength

Figure 5.11: X-band EPR spectra of SrZrO₃ sample recorded at RT

Figure 5.12: Decay curves of SrZrO₃ sample. Samples were excited at 243 nm and the emission was monitored at different wavelength.

Figure 5.13: Excitation spectra SrZrO₃:Sm³⁺. Inset shows the f-f lines of Sm³⁺

Figure 5.14: Emission spectra of air sintered SrZrO₃:Sm³⁺ at excitation wavelength (a) 243 nm (CTB) (b) 407 nm (f-f band)

Figure 5.15: Luminescence decay time profile of SrZrO₃:Sm³⁺ at λ_{ex} -407 nm under λ_{em} -565, 597 and 643.

Figure 5.16: Time-resolved emission spectra of SrZrO₃:Sm³⁺ nanophosphor under the excitation at 243 nm (a) after giving suitable delay time

Figure 5.17: Time-resolved emission spectra of for short and long lived Sm³⁺ ion in SrZrO₃

Figure 5.18: Emission spectra SrZrO₃ (λ_{ex} -243 nm) and excitation spectra of SrZrO₃:Sm³⁺ (λ_{em} -597 nm)

Figure 5.19 Energy transfer from host to Sm³⁺ ion (Vacuum sintered sample).

Figure 5.20: Total DOS for Sm doped fm-SZ in (a) Sr position and (b) Zr position. Total and partial DOS of Sm doped fm-SZ in both Sr and Zr position (c). The vertical lines represent Fermi level (E_{F}).

Figure 5.21: Schematic of energy transfer mechanism from SrZrO₃ host to Sm³⁺ ions.

Figure 5.22: (a) CIE index diagram of (a) SrZrO₃ and (b) SrZrO₃:Sm³⁺ system showing violet blue white and red emission (point *) respectively.

Figure 5.24: Variations in PL emission and decay time with annealing temp.

Figure 5.25: Excitation spectra of the powder sample of SrZrO₃:Eu³⁺ 0.5 mol% annealed at 800°C.

Figure 5.26 (a): Emission spectra at (a) 229 nm excitation (b) 296 nm excitation and (c) 393 nm excitation of the powder sample of SrZrO₃:Eu³⁺ 0.5 mol% annealed at 800°C .

Figure 5.27: Luminescence decay time profile of the Eu doped strontium zirconate annealed at 800°C (a) λ_{ex} -229 nm (b) λ_{ex} -296 nm and (c) 393 nm under λ_{em} – 594 nm

Figure 5.28: Time-resolved emission spectra of SrZrO₃:Eu³⁺ nanophosphors annealed at 800°C under the excitation at 229 nm (a) after giving suitable delay time (b) for short and long lived species

List of figures and tables

Figure 5.29: Time-resolved emission spectra of SrZrO₃:Eu³⁺ nanophosphors annealed at 800°C under the excitation at 296 nm (a) after giving suitable delay time (b) for short and long lived species

Figure 5.30: Time-resolved emission spectra of SrZrO₃:Eu³⁺ nanophosphor annealed at 800°C under the excitation at 393 nm for short and long-lived species.

Figure 5.31: CIE index diagram of SrZrO₃:Eu³⁺ system annealed at various temperatures and at different excitation wavelength.

Figure 5.32: Photoluminescence spectra of the Gd³⁺ doped SrZrO₃ calcined at 600°C (a) Excitation spectrum of SrZrO₃:Gd³⁺ (λ_{em} = 313 nm) and (b) Emission spectrum of SrZrO₃:Gd³⁺ (λ_{ex} = 274 nm)

Figure 5.33: Luminescence decay time profile of the Gd³⁺ doped SrZrO₃ annealed at 600°C (as prepared sample) at λ_{ex} -274 nm under λ_{em} – 313 nm

Figure 5.34: X-band EPR spectra of Gd³⁺ doped SrZrO₃ at room temperature

Figure 5.35: Excitation spectra of the powder sample of SrZrO₃:Dy³⁺ annealed at 600°C (as prepared sample).

Figure 5.36: Emission spectra of the powder sample of SrZrO₃:Dy³⁺ (as prepared sample) on excitation with (a) 229 nm (host absorption band) b) 243 nm (charge transfer band) and (c) 351 nm (f-f band)

Figure 5.37: Effect of excitation wavelength on emission intensity of blue and yellow line

Figure 5.38: Luminescence decay time profile of the Dy doped strontium zirconate annealed at 600°C (as prepared sample) (a) λ_{ex} -229 nm (host absorption band) (b) λ_{ex} -243 nm (charge transfer band) and (c) 351 nm (f-f band) under λ_{em} – 576 nm

Figure 5.39: Emission intensity of the SrZrO₃:Dy³⁺ as a function of annealing temperature.

Figure 5.40: Influence of annealing temperature on the Y/B value of the as-prepared SrZrO₃:Dy³⁺.

Figure 5.41: CIE index diagram of the SrZrO₃:Dy³⁺ annealed at different temperatures, a-(as prepared sample), b-700°C, c-800°C and d-900°C.

Chapter 6

Figure 6.1: XRD pattern of Sr_{1.995}Eu_{0.005}CeO₄ at different temperature

Figure 6.2: XRD pattern of Sr_{1.95}Eu_{0.05}CeO₄ at different temperature

List of figures and tables

Figure 6.3: XRD pattern of $\text{Sr}_{1.97}\text{Eu}_{0.13}\text{CeO}_4$ at different temperature

Figure 6.4: XRD pattern of undoped and doped strontium cerate at synthesized at 1323 K.

Figure 6.5: TG-DTA curves for the precursor of $\text{Sr}_{1.995}\text{Eu}_{0.005}\text{CeO}_4$ and $\text{Sr}_{1.97}\text{Eu}_{0.13}\text{CeO}_4$ prepared by complex polymerization method

Figure 6.6: SEM micrograph of strontium cerate sample calcined at 1000 °C for 30 in air at different magnifications (a) 2000X (b) & (c) 5000 X and (d) 10000 X

Figure 6.7: (a) Excitation and (b) emission spectra of Sr_2CeO_4 sample calcined at 1000 °C for 30 h in air

Figure 6.8: Luminescence decay time profile for Sr_2CeO_4 sample calcined at 1000 °C for 30 h in air

Figure 6.9: Excitation spectra of $\text{Sr}_{2-x}\text{Eu}_x\text{CeO}_4$ ($x=0.005, 0.008, 0.01, 0.03, 0.05,$ and 0.13) calcined at 1000 °C for 30 h in air

Figure 6.10: Emission spectra of the powder sample of Sr_2CeO_4 : 0.5 mol % Eu^{3+} on excitation with 280 nm (charge transfer band) calcined at 1000 °C for 30 h in air

Figure 6.11: Luminescence decay time profile of the Sr_2CeO_4 : 0.5 mol % Eu^{3+} , $\lambda_{\text{ex}}=280$ nm $\lambda_{\text{em}}=614$ nm. The black line gives the observed points and the red line gives its exponential fitting.

Figure 6.12: The emission spectra at $\lambda_{\text{ex}} = 280$ nm for Sr_2CeO_4 doped with different concentration of Eu^{3+} ions calcined at 1000 °C for 30 h in air

Figure 6.13: The relationship between the average life time of $^5\text{D}_0$ state and Eu^{3+} ion concentrations.

Figure 6.14: (a) CIE index diagram of (a) Sr_2CeO_4 and (b) Sr_2CeO_4 :5 mol% Eu^{3+} system calcined at 1000 °C for 30 h in air showing bluish white and red emission (point *) respectively.

Chapter 7

Figure 7.1: Rietveld- refined X-ray diffraction pattern of $\alpha\text{-Zn}_2\text{P}_2\text{O}_7$

Figure 7.2: Crystal structure of $\alpha\text{-Zn}_2\text{P}_2\text{O}_7$

Figure 7.3: FTIR spectrum of zinc pyrophosphate crystals. (a) Full range 4000-400 (extended range) and (b) 1200-430 cm^{-1} (absorption band of phosphate)

Figure 7.4a: XRD pattern of 2 mol% Mn^{2+} in $\text{Zn}_2\text{P}_2\text{O}_7$ at various temperatures. Asterisk indicates the pattern of Pt which arises due to usage of Pt-Rh as a sample

List of figures and tables

holder in HTXRD

Figure 7.4b: XRD pattern α and β phase and their standard pattern of 2 mol% Mn^{2+} in $\text{Zn}_2\text{P}_2\text{O}_7$. Arrows indicate missing reflections in β -phase.

Figure 7.5: The temperature variation of unit cell volume of 2 mol% Mn^{2+} in $\text{Zn}_2\text{P}_2\text{O}_7$. Error bars are smaller than symbols.

Figure 7.6: DSC studies of Mn doped $\text{Zn}_2\text{P}_2\text{O}_7$

Figure 7.7: EPR spectra of 2 mol% Mn^{2+} in $\text{Zn}_2\text{P}_2\text{O}_7$ at various temperatures

Figure 7.8: The temperature variation of the zero field splitting parameter for $\text{Zn}_2\text{P}_2\text{O}_7$: Mn^{2+}

Figure 7.9: Excitation spectra of $\text{Zn}_2\text{P}_2\text{O}_7$: Eu^{3+} powder sample ($\lambda_{\text{em}}=592$ nm)

Figure 7.10: Emission spectra at 230 nm excitation wavelength of undoped and doped zincpyrophosphate

Figure 7.11: Emission spectra at different excitation wavelength of $\text{Zn}_2\text{P}_2\text{O}_7$: Eu^{3+}

Figure 7.12: Luminescence decay time profile of Eu doped zinc pyrophosphate at $\lambda_{\text{ex}}=395$ nm under $\lambda_{\text{em}}=592$ nm

Figure 7.13: Time-resolved emission spectra of $\text{Zn}_2\text{P}_2\text{O}_7$: Eu^{3+} under the excitation at 395 nm after giving suitable delay

Figure 7.14: Time-resolved emission spectra of $\text{Zn}_2\text{P}_2\text{O}_7$: Eu^{3+} under the excitation at 395 nm for short and long lived species

Figure 7.16: Site selective emission of Eu^{3+} in $\text{Zn}_2\text{P}_2\text{O}_7$

Figure 7.17: Crystal field splitting in octahedral and square pyramidal coordination.

Figure 7.18: EPR spectra of monoclinic 2 mol% Mn doped $\text{Zn}_2\text{P}_2\text{O}_7$ (a) at 300 K and (b) 100 K.

Figure 7.19: Second derivative EPR spectra of Mn in $\text{Zn}_2\text{P}_2\text{O}_7$.

Figure 7.20: Emission spectra of Mn doped zinc pyrophosphate

Figure 7.21: Excitation spectra of Mn doped zinc pyrophosphate

Figure 7.22: Emission spectra of Mn doped zinc pyrophosphate heated in oxidizing and reducing atmosphere

List of figures and tables

Figure 7.23: CIE index diagram of 2 mol% Mn doped $\text{Zn}_2\text{P}_2\text{O}_7$ in air showing the white emission (point *).

Figure 7.24: The PL emission intensity of Sm^{3+} as a function of its (a) concentration (b) annealing temperature in crystalline $\text{Zn}_2\text{P}_2\text{O}_7$.

Figure 7.25: Excitation spectra of $\text{Zn}_2\text{P}_2\text{O}_7$ and $\text{Zn}_2\text{P}_2\text{O}_7:\text{Sm}^{3+}$. Inset in spectra of doped sample shows the expanded f-f region of Sm^{3+} .

Figure 7.26: Emission spectra $\text{Zn}_2\text{P}_2\text{O}_7$ and $\text{Zn}_2\text{P}_2\text{O}_7:\text{Sm}^{3+}$

Figure 7.27: CIE index diagram of the $\text{Zn}_2\text{P}_2\text{O}_7:\text{Sm}^{3+}$

LIST OF TABLES:

Chapter 1

Table 1.1: Electronic configuration of lanthanide atoms and trivalent ions as well as the radii of the trivalent ions

Table 1.2: Selection rules for f–f transitions between spectroscopic levels

Table 1.3: Important emission lines of some lanthanide ions.

Table 1.4: Experimentally observed hypersensitive transitions for Ln^{III} ions in optical spectra

Chapter 2

Table 2.1: Advantages and disadvantages of electron microscope.

Table 2.2: Comparison of light optical microscope and electron microscope

Table 2.3: Comparison between SEM and TEM

Table 2.4: Different region in IR

Table 2.5: List of fields for resonance for g=2 signal at microwave frequencies commonly available in EPR spectrometers

Chapter 3

Table 3.1: Average particle size and unit cell volume of thoria nanoparticles at different annealing temperature

Table 3.2: Life time data for ThO₂: Eu at λ_{ex} -403 nm and λ_{em} -592 nm under different annealing temperature (parentheses represents the percentage of that particular species)

Table 3.3: Life time for the Eu³⁺ species in zirconium oxalate and zirconia

Table 3.4: J-O intensity parameters and radiative properties for Eu³⁺ in ZrO₂

Chapter 4

Table 4.1: Fluorescence decay for the Sr₂SiO₄:Eu³⁺ with λ_{ex} = 243 nm

List of figures and tables

Table 4.2: Fluorescence decay time for the $\text{Sr}_2\text{SiO}_4:\text{Eu}^{3+}$ with $\lambda_{\text{ex}} = 296$ nm.

Table 4.3: J-O intensity parameters of the Eu^{3+} doped Sr_2SiO_4 . ($\lambda_{\text{ex}} = 243$ nm).

Table 4.4: Structural parameters for undoped and Lanthanide ion doped strontium silicate as obtained by EXAFS fitting.

Table 4.5: Positron life time values with their intensity

Table 4.6: Energetics for various lanthanides in Sr_2SiO_4 for two different sites of Sr

Chapter 5

Table 5.1: XRD data of strontium zirconate ($\lambda = 0.15406$ nm) annealed at 600°C .

Table 5.2: Life time and % occupancy for the life time of SrZrO_3 host with different emission wavelength

Table 5.3: Life time and % occupancy for the Eu^{3+} species in 800°C annealed sample with different excitation wavelength.

Table 4.4: J-O intensity parameters of the Eu^{3+} doped SrZrO_3 annealed at 800°C .

Table 5.5: Spectral characteristics of three different types of Eu^{3+}

Table 5.6: Chromaticity coordinates for sample annealed at different temperature and at different excitation wavelength.

Table 5.7: The observed band positions Gd^{3+} doped SrZrO_3 along with their assignments.

Table 5.8: Life time and % occupancy for the Dy^{3+} species in as-prepared sample with different excitation wavelength.

Table 5.9: CIE indices and the CCT of the Dy^{3+} doped SrZrO_3 samples annealed at different temperatures.

Chapter 6

Table 6.1: Luminescence lifetimes, radiative and non-radiative decay rates, quantum efficiencies ($^5\text{D}_0$ level), intensity ratio between the $^5\text{D}_0 \rightarrow ^7\text{F}_2$ and $^5\text{D}_0 \rightarrow ^7\text{F}_1$ transitions, Judd–Ofelt intensity parameters, and chromaticity coordinates of the Eu^{3+} doped strontium cerate

Chapter 7

Table 7.1: Assignments of different absorption bands in the FT-IR spectrum of zinc pyrophosphate crystals.

Table 7.2: Allotropic forms and crystallographic data of $Zn_2P_2O_7$

Table 7.3: Comparison of J-O intensity parameters and radiative properties for two different species Eu^{3+} in $Zn_2P_2O_7$

Table 7.4: EPR parameters of isolated Mn^{4+} in monoclinic zincpyrophosphate matrix.

Table 7.5: Peak assignments of isolated Mn^{4+} species in monoclinic Zinc pyrophosphate matrix.

Table 7.6: Life time data for $Zn_2P_2O_7: Sm^{3+}$ at $\lambda_{ex}=403$ nm under different λ_{em}

Chapter 1
INTRODUCTION

CHAPTER 1

1.1. General Introduction

Photonics broadly defined as the science and technology for understanding, controlling and exploiting the interaction of light and matter, furnishes enabling technologies for telecommunications, solar energy, lighting, displays, biotechnology, medical diagnostics, bio-imaging etc. Lanthanide ions hold a special place in photonics, because of their unique photophysical properties, especially with respect to the generation and amplification of light. The luminescence of trivalent lanthanide ions (Ln^{3+}) has been and is being studied in several scientific domains, ranging from laser physics to molecular biology.

Optical materials doped with rare earth elements are of great relevance in science and technology. Modern solid state optical technology is mainly based on lanthanide doped materials, with applications ranging from solid state lasers for industry, medicine and environmental monitoring, to active optical fibers for telecommunication purposes and phosphors for cathode ray tubes, displays, plasma monitors and lightning applications. From the scientific point of view, lanthanide doped materials attract increasing interest due to their particular physical properties. Indeed their electron configuration involving *f*-electrons and the exceptional time and space coherence properties led to the observation of new and fascinating phenomena. Among the materials evaluated as host for lanthanide ions in this work, our attention was mostly focused on alkaline earth silicate, zirconate and cerate. These materials are characterized by good transmission properties in the visible part of the electromagnetic spectrum and by relatively low phonon energies. They can be efficiently doped with lanthanide ions, due the similarity between the ionic radius of the alkaline earth and the lanthanide ions. Therefore these materials are prospective high efficiency luminophors and are attracting increasing interest for photonics and optoelectronics applications. Indeed alkaline earth silicate, zirconate and cerate are resistant to many chemicals and air exposure and can also be grown with low-cost techniques. Few new oxide hosts were also tried to venture into novel lanthanide luminescent materials viz. $\text{Zn}_2\text{P}_2\text{O}_7$, ThO_2 and ZrO_2 .

Luminescent dopants are extensively used as local probes for identifying local structures in crystalline material, understanding the effect of chemical and thermal

treatment on catalysts and probing the structure of biological molecules. In view of its non-degenerate emissive state, 5D_0 , Eu (III) ion is most appropriate as luminescent structural probe for the determination of the number of metal ion sites in a compound, their symmetry, and their respective population. Other lanthanide ions have transitions that are usually the mixtures of EDT and MDT and the effects of symmetry are less pronounced.

1.2. Luminescence of trivalent lanthanide ion:

In the periodic table of elements, lanthanides are the group of atoms ranging from lanthanum (atomic number 57) to lutetium (atomic number 71) (see Figure 1.1). They are characterized by gradual filling of the 4f electron shell and are therefore called f-block elements.

1 H																	2 He
3 Li	4 Be											5 B	6 C	7 N	8 O	9 F	10 Ne
11 Na	12 Mg											13 Al	14 Si	15 P	16 S	17 Cl	18 Ar
19 K	20 Ca	21 Sc	22 Ti	23 V	24 Cr	25 Mn	26 Fe	27 Co	28 Ni	29 Cu	30 Zn	31 Ga	32 Ge	33 As	34 Se	35 Br	36 Kr
37 Rb	38 Sr	39 Y	40 Zr	41 Nb	42 Mo	43 Tc	44 Ru	45 Rh	46 Pd	47 Ag	48 Cd	49 In	50 Sn	51 Sb	52 Te	53 I	54 Xe
55 Cs	56 Ba	57 La	72 Hf	73 Ta	74 W	75 Re	76 Os	77 Ir	78 Pt	79 Au	80 Hg	81 Tl	82 Pb	83 Bi	84 Po	85 At	86 Rn
87 Fr	88 Ra	89 Ac	104 Rf	105 Db	106 Sg	107 Bh	108 Hs	109 Mt	110 Ds	111 Rg	112 Cn	113 Uut	114 Fl	115 Uup	116 Lv	117 Uus	118 Uuo
58 Ce	59 Pr	60 Nd	61 Pm	62 Sm	63 Eu	64 Gd	65 Tb	66 Dy	67 Ho	68 Er	69 Tm	70 Yb	71 Lu				
90 Th	91 Pa	92 U	93 Np	94 Pu	95 Am	96 Cm	97 Bk	98 Cf	99 Es	100 Fm	101 Md	102 No	103 Lr				

Figure 1.1: The periodic table of elements. The lanthanides are highlighted in green.

The different lanthanides have very similar chemical behaviour so that their properties can be discussed in a general way. Lanthanide ions are most frequently found in the trivalent (3+) oxidation state (see Table 1.1), although tetravalent (4+) cerium/terbium and divalent (2+) europium/ytterbium also occur. The f-orbitals are shielded by the 5s and 5p orbitals. Therefore, the f-electrons do not participate in chemical bonding so that the predominant interactions in lanthanide complexes are electrostatic ones. The

shielding of the spectroscopically active 4f-electrons by filled 5s and 5p orbitals results in distinct spectroscopic characteristics for the trivalent lanthanide ions. In contrast to the broad bands observed for transition metal ions, the lanthanide f-f electronic transitions exhibit typically very narrow lines in the luminescence and absorption spectra. Since changes in the local environment of the lanthanide ion has a negligible influence on the 4f-electrons, coordination will only affect the fine structure of the absorption and emission bands, rather than result in major shifts in the peak position. Lanthanide ions can show emission in the near-UV, visible, near-infrared and infrared spectral regions. Each lanthanide ion has a characteristic absorption and emission spectra.

Table 1.1: Electronic configuration of lanthanide atoms and trivalent ions as well as the radii of the trivalent ions

Z	Element	Symbol	Atom	M ³⁺	M ³⁺ radius (Å)
57	Lanthanum	La	[Xe]5d ¹ 6s ²	[Xe]	1.061
58	Cerium	Ce	[Xe]4f ¹ 5d ¹ 6s ²	[Xe]4f ¹	1.034
59	Praseodymium	Pr	[Xe]4f ³ 6s ²	[Xe]4f ²	1.013
60	Neodymium	Nd	[Xe]4f ⁴ 6s ²	[Xe]4f ³	0.995
61	Promethium	Pm	[Xe]4f ⁶ 6s ²	[Xe]4f ⁴	0.979
62	Samarium	Sm	[Xe]4f ⁶ 6s ²	[Xe]4f ⁶	0.964
63	Europium	Eu	[Xe]4f ⁷ 6s ²	[Xe]4f ⁶	0.950
64	Gadolinium	Gd	[Xe]4f ⁷ 5d ¹ 6s ²	[Xe]4f ⁷	0.938
65	Terbium	Tb	[Xe]4f ⁹ 6s ²	[Xe]4f ⁸	0.923
66	Dysprosium	Dy	[Xe]4f ¹⁰ 6s ²	[Xe]4f ⁹	0.908
67	Holmium	Ho	[Xe]4f ¹¹ 6s ²	[Xe]4f ¹⁰	0.899
68	Erbium	Er	[Xe]4f ¹² 6s ²	[Xe]4f ¹¹	0.881
69	Thulium	Tm	[Xe]4f ¹³ 6s ²	[Xe]4f ¹²	0.869
70	Ytterbium	Yb	[Xe]4f ¹⁴ 6s ²	[Xe]4f ¹³	0.858
71	Lutetium	Lu	[Xe]4f ¹⁴ 5d ¹ 6s ²	[Xe]4f ¹⁴	0.848

The luminescence properties of the trivalent rare earth or lanthanide cations in solution and in the solid state are characterized by narrow emission bands and relatively long luminescence lifetimes of upto milliseconds [1]. The characteristic shape of the bands is explained by the fact that the ground and excited states of these transitions have the same equilibrium geometry, since excitation only involves rearrangement of the electrons within f-orbitals.

Except for lanthanum (La^{3+}) and lutetium (Lu^{3+}), each lanthanide ion has its specific emission bands: for example, the lanthanide ions europium (Eu^{3+}) and samarium (Sm^{3+}) emit red light, terbium (Tb^{3+}) green light, gadolinium (Gd^{3+}) UV-light and neodymium (Nd^{3+}), ytterbium (Yb^{3+}), and erbium (Er^{3+}) near-infrared light. These characteristics have led to the application of lanthanide ions as probes in fluoroimmunoassays (Eu^{3+} and Tb^{3+}) [2, 3], laser systems (e.g. Nd^{3+}) [4], and optical amplifiers (Er^{3+} and Pr^{3+}) [5].

1.2.1. The 4f energy levels and selection rules

The occurrence of different energy levels belonging to the same configuration is a result of several interactions within the ion. The energy levels of 4f orbitals are not degenerate, because of electronic repulsion, spin-orbit coupling, and (in a coordination environment) the ligand field (see Figure 1.2). The strongest interaction, the electronic repulsion between the electrons known as columbic interaction, disrupts the degeneracy of the 4f energy levels and yields terms with separations in the order of 10^4 cm^{-1} . Each of these terms is split into several J-levels by spin-orbit coupling, which is relatively large (10^3 cm^{-1}) in lanthanide ions, because of their heavy nuclei. Spin-orbit coupling is the interaction between the magnetic moments of the electrons due to their spin (spin angular momentum) and the magnetic moments due to their movement around the nucleus (orbital angular momentum). We have now arrived at the free ion levels that are described by the term symbols $^{(2S+1)}L_J$. $2S+1$ represent the total spin multiplicity, L the total orbital angular momentum and J the total angular momentum of the f electrons. When present in a coordinating environment, such as a crystal or an organic ligand, the individual J-levels are split up further by the electric field of the matrix, which is usually referred to as the crystal field. These splitting are usually small (10^2 cm^{-1}) and, depending on the spectral resolution of the spectrometer, appear as fine structure on the individual bands. Often this fine structure is ignored, although it may be used to gather information about the symmetry of the coordination environment.

The term symbol of the J-states is written as $^{(2S+1)}L_J$ according to the Russell-Saunders coupling scheme [6]. The spin multiplicity $2S+1$, where S is the total spin-impulse momentum of the system gives the maximum of possible spin orientations and denotes the degeneracy of the J-states. The value of the total orbital angular

momentum L is represented by the symbols S ($L=0$), P ($L=1$), D ($L=2$), F ($L=3$), G ($L=4$) etc. The value of L is obtained by coupling the individual orbital angular momenta l_i : $L = (l_1+l_2+\dots+l_i), (l_1+l_2+\dots+l_{i-1}), (l_1- l_2-\dots-l_i)|$. The total angular momentum J indicates the relative orientation of the spin and the orbital momenta: $J = L+S, L+S-1, L+S-2, \dots, |L-S|$.

The energy levels of some of the trivalent lanthanide ions are depicted in Figure 1.3.

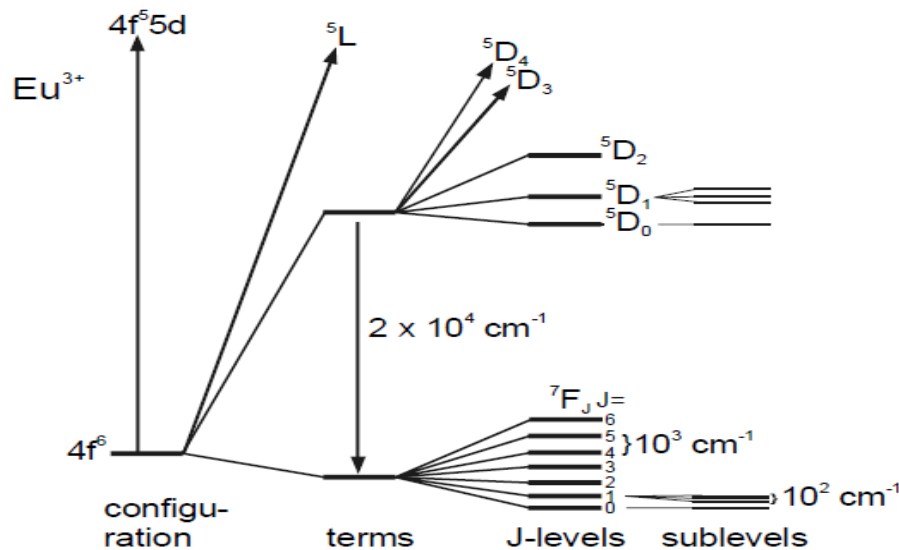


Figure 1.2: Splitting of the 4f energy levels of Eu^{3+} as a result of electronic repulsion, spin-orbit coupling, and the ligand field

In general the atomic spectra have to obey the following selection rules:

- $\Delta S = 0$, the overall spin is not allowed to change, because light does not affect the spin.
- $\Delta L = 0, \pm 1$, with $\Delta l = \pm 1$, the orbital angular momentum of an individual electron must change.
- $\Delta J = 0, \pm 1$, but $J = 0$ to $J = 0$ is forbidden.
- The parity selection rule, which forbids electric dipole transitions between levels with the same parity, examples are electronic transitions within the d-shell, within the f-shell, and between d and s shells.

The absorption of light by an electron moving around a nucleus occurs thanks to operators linked to the nature of light: the odd-parity electric dipole (ED) operator, the even-parity magnetic dipole (MD) and electric quadrupole (EQ) operators. Not all transitions are permitted, since they have to obey selection rules. One of these is the so-called Laporte's (or parity rule) requiring that for ED transitions, the sum of the

angular momenta of the electrons in the initial and final states must change by an odd integer.

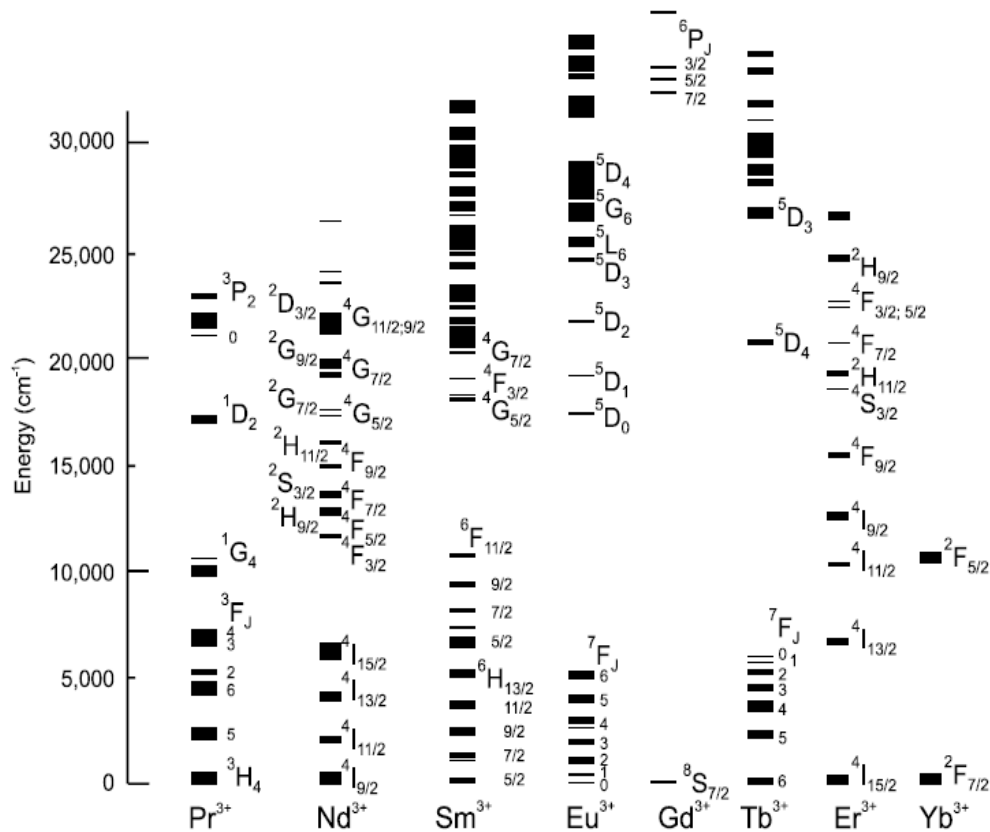


Figure 1.3: Energy diagram of the 4f levels responsible for the lanthanide luminescence [7].

Magnetic dipole transitions within the 4fⁿ configuration, which obey the selection rule $\Delta J = 0, \pm 1$ are allowed (except for $J = 0$ to $J = 0$), but have low oscillator strengths. The electric dipole intra-4f transitions are in principle parity forbidden and those transitions that do not occur within the ground multiplets may also be spin-forbidden ($\Delta S \neq 0$). However in an asymmetric environment, the electric dipole f-f transitions become weakly allowed (with oscillator strength of 10^{-6}) by mixing of opposite parity wave functions (primarily the 5d wave functions) into the 4f wave functions. In other words the parity forbidden intra-4f transitions ‘steal’ some intensity from the allowed 4f-5d transitions. The spin selection rule is relaxed by the fact that heavy atoms have large spin-orbit couplings. Because the oscillator strengths of these induced electric dipole transitions are in the same order of magnitude as those of magnetic dipole transitions, both transitions can be observed in lanthanide absorption and emission spectra. The forbidden character of intra-4f transitions causes them to have low

absorptivities, with absorption coefficients in the visible spectral range of less than $10 \text{ M}^{-1}\text{cm}^{-1}$ and relatively long luminescence lifetimes (in the range of μs to ms).

For certain induced electric dipole transitions that have $|\Delta J| < 2$, $|\Delta L| < 2$, and $\Delta S = 0$, the intensities are much more sensitive to complexation than other transitions, and have been termed *hypersensitive transitions*. The intensities of these transitions may be up to 200 times larger than the corresponding transition in the hydrated ion, whereas the intensities of the other transitions are generally approximately the same.

The other selection rules applying to S, L and J quantum numbers for f–f transitions between spectroscopic states are listed in Table 1.2. They are derived assuming that the wave functions of the 4f electrons are described by $f^n[\text{SL}]J$ functions (i.e. that Russell–Saunders spin–orbit coupling scheme is valid).

Table 1.2: Selection rules for f–f transitions between spectroscopic levels [8]

Operator	Parity	ΔS	ΔL	ΔJ^*
ED	Opposite	0	≤ 6	≤ 6 (2,4,6 if J or J' = 0)
MD	Same	0	0	0, ± 1
EQ	Same	0	0, ± 1 , ± 2	0, ± 2
* $J=0$ to $J'=0$		always		forbidden

The selection rules are derived under several hypotheses, which are not always completely fulfilled in reality (in particular 4f wavefunctions are not totally pure); so that the terms “forbidden” and “allowed” transitions cannot be taken too rigidly. A more correct wording would be that a forbidden transition has a low probability and an allowed transition a high probability of occurring.

1.2.2. Radiative and Non-radiative transitions in lanthanide

In the hypothetical free lanthanide ion, only magnetic dipole (MD) transitions are allowed. These are selected by the $\Delta J = 0, \pm 1$ (but $J = 0 \rightarrow J = 0$ is forbidden) rule. Their probability is relatively easily calculated [9] and practically independent of the surrounding matrix. One example of a purely MD transition is the ${}^5\text{D}_0 \rightarrow {}^7\text{F}_1$ emission line of Eu^{3+} . In a coordinating environment, electric dipole (ED) transitions are

induced, as the ligand field mixes odd parity configurations slightly into the [Xe] $4f^n 5d^0$ configuration.

Most of the absorption and emission lines are such induced ED transitions. Some transitions acquire strength both by MD and ED schemes: the emission spectrum of Tb^{3+} is dominated by mixed ED/MD transitions. Since ED transitions in lanthanide ions are induced by the ligand field, their strengths (or probabilities) are quite sensitive to it. Strongly asymmetric or strongly interacting ligand fields lead to relatively intense ED transitions. The intensities of some ED transitions are extremely sensitive to coordinating environment, which means that they can be either completely absent or very intense, depending on the ligand field.

The emission spectrum of the Eu^{3+} ion is strongly influenced by the symmetry of the surroundings. The main emissions of this ion occur from the 5D_0 to the 7F_1 ($J = 0-6$) levels. The $^5D_0 \rightarrow ^7F_1$ transition is a pure magnetic dipole transition, which is practically independent of the symmetry of the surroundings and the strength can be calculated theoretically. The transitions to the $^7F_{0, 3, 5}$ levels are forbidden both in magnetic and electric dipole schemes and are usually very weak in the emission spectrum. The remaining transitions to the $^7F_{2, 4, 6}$ levels are pure electric dipole transitions and they are strongly dependent on the symmetry of the environment. In a crystal site with inversion symmetry, the electric dipole transitions are strictly forbidden and the $^5D_0 \rightarrow ^7F_1$ transition is usually the dominant emission line. In a site without inversion symmetry, the strength of the electric dipole transition is higher. The $^5D_0 \rightarrow ^7F_2$ transition is usually the strongest emission line in this case, because transitions with $\Delta J = \pm 2$ are hypersensitive to small deviations from inversion symmetry. The symmetry around the lanthanide ion can thus be obtained from the shape of the emission spectrum of the Eu^{3+} ion. The other lanthanide ions have transitions that are usually mixtures of electric and magnetic dipole transitions and the effects of the symmetry are less pronounced. The symmetry also has an influence on the radiative lifetime of the 5D_0 level. The radiative lifetime is the time for the luminescence to drop to $1/e$ in intensity in absence of quenching. In the case of Eu^{3+} ion without inversion symmetry, the rate of the forced electric dipole transition is higher than in the case of a Eu^{3+} ion with inversion symmetry. This automatically means that the radiative lifetime of a Eu^{3+} ion in a site with inversion symmetry is longer. Radiative lifetimes of lanthanide ions have been calculated with several methods, of which the Judd-Ofelt theory is the most popular [10]. In this theory, the

strength of the electric dipole transitions are calculated from the absorption spectrum and these strengths can be related to the radiative lifetime. Werts *et al.* have formulated an equation to calculate the radiative lifetime of the Eu^{3+} ion from the shape of the emission spectrum (Equation 1.1) [11].

$$\frac{1}{\tau_R} = A_{MD,0} n^3 \left(\frac{I_{tot}}{I_{MD}} \right) \quad (1.1)$$

In this equation, the strength of the magnetic dipole transition (IMD) is compared to the intensity of the total spectrum (I_{tot}). $A_{MD,0}$ is the spontaneous emission probability of the $^5D_0 \rightarrow ^7F_1$ transition in vacuo and n^3 is a correction for the refractive index. $A_{MD,0}$ could be calculated and was found to be 14.65 s^{-1} .

Both MD and induced ED transitions of lanthanide ions are weak compared to the ‘fully allowed’ transitions found in organic chromophores. In the case of luminescence, this gives rise to radiative lifetimes of the order of milliseconds, depending on the lanthanide ion and its matrix. This is 6 orders of magnitude as long as the radiative lifetimes of organic fluorophores. On the other hand, the absorption bands are also weak, typically resulting in extinction coefficients of the order of $1 \text{ M}^{-1} \text{ cm}^{-1}$ with bandwidths less than 0.2 nm. This makes the long-lived photoluminescence of lanthanide ions difficult to excite. Figure 1.4 schematises the types of electronic transitions in lanthanide ions, both of radiative and non-radiative nature. If highly excited lanthanide ions could only decay radiatively, their emission spectra would become extremely rich in lines, since in principle radiative transitions between any two states can take place. Under favourable conditions, emission from ‘higher’ excited states is indeed observed. Such processes are the basis of upconversion (UC) [9], in which an already excited ion is excited into a higher lying luminescent state, converting two low-energy photons into one high-energy photon, and quantum cutting (QC) [12], in which a highly excited ion emits sequentially two photons. Both UC and QC have important technological implications. UC can convert a flux of near-infrared light into visible light, whereas QC offers the prospect of highly energy-efficient conversion of ultraviolet light into visible light.

The excited states of lanthanide ions, however, do not decay solely by radiative processes. In glasses and crystals, the electronic excitation energy can be dissipated by vibrations of the surrounding matrix, a process known as multiphonon relaxation

(MPR) [13]. MPR is inversely proportional to number of vibrational quanta needed to bridge the gap between given energy level and the next lower one. A similar process occurs also in complexes with organic ligands and is even of bigger importance in such systems, since in organic media, suitable high-energy vibrations are more common. The efficacy of matrix vibration mediated nonradiative relaxation is inversely proportional to the number of vibrational quanta that are needed to bridge the gap between a given energy level and the next-lower one. This energy gap law is a result of the overlap between the vibronic wavefunctions. A semi-quantitative treatment was given by Haas and Stein [14].

The rate of phonon emission, ω , depends on the number of phonons emitted simultaneously to bridge the energy gap and is expressed by equation 1.2:

$$\omega \propto \left(\frac{-k\Delta E}{h\nu_{\max}} \right) \quad (1.2)$$

Where, ΔE is the energy gap to the nearest lower level and $h\nu_{\max}$ is the maximum energy of phonons coupled to the emitting states. The phonon emission rate, ω , decreases rapidly with an increase in ΔE , so that the competitive light emission or radiative process becomes dominant.

The nonradiative decay rate does not depend exclusively on the energy gap and the number of matrix vibrations that fit this gap. Multiphonon relaxation still involves electronic transitions in the ion without a change in parity. Weber [13] has pointed out that for this process also; selection rules apply, although these only affect a few transitions, such as ${}^5D_1 \rightarrow {}^5D_0$ in Eu^{3+} (and Tb^{3+}). Indeed even in organic media, weak luminescence from the ‘higher excited’ 5D_1 state can be observed. As a result of vibration (or phonon)-mediated nonradiative (NR) decay, luminescence of a given lanthanide ion occurs mainly from one state, which is the state that has a large gap with the next lower lying level. More highly excited states are quickly deactivated to this state, since the higher states form a ‘ladder’ consisting of relatively small gaps that efficiently undergo multiphonon relaxation. Especially in organic media and in aqueous solution, where matrix vibrations of high energy are ubiquitous [15, 16] the emission of lanthanide ions stems (almost) exclusively from one level and therefore the number of emission lines is limited.

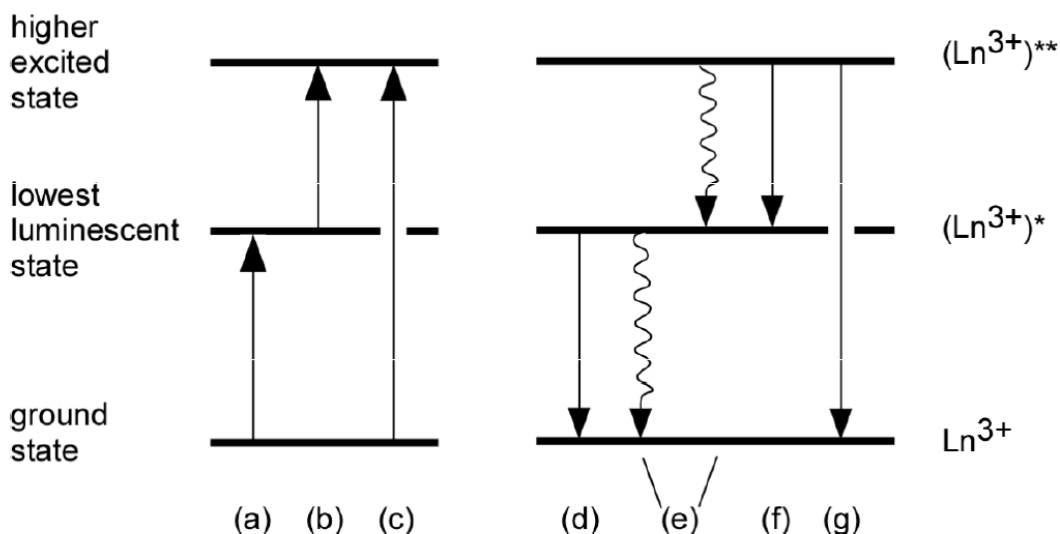


Figure 1.4: Electronic transitions in lanthanide ions: (a) absorption/excitation, (b) excited state absorption, (c) direct excitation into a higher excited state, (d) “conventional” emission from the lowest luminescent state, (e) non-radiative relaxation, (f) radiative transition between excited states, (g) emission from a higher excited state

In most cases, the decay of the lanthanide luminescent level is not controlled by the radiative rate constant, which is the rate constant of spontaneous emission, but by non-radiative processes. For lanthanide ions, the most important nonradiative processes are those that emerge from interaction of the lanthanide 4f electronic states with suitable vibrational modes of the environment. The *luminescent* trivalent rare earth cations can be classified into two groups: The first group of lanthanides consists of praseodymium, neodymium, holmium, erbium, thulium, and ytterbium, and this group exhibits only weak luminescence in the visible and/or the near-infrared region. The main reason for this is that the energy difference between the lowest luminescent state and the highest non-luminescent state is relatively small. This small energy gap makes the competing radiationless decay more likely to occur, *i.e.* vibronic quenching by high frequency oscillators. The second group of lanthanides consists of samarium, europium, terbium, and dysprosium, and exhibits strong luminescence. These lanthanide ions have large energy gaps between the lowest luminescent state and the highest non-luminescent state, and are therefore less sensitive towards vibronic quenching by high frequency oscillators. These energy gap considerations are known as the energy gap law theory. The lanthanide ions lanthanum, lutetium and gadolinium do not exhibit any luminescence. Because the 4f subshells are completely empty or completely filled in La^{3+} and Lu^{3+} respectively, no intra-4f transitions are

possible. Luminescence is seldomly observed for Gd^{3+} , because of the large energy gap between the ground and the first excited state.

The measured lifetimes of luminescent species are generally shorter than the natural lifetimes, because non-radiative processes compete with the radiative decay. High frequency O-H and C-H vibrations in the local environment and the size of the energy gap between the excited and the ground state of the lanthanide ion, play an important role in removing energy non-radiatively from the lanthanide excited state [17,18]. The deactivation arises from a weak vibronic coupling between the f-electronic states of the lanthanide ions and the vibrational states of O-H and C-H. To provide an efficient deactivation route, the energy gap between the excited and the ground state of an excited lanthanide ion must be bridged by these vibrational states. According to the theory of the energy gap law [14] the smaller the harmonic number of vibrational quanta that is required to match the energy gap between the lowest luminescent state and the highest non-luminescent state of the lanthanide ion, the more effective the vibronic quenching will be. The harmonic number of vibrational quanta (ν) of several vibrations that is required to match the energy gap in Tb^{3+} , Eu^{3+} , Yb^{3+} , Er^{3+} , and Nd^{3+} are indicated in Figure 1.5.

The Tb^{3+} ion, which has a large energy gap, is the least sensitive towards quenching by high frequency oscillators, and as a result has a higher luminescence quantum yield than for example, Eu^{3+} . It can furthermore easily be seen from Figure 1.5 that the near-infrared luminescent lanthanide ions are more prone to quenching by vibrations in their environment than the visible emitting lanthanide ions. Indeed, the observed lifetimes of Eu^{3+} and Tb^{3+} complexes in solution are in the ms range, whereas the observed lifetimes of the near-infrared luminescent lanthanide complexes are in the μs range. It has been shown that by replacing the C-H bonds in the ligands by C-D bonds the luminescence lifetimes of the complexed lanthanide ions are increased [19, 20].

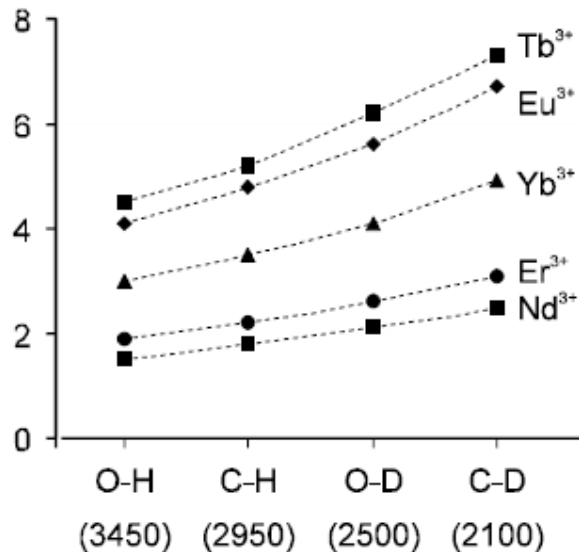


Figure 1.5: Graphical representation of the number of vibrational quanta of four high frequency oscillators that is required to match the energy gap between the lowest luminescent state and the highest non-luminescent state of the lanthanide ion (the dashed line is merely a guide to the eye).

1.2.3. Phosphor Design: Selection of dopant and hosts

Phosphors are luminescent inorganic materials with preferably a homogeneous grain size, which is usually on the order of several micrometers. The grains can be smaller, in which case they may be called nanophosphors. Phosphors are luminescent, because of the presence of small amounts of activators. The stable luminescences of trivalent lanthanide ions make them attractive activators. In fluorescent lighting, phosphors convert ultraviolet radiation generated by mercury or Xe plasma into visible light. In cathode ray tubes, phosphors emit light upon electron bombardment. Most Ln (III) ions are luminescent, but some are more emissive than others. The emissive properties of a lanthanide ion are governed by the facility with which its excited state(s) can be populated and the non-radiative de-activation paths minimized. To meet the first requirement, sensitization via the surroundings of the ion is often used so that the overall quantum yield of a lanthanide-containing molecular edifice is given by equation 1.3

$$Q_{Ln}^E = \eta_{sens} Q_{Ln}^{Ln} \quad (1.3)$$

Whereby Q_{Ln}^E and Q_{Ln}^{Ln} are the quantum yields resulting from indirect and direct excitation, respectively, while η_{sens} represents the efficacy with which electromagnetic energy is transferred from the surroundings onto the metal ion. The intrinsic quantum yield Q_{Ln}^{Ln} essentially depends on the energy gap between the lowest

lying excited (emissive) state of the metal ion and the highest sublevel of its ground multiplets. The smaller this gap, the easier is its closing by non-radiative deactivation processes, for instance through vibrations of bound ligands, particularly high energy vibrations such as O–H.

With respect to the energy gap requirement, it is obvious that Eu (III), Gd (III), and Tb (III) are the best ions, with $\Delta E = 12\,300$ ($^5D_0 \rightarrow ^7F_6$), $32\,200$ ($^6P_{7/2} \rightarrow ^8S_{7/2}$) and $14\,800$ ($^5D_4 \rightarrow ^7F_0$) cm^{-1} , respectively. However, Gd (III) emits in the UV and it is not very useful as luminescent probe for bioanalyses, because its luminescence interferes with either emission or absorption processes in the organic part of the complex molecules. On the other hand, it can efficiently transfer energy onto Eu (III) upon vacuum-UV excitation, resulting in the emission of two red photons (the so-called quantum cutting or down-conversion effect) [12]; Gd (III) is therefore a potential phosphor component for mercury-free fluorescent lamps. The sizeable energy gap displayed by Eu (III) and Tb (III) explains why luminescent probes containing these ions have been so popular during the last decades. Nevertheless, development of dual luminescent time-resolved immunoassays has also stirred interest for Sm (III) ($\Delta E = 7\,400$ cm^{-1} , $^4G_{5/2} \rightarrow ^6F_{11/2}$) or Dy (III) ($7\,850$ cm^{-1} , $^4F_{9/2} \rightarrow ^6F_{3/2}$) [21, 22]. The other ions have all very low quantum yield in aqueous solutions and appear to be less useful with respect to similar applications. Pr (III) emits both in visible and NIR ranges [23] and is often a component of solid state optical materials, in view of its ability to generate up-conversion, which is blue emission from 3P_0 upon two- or three-photon pumping of the 1G_4 or 1D_2 states [9]. Thulium is a blue emitter from its 3P_0 , 1D_2 , and 1G_4 levels and is used as such in electroluminescent devices [24]; it is the first Ln (III) ion for which up-conversion has been demonstrated [9]; several other ions (Nd(III), Dy(III), Ho(III), Er(III)) present up-conversion processes as well. In addition, Nd(III), Ho(III), Er(III) and Yb(III) have special interest in that they emit in the NIR spectral range and are very useful in the design of lasers (especially Nd(III) with its line at 1.06 μm) and of telecommunication devices [25]. The telecommunication windows lie usually between 1 and 1.6 μm and Yb(III), which emits slightly under 1 μm is less useful than Pr(III) for instance (emitting at 1.33 μm); but it acts as an efficient sensitizer of Er(III) (emitting at 1.55 μm) [25]. Finally, the three ions Nd(III), Er(III) and Yb(III) (and partially Pr(III)) have recently gained in popularity, because technical developments facilitating the detection of weak NIR emission and

identification of efficient sensitizing groups. As a consequence of efficient light transmission of biological tissues in part of the NIR spectral range (0.9 to 1.5 mm approximately), lanthanide containing luminescent probes based on these ions are now being used for time-resolved imaging of these tissues; cancer detection is obviously a highly sought for application. Trivalent cerium emits a broad band spectrum in the range 370–410 nm due to the interconfigurational allowed 5d–4f transition. Table 1.3 gives some important emissions of lanthanide ions and their technological interest. Figure 1.6 shows some of these applications.

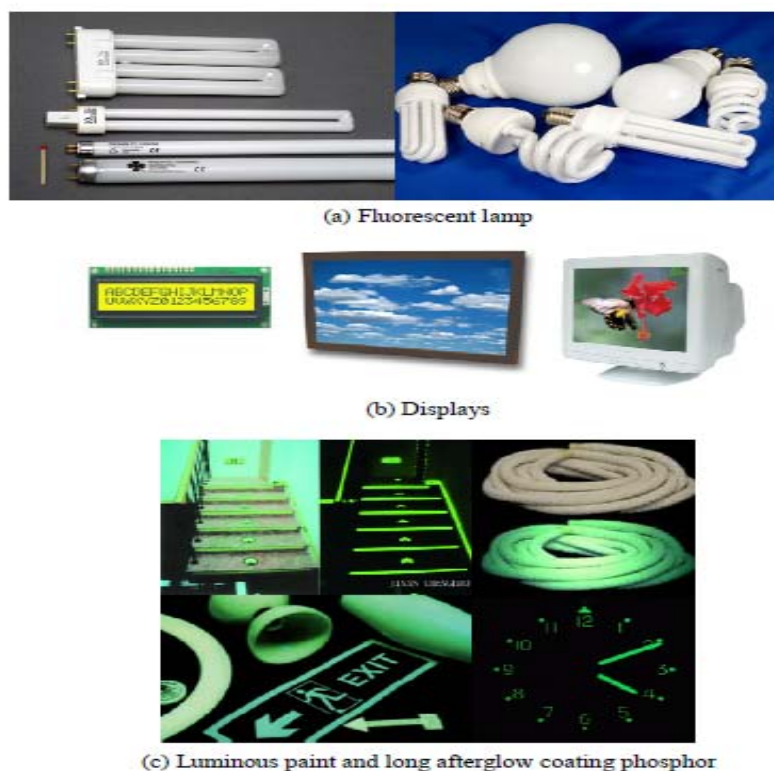


Figure 1.6: Some of the phosphor applications

Table 1.3: Important emission lines of some lanthanide ions.

Ion	Transition	Wavelength (nm)	Application
Pr^{3+}	$^1\text{G}_4 \rightarrow ^3\text{H}_5$	1300	Optical amplifier
Nd^{3+}	$^4\text{F}_{3/2} \rightarrow ^4\text{I}_{11/2}$	1064	Solid state laser
Eu^{3+}	$^5\text{D}_0 \rightarrow ^7\text{F}_2$	615	Displays, Lighting

Chapter 1

Tb ³⁺	⁵ D ₄ → ⁷ F ₅	545	Lighting
Dy ³⁺	⁶ F _{11/2} + ⁶ H _{9/2} → ⁶ H _{15/2}	1300	Optical amplifier
Er ³⁺	⁴ I _{13/2} → ⁴ I _{15/2}	1530	Optical amplifier
Tm ³⁺	¹ G ₄ → ³ H ₅	1480	Optical amplifier
Yb ³⁺	² F _{5/2} → ² F _{7/2}	980	Sensitizer

In a sense, the host is regarded as the “home” of optically active ions. It is necessary to optimize the distribution of the activators and prevent rapid non-radiative processes from occurring. Since dopant ions in a solid host are impurities embedded in the host lattice, the host ions are substitutionally replaced by dopant ions. Therefore, the host lattice determines the distance between the dopant ions as well as their relative spatial position. The host materials generally require close lattice matches, and the valence of the host cation should be the same or similar to those of dopant ions in order to prevent the formation of crystal defects and lattice stresses arising from doping. Another consideration of selecting the host is the magnitude of phonon energy. It is believed that host materials with low phonon energies will minimize non-radiative relaxation losses and increase the overall metastable energy lifetime [26]. For display and LED applications, host materials (oxide, sulfide, Fluoride, etc.) must have a wide band-gap so as to allow full visible light transmission. Hence, hosts selected are usually insulators. Some semiconductors can also serve as hosts for optically active ions as long as the luminescent excited state does not overlap with the conduction band leading to luminescence quenching. Therefore, wide band-gap semiconductors, including GaN and ZnO have extensively been utilized as hosts for optical and electronic applications. Other general requirements for host materials include mechanical and chemical stability. To some extent, host materials have an influence on the optical and luminescent properties of metal-ion doped phosphors, depending upon the nature of the dopant ions. Emissions originating from 4f–4f transitions of lanthanide ions as well as 3d–3d transitions of transition-metal ions are both parity forbidden. However when the dopant ion is placed in a non-centrosymmetric lattice, the parity selection rules are relaxed. Low-symmetry hosts exert a crystal field

containing more uneven components around the dopant ions. The perturbation caused by the odd-order terms of the crystal field forces the parity forbidden transitions to become allowed. In principle, the lower symmetry at the dopant ion site corresponds to higher transition probabilities. It should be emphasized that much attention has been paid on the development of multifunctional luminescent materials. Researchers are attempting to seek the potentials of metal-ion doped functional hosts as multifunctional systems, which combine light emission with other intrinsic properties of the host such as ferroelectricity, [27,28] magnetism [29] , piezoelectricity [30] and electro-optic properties [31].

1.2.4. Lanthanide Photophysics:

1.2.4.1. Absorption spectra

Description of the interaction between photons (massless elemental particles of light) and matter considers the former behaving as waves comprised of two perpendicular fields, electric and magnetic, oscillating in time (henceforth the denomination of electromagnetic wave or radiation). When a photon is absorbed, its energy is transferred to an electron, which then may be “pushed” into an orbital with higher energy. The absorption is promoted by “operators” linked to the nature of light: the odd-parity electric dipole (ED) operator \vec{P} , the even-parity magnetic dipole (MD) operator \vec{M} and electric quadrupole (EQ) operator \vec{Q} operators:

$$\vec{P} = -e \sum_{i=1}^n \vec{r}_i, \quad \vec{M} = -\frac{e\hbar}{4\pi mc} \sum_{i=1}^n (\vec{l}_i + 2\vec{s}_i), \quad \vec{Q} = \frac{1}{2} \sum_{i=1}^n (\vec{r}_i \cdot \vec{r}_i) \cdot \vec{r}_i \quad (1.4)$$

There are three types of electronic transitions involving lanthanide ions: sharp interconfigurational 4f–4f transitions, broader 4f–5d transitions, and broad charge-transfer transitions (metal-to-ligand, MLCT or ligand-to-metal, LMCT). Not all transitions are permitted and the allowed ones are described by selection rules. Laporte’s parity selection rule implies that states with the same parity cannot be connected by electric dipole transitions; as a consequence f–f transitions are forbidden by the ED mechanism. However, when the lanthanide ion is under the influence of a ligand-field, non-centrosymmetric interactions allow the mixing of electronic states of opposite parity into the 4f wavefunctions, which somewhat relaxes the selection rules and the transition becomes partially allowed; it is called an induced (or forced)

electric dipole transition. Magnetic dipole transitions are allowed, but their intensity is weak; in 4f–4f spectra, however, they often have intensity of the same order of magnitude as induced electric dipole transitions. Quadrupolar transitions are also parity allowed, but they are much weaker than MD transitions so that they are usually not observed. Some induced ED transitions are highly sensitive to minute changes in the Ln^{III} environment and are called hypersensitive or sometimes pseudo-quadrupolar transitions, because they apparently follow the selection rules of EQ transitions. A listing of such transitions (experimentally identified) is presented in Table 1.4; note that these transitions are not necessarily the most intense ones in the optical spectra.

In addition to the parity selection rule, other rules are operative; for instance, on ΔS (spin selection rule, requiring no change of spin for all three mechanisms, $\Delta S = 0$), ΔL , and ΔJ ; they will be detailed below. The selection rules are derived under several hypotheses, which are not always completely fulfilled in reality (in particular 4f wavefunctions are not completely pure), so that the terms “forbidden” and “allowed” transitions are not accurate. In general, a forbidden transition has a low probability and an allowed transition a high probability of occurring.

Table 1.4: Experimentally observed hypersensitive transitions for Ln^{III} ions in optical spectra [5]. Energies/wavelengths are approximate

Ln	Transition	$\tilde{\nu}/\text{cm}^{-1}$	λ/nm
Pr	$^3F_2 \leftarrow ^3H_4$	5,200	1,920
Nd	$^4G_{5/2} \leftarrow ^4I_{9/2}$ ^a	17,300	578
	$^2H_{9/2}, ^4F_{5/2} \leftarrow ^4I_{9/2}$	12,400	806
	$^4G_{7/2}, ^3K_{13/2} \leftarrow ^4I_{9/2}$	19,200	521
Sm	$^4F_{1/2}, ^4F_{3/2} \leftarrow ^6H_{5/2}$	6,400	1,560
Eu	$^5D_2 \leftarrow ^7F_0$	21,500	465
	$^5D_1 \leftarrow ^7F_1$	18,700	535
	$^5D_0 \rightarrow ^7F_2$	16,300	613
Gd	$^6P_{5/2}, ^6P_{7/2} \leftarrow ^8S_{7/2}$	32,500	308
Tb	– ^b	–	–
Dy	$^6F_{11/2} \leftarrow ^6H_{15/2}$	7,700	1,300
	$^4G_{11/2}, ^4I_{15/2} \leftarrow ^6H_{15/2}$	23,400	427
Ho	$^3H_6 \leftarrow ^5I_8$	27,700	361
	$^5G_6 \leftarrow ^5I_8$	22,100	452
Er	$^4G_{11/2} \leftarrow ^4I_{15/2}$	26,400	379
	$^2H_{11/2} \leftarrow ^4I_{15/2}$	19,200	521
Tm	$^1G_4 \leftarrow ^3H_6$	21,300	469
	$^3H_4 \leftarrow ^3H_6$	12,700	787
	$^3F_4 \leftarrow ^3H_6$	5,900	1,695

^aThe transition $^4G_{5/2} \leftarrow ^4I_{9/2}$ overlaps with $^2G_{7/2} \leftarrow ^4I_{9/2}$

^bNone identified positively, but the $^5D_4 \rightarrow ^7F_5$ transition shows sometimes ligand-induced pseudo-hypersensitivity

A. Induced ED f-f Transitions: Judd-Ofelt Theory [32, 33]

Judd-Ofelt (JO) theory has been established within the frame of the crystal-field concept and it provides a simple model for reproducing the intensities of f-f transitions both in solids and solutions. It only takes into account the 4fⁿ electronic configuration, i.e. inter-configurational 4fⁿ-4fⁿ⁻¹5d¹ interaction is neglected. On the other hand, spin-orbit coupling is treated within the frame of the intermediate coupling scheme. The dipole strength in esu²cm² (=10³⁶ debye²) of an induced ED f-f transition between states Ψ and Ψ' is given by:

$$D_{ED} = e^2 \sum_{\lambda=2,4,6} \Omega_{\lambda} \left| \langle \Psi J \| U^{(\lambda)} \| \Psi' J' \rangle \right|^2$$

(1.5)

in which e is the electric charge of the electron, wavefunctions Ψ and Ψ' are full intermediate-coupled functions fn[SL]J, U^(λ) are the irreducible tensor forms of the ED operator, and Ω_λ are the phenomenological JO parameters, expressed in cm². The bracketed expressions in (1.5) are dimensionless doubly-reduced matrix elements, which are tabulated (and insensitive to the metal-ion environment). Mathematical treatment of the parity mixing by the crystal-field perturbation leads to the selection rules for f-f transitions mentioned in Table 1.2.

JO parameters are adjustable parameters and they are calculated from the absorption spectrum ε(ν̄). For an isotropic crystal or a solution, the experimental dipole strength is defined as:

$$D(\text{exp}) = \frac{10^{36}}{108.9 \cdot \nu_{\text{mean}} \cdot X_A} \left((2J + 1) \cdot \frac{n}{(n^2 + 2)^2} \right) \int \varepsilon(\nu) d\nu$$

(1.6)

with X_A being the fractional population of the initial state, while ν_{mean} is given by:

$$\nu_{\text{mean}} = \frac{\int \nu \varepsilon(\nu) d\nu}{\int \varepsilon(\nu) d\nu}$$

(1.7)

The above equations assume that the absorption bands are symmetrical, i.e., either Gaussian or Lorentzian. If not, (1.6) has to be replaced with:

$$D(\text{exp}) = \frac{10^{36}}{108.9 \cdot X_A} \left((2J + 1) \cdot \frac{n}{(n^2 + 2)^2} \right) \int \frac{\varepsilon(\nu)}{\nu} d\nu$$

(1.8)

Finally, (2J + 1) is the degeneracy of the initial state and the expression involving the refractive index n is known as Lorentz's local-field correction. Calculations of

transition probabilities within the frame of JO theory are usually made assuming that all Stark sublevels within the ground level are equally populated and that the material under investigation is optically isotropic. The former hypothesis is only reasonable in some cases, e.g., when transitions initiate from non-degenerate states such as $\text{Eu} (^7\text{F}_0)$. Otherwise, there is a Boltzmann distribution of the population among the crystal-field sublevels. The second assumption is not valid for uniaxial or biaxial crystals, but, of course, holds for solutions. The phenomenological JO parameters are determined from a fit of equation 1.5 to the experimental values defined by equation 1.6, using adequate matrix elements. The exact procedure is described in details in reference [33]. In the case of Eu^{III} the procedure is quite simple, since Ω_2 , Ω_4 and Ω_6 can be directly extracted from the dipole strength of the $^5\text{D}_2 \leftarrow ^7\text{F}_0$, $^5\text{D}_4 \leftarrow ^7\text{F}_0$, and $^5\text{D}_6 \leftarrow ^7\text{F}_0$ transitions, respectively. Extensive tabulations of JO parameters can be found in reference [32], while spectra for all Ln^{III} ions are presented in reference [34]; molar absorption coefficients are, with a few exceptions, smaller than $10 \text{ M}^{-1}\text{cm}^{-1}$ and very often smaller than 1 or even $0.1 \text{ M}^{-1}\text{cm}^{-1}$.

B. 4f-5d and CT transition

The promotion of a 4f electron into the 5d sub-shell is parity allowed; the corresponding transitions are broader than f–f transitions and their energy depends largely on the metal environment, since the 5d orbitals are external and interact directly with the ligand orbitals. The 4f–5d transitions have high energies (Fig. 1.7) and only those of Ce^{III} , Pr^{III} , and Tb^{III} are commonly observed. Figure 1.8 shows the crystal-field splitting of both the $4\text{f}^1(^2\text{F}_{5/2}, ^2\text{F}_{7/2})$ and $5\text{d}^1(^2\text{D}_{3/2}, ^2\text{D}_{5/2})$ electronic configurations of Ce^{III} in $\text{D}_{3\text{h}}$ symmetry. In the spectrum displayed, the third transition to $^2\text{D}_{5/2}$ is not observed, because it lies at too high energy. Conversely, the Ce^{III} luminescence can be tuned from about 290 to 450 nm, depending on the matrix into which the metal ion is inserted, because of large crystal-field effects on the 5d^1 excited configuration. Charge-transfer transitions, both LMCT and MLCT, are allowed and have also high energies (Fig. 1.7), so that only the LMCT of Eu^{III} and Yb^{III} (possibly Sm^{III} and Tm^{III}) are commonly observed in ordinary solvents, contrary to d-transition metal ions for which this type of transition is widespread. This is sometimes not well understood; the literature features many wrong assignments to MLCT transitions made by analogy to d-metal complexes.

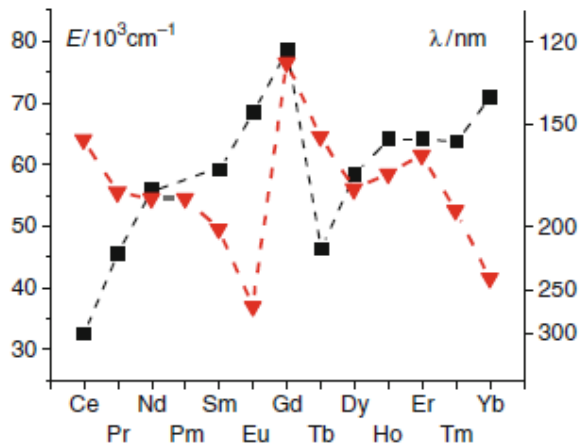


Figure 1.7: Energy of the 4f–5d transitions in $\text{Ln}^{\text{III}}:\text{CaF}_2$ (squares, [35]) and of the 2p (O)-4f LMCT transitions (triangles, [36])

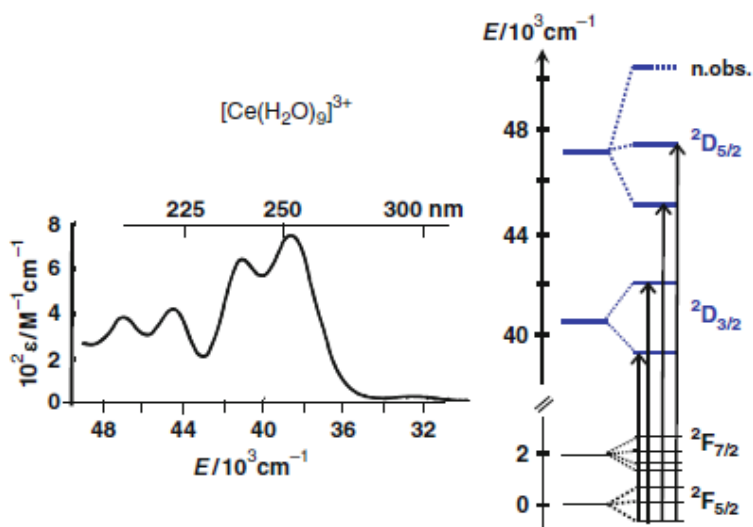


Figure 1.8: Left: Absorption spectrum of $[\text{Ce}(\text{H}_2\text{O})_9]^{3+}$ and right: its assignment (D_{3h} symmetry)

1.2.4.2. Emission spectra

With the exception of La^{III} and Lu^{III} , all Ln^{III} ions are luminescent and their f–f emission lines cover the entire spectrum, from UV (Gd^{III}) to visible (e.g., Pr^{III} , Sm^{III} , Eu^{III} , Tb^{III} , Dy^{III} , Tm^{III}) and near-infrared (NIR, e.g., Pr^{III} , Nd^{III} , Ho^{III} , Er^{III} , Yb^{III}) ranges. Some ions are fluorescent ($\Delta S = 0$), others are phosphorescent ($\Delta S \neq 0$), and some are both. The f–f emission lines are sharp, because the rearrangement

consecutive to the promotion of an electron into a 4f orbital of higher energy does not perturb much the binding pattern in the molecules, since 4f orbitals do not participate much in this binding (the covalency of a Ln^{III}-ligand bond is at most 5–7%). Therefore, the internuclear distances remain almost the same in the excited state, which generate narrow bands and very small Stokes' shifts. A different situation is met in organic molecules for which excitation leads frequently to a lengthening of the chemical bonds, resulting in large Stokes' shifts and since the coupling with vibrations is strong, in broad emission bands (Fig. 1.9). As for absorption, emission of light through f–f transitions is achieved by either electric dipole or magnetic dipole mechanisms, and the selection rules detailed in table 1.2 apply.

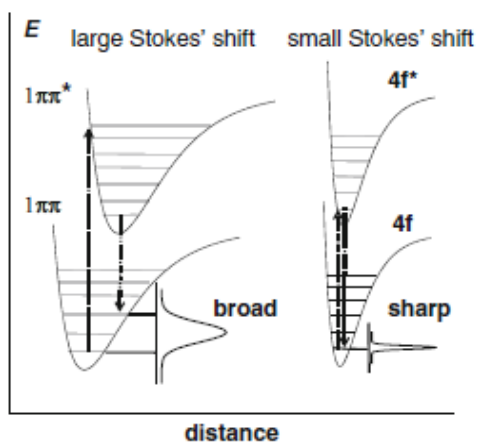


Figure 1.9: Configurational coordinate diagram for emission from (left) an organic chromophore and (right) a lanthanide ion

Important parameters characterizing the emission of light from a Ln^{III} ion are the lifetime of the excited state $\tau_{obs} = \frac{1}{k_{obs}}$ and the quantum yield Q . A general expression for the latter is simply

$$Q = \frac{\text{no of emitted photons}}{\text{no of absorbed photons}} \quad (1.9)$$

The quantum yield is related to the rate at which the excited level is depopulated k_{obs} and to the radiative rate constant k_{rad}

$$Q_{Ln} = \frac{k_{rad}}{k_{obs}} = \frac{\tau_{obs}}{\tau_{rad}} \quad (1.10)$$

Subscript and superscript “Ln” have been added to avoid confusion with the other definition of quantum yield discussed below. The quantity defined in (1.10) is called

the intrinsic quantum yield, that is, the quantum yield of the metal-centered luminescence upon direct excitation into the 4f levels. Its value reflects the extent of nonradiative deactivation processes occurring both in the inner- and outer-coordination spheres of the metal ion. The rate constant k_{obs} is the sum of the rates of the various deactivation processes:

$$k_{\text{obs}} = k^{\text{rad}} + \sum_{\text{n}} k_{\text{n}}^{\text{nr}} = k^{\text{rad}} + \sum_{\text{l}} k_{\text{l}}^{\text{vibr}}(T) + \sum_{\text{j}} k_{\text{j}}^{\text{pet}} + \sum_{\text{k}} k_{\text{k}}^{\text{nr}} \quad (1.11)$$

Where k^{rad} and k^{nr} are the radiative and nonradiative rate constants, respectively; the superscript vibr points to vibration-induced processes, while pet refers to photoinduced electron transfer processes such as those generated by LMCT states, for instance; the rate constants k' are associated with the remaining deactivation paths. In absence of nonradiative deactivation processes, $k_{\text{obs}} = k^{\text{rad}}$ and the quantum yield would be equal to 1, which is very rare. Examples are, in solid state and under excitation at 254 nm, $\text{Y}_2\text{O}_3:\text{Eu}$ (5%) with $Q = 0.99$ and terbium benzoate with $Q = 1$ [37]; in solution, a terbium complex with a dipyrazoylpyridine bearing aminocarboxylate coordinating groups was reported having $Q = 0.95$ [38].

Temperature-dependent vibrational deactivation processes can often be fitted to an Arrhenius-type of equation [39]:

$$\ln(k_{\text{obs}} - k_0) = \ln A - \frac{E_A}{RT} \quad (1.12)$$

where k_0 is the rate constant at 0 K (practically: at 4 K, or even at 77 K), which allows one to decipher the vibration responsible for it; examples are presented in references [40].

The intrinsic quantum yield essentially depends on the energy gap ΔE between the emissive state of the metal ion and the highest sublevel of its ground, or receiving multiplet. The smaller this gap, the easier is its closing by nonradiative deactivation processes; for instance, through vibrations of bound ligands, particularly those with high energy such as O–H, N–H, or C–H. With the assumption that the deactivating phonons involved have all the same energy $h\omega$, the temperature dependent rate constant $k_{\text{vibr}}(T)$ for the quenching of a single excited level is described by the following expression [41]

$$k^{\text{vibr}}(T) = k^{\text{vibr}}(0) \left(1 - e^{\frac{-h\omega}{k_B T}} \right)^{-1} \text{ with } l = \frac{\Delta E}{h\omega} \quad (1.13)$$

Where k_B is Boltzmann's constant ($1.38 \times 10^{-23} \text{ J K}^{-1} \sim 0.695 \text{ cm}^{-1}$), i the number of phonons required to bridge the gap, and $k_{\text{vibr}}(0)$ the spontaneous rate at 0 K. The latter heavily depends on the order n of the process. In practice, the excited level possesses several crystal-field sublevels, the population of which is in thermal equilibrium. This equilibrium is reached in times short compared to the multiphonon decay time; but since phonon-induced decay rates are significantly slower for the upper levels in view of the larger energy gaps, depopulation of the lower crystal field sublevel is the major contribution to the deactivation process. A rule of thumb is that radiative de-excitation will compete efficiently with multi-phonon processes if the energy gap is more than 6 quanta of the most energetic vibration present in the molecule. This type of nonradiative deactivation is especially detrimental to NIR luminescence because of closeness their energy levels as can be seen from Figure 1.3: for Er^{III} , for instance, a C–H vibrator located outside the inner coordination sphere at a distance between 20 and 30 Å from the emitting center induces a radiationless rate equal to the radiative one. Determination of the intrinsic quantum yield with (1.10) requires evaluation of the radiative lifetime, which is related to Einstein's rates of spontaneous emission A from an initial state $|\psi_j\rangle$ characterized by a quantum number J , to a final state $|\psi_{j'}\rangle$:

$$A(\psi_j, \psi_{j'}) = k^{\text{rad}} = \frac{1}{\tau^{\text{rad}}} = \frac{64\pi^4 \bar{\nu}^3}{3h(2J+1)} \left[\frac{n(n^2+2)^2}{9} D_{\text{ED}} + n^3 D_{\text{MD}} \right] \quad (1.14)$$

where $\bar{\nu}$ is the average transition energy (in cm^{-1}), h is the Planck constant ($6.63 \times 10^{-27} \text{ erg s}$) and $2J+1$ is the degeneracy of the initial state (1 for 5D_0). D_{ED} and D_{MD} are the electric and magnetic dipole strengths (in $\text{esu}^2 \text{ cm}^2$), respectively. The factors containing medium's refractive index n result from local field corrections, which convert the external electromagnetic field into an effective field at the location of the active center in the dielectric medium. D_{ED} is given by (1.5) and D_{MD} by (1.15):

$$D_{\text{MD}} = \left(\frac{eh}{4\pi m_e c} \right)^2 |\langle \psi_j \| \mathbf{L} + 2\mathbf{S} \| \psi_{j'} \rangle|^2 \quad (1.15)$$

The bracketed matrix elements are tabulated and the radiative lifetime can, therefore, be extracted from the spectral intensity, i.e. from (1.5), (1.14), and (1.15). Except in few cases, this calculation is not trivial and large errors may occur, including those pertaining to the hypotheses made within JO theory. In particular, it has been assumed that the emitting and receiving levels are $(2J + 1)$ -fold degenerate or if split by crystal field effects, that all the sublevels are equally populated. This is obviously not true

and in the case of Er^{III} this may lead to up to 20% errors. Even larger errors have been found for Ln^{III} tris (dipicolinate) [42].

On the other hand, if the absorption spectrum corresponding to an emission spectrum is known, which may be the case, when the luminescence transitions terminate onto the ground level, the radiative lifetime can be simply calculated from the following equation where N_A is Avogadro's number

$$\frac{1}{\tau_{\text{rad}}} = 2.303 \times \frac{8\pi n^2 \nu^2 (2J+1)}{N_A (2J'+1)} \int \epsilon(\nu) d\nu \quad (1.16)$$

In the special case of Eu^{III} for which one transition (⁵D₀→⁷F₁) has pure magnetic origin, a convenient simplified equation can be derived [11] as already mentioned in equation 1.1.

$$A(\psi_J, \psi_{J'}) = \frac{1}{\tau_R} = A_{MD,0} n^3 \left(\frac{I_{\text{tot}}}{I_{MD}} \right)$$

with $A_{MD,0}$ being a constant equal to 14.65 s⁻¹ and (I_{tot}/I_{MD}) the ratio of the total integrated emission from the Eu(⁵D₀) level to the ⁷F_J manifold (J = 0–6) to the integrated intensity of the MD transition ⁵D₀→⁷F₁. Finally, there are two important points to be stressed here in order to correct many errors reported in the literature. Firstly, the radiative lifetime is characteristic of one emitting state. If several excited states of an Ln^{III} ion emit light, then each of them will have a characteristic radiative lifetime. Moreover, the radiative lifetime is not a constant for a given ion and a given electronic level. Indeed, there is a dependence on the refractive index, as clearly shown in (1.14), so that transposition of a literature value to a specific compound cannot be made directly.

1.2.5. Information gained from lanthanide luminescence: Structural probing

Any luminescent lanthanide ion may act as a probe, but some ions bring more information (e.g. Eu^{III}), or are more luminescent (e.g. Tb^{III}) than others, which explains their preferential use. The following section will mainly deal with Eu^{III}. Generally speaking a lanthanide luminescent tag functions either as a structural probe deciphering the symmetry of the chemical environment and, partly, the composition of the inner coordination sphere, or as simple analytical (bio)marker, the switching on (or off) or the modulation of its luminescence representing the analytical signal. In

view of its non-degenerate emissive state 5D_0 , the Eu^{III} ion is most appropriate as luminescent structural probe for the determination of the number of metal ion sites in a compound, their symmetry, and their respective population.

1.2.5.1. Number of Metal Ion Sites: N

High resolution of the Eu ($^5D_0 \rightarrow ^7F_0$) transition, which is unique for a given chemical environment associated with spectral decomposition with Lorentzian–Gaussian shape functions [43,44] gives a direct access to N. Experimentally, laser-excited excitation spectra of the $^5D_0 \rightarrow ^7F_0$ transition yield more sensitive results. It is best detected in excitation mode by analyzing the emission of the hypersensitive transition $^5D_0 \rightarrow ^7F_2$, since both the emitting and end states are non-degenerate, its number of components indicates the number of different metal–ion sites.

1.2.5.2. Composition of the first coordination sphere

The energy of the $^5D_0 \rightarrow ^7F_0$ transition at 298 K, ν_{calc} in cm^{-1} , is correlated with the nephelauxetic effect δ_i generated by each coordinated group [45]:

$$\nu_{\text{calc}} = 17374 + C_{\text{CN}} \sum_{i=1}^{\text{CN}} n_i \delta_i$$

(1.17) with C_{CN} being a constant depending on the coordination number and n_i the number of a given type of bound atom. This phenomenological equation is helpful but one has to realize that δ_i strongly depends on the Eu-L distance; so that the relationship does not always yield satisfying results, if distances are not standard. Moreover only a limited number of δ_i parameters have been worked out.

1.2.5.3. Population analysis

When several Ln^{III} sites are present, their relative populations P_i can be determined by analysis of the multi-exponential luminescence decay

$$I(t) = A + I_0 \sum_{i=1}^n B_i e^{-k_i t}, \quad P_i = \frac{B_i/k_i}{\sum_{i=1}^n \frac{B_i}{k_i}} \quad (1.18)$$

In these cases, an average lifetime can be defined:

$$\langle \tau \rangle = \frac{\sum_i B_i \tau_i^2}{\sum_i B_i \tau_i} = \frac{\sum_i B_i k_i}{\sum_i B_i k_i^2} \quad (1.19)$$

While recording the decay, one has to make sure that (1) there is no artefact at the beginning of the decay (remaining light from the light pulse), (2) the decay is

recorded during at least 5–6 lifetimes, (3) the signal at the end goes back to the background value, and (4) the decay is defined by a sufficient number of data points. Even if experimental data are of high quality, it is difficult to determine populations smaller than 5 % and to decompose decays with more than 2 or 3 exponential functions or when the two lifetimes are either very different or quite similar. The example given on Fig. 1.10 illustrates a bi-exponential analysis of Eu (5D_0) decay.

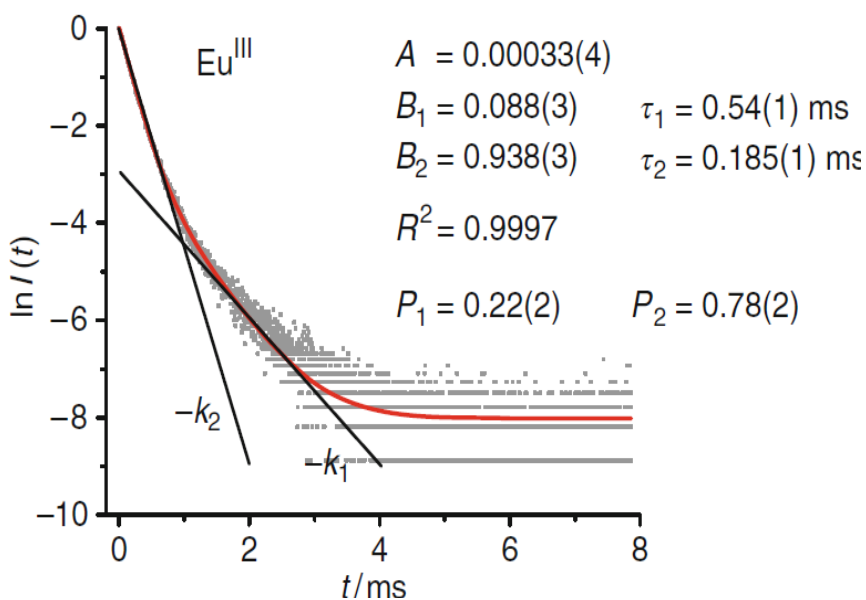


Fig 1.10: Luminescence decay for an Eu^{III} sample with its bi-exponential analysis; straight lines correspond to the two decay rates and the red line is the calculated fit

Alternatively since the intensity of the MD transition $^5D_0 \rightarrow ^7F_1$ for Eu^{III} is independent of the metal–ion environment, a spectral decomposition of the transition recorded under broad band excitation into its components measured under selective laser excitation, followed by integration yields the population P_i of each site [46].

1.2.5.4. Site symmetry

This aspect is related to the Stark splitting of the levels described in Table 1.5. Again here, Eu^{III} luminescence is the easiest to analyze given the non-degeneracy of the emissive 5D_0 level. When allied to high-resolution selective laser excitation of components of the $^5D_0 \rightarrow ^7F_0$ transition, symmetry of multi-site molecules and materials can be worked out easily, based on group-theoretical considerations [46, 47]. Such detailed analyses are not discussed here. On the other hand, the Eu($^5D_0 \rightarrow ^7F_1$) transition represents an interesting case. A simple examination of its splitting

tells immediately at which crystal system the compound belongs: cubic if only 1 component is seen, axial (i.e., hexagonal, tetragonal, or trigonal, labeled A and E in group-theoretical notation) if there are two components and low symmetry if the maximum splitting of three appears. For truly low-symmetry species, the three components are equally spaced and tend to have the same intensity. However, when the coordination sphere is close to an idealized higher symmetry, the splitting is unsymmetrical. In this case, three important pieces of information can be extracted for symmetries close to axial symmetry: (1) the sign of the 5^9 crystal-field parameter, which depends on the relative energetic position of the A and E sublevels of 7F_1 , (2) its value thanks to a phenomenological relationship between $\Delta E(A-E)$ and this parameter [48], and (3) the extent of the deviation from the idealized symmetry given by the splitting of the E sublevel. In the example depicted in Fig. 1.11, the crystal field parameter has a value of ca-600 cm^{-1} and the coordination polyhedron EuN_6O_3 appears to be only slightly distorted from the idealized D_{3h} symmetry with $\Delta E(A-E)$ equal to 31 cm^{-1} .

Table 1.5: Number of stark sub-levels versus the value of quantum number J

Symmetry	Site symmetry	Integer J									
		0	1	2	3	4	5	6	7	8	
Cubic	T, T_d, T_h, O, O_h	1	1	2	3	4	4	6	6	7	
Hexagonal	$C_{3h}, D_{3h}, C_6, C_{6h}, C_{6v}, D_6, D_{6h}$	1	2	3	5	6	7	9	10	11	
Trigonal	$C_3, S_6, C_{3v}, D_3, D_{3d}$										
Tetragonal	$C_4, S_4, C_{4h},$ $C_{4v}, D_4, D_{2d}, D_{4h}$	1	2	4	5	7	8	10	11	13	
Low	$C_1, C_s, C_2, C_{2h}, C_{2v}, D_2, D_{2h}$	1	3	5	7	9	11	13	15	17	
Symmetry	Site symmetry	Half-integer J									
		1/2	3/2	5/2	7/2	9/2	11/2	13/2	15/2	17/2	
Cubic	T, T_d, T_h, O, O_h	1	1	2	3	3	4	5	6	6	
All others ^a	See above	1	2	3	4	5	6	7	8	9	

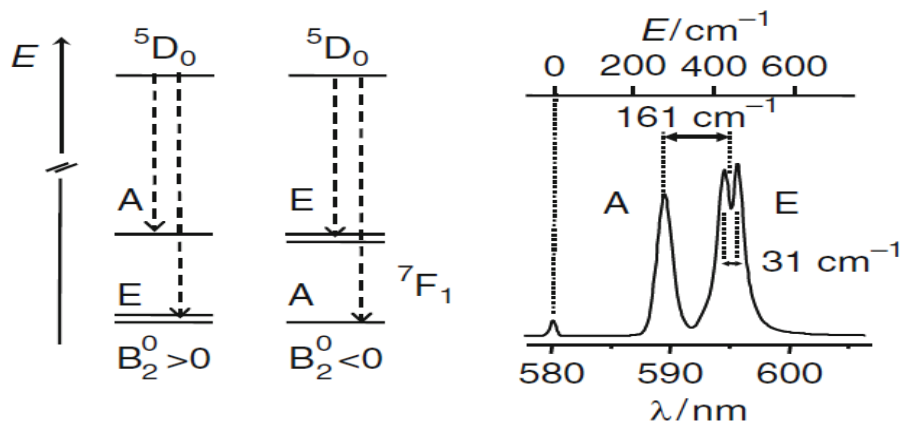


Figure 1.11: Left: Ligand-field splitting of the Eu (7F_1) sublevel and sign of the B_2^0 parameter. Right: High resolution ${}^5D_0 \rightarrow {}^7F_1$ spectra [49].

1.2.5.5. Strength of Ln-L bond

The intensity of vibronic satellites, which are particularly intense, when associated with hypersensitive transitions, is proportional to the ligand-to-metal bond strength and constitutes a useful measure of the latter [50]. For instance, $\text{Eu}({}^5D_0 \rightarrow {}^7F_2)$; in addition, the 7F_2 level corresponds to an energy range (1,000–1,500 cm^{-1}), in which the density of phonon states is usually large.

1.2.5.6. Solvation state of Ln^{III} ion

Lanthanide luminescence is very sensitive to the quenching by high-energy vibrations, particularly O–H as explained in earlier section. This quenching can be turned into an advantage for calculating the number q of inner-sphere bonded water molecules by measuring the lifetime in both water and deuterated water. Provided that the O–H quenching is the main non-radiative process operating (i.e. in absence of other temperature-dependent processes such as photo-induced electron transfer or back transfer), phenomenological equations can be worked out:

$$q = A(\Delta k_{\text{obs}} - B) - C, \quad \Delta k_{\text{obs}} = k_{\text{H}_2\text{O}} - k_{\text{D}_2\text{O}} = \frac{1}{\tau_{\text{H}_2\text{O}}} - \frac{1}{\tau_{\text{D}_2\text{O}}} \quad (1.20)$$

where A, B, and C are phenomenological Ln-dependent (and sometimes ligand depending) parameters determined using series of compounds with known hydration numbers. Parameter A describes the inner-sphere contribution to the quenching, parameter C the outer-sphere contribution of closely diffusing solvent molecules, while the corrective factor B, which has the same units as k , accounts for the presence of other deactivating vibrations (C–H, N–H etc).

1.2.5.7. Donor-Acceptor distances

Distances between two metal-ion sites or between a chromophore and an ion, R_{DA} , may be determined by measuring the lifetimes of the donor (D) in presence (τ_{obs}) and in absence (τ_0) of the acceptor (A):

$$\eta_{et} = 1 - \frac{\tau_{obs}}{\tau_0} \quad (1.21)$$

Assuming Forster's dipole-dipole mechanism of transfer, the efficiency of the latter is given by:

$$\eta_{et} = \frac{1}{1 + (R_{DA}/R_0)^6} \quad (1.22)$$

R_0 being the D-A distance, for which the quantum yield is 50%; this parameter depends on the nature of the D-A pair involved.

1.3. Luminescence Quenching:

Quenching refers to any process which decreases the fluorescence intensity of a given substance. A variety of processes can result in quenching, such as excited state reactions, energy transfer, complex-formation and collisional quenching. As a consequence, quenching is often heavily dependent on pressure and temperature. Quenching processes broadly involves two processes – electron transfer or energy transfer. In both cases, the excited state energy of the luminophore (the luminescent species) is deactivated due to the presence of the quencher. There are two scenarios by which, quenching are generally modelled: Dynamic (collisional) and static.

Dynamic quenching results from collisions between excited state and quencher. In this case, the excited fluorophores experience contact with an atom or molecule that can facilitate non-radiative transitions to the ground state. Common quenchers include O_2 , I^- , Cs^+ and acrylamide.

In the simplest case of collisional quenching, the following relation, called the Stern-Volmer equation, holds:

$$\frac{F_0}{F} = 1 + K_{SV}[Q]$$

(1.23)

where F_0 and F are the fluorescence intensities observed in the absence and presence, respectively, of quencher, $[Q]$ is the quencher concentration and K_{SV} is the Stern-Volmer quenching constant. Thus, a plot of F_0/F versus $[Q]$ should yield a straight

line with a slope equal to K_{SV} . Such a plot, known as a Stern-Volmer plot (Fig. 1.12), is shown below for the case of fluorescein quenched by iodide ion (I⁻).

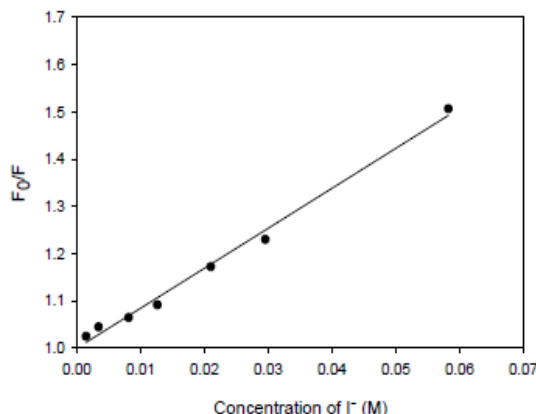


Figure 1.12: Stern Volmer plot in case of dynamic quenching [51].

$K_{SV} = k_q \tau_0$ where k_q is the bimolecular quenching rate constant (proportional to the sum of the diffusion coefficients for fluorophore and quencher) and τ_0 is the excited state lifetime in the absence of quencher. Collisional quenching also shortens the lifetime of fluorophore as can be seen from Figure 1.13. For purely collisional quenching, also known as dynamic quenching:

$$\frac{F_0}{F} = \frac{\tau_0}{\tau} = 1 + k_q \tau [Q] \quad (1.24)$$

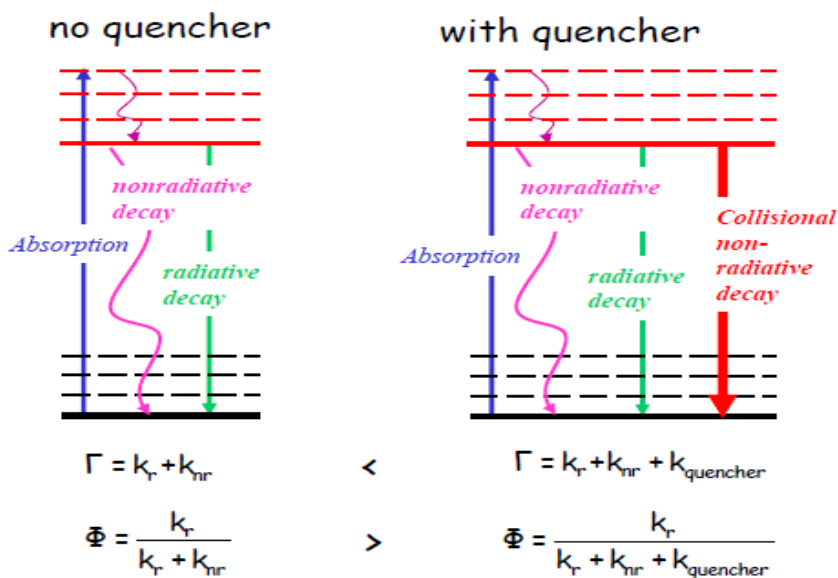


Figure 1.13: Effect of collisional quenching on lifetime of fluorophore [51]

In some cases, the fluorophore can form a stable complex with another molecule. If this ground-state is non-fluorescent, then we say that the fluorophore has been

statically quenched. In such a case, the dependence of the fluorescence as a function of the quencher concentration follows the relation:

$$\frac{F_0}{F} = 1 + K_a [Q] \quad (1.25)$$

where K_a is the association constant of the complex. Even in this case, plot of F_0/F versus $[Q]$ should yield a straight line with a slope equal to K_a . Figure 1.14 pictorially represents static quenching phenomenon. Static quenching only affects the complexed fluorophores. The properties of the uncomplexed fluorophores are not changed.

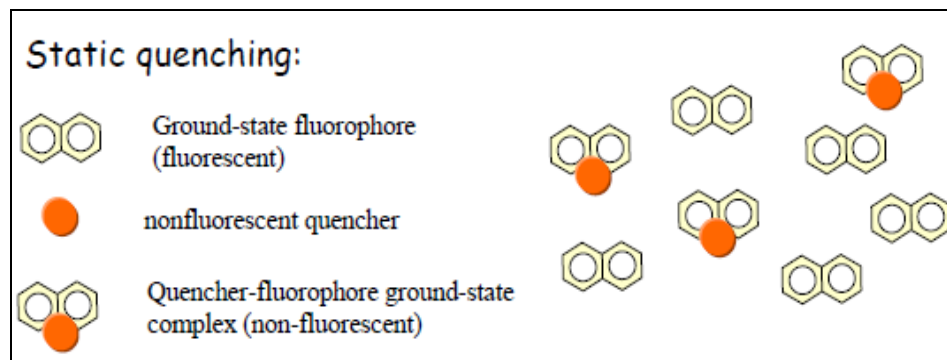


Figure 1.14: Schematic of static quenching [51]

The question that immediately arises now is that if plots of emission intensity against quencher concentration both produce straight line graphs, how do we know which type of quenching is occurring? The answer lies in the nature of each type of quenching. For dynamic quenching as can be seen from Figure 1.15, all luminophores are affected by the quenching process, as it is probable that they will all collide with a quencher during their excited state lifetime; so both emission intensity and lifetime reduced on increasing quencher concentration. For static quenching by association as can be seen from Figure 1.15, only luminophore-quencher associations result in reduction in emission; unassociated luminophores are free to luminesce as if there was no quencher present. Increasing quencher concentration affects emission intensity, because there are more associations, but not emission lifetime, as the unassociated luminophores can emit in the absence of quencher. (Note that these two scenarios are the extremes, and there are cases where a mixture of both static and dynamic quenching may occur simultaneously.) Therefore the diagnostic test for assigning whether a quenching mechanism is dynamic or static is to compare how the emission intensity and emission lifetime change as a function of increasing concentration as can be seen from Figure 1.16. In the case of dynamic quenching, plots of relative emission intensities and emission lifetimes will be the same, changing on increasing quencher

concentration. For static quenching, only a plot of relative emission intensity will change, the emission lifetime plot will have slope close to zero.

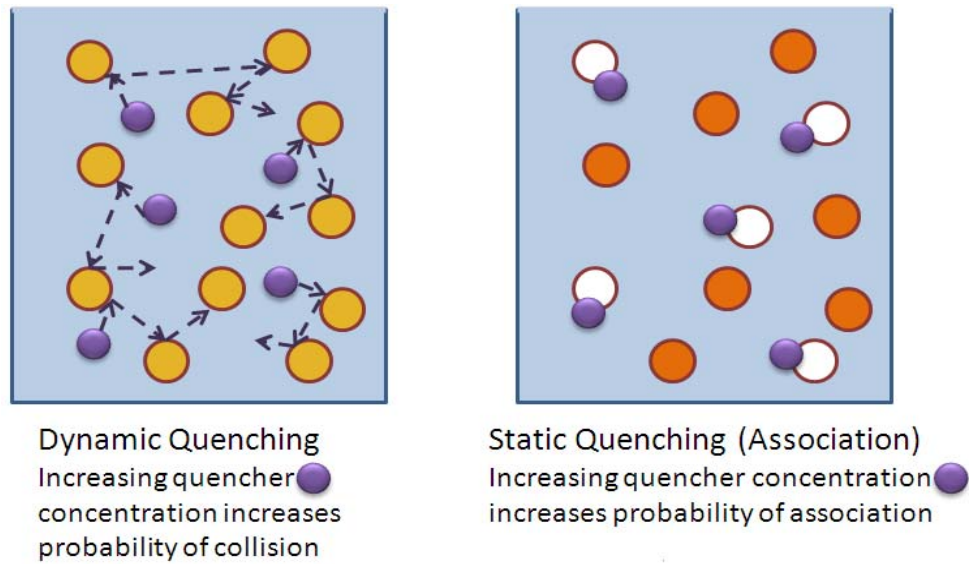


Figure 1.15: Schematic of dynamic versus static (association) quenching [52]

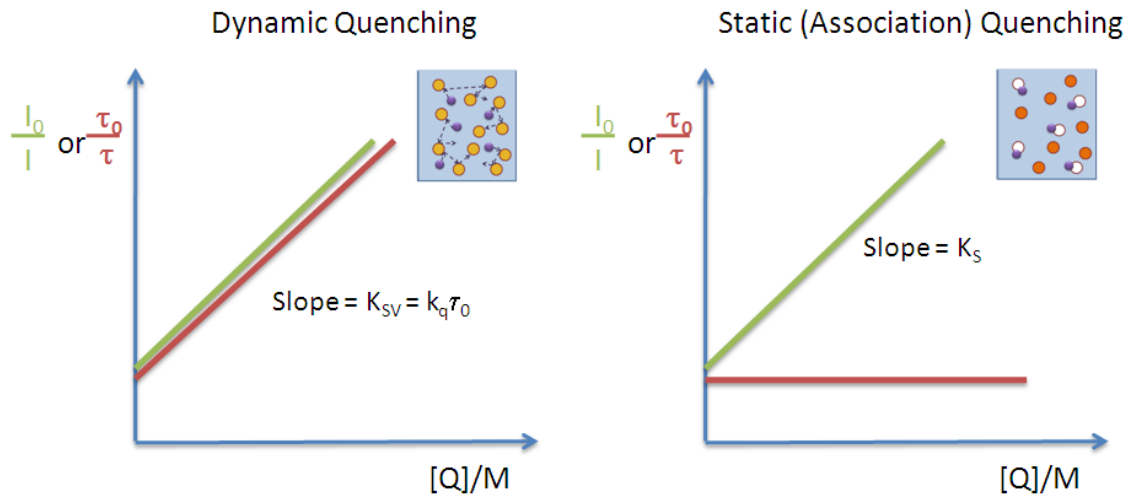


Figure 1.16: Model diagnostic plots to distinguish between dynamic and static quenching [52]

If both static and dynamic quenching occur in the sample, the following relation holds:

$$\frac{I_0}{I} = (1 + k_q \tau_0 [Q]) * (1 + k_a \tau [Q]) \quad (1.26)$$

In such a case, then a plot of F_0/F versus $[Q]$ will give an upward curving plot as can be seen from Figure 1.17. The upward curvature occurs because of the $[Q]^2$ term in the equation.

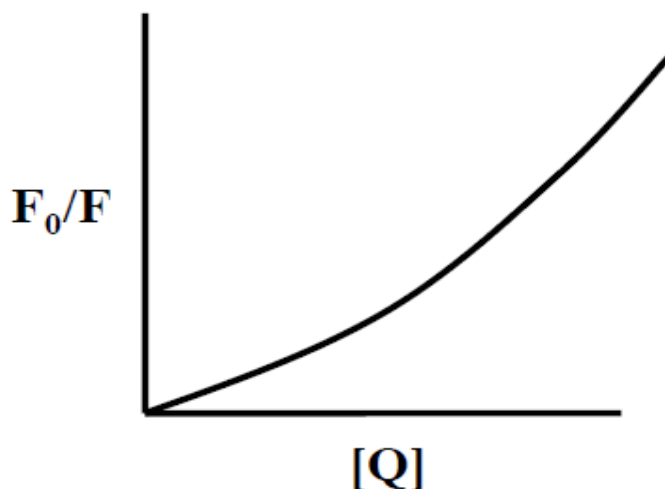


Figure 1.17: Stern Volmer plot in case of when both dynamic and static quenching occur simultaneously [51].

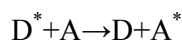
1.3.1. Multiphonon Emission

Non-radiative processes can also play an important role. The energy of the excited state can be taken up by the surroundings in the form of vibrational energy, often referred to as phonon emission. The effectiveness of this process depends on the availability of high-energy vibrations in the surroundings and the energy difference between the energy levels of the lanthanide ion. The fundamental vibrations of the chemical bonds in the surroundings and the energy of the vibration are determined by the reduced mass of a bond. Especially bonds with hydrogen have a small reduced-mass and therefore high vibrational energies. These bonds are therefore able to take up large amounts of energy and effectively quench lanthanide ions with large separations between the energy levels. The visible emitting ions Eu^{3+} and Tb^{3+} have large gaps between the emissive $^5\text{D}_0$ and $^5\text{D}_4$ level of 12,000 and 15,000 cm^{-1} , respectively; but still these ions and especially Eu^{3+} are quenched substantially, when the ions are dissolved in water (vibrational energy: ν_{max} 3500 cm^{-1}). The quenching efficiency is strongly dependent on the number of vibrational quanta that are needed to bridge the gap between the lowest emitting level and the highest non-emitting level of the lanthanide ion. The intensity of the vibronic transition is dependent on the square overlap integral (Franck-Condon factor) of the initial and final vibrational

states and this overlap decreases rapidly as the number of vibrational quanta increases [53]. This is summarized in the theory of the energy gap law [14]. The observation of luminescence of a lanthanide ion in solvents with high vibrational energies (water) is dependent on the energy difference between the lowest radiative level and the highest non-radiative level. For example, Tb^{3+} in water shows reasonable luminescence but Eu^{3+} luminescence is almost completely quenched. The Eu^{3+} ion is quenched by energy transfer to the 4th overtone of the OH bonds, while the Tb^{3+} ion is quenched by energy transfer to the 5th overtone of the OH bond. Another important factor governing the efficiency of quenching is the distance between the lanthanide ion and the quencher group.

There are a few distinct mechanisms by which energy can be transferred nonradiatively (without absorption or emission of photons) between the lanthanide ion (donor) and the quenching site (acceptor). Non-radiative energy transfer has been observed and treated theoretically by Forster [54] and was developed by Dexter [55]. Forster developed a theory for the rate of energy transfer by electric dipole-dipole interaction [54], which was later extended by Dexter to involve the higher multipole interactions [55]. Dexter also created a model for the short donor-acceptor distance based on the exchange interaction [55]. Inokuti and Hirayama [56] developed numerical methods on energy transfer that can be used to determine the mechanism responsible for energy transfer.

The non-radiative transfer of an electronic excitation from a donor to an acceptor is represented by



Where D and A represent the ground states of donor and acceptor respectively, while D^* and A^* represents the excite state (see Figure 1.17).

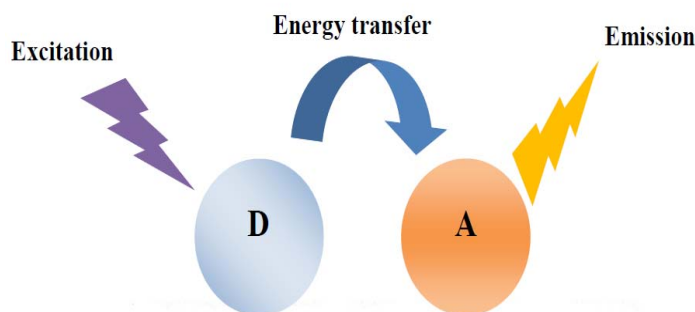


Figure 1.18: Illustration of energy transfer phenomenon.

The process consists of the following steps [57]:

- Absorption of the excitation energy by the donor center D
- Relaxation of the lattice about the donor
- Transfer of energy from donor center D to the acceptor center A
- Relaxation of the lattice about the acceptor
- Emission of luminescence by the acceptor center A

Figure 1.18 illustrates these steps [58].

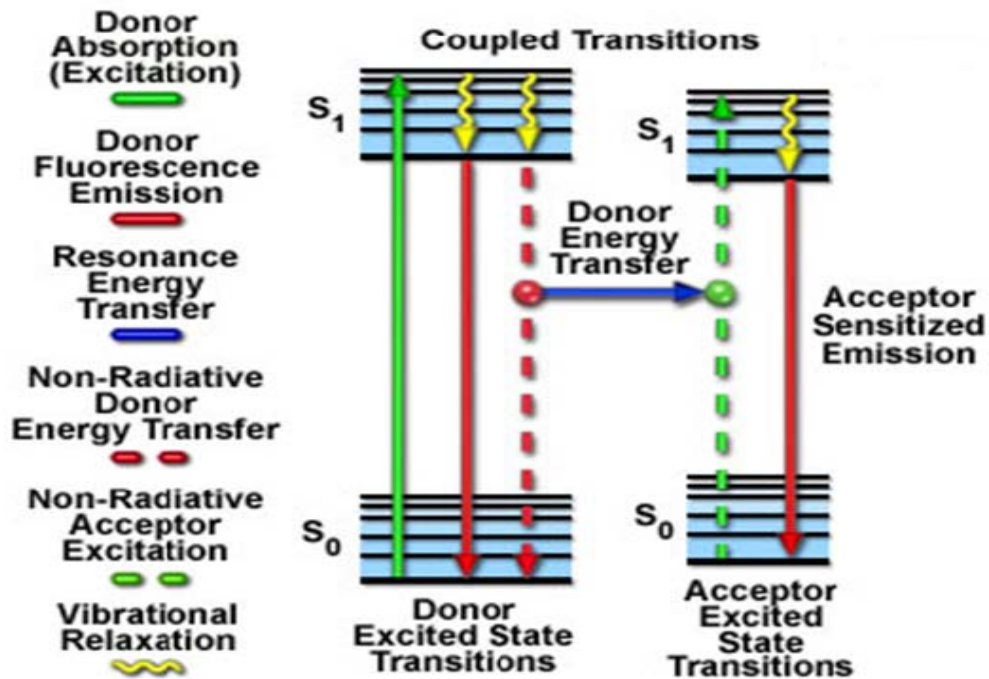


Figure 1.19: Coupled transitions between donor emission and acceptor absorbance in fluorescence resonance energy transfer. The coupled transitions are drawn with dashed lines. The phenomenon of energy transfer is illustrated by a blue arrow [58].

Förster resonance energy transfer (FRET or FET) is a dynamic quenching mechanism because energy transfer occurs, while the donor is in the excited state. FRET is based on classical dipole–dipole interactions between the transition dipoles of the donor and acceptor and is extremely dependent on the donor–acceptor distance, R , falling off at a rate of $1/R^6$. FRET also depends on the donor–acceptor spectral overlap (see Figure 1.19) and the relative orientation of the donor and acceptor transition dipole moments. FRET can typically occur over distances up to 100 Å. Dexter (also known as exchange or collisional energy transfer) is another dynamic quenching mechanism.

Dexter energy transfer is a short-range phenomenon that falls off exponentially with distance (proportional to e^{-R}) and depends on spatial overlap of donor and quencher molecular orbitals. In most donor-fluorophore–quencher-acceptor situations, the Förster mechanism is more important than the Dexter mechanism. With both Förster and Dexter energy transfer, the shapes of the absorption and fluorescence spectra of the Ln^{3+} are unchanged. In Förster's model, energy is transferred from the donor D to the acceptor A by multipole interactions, while in Dexter's model energy transfer occurs by quantum-mechanical exchange of the excited electron between D and A. Although the nature of the two models is different, both of them require overlap between the emission spectrum of the donor and the excitation spectrum of the acceptor. Figure 1.20 represents spectral overlap between the donor (Ln^{3+}) emission spectrum and the acceptor (Quencher) absorption spectrum.

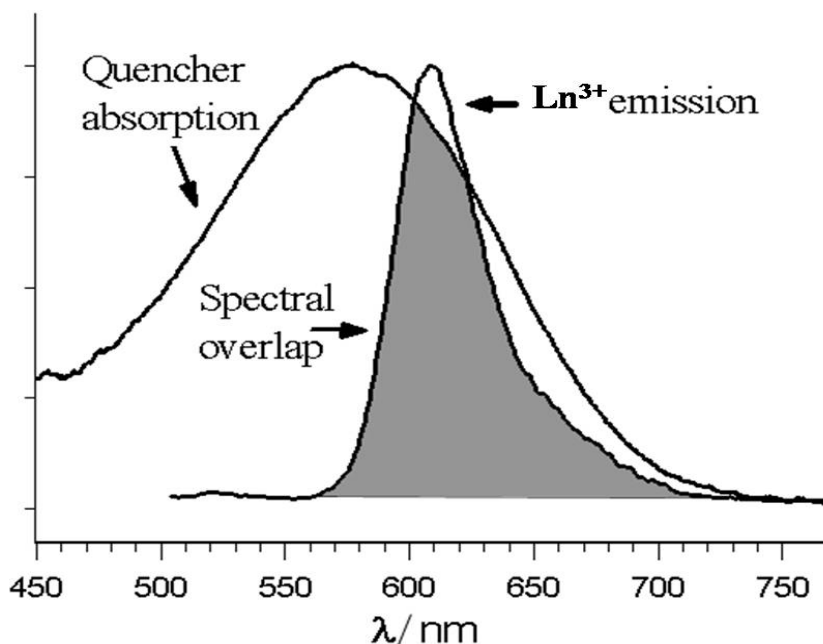


Figure 1.20: Donor emission and quencher absorption spectral overlap [59].

Schematic diagram for Förster's and Dexter's models of energy transfer is illustrated in Figure 1.21 [60]. Singlet-singlet energy transfer can happen via Förster's model. However, the multipole interaction will not involve the triplet-triplet energy transfer, because that violates the Wigner spin conservation law, which states that the exchange mechanism (Dexter's model) is based on the Wigner spin conservation rule;

thus the spin-allowed process could be either singlet-singlet energy transfer or triplet-triplet energy transfer.

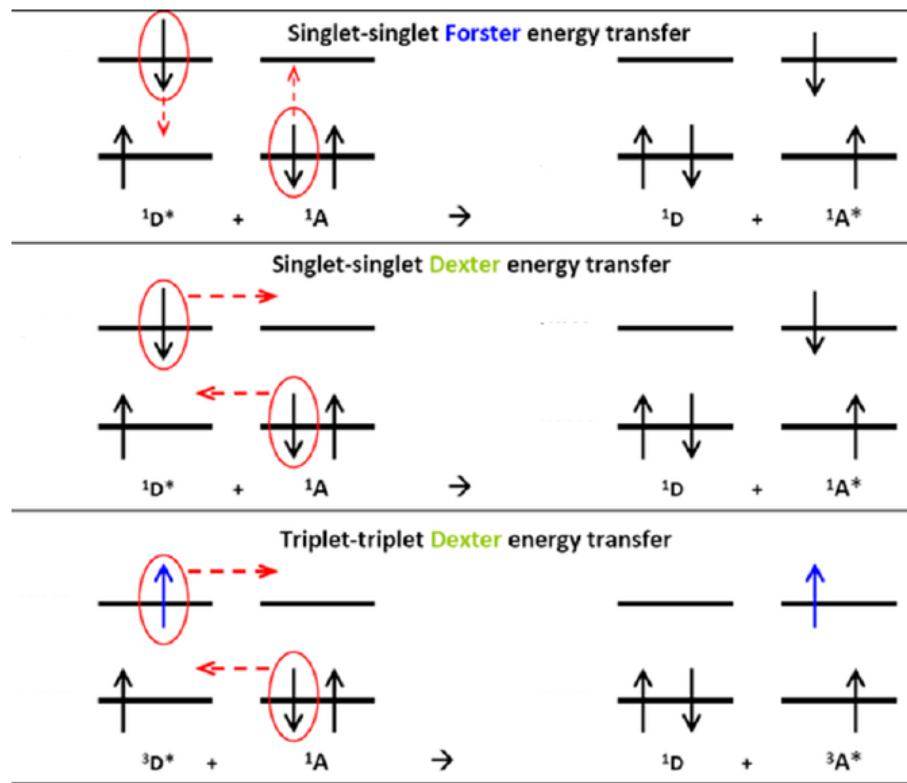


Figure 1.21: Schematic diagram for Forster and Dexter energy transfer [60].

1.3.2. Energy transfer between lanthanide ions

Another factor in the quenching of lanthanide ions is the interaction between the lanthanide ions, of the same or different type. Two different lanthanide ions can transfer energy, when they have similar separations between the energy levels. The small mismatch in energy can be compensated for by the emission or uptake of a phonon. Energy transfer of one lanthanide ion can be used to enhance luminescence of the other lanthanide ion. For example, the lanthanide couple Yb^{3+} - Er^{3+} , where the Yb^{3+} ion is excited at 980 nm and then transfers its energy to the Er^{3+} ion. The advantage of co-doping with Yb^{3+} is that the Yb^{3+} ions have a much higher absorption cross-section at 980 nm [61]. The optical gain of an amplifier co-doped with both these ions can be increased compared to an amplifier with only Er^{3+} ions [62]. Another example is the Tm^{3+} - Ho^{3+} couple, where Tm^{3+} is used as the sensitizer and Ho^{3+} as the emitter around 2 μm . The Tm^{3+} ion has an absorption peak around 790

nm, a wavelength where a lot of cheap semiconductor pump lasers are available. Pumping at this wavelength leads to an excited Tm^{3+} ion in the $^3\text{H}_4$ level, which self-quenches to the $^3\text{F}_4$ level producing two Tm^{3+} ions excited in the $^3\text{F}_4$ level. Energy transfer from the $^3\text{F}_4$ level of Tm^{3+} to the $^5\text{I}_7$ level of Ho^{3+} could theoretically lead to two excited Ho^{3+} ions per absorbed photon [63]. The same energy transfer process could also be used to enhance laser action of Tm^{3+} around 1480 nm [64]. Pumping of the Tm^{3+} ion into the $^3\text{H}_4$ level can lead to Tm^{3+} emission at 1480 nm by radiative decay to the $^3\text{F}_4$ level. If this $^3\text{F}_4$ level is relatively long lived, which is the case in some host materials, it is difficult to create a population inversion between the $^3\text{H}_4$ and $^3\text{F}_4$ level. Co-doping with Ho^{3+} leads to a fast depopulation of the $^3\text{F}_4$ level making population inversion possible.

1.3.3. Cross Relaxation

In a cross-relaxation process, two ions that are closely together interact and exchange energy. Examples of these processes are given in Figure 1.22 for Eu^{3+} and Pr^{3+} . A Eu^{3+} ion in the $^5\text{D}_1$ excited state can transfer its energy to a neighboring Eu^{3+} ion promoting it to the $^7\text{F}_3$ level. This leads to one ion in the $^5\text{D}_0$ excited state and one in the $^7\text{F}_3$ level. In the case of Pr^{3+} , the $^3\text{P}_0$ level can be quenched by cross-relaxation leading to an ion in the $^3\text{H}_6$ and an ion in the $^1\text{D}_2$ level. The $^1\text{D}_2$ level can be quenched again by cross-relaxation leading to an ion in the $^1\text{G}_4$ state and an ion in the $^3\text{F}_3$ level. Energy migration is another form of cross-relaxation between two ions of the same sort. The excited state energy levels of two identical ions are resonant, so the energy can be transferred to the neighboring ion by cross-relaxation and travel through the material hopping from one ion to the other. An increase in the doping concentration leads to a faster energy migration through the material, making the chance of meeting a quenching site higher. For reasons of cross-relaxation and energy migration, high doping concentrations often lead to a decrease in luminescence intensity and luminescence lifetime.

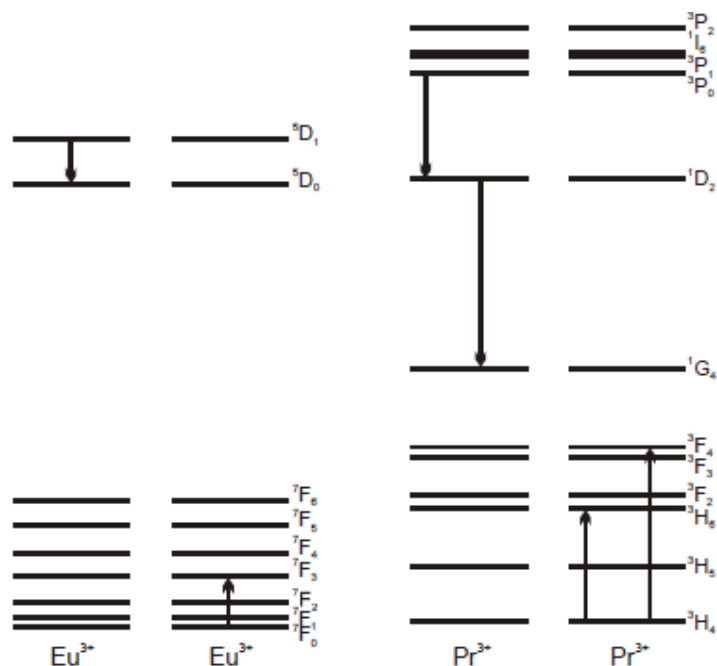


Figure 1.22: Cross-relaxation processes in Eu^{3+} and Pr^{3+} .

1.4. Lanthanide doped nanoparticles:

1.4.1 Significance of Lanthanide doped nanoparticles

Research and development of nanoscale luminescent and laser materials are part of the rapidly advancing nanoscience and nanotechnology. Because of unique spectroscopic properties and luminescent dynamics of f -electron states, doping luminescent rare earth ions into nano-hosts has been demonstrated as an optimistic approach to develop highly efficient and stable nanophosphors for various applications. Luminescence- or fluorescence-based technologies have been widely utilized in various areas such as solid state lighting, displays, illuminations, optical communications, biological detection, diagnosis, medical imaging, radiation detection, homeland security, forensic tracking, equipment control, safety and alarm systems, pressure measurement, temperature sensing and dark matter exploration. Luminescence is a ubiquitous phenomenon, which can be seen day in and day out. Our life would not be so beautiful and our society would not be so safe without luminescence. The emerging field of nanotechnology has become an important area in science and technology. Nanotechnology is a major factor in the advancement of luminescence technology—it makes luminescence much brighter and enables luminescence for some special applications. Of the numerous publications and reports on nanomaterials, half are related to luminescence in one way or another. More than

half of nanoscale materials exhibit intense luminescence— these include semiconductor nanoparticles or quantum dots, organic nanoparticles, metallic nanoparticles, doped nanoparticles, carbon nanotubes, and insulator nanoparticles. Quantum size confinement results in brighter luminescence and easy tunability of the emission color of semiconductor nanoparticles. Along with other advantages, such as small size, water-solubility, good photo-stability, narrow emission bandwidth, and surface functionalities—luminescence nanomaterials have tremendous potential for practical applications. One special application is for biological *in vivo* detection, because the nanoscale size makes it possible for nanoparticles to penetrate into deep into tissue and even into the cellular nucleus. Quantum size confinement can not only modify the energy structure and luminescence behaviors of pure semiconductor nanoparticles, but also affect the energy structure and physical properties of doped nanomaterials. ZnS: Eu²⁺ is a good example of how quantum size confinement affects doped nanomaterials can result in applications such as a new type of solid-state source for lighting. No luminescence from Eu²⁺ could be seen in bulk ZnS, while strong green emission can be observed from Eu²⁺ in ZnS nanoparticles as a result of quantum size confinement. There are many other examples of using the quantum size effect to modify and enhance luminescence materials. Bulk luminescence materials or phosphors are employed in a broad range of applications such as cathode ray tubes, projection television screens, fluorescent tubes, X-ray detectors, and biomedical probes. However, luminescence based on bulk materials offer extremely limited opportunities for further reduction in size, complexity, and power consumption.

Fortunately, due to the physics of quantum size confinement, nanoscale phosphors provide an avenue for further advancing solid-state luminescence. Compared to bulk materials, nanoparticles exhibit greater electron–hole overlap, thereby yielding greater oscillator strength and enhanced luminescence quantum efficiency. Improved oscillator strength is important because a phosphor’s emission decay lifetime is inversely proportional to its oscillator strength and typically shortens as particle size decreases. Similarly, by overcoming the inherent loss of luminescence efficiency normally associated with smaller size materials, luminescence nanoparticles hold the promise of practical phosphors that are considerably smaller than what can be achieved currently. One interesting phenomenon of optically excitable nanoparticles is upconversion luminescence, in which the energy of the emitted photon is higher than that of the excitation photon. Upconversion luminescence is being investigated

extensively in doped nanoparticles and may find applications in optical storage, radiation detection, infrared detection, and dosimetry. Upconversion nanoparticles are particularly promising for biological imaging, because auto-fluorescence can be overcome and higher imaging resolution can be obtained. Rare earth-doped insulator nanoparticles such as $\text{Y}_2\text{O}_3:\text{Eu}^{3+}$ and $\text{LaPO}_4:\text{Tb}^{3+}$ represent a new type of high efficiency luminescence material. Quantum size confinement is not as critical for insulator nanoparticles as it is for semiconductor nanoparticles; however, because of their large surface-to-volume ratios, insulator nanoparticles exhibit some novel properties that make them suitable for numerous useful applications. For example, as phosphors, nanoparticle insulators are more efficient and produce less light-scattering than micro-sized particles. Also, as biological labelling agents, insulator nanoparticles are much less toxic than semiconductor nanoparticles [65]. Most recently, doped luminescence nanoparticles have been proposed for biological activation. The strong scintillation luminescence of doped nanoparticles has been investigated as a light source for photodynamic activation to enable photodynamic therapy for deep cancer treatment. RE-doped nanoparticles have been suggested as a promising new class of fluorescent probes. In comparison to organic dyes and semiconductor quantum dots, RE-doped nanocrystals show superior chemical and optical properties, including low toxicity, large effective Stokes shifts, sharp emissions, long fluorescence lifetimes, and high resistance to photobleaching [66]. In addition, these nanoparticles can enable time-resolved fluorescence imaging for quantitative detection of antigens as well as tissue-specific transcripts and genes. More importantly, the RE nanoparticles have the potential to be used for non-invasive, non-destructive, and real-time in vivo diagnosis of various diseases, including atherosclerotic plaques, which can lead to stroke and heart disease [67].

1.4.2 Difference in Luminescent properties of Lanthanide doped nanoparticles w.r.t bulk

1.4.2.1. Excitation and emission spectra

Nanoparticles due to an enlarged surface area and small domain of the crystal itself, different properties compared to the bulk materials are observed. First of all, the emission lines in nanocrystalline materials show extra inhomogeneous broadening [68]. Not all crystal sites are the same, especially due to the enormous increase in surface sites compared to bulk sites. The increase in surface area was found to be an advantage for $\text{Y}_2\text{O}_3:\text{Eu}$ nanoparticles excited with cathode rays [69]. The synthesized

nanocrystalline materials have a much better surface termination than the powdered bulk material leading to higher luminescence efficiency. A blue shift in the peak emission wavelength with decreasing particle size was also reported for Y_2O_3 nanoparticles doped with Eu^{3+} [70]. $\text{Y}_2\text{O}_2\text{S}$ nanoparticles doped with Er^{3+} showed a population of the energy levels that was only observed in nanocrystalline materials and not in the bulk [71]. Laser excitation of the Er^{3+} ions in nanocrystals at a temperature below 7 K, led to a saturation of the levels just above the ground state. Figure 1.23 shows a schematic and simplified excitation spectrum of Er^{3+} emission in bulk and nanocrystalline $\text{Y}_2\text{O}_2\text{S}$ at 2.6 K.

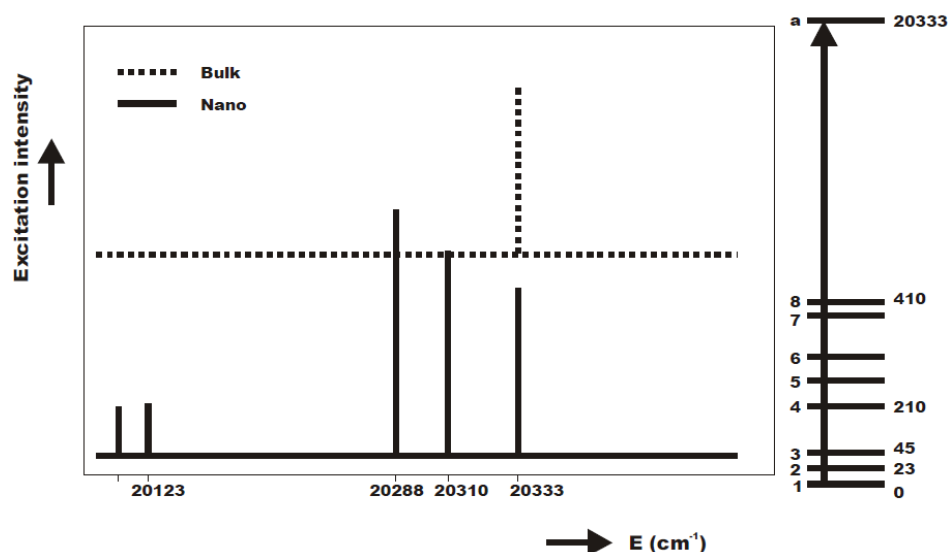


Figure 1.23: Schematic excitation spectrum of $\text{Y}_2\text{O}_2\text{S}:\text{Er}$ nanoparticles and bulk $\text{Y}_2\text{O}_2\text{S}:\text{Er}$ at 7 K [71].

The excitation spectrum of the bulk material only shows a single line at $20,333\text{ cm}^{-1}$ from the absorption of the lowest level of the ground state to level **a** of the excited state. In the nanocrystals absorptions from level **2**, **3**, **4**, and **5** were also observed in the excitation spectrum of the Er^{3+} emission. At low temperatures, the levels just above the ground state become populated, because after excitation the ion does not fully decay to the ground state. The explanation given for this behavior is the absence of the very small phonon energies in nanocrystals, because of the “ending” character of the crystal domain. The vibrational modes in a nanocrystal become discrete and are no longer band-like as in bulk materials. In bulk materials, the higher levels of the ground state decay very rapidly to the lowest level even at low temperatures. A

similar effect was found for Eu_2O_3 nanoparticles [72]. A lot of energy transfer processes rely on the matching of the energy levels by the uptake or emission of low energy phonons. The absence of low energy phonons can have a significant effect on efficiency of energy transfer processes in nanoparticles [73].

1.4.2.2. Symmetry of the lanthanide site

The symmetry of the lanthanide site can also be changed in nanocrystalline materials [74]. Decreasing the size of YBO_3 : Eu nanoparticles leads to an increase of the $^5\text{D}_0 \rightarrow ^7\text{F}_2$ emission peak compared to the other emission lines indicating that the symmetry around the Eu^{3+} ion is lowered. A similar effect was found for 14 nm sized YVO_4 : Eu particles [75]. These nanoparticles were excited using a narrow laser line and the excitation wavelength was slowly scanned over an absorption peak. Different Eu^{3+} sites with different site symmetries and corresponding different luminescence lifetimes were found. The sites with decreased site symmetry were attributed to surface sites, so the lower lifetimes are found at the nanoparticle surface. Lanthanide-doped nanoparticles also offer the possibility to change the environment around the lanthanide ion, while keeping the lanthanide ion in the same crystal site. This proved to be valuable in the determination of the influence of the refractive index on the luminescence lifetime. The influence of the refractive index on the luminescence lifetime of Eu^{3+} organic complexes was studied by varying the solvent in which the complex was dissolved [76]. In these complexes, special care has to be taken that the coordination of the lanthanide is not changed, while changing the solvent. In nanoparticles, the ions are doped inside the crystal and local coordination of the ion is not changed with variation of the solvent. Y_2O_3 : Eu particles showed a correlation between the refractive index and the luminescence lifetime of the Eu^{3+} ion, when the particles were dispersed in different environments [77].

1.4.3 Lanthanide ion in semiconductor nanoparticles

The shielding of lanthanide ions could be achieved by doping them in the core of nanoparticles and as a result the luminescence properties of the ions in an organic environment could be improved. Semiconductor nanoparticles have the advantage of high molar absorption coefficients and the possibility to excite them with charge carriers generated by electricity. Doping of lanthanide ions in semiconductor nanoparticles could have enormous advantages over the doping in nanoparticles of

isolator host materials. Energy transfer from the semiconductor host to the lanthanide ion would have the advantage of a broad excitation band for photo-excitation and offer the possibility of electroluminescence of the lanthanide ion. At the same time the lanthanide ion is shielded from the organic environment. Energy transfer from semiconductor nanoparticles to lanthanide ions has been reported in a large number of publications. The best known example is the energy transfer of silicon nanoparticles to Er^{3+} ions doped in silicon enriched SiO_2 waveguides [78]. Energy transfer of other semiconductor nanoparticles to other lanthanide ions is also described, like from CdS to Eu^{3+} and SnO_2 to Eu^{3+} [79, 80]. These examples are all in solid state glasses or sol-gel derived samples. Reports about the doping of lanthanide ions in nanoparticles passivated by organic ligands have also appeared. The doping of Tb^{3+} ions in ZnS nanoparticles was described in several papers [81]. Okamoto *et al.* reported luminescence studies on CdS doped with Eu^{3+} [82], and ZnS doped with Eu^{3+} was reported by Qu *et al* [83]. The results of these studies have been under discussion recently, when Bol *et al.* tried to reproduce the results [84]. They conclude that the lanthanide ions are not incorporated in the nanoparticles, but probably adsorbed at the surface. The excitation spectra of their reaction products are dominated by the $4f$ absorption bands of the lanthanide ions suggesting that no energy transfer takes place from the semiconductor host to the lanthanide ion

1.5. Motivation for the present work:

Studies of lanthanide ion distribution in inorganic oxides with multiple sites have attracted much attention, because they may allow better understanding of the correlations between structure and properties such as color, magnetic behavior, catalytic activity, and optical properties, *etc.*, which are strongly dependent on the occupation of various sites by metals ion. Lanthanide dopants are well known structural probes and can be used to understand the local structures in crystalline materials, probing the structure of biological molecules etc. The absorption of light by an electron moving around a nucleus occurs, thanks to operators linked to the nature of light: the odd-parity electric dipole (ED) operator, the even-parity magnetic dipole (MD) and electric quadrupole (EQ) operators. Not all transitions are permitted, since they have to obey selection rules. One of these is the so-called Laporte's (or parity

rule) requiring that for ED transitions, the sum of the angular momenta of the electrons in the initial and final states must change by an odd integer.

Magnetic dipole transitions within the $4f^n$ configuration, which obey the selection rule $\Delta J = 0, \pm 1$ are allowed (except for $J = 0$ to $J = 0$), but have low oscillator strengths. The electric dipole intra- $4f$ transitions are in principle parity forbidden, and those transitions that do not occur within the ground multiplets may also be spin-forbidden ($\Delta S \neq 0$). However in an asymmetric environment, the electric dipole f - f transitions become weakly allowed (with an oscillator strength of 10^{-6}) by mixing of opposite parity wave functions (primarily the $5d$ wave functions) into the $4f$ wave functions. In other words the parity forbidden intra- $4f$ transitions 'steal' some intensity from the allowed $4f$ - $5d$ transitions. The spin selection rule is relaxed by the fact that heavy atoms have large spin-orbit couplings. Because the oscillator strengths of these induced electric dipole transitions are in the same order of magnitude as those of magnetic dipole transitions, both transitions can be observed in lanthanide absorption and emission spectra. Since ED transitions in lanthanide ions are induced by the ligand field their strengths (or: probabilities) are quite sensitive to it. Strongly asymmetric or strongly interacting ligand fields lead to relatively intense ED transitions. The intensities of some ED transitions are extremely sensitive to coordinating environment, which means that they can be either completely absent or very intense, depending on the ligand field.

Based on asymmetry ratio, ED/MD one can have idea about the local site occupancy of lanthanide ion. Any luminescent lanthanide ion may act as a probe, but some ions bring more information (e.g. Eu^{III}), or are more luminescent (e.g. Tb^{III}) than others, which explains their preferential use. In view of its non-degenerate emissive state $^5\text{D}_0$, Eu^{III} ion is most appropriate as luminescent structural probe for the determination of the number of metal ion sites in a compound, their symmetry and their respective population. Other lanthanide dopants, such as Sm^{3+} and Dy^{3+} have rarely been used as a probe to understand the local structure of inorganic material. This really opens a new avenue for researcher working in the field of lanthanide luminescence.

Also understanding why different lanthanide ions behave differently in same host is an interesting problem, which can be solved by theoretical validation of experimental results. Time resolved fluorescence spectroscopy is an extremely sensitive method to

bring out the difference in luminescent properties of lanthanide ion occupying various sites.

Synthesizing nanoparticles of refractory oxide like ThO_2 and ZrO_2 at lower temperature is another challenge. Hosts like ThO_2 and Sr_2CeO_4 are having very low phonon energy are good candidates for luminescent materials; but they are relatively unexplored.

Bulk luminescence materials, or phosphors, are employed in a broad range of applications such as cathode ray tubes, projection television screens, fluorescent tubes, X-ray detectors, and biomedical probes. However, luminescence based on bulk materials offer extremely limited opportunities for further reduction in size, complexity, and power consumption.

Fortunately, due to the physics of quantum size confinement, nanoscale phosphors provide an avenue for further advancing solid-state luminescence. Compared to bulk materials, nanoparticles exhibit greater electron-hole overlap, thereby yielding greater oscillator strength and enhanced luminescence quantum efficiency. Improved oscillator strength is important because a phosphor's emission decay lifetime is inversely proportional to its oscillator strength and typically shortens as particle size decreases. Similarly, by overcoming the inherent loss of luminescence efficiency normally associated with smaller size materials, luminescence nanoparticles hold the promise of practical phosphors that are considerably smaller than what can currently be achieved. Rare earth-doped insulator nanoparticles such as $\text{Y}_2\text{O}_3:\text{Eu}^{3+}$ and $\text{LaPO}_4:\text{Tb}^{3+}$ represent new type of high efficiency luminescence materials. Quantum size confinement is not as critical for insulator nanoparticles as it is for semiconductor nanoparticles; however, because of their large surface-to-volume ratios, insulator nanoparticles exhibit some novel properties that make them suitable for numerous useful applications. For example, as phosphors, nanoparticle insulators are more efficient and produce less light-scattering than microsized particles. The symmetry of the lanthanide site can also be changed in nanocrystalline materials. Understanding the reason behind the same opens a new area of research.

Rare earths are really rare and most of their production is from china. Synthesising rare earth free luminescent materials and understanding the mechanism of their emission experimentally and theoretically is very important.

1.6. Scope of the thesis:

In the present investigation, a variety of inorganic matrices varying from binary oxides (ThO_2 , ZrO_2), silicates (Sr_2SiO_4), cerate (Sr_2CeO_4), zirconate (SrZrO_3) to phosphate ($\text{Zn}_2\text{P}_2\text{O}_7$)- undoped and doped with lanthanide ions- have been synthesised and their luminescent properties are investigated. The idea is to synthesize low phonon-energy luminescent materials (micro and nano regime) to minimize non-radiative losses. Nanoparticles - exhibit greater electron-hole overlap, thereby yielding greater oscillator strength and enhanced luminescence quantum efficiency. Another focus is to explore novel white light emitting material with high CRI index and efficiency. Synthesizing nanoparticles of refractory oxides like ThO_2 and ZrO_2 at lower synthesis temperature is another challenge. Host like ThO_2 , $\text{Zn}_2\text{P}_2\text{O}_7$, Sr_2CeO_4 having very low phonon energy are good candidates for luminescent materials; but they are relatively unexplored. Another novel approach is to use lanthanide ion as a structural probe (structure properties correlation). Further understanding why different lanthanides (Sm, Eu and Dy) behave differently in same host is an interesting problem, which can be solved by theoretical validation of experimental results.

Although numbers of reports are available on lanthanide doped ZrO_2 nanoparticles, very few reports are there on luminescence properties of lanthanide ion in ThO_2 . Eu^{3+} is used as a structural probe to understand its local site symmetry in nanocrystalline ThO_2 . For the first time, reverse micellar route is used to synthesize ThO_2 . Although reports exist on luminescence properties of lanthanide ion in Sr_2SiO_4 and SrZrO_3 , none of them explain the site occupancy of Ln^{3+} and their related effect on luminescence properties in these matrices. TRES is extensively used as to understand such phenomena. In Sr_2SiO_4 , there are two types of sites for Sr^{2+} . One is a more symmetric 10 coordinated site Sr (1) and the other is a less symmetric 9 coordinated site Sr (2). In SrZrO_3 also there is 8-coordinated Sr and 6-coordinated Zr. Different lanthanide ion viz. Eu, Sm and Dy ion are used as structural probe to understand their site occupancy in Sr_2SiO_4 and SrZrO_3 . These ions are found to behave differently in terms of their local site occupancy in these matrices. This aspect is investigated in detail in the present work. Theoretical modelling and EXAFS studies were carried out to explain such anomaly. Effect of replacing Si (IV) by Ce (IV) in Sr_2SiO_4 is investigated in Sr_2CeO_4 system. Ionic size of silicon 0.40 Å; not ideal for Eu^{3+} substitution- entire Eu is distributed to Sr^{2+} site. Si (IV) is replaced by Ce (IV) whose ionic radius is very close to Eu (III). Also synthesizing Sr_2CeO_4 is a challenge,

because it decomposes peritectically to SrO and SrCeO₃ at higher temperatures. Luminescence properties of hosts like Zn₂P₂O₇ (both undoped and doped) with lanthanide ions are investigated for the first time with a view to develop new and robust phosphor materials having multifunctional applications.

Compounds like SrZrO₃, Zn₂P₂O₇, etc. have host emission in the visible region over the range of 400-550 nm. Hence, it is expected that suitable modification in the synthesis procedure as well doping them with lanthanide ions can give efficient luminescent materials, which can have multi colour emission. Keeping the above mentioned aspects in mind, the luminescence properties of these nanomaterials have been investigated during the course of the present investigation.

Chapter 2
EXPERIMENTAL

CHAPTER 2

2.1. Synthesis of luminescent materials:**2.1.1 Conventional Solid state route:**

The solid-state reaction route is the most widely used method for the preparation of polycrystalline solids from a mixture of solid starting materials. Solids do not react together at room temperature over normal time scales and it is necessary to heat them to much higher temperatures, often to 1000 to 1500 °C in order for the reaction to occur at an appreciable rate. The factors on which the feasibility and rate of a solid state reaction include, reaction conditions, structural properties of the reactants, surface area of the solids, their reactivity and the thermodynamic free energy change associated with the reaction. The mechanism of solid state reactions is diffusion control; and hence, repeated grinding and repeated heating are required.

Consequences of high reaction temperatures

- It can be difficult to incorporate ions that readily form volatile species (i.e. Ag⁺).
- It is not possible to access low temperature, metastable (kinetically stabilized) products.
- High (cation) oxidation states are often unstable at high temperature, due to the thermodynamics of the following reaction:



Due to the release of a gaseous product (O₂), the products are favored by entropy, and the entropy contribution to the free energy become increasingly important as the temperature increases.

Preparation of single phase compound is difficult by the conventional solid state method. Hence, doping a low concentration (of the order of 1–3%) of activator has always been delicate. Thus, the limitations of conventional solid state are:

1. Inhomogeneity of the product.
2. Formation of large particles with low surface area and hence, mechanical particle size reduction is required, which introduces impurity and defects.
3. Presence of defects, which are harmful to luminescence.

The problem of inhomogeneity could be mitigated by the use of non-conventional methods (wet-chemical). These techniques are defined as techniques which do not comprise of the normal mixing, calcinations and grinding operations. Wet-chemical

methods such as sol-gel, combustion, polymeric precursor, reverse micellar etc have been employed to synthesize rare-earth activated phosphors. These wet-chemical methods facilitate doping of rare earth activators uniformly. But, calcination is required to get crystalline (required) phosphor.

2.1.2 Sol-gel Method:

The most widely used synthetic technique for bulk metal oxides has been the solid state method, which is based on the direct reaction of powder mixtures. These reactions are completely controlled by the diffusion of the atomic or ionic species through the reactants and products. To bring the reaction partners sufficiently close together and to provide high mobility, these solid state processes require high temperature and small particle sizes. Although the harsh reaction conditions only lead to thermodynamically stable phases, preventing the formation of metastable solids, these approaches gave access to a large number of new solid compounds, enabling the development of structure-properties relationships. However, in comparison to organic chemistry, where highly sophisticated synthetic pathways are employed to make and break chemical bonds in a controlled way, the ceramic method is a rather crude approach. It is therefore no surprise that for the size- and shape-controlled synthesis of nanoparticles especially liquid-phase routes represent the most promising alternatives. In contrast to solid-state processes, but analogous to organic chemistry, “chimie douce” approaches offer the possibility to control the reaction pathways on a molecular level during the transformation of the precursor species to the final product, enabling the synthesis of nanoparticles with well-defined and uniform crystal morphologies and with superior purity and homogeneity [85]. Among the various soft-chemistry routes, sol-gel procedures were particularly successful in the preparation of bulk metal oxides (e.g., ceramics, glasses, films and fibers) [86, 87], and therefore they have also been applied for nanoparticle synthesis. But in spite of great efforts, the number of oxidic nanoparticles obtained by sol-gel chemistry is still rather small compared to the variety of compounds obtained via powder routes. In many cases a synthesis protocol developed for a bulk metal oxide could not directly be adapted to its corresponding counterpart on the nanoscale. The reasons for this observation are manifold. Aqueous sol-gel chemistry is quite complex, on the one hand due to the high reactivity of the metal oxide precursors towards water and the double role of water as ligand and solvent, and, on the other hand, due to the large

number of reaction parameters that have to be strictly controlled (hydrolysis and condensation rate of the metal oxide precursors, pH, temperature, method of mixing, rate of oxidation, the nature and concentration of anions, ...) in order to provide good reproducibility of the synthesis protocol [86]. Another fundamental problem of aqueous sol-gel chemistry is that the as-synthesized precipitates are generally amorphous. The required post-synthetic annealing step to induce the crystallization process prevents any subtle control over crystal size and shape. For the preparation of bulk metal oxides, these limitations play only a minor role; however, in the case of nanoparticle synthesis, they constitute a major issue.

In material science, the sol-gel process is a method for producing solid materials from small molecules. The method is used for the fabrication of metal oxides, especially the oxides of silicon and titanium. The process involves conversion of monomers into a colloidal solution (sol) that acts as the precursor for an integrated network (or gel) of either discrete particles or network polymers.

In general, the precursor or starting compound is either an inorganic (no carbon) metal salt (chloride, nitrate, sulfate etc) or a metal organic compound such as an alkoxide. Metal alkoxides are the most widely used precursors, because they react readily with water and are known for many metals. Some alkoxides, which are widely used in industry, are commercially available at low cost (Si, Ti, Al, Zr), whereas other ones are hardly available or only at very high costs (Mn, Fe, Co, Ni, Cu, Y, Nb, Ta ...).

In general, the sol-gel process consists of the following steps (Figure 2.1) [88]: i) Preparation of a homogeneous solution either by dissolution of metal organic precursors in an organic solvent that is miscible with water, or by dissolution of inorganic salts in water; ii) conversion of the homogeneous solution into a sol by treatment with a suitable reagent (generally water with or without any acid/base); iii) aging; iv) shaping; and v) thermal treatment/ sintering. The first step in a sol-gel reaction is the formation of an inorganic polymer by hydrolysis and condensation reactions, i.e., the transformation of the molecular precursor into a highly cross-linked solid. Hydrolysis leads to a sol, a dispersion of colloidal particles in a liquid, and further condensation results in a gel, an interconnected, rigid and porous inorganic network enclosing a continuous liquid phase. This transformation is called the sol-gel transition. There are two possibilities to dry the gels. Upon removal of the pore liquid under hypercritical conditions, the network does not collapse and aerogels are produced. When the gel is dried under ambient conditions, shrinkage of the pores

occurs, yielding a xerogel. One of the highly attractive features of the sol-gel process is the possibility to shape the material into any desired form such as monoliths, films, fibers, and monosized powders, and subsequently to convert it into a ceramic material by heat treatment.

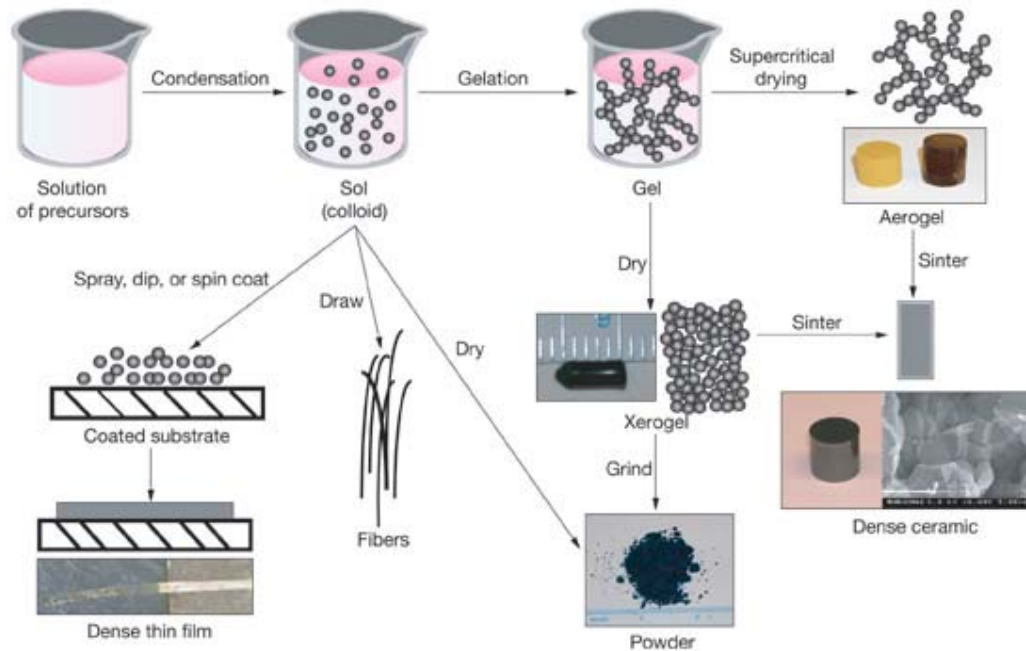
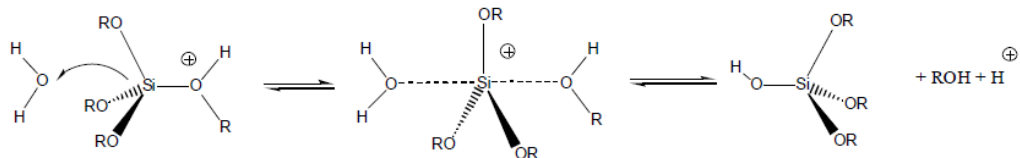


Figure 2.1: Various steps in the sol-gel process to control the final morphology of the product [88].

The sol-gel conversion of metal alkoxides involves two main reaction types: hydrolysis and condensation (Scheme 2.1). During hydrolysis, the alkoxide groups ($-OR$) are replaced via the nucleophilic attack of the oxygen atom of a water molecule under release of alcohol and the formation of a metal hydroxide. In most cases hydrolysis step requires catalyst as can be seen from Figure 2.2. Condensation reactions between two hydroxylated metal species leads to $M-O-M$ bonds under release of water (oxolation), whereas the reaction between a hydroxide and an alkoxide leads to $M-O-M$ bonds under release of an alcohol (alkoxolation). Steps involved in the condensation of tetra ethyl orthosilicate (TEOS) during sol-gel process are shown in Figure 2.3. In the present work, Sr_2SiO_4 has been synthesized using sol-gel method. Main reactions in the sol-gel process using metal alkoxides. Hydrolysis (Eq. 2.1) and condensation, involving oxolation (Eq. 2.2) and alkoxolation (Eq. 2.3)



Acid catalysed hydrolysis



Base catalysed hydrolysis

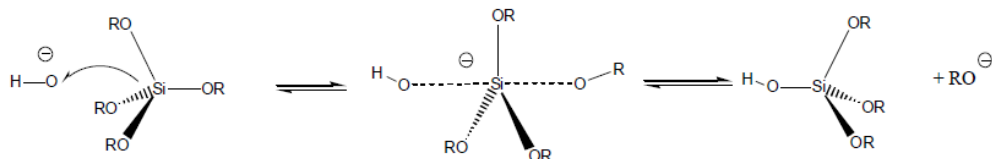


Figure 2.2: Acid and base catalyzed hydrolysis step

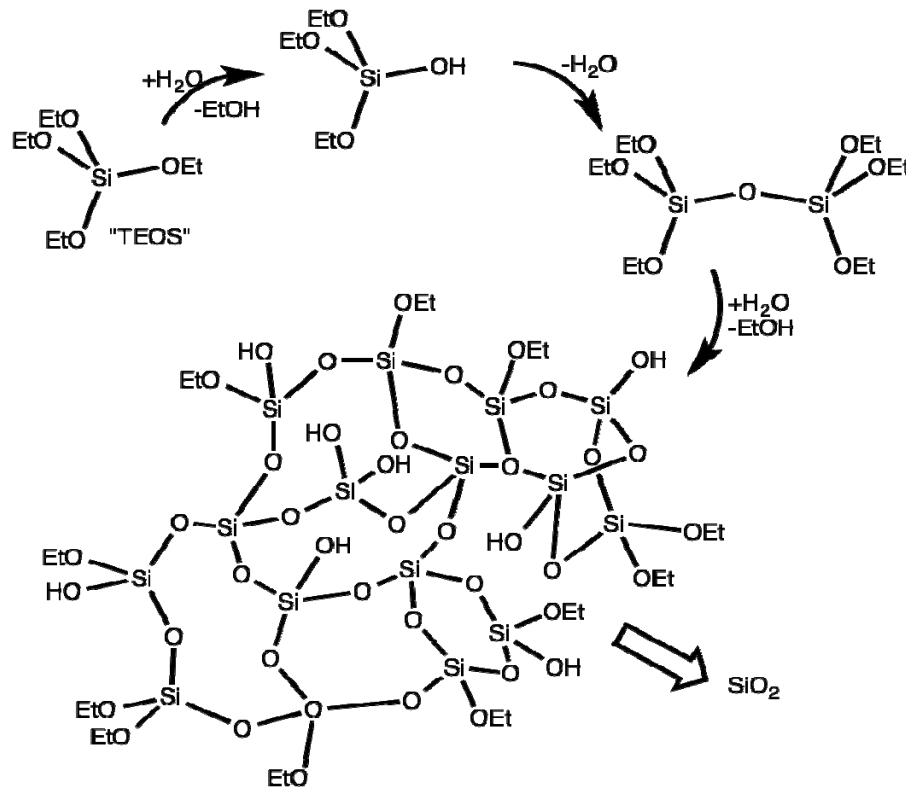


Figure 2.3: Simplified representation of the condensation of TEOS in sol gel process

2.1.3 *Gel-combustion Method:*

Combustion synthesis (CS) or self-propagating high-temperature synthesis (SHS) is an effective, low-cost method for production of various industrially useful bulk/ nano-crystalline powders of oxide ceramics, at a lower calcination temperature in a surprisingly short time.

The solution-combustion is a two-step process viz. (i) formation of a precursor and (ii) auto-ignition.

In a typical reaction, the precursor (mixture of water, metal nitrates and fuel) on heating decomposes, dehydrates and ruptures into a flame. The resultant product is a voluminous, foamy powder, which occupies the entire volume of the reaction vessel. The chemical energy released from the exothermic reaction between the metal nitrates and fuel can rapidly heat the system to high temperatures without an external heat source. Nanomaterials synthesized by combustion route are generally homogeneous, contain fewer impurities, and have higher surface areas than powders prepared by conventional solid-state methods. The parameters that influence the reaction are the nature of fuel, fuel to oxidizer ratio, ignition temperature and water content of the precursor mixture. The major advantage of this method is that large-scale production can be made at relatively low temperatures and disadvantage is that the particles obtained are highly agglomerated and cannot be dispersed in solvents.

The formation of the precursor (viscous liquid or gel), is a primary condition for an intimate blending of the starting constituents and preventing the random redox reaction between a fuel and an oxidizer. The very high exothermicity generated during combustion manifests in the form of either a flame or a fire and hence, the process is termed as auto-ignition process. The nature of the fuel and its amount, are some of the important process parameters, for getting the transparent viscous gel without any phase separation or precipitation [89]. Thus, the basic characteristics of the fuel are that it should be able to maintain the compositional homogeneity among the constituents and also undergo combustion with an oxidizer at a low ignition temperature. The commonly used fuels are: glycine, citric acid, urea, ascorbic acid etc. The two events, which occur during combustion, are (i) generation of heat of combustion, and (ii) gas evolution. Heat of combustion (or flame temperature) helps in crystallization and formation of the desired phase. However, a very high flame temperature can adversely affect powder characteristics like increase in the crystallite

size, formation of hard agglomerates and thereby reduction in the surface area and sinterability. The evolution of gaseous products during combustion dissipates the heat of combustion and limits the rise of temperature, thus reducing the possibility of premature local partial sintering among the primary particles. The powder characteristics are primarily governed by heat of combustion and gas evolution, which themselves are dependent on nature of the fuel and oxidant-to-fuel ratio [90].

Depending on the type of the precursors, as well as on conditions used for the process organization, the SCS may occur as either volume or layer-by-layer propagating combustion modes. This process not only yields nanosize oxide materials but also allows uniform (homogeneous) doping of trace amounts of rare-earth impurity ions in a single step. Among the gamut of papers published in recent years on SCS, synthesis of luminescent materials and catalysts occupy the lion share. The latest developments in SCS technique are discussed based on the materials applications. The synthesis of nanophosphors is currently a hot topic in the field of CS.

There are various advantages and disadvantages of gel-combustion method over other routes as mentioned in table 2.1. We have synthesized SrZrO₃ using gel-combustion method.

Table 2.1: Advantages and disadvantages of Combustion route

	Advantages	Disadvantages
1	Decreases diffusion path length	Safety related issues
2	Size control	Evolution of NOX
3	Less Energy and time consuming	Shape control is a problem
4	Metastable state can be synthesized	Synthesis of non-oxide ceramic is difficult
5	Better powder characteristics	Scaling up is an issue

2.1.4 Polymeric precursor Method:

The polymerized complex technique, known originally as the Pechini method [91] (wherein a solution of ethylene glycol (EG), citric acid (CA) and metal ions is

polymerized to form a polyester-type resin), has received considerable attention among others. This technique offers a convenient means in which a wide range of metal compounds stay as soluble species throughout the resin formation, and leaves enough flexibility for the system to persist without undergoing precipitation. Because of the high degree of compositional control afforded by the polymerized complex technique, it has been preferably used to study the effects of slight change in composition on electrical properties of high technology multicomponent oxides [92, 93].

The polymeric citrate method is based on the Pechini-type reaction route [91, 94]. It involves reacting a mixed solution of citric acid, ethylene glycol and the desired cations to form a polyester type of gel. The metal ions can be immobilized in a rigid polyester network, which is charred off by heating the gel. This can greatly reduce the diffusion path lengths of a particular reactant during the processing. Thus a distinct advantage over most other methods is that very pure mixed metal oxides can be prepared. Also compared to the ceramic route, this method can give rise to homogeneous and fine-grained powders at relatively lower reaction temperature. Figure 2.4 shows various stages involved in the synthesis using polymeric precursor route or polymerization complex method.

Approach: Decrease diffusion distances through intimate mixing of cations.

Advantages: Lower reaction temps, possibly stabilize metastable phases, eliminate intermediate impurity phases, and produce products with small crystallites/high surface area.

Disadvantages : Reagents are more difficult to work with, can be hard to control exact stoichiometry in certain cases, sometimes it is not possible to find compatible reagents (for example ions such as Ta^{5+} and Nb^{5+} immediately hydrolyze and precipitate in aqueous solution).

Methods: With the exception of using mixed cation reactants, all precursor routes involve the following steps:

- Mixing the starting reagents together in solution.
- Removal of the solvent, leaving behind an amorphous or nano-crystalline mixture of cations and one or more of the following anions: acetate, citrate, hydroxide, oxalate, alkoxide, etc.

- Heat the resulting gel or powder to induce reaction to the desired product.

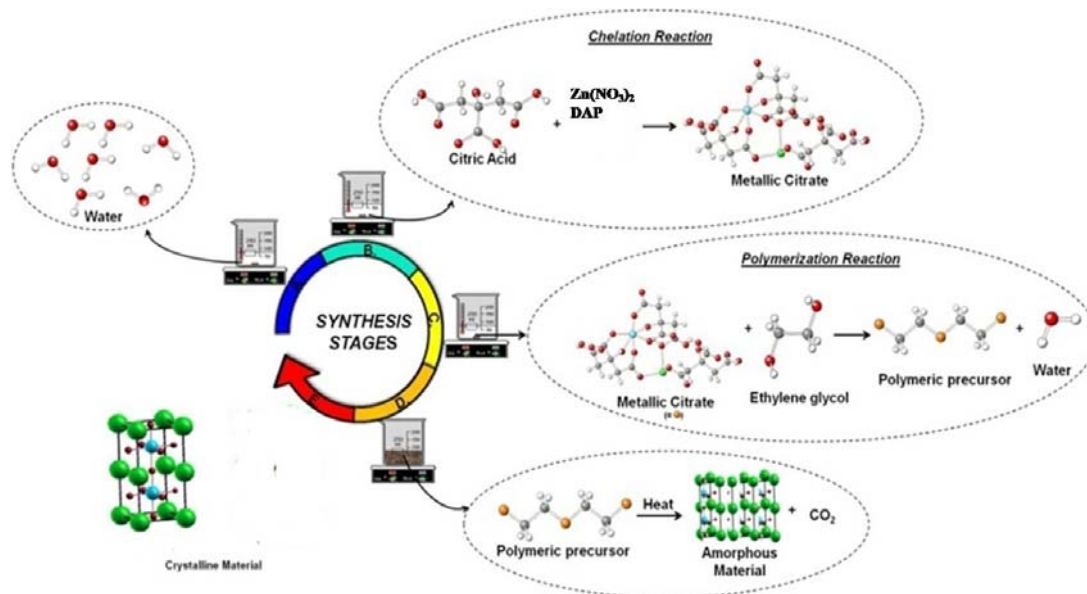


Figure 2.4: Typical synthesis stages in polymeric precursor route

2.1.5 Microemulsion method/Reverse micellar route:

A micro-emulsion is a mixture of water, water-insoluble and water-soluble components forming a visually homogeneous, transparent liquid. One or more active ingredients may be present in either the aqueous phase, the non-aqueous phase, or in both phases. A variety of micro-emulsion formulations may be prepared in which the aqueous phase can be considered the dispersed phase, the continuous phase or, alternatively, where the two phases are considered to be bicontinuous. In all cases micro-emulsions will disperse into water to form either conventional emulsions or dilute micro-emulsions. Synthesis of nano particles via micro emulsions is a simple and powerful technique, which does not require specialized or expensive equipments. Here precipitation reaction is carried out in mono dispersed aqueous cores dispersed in non-polar solvent and are stabilized by surfactant / co surfactant molecules. The material obtained is micro homogeneous, because the desired stoichiometry is maintained. The advantage of this technique over other methods of synthesis lies in the fact that a micro emulsion may assume a variety of structures depending on the constituents and the location within the phase diagram. It may therefore be possible to

control not only the size but also the morphology of the product nano particles by proper choice of the composition of the micro emulsion system.

It is a macro homogenous transparent solution formed by dissolving surfactant in organic solvent with limited amount of water. Reverse micelles can be defined as “Water in oil micro emulsion (see Figure 2.5) in which polar head groups of surfactant molecules are attracted by aqueous core and directed towards inside and hydrocarbon chain i. e. apolar part is attracted by non aqueous phase and directed towards outside.” The non-polar tail of surfactant molecules come into contact with the organic phase and the polar heads sequester together, forming a vesicle, which encloses the water pool inside the cavity. It consists of nanometer sized, monodisperse water droplets. It can easily control the size and shape of the aqueous core by varying the value of water to surfactant ratio (W_o). The reverse-micelles obtained at a particular ratio of the aqueous phase to the surfactant leads to uniform-size nano-reactors and have an aqueous core of 5-10 nm in which it is possible to precipitate the inorganic material.. It was initially assumed that these nanodroplets could be used as templates to control the final size of the particles, however, the research carried out in the last few years has shown that besides the droplet size, several other parameters also play an important role in the final size distribution.

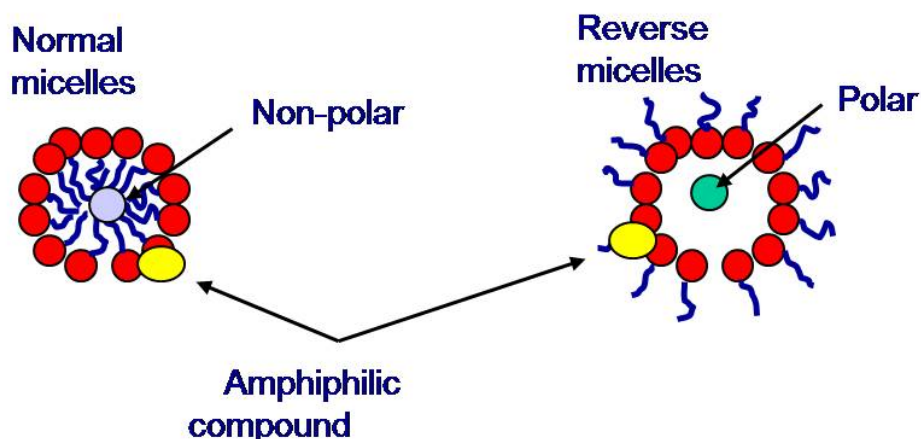


Figure 2.5: A typical structure of micelle.

Among all the chemical processes, the microemulsion processing (reverse micelle synthesis) has been demonstrated as a very versatile and reproducible method [95–98]. This method is superior to many others in terms of being able to deliver homogeneous and monodisperse nanoparticles of a variety of metals [99-100], oxides

[101-102], and chalcogenides [103]. The reaction takes place in the aqueous cores of the reverse micelles which are dispersed in an organic solvent and are stabilized by a surfactant. The dimensions of these aqueous cores are in the nanoregime and are thus being referred to as nanoreactors. The product obtained after the reaction is homogeneous. The other advantage of using this methodology is that the morphology of the product can also be controlled as the surfactant aggregates from a variety of structures which are used as templates. The size of the core of the reverse micelles can also be controlled by changing W_o ($[H_2O]/ [surfactant]$). Thus, the size and morphology of the product can be controlled by proper choice of the composition of the microemulsion system.

2.2. Characterization Techniques:

2.2.1. X-ray diffraction:

XRD is a technique to determine the structural properties of materials. This technique can inform researchers on the degree of crystallinity, phase identification, lattice parameters, and grain size. The use of the diffraction of waves from the periodic arrangement of atoms in solids to determine the crystal structure was first suggested by Von Laue in 1912, developed by Bragg in 1913 and is now a well-developed science. The typical interatomic distances in solids are a few angstroms, so waves with approximately this wavelength are required to explore this structure. The wavelengths of x-rays commonly applied for x-ray diffraction are between 0.7 and 2.3 Å, which is close to the interplanar spacings of most crystalline materials.

2.2.1.1. Principle:

X-rays interact primarily with electrons in atoms. When an incident x-ray wave approaches an atom, it is scattered and interference of these scattered waves occur. If the atoms have a periodic arrangement, as in a crystal, the scattering produces a diffraction pattern with sharp maxima (peaks) at certain angles. The peaks in the x-ray diffraction pattern are directly related to the interatomic distances. An incident x-ray beam interacting with the atoms arranged in a periodic manner is shown in two dimensions (2-D) in Figure 2.6. The atoms can be viewed as forming different sets of planes in the crystal. For a given set of lattice plane with an interplanar distance of, the condition for a diffraction (peak) to occur can be written as:

$$2d \sin \theta = n\lambda \quad (2.1)$$

This is known as Bragg's law, after W.L. Bragg, who first proposed it. In equation θ is the Bragg angle, which is half of the scattering angle; an integer representing the order of the diffraction peak and λ is the wavelength of the x-rays.

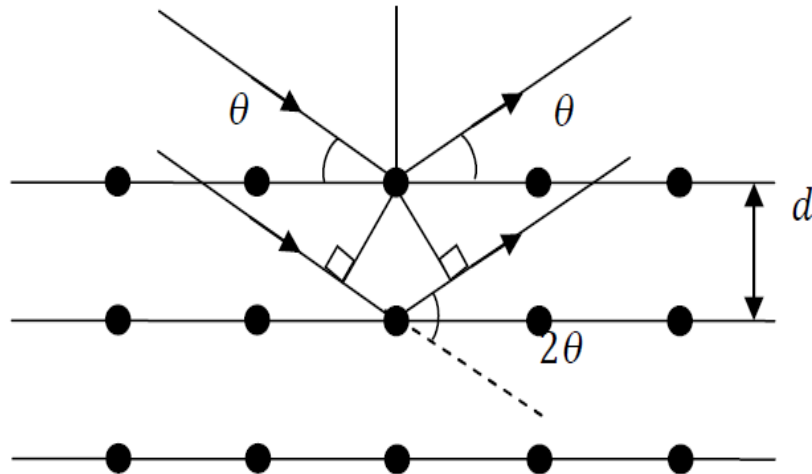


Figure 2.6: Scattering of x-rays from atoms and Bragg's law

2.2.1.2. X-ray production:

X-rays are a part of the spectrum of electromagnetic radiation in the region between ultraviolet and gamma rays. X-rays have a wavelength between 10.0 and 0.1 Å. They are produced when fast-moving electrons of sufficient energy are decelerated. In an x-ray tube, the high voltage maintained across the electrodes draws electrons toward a metal target (the anode). X-rays are produced at the point of impact, and radiated in all directions. The kinetic energy of the electrons is transformed into electromagnetic energy (x-rays). Since energy must be conserved, the energy loss results in the release of x-ray photons of energy equal to the energy loss. This process generates a broad band of continuous radiation (called Bremsstrahlung, or braking radiation) as shown in Figure 2.7.

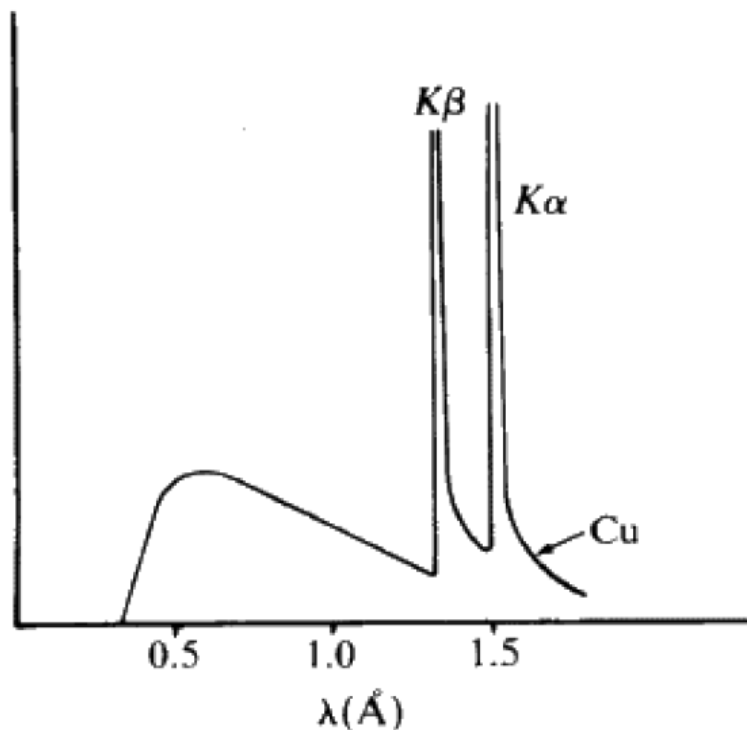


Figure 2.7: Continuous and characteristic x-rays for copper [104]

If the moving electron interacts with an inner-shell electron of the target atom, characteristic x-rays can be produced. When the moving electron ionizes a target atom by removal of a K-shell electron, transition of an orbital electron from an outer to an inner shell will occur, accompanied by the emission of an x-ray photon. The x-ray photon has energy equal to the difference in the binding energies of the orbital electrons involved. If an L-shell electron moves to replace a K-shell electron, a $K\alpha$ x-ray is produced (with wavelength 1.54178 Å for Cu). If an M-shell electron moves to replace a K-shell electron, a $K\beta$ x-ray is produced (with wavelength 1.39217 Å for Cu). These characteristic x-rays, also shown in Figure 2.7, are suitable for diffraction experiments. To obtain monochromatic x-rays a suitable metal filter can be used. Nickel strongly absorbs x-rays below 1.5 Å and can be used to filter the $K\beta$ x-rays from copper, as shown in Figure 2.8 [105].

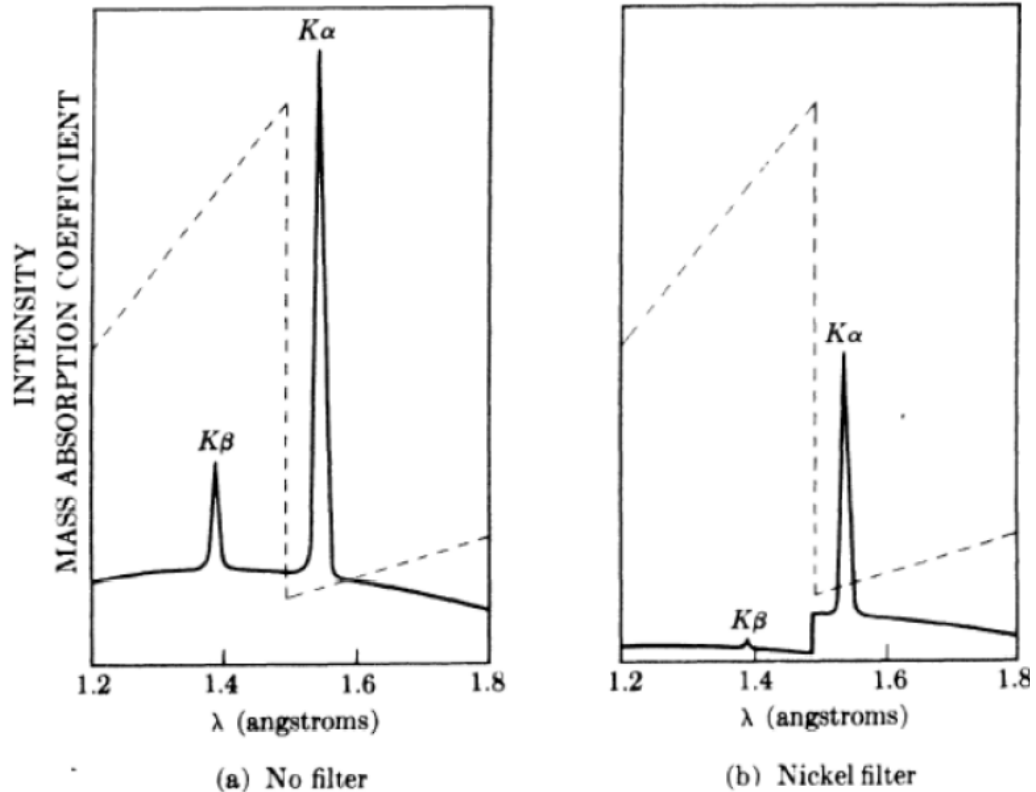


Figure 2.8: Using a Nickel filter for Cu X-rays [105]

2.2.1.3. XRD diffractometer:

A diffractometer records the diffraction pattern of a sample. The essential features of a diffractometer are presented schematically in Figure 2.9. It consists of an x-rays source (usually an x-ray tube) producing monochromatic x-rays of known wavelength, a sample stage, a detector, and a way to vary the angle. The x-rays are focused on the sample at some angle θ , while the detector reads the intensity of the diffracted x-rays it receives at the scattering angle 2θ .

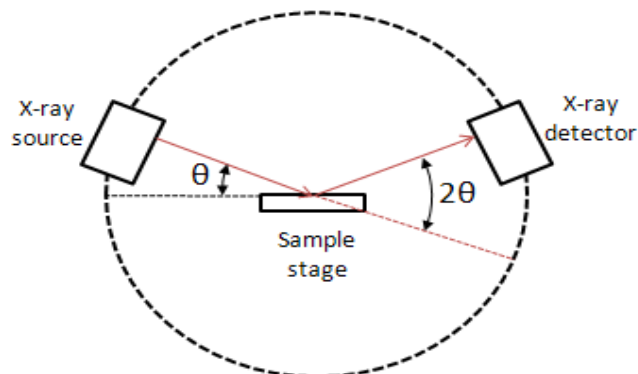


Figure 2.9: X-ray diffractometer [106].

2.2.1.2. XRD applications: phase purity and crystallite size:

With the XRD pattern the identification of an unknown crystalline material becomes possible. Bragg's law is used to convert the angles where peaks occur to interplanar spacings (d-spacings) using Bragg's law (Equation 2.1). Files of d-spacings for hundreds of thousands of inorganic compounds for comparison are available in the Powder Diffraction Files (PDF) of the International Centre for Diffraction Data (ICDD).

When crystallites are less than 100 nm in size, appreciable broadening in the x-ray diffraction reflections will occur. These regions may in fact correspond to the actual size of the particles. The grain size can be calculated from the broadening of the diffracted beam using the Scherer's formula:

$$t = K\lambda / B \cos\theta \quad (2.4)$$

Where, t = Diameter of the grain, λ = Wavelength of the X-ray (for Cu-K α , λ = 1.5418 Å), θ = Bragg angle or diffraction angle, B = Full width at half maximum (FWHM) of a diffraction peak, K = Scherer's constant and its value is the order of unity for usual crystals. Normally, $K = 0.9$ is used. Hence,

$$t = 0.9\lambda / B \cos\theta \quad (2.5)$$

The line broadening B is measured from the broadened peak at full width at half maxima and obtained from the Warren's formula:

$$B^2 = B_M^2 - B_S^2 \quad (2.6)$$

Where, B_M = Full width at half maximum of the sample, B_S = Full width at half maximum of a standard sample of grain size of around 2 μm . Quartz was used as the standard and the reflections were chosen such that the sample and standard had closest possible 2θ values and the operations carried out on two reflections were identical.

In the present case measurements were carried out on a STOE X-ray diffractometer equipped with Ni filter, scintillation counter and graphite monochromator. The diffraction patterns were obtained using monochromatic Cu-K α radiation ($\lambda = 1.5406\text{\AA}$) keeping the scan rate at 1sec./step in the scattering angle range (2θ) of 10° to 60° . The $K_{\alpha 2}$ reflections were removed by a stripping procedure to obtain accurate lattice constants. The goniometer was calibrated for correct zero position using silicon standard. Samples are well grounded and made in the form of a slide. As all the micro

crystals are randomly oriented, at any point on the sample different planes from crystals will be exposed to X-rays.

2.2.2. *Thermal analysis: TGA/DTA/DSC*

Thermal analysis is a branch of materials science where the properties of materials are studied as they change with temperature. Several methods are commonly used – these are distinguished from one another by the property which is measured:

- Dielectric thermal analysis (DEA): dielectric permittivity and loss factor
- Differential thermal analysis (DTA): temperature difference
- Differential scanning calorimetry (DSC): heat difference
- Dilatometry (DIL): volume
- Dynamic mechanical analysis (DMA) : mechanical stiffness and damping
- Evolved gas analysis (EGA) : gaseous decomposition products
- Laser flash analysis (LFA): thermal diffusivity and thermal conductivity
- Thermogravimetric analysis (TGA): mass
- Thermomechanical analysis (TMA): dimension
- Thermo-optical analysis(TOA): optical properties

Thermal analysis methods are essential for understanding the compositional and heat changes involved during reaction. They are useful for investigating phase changes, decomposition and loss of water or oxygen and for constructing phase diagrams.

In TGA, the weight of a sample is monitored as a function of time as the temperature is increased at a controlled uniform rate. Loss of water of crystallization or volatiles (such as oxygen, CO₂, etc.) is revealed by a weight loss. Oxidation or adsorption of gas shows up as a weight gain. A phase change is generally associated with either absorption or evolution of heat. In DTA experiments, the sample is placed in one cup and a standard sample (like Al₂O₃) in the other cup. Both cups are heated at a controlled uniform rate in a furnace, and the difference in temperature (ΔT) between the two is monitored and recorded against time or temperature. Any reaction involving heat change in the sample will be represented as a peak in the plot of ΔT vs. T. Exothermic reactions give an increase in temperature, and endothermic reaction leads to a decrease in temperature and the corresponding peaks appear in opposite directions.

DSC is a thermoanalytical technique in which the difference in the amount of heat required to increase the temperature of a sample and reference is measured as a function of temperature. Both the sample and reference are maintained at nearly the same temperature throughout the experiment. Generally, the temperature program for a DSC analysis is designed such that the sample holder temperature increases linearly as a function of time. The reference sample should have a well-defined heat capacity over the range of temperatures to be scanned. The result of a DSC experiment is a curve of heat flux versus temperature or versus time. There are two different conventions: exothermic reactions in the sample shown with a positive or negative peak, depending on the kind of technology used in the experiment. This curve can be used to calculate enthalpies of transitions. This is done by integrating the peak corresponding to a given transition

2.2.3. *Electron microscopy: SEM/TEM*

Micro-structural characterization has become important for all types of materials as it gives substantial information about the structure-property correlation. Micro-structural characterization broadly means ascertaining the morphology, identification of crystallographic defects and composition of phases, estimating the particle size, etc. Electron microscopic techniques are extensively used for this purpose. Electron microscopy is based on the interaction between electrons (matter wave) and the sample.

Electron microscopes are scientific instruments that use a beam of highly energetic electrons to examine objects on a very fine scale. They are widely used as tools for research, quality assurance and failure analysis in material science. They are indispensable implements in biological and life sciences. In electron microscopy beams of electrons are used to produce images wavelength of electron beam is much shorter than light, resulting in much higher resolution. Table 2.1 shows the advantages and disadvantages of electron microscope while Table 2.2 shows the comparison between light optical microscope and electron microscope. Figure 2.10 depicts the range of optical and electron microscope.

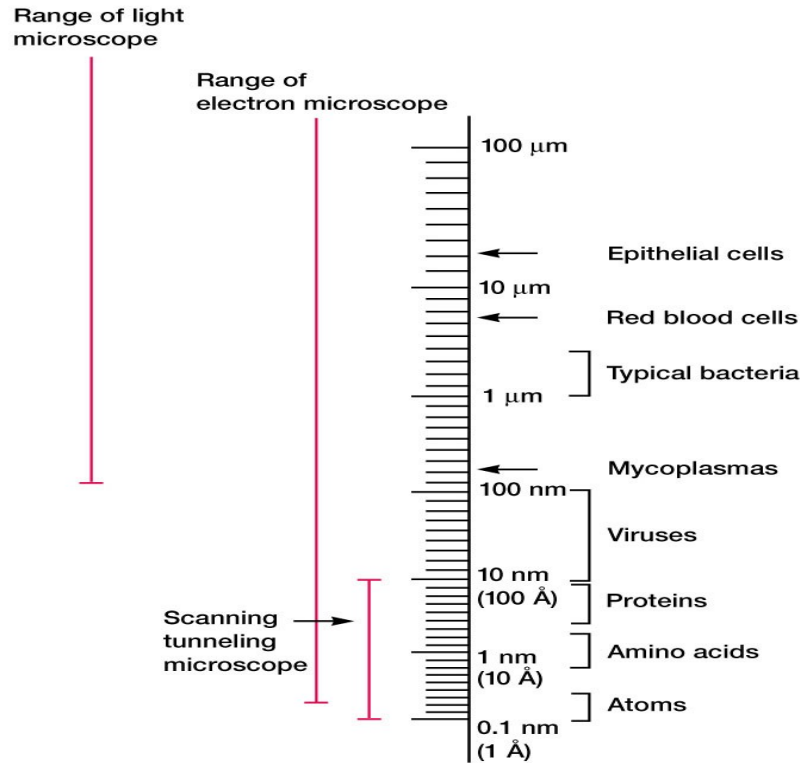


Figure 2.10: Typical range of light and electron microscope

Table 2.1: Advantages and disadvantages of electron microscope

Advantages	
	<p><i>Shorter wavelength</i> Better resolution</p>
	<p><i>Low mass</i> Non-destructive for most specimens</p>
	<p><i>Negative charge</i> Beam focused / deflected via electric coils</p>
	<p><i>Strong interaction electron-matter</i> Different signals available</p> <ul style="list-style-type: none"> - Elastic scattering: imaging - Phase shift: weak-scatter imaging - Diffraction: crystallography - Inelastic scattering / ionisation: chemical analysis
Disadvantages	
	<p><i>Strong interaction electron-matter</i> Excellent vacuum and thin specimen for TEM, conductive specimen for SEM</p>

Table 2.2: Comparison between light optical microscope and electron microscope

	Light Microscopy	Electron Microscopy
<i>Carrier</i>	Photons	Electrons
<i>Wavelength</i>	400–800 nm (visible) 200 nm (ultra violet)	0.0037 nm (at 100kV) 0.0020 nm (at 300kV)
<i>Medium</i>	Air	Vacuum
<i>Observation</i>	Direct	Via fluorescent screen/TV screen
<i>Contrast by</i>	Absorption, reflection, phase changes, polarisation...	Scattering, phase changes and diffraction
<i>Information</i>	Mass Density Distribution	Mass Density Distribution, Crystallographic and Chemical
<i>Resolving Power</i>	0.2 μm (visible) 0.1 μm (ultra violet)	0.2 nm (point) 0.1 nm (line)
<i>Lenses</i>	Glass	Electromagnets
<i>Focusing and Alignment</i>	Mechanically	Electronically
<i>Aperture Angle</i>	$<64^\circ$	0.2–0.7 $^\circ$
<i>Depth of Focus</i>	0.1 μm –0.1m (1-1k)	1–10,000m (1k–1000k)
<i>Depth of Field</i>	$<0.1 \mu\text{m}$	$<1 \mu\text{m}$

In the present study, Scanning Electron Microscopy (SEM) and Transmission Electron Microscopy (TEM) have been used to characterize the nano powders. The principle and experimental details of these two techniques are given below.

They can be used to study the following in **MATERIALS SCIENCE**:

- ❖ Topography - the surface features of an object or 'how it looks', its texture, direct relation between these features and material's properties like hardness, reflectivity etc.
- ❖ Morphology - the shape and size of the particles making up the object. There is a direct relation between these structures and material's properties like strength, ductility, reactivity etc.
- ❖ The composition of the specimen - the elements and compounds that the specimen is composed of and their relative amounts. The uniformity of composition and its relation between properties like melting point, mechanical properties can be evaluated using an electron microscope.
- ❖ · Crystallographic information - how the atoms arranged in the specimen of the object. This gives a direct relation between the atomic arrangements and the properties like conductivity, electrical characteristics, strength etc., of the material under investigation.

In fact, a complete *structure – property* correlation is possible using an electron microscope.

Scanning Electron Microscopy (SEM):

In a typical scanning electron microscope, a well-focused electron beam is incident and scanned over the sample surface by two pairs of electro-magnetic deflection coils. The signals generated from the surface by secondary electrons are detected and fed to a synchronously scanned cathode ray tube (CRT) as intensity modulating signals. Thus, the specimen image is displayed on the CRT screen. Changes in the brightness represent changes of a particular property within the scanned area of the specimen. The SEM has a large depth of field, which allows a large amount of the sample to be in focus at one time. The SEM also produces images of high resolution, which means that closely spaced features can be examined at a high magnification. For carrying out SEM analysis, the sample must be vacuum compatible ($\sim 10^{-6}$ Torr or more) and electrically conducting. The surfaces of non-conductive materials are made conductive by coating with a thin film of gold or platinum or carbon.

Schematic representation of SEM is shown in Fig.2.11. Image formation in a SEM depends on the acquisition of signals produced from the interaction of the specimen and the electron beam. Figure 2.12 pictorially represent the types of information that can be obtained from SEM.

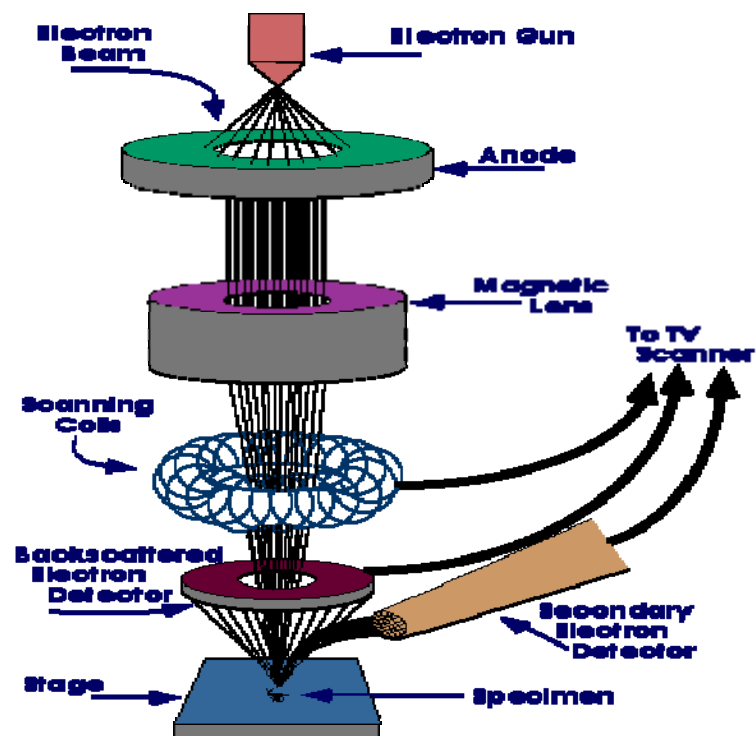


Figure 2.11: Schematic of scanning electron microscope

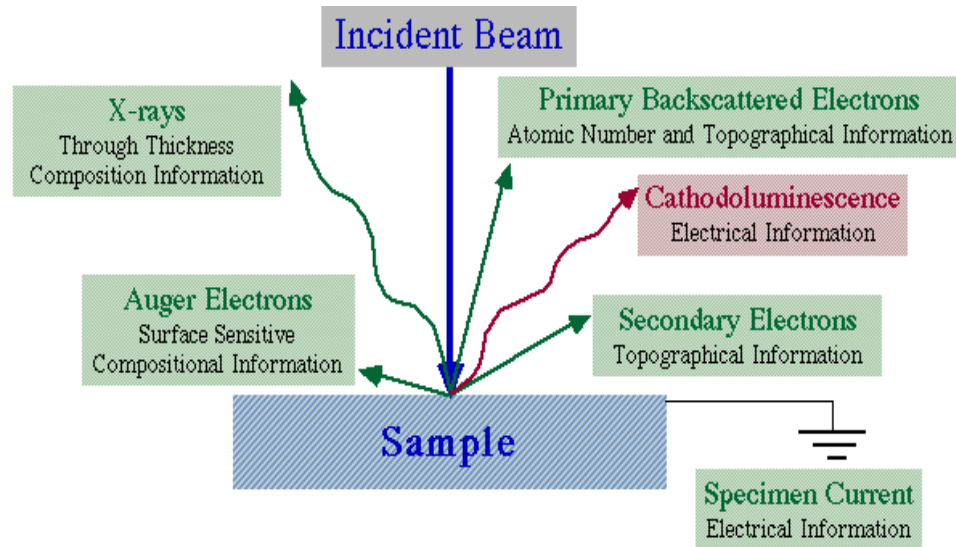


Figure 2.12: Various electron and photon emitted in SEM and information's gathered from them.

Transmission electron microscopy (TEM):

Transmission electron microscopy (TEM) is a microscopy technique in which a beam of electrons is transmitted through an ultra-thin specimen, interacting with the specimen as it passes through. An image is formed from the interaction of the electrons transmitted through the specimen; the image is magnified and focused onto an imaging device, such as a fluorescent screen, on a layer of photographic film, or to be detected by a sensor such as a charge couple device (CCD) camera. TEMs are capable of imaging at a significantly higher resolution than light microscopes, owing to the small de Broglie wavelength of electrons. This enables the instrument's user to examine fine detail—even as small as a single column of atoms, which is thousands of times smaller than the smallest resolvable object in a light microscope. Schematic representation of TEM is shown in Fig.2.13. Table 2.3 represents the comparison between SEM and TEM.

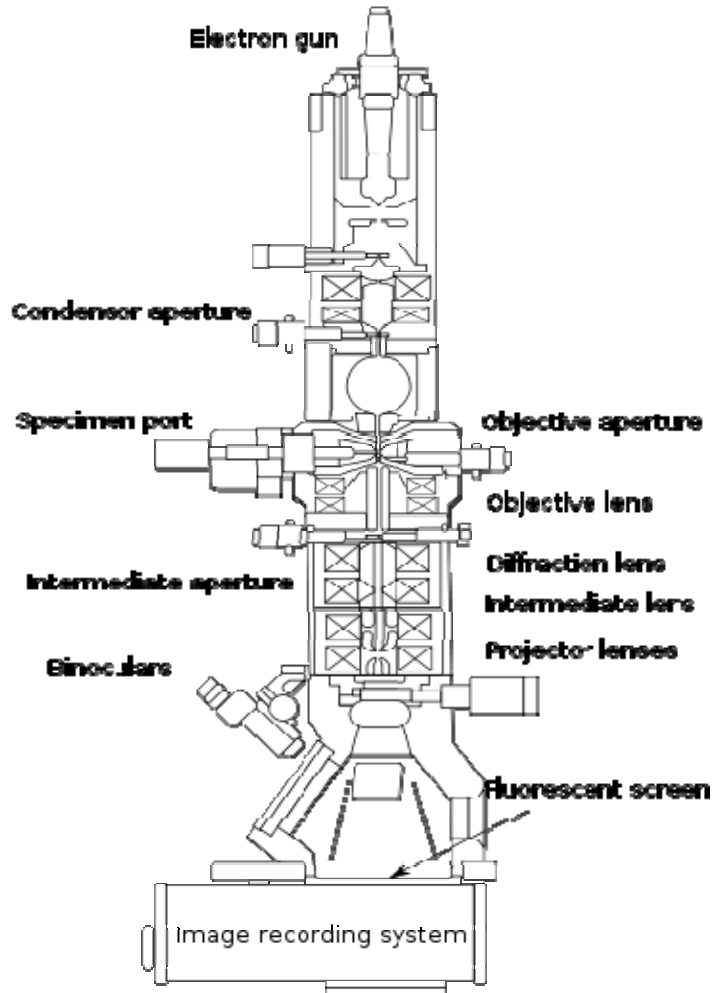


Figure 2.13: Schematic of transmission electron microscope.

Table 2.3: Comparison between SEM and TEM

SEM	TEM
Electrons scan the surface	Electron is transmitted through the specimen
Bulk sample can be done	Extremely thin sample
Larger depth of field	Comparatively less
Resolution-10 nm	Resolution-0.1 nm

2.2.4. *Dynamic light scattering (DLS):*

Dynamic light scattering (also known as photon correlation spectroscopy or quasi-elastic light scattering) is a technique in physics that can be used to determine the size distribution profile of small particles in suspension or polymers in solution. This method is used to determine the size of particles in the 5 to 5000 nanometre range. It uses the scattered light to measure the rate of diffusion of the particles. This motion data is conventionally processed to derive a size distribution for the sample, where the size is given by the "Stokes radius" or "hydrodynamic radius" of the particle. This hydrodynamic size depends on both mass and shape (conformation). Dynamic scattering is particularly good at sensing the presence of very small amounts of aggregated protein (<0.01% by weight) and studying samples containing a very large range of masses. It can be quite valuable for comparing stability of different formulations, including real-time monitoring of changes at elevated temperatures. Hydrodynamic radius is given by Stoke – Einstein equation which is given by

$$R_h = kT / 6\pi\eta D \quad (2.7)$$

where, k = Boltzmann constant, T = Temperature, η = viscosity of suspension, D = diffusion coefficient. So, the hydrodynamic particle radius can be calculated if the shear viscosity of the suspension and the temperature is known.

2.2.5. *Fourier transform infrared spectroscopy (FTIR):*

Fourier Transform Infrared Spectroscopy (FTIR) is an analytical technique which can be used to identify chemical group in organic or inorganic materials. Infrared (IR) light passing through a sample is measured in order to determine the chemical functional groups in the sample. Different functional groups absorb characteristic frequencies of IR radiation. The FTIR spectrometers with especial accessory can measure a wide variety of sample types such as gases, liquids, and solids. Infrared rays are a part of the electromagnetic spectrum and cover the range between 0.78 and 1000 μm . The wavelength in infrared spectroscopy is often expressed as the reciprocal of the wavelength in cm, with unit as cm^{-1} . For convenience the infrared region can be divided into three parts: near, mid and far infrared (Table 2.4). The part of the mid infrared region between 4000 – 670 cm^{-1} is the most useful one.

Table 2.4: Different region in IR

Region	Wavelength range	
	μm	cm^{-1}
Near	0.78-2.5	12800-4000
Mid	2.5-50	4000-200
Far	50-1000	200-10

“Molecular bonds vibrate at various frequencies depending on the elements and the type of bonds. For any given bond, there are several specific frequencies at which it can vibrate. According to quantum mechanics, these frequencies correspond to the ground state (lowest frequency) and several excited states (higher frequencies). One way to increase the frequency of a molecular vibration is to excite the bond by having it absorb light energy. For any given transition between two states the light energy must equal the difference in the energy between the two states exactly (usually ground state (E_0) and the first excited state (E_1)). The energy corresponding to these transitions...” “...corresponds to the infrared portion of the electromagnetic spectrum. Thus absorption of IR is restricted to vibrational states. For a molecule to absorb IR, the vibrations within a molecule must cause a net change in the dipole moment of the molecule. The alternating electrical field of the radiation interacts with fluctuations in the dipole moment of the molecule. If the frequency of the radiation matches the vibrational frequency of the molecule, then radiation will be absorbed, causing a change in the amplitude of molecular vibration.” In solids the same principles apply, but the vibrations of the lattice instead of individual molecules must be considered.

2.2.6. Positron annihilation spectroscopy (PAS):

Positron annihilation spectroscopy (PAS) or sometimes specifically referred to as Positron annihilation lifetime spectroscopy (PALS) is a non-destructive spectroscopy technique to study voids and defects in solids. Positron annihilation spectroscopy (PAS) is a well established technique to study the electronic structure and defects in materials [107-110]. The lifetime of positrons depends on the electron density at the annihilation site. The technique operates on the principle that a positron or

positronium will annihilate through interaction with electrons. This annihilation releases gamma rays that can be detected; the time between emission of positrons from a radioactive source and detection of gamma rays due to annihilation corresponds to the lifetime of positron or positronium. When positrons are injected into a solid body, they interact in some manner with the electrons in that species. For solids containing free electrons (such as metals or semiconductors), the implanted positrons annihilate rapidly unless voids such as vacancy defects are present. If voids are available, positrons will reside in them and annihilate less rapidly than in the bulk of the material, on time scales up to ~ 1 nanosecond. Positrons have high affinity for open volume defects and in the presence of defects; the electron density experienced by positron is reduced leading to increase in its lifetime. Thus, positron lifetime spectroscopy is capable of giving information about the size, type and relative concentration of various defects/vacancies even at ppm level concentration. Doppler broadening technique, on the other hand, measures the momentum distribution of the annihilating electrons. The low momentum part of the Doppler spectrum (511 keV gamma line) arises mainly from the annihilation with the valence electrons and the core electrons that can be taken as signature of an element, contribute to the high momentum part of the spectrum. A very small fraction of positrons annihilate with core electrons due to the repulsion of positron by the positively charged nucleus. The amplitude of the high momentum or core electron component is, therefore, low and it is buried in the Compton background in conventional Doppler spectrum. Coincidence Doppler broadening (CDB) technique using two HPGe detectors [111], is capable of eliminating the background to a great extent, e.g., peak to background ratio of $\sim 10^6$ can be obtained as compared to a few hundreds in conventional Doppler technique. This enables unambiguous extraction of the shape and magnitude of the high momentum part of the Doppler spectrum. The chemical surrounding of the annihilation site or elemental specificity is obtained from the shape/magnitude of the high momentum core component, which carry the signature of the element. Since the core electron momentum distribution is not influenced by the physical or chemical state of the element, the CDB technique is capable of identifying the elements at the annihilation site irrespective of its physical or chemical state in the sample. Therefore, combined use of lifetime spectroscopy (LTS) and CDB technique can provide valuable information about the vacancy structure. A schematic representation of

positron annihilation is shown in Figure 2.14. Figure 2.15 shows the schematic of instrument used in positron lifetime measurement.

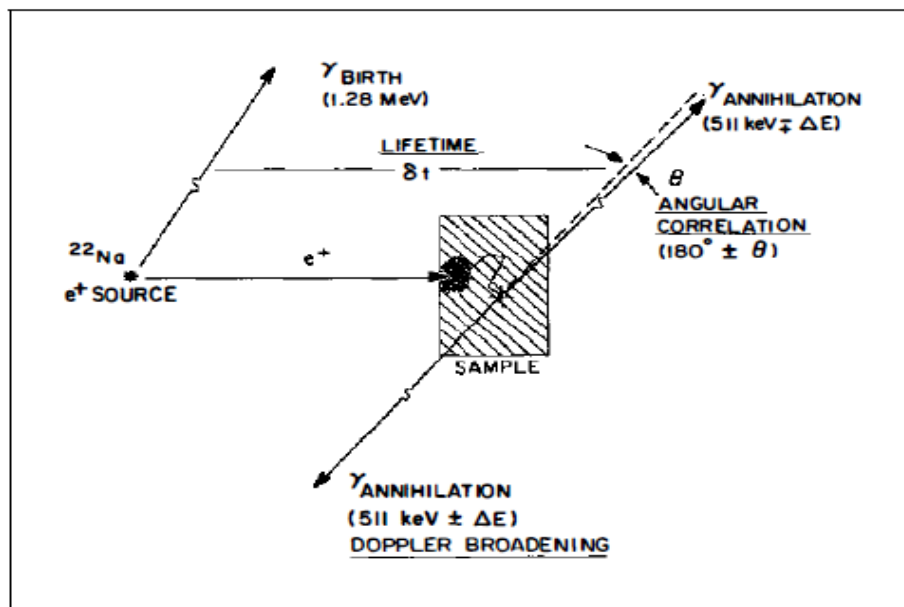


Figure 2.14: Schematic representation of positron annihilation indicating the basis for the three experimental techniques of positron annihilation spectroscopy (PAS): lifetime, angular correlation, and Doppler broadening

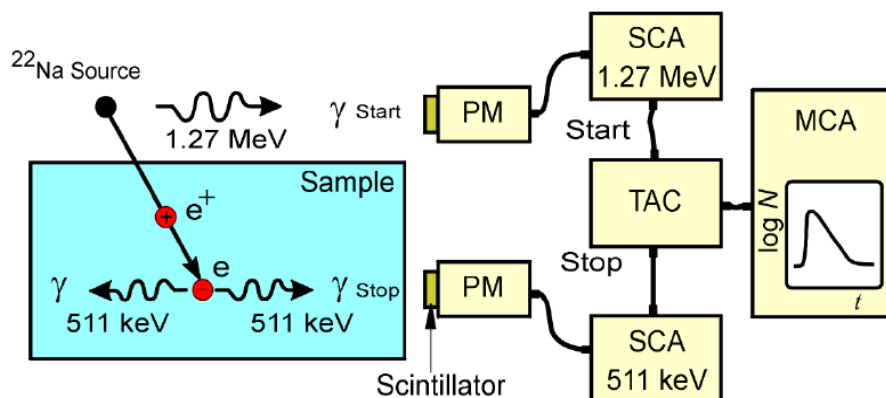


Figure 2.15: The conventional positron lifetime measurement system

2.2.7. Electron paramagnetic resonance (EPR) spectroscopy:

Electron Paramagnetic Resonance, EPR, is a spectroscopic technique which detects species that have unpaired electrons. It is also often called ESR, Electron Spin Resonance. A surprisingly large number of materials have unpaired electrons. These include free radicals, many transition metal ions, and defects in materials. Free electrons are often short-lived, but still play crucial roles in many processes such as

photosynthesis, oxidation, catalysis, and polymerization reactions. As a result EPR crosses several disciplines including: chemistry, physics, biology, materials science, medical science and many more.

EPR is a magnetic resonance technique very similar to NMR, Nuclear Magnetic Resonance. However, instead of measuring the nuclear transitions in our sample, we are detecting the transitions of unpaired electrons in an applied magnetic field. Like a proton, the electron has spin, which gives it a magnetic property known as a magnetic moment. The magnetic moment makes the electron behaves like a tiny bar magnet. When we supply an external magnetic field, the paramagnetic electrons can either orient in a direction parallel or antiparallel to the direction of the magnetic field. This creates two distinct energy levels for the unpaired electrons and allows us to measure them as they are driven between the two levels.

Initially, there will be more electrons in the lower energy level (i.e., parallel to the field) than in the upper level (antiparallel). We use a fixed frequency of microwave irradiation to excite some of the electrons in the lower energy level to the upper energy level. In order for the transition to occur we must also have the external magnetic field at a specific strength, such that the energy level separation between the lower and upper states is exactly matched by our microwave frequency as shown in Figure 2.16. In order to achieve this condition, we sweep the external magnet's field while exposing the sample to a fixed frequency of microwave irradiation. The condition where the magnetic field and the microwave frequency are "just right" to produce an EPR resonance (or absorption) is known as the resonance condition and is described by the equation shown in the above Figure 2.16.

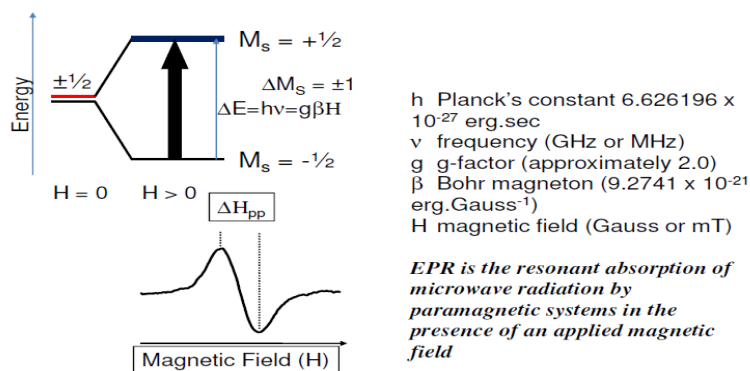


Figure 2.16: Separation between the lower and the upper state for unpaired free electrons in EPR

Chapter 2

The factor g is the measure of the total magnetic moment associated with the paramagnetic molecule and it is represented by the following equation.

$$g = 1 + \frac{J(J+1) + S(S+1) - L(L+1)}{2J(J+1)} \quad (2.8)$$

For free electron, $S = 1/2$, $L = 0$, $J = S = 1/2$. This gives $g = 2.0$. The g factor is a dimensionless constant. For most of the free radicals g value is very close to 2.0000. This is because in case of free radicals the unpaired electron is not confined to a localized orbital but can move freely over the orbital resulting in the quenching of the orbital contribution ($L=0$). In case of transition metal complexes, on the other hand, the unpaired electron is confined in a particular orbital. Because of the loss of orbital degeneracy and the spin orbit coupling the g value of the complex is different from 2.0000. The g value of the transition metal complexes depends on the relative magnitude of the spin orbit coupling and the crystal field splitting. The spin orbit contribution makes “ g ” as a characteristic property of a transition metal ion and its oxidation state. The g factor is an anisotropic quantity i.e. its value depends on the direction of observation (orientation dependent). From the g value of a transition metal complex, one can obtain important information about the structure of the complex. In solids, the movement of the molecule is restricted and thus one can have different g values for different direction of observations. In a cubic crystal field, the metal ligand bond lengths are same along three crystallographic axes and hence g value remains the same (isotropic), that is $g_x = g_y = g_z$.

If the crystal field is tetragonal, the metal - ligand distance along the x and y axis are the same but different from the metal ligand distance along the z direction. The g value for such complex is anisotropic and they are expressed as $g_z = g_{||}$ and $g_x = g_y = g_{\perp}$. This is because it is always assumed that, the principal axis (along which the magnetic field is aligned) is along the z axis. Whereas if the symmetry of the complex is orthorhombic, all the three g values will be different that is $g_x \neq g_y \neq g_z$.

However, for most systems in solution or gas phase, the g value is averaged over all the orientations because of the free motion of the molecules. In this case, the

$$g_{av} = (g_x + g_y + g_z)/3. \quad (2.9)$$

The simplest possible spectrometer for any spectroscopic technique has three essential components: a source of electromagnetic radiation (EMR), a sample, and a detector. To acquire a spectrum, we can vary the frequency of the EMR and measure the

amount of radiation which passes through the sample with a detector to observe the spectroscopic absorptions. In an EPR spectrometer, the source of the microwave radiation is a Klystron or a Gunn-diode. The source provides a limited range of variable frequency. The microwave source and the detector are in a box called the microwave bridge.

To measure the EPR spectrum of a paramagnetic sample, the sample is placed in a magnetic field of a resonator cavity in which microwave power is concentrated. The sample is so positioned inside the resonator cavity that the electrical component of the EMR is at its minimum and the magnetic component is at its maximum.

At the sample, the static magnetic field (H) is perpendicular to the microwave magnetic field. The interaction of magnetic spins with the oscillating magnetic field of the electromagnetic radiation leads to the EPR transitions. The EPR spectrum can be recorded by either varying the magnetic field strength or the microwave frequency. As it is easier to vary the magnetic field than the frequency due to restriction in the electronics, usually the magnetic field H is varied over a wide range and the frequency is kept constant.

An electromagnet having sweep width ranging from 5000 G to 15000 G can be used. The microwave energy is modulated and the microwave power absorbed by the sample at the resonance is measured by the phase sensitive detector, the signal is amplified and fed to a computer for data processing. A semiconductor silicon-tungsten diode is used as a detector. Earlier, the EPR spectrum used to be recorded as a function of absorption intensity against magnetic field. Such a curve often produces broad absorption bands. In modern instrument, the first derivative of the absorption intensity (dA/dH , i.e. slope) is plotted against H . This type of plot gives more accurate g values. It may be noted that the resonance field H is not a unique fingerprint for identification of the paramagnetic species because spectra can be acquired at different frequencies. The g -factor, $g = hv/\beta H$ being independent of the microwave frequency, is much better for that purpose. Notice that higher values of ' g ' occur at low magnetic fields and vice versa. A list of fields for resonance for a $g=2$ signal at microwave frequencies commonly available in EPR spectrometers is presented in the Table 2.5. Figure 2.17 shows the block diagram of typical EPR spectrometers. Figure 2.18 shows the photographs of EPR spectrometer used in current studies.

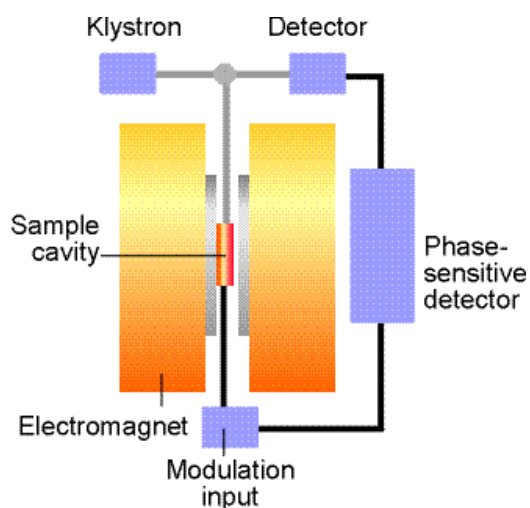


Figure 2.17: Block diagram of typical EPR spectrometers



Figure 2.18: Photograph of Bruker ESP-300 EPR spectrometer

Table 2.5: List of fields for resonance for a $g=2$ signal at microwave frequencies commonly available in EPR spectrometers

Designation	ν/GHz	$H_{(\text{electron})}/\text{Tesla}$
L	1.1	0.0392
S	3.0	0.107
X	9.5	0.339
K	23	0.82
Q	35	1.25
W	95	3.3

The most widely used EPR spectrometer is the X-band spectrometer operating in the frequency range 9-10 GHz. The sensitivity of an EPR spectrometer is directly proportional to the square of the frequency, and a high frequency is preferred for a better resolution of the EPR signal. The sensitivity of the Q band spectrometer is fifteen times than that of X band spectrometers.

2.2.8. Thermally stimulated luminescence (TSL):

Thermoluminescence is a form of luminescence that is exhibited by certain crystalline materials, such as some minerals, when previously absorbed energy from electromagnetic radiation or other ionizing radiation (like gamma) is re-emitted as light upon heating of the material. The phenomenon is distinct from that of black body radiation. High energy radiation creates electronic excited states in crystalline materials. In some materials, these states are *trapped*, or *arrested*, for extended periods of time by localized defects, or imperfections, in the lattice interrupting the normal intermolecular or inter-atomic interactions in the crystal lattice. Quantum-mechanically, these states are stationary states which have no formal time dependence; however, they are not stable energetically. Heating the material enables the trapped states to interact with phonons, i.e. lattice vibrations, to rapidly decay into lower-energy states, causing the emission of photons in the process. Figure 2.19 pictorially represent the process thermally stimulated luminescence.

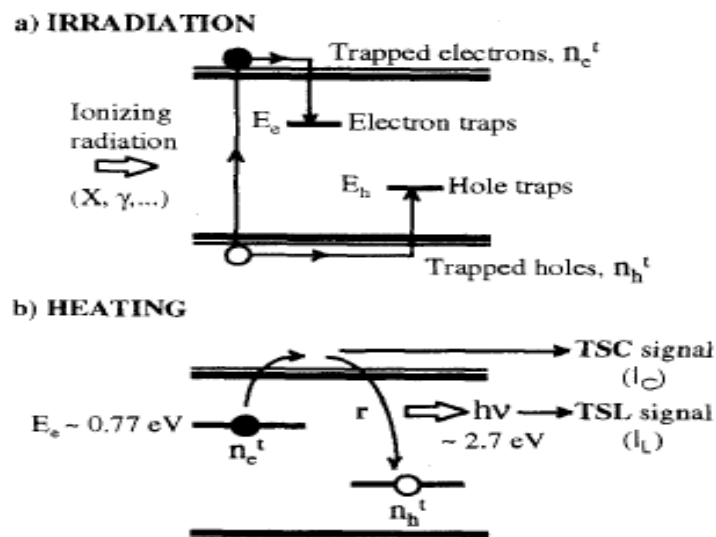


Figure 2.19: Thermally stimulated luminescence

TL or more specifically Thermally Stimulated Luminescence (TSL) is stimulated thermally after initial irradiation given to a phosphor by some other means (α - rays, β -rays, γ - rays, UV rays and X-rays). Thermally stimulated luminescence (TSL) is the phenomenon of emission of light from a solid which has been previously exposed to ionizing radiation under conditions of increasing temperature. Unlike other luminescence process such as Electroluminescence, Chemiluminescence, here heat is not an exciting agent, but it acts only as a stimulant. Hence it is better known as thermally stimulated luminescence (TSL). Excitation is achieved by any conventional sources like ionizing radiation, α -rays, β -rays, γ - rays and UV rays and X-rays. TSL is exhibited by a host of materials, glasses, ceramics, plastics and some organic solids. By far insulating solids doped with suitable chemical impurities, termed as activator, are the most sensitive TL materials. The band theory of solids is normally used to explain this phenomenon. When a solid is irradiated, electrons and holes are produced. The defects in the solid results in the presence of localized energy levels within the forbidden gap. On irradiation, electron and holes can be trapped at these defect sites. When the solid is heated, these trapped electrons/holes get enough thermal energy to escape from the trap to the conduction band (or valence band). From here they may get re-trapped again or may recombine with trapped holes/electrons. The site of recombination is called recombination center. If this recombination is radiative, then center is called luminescence center. Alternatively a trapped hole can be released by heating which can recombine with a trapped electron resulting in luminescence. These features are shown diagrammatically in Fig.2.20. It is not required that all charge recombination should result in luminescence, they may be non- radiative too. The plot of intensity of emitted light versus the temperature known as a TL glow curve. A glow curve may exhibit one or many peaks depending upon the number of electron/hole traps with different trap depths, present in the lattice. These peaks may or not be well separated. The position, shape and intensity of the glow peaks therefore are characteristic of the specific material and the impurities and defects presents. Therefore each TSL peak corresponds to the release for an electron (or hole) from a particular trap level within the band gap of the material. The nature of the TL glow peaks gives information about the luminescent centers present in the material. It may be mentioned that TSL is highly sensitive to structural imperfections in crystals. Defects densities as low as $10^7/\text{cm}^3$ also can give measurable TSL if radiative recombination are dominant whereas techniques such as

EPR and OAS are sensitive only for relatively higher defect concentrations such as $10^{12}/\text{cm}^3$. The first step towards understanding the mechanism for TSL glow peaks is the identification of the trapping center and the recombination centers for the observed light emission. Apart from being a tool for the study of defects in solids, TSL has also found widespread use in radiation dosimetry, archaeological dating of pottery, ceramics, minerals etc; and meteorite research.

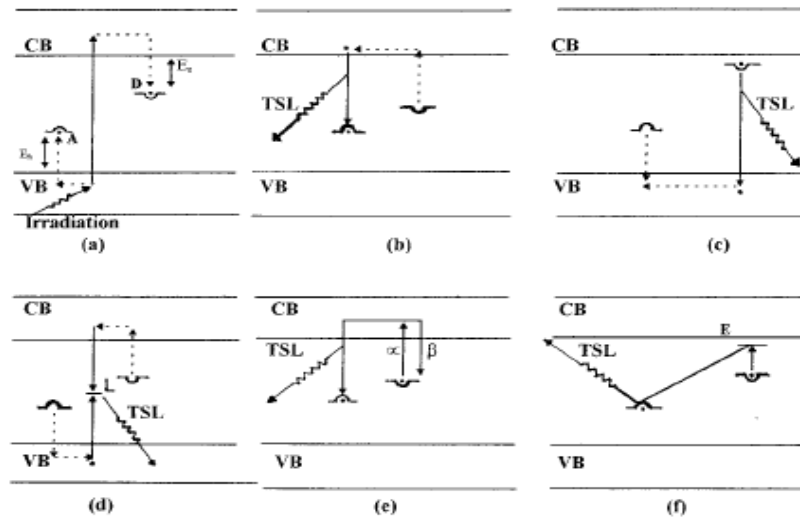


Figure 2.20: Processes involved in radiation induced electron/hole trapping and subsequent recombination on thermal stimulation with associated luminescence emission.

VB- Valence band, CB - Conduction band, Eh - Trap depth for hole, Ee - Trap depth for electron, L - Luminescent center, A - Hole trap and D - Electron trap.

(a) On gamma irradiation, electrons and holes are produced and trapped at electron hole traps. (b) On thermal stimulation, trapped electron is released and recombines at trapped hole site. (c) e-h recombination at trapped electron site. (d) e-h recombination at luminescent center site. (e) Process of de trapping and re trapping (second order kinetics, α - de trapping probability and β - re trapping probability); (f) e-h recombination via an excited state 'E' and tunnelling.

2.2.9. Photoluminescence spectroscopy (PL):

Photoluminescence spectroscopy is analytical technique that can determine quantities such as emission and excitation spectra and luminescence lifetimes. By this technique, a sample is excited by photons (generally in UV range) and the excess energy released by the sample through the emission of light can be detected and recorded for different modes, i.e. excitation, emission and luminescence decay lifetime. A spectrofluorometer is an instrument capable of recording the emission spectrum or both the excitation and emission spectra. An emission spectrum is the wavelength distribution of an emission measured at a single constant excitation wavelength. An

excitation spectrum is the dependence of emission intensity, measured at a single emission wavelength, upon scanning the excitation wavelength. With a pulsed excitation source and a fast detector the spectrofluorometer can record the luminescence lifetime decay curve. A fluorescence decay time is a measurement, at fixed wavelength, of fluorescence signals as a function of time. A decay curve is a spectrum measured within a narrow time-window during the decay of the fluorescence of interest. Two requirements for lifetime measurements are a pulsed excitation source (pulse duration short in comparison with the excited-state lifetime of the molecule) and a fast detector.

2.2.9.1. Physical principle:

In photoluminescence spectroscopy, the species is first excited (by absorbing a photon) from its ground electronic state to one of the various vibrational states in the excited electronic state. Collisions with other molecules cause the excited molecule to lose vibrational energy until it reaches the lowest vibrational state of the excited electronic state. The molecule then drops down to one of the vibrational levels of the ground electronic state, emitting a photon in the process. As molecules may drop down into any of several vibrational levels in the ground state, the emitted photons will have different energies. These processes are often visualised with the Jablonski diagram shown in Figure 2.21. There are factors which can affect fluorescence intensity which is pictorially represented in Figure 2.22.

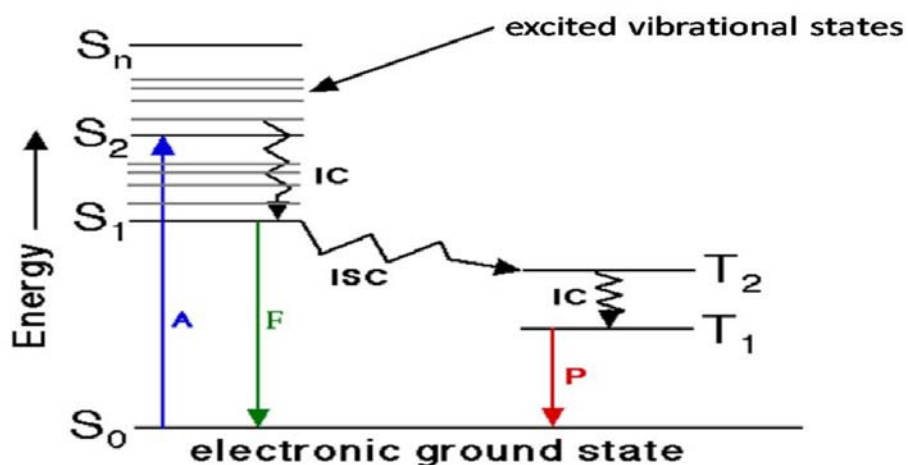


Figure 2.21: A Jablonski diagram shows the possible relaxation processes in a molecule after the molecule has absorbed a photon (A): IC = internal conversion, ISC= intersystem conversion, F= fluorescence, P= phosphorescence

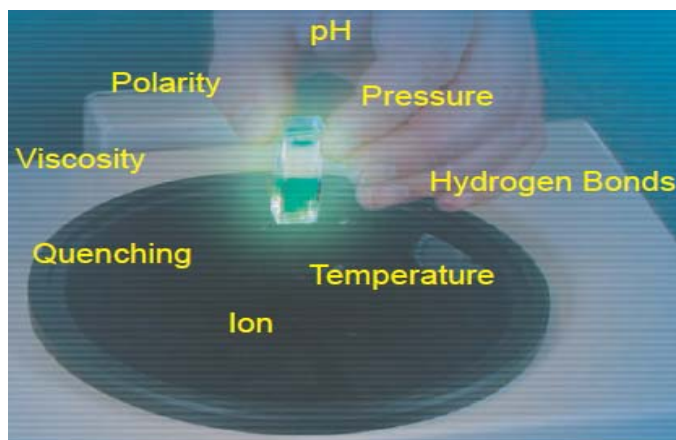


Figure 2.22: Parameters affecting fluorescence emission

2.2.9.2. Instrumentation: Excitation and emission spectroscopy

The source produces light photons. Various light sources may be used as excitation sources, including lasers, photodiodes, and lamps. Photons impinge on the excitation monochromator, which selectively transmits light in a narrow range around the specified excitation wavelength. With a laser excitation sources, filters may be used instead of a monochromator, or with a monochromator to give high quality monochromatic light. The transmitted light passes through adjustable slits that control intensity and resolution by further limiting the range of transmitted light. The filtered light passes into the sample. Emitted light goes through a filter to prevent the excitation light entering the detector and causing second order peaks. The filtered light then enters the emission monochromator, which is often positioned at a 90° angle from the excitation light path to eliminate background signal and minimize noise due to stray light. Again, emitted light is transmitted in a narrow range centred on the specified emission wavelength and exits through adjustable slits, finally entering the photomultiplier tube (PMT). Schematic diagram of a general purpose spectrofluorometer are illustrated in Figure 2.23. With most spectrofluorometer it is possible to record both excitation and emission spectra. An emission spectrum is the wavelength distribution of an emission measured at a single constant excitation wavelength. Conversely, an excitation spectrum is the dependence of emission intensity, measured at a single emission wavelength, upon scanning the excitation wavelength. For an ideal instrument, the directly recorded emission spectra would represent the photon emission rate or power emitted at each wavelength, over a wavelength interval determined by the slit widths and dispersion of the emission

monochromator. Similarly, the excitation spectrum would represent the relative emission of the fluorophore at each excitation wavelength. This instrument has a xenon lamp as a source of exciting light. Such lamps are generally useful because of their high intensity at all wavelengths ranging upward from 250 nm. The instrument shown is equipped with monochromators to select both the excitation and emission wavelengths. The excitation monochromator in this schematic contains two gratings, which decreases stray light, that is, light with wavelengths different from the chosen one. In addition, these monochromators use concave gratings, produced by holographic means to further decrease stray light. Both monochromators are motorized to allow automatic scanning of wavelength. The fluorescence is detected with photomultiplier tubes and quantified with the appropriate electronic devices. The output is usually presented in graphical form and stored digitally. Figure 2.24 shows the fluorescence spectrometer used in current studies.

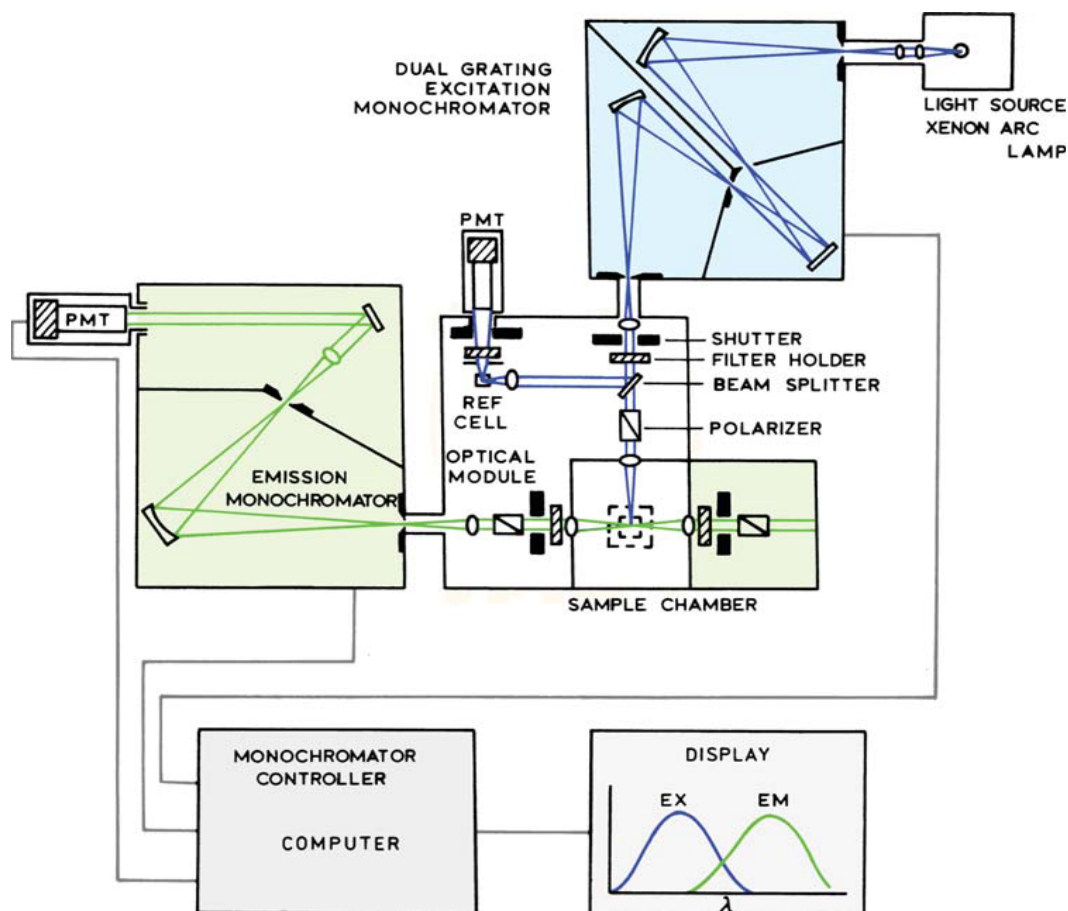


Figure 2.23: Block diagram of spectrofluorometer [113].

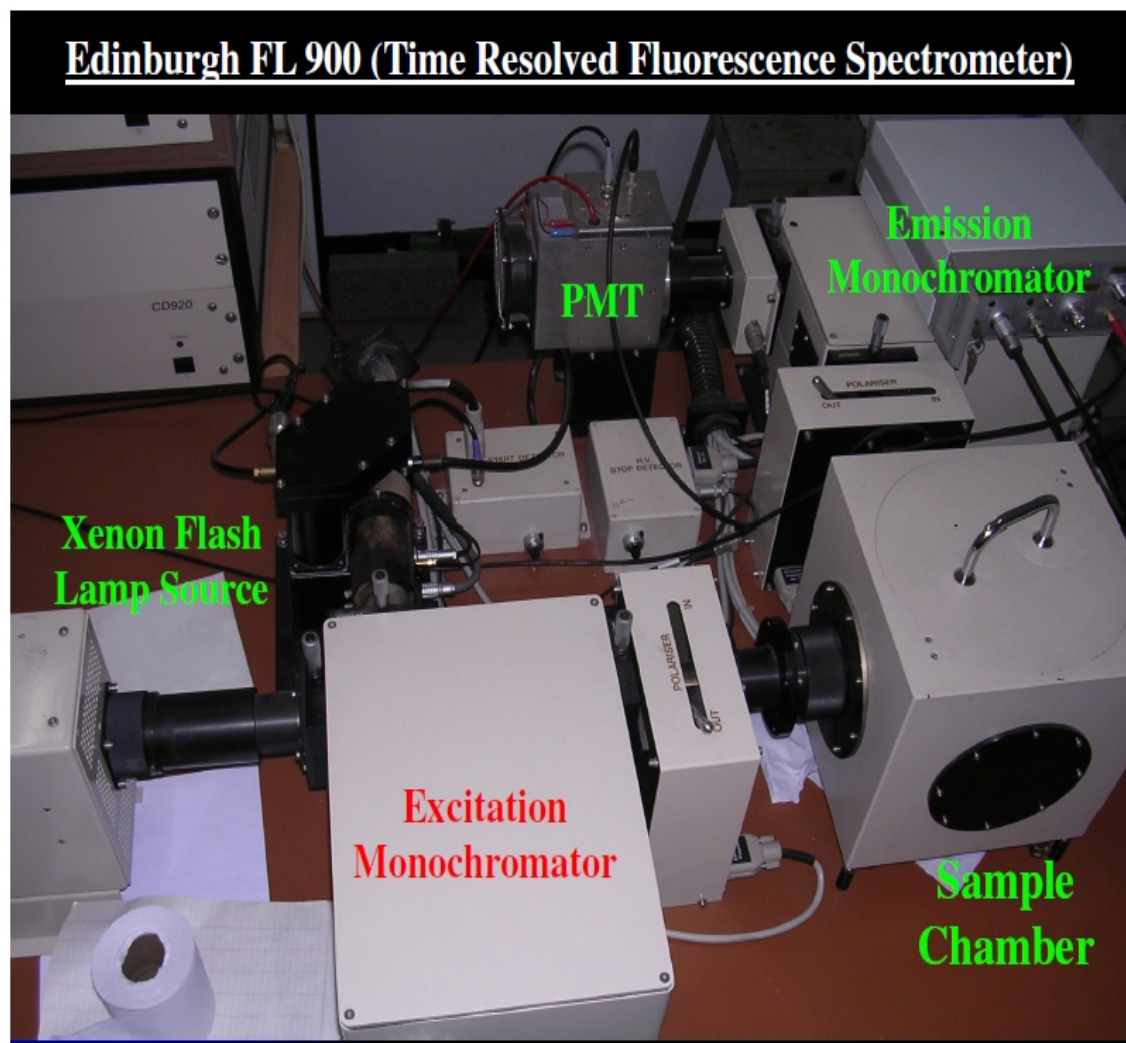


Figure 2.24: Photograph of the time resolved fluorescence spectrometer

2.2.9.3. Instrumentation: Luminescence lifetime

Time-correlated single-photon counting (TCSPC) is a well established and a common technique for fluorescence lifetime measurements, it is also becoming increasingly important for photon migration measurements, optical time domain reflectometry measurements and time of flight measurements.

The principle of TCSPC is the detection of single photons and the measurement of their arrival times in respect to a reference signal, usually the light source. TCSPC is a statistical method requiring a high repetitive light source to accumulate a sufficient number of photon events for a required statistical data precision. TCSPC electronics

can be compared to a fast stopwatch with two inputs (Fig 2.25). The clock is started by the START signal pulse and stopped by the STOP signal pulse. The time measured for one START – STOP sequence will be represented by an increase of a memory value in a histogram, in which the channels on the x-axis represent time. With a high repetition rate light source millions of START – STOP sequences can be measured in a short time. The resulting histogram counts versus channels will represent the fluorescence intensity versus time. Generally, one of the inputs to the TCSPC electronics (either START or STOP) will be a pulse generated by a single photon. Single photons can be detected by photodetectors with intrinsically high gain. The majority of those photodetectors are photomultipliers or micro-channel plate photomultipliers, but also single photon avalanche photodiodes. For statistical reasons it is important to ensure no more than one single photon event per light flash is detected. Multi-photon events will affect the histogram statistics and will yield to erroneous measurement results. (This is known in literature as the “pulse pile-up problem”.) In order to ensure that only one photon per light flash is detected; the photon rate is kept low in comparison to the rate of the exciting lamp; usually 5% or lower.

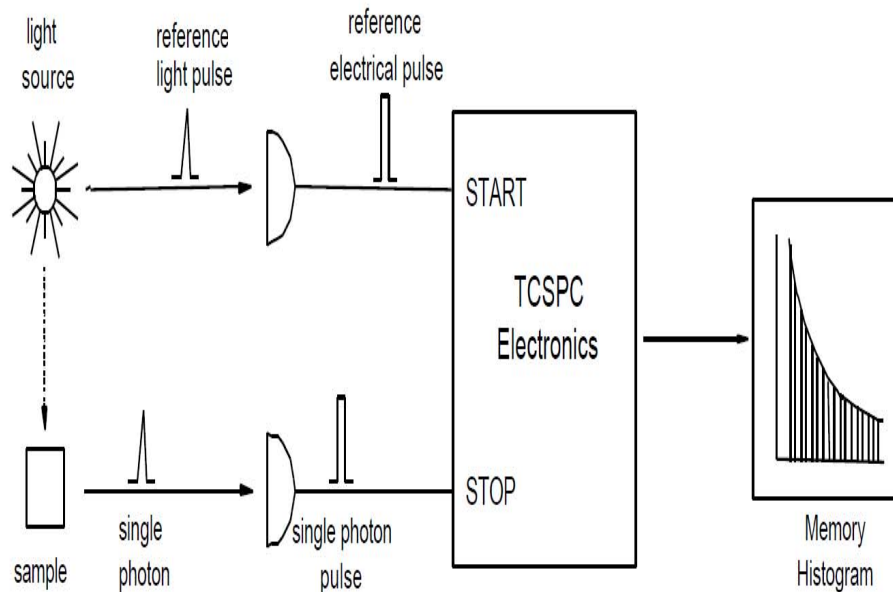


Figure 2.25: TCSPC - A fast stopwatch with two inputs [114].

The main components for signal processing in TCSPC as shown in Figure 2.26 are constant fraction discriminators (CFD), electrical delays (DEL), the Time-to-Amplitude Converter (TAC), Amplifier (between the TAC and ADC), Analogue to Digital Converter (ADC) and digital memory (Mem).

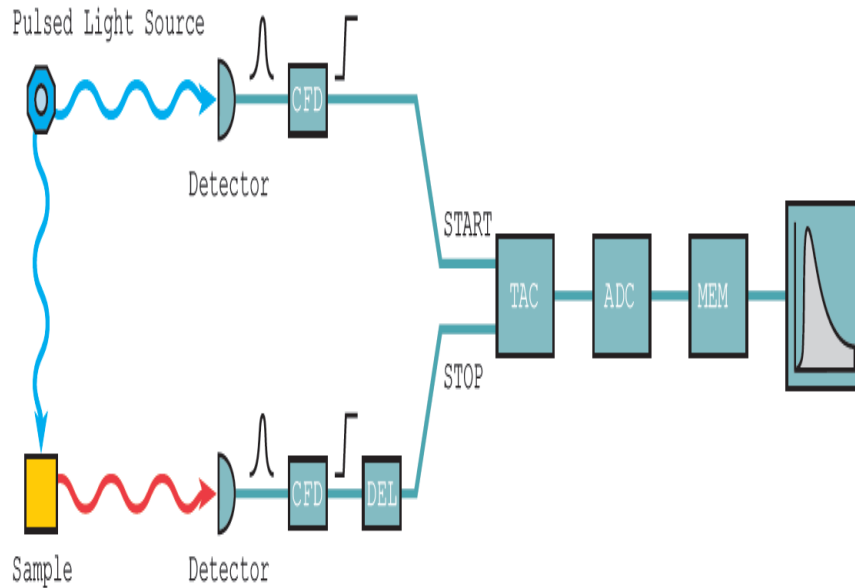


Figure 2.26: The main components for signal processing in TCSPC [114]

At the input of the electronics, incoming pulses are evaluated with respect to pulse height. Only pulses higher than a given threshold will be accepted for further signal processing. Thus small amplitude noise pulses are readily eliminated. The constant fraction discriminators on both the START and the STOP input then analyse the pulse shape of the individual pulses. The portion of the incoming (generally negative) pulses with the steepest slope on the leading edge is taken as a criterion for the temporal position. Which portion of the slope is taken will depend on the fraction, the constant fraction delay (or shaping delay), and the zero crossing level. Threshold, fraction, constant fraction delay, and zero crossing level will depend on the type of detector used and need to be matched to the individual detector. At the output of the CFD pulses are re-shaped to a standard height and shape. They then can be delayed by an electronic shifting delay. This delay will later result in a left or right shift of the entire measurement on the time axis. The TAC is the fast clock, started by the START and stopped by the STOP pulse. The START pulse initiates the growth of a ramp signal. Depending on the arrival time of the STOP pulse the ramp will have a lower or higher height. Once the growth of the ramp has been stopped, the level will remain

Chapter 2

constant for a defined period. The TAC output pulse can then be amplified, thus effectively stretching the time axis. Minimum and maximum available (amplified) TAC amplitude determine the time range. The amplified TAC output pulse is effectively an analogue pulse of a height corresponding to a measured time of a single START – STOP sequence. For further processing the pulse height will be measured by a digital pulse height measure device, the ADC. The ADC resolution determines how many discrete time values are possible. All possible measured TAC pulse amplitudes will therefore put into different time bins. The width of the time bin is the ratio of the full time range and the resolution of the ADC in channels. It is the time resolution, usually given in picoseconds / channel or nanoseconds / channel.

Chapter 3
Lanthanide doped Binary oxides
(Thoria and zirconia)

CHAPTER 3

3.1. General Introduction

Oxides like ThO_2 and ZrO_2 find extensive application in the field of catalysis, fuel cell, sensor, luminescent materials etc. During the past decade, luminescent inorganic nanoparticles have attracted great research interest for their unique optical properties and potential applications in nanoscale optics, optoelectronics, optical bioprobes and biological detection [115-118]. Oxides with one dimensional structure like nanorods and nanowires are interesting due to the unique optical and catalytic properties. ThO_2 and ZrO_2 are found to be very efficient hosts for luminescent materials because of their low phonon energy (thoria~ 450 cm^{-1} and zirconia~ 470 cm^{-1}). This low phonon energy decreases the probability of nonradiative multi-phonon relaxation of excited rare earth dopant ions throughout the vibrational bands of the host lattice, which is considered one of the most competitive non-radiative relaxation processes for optical activator ions in a luminescent material. Also it is known for ThO_2 that it crystallizes in the fluorite structure with a lattice constant of 0.56 nm. The ionic radius of Th^{4+} is 0.104 nm, making the substitution of all the rare earths possible. On the other side, zirconium oxide (ZrO_2) has also attracted a lot of attention in technology and science because of its properties such as superior hardness, good chemical and photochemical stability, high resistance to corrosion, low thermal conductivity, high thermal expansion coefficient, high thermo-mechanical resistance, a large dielectric constant, a high refractive index of 2.17 and a high optical transparency in the $0.3\text{--}8.0\mu\text{m}$ range with a wide optical band gap of about 5.2 eV [119]. Due to some of these properties, it can be used in a variety of photonics and industrial applications [120-123]. The optical gap of ZrO_2 is commonly affected by the incorporation of activators ions that generally induce new optical properties in the host material. Nanocrystalline ZrO_2 doped with different rare earths has been demonstrated to present suitable optical properties for photonics applications due to its enhanced luminescence [124-127], which in turn is due to nanosized effects. Zirconia can adopt three different crystalline structures, that is, cubic, tetragonal, and monoclinic polymorphs. The monoclinic phase, stable at room temperature, is transformed to tetragonal at 1170°C , and then to cubic at 2370°C . These two high-temperature phases are unstable in bulk forms at ambient temperature. This is unfortunate because they are more valuable for the technological applications mentioned above than the room-temperature monoclinic

phase. Consequently, many divalent and trivalent cationic species such as Mg^{2+} , Ca^{2+} and Y^{3+} have been incorporated into zirconia to prepare cubic and tetragonal zirconia that is stable at room temperature [128].

As far as thorium dioxide is concerned; most of the earlier luminescence reports are with dopant like Eu, Pr, Dy, Tb, Er [129-136]. To the best of our knowledge, no literature is available on spectroscopic investigation of Sm^{3+} ions in ThO_2 . Further little attention has been paid to the optical spectroscopy of Eu^{3+} doped ThO_2 nanocrystals such as site symmetry and luminescence dynamics. The optical properties of $Eu^{3+}:ThO_2$ with nanometre dimension may differ significantly from those of bulk material. This is the first report of its kind, where effect of annealing temperature on luminescence dynamics of Eu^{3+} in ThO_2 is investigated in detail.

Here, we introduced Sm^{3+}/Eu^{3+} ions in nanocrystalline ThO_2 materials by means of a versatile microemulsion based synthesis (reverse micellar route) in order to obtain multifunctional materials which combine the optical properties of the lanthanides with the matrix's own properties. The main idea behind this technique is that by appropriate control of the synthesis parameters, one can use these nanoreactors to produce tailor-made products down to nanoscale level with new and special properties. The aim of this study was to lower the synthesis temperature for preparing thoria nanorods from thorium oxalate precursor via the surfactant (Cetyl Trimethyl ammonium bromide, CTAB) assisted reverse micellar route and characterize the same with Thermogravimetric analysis (TGA), X-ray diffraction (XRD), High resolution transmission electron microscopy (HRTEM) and Photoluminescence (PL) spectroscopy. Through the present work, we have tried to investigate the emission, excitation and lifetime studies of the samarium/europium ion in thoria matrix. The sites occupied by Sm^{3+} ions and effect of site symmetry were also studied using time resolved emission spectrometry. PL spectra of $Eu^{3+}:ThO_2$ nanocrystals was studied after annealing at higher temperatures in the range 500-900°C. Eu^{3+} ion occupied two different sites in the host and relaxes at different time intervals. The change in lifetime of Eu^{3+} at two sites with annealing temperature could be related with changes in structure of the host by investigating the changes in intensity of time resolved emission spectra of Eu^{3+} at two different sites.

There are quite a few reports also available on photoluminescence of europium doped zirconia [137-144]. But we have employed different approach to synthesize zirconia

nanocubes by non-ionic assisted reverse micellar synthesis. Through this route we can stabilize metastable tetragonal phase at 500°C through addition of 1 mol % Eu^{3+} which is technologically more important. We have tried to investigate the effect of ligand field (oxalate and oxide) on emission, excitation and lifetime studies of the Europium doped zirconium oxalate (precursor stage) and zirconium dioxide samples. In addition, Judd-Ofelt parameter and other Photophysical properties like (radiative transition rate, radiative lifetime, efficiency, branching ratio) of the Eu^{3+} ion in the zirconium oxalate and zirconium dioxide was evaluated by adopting standard Judd-Ofelt (J-O) analysis procedures. These J-O parameters reflect the local structure around the metal ion in the host and provide information regarding nature of the metal-ligand bonding in the matrix.

3.2. Synthesis and characterization of $\text{ThO}_2:\text{Sm}^{3+}$ nanoparticles

3.2.1. *Synthesis of $\text{ThO}_2:\text{Sm}^{3+}$ nanorods*

ThO_2 nanoparticles were synthesized by the thermal decomposition of thorium oxalate precursor. The precursors were synthesized by the reverse micellar route with CTAB (Cetyl trimethyl ammonium bromide as the surfactant, 1-butanol as the co-surfactant and iso-octane as the nonpolar solvent. The weight fraction of various constituents in the microemulsion was 16.76% of CTAB, 13.9% of n-butanol, 59.29% of isooctane, and 10.05% of aqueous phase. For the synthesis of thorium oxalate precursor two different microemulsion, one containing 0.1M aqueous solution of thorium nitrate and the other containing the aqueous solution of ammonium Oxalate were slowly mixed and stirred for 15 h. The product was separated from microemulsion by centrifugation and washed with 1:1 mixture of chloroform and methanol and dried at room temperature. The product was decomposed at 500°C for 6 h to obtain thorium oxide. For preparation of samarium doped sample, appropriate quantities (1mol %) of samarium nitrate, $\text{Sm}(\text{NO}_3)_3$ were added at the initial stage in thorium nitrate microemulsion. Thorium nitrate (99.99%) and 1 mol % of samarium nitrate (99.99%) were dissolved in quartz double distilled water and stirred for 2 h at 80–90 °. Based on ionic radii analogy composition is like $\text{Th}_{1-x}\text{Sm}_x\text{O}_2$, samarium occupies thorium site.

3.2.2. Characterization of $\text{ThO}_2\text{:Sm}^{3+}$ nanorods

3.2.2.1. Thermal studies of oxalate: TGA/DTA

TGA and DTA plots of the oxalates are given in Figures. 3.1a and b, respectively. Fig. 3.1 show that total mass loss {49.2%} obtained during steps A–F, by heating the sample to 800 °C is in good agreement with that for the formation of thorium oxide from thorium oxalate hexahydrate {48.8%} [145]. Raje et al [145] have reported mechanism for thermal decomposition of thorium oxalate hexahydrate which was found to takes places in six stages. They have reported that thorium oxalate hexahydrate dehydrates during step A in the temperature range of 70–165 °C to form thorium oxalate dihydrate. Formation of thorium oxalate dihydrate was also confirmed by the recorded HTXRD pattern [145] which matches well with the reported JCPDS card no. 18-1385 of thorium oxalate dihydrate. This compound has an orthorhombic structure with four molecular formula units per unit cell [146].

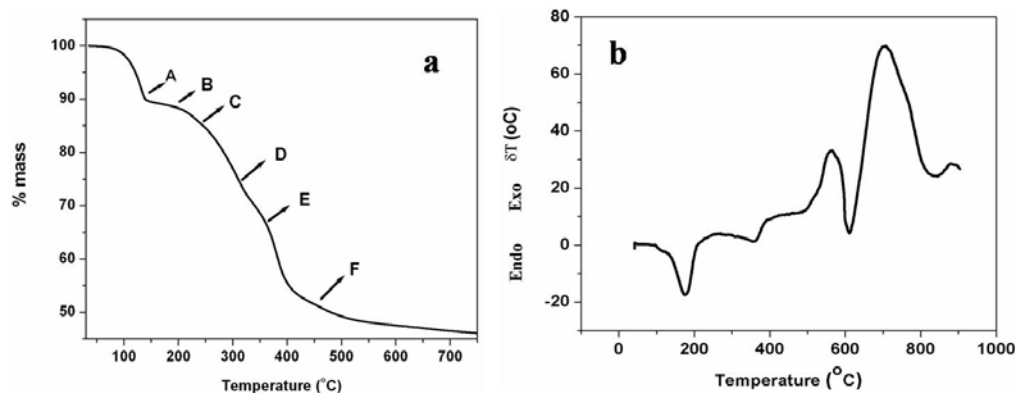


**Figure 3.1: (a) TGA of thorium oxalate hexahydrate powders in air atmosphere
(b) DTA of thorium oxalate dihydrate powders**

Step A: 70–165°C, Step B: 165–215 °C, Step C: 215–280°C, Step D: 280–400°C, Step E: 400–450 °C, Step F: 450–520°C

3.2.2.2. Phase purity and Structure: XRD

Based on TGA/DTA analysis (refer to Fig.3.1a) thorium oxalate precursor was heated at 500°C for 6 h to obtain Thorium oxide.

Figure 3.1b shows the DTA curve for thorium oxalate. Various exotherm shows the reaction taking place during the decomposition of thorium oxalate hexahydrate. Peak corresponding to step; A (70–165°C), B (165–215°C), C (215–280 °C) and D (280–400°C) corresponds to loss of six water molecules in various steps. Peak D (400–450°C) and E (450°C) correspond to $\text{Th}(\text{OH})_2\text{C}_2\text{O}_4 \rightarrow \text{ThO}_2 + \text{H}_2\text{O} + \text{CO}_2 + \text{CO}$.

Figure 3.2 shows the XRD patterns of the Thorium oxalate and thorium dioxide. The recorded XRD pattern for the Thorium oxalate matches well with the reported XRD pattern of thorium oxalate hexahydrate with JCPDS files no. 22-1485. Based on X-ray line broadening technique, crystallite size of thorium oxalate nanoparticles was found to be about 20 nm. ThO_2 crystallized in a cubic geometry with space group $Fm\bar{3}m$ (JCPDS file no-78-0685, shown in Fig. 3.2). The XRD data were indexed on a cubic system with cell parameters $a = 5.597\text{\AA}$ which. The grain size of thoria powder was obtained by X-ray line broadening as well as from TEM studies. Thorium oxide was found to have a grain size of 62 nm from X-ray line broadening studies.

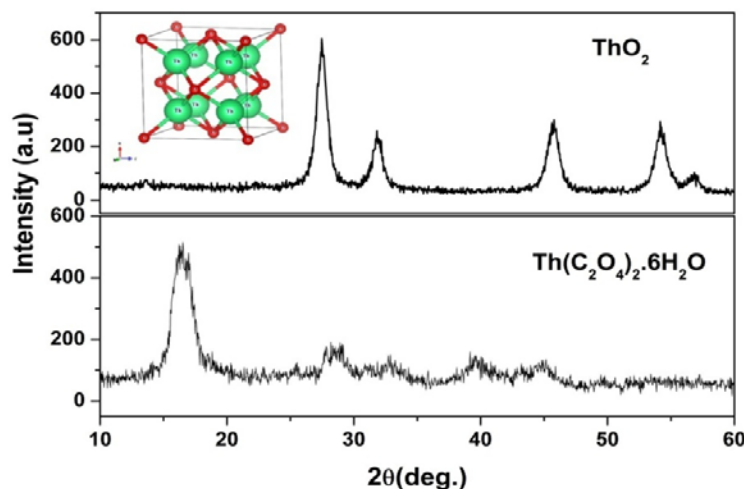


Figure 3.2: PXRD pattern of thorium oxalate hexahydrate and thorium oxide doped. Inset in figure shows the crystal structure of thoria.

3.2.2.3. Morphological studies: TEM

To check the morphology of thoria nanoparticles, TEM images were recorded and the TEM image of a representative ThO_2 sample is shown in Fig. 3.3. The image consists of nano-rods having length 2-2.5 μm and diameter less than 50 nm (Fig. 3.3c). It is interesting to note that the surface charge (obtained by zeta potential measurements on thorium oxalate nanorods) was found to be negative (-9.42). Cationic surfactants such as CTAB have a positive charge on their head group. This would lead to an assembly of surfactant molecules with a positively charged group on the surface of the nanorods (negative zeta potential) and subsequently affect the growth along the diameter (surface of the nanorods). Growth hence would be easier along the axis of the rod.

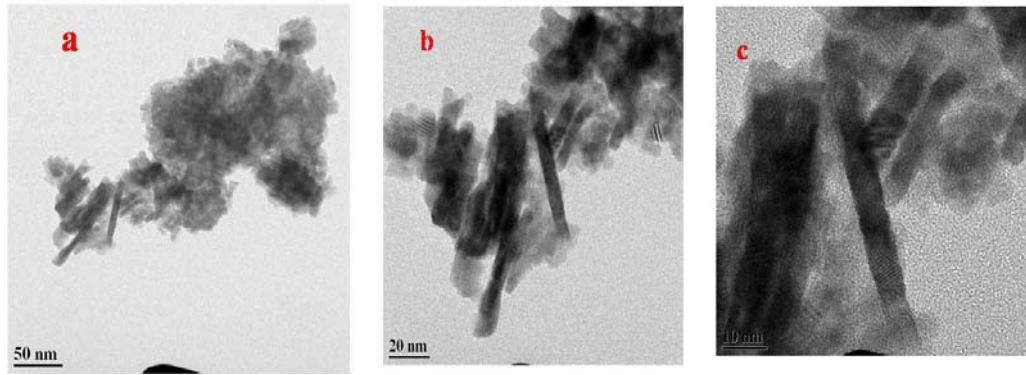


Figure 3.3: High resolution TEM micrograph of ThO₂

3.3. Photoluminescence properties of ThO₂:Sm³⁺ nanorods:

The excitation spectra of the 1 mol% sample with $\lambda_{em} = 569$ corresponding to ${}^4G_{5/2} \rightarrow {}^6H_{5/2}$ emission showed intense and broad band in the range of 200–275 nm and was assigned to the charge transfer band $O^{2-} \rightarrow Sm^{3+}$ (CTB). The peaks seen at 358, 406, 422 and 488 nm (the enlarger in the inset of Fig. 3.4a) were assigned to the f-f transitions from the ${}^6H_{5/2}$ ground state to ${}^4F_{9/2}$, ${}^4K_{11/2}$, ${}^6P_{3/2} + {}^5P_{3/2}$ and ${}^4I_{9/2} + {}^4M_{15/2}$ levels, respectively [147]. Upon excitation with the 250 nm, the emission spectrum (see Fig. 3.4b) is characterized by four bands located at 569, 609, 662 and 720 nm corresponding to the transitions ${}^4G_{5/2} \rightarrow {}^6H_{5/2}$, ${}^4G_{5/2} \rightarrow {}^6H_{7/2}$, ${}^4G_{5/2} \rightarrow {}^6H_{9/2}$ and ${}^4G_{5/2} \rightarrow {}^6H_{11/2}$, respectively. Spectral features remain same on excitation with 245 nm (charge transfer) and 406 nm (f-f band). Broad band at 447 nm is assigned to host emission [148].

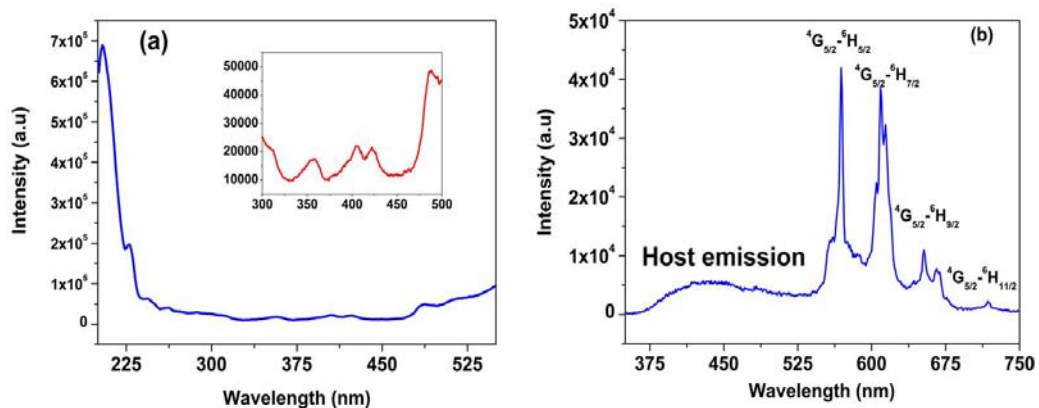


Figure 3.4: (a) Excitation spectra (λ_{em} - 569 nm) (b) Emission spectra (λ_{ex} - 245 nm) of the ThO₂: Sm³⁺

The room temperature decay curves (see Fig. 3.5a) of the PL emission showed a non-exponential shape. Therefore, we applied double exponential fitting equation, which takes into account both the fast and the slow component of the decay

$$I(t) = A_0 + A_1 \exp\left(\frac{-t}{\tau_1}\right) + A_2 \exp\left(\frac{-t}{\tau_2}\right) \quad (3.1)$$

It was reported that in ThO₂ there are two sites for Th⁴⁺ ion; cubic (*O_h*) and trigonal (*C_{3v}*) sites and can be occupied by rare earth ions. Two life-times values (1.17 and 4.90 ms) indicate the presence of Sm³⁺ ions in these different environments. Time resolved emission spectroscopy (TRES) was carried to identify the two species. TRES spectra after giving suitable delay time and proper gate width has been shown in Figure 3.5(b). The ⁴G_{5/2}→⁶H_{5/2} line is observed at 569 nm, which originates from the magnetic dipole (MD) transition, and does not depend on chemical surroundings of the luminescent centre and its symmetry. However, the hypersensitive ⁴G_{5/2}→⁶H_{9/2} transition at 662 nm is magnetic-dipole forbidden and electric-dipole allowed and its intensity increases as the environmental symmetry become lower. The asymmetry ratio was found to be 0.46 and 0.39 for short lived (τ= 1.1 ms) and long lived (τ= 4.9 ms) species respectively. The existence of two different lifetimes should be linked to the presence of oxygen vacancies in the structure. In these conditions, Sm³⁺ could adopt two different environments: one with eight oxygen atoms coordinated the other one with oxygen atoms and vacancies. Short lived species is at more asymmetric environment (nearer to oxygen vacancies) in comparison to long lived species which occupy *O_h* site.

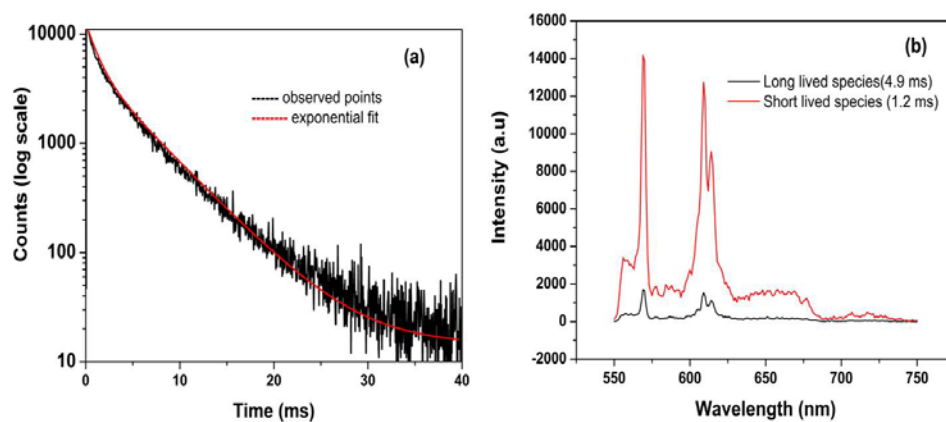


Figure 3.5: (a) Luminescence decay time profile of the ThO₂: Sm³⁺ (b) TRES spectra for short and long lived samarium ion in thorium dioxide.

In order to evaluate the colorimetric performance of the phosphor, the color coordinates for the sample $\text{ThO}_2:\text{Sm}^{3+}$ (1mol %) were calculated using the intensity-corrected emission spectra excited by 245 nm. The calculated CIE coordinates for $\text{ThO}_2:\text{Sm}^{3+}$ (1mol %) nanorods are found to be 0.443 and 0.370, which are indicated in the CIE chromaticity coordinate diagram and confirm the warm white color (on the boundary line of CIE white domain), as shown in Fig. 3.6. The correlated color temperatures (CCT) is also calculated using McCamy and Kelly approximation [149, 150].

$$\text{CCT}(x,y) = -449n^3 + 3525n^2 - 6823.3n + 5520.33 \quad (3.2)$$

Where $n = (x - x_e)/(y - y_e)$ is the inverse slope line and $(x_e = 0.3320, y_e = 0.1858)$ is the "epicentre"; quite close to the intersection point mentioned by Kelly. The value of CCT ($x = 0.443$ and $y = 0.370$) for $\text{ThO}_2:\text{Sm}^{3+}$ (1mol %) is 2600 K which indicated that White light is more close to yellowish white through red (warm color).

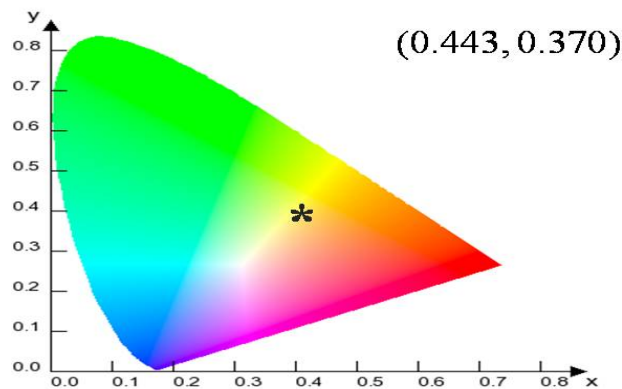


Figure 3.6: CIE index diagram of the $\text{ThO}_2:\text{Sm}^{3+}$

3.4. Synthesis and characterization of $\text{ThO}_2:\text{Eu}^{3+}$ nanoparticles

3.4.1. Synthesis of $\text{ThO}_2:\text{Eu}^{3+}$ nanoparticles

Eu-doped ThO_2 nanoparticles were synthesized by urea combustion method [151,152]. In a combustion reaction, thorium nitrate gel containing appropriate amounts of europium [in the form of $\text{Eu}(\text{NO}_3)_3$] was mixed with urea solution in a molar ratio of 1:1. This solution was dried and heated at 573 K to give nanocrystalline powders of $\text{Th}_{1-x}\text{Eu}_x\text{O}_2$ ($x=0.01$). The ThO_2 nanopowders thus obtained were annealed at 500, 700 and 900°C for 90 minutes.

3.4.2. Characterization of $\text{ThO}_2\text{:Eu}^{3+}$ nanoparticles

3.4.2.1. Thermal studies: TGA/DTA

The DTA and TGA investigations of combustion reaction indicated that combustion temperature to be around 275 °C (Fig. 3.7). Thermogravimetric curve of the Th–Eu nitrate/urea gel showed that the gel decomposed sharply at around 275 °C, yielding Eu-doped ThO_2 as the final product. The exothermic peak in the differential thermal analysis curve at 275 °C is related to combustion of urea, releasing sufficient heat energy for the decomposition of thorium nitrate–europium nitrate leading to the formation of the final product.

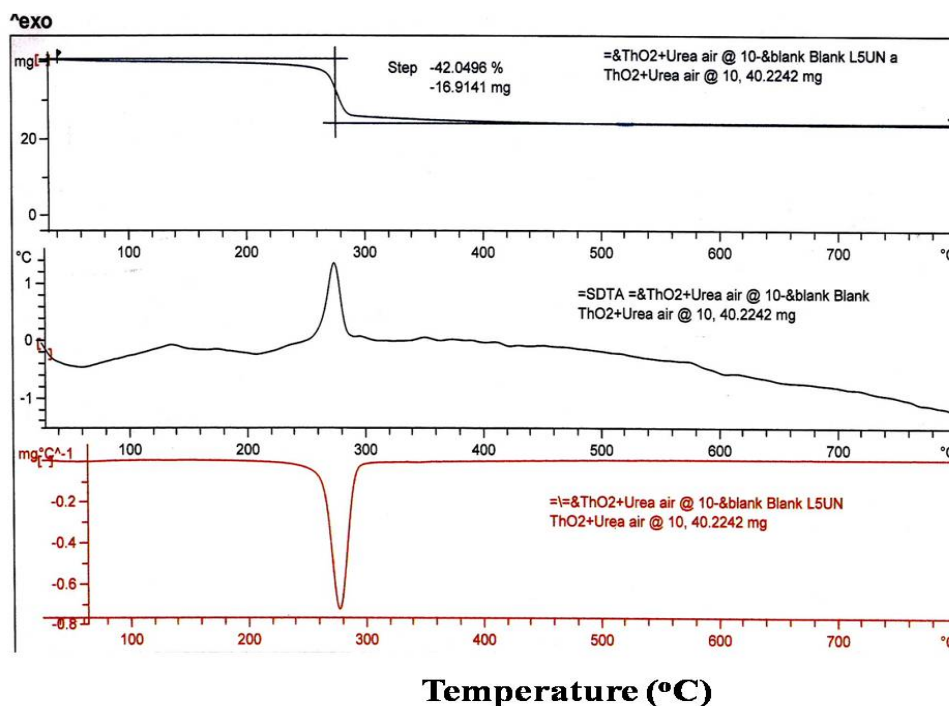


Figure 3.7: Thermogram for $\text{ThO}_2\text{:Eu}$ prepared via combustion synthesis route using Urea

3.4.2.2. Phase purity and Structure: XRD

The X-ray diffraction patterns of the product obtained by the thermal decomposition of metal nitrate precursor gel indicate that $\text{Th}_{1-x}\text{Eu}_x\text{O}_2$ crystallized in the cubic structure (lattice parameter $a = 0.56$ nm). The crystallite size of the ThO_2 nanocrystals was estimated from the diffraction data using the Scherrer formula $D = 0.9 \lambda / \beta \cos \theta$. In this equation D is the mean crystallite size in nm, λ is the X ray wavelength (0.154249 nm), and β is the full width at half maximum (FWHM) of the

selected XRD peak (rad) and θ is half of the Bragg's angle (2θ). The reflection broadening due to the diffractometer was eliminated from the β_s value using a microcrystalline reference (silicon) β_r as given in equation, $\beta^2 = \beta_s^2 - \beta_r^2$. In the present work, the [111] reflection of the ThO_2 ($2\theta = 28^\circ$) was used in the calculation. As prepared $\text{Th}_{1-x}\text{Eu}_x\text{O}_2$ sample (annealed 300°C) crystallized in cubic geometry with space group $\text{Fm}\bar{3}\text{m}$ (JCPDS file no-78-0685, shown in Fig. 3.8). The XRD data were indexed on a cubic system with cell parameters $a = 5.597\text{\AA}$. Intensity of all the diffraction lines increased with increasing annealing temperatures suggesting the improved crystallinity for the host.

The average crystallite size was determined using Scherrer's formula from half width of the most intense emission (Fig. 3.8) which varied from 5 to 43 nm on high temperature annealing (Table 3.1). As can be seen from Table 3.1, with increase in annealing temperature, unit cell volume decreases, which indicates substitution of Eu^{3+} at Th^{4+} site.

X-ray line broadening takes place because of various reason like instrumental artefacts (Non-monochromaticity of the source, imperfect focusing) crystallite size, and residual strain arising from dislocations, coherent precipitates etc. Grain size from X-ray line broadening is obtained from Scherer's formula.

$$t = \frac{0.94\lambda}{B \cos \theta} \quad (3.3)$$

Where t is the crystallite size, λ is the wavelength (for $\text{Cu-K}\alpha$, $\lambda=1.5418\text{ \AA}$) and $B=\sqrt{(B_M^2 - B_S^2)}$ (B_M is the full width at half maximum of the sample and B_S is that of a standard grain size of around $2\text{ }\mu\text{m}$). From the Scherer formula, Peak width (B) is inversely proportional to crystallite size (L). As the crystallite size gets smaller, the peak gets broader. With increase in temperature; size of crystallite increases and so B decreases. A smaller particle gives a broader Bragg peak. Effect of temperature on the broadness of strong diffraction peak (30°) is shown in inset of Figure 3.8.

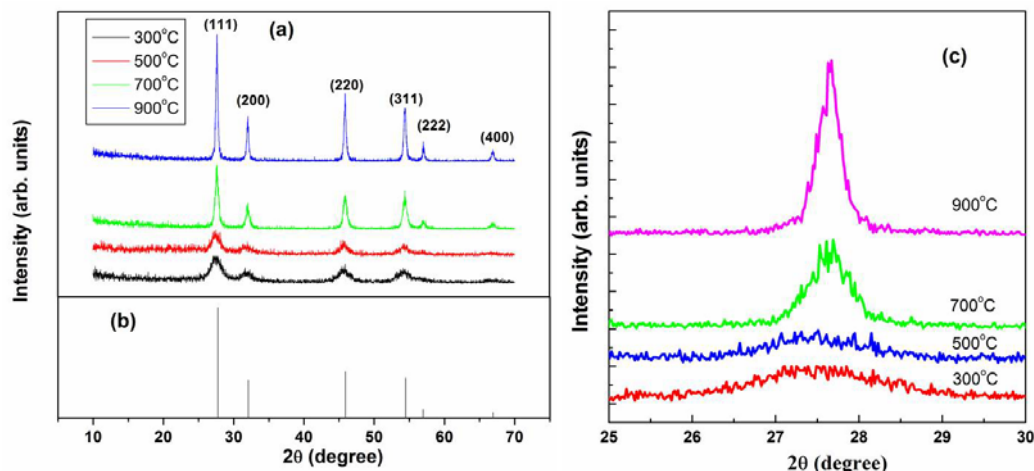


Figure 3.8: Figure 2: (a) X-ray diffraction patterns for the powder samples obtained via combustion synthesis by annealing at different temperatures along with their hkl values. (b) The standard ICDD stick patterns (JCPDS-78-0685) that matched with the experimental pattern. (c) Effect of temperature on the line broadening of peak at $2\theta=28^\circ$ which was used for the calculation of crystallite size.

Table 3.1: Average particle size and unit cell volume of thoria nanoparticles at different annealing temperature

Sr. No.	Annealing Temp. ($^\circ\text{C}$)	Average Particle size (nm)	Cell Volume (\AA^3)
1	300	4.8	5.61803
2	500	5.6	5.60434
3	700	17.6	5.59035
4	900	43.3	5.58566

3.4.2.3. Morphological studies: TEM

Figures 3.9 and 3.10 show TEM and SAED micrographs of thoria nanoparticles. Transmission electron microscopy (TEM) was utilized to examine the morphology of thoria nanoparticles. Qualitatively, the material appears to be comprised of interconnected thoria particles that define cavities of mesoporous (20–50 nm) dimensions. The nanostructure is composed of cubical primary particles with features in the 2-5 nm range. These particles are connected to one another to form the larger clusters. Selected area electron diffraction (SAED) pattern of the oxide nanoparticles shows crystalline nature. It exhibits diffuse rings, indicating the nanocrystalline nature of the sample. These rings can be indexed to thoria phase.

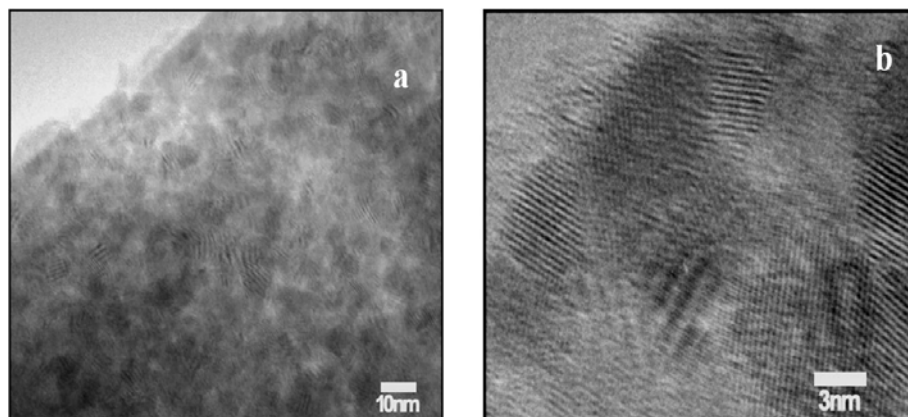


Figure 3.9: TEM micrographs of $\text{ThO}_2:\text{Eu}^{3+}$ annealed at 300°C (as prepared samples) under different magnifications

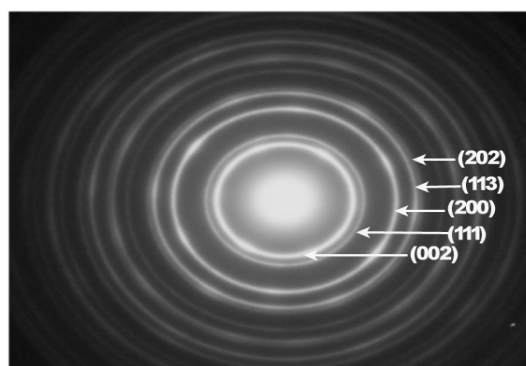


Figure 3.10: SAED micrographs of $\text{ThO}_2:\text{Eu}^{3+}$ annealed at 300°C (as prepared samples)

3.5. Photoluminescence properties of $\text{ThO}_2:\text{Eu}^{3+}$ nanoparticles

3.5.1. Effect of annealing temperature on PL properties $\text{ThO}_2:\text{Eu}^{3+}$ nanoparticles

To investigate the effect of annealing temperature on the PL properties of the 1.0 mol% Eu doped thorium dioxide phosphors, the as-formed sample (finally heated at 300°C) was further annealed at 500, 700 and 900°C and the changes in PL emission intensity were measured (Figure 3.11). It was observed that, emission intensity increases with increase in temperature. This can be attributed to reduction in non-radiative transitions as a result of reducing surface defects with increasing annealing temperature. Another interesting observation, which can be inferred from these studies is that in sample annealed at 300°C , ${}^5\text{D}_0 \rightarrow {}^7\text{F}_0$ intensity is negligible and crystal field splitting in ${}^5\text{D}_0 \rightarrow {}^7\text{F}_1$ and ${}^5\text{D}_0 \rightarrow {}^7\text{F}_2$ is not that prominent as in the case of

samples annealed at 700/900°C. At 900 °C, along with enhancement in emission intensity, the peak ${}^5D_0 \rightarrow {}^7F_1$ and ${}^5D_0 \rightarrow {}^7F_2$ splits into three and five peaks respectively, which indicates that the symmetry around the Eu^{3+} ions is significantly lowered in this sample compared with in the samples heated up to 500 °C. These results confirm the fact that the symmetry around Eu^{3+} is very low for samples heated above 500 °C.

Figure 3.12 shows the variation in asymmetric ratio ('X') with annealing temperature. This is defined as the ratio of the intensity of the ${}^5D_0 \rightarrow {}^7F_2$ and the ${}^5D_0 \rightarrow {}^7F_1$ transitions (I_{615}/I_{592}). The electric dipole transition (${}^5D_0 \rightarrow {}^7F_2$) is hypersensitive in nature than the magnetic dipole transition (${}^5D_0 \rightarrow {}^7F_1$). Thus 'A' value gives indication regarding the symmetry and the covalence of the rare earth ion. Its value increases with increasing covalence of the ligands or decreasing site symmetry. As shown in Figure 3.12, the value of X increases with increase in temperature which indicate that extent of asymmetry around Eu^{3+} at 700/900°C is very high as compared to as prepared or 500°C annealed sample. Based on these observations, further investigations on the system were carried out on the sample, which was giving the best output (1.0 mol% sample annealed at 900°C).

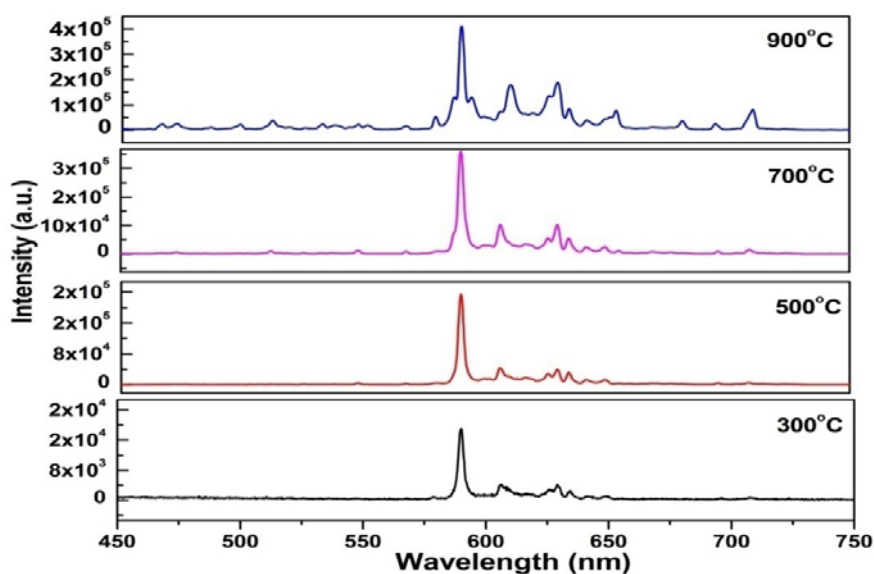


Figure 3.11: Variation in PL emission intensity with annealing temperature.

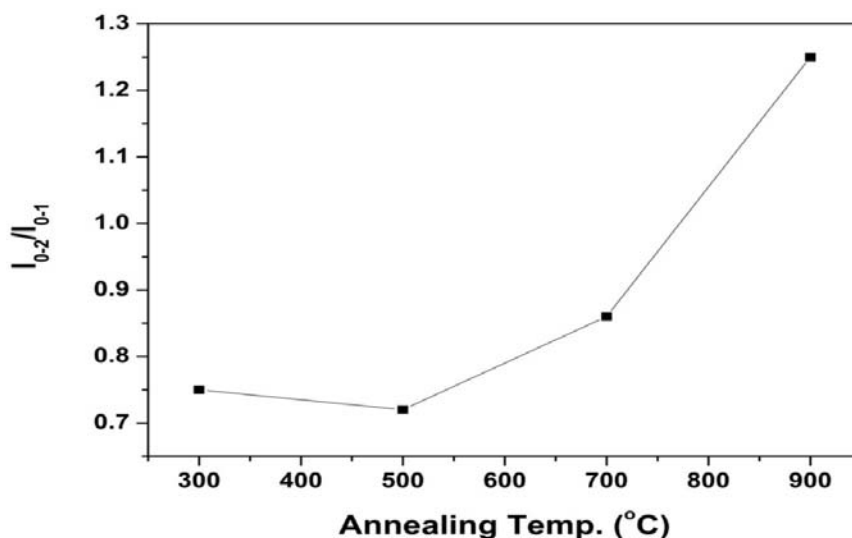


Figure 3.12: Variation in asymmetry ratio with annealing temperature

3.5.2. Excitation and emission spectroscopy of $\text{ThO}_2\cdot\text{Eu}^{3+}$ (1.0 mol% sample annealed at 900°C)

Figure 3.13 shows the excitation spectra ($\lambda_{\text{em}} = 592 \text{ nm}$) of Eu doped thorium oxide sample. A broadband in the region of 220–280 nm peaking at around 256 nm has been attributed to the $\text{O}^{2-} \rightarrow \text{Eu}^{3+}$ charge transfer band (CTB), which is caused by the electron transfer from 2p orbits of O^{2-} ions to 4f shells of Eu^{3+} ions. The sharp lines in 300–400 nm are attributed to intra-configurational 4f–4f transition of Eu^{3+} in host lattice. The peaks observed at 320, 360, 380, 395, 420, 460, 480 and 500 nm were assigned to electronic transitions of ${}^7\text{F}_0 \rightarrow {}^5\text{H}_3$, ${}^5\text{L}_9$, ${}^5\text{L}_7$, ${}^5\text{L}_6$, ${}^5\text{D}_4$, ${}^5\text{D}_3$, ${}^5\text{D}_2$ and ${}^5\text{D}_1$ respectively. Expanded spectra of f–f lines at different annealing temperature are shown in Figure 3.13.

In ThO_2 , Th^{4+} ions occupy a site of O_h symmetry. Replacing tetravalent ions by trivalent ions will require positive charge compensation to maintain the electrical neutrality. The compensation can be achieved at some distance by Th^{4+} interstitial ions. Then several centers are expected in this matrix. Apparently, the doping concentration has a very important role in determining the site symmetry [153]. Linares [153] studied this aspect and came to the conclusion that the cubic sites O_h would be predominated at low rare-earth concentration and the trigonal C_{3v} at high concentration.

Upon excitation at charge transfer band, the emission spectrum exclusively contains very weak lines of ${}^5\text{D}_2 \rightarrow {}^7\text{F}_0$ (465 nm), ${}^5\text{D}_2 \rightarrow {}^7\text{F}_2$ (490 nm), ${}^5\text{D}_2 \rightarrow {}^7\text{F}_3$ (510 nm),

$^5D_1 \rightarrow ^7F_1$ (535 nm), and $^5D_1 \rightarrow ^7F_2$ (555 nm) and the relatively strong bands of $^5D_0 \rightarrow ^7F_0$ (579 nm), $^5D_0 \rightarrow ^7F_1$ (592 nm), $^5D_0 \rightarrow ^7F_2$ (614 nm), $^5D_0 \rightarrow ^7F_3$ (653 nm) and $^5D_0 \rightarrow ^7F_4$ (704 nm). $^5D_{1,2,3} \rightarrow ^7F_1$ lines usually appear in a compound with low-lattice phonon energy, which leads to multiphonon relaxation. They are usually difficult to occur among the levels of Eu^{3+} . As shown in Fig. 3.14, the emission spectra of $\text{ThO}_2:\text{Eu}^{3+}$ nanoparticles consist of emissions from the higher energy levels (5D_1 and 5D_2) also. The presence of emission lines from higher excited states of Eu^{3+} is attributed to the low vibration energy of Th-O groups. Multiphonon relaxation by thoria is not able to bridge the gaps between the higher energy levels and the 5D_0 level of Eu^{3+} completely, resulting in weak emissions from these levels.

The orange emission at 592 nm belongs to the magnetic dipole $^5D_0 \rightarrow ^7F_1$ transitions of Eu^{3+} , and the transition hardly varies with the crystal field strength. The red emission at about 615 nm ascribes to the electric dipole $^5D_0 \rightarrow ^7F_2$ transitions of Eu^{3+} , which is very sensitive to the local environment around the Eu^{3+} and depends on the symmetry of the crystal field. The intensity ratio of $^5D_0 \rightarrow ^7F_2$ to $^5D_0 \rightarrow ^7F_1$ may provide structural hints such as the distortion of CF environment and the site symmetry. The fact that $^5D_0 \rightarrow ^7F_1$ line at 594 nm (MD) is very strong in comparison to $^5D_0 \rightarrow ^7F_2$ line at 614 nm (ED) as can be seen from Figure 3.14 indicates that Eu^{3+} occupy (cubic) symmetric environment with inversion symmetry (O_h). But the appearance of several weak lines in the spectra in addition to the allowed transitions for O_h symmetry indicates that other Eu^{3+} sites may be coexisting.

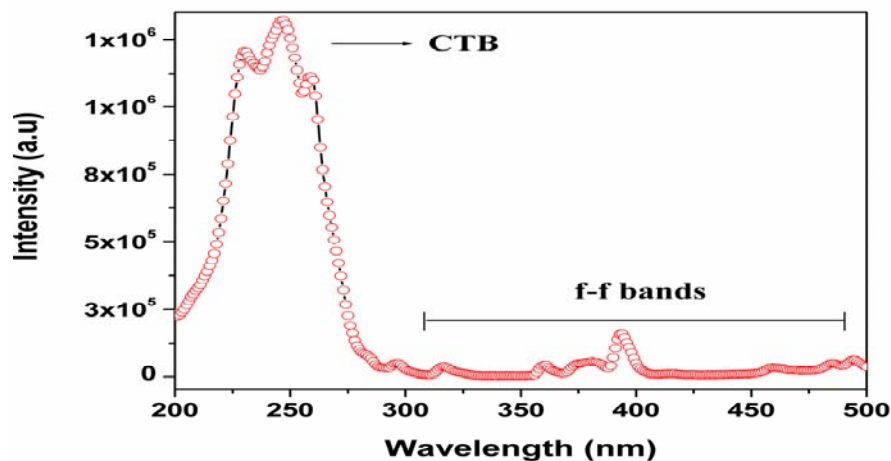


Figure 3.13: Excitation spectra of powder sample of $\text{ThO}_2:\text{Eu}^{3+}$ 1.0 mol% annealed at 900°C .

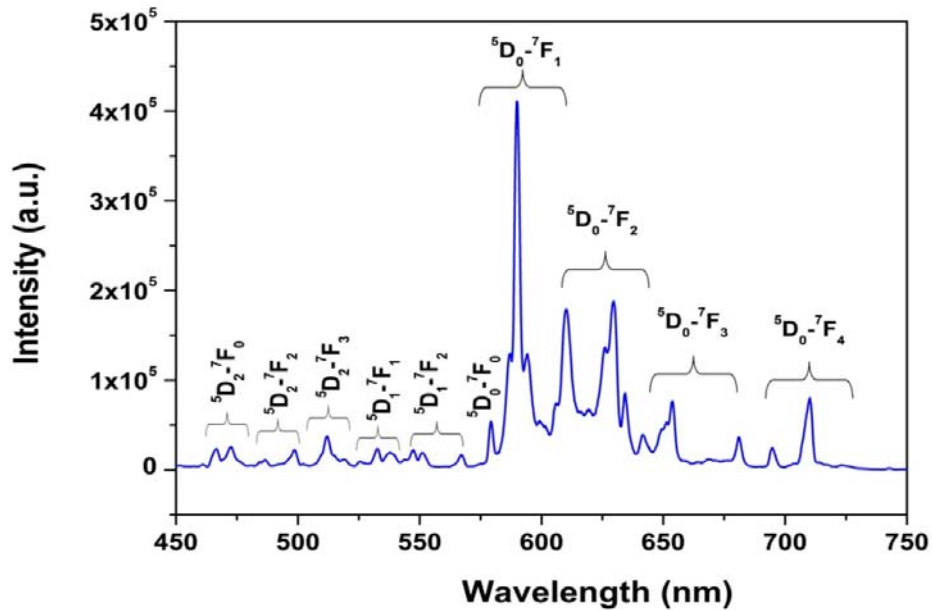


Figure 3.14: Emission spectra ($\lambda_{\text{ex}}=256$ nm) of $\text{ThO}_2:\text{Eu}^{3+}$ 1.0 mol% annealed at 900°C

When the Eu^{3+} ion is inserted into a chemical environment, the $(2J + 1)$ -degenerate J -levels are split by ligand-field effects into so-called Stark sub-levels, the number of which depends on the site symmetry of the metal ion. Here again, the Eu^{3+} ion is used as a local crystal-field probe to characterize the structure and site symmetry, as done by different groups including ours [154-158].

Radiative transitions from ${}^5\text{D}_0$ to levels with $J = 0$ or odd J ($J = 3, 5$) are both ED and MD forbidden, and only weak transitions from ${}^5\text{D}_0$ to these levels are observed due to CF induced J -mixing effect [159]. Moreover, the ${}^5\text{D}_0 \rightarrow {}^7\text{F}_0$ transition is only allowed in the following 10 site symmetries: C_s , C_1 , C_2 , C_3 , C_4 , C_6 , C_{2v} , C_{3v} , C_{4v} , and C_{6v} , according to the ED selection rule [160].

The fact that ${}^5\text{D}_0 \rightarrow {}^7\text{F}_1$ line at 594 nm (MD) is very strong in comparison to ${}^5\text{D}_0 \rightarrow {}^7\text{F}_2$ line at 614 nm (ED) indicates that Eu^{3+} occupies (cubic) symmetric environment with inversion symmetry (O_h). The ${}^5\text{D}_0 \rightarrow {}^7\text{F}_0$ transition, which is only allowed in the 10 point group symmetries aforementioned, was observed in the emission spectrum. In cubic ThO_2 structure, Th^{4+} ions occupy a site of O_h symmetry. The substitution of Th^{4+} with Eu^{3+} may result in significant lattice distortion and thus descend the original O_h site symmetry to very low symmetry viz. C_n or C_{nv} . According to the branching rules of various point groups [161], if Eu^{3+} ions at Th^{4+} site situate at C_{4v}/C_{6v} or C_4/C_6 site, only two lines for $J = 0 \rightarrow J = 1$ transition and two lines for $J = 0 \rightarrow J = 2$ transition are allowed. If Eu^{3+} ions are situated at C_3/C_{3v} , there should be two lines for

$J = 0 \rightarrow J = 1$ transition and three lines for $J = 0 \rightarrow J = 2$ transition. If Eu^{3+} ions are situated at C_{2v} , there should be three lines for $J = 0 \rightarrow J = 1$ transition and four lines for $J = 0 \rightarrow J = 2$ transition. As a matter of fact and as can be seen from Figure 3.15, three lines for $J = 0 \rightarrow J = 1$ transition and five lines for $J = 0 \rightarrow J = 2$ transition of Eu^{3+} were resolved. It infers that the actual site symmetry of Eu^{3+} is very likely reduced to a lower symmetry than C_{2v} (that is, C_2 , C_s , or C_1), due to the difference of ionic radius and charge imbalance between Eu^{3+} and Th^{4+} . So it can be inferred from these discussions that Eu^{3+} occupies two sites in nanocrystalline ThO_2 , cubic (O_h) and non-cubic ($<C_{2v}$). It is contrary to the result obtained by Yin et al [162] in bulk ThO_2 , where they have found the site symmetry of europium ion to be O_h and C_{3v} . Because of smaller particle size and higher surface –to–volume ratio, oxygen can easily be adsorbed and thus oxygen defect were formed in nanocrystalline ThO_2 during the synthesis procedure in air. These oxygen defects significantly influenced the crystal field environment of Eu^{3+} .

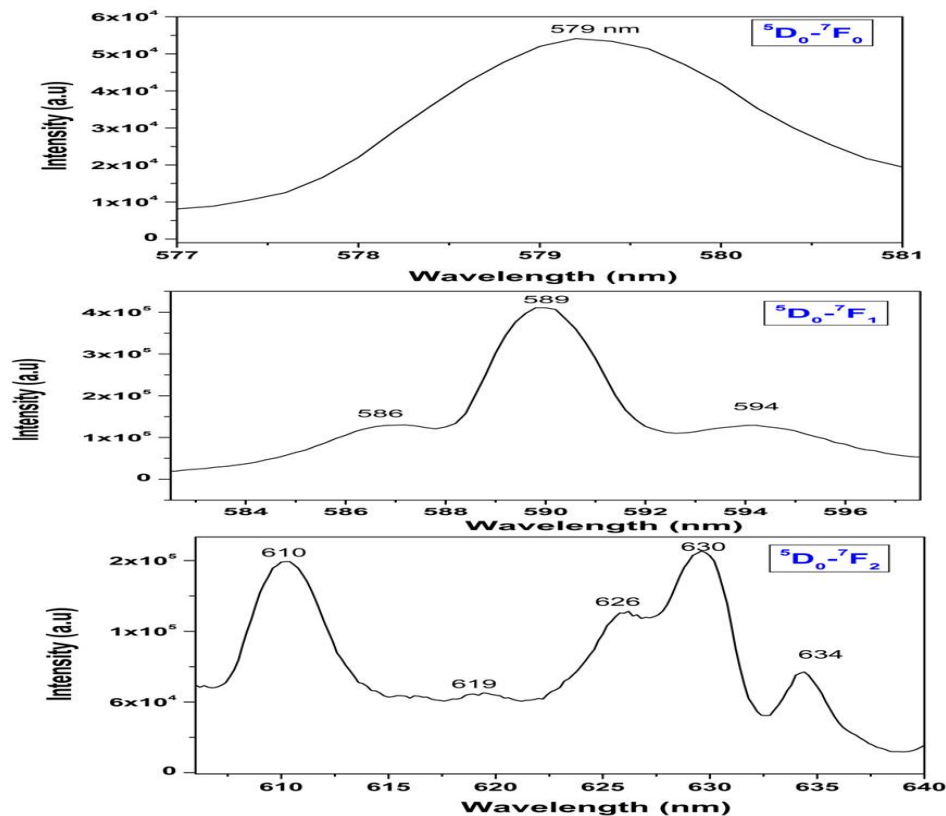


Figure 3.15: Emission spectra ($\lambda_{\text{ex}}=256 \text{ nm}$) of $\text{ThO}_2:\text{Eu}^{3+}$ in different transition region

3.5.3. Time resolved emission spectroscopy of $\text{ThO}_2:\text{Eu}^{3+}$ (1.0 mol% sample annealed at 900°C)

In ThO_2 structure; Eu^{3+} occupy two sites cubic (O_h) and non-cubic ($<\text{C}_{2v}$) as can be confirmed from our emission studies. To get an idea about the nature of the dopant ion occupancy in these lattice sites, PL decay time (life time) studies were conducted. The decay curves corresponding to the $^5\text{D}_0$ level of Eu^{3+} ions in the 1.0 mol % Eu^{3+} doped ThO_2 shown in Figure 3.16 at excitation wavelength of 256 nm, monitoring emission at 592 nm. For $\text{ThO}_2:\text{Eu}$, a good fit was found to a biexponential decay using the similar equation as mentioned in equation (3.4).

$$I(t) = A_0 + A_1 \exp\left(\frac{-t}{\tau_1}\right) + A_2 \exp\left(\frac{-t}{\tau_2}\right) \quad (3.4)$$

Here the τ_f represents the lifetime of the fast decaying component and τ_s represents the lifetime of the slow decaying component. A_1 and A_2 are residual weightage.

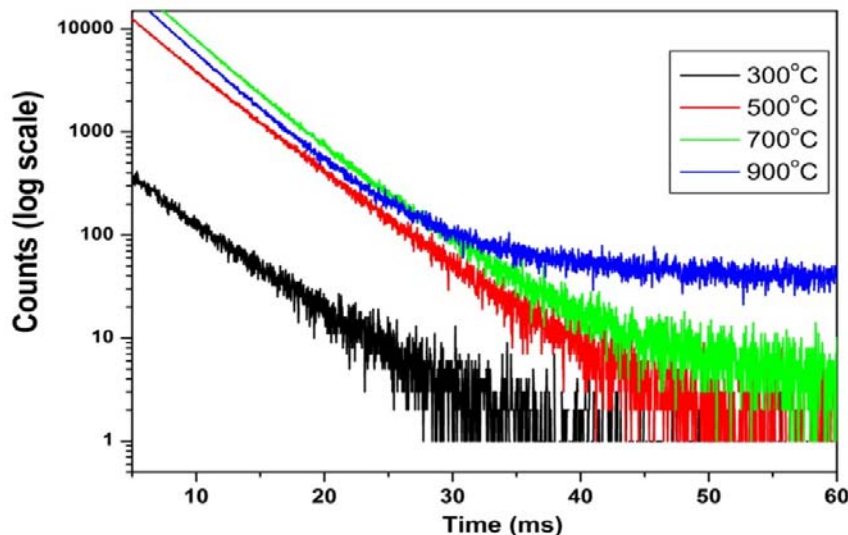


Figure 3.16: Decay curves for the $^5\text{D}_0$ level of Eu^{3+} in $\text{ThO}_2:\text{Eu}$ samples annealed at different temperatures. Samples were excited at 256 nm and emission was monitored at 592 nm for the as-prepared (300°C) and 500, 700 $^\circ\text{C}$ and 900°C heated samples.

Broadly, the analysis showed the presence of two components; one short lived and one long lived. The life time values and their relative fraction at different annealing temperature are tabulated in table 3.2.

This suggested that the Eu^{3+} occupied two different sites in ThO_2 in all the samples annealed at different temperatures. Assuming a given phonon energy (same host for the lanthanide ions), a relatively longer PL decay time should be attributed to a more

symmetric site, as the f-f transition becomes more forbidden, whereas a shorter decay time is often associated with an asymmetric site due to relaxation in the selection rules. In ThO₂ structure, Eu³⁺ ions occupy two sites; cubic (O_h) and non-cubic (<C_{2v}) as can be confirmed from our emission studies. Short lived species T₁ (~1.3-3.4 ms) (which is predominates at higher annealing temperature) arises, because of Eu³⁺ ions occupying non-cubic (<C_{2v}) site without inversion symmetry, whereas long-lived species T₂ (~4.6-6.6 ms) can be ascribed to Eu³⁺ ions occupying cubic (O_h) with inversion symmetry. Such site selective spectroscopy of Eu³⁺ in hosts like silicate, cerate, zirconate and pyrophosphate where multiple sites are available for occupancy, has already been reported by our group [154, 157-158].

Table 3.2: Life time data for ThO₂: Eu at λ_{ex} -403 nm and λ_{em} -592 nm under different annealing temperature (parentheses represents the percentage of that particular species)

Temperature(°C)	Short lived species, T ₁ (in ms)	Long lived species, T ₂ (in ms)
300	1.30 (13 %)	4.60 (87%)
500	2.15 (19 %)	4.85 (81 %)
700	3.25 (65 %)	5.25 (35 %)
900	3.35 (85 %)	6.55 (15 %)

The lifetime values for both T₁ and T₂ increase with annealing temperature. Increase in decay time can be attributed to reduction in non-radiative transitions as a result of reducing surface defects with increasing annealing temperature up to 900°C. But the interesting observation as can be seen from Figure 3.17 is that for the as-prepared sample and 500°C annealed sample the percentage of short lived species is considerably small and long lived is fairly large. But situation reverses at higher temperature; wherein percentage of short lived species is larger than long lived species. This is because of the fact that at higher temperature majority of Eu³⁺ ions tunnels to low symmetry non-cubic site (<C_{2v}) as discussed earlier using emission spectra.

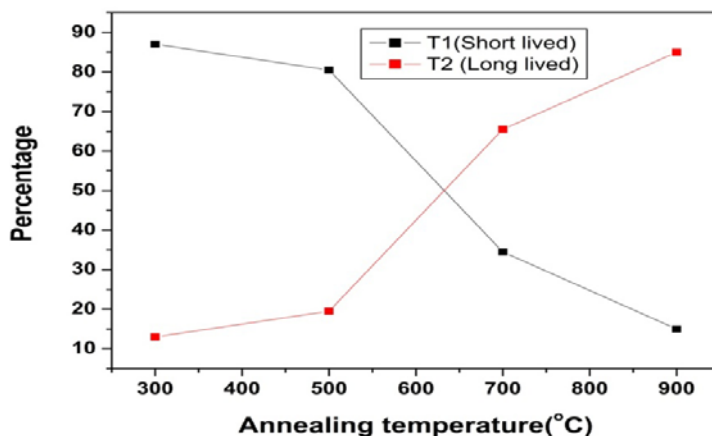


Figure 3.17: Effect of annealing temperature on the fraction of short and long lived species

In case of as prepared sample and 500°C annealed sample, fraction of long lived species (T_2) is larger than short lived species (T_1). This is because of the fact that at 330 and 500°C, the predominant site occupied by Eu^{3+} is cubic (O_h) as is evidenced from figure 3.11 and the related explanations mentioned there. At 700/900 °C, along with enhancement in emission intensity, the peaks ${}^5D_0 \rightarrow {}^7F_1$ and ${}^5D_0 \rightarrow {}^7F_2$ split into three and five peaks respectively, which indicates that the symmetry around the Eu^{3+} ions is significantly lowered compared with that in the samples heated up to 500 °C. These results confirm the fact that the symmetry around Eu^{3+} is very low for samples heated above 500 °C.

In order to identify the environment associated with the species exhibiting different life-times, time resolved emission spectra (TRES) were recorded at different time-delays with constant integration time. Spectra for long lived (T_2) and short lived (T_1) species obtained after mathematical calculations at different annealing temperature are shown in the Figures 3.18 and 3.19 respectively. The ${}^5D_0 \rightarrow {}^7F_1$ line is observed at 592 nm, which originates from the magnetic dipole (MD) transition, and does not depend on chemical surroundings of the luminescent centre and its symmetry. However, the hypersensitive ${}^5D_0 \rightarrow {}^7F_2$ transition at 615 nm is magnetic-dipole forbidden and electric-dipole allowed and its intensity increases as the environmental symmetry become lower. It can be seen from Figure 3.18 that for long lived species ${}^5D_0 \rightarrow {}^7F_1$ line at 594 nm (MD) is stronger than ${}^5D_0 \rightarrow {}^7F_2$ line at 615 nm (ED) in samples annealed at all the temperatures. This is in correspondence with phonon energy concept, where long lived species will have more symmetric component than short lived species. As far as short lived species is concerned, integral

intensity of ${}^5D_0 \rightarrow {}^7F_2$ line at 615 nm (ED) is stronger than ${}^5D_0 \rightarrow {}^7F_1$ line at 594 nm (MD); as can be seen from Figure 3.19.

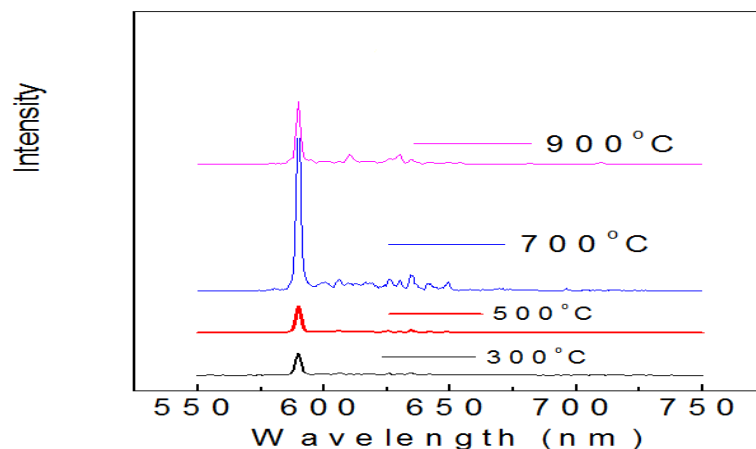


Figure 3.18: Time resolved emission for long lived component

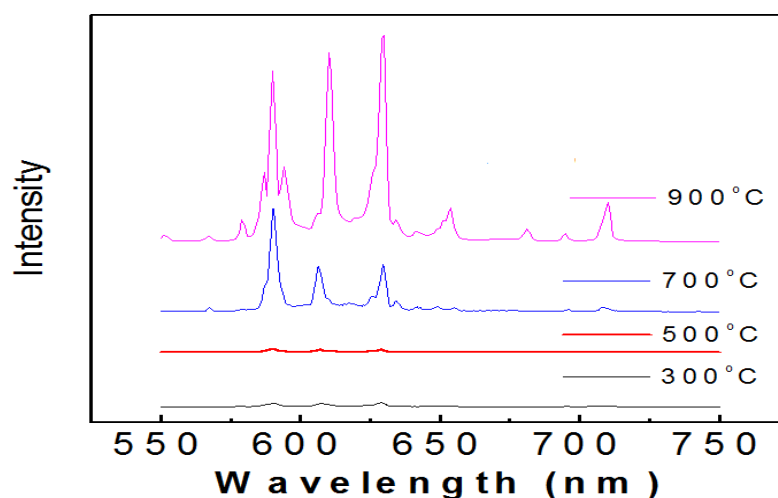


Figure 3.19: Time resolved emission for short lived component

3.6. Synthesis and characterization of $ZrO_2:Eu^{3+}$ nanocubes

3.6.1. Synthesis of $ZrO_2:Eu^{3+}$ nanocubes

ZrO_2 nanoparticles were synthesized by the thermal decomposition of zirconium oxalate precursor using the similar way as explained in section 3.2.1 for synthesis of ThO_2 . The precursors were synthesized by the reverse micellar (microemulsion) route with Tergitol [(C_9H_{19} (C_6H_4) (OCH_2CH_2) $_2$ OH)] (Sigma Aldrich) as the surfactant, 1-octanol (Qualigen, Mumbai, India) as the co-surfactant and cyclohexane (Spectrochem) as the nonpolar solvent. Two different micro emulsions A and B were prepared. Micro-emulsions A consist of 9 mL of 0.1 M zirconium nitrate, 27 mL of

Tergitol (surfactant), 18 mL of 1-octanol (co-surfactant) and 180 mL cyclohexane (non polar solvent). Micro-emulsions B consist of 9 mL of 0.1 M ammonium oxalate, 27 mL of Tergitol (surfactant), 18 mL of 1-octanol (co-surfactant) and 180 mL cyclohexane (non polar solvent) These two micro-emulsion were mixed slowly and stirred overnight on a magnetic stirrer, and the resulting precipitate was separated from apolar solvent and surfactant by centrifuging at the rate of 4000 rpm for 30 min and washing it with acetone. The precipitate was then dried in air. The product was decomposed at 500°C for 6 h to obtain zirconium oxide. For preparation of Eu doped sample, appropriate quantities of europium nitrate, $\text{Eu}(\text{NO}_3)_3$ were added at the initial stage, after adding zirconium nitrate.

3.6.2. Characterization of $\text{ZrO}_2:\text{Eu}^{3+}$ nanocubes

3.6.2.1. Thermal analysis: TGA

Figure 3.20 shows recorded thermogram of the undoped zirconium oxalate sample in air up-to 800°C. Weight loss was observed in two distinct steps; first step corresponds to the water loss (17.8154 %, 6.8589 mg) with observed weight loss matching with the calculated loss. Second step corresponds to the decomposition of the zirconium oxalate and finally forming ZrO_2 , observed weight loss was in agreement with the of calculated weight loss (41.5612 %, 16.0010 mg). Based on TGA/DTA analysis (refer to Fig. 3.20) zirconium oxalate precursor was heated at 500°C for 6 h to obtain zirconium oxide. The zirconium oxalate precursor, obtained using reverse micellar method was found to be amorphous.

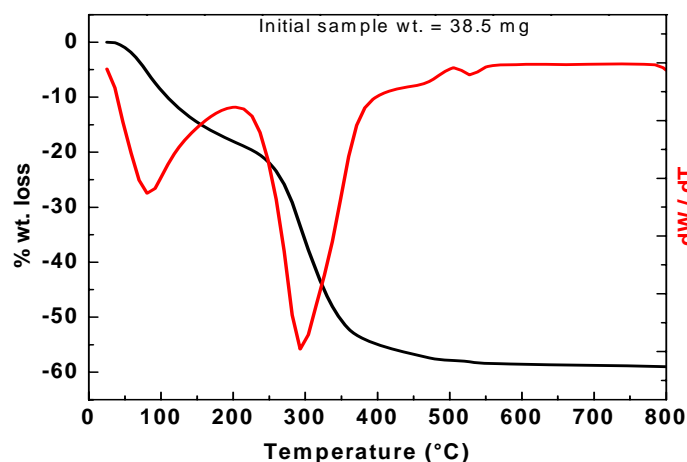


Figure 3.20: TGA/DTA plot for the decomposition of zirconium oxalate. The black line represents the TGA curve. The red line represents the DTA curve

3.6.2.2. Structural analysis: XRD

Figure 3.21a shows the XRD recorded of the final ZrO_2 formed. XRD shows it is the mixture of Monoclinic and tetragonal phases. Monoclinic phase was found in majority with 93% by weight basis.

Figure 3.21b displays the XRD patterns of Eu^{3+} doped ZrO_2 sample obtained after heating zirconium oxalate at 500 °C for 6 hours that shows reflections peaks that can be indexed to the fluorite-like tetragonal structure. Evidence of the tetragonal symmetry might be obtained in the high angle region of the XRD pattern, i.e. a non-symmetric line shape around $2\theta = 35^\circ$ which is originated from the splitting between $[0\ 0\ 2]$ and $[1\ 1\ 0]$ peaks.

Majority phase observed in the XRD pattern corresponds to the tetragonal phase (high temperature phase) which is stabilized by the doping of 1 % Eu^{3+} . Small amount of monoclinic phase (room temperature phase) approximately 5% on weight basis was also detected. The reflections are markedly broadened, which indicate that crystallite size of $\text{ZrO}_2:\text{Eu}^{3+}$ nanoparticles are small.

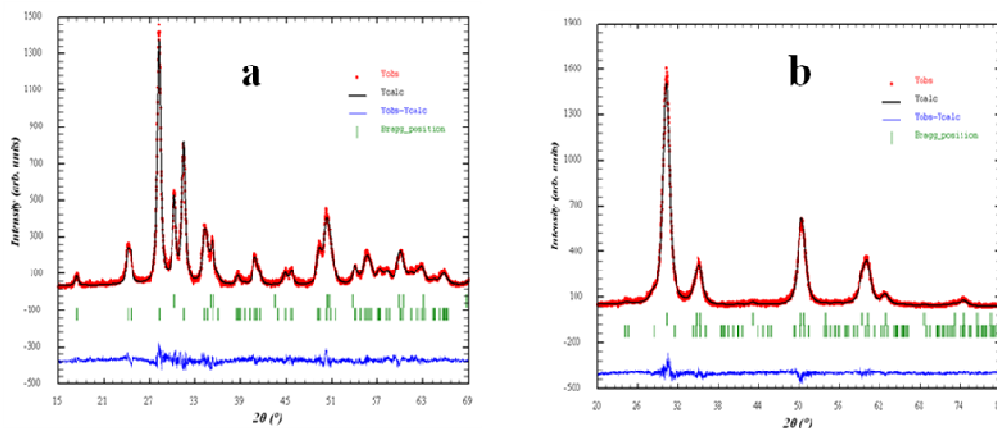


Figure 3.21: Rietveld- refined X-ray diffraction pattern of (a) ZrO_2 (b) $\text{ZrO}_2:\text{Eu}^{3+}$

Approximate crystallite size determined by XRD analysis is 10 nm. This size is small compared to the particle size determined from HRTEM analysis thus indicating that many crystallite agglomerates to form single particle. Structure of monoclinic and tetragonal phase of zirconia is pictorially represented in Figure 3.22.

The crystal structure of tetragonal ZrO_2 is a simple cubic (primitive) with the space group $P42/nmc$. The symmetry of lattice for monoclinic is $2/m$ (C_{2h}) and the symmetry lattice for tetragonal is $4/mmm$ (D_{4h}). It is known that synthesizing ZrO_2

particles with metastable tetragonal crystal structures is very important for technological purposes. On doping Eu^{3+} oxygen vacancies are created which are responsible for the formation of the tetragonal phase instead of the thermodynamically stable monoclinic phase upon crystallization. The process is assigned to the creation of oxygen vacancies and their association with the Zr^{4+} cations whereas the dopants tend to form 8-fold coordination with oxygen [163]. It is acknowledged that the thermally treated ZrO_2 doped with an oversized trivalent ion (Eu^{3+} has an ionic radius of 1.066 Å compared to 0.84 Å of Zr^{4+}) in eight-fold coordination generates minor host distortion and oxygen vacancies that are supposed to associate with the europium in the next nearest-neighbour sites. This induces the eight-fold coordination of europium and seven-fold coordination of Zr^{4+} to oxygen (O) similar to its environment in the monoclinic zirconia.

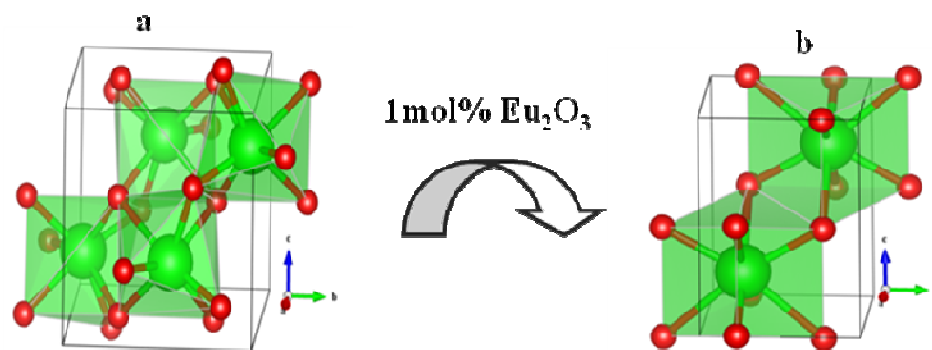


Figure 3.22: Structure of (a) monoclinic and (b) tetragonal phases of zirconia

For incorporation of Eu^{3+} ion at the Zr^{4+} site, three Zr^{4+} ions must be replaced with four Eu^{3+} ions; during this process, an anion vacancy is generated in the lattice. This is schematically represented using Kroger-Vink notation as



3.6.2.3. Vibrational spectroscopy-FTIR

The IR spectra of zirconium oxalate nano particles prepared from Tergitol have been given below in Fig. 3.23. The structural functionality present in the oxalate nano particles may be explained from the characteristic absorption bands in the IR spectra, especially those associated with the keto and carboxylato groups. We find IR bands for OH stretch at 3457 cm^{-1} due to presence of water of crystallization, C=O stretching mode at 1715 cm^{-1} , C-C=O bending mode at 503.7 cm^{-1} , COO^{-1}

(carboxylate group) stretching mode at 1319 cm^{-1} and C-O stretching mode at 1362 cm^{-1} in oxalate.

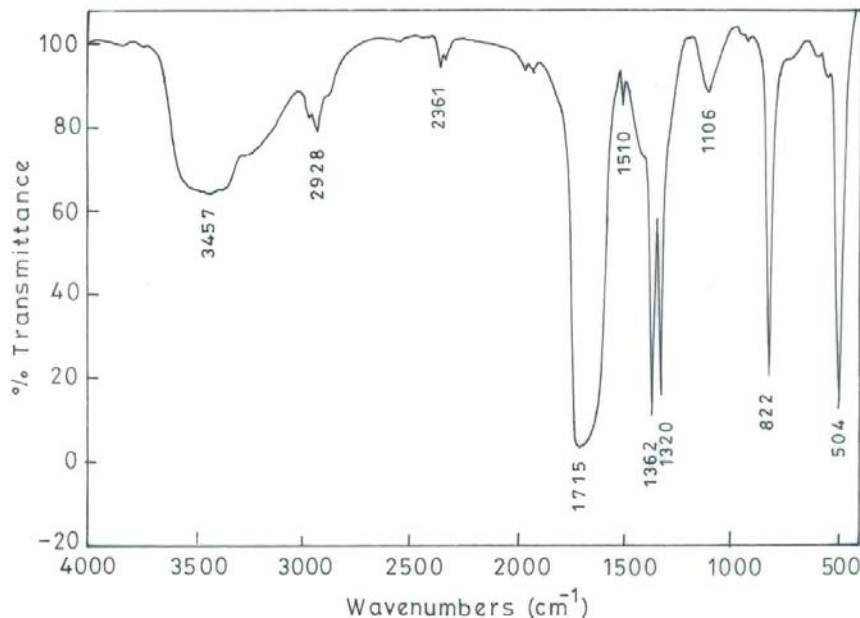


Figure 3.23: FTIR spectra of zirconium oxalate

3.6.2.4. Size and morphology-HRTEM

HRTEM studies showed that, the particles are uniformly distributed and mostly of cube morphology as shown in Figure 3.24. Moreover the ZrO_2 nanocubes show 70 nm size grain, which were highly uniform and monodisperse in nature. It is remarkable that all the samples have same morphology. These images exhibited homogeneous aggregates with a cube-like aspect, which are composed of large number of small grains. The average grain size of the particles of ZrO_2 obtained from the X-ray studies is found to be 10 nm. TEM studies shows nearly uniform, but slightly agglomerated particles having a grain size of 70 nm (Fig. 3.24). TEM studies showed that, the particles in both the samples (zirconium oxalate and zirconia) are uniformly distributed and mostly of cube morphology. Moreover the initial precursor, obtained at room temperature (Fig. 3.24a), shows 10-20 nm size particles, which were highly uniform and monodisperse in nature. After heating at 500°C , the particle size was found to be 80-100 nm.

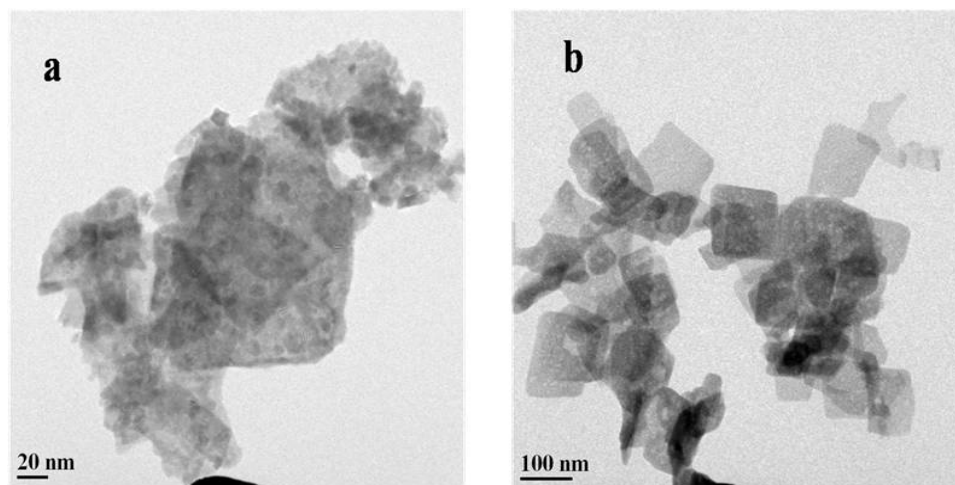


Figure 3.24: HRTEM image of (a) zirconium oxalate (precursor) (b) zirconia nanoparticles

3.7. Photoluminescence spectroscopy

3.7.1. Emission and life time spectroscopy of undoped zirconium oxalate and zirconia:

Under steady state excitation into the charge transfer band at 365 nm, nanocubes shows a broad band ranging (Figure 3.25 a) from 400- 600 nm centered at 475 nm in case of zirconium oxalate and 450 nm in case of zirconia. Zr^{4+} itself is nonluminous and has no extrinsic activators; so the observed luminescence from ZrO_2 is attributed to presence of surface defects and oxygen vacancies. Large amounts of surface defects should exist on the as-synthesized nano- ZrO_2 particles, because of their high surface area built into the -Zr-O- networks [164, 165].

The luminescence decay curves (Figure 3.25b) can be also fitted to a single-exponential function such as $I = I_0 \exp(-t/\tau)$ (τ is the lifetime), from which the lifetimes are determined to be 6.02 and 5.81 ns, respectively for zirconium oxalate and zirconium oxide samples.

When the reaction was finished, zirconium oxalate cubes were collected and washed with 1:1 chloroform –methanol mixture by centrifugation to remove the mostly organic compounds. The residual Tergitol and other organic moiety (cyclohexane and 1-octanol) still existed in the zirconia networks. In the subsequent annealing process, part of the organic groups decomposed into H_2O and CO_2 and escaped from the system. However, minor amounts of them might have decomposed to create a carbon

substitutional defect for Zr in zirconia networks ($-\text{Zr}-\text{O}-\text{C}-\text{O}-\text{Zr}-$), which is assumed to be the luminescent species in the lattice [166].

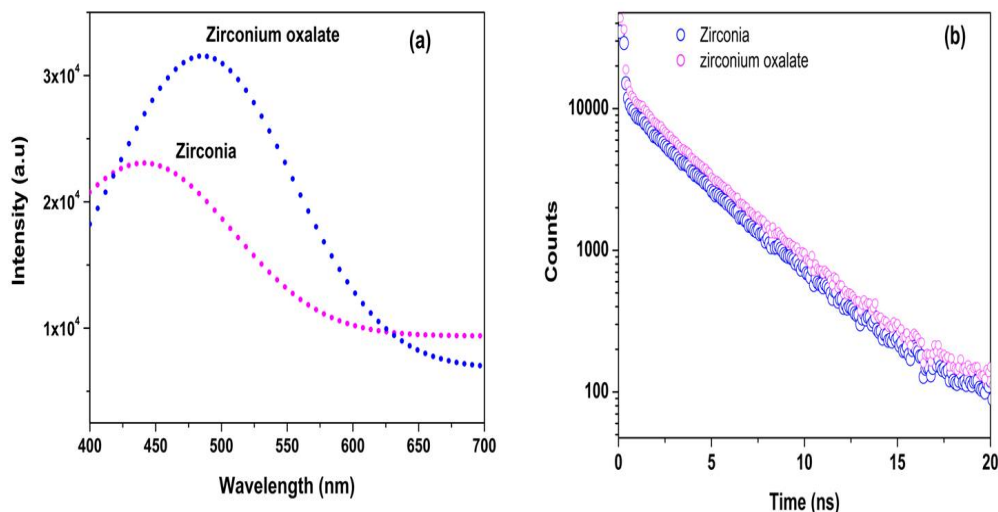


Figure 3.25: Emission spectra (a) and fluorescence decay profile (b) of zirconium oxalate and zirconium oxide nanoparticles

3.7.2. Excitation, emission and life time spectroscopy of Eu^{3+} doped zirconium oxalate and zirconia:

The excitation spectra (Figure 3.26(a)) were acquired by fixing the emission wavelength at 613 nm corresponding to the ${}^5\text{D}_0 \rightarrow {}^7\text{F}_2$ transition of Eu^{3+} ion for Zr $(\text{C}_2\text{O}_4)_2 \cdot n\text{H}_2\text{O}: 1\% \text{Eu}$ and 606 nm related to the ${}^5\text{D}_0 \rightarrow {}^7\text{F}_2$ transition for $\text{ZrO}_2: 1\% \text{Eu}$. In order to distinguish the differences in the spectra of the two samples, the intensities of these excitation spectra were normalized. The principle features consist of a broad band corresponding to transitions from the ${}^7\text{F}_0$ ground state to charge transfer (CT) state due to the europium–oxygen interaction and some weak peaks between 340 and 450 nm corresponding to f–f transitions of Eu^{3+} .

The excitation peaks of oxalate and oxide samples are centered at 248 and 270 nm, respectively, indicative of a red-shift orientation, when ligand is changed from oxalate to oxide ion. Oxalate is strong ligand compared to oxide ion. Therefore, it could be easier for the electronic transition from the 2p orbital of O^{2-} to the 4f orbital of Eu^{3+} in the zirconia compared to zirconium oxalate and thus the CTB energy of Eu^{3+} is less in zirconia than zirconium oxalate. Figure 3.26(b) shows the emission spectra of zirconium samples under the different excitation wavelengths of 248 nm (Zr $(\text{C}_2\text{O}_4)_2 \cdot n\text{H}_2\text{O}: \text{Eu}$), and 270 nm ($\text{ZrO}_2: \text{Eu}$) respectively.

In europium, the ${}^5D_0-{}^7F_1$ transition is mainly magnetically allowed (a magnetic-dipole transition), while ${}^5D_0-{}^7F_2$ is a hypersensitive forced electric-dipole transition, being allowed only at low symmetries with no inversion centre. Thus, the intensity ratio $I_{5D_0-7F_2} / I_{5D_0-7F_1}$ serves as an effective spectroscopic probe of the site symmetry in which europium is situated i.e. the higher the ratio, the lower the site symmetry.

Upon excitation into CTB of Eu^{3+} , the emission spectra of both the samples showed similar profiles, which are composed of ${}^5D_0-{}^7F_J$ ($J = 1-4$) emission lines of Eu^{3+} , with the ${}^5D_0-{}^7F_2$ transition being dominant. The ${}^5D_0-{}^7F_2$ transition belongs to the forced electric-dipole transition, indicating that Eu^{3+} is located at a low symmetry without an inversion centre. From the results of the XRD, $\text{ZrO}_2:\text{Eu}^{3+}$ adopts tetragonal symmetry with space group of P42/nmc and the site symmetry for Zr^{4+} is D_{4h} . The substitution of Eu^{3+} for Zr^{4+} will cause defects ($4\text{Eu}^{3+} = 3\text{Zr}^{4+} + \text{anion vacancy}$) in the host lattice, making the site symmetry of Eu^{3+} deviate from the D_{4h} symmetry. So, ${}^5D_0-{}^7F_2$ red emission of Eu^{3+} dominates the emission spectra in ZrO_2 with an asymmetry ratio value of 1.66.

The enhancement of the emission intensities in case of zirconia nanoparticles w.r.t to zirconium oxalate is related to the temperature of heating and is ascribed to two other factors as well: one is the growth of the ZrO_2 particles, and the second is the loss in the amount of oxalate and hydroxyl groups, which lowers the multiphonon relaxation rate. Here, we believe that the loss of hydroxyl groups is the dominant factor to increase the emission intensity with increasing the temperature of heating. FTIR spectra (Figure 3.23) support the presence of high frequency oscillator like OH and CO groups, which are known fluorescence quenchers. According to configurational-coordinate model [167], it is known that emission band shifts to lower wavelength, if the crystal field is weak. The emission band due to ${}^5D_0-{}^7F_2$ shifts from 613 to 606 nm in case of zirconia because oxide ion (O^{2-}) exerts less crystal field than oxalate ion ($\text{C}_2\text{O}_4^{2-}$).

Further the appearance of a narrow 606 nm peak is a strong indication of emergence of a symmetrical crystalline phase, which is typically related to tetragonal phase [163].

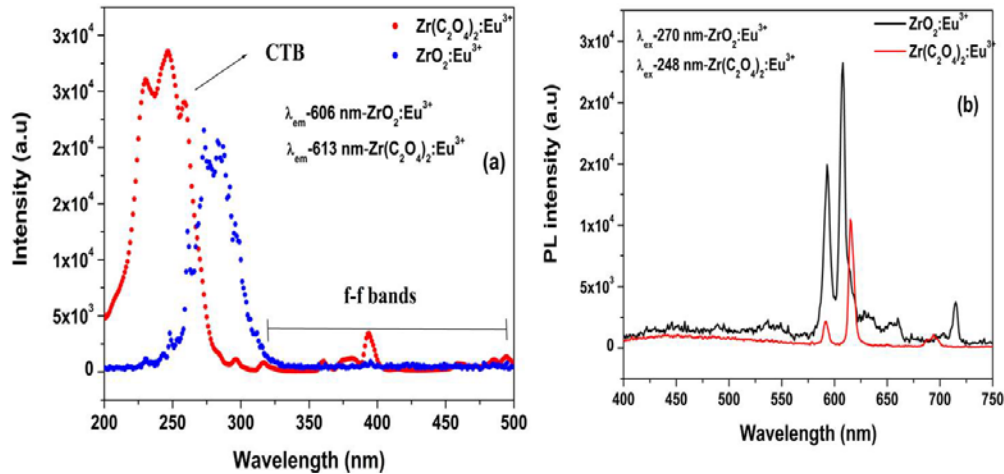


Figure 3.26 (a): Excitation spectra (b): Emission spectrum powder sample of zirconium oxalate and zirconium oxide nanoparticles

The room temperature decay curves of the PL emission showed non-exponential shape. Therefore, we applied double exponential fitting equation same as 3.4, which takes into account both the fast and the slow components of the decay

It is worth mentioning that this provides a mathematical strategy, useful for the calculation of a representative effective lifetime τ_{av} for each system, according to the following equation:

$$\tau_{av} = \frac{(A_1 \tau_1^2 + A_2 \tau_2^2)}{(A_1 \tau_1 + A_2 \tau_2)} \quad (3.6)$$

As seen from Figure 3.27 and Table 3.3, for both the systems, decay curves display two life-times indicating the presence of Eu^{3+} ions in two different environments. It is reported that in nano-sized phosphors rare earth ions exhibit two lifetimes, one arising out of conventional emission and other is the lifetime of the same level of rare earth ions near and/or on the surface [168-170]. $\text{ZrO}_2:\text{Eu}^{3+}$ exhibits long lifetime than $\text{Zr}(\text{C}_2\text{O}_4)_2 \cdot n\text{H}_2\text{O}:\text{Eu}^{3+}$, because of removal of high frequency oscillators like C-H, O-H etc in case of zirconia which are fluorescence quenchers. It can be seen from the values that, when excited at the CTB position, biexponential behavior is observed, indicating that, there are two different types of europium species in the in zirconia matrix; one short lived species ($\tau \sim 197 \mu\text{s}$, fast decaying species- t_1) and one long lived species ($\tau \sim 870 \mu\text{s}$, slow decaying species- t_2). Fast decaying species corresponds to conventional/surface emission.

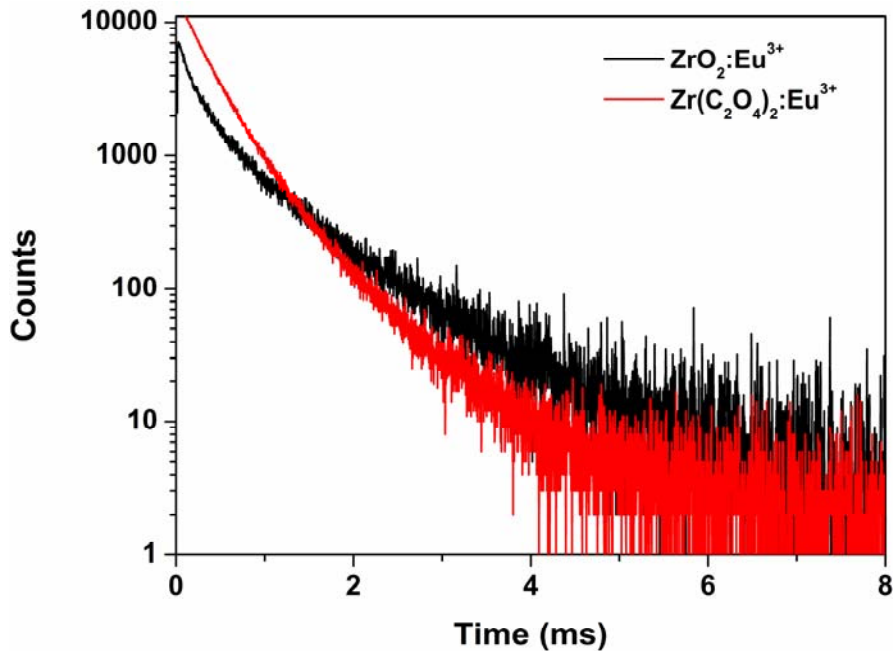


Figure 3.27: Luminescence decay time profile of the Eu doped zirconium oxalate and zirconium oxide nanoparticles

Table-3.3: Life times for Eu^{3+} species in zirconium oxalate and zirconia

Systems	$\tau_1(\mu\text{s})$	$\tau_2(\mu\text{s})$	$\tau_{\text{avg}}(\mu\text{s})$
$\text{Zr}(\text{C}_2\text{O}_4)_2 \cdot n\text{H}_2\text{O}:\text{Eu}^{3+}$	273	644	398
$\text{ZrO}_2:\text{Eu}^{3+}$	197	870	622

The J–O analysis of the emission spectrum is a powerful tool for calculating the parity-forbidden electric-dipole radiative transition rates between the various levels of a rare earth ion such as Eu^{3+} . Through these analyses, the local environment around the metal ion can be interpreted. It is possible to determine the J–O intensity parameters Ω_λ (where $\lambda = 2, 4$ and 6 etc.) from the emission spectral data. For these analyses, the corrected emission spectra with respect to the source and detector response were taken into consideration. The details of these analyses of the emission spectra for calculating the J–O parameters of Eu^{3+} ion in various matrices are discussed 1.2.4.2. The J–O parameter, Ω_2 exhibits dependence on the covalence between rare-earth ions and ligands and gives information about the asymmetry of the local environment of Eu^{3+} site. The Judd-Ofelt parameter and other properties calculated for Eu^{3+} in zirconia is mentioned in table 3.4.

Table 3.4: J-O intensity parameters and radiative properties for Eu³⁺ in ZrO₂

Transition	A_{Red} (s ⁻¹)	A_{Rmd} (s ⁻¹)	Ω_J (10 ⁻²⁰ cm ²)	β_J (%)	η (%)	A_R (s ⁻¹)	A_{NR} (s ⁻¹)
⁵ D ₀ → ⁷ F ₁	0	147	-	14.3	64.1	1030	578
⁵ D ₀ → ⁷ F ₂	628	0	5.63	60.9			
⁵ D ₀ → ⁷ F ₄	116	0	2.35	11.3			

It is well known that the parameter Ω_2 , is an indication of the dominant covalent nature and/or structural changes in the vicinity of the Eu³⁺ ion (short range effects), while Ω_4 intensity parameters are long range parameters that can be related to the bulk properties such as viscosity and rigidity of the inorganic matrices. The Ω_2 parameter is related to the degree of covalence and polarizability of the chemical environment experienced by the Eu³⁺ ion; higher Ω_2 values point to more covalent and polarizable environments. High values of the Ω_2 parameters can also be related to high asymmetry of the Eu³⁺ surrounding environment. This is well in agreement with high asymmetry value of Eu³⁺ in zirconia. The calculated τ_R for the excited ⁵D₀ level of Eu³⁺ ion is found to be 0.97 ms, which is larger than the τ_{exp} (0.622 ms). This difference in τ_{exp} and τ_{cal} can be attributed to nonradiative decays. The trend in branching ratio suggests most of radiative energy goes in the ⁵D₀ → ⁷F₂ transition.

3.8. Summary:

Sm³⁺ and Eu³⁺ behave differently in nanocrystalline ThO₂. Emission spectroscopy shows warm white light emission in ThO₂:Sm³⁺, whereas intense red emission is observed in case of ThO₂:Eu³⁺. Biexponential decay is observed for Sm³⁺ as well as for Eu³⁺ in ThO₂. In both cases, longer lived species is due to the presence of Sm³⁺/Eu³⁺ ion in cubic (O_h) site with inversion symmetry. But in case of Sm³⁺ doped thoria, shorter species is due to its presence on the surface of nanocrystals, whereas europium behaves distinctly in nano ThO₂; short lived species T₁ (~1.3-3.4 ms) arises because of Eu³⁺ ions occupying non-cubic (<C_{2v}) site without inversion symmetry. It was also observed in case of ThO₂:Eu³⁺ that extent of asymmetry around Eu³⁺ at 700/900°C is very high as compared to as prepared or 500°C annealed sample. Short lived species T₁ (~1.3-3.4 ms) predominating at higher annealing temperature arises because of Eu³⁺ ions occupying non-cubic (<C_{2v}) site without inversion symmetry,

whereas long-lived species T_2 (~4.6-6.6 ms) can be ascribed to Eu^{3+} ions occupying cubic (O_h) sites with inversion symmetry.

Nanocrystalline ZrO_2 and $\text{ZrO}_2:\text{Eu}^{3+}$ were prepared using non-ionic surfactant (Tergitol) assisted reverse micellar route. Through this route, we could stabilize metastable tetragonal phase of zirconia at 500°C through addition of 1 mol % Eu^{3+} , which is technologically more important. Eu (III) in zirconia behaves similar to Sm (III) in thoria in terms of site occupancy. It was observed that emission intensity and lifetime of europium ion in the oxalate phase is less than in zirconia. This is related to the association of the water molecules in the oxalate phase, wherein the nonradiative process from the water molecules surrounding Eu^{3+} is dominating over the radiative process. On annealing above 500°C , luminescence intensity increases due to significant removal of water and conversion of oxalate to oxide. In addition, Judd-Ofelt parameter and other photo-physical properties (radiative transition rate, radiative lifetime, efficiency, and branching ratio) of Eu^{3+} ion in zirconium dioxide were evaluated by adopting standard Judd-Ofelt (J-O) analysis procedures.

Chapter 4

Luminescent properties of various lanthanide ions (Sm, Eu, and Dy) in α' - Sr_2SiO_4 : understanding differences in their local environment

CHAPTER 4

4.1. General Introduction

The energy levels of the lanthanide ions in a range of crystals were investigated and tabulated by Dieke et al. in 1968 [171], and rare-earth ions have been extensively used as the active ions in phosphors for several decades. The rare-earth ions are characterized by a partially filled 4f shell that is well shielded by 5s² and 5p⁶ orbitals. The emission transitions, therefore, yield sharp lines in the optical spectra. The use of rare-earth element-based phosphor, based on “line-type” f–f transitions, can narrow to the visible, resulting in both high efficiency and a high lumen equivalent. It is therefore, necessary to find a stable, inorganic rare-earth-based phosphor with high luminescent efficiency. The luminescence properties of the trivalent rare earth or lanthanide cations in solution and in the solid state are characterized by narrow emission bands and relatively long luminescence lifetimes of up to milliseconds. Except for lanthanum (La³⁺) and lutetium (Lu³⁺), each lanthanide ion has its specific emission bands: for example, the lanthanide ion europium (Eu³⁺) emits red light, terbium (Tb³⁺) green light, and neodymium (Nd³⁺), ytterbium (Yb³⁺), and erbium (Er³⁺) near-infrared light. These characteristics have led to the application of lanthanide ions as probes in fluoroimmunoassays (Eu³⁺ and Tb³⁺), [172, 173] laser systems (e.g. Nd³⁺), [174] and optical amplifiers (Er³⁺ and Pr³⁺) [175]. The host material of the lanthanide ions can be organic (an organic ligand with lanthanide complexing moieties) or inorganic (a glass or a crystal), which can have a profound influence on the luminescence properties. Among the materials currently evaluated as host for lanthanide ions, in this work our attention was focused on alkaline earth silicates. These materials are characterized by good transmission properties in the visible part of the electromagnetic spectrum and by relatively low phonon energies. They can be efficiently doped with lanthanide ions, due the similarity between the ionic radius of the alkaline earth and the lanthanide ions. Therefore these materials are prospective high efficiency luminophors and are attracting increasing interest for photonics and optoelectronics applications. Indeed alkaline earth silicates are resistant to many chemicals and air exposure and can also be grown with low-cost techniques.

Oxide-based hosts have received considerable attention for use in flat-panel displays due to their luminescent characteristics, stability in high vacuum, and the absence of corrosive gas emission under electron bombardment, as compared to currently used sulfide-based phosphors [176]. Therefore, oxide-based phosphors are likely to emerge as the choice for field emission diodes (FED) green or red phosphors. Among these, strontium silicate is an excellent matrix due its stable crystal structure, good mechanical strength and high thermal stability provided by the tetrahedral silicate $(\text{SiO}_4)^{2-}$ group [177]. Sr_2SiO_4 has attracted interest due to its special structural features and potential application in developing white light-emitting-diodes (LEDs), because GaN (400 nm chip) coated with $\text{Sr}_2\text{SiO}_4 : \text{Eu}^{2+}$ exhibits better luminous efficiency than that of industrially available products such as InGaN (460 nm chip) coated with YAG : Ce [178]. The optical band gap of alkaline earth silicate is in the range of 4-7 eV and therefore these materials are characterized by good transmission properties in the visible part of the electromagnetic spectrum.

Eu^{3+} is often used as a structural probe [154, 157, 158, 177-178], because of the relative simplicity of its energy-level structure and the fact that it possesses non-degenerate ground ($^7\text{F}_0$) and excited ($^5\text{D}_0$) states, and because the absorption and emission spectra of this ion show marked dependence on its site symmetry in the host material. The orange emission (590–600 nm) of Eu^{3+} due to the magnetic dipole transition (MDT) $^5\text{D}_0 \rightarrow ^7\text{F}_1$ is not affected much by the site symmetry, because it is parity-allowed, while the red emission (~610–630 nm) due to the electric dipole transition (EDT) of $^5\text{D}_0 \rightarrow ^7\text{F}_2$, being hypersensitive, is affected by the site symmetry of Eu^{3+} ion [154, 157, 158, 177-179]. In a crystal site with inversion symmetry the EDT are strictly forbidden and the MDT are usually the dominant emission lines. In a site without inversion symmetry the strength of EDT is higher. The $^5\text{D}_0 \rightarrow ^7\text{F}_2$ transition is usually the strongest emission line in this case, because transition with $\Delta J = \pm 2$ is hypersensitive to small deviation from inversion symmetry. The symmetry around the lanthanide ion can thus be obtained from the shape of the emission spectrum of Eu^{3+} ion. Luminescence spectrum of Dy^{3+} consists of two relatively intense bands in the visible spectral region that correspond to the $^4\text{F}_{9/2} - ^6\text{H}_{15/2}$ (blue) and $^4\text{F}_{9/2} - ^6\text{H}_{13/2}$ (yellow) transitions, respectively. The yellow emission of Dy^{3+} is especially hypersensitive to the local environment, while its blue emission is not. Generally, when Dy^{3+} is located at a low symmetry (without an inversion center), the yellow emission is dominant, whereas the blue emission is stronger when Dy^{3+} is

located at a high symmetry (with an inversion center) [180, 181]. In case of Sm^{3+} ; ${}^4\text{G}_{5/2} \rightarrow {}^6\text{H}_{7/2}$ ($\Delta J = \pm 1$) is a partly magnetic dipole (MD) and partly electric dipole (ED) nature emission band whereas ${}^4\text{G}_{5/2} \rightarrow {}^6\text{H}_{5/2}$ is purely MD natured and ${}^4\text{G}_{5/2} \rightarrow {}^6\text{H}_{9/2}$ is purely ED natured [182]. The magnetic dipole transition (MDT) ${}^4\text{G}_{5/2} \rightarrow {}^6\text{H}_{5/2}$ does not depend on chemical surroundings of the luminescent centre and its symmetry. However, the hypersensitive ${}^4\text{G}_{5/2} \rightarrow {}^6\text{H}_{9/2}$ transition is magnetic-dipole forbidden and electric-dipole allowed. Its intensity increases as the environmental symmetry become lower.

Eu^{2+} is the most stable lanthanide divalent ion due to its half-filled valence shell. Emission and absorption spectra of Eu^{2+} ion usually consist of broad bands due to transition between $4f^7$ (${}^8\text{S}_{7/2}$) ground state and crystal field components of the $4f^6 5d^1$ excited state configuration [183]. For most hosts, the emission spectra of Eu^{2+} are observed in the UV to visible range, specifically in the wavelength range from 390 nm to 640 nm [183]. The decay times of these transitions are usually in the range from 0.2 to 2 μs , reflecting the dipole allowed nature of these transitions [184]. The host dependence of the emission spectra of Eu^{2+} can be explained as follows: In the divalent state, the europium ion has seven f electrons which form a stable half-filled 4f valence shell. These electrons do not strongly interact with environment of the host material because they are effectively shielded by filled $5s^2$ and $5p^6$ shells and thus are affected weakly by changes in its environment. After one 4f electron is excited to the 5d level, this electron is strongly influenced by the crystal field, leading to broad, host dependent 5d-4f emission bands. The host lattice dependence of the emission is mainly connected with covalency (the nephelauxetic effect), the strength of the crystal field and the Stokes shift [185]. For Eu^{2+} ions, two different emission types were distinguished: normal broad-band $4f^6 5d^1 \rightarrow 4f^7$ (${}^8\text{S}_{7/2}$) emission, and anomalous Eu^{2+} emission (the 4f-4f transitions are not observed for Eu^{2+} , because the ${}^6\text{P}$ f-levels are energetically above the 5d levels). In each case the emission can be excited via the lowest f-d level of the Eu^{2+} , the final state is the $4f^7$ (${}^8\text{S}_{7/2}$) ground state for each emission types [186].

Sr_2SiO_4 has been prepared by several synthetic routes including conventional solid-state reaction [178]; liquid phase reaction [187] and microwave assisted sintering [188]. Few reports are also available on the sol-gel synthesis of strontium silicate [189-191]. The conventional solid state reaction route requiring temperatures in excess of 1400 K suffers from inhomogeneous and coarse sample formation with non

uniform size distribution. Large and non-uniform phosphor particles are more likely to be prone to poor adhesion to the substrate and loss of coating. For good luminescence characteristics, phosphors should have fine size, narrow size distribution, non-aggregation and spherical morphology. Similarly, several disadvantages have also been noted with other synthetic techniques such as the evaporation of solvents resulting in phase segregation, alteration of the stoichiometry due to incomplete precipitation, expensive chemicals and time consuming processes. This process provides molecular level of mixing, high degree of homogeneity and short reaction time that leads to reduction in crystallization temperature and prevents from segregation during heating.

TRFS was used to establish the local environment around various lanthanide ions in a same host. For Sr_2SiO_4 doped with europium and dysprosium ions EXAFS studies were carried out at Sr K-edge to see the changes in Sr(9) and Sr(10) polyhedra.

4.2. Synthesis and characterization of $\text{Sr}_2\text{SiO}_4:\text{Ln}^{3+}$ (Ln=Sm, Eu, Dy)

4.2.1. Synthesis of $\text{Sr}_2\text{SiO}_4:\text{Ln}^{3+}$ (Ln=Sm, Eu, Dy)

All the chemicals used in the sample preparation were of Analytical reagent (AR) grade and procured from Sigma Aldrich. The alkaline earth silicate samples were prepared via a sol-gel route using tetraethyl orthosilicate (TEOS) and strontium nitrate.

At first, hydrolysis reaction of TEOS and ethanol catalyzed by dilute nitric acid was carried out. Appropriate quantity of strontium nitrate solution, prepared by dissolving strontium carbonate in dilute nitric acid, was added to the hydrolyzed solution drop wise with vigorous stirring at 60°C . After stirring for 2 h, the solution was allowed to cool and settle down. After a cooling period of about 2 h, a gel like compound was formed. This gel type mass was dried under infra red (IR) lamp for 1 hr and then at room temperature (RT) so as to get a white crystalline solid. This solid mass was repeatedly washed with liquid ammonia and quartz double distilled water to get a white mass. This mass was ground thoroughly in agate mortar and heated at 400°C for 4 h and at 600°C for 2 h. The final product obtained was a free flowing white crystalline powder. For preparation of lanthanide doped sample (0.5 mol %), appropriate quantities of $\text{Eu}(\text{NO}_3)_3$, $\text{Dy}(\text{NO}_3)_3$ and $\text{Sm}(\text{NO}_3)_3$ were added to the

hydrolyzed TEOS solution. For Eu^{2+} doped sample $\text{Sr}_2\text{SiO}_4:\text{Eu}^{3+}$ the mixtures were ground thoroughly and fired at 600°C for 6 h under reducing atmosphere (92 % Ar + 8% H_2) for conversion of Eu^{3+} to Eu^{2+} .

4.2.2. Characterization of $\text{Sr}_2\text{SiO}_4:\text{Ln}^{3+}$ (Ln=Sm, Eu, Dy)

4.2.2.1. Phase purity and Structure: XRD

The purity and crystallinity of the as-prepared Sr_2SiO_4 and $\text{Sr}_2\text{SiO}_4:\text{Ln}^{3+}$ (Ln = Eu, Dy, Sm) samples were characterized using powder X-ray diffraction (XRD). It can be seen that the from the XRD pattern in Fig. 4.1 that diffraction peaks of both Sr_2SiO_4 and $\text{Sr}_2\text{SiO}_4:\text{Ln}^{3+}$ samples were could be indexed to the orthorhombic phase of α' - Sr_2SiO_4 (JCPDS card No. 39-1256). Incorporation of lanthanide ion has not changed the XRD pattern which confirms that doping is proper and has not distorted the structure of strontium silicate. Since no impurity peaks were observed, it is feasible to suggest that both samples are a single phase of α' - Sr_2SiO_4 . No obvious shifting of peaks or other impurity phases could be detected in the Ln^{3+} -doped samples, indicating that the Ln^{3+} ions are efficiently dissolved in the Sr_2SiO_4 host lattice by replacing the Sr^{2+} because of the similar ionic radius and very small level of doping (0.5 mol %).

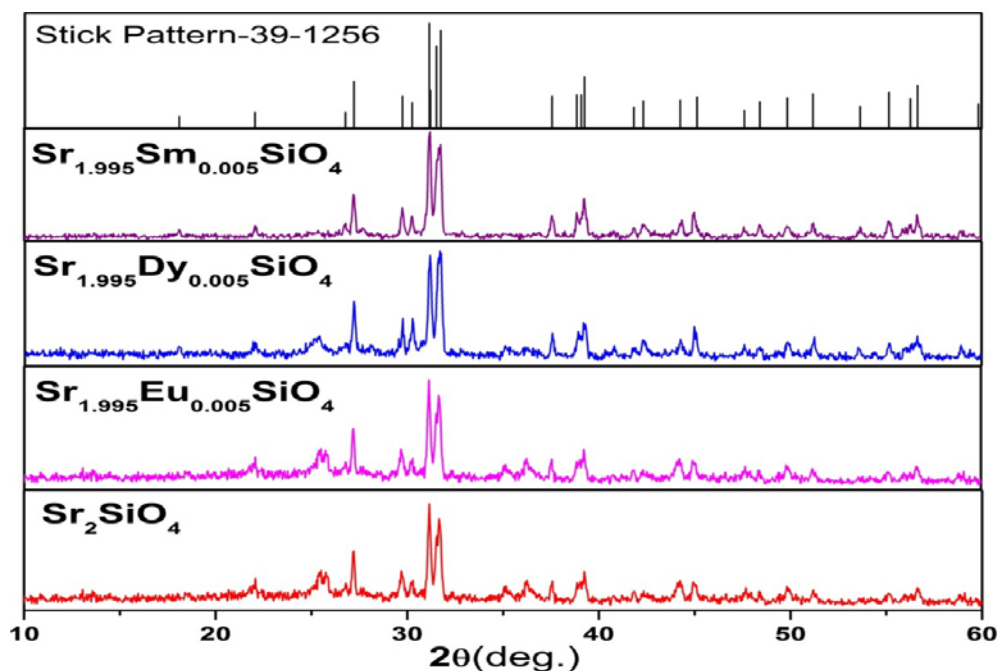


Figure 4.1: XRD pattern Sr_2SiO_4 and $\text{Sr}_2\text{SiO}_4:\text{Ln}^{3+}$ (Ln = Eu, Dy, and Sm)

The structure of Sr_2SiO_4 has been well described in literature and is similar to the non-close packing structure of K_2SiO_4 [191]. One unit cell of Sr_2SiO_4 comprises of 4 formula unit sharing 28 atoms (8, 4 and 16 atoms of Sr, Si and O respectively). Its structure can be best described as comprising of corner sharing SiO_4 tetrahedra (Td) forming parallel chains. The oxygen ions are located at three types of unequivalent lattice sites with D_{2h} space group and the Si^{4+} ions are located at the center of the oxygen tetrahedron. In the structure of Sr_2SiO_4 , there are two different Sr sites: one having coordination number 9 and the other with coordination number 10. The ten coordinated Sr(1) sites form linear three-membered rows of (Si–O–Sr(1)–O–Sr(2)) whereas the nine coordinated Sr(2) sites form zig-zag chains of (Sr(1)–O–Sr(2)–O–Sr(1)) along the b-axis [178]. A schematic of the crystal structure for the strontium silicate is presented in Figure 4.2.

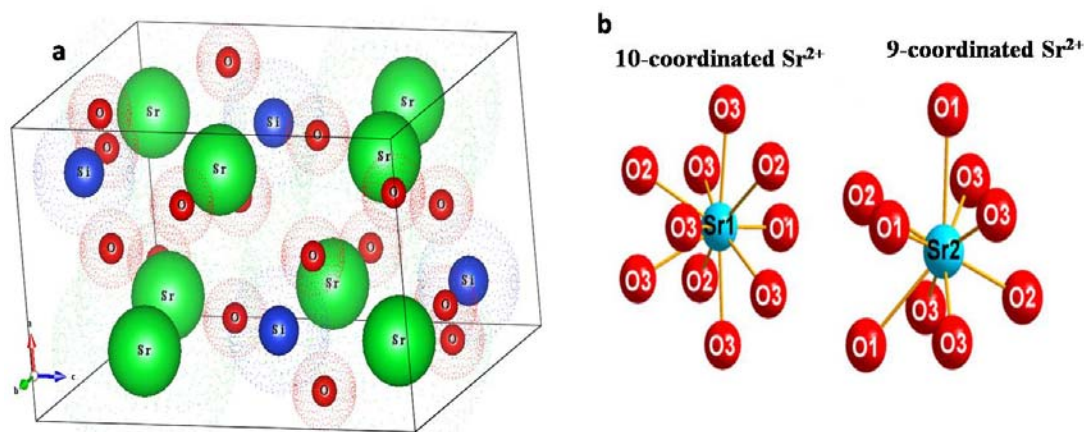


Figure 4.2: (a) Crystal structure of α' - Sr_2SiO_4 (b) Pictorial representation of 9- and 10-coordinated Sr^{2+} in strontium silicate

4.2.2.2. Morphological studies and particle size distribution: AFM, SEM and DLS Results

Figures 4.3(a) and (b) show AFM images and size distribution obtained in AFM measurement of as- prepared sample respectively. The AFM images reflect highly dense microstructures without much porosity. The particle size distribution was narrow with average size of ~ 300 nm. A SEM image of same sample is depicted in

Figure 4.4. SEM image of the sample is depicted in Figure 4.4. SEM studies showed that the particles tend to agglomerate forming small clusters with irregular shapes as can be observed from the micrograph. Furthermore, the particle size is in a wide distribution, the average size being about 300-400 nm in diameter at 600°C. These results were also corroborated by DLS measurements where the particle size distribution is given by the "Stokes radius" or "hydrodynamic radius" represented by the following Stoke – Einstein equation -

$$R_h = k T / 6\pi\eta D \tag{4.1}$$

Where, k = Boltzmann constant

T = Temperature

η = Viscosity of suspension

D = Diffusion coefficient

This method also known referred as "photon correlation spectroscopy" (PCS) or "quasi-elastic light scattering" (QELS) technique, uses the scattered light to measure the rate of diffusion of the particles. This motion data is conventionally processed to derive a size distribution for the sample. (If this part is in introduction, do not repeat the equation, just quote) For the present Sr_2SiO_4 system, a narrow size distribution of particles centered at 278 nm was obtained (Fig. 4.5), which is in good agreement with the AFM and SEM data.

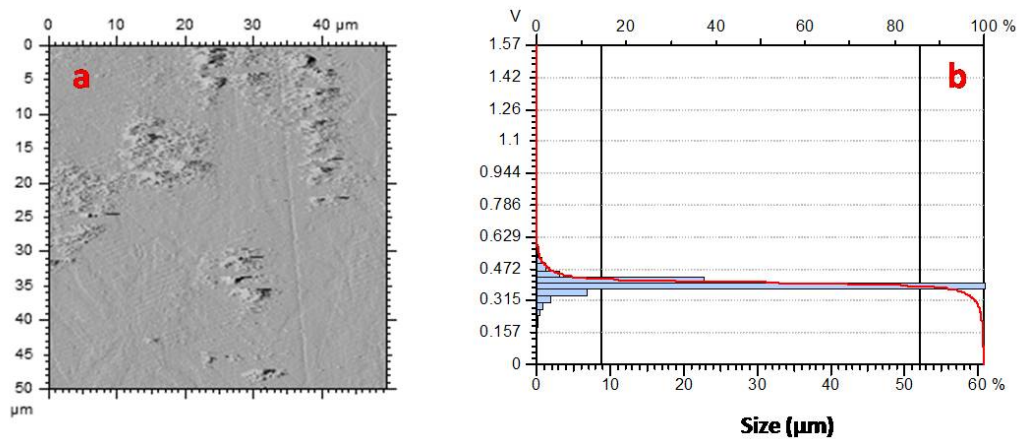


Figure 4.3: (a) 2D (XY)-AFM topographies (~50µ x 50µ) of silicate host matrix (b) Particle size distribution of as prepared sample obtained from AFM topographies.

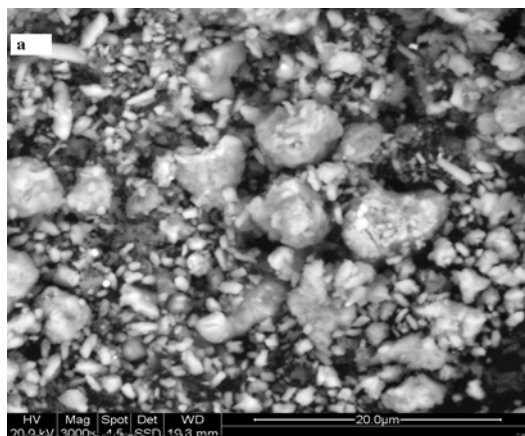


Figure 4.4: SEM micrographs of as prepared samples at magnification of 3000X.

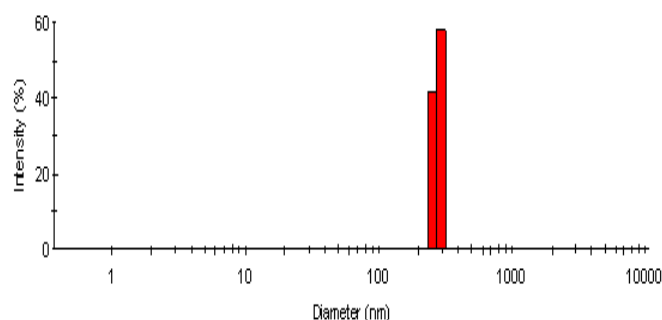


Figure 4.5: Size distribution plot obtained by dynamic light scattering studies of Sr_2SiO_4 powder after heating at 600°C .

4.3. Photoluminescence properties of $\text{Sr}_2\text{SiO}_4:\text{Eu}^{3+}$:

The excitation spectra of the 0.5 mol% sample with $\lambda_{\text{em}} = 592 \text{ nm}$ (Fig. 4.6) shows intense and broad band at $\sim 243 \text{ nm}$ and another relatively less intense band at $\sim 296 \text{ nm}$, both of which are assigned to the charge transfer band ; CTB-1 and CTB-2 respectively. The peaks seen at 320, 360, 380 and 395 nm (very intense) were assigned to the f-f transitions from the $^7\text{F}_0$ ground state to $^5\text{H}_3$, $^5\text{L}_9$, $^5\text{G}_3$ and $^5\text{L}_6$ levels respectively. The existence of two charge transfer bands is because of presence of 9- and 10-coordinated SrO polyhedra in α' - Sr_2SiO_4 .

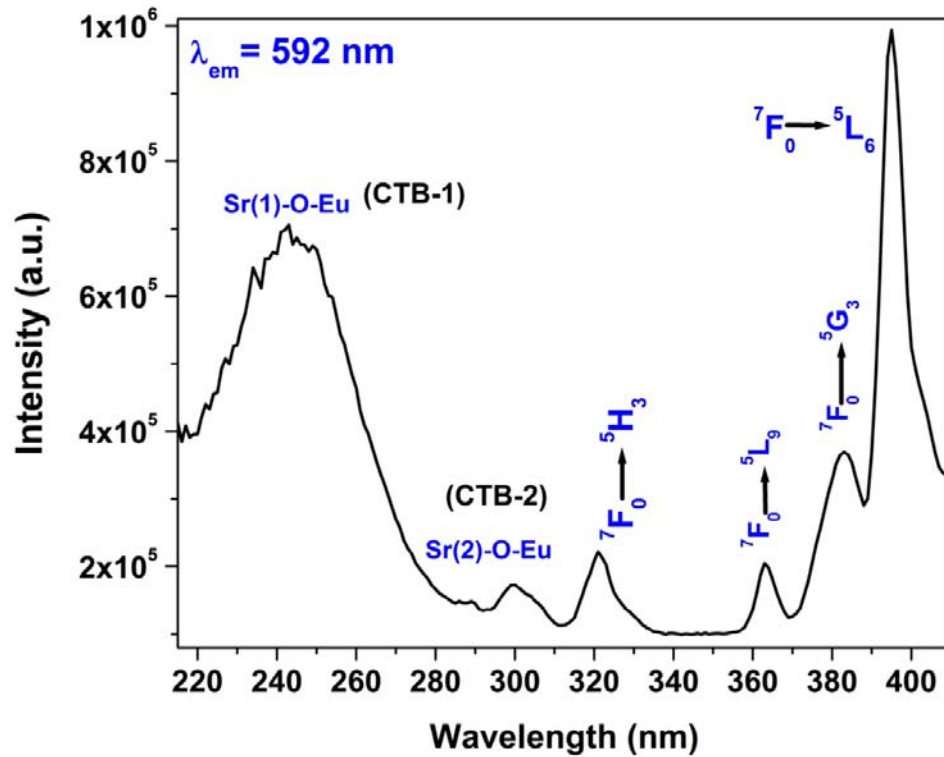


Figure 4.6: Excitation spectrum $\text{Sr}_2\text{SiO}_4: \text{Eu}^{3+}$

Figure 4.7 shows the PL emission spectra of 0.5 mol% Eu doped strontium silicate sample respectively. The emission spectrum with $\lambda_{\text{ex}} = 243 \text{ nm}$ (CTB-1) shows a number of sharp lines at 592, 610-618, 653 and 689-704 nm associated with the transitions from the excited $^5\text{D}_0$ to $^7\text{F}_J$ levels of Eu^{3+} where $J = 1, 2, 3 \text{ \& } 4$ respectively. The orange emission at 592 nm belongs to the magnetic dipole $^5\text{D}_0$ - $^7\text{F}_1$ transitions of Eu^{3+} and the transition hardly varies with the crystal field strength. The red emission at about 614 nm ascribes to the magnetic dipole $^5\text{D}_0$ - $^7\text{F}_2$ transitions of Eu^{3+} , which is very sensitive to the local environment around Eu^{3+} and depends on the symmetry of the crystal field. It was found that 614 nm emission is almost as strong as 590 nm emission, indicating that there are two Sr^{2+} sites in α - Sr_2SiO_4 lattice; one site Sr (1) is centrosymmetric and the other site Sr (2) is non-centrosymmetric. When doped in α - Sr_2SiO_4 , Eu^{3+} ions occupy the two different sites of Sr (I) and Sr (II). Another interesting feature is the presence of $^5\text{D}_0$ - $^7\text{F}_0$ line at high energy position (575 nm) than its usual position at around 580 nm.

Other interesting observation was the presence of very intense $^5\text{D}_0$ - $^7\text{F}_0$ on excitation with 296 nm (CTB-2); this is forbidden by both ED and MD transition and observed

mainly in very low symmetry environment, this is more intense than magnetic dipole 5D_0 - 7F_1 and electric dipole 5D_0 - 7F_2 transitions as can be seen from Fig. 4.8. Further when we used 575 as an emission wavelength, an intense CTB-2 peak (296 nm) was observed in excitation spectra.

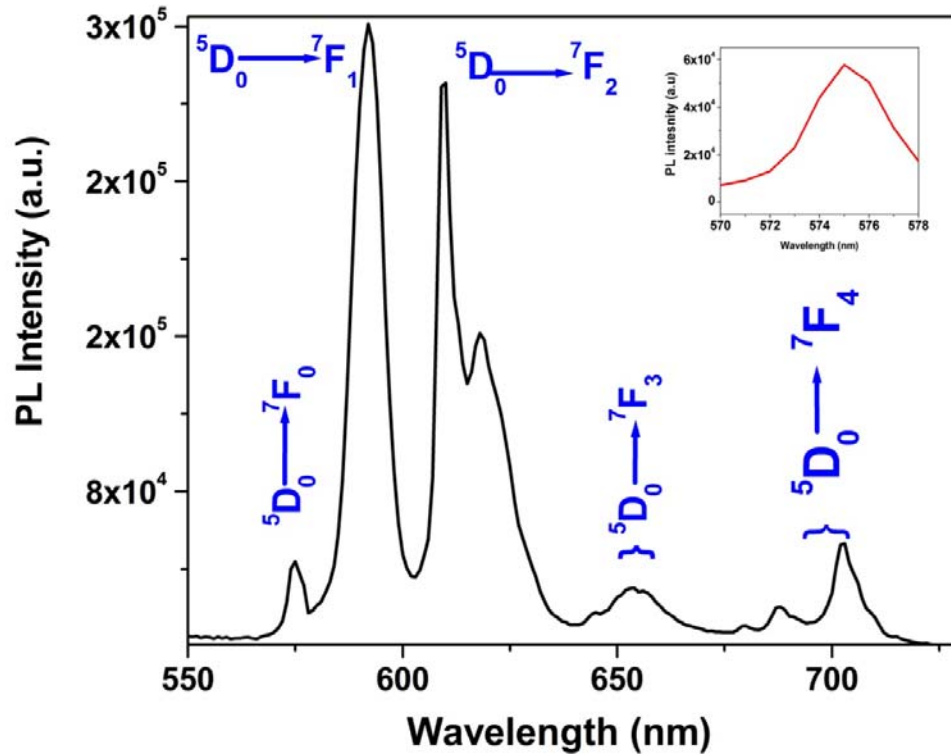


Figure 4.7: Emission spectrum of $\text{Sr}_2\text{SiO}_4:\text{Eu}^{3+}$ with $\lambda_{\text{ex}} = 243$ nm. The inset figure shows the 5D_0 to 7F_0 transition at 575 nm.

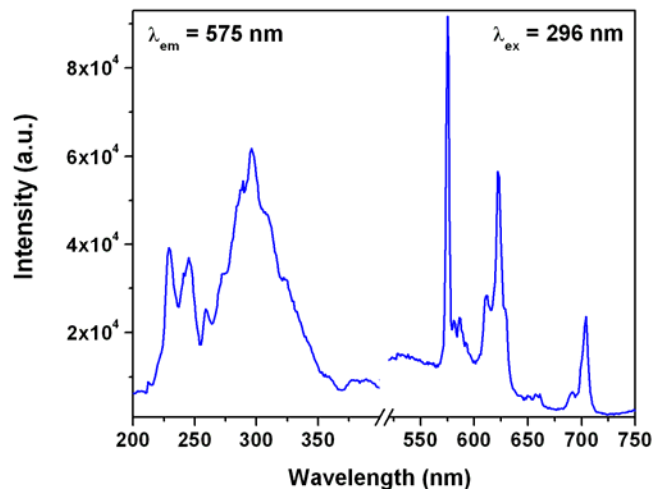


Figure 4.8: Excitation and emission spectra of the strontium silicate doped Eu sample with $\lambda_{\text{em}} = 575$ nm and $\lambda_{\text{ex}} = 296$ nm.

It can be inferred that that emission spectra corresponding to CTB-1 and CTB-2 are entirely different and both may be exciting Eu^{3+} sitting in two different environments. To further validate this result, fluorescence decay measurements were carried out corresponding to $\lambda_{\text{ex}} = 243$ nm and 296 nm at all the λ_{em} . The obtained lifetime values are listed in Tables 4.1 and 4.2.

Table 4.1: Fluorescence decay time for the $\text{Sr}_2\text{SiO}_4:\text{Eu}^{3+}$ with $\lambda_{\text{ex}} = 243$ nm.

	575	592	611	653	704
τ_1 (ms)	-	4.8	5.0	4.5	4.6
τ_2 (ms)	1.1	1.3	1.0	1.2	1.4

As shown in Table 4.1, when excited at the CTB-1 position, single lifetime is observed at 575 nm whereas at other wavelength biexponential behavior is observed, indicating that, there are two different types of europium species in the matrix; one short lived species ($\tau \sim 1.2$ ms, fast decaying species- S_1) and one long lived species ($\tau \sim 4.7$ ms, slow decaying species- S_2). But on recording fluorescence decay with excitation wavelength of 296 nm, monoexponential behavior is observed irrespective of emission wavelength as shown in Table -4.2.

Table 4.2: Fluorescence decay time for the $\text{Sr}_2\text{SiO}_4:\text{Eu}^{3+}$ with $\lambda_{\text{ex}} = 296$ nm.

λ_{em} (nm)	575	581	586	589	623	629	650	661	692	703
τ (ms)	1.1	1.2	1.3	1.4	1.3	1.2	1.3	1.2	1.2	1.4

From Table 4.2, it can be seen that all the lifetime values are very close to each other suggesting that they belong to a single Eu^{3+} species, which is different from the S_2 ($\tau \sim 4.7$ ms).

In order to, identify the species responsible bi-exponential decay time observed with 243 nm (CTB-1), a detailed time resolved emission spectrometric (TRES) investigation was carried out on the system. Through this analyses, by giving suitable delay times and choosing a proper gate width (TRES data slicing range), the emission spectrum responsible for the particular decay time was obtained (Figure 4.9).

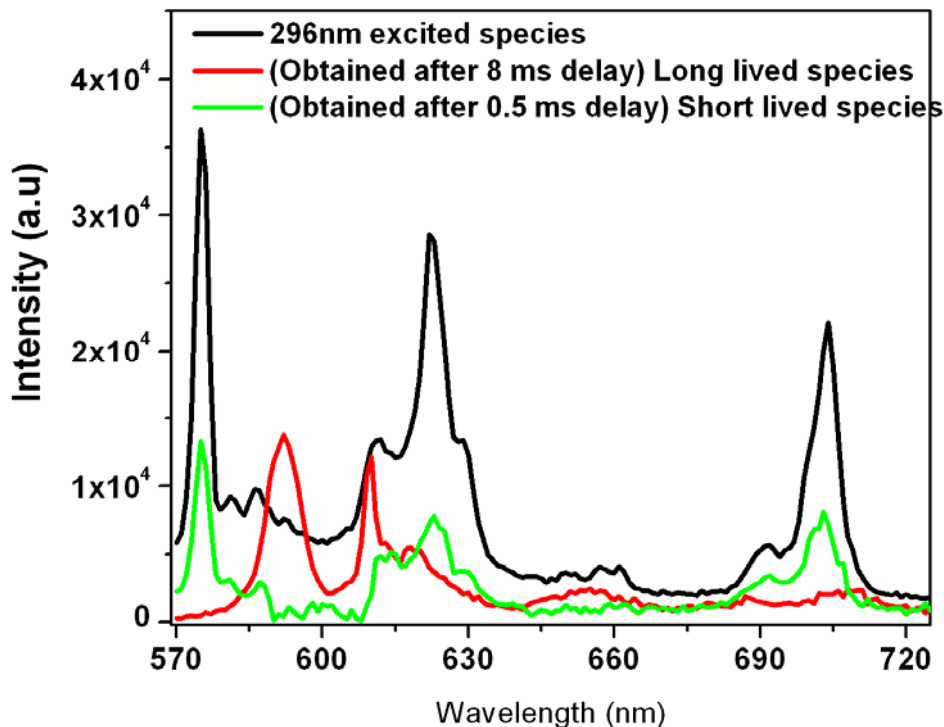


Figure 4.9: Emission spectra of the two RE ions species obtained after giving suitable delay times following TRES measurements (with 243 nm excitation). The emission spectrum of the species getting selectively excited at 296 nm is also shown.

As seen from the TRES data, the emission characteristics of the S_1 obtained by 243 nm excitation and the species getting selectively excited by 296 nm have same spectral features. Moreover, these two species have similar decay time values suggesting the fact that, these are due to the same type of Eu^{3+} ions. In this species, the transition ${}^5\text{D}_0 \rightarrow {}^7\text{F}_0$ is markedly more intense as compared with those of (0, 1) and (0, 2) line and a large splitting is found in ${}^5\text{D}_0 \rightarrow {}^7\text{F}_1$ and ${}^5\text{D}_0 \rightarrow {}^7\text{F}_2$ transition. This suggests that the particular type of Eu^{3+} is present in a lower symmetric environment. From the detailed structural investigation of α' - Sr_2SiO_4 , it was earlier mentioned that the Sr (2) polyhedron is much less symmetrical and shares neither edges nor faces with any SiO_4 tetrahedra [192]. According to the crystal field theory, the crystal field strength is influenced by the site symmetry, covalency, ligand charge and bond length. Among these parameters, the bond length (R) of Sr–O affects the crystal field strength significantly, i.e., the crystal field strength is proportional to $1/R^5$ [193]. A strong anisotropic crystal field is exerted on the Sr^{2+} (2) sites due to the short bond length ($\sim 2.698 \text{ \AA}$). This may be the reason for larger splitting of ${}^5\text{D}_0 \rightarrow {}^7\text{F}_1$ and ${}^5\text{D}_0$

→ 7F_2 lines. A strong crystal field also causes ${}^5D_0 \rightarrow {}^7F_0$ to steal some energy from ${}^5D_0 \rightarrow {}^7F_1$ and ${}^5D_0 \rightarrow {}^7F_2$. So we can conclude that this particular emission is because of europium ion sitting in 9-coordinated Sr (2).

Emission spectrum of the S_2 species ($\tau \sim 4.7$ ms) with $\lambda_{\text{ex}} = 243$ nm, shows that intensity of ${}^5D_0 \rightarrow {}^7F_1$ transition is more than that of ${}^5D_0 \rightarrow {}^7F_2$ transition. Moreover, it indicates the complete absence of ${}^5D_0 \rightarrow {}^7F_0$ line. This suggests that this particular Eu^{3+} species is in more symmetric environment.

Sr (1) polyhedron has more symmetric environment having hexagonal pseudo-symmetry along the y-axis [192]. It shares the face and the vertex with the two SiO_4 tetrahedra which are vertically above and below it and the three edges with three SiO_4 tetrahedra. Moreover, in the range spanning ${}^7F_{0, 1, 2}$ multiplets, it can be noted that, smaller number of peaks are observed and the overall splitting of the levels within these multiplets is significantly smaller. This indicates the crystal field is noticeably reduced in this case. A weak crystal field is exerted on the Sr^{2+} (1) site with a longer bond length. So we can conclude that this particular emission is because of europium ion sitting in 10-coordinated Sr (1).

The J–O analysis of the emission spectrum is a powerful tool for calculating the parity-forbidden electric-dipole radiative transition rates between the various levels of a rare earth ion such as Eu^{3+} . Through these analyses, the local environment around the metal ion can be interpreted. It is possible to determine the J-O intensity parameters Ω_λ (where $\lambda = 2, 4$ and 6 etc.) from the emission spectral data. For these analyses, the corrected emission spectra with respect to the source and detector response were taken into consideration. The J-O parameters for the two types of Eu^{3+} species (obtained from the TRES spectra after suitable delay time) and the species selectively getting excited at 296 nm are listed in Table-4.3. Since, the ${}^5D_0 \rightarrow {}^7F_6$ transition was not observed in the present case, its J-O parameters could not be evaluated.

Table 4.3: J-O intensity parameters of the Eu^{3+} doped Sr_2SiO_4 . ($\lambda_{\text{ex}} = 243\text{nm}$).

Eu^{3+} Species	$\Omega_2 (10^{-20} \text{ cm}^2)$	$\Omega_4 (10^{-20} \text{ cm}^2)$
S_2 ($\tau = 4.7$ ms)	1.40	0.493
S_1 ($\tau = 1.2$ ms)	8.75	14.7
Species getting selectively excited at 296 nm ($\tau = 1.2$ ms)	8.23	14.3

The J-O parameter, Ω_2 exhibits dependence on the covalence between rare-earth ions and ligands and gives information about the asymmetry of the local environment of Eu^{3+} site. From the table it is observed that the J-O parameters for both the S_1 species getting excited at 243 and 296 nm are similar. This unequivocally confirms our earlier argument that, the two Eu^{3+} species are similar in nature. Moreover, the trend observed in the parameters ($\Omega_2 < \Omega_4$) also proves that the particular species is present in an asymmetric environment. On the other hand, for the S_2 species the trend observed in the J-O parameter was $\Omega_2 > \Omega_4$ which confirms our observation that S_2 sits at more symmetric 10-coordinated Sr site (Sr(1)) where as S_1 sits at relatively less symmetric 9-coordinated Sr site (Sr(2)). The ${}^5\text{D}_0 \rightarrow {}^7\text{F}_3$ transition could not be accounted for by either the magnetic or electric dipole mechanisms. Its presence is considered to be a small deviation from theory at the level used in this work.

4.4. Reduction of Eu^{3+} to Eu^{2+} : *EPR spectroscopy*

Eu^{3+} is EPR silent, while for Eu^{2+} with electron configuration of $4f^7$ (${}^8\text{S}_{7/2}$ ground state), EPR could be observed at room temperature. The EPR spectrum due to Eu^{2+} with an effective spin quantum number of $S=7/2$ in non cubic symmetry is expected to show seven fine structure transitions. In the present study, EPR spectra of $\text{Sr}_2\text{SiO}_4:\text{Eu}$ was recorded at room temperature (Fig. 4.10) and spectral features are typical of Eu^{2+} [194-196]. The spectrum consists of no. of broad and intense fine structure lines in the region 0-4200 G. The 7 line spectrum observed at 208, 1145, 1632, 2017, 2584, 3003 and 4133 G was anisotropic due strong crystal field splitting and suggested presence of Eu^{2+} at site having lower symmetry. In addition to this, an isotropic signal around $g = 1.991$ was also observed in the EPR spectrum of sample. The resolved spectrum of Eu^{2+} at isotropic site is shown in Fig.4.10 b; it was made up of 12 line structure resulting from magnetically non-equivalent pairs of europium ${}^{151}\text{Eu}$ and ${}^{153}\text{Eu}$ ($I=5/2$) ions having different hyperfine splitting (hfs). From analysis of EPR spectrum in Fig.4.10 b, hfs constant(A) was found to be of the order of 32.3 G and 14.2 G respectively for ${}^{151}\text{Eu}$ and ${}^{153}\text{Eu}$ isotopes.

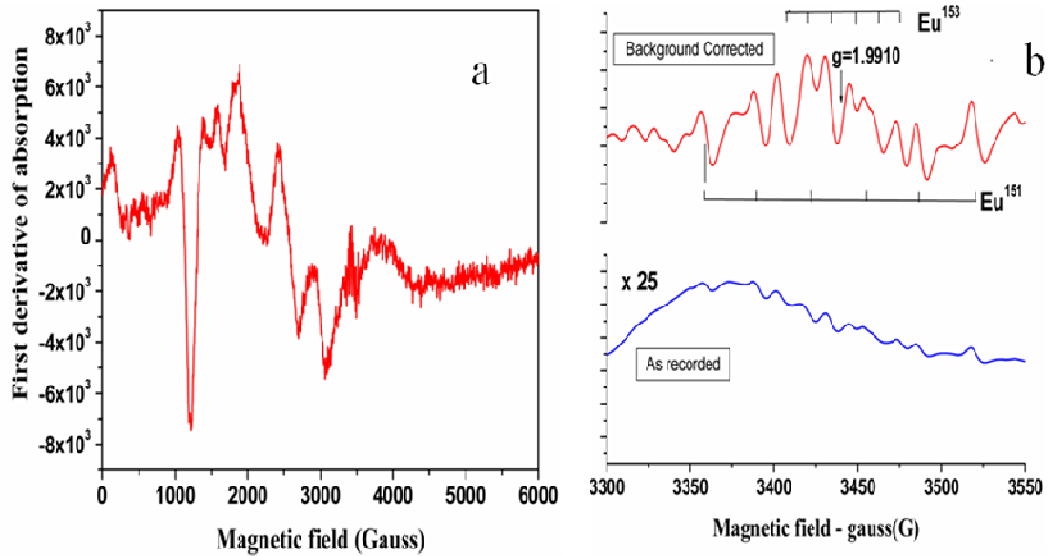


Figure 4.10: (a) EPR spectra of $\text{Sr}_2\text{SiO}_4:\text{Eu}$ (b) EPR showing hfs of Eu^{2+} signal in Sample

4.5. Photoluminescence properties of $\text{Sr}_2\text{SiO}_4:\text{Eu}^{2+}$:

By monitoring the emission at ($\lambda_{\text{em}} = 485$), the excitation spectrum $\text{Sr}_2\text{SiO}_4:\text{Eu}$ exhibited a broad band in the wavelength range from 300 nm to 400 nm peaking at around 350 nm, which is mainly due to $4f^7(^8S_{7/2}) - 4f^65d^1$ transition of the Eu^{2+} ions. Figure 4.11 (a) and (b) shows the excitation and emission spectra of 0.5 mol% Eu^{2+} doped Sr_2SiO_4 respectively.

There are two cation sites of Sr^{2+} α' - Sr_2SiO_4 phase: Sr (1) is 10-coordinated and Sr (II) is nine-coordinated by oxygen atoms as discussed earlier. Average Sr–O distances are significantly different in the two polyhedra: Sr (2) shows a regular value (0.27 nm), whereas Sr (I) is loosely coordinated with a very large value (0.29 nm). Based on the crystal field theory, the 4f electrons of Eu^{2+} are not sensitive to their surroundings, due to the shielding by the electrons present in the outer shell, but the 5d electrons are split by the crystal field. In the $\text{Sr}_2\text{SiO}_4:\text{Eu}^{2+}$ phosphors, Eu^{2+} substitutes Sr^{2+} due to their similar ionic radius and bonding properties. So the emission spectra (Fig. 4.11 b) verify the fact that both sites of Sr can be substituted by Eu and the two emission bands are corresponding to Eu^{2+} at different sites. When Eu occupies Sr(1) site with weak crystal field, the emission band is about 470–490 nm, while the Sr(2) site has a more compact environment and stronger crystal field effect, leading to a longer emission wavelength of 590–610 nm.

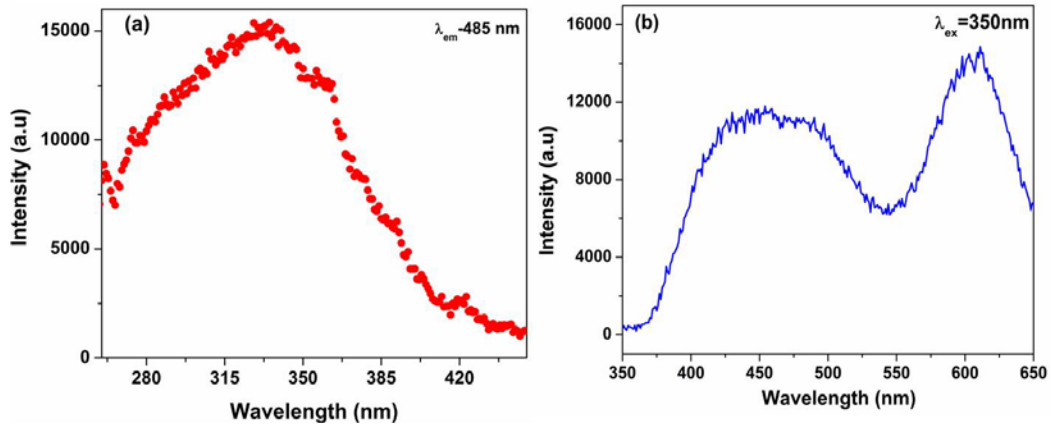


Figure 4.11: (a) Excitation spectra (λ_{em} -485 nm) and (b) Emission spectra (λ_{ex} -350 nm) of 0.5 mol% Eu^{2+} doped Sr_2SiO_4

The decay curve corresponding to the 0.5 mol % Eu^{2+} doped Sr_2SiO_4 are shown in Figure 4.12. For the 0.5 mol % Eu^{3+} doped sample the decay has been found to be monoexponential with a lifetime component of 0.483 μs and a long lifetime component of 1.73 μs . Longer lifetime component arises due to the Eu^{2+} ions sitting at symmetric 10-coordinated Sr sites and the short lifetime component arises due to the Eu^{2+} ion at non-centrosymmetric 9-coordinated Sr sites. The bi-exponential decay time curves have been fitted using the following equation.

$$y = A_1 \exp(-t/\tau_f) + A_2 \exp(-t/\tau_s) + y_0 \quad (4.2)$$

Where A_1 and A_2 are the pre-exponential factors obtained from the curve fitting, and τ_f and τ_s stand for the lifetimes for the fast and slow decay times, respectively.

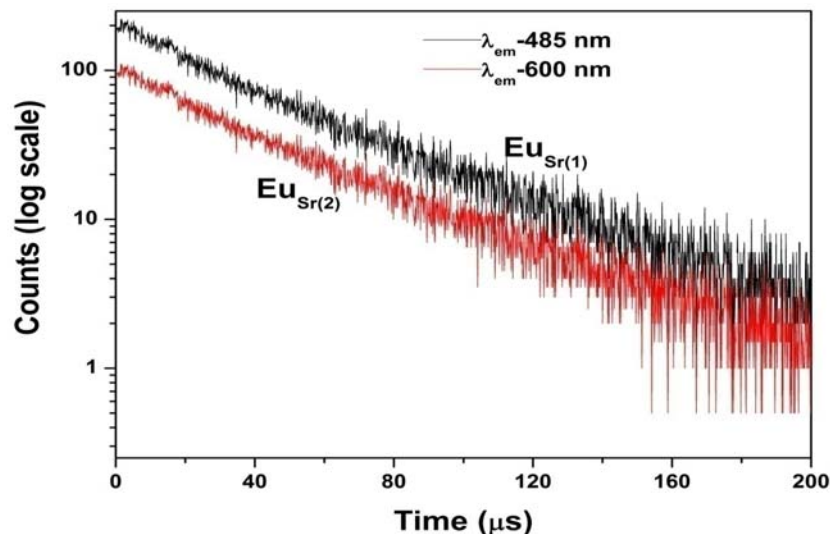


Figure 4.12: Luminescence decay time profile of Eu^{2+} doped Sr_2SiO_4 with λ_{ex} -350 nm under λ_{em} - 485 and 600 nm

4.6. Photoluminescence properties of $Sr_2SiO_4:Dy^{3+}$:

Figure 4.13(a) shows excitation spectra ($\lambda_{em} = 575$ nm) of the 0.5 mol% Dy doped strontium silicate (as prepared sample). In the excitation spectrum, a broad hump observed in the region of 220–270 nm has been attributed to the $O^{2-} \rightarrow Dy^{3+}$ charge transfer band (CTB), which is caused by the electron transfer from 2p orbits of O^{2-} ions to 4f shells of Dy^{3+} ions. The sharp lines observed in the wavelength range 300–450 nm, are attributed to the 4f-4f transition of Dy^{3+} . The peaks seen at 326, 351, 366, 387, 427 and 450 nm were assigned to electronic transitions of ${}^6H_{15/2} \rightarrow {}^6P_{3/2}$, ${}^6P_{7/2}$, ${}^6P_{5/2}$, ${}^4I_{13/2}$, ${}^4G_{11/2}$ and ${}^4I_{15/2}$ respectively. Figures 4.13(b) show the emission spectra for $Sr_2SiO_4:Dy^{3+}$ annealed at 600°C at 250 nm (charge transfer band) and 351 nm (f-f band) respectively.

Upon excitation with 250 nm, the emission spectrum is characterized by three bands located at 480, 575 and 665 nm corresponding to the transitions ${}^4F_{9/2} \rightarrow {}^6H_{15/2}$ (blue), ${}^4F_{9/2} \rightarrow {}^6H_{13/2}$ (yellow) and ${}^4F_{9/2} \rightarrow {}^6H_{11/2}$ (red) respectively. Spectral features remain same on excitation with 250 nm (charge transfer) and 351 nm (f-f band). It is also known that the Dy^{3+} emission around 480 nm is of magnetic dipole and 575 nm is of electric dipole (ED) origin. Generally, when Dy^{3+} is located at a low symmetry (without an inversion center), the yellow emission is dominant, while the blue emission is stronger when Dy^{3+} is located at a high symmetry (with an inversion center). However yellow emission at 575 nm (${}^4F_{9/2} \rightarrow {}^6H_{13/2}$) is predominant in Dy^{3+} ion-doped Sr_2SiO_4 suggesting that the ligand field deviates from inversion symmetry. This indicates that the luminescence centers are situated at low-symmetry local sites with no inversion centre. Average ionic radius of Dy^{3+} is around 100 pm, which is closer to 9-coordinated Sr^{2+} and unfavorable geometry in 10-coordination causes most of the Dy^{3+} to occupy 9-coordinated Sr^{2+} sites in strontium silicate. Ionic size and charge differences between Dy^{3+} and Sr^{2+} sites disturbs the local field, where such disturbance is evidenced by the more intense emission of ${}^4F_{9/2} \rightarrow {}^6H_{13/2}$. It can be concluded that the 9-coordinated strontium polyhedra in host lattice are distorted and there is lack of inversion symmetry at the Dy^{3+} site.

An energy level scheme is given in Figure 4.14 to explain the mechanism involved in the emission/excitation process in $Sr_2SiO_4:Dy^{3+}$.

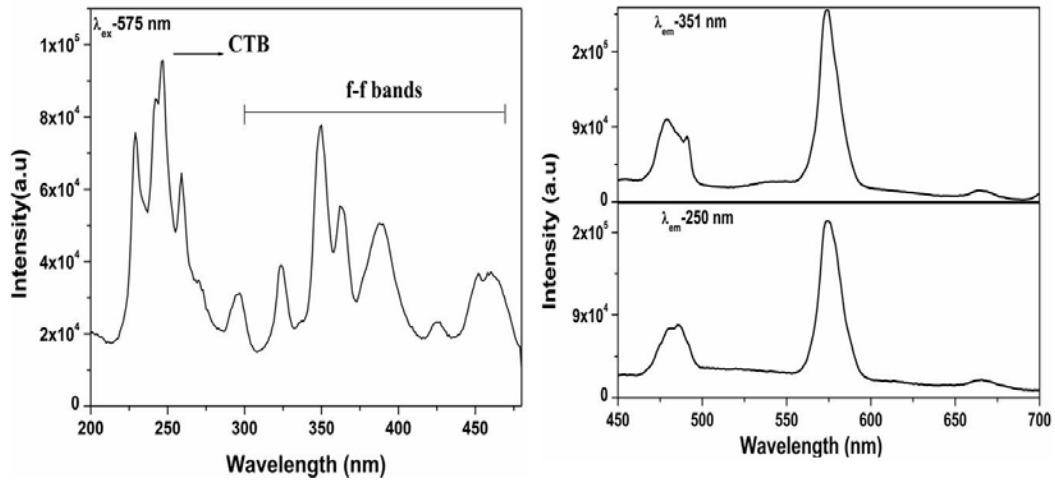


Figure 4.13: (a) Excitation spectrum and (b) Emission spectrum of the powder sample of $\text{Sr}_2\text{SiO}_4:\text{Dy}^{3+}$ with excitation wavelength 250 nm and 351 nm (0.1 mol % annealed at 600°C)

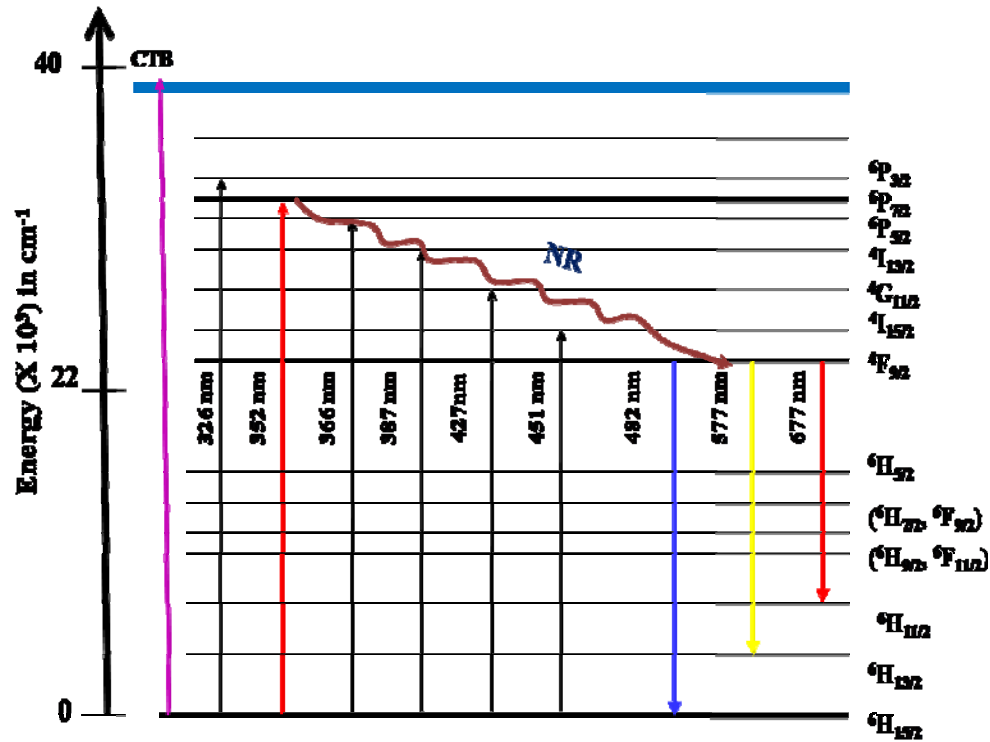


Figure 4.14: Energy level scheme for $\text{Sr}_2\text{SiO}_4:\text{Dy}^{3+}$ (0.5 mol % annealed at 600°C)

The decay curves corresponding to the ${}^6\text{H}_{15/2}$ level of Dy^{3+} ions in 0.5 mol % dysprosium doped Sr_2SiO_4 annealed at 800°C are shown in Figure 4.15 at excitation wavelengths of 250 nm monitoring emission at 577 nm on a 10 ms scale and fitted using the same exponential decay equation as mentioned in 4.2. As seen from Figure 4.15, decay curves display two life-times (291 μs and 1.56 μs) indicating the presence of Dy^{3+} ions in two different environments. Both these species are present in 9-

coordinated environment, but species is having relatively lower life time value is nearer to charge compensating defects and the one having higher lifetime is far off from charge compensating defects. A detailed time resolved emission spectrometric study (TRES) was carried out by giving suitable delay times in order to identify the two species responsible for the bi-exponential life times. However, the two emission spectra obtained from the TRES experiments were similar in nature and could not be differentiated.

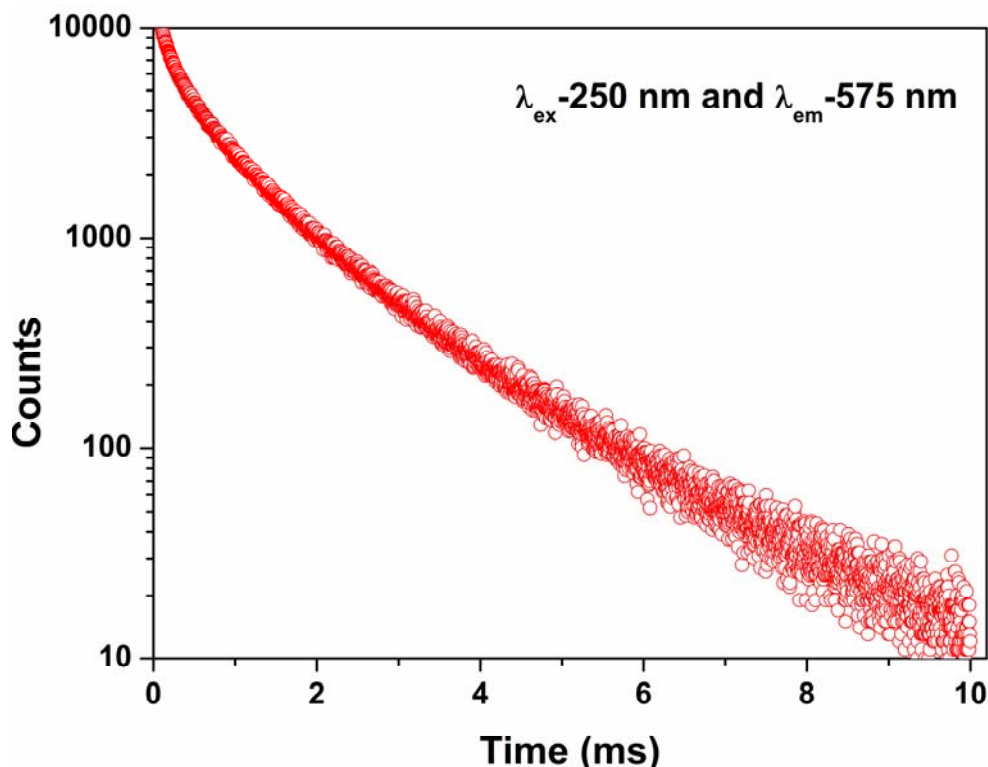


Figure 4.15: Luminescence decay time profile of the D 18 sample (λ_{ex} -250 nm and λ_{em} - 575 nm)

4.7. Photoluminescence properties of $\text{Sr}_2\text{SiO}_4:\text{Sm}^{3+}$:

Trivalent samarium ions emit a considerably bright luminescence in the visible and near infrared region in various kinds of host materials. The luminescence bands observed in this ion emission are due to transitions between the energy levels in the $4f^5$ electron configuration.

The excitation spectrum of the system at 597 nm emission is shown in Figure 4.16. Broad band in the range of 200–275 nm and was assigned to the charge transfer band $\text{O}^{2-} \rightarrow \text{Sm}^{3+}$ (CTB) peaking at 243 nm. In the wavelength region 320–550 nm, several

excitation peaks are observed and are located at 346 nm (${}^6\text{H}_{5/2}-{}^6\text{H}_{13/2}$), 365 nm (${}^6\text{H}_{5/2}-{}^4\text{D}_{3/2}$), 379 nm (${}^6\text{H}_{5/2}-{}^6\text{P}_{7/2}$), 407 nm (${}^6\text{H}_{5/2}-{}^4\text{F}_{7/2}$), 417 nm (${}^6\text{H}_{5/2}-{}^6\text{P}_{5/2}$), 438 nm (${}^6\text{H}_{5/2}-{}^4\text{G}_{9/2}$), 462 nm (${}^6\text{H}_{5/2}-{}^4\text{I}_{9/2}$), 469 nm (${}^6\text{H}_{5/2}-{}^4\text{I}_{11/2}$), 473 nm (${}^6\text{H}_{5/2}-{}^4\text{I}_{13/2}$) and 485 nm (${}^6\text{H}_{5/2}-{}^4\text{I}_{15/2}$) which are attributed to f-f transitions of Sm^{3+} . From the excitation spectrum, it was found that the intensity of f-f transition at 407 nm is high compared with the other transitions, this was chosen for the measurement of emission spectra of $\text{Sr}_2\text{SiO}_4: \text{Sm}^{3+}$ phosphors. The most intense peak at 407 nm clearly indicates that these phosphors are effectively excited by near ultraviolet light emitting diodes.

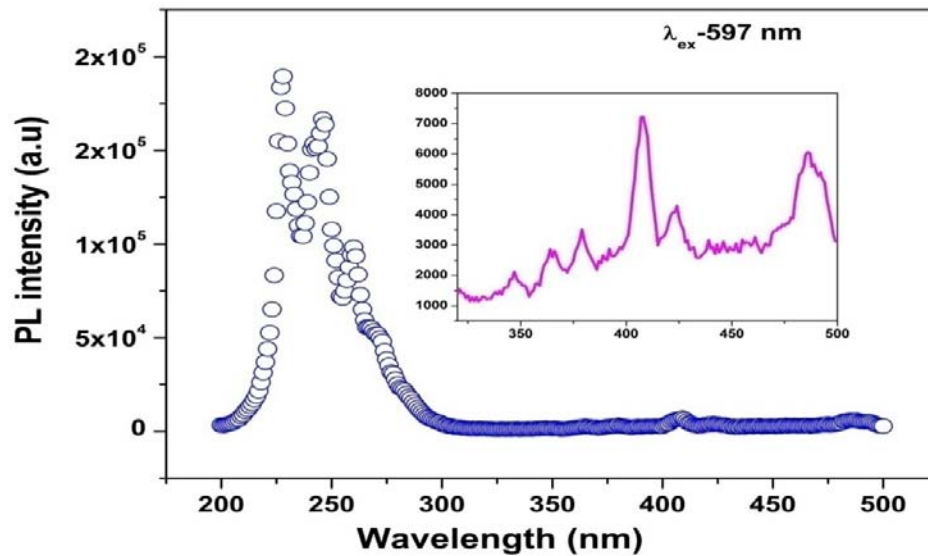


Figure 4.16: Excitation spectra $\text{SrZrO}_3:\text{Sm}^{3+}$. Inset shows the f-f lines of Sm^{3+}

Fig. 4.17 reveals that the emission spectra of Sm^{3+} ions doped Sr_2SiO_4 with an excitation wavelength of 243 nm (CTB)/ 407 nm (f-f band). Spectral features remain same on excitation with 250 nm (charge transfer) and 406 nm (f-f band). The intensities of emission bands were found to be low, when excited with the characteristic absorption band at 407 nm of Sm^{3+} ions, compared to that of emission intensities obtained with LMCT excitation band (250 nm).

This is due to the fact that the Sm^{3+} absorption bands corresponding to the f-f transitions are forbidden and exhibit poor absorptivities in UV region. The high intensities of emission bands when excited with LMCT are due to the intramolecular energy transfer (IMET) process, which occurs in the UV region.

The emission spectra consist of two parts: one is due to host in the region of 400-550 nm, another region comprising three sharp emission lines from 550 to 700 nm are the

characteristic of the samarium ions. Three peaks are ascribed to the ${}^4G_{5/2}$ - ${}^6H_{5/2}$, ${}^4G_{5/2}$ - ${}^6H_{7/2}$ and ${}^4G_{5/2}$ - ${}^6H_{9/2}$ transitions at 565, 597 and 643 nm of the Sm^{3+} ions, respectively. The peak at 703 nm is due to ${}^4G_{5/2}$ - ${}^6H_{11/2}$ transition. Among these, the transition at 597 nm (${}^4G_{5/2}$ - ${}^6H_{7/2}$) has the maximum intensity, which corresponds to the red emission of $SrZrO_3:Sm^{3+}$ phosphors. It can be stated that the strong red emitting transition ${}^4G_{5/2}$ - ${}^6H_{7/2}$ at 597 nm ($\Delta J = \pm 1$) is a partly magnetic dipole (MD) and partly electric dipole (ED) nature emission band. The other transition at 565 nm (${}^4G_{5/2}$ - ${}^6H_{5/2}$) is purely MD natured and at 643 nm (${}^4G_{5/2}$ - ${}^6H_{9/2}$) is purely ED natured, which is sensitive to crystal field. Generally, the intensity ratio of ED and MD transition has been used to measure the symmetry of the local environment of the trivalent 4f ions. The greater the intensity of the ED transition, the more the asymmetric nature. In the present study, the ${}^4G_{5/2}$ - ${}^6H_{5/2}$ (MD) transition of Sm^{3+} ions is less intense than ${}^4G_{5/2}$ - ${}^6H_{9/2}$ (ED) transition, indicating Sm^{3+} occupied asymmetric site in 9-coordinated Sr in Sr_2SiO_4 . From symmetry considerations, it is known that in a noncubic environment a ${}^{2S+1}L_J$ manifold of RE^{3+} ion containing an odd number of electrons is split to $J + 1/2$ Stark levels with each level maintaining two-fold Kramers degeneracy. Indeed, in the case of ${}^6H_{5/2}$ and ${}^6H_{7/2}$, the corresponding number of spectral lines can be counted. For ${}^6H_{9/2}$ and ${}^6H_{11/2}$, some of the transitions are probably too weak to be resolved. Splitting in the spectral line of Sm^{3+} further supports the fact that majority of samarium ion occupy low symmetric 9-coordinated Sr site.

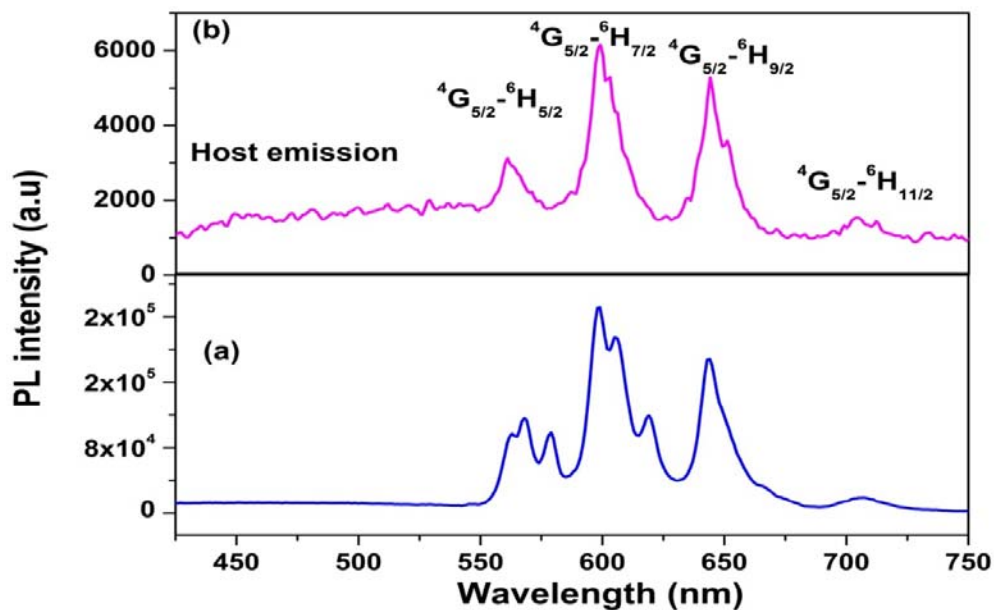


Figure 4.17: Emission spectra of air sintered $Sr_2SiO_4:Sm^{3+}$ at excitation wavelength (a) 243 nm (CTB) (b) 407 nm (f-f band)

Fluorescence life time measurement showed monoexponential behavior for Sm^{3+} in strontium silicate with a lifetime value of 2.23 ms. This indicates homogenous environment for Sm^{3+} as can be seen from Figure 4.18. Based on lifetime and emission spectra, it can be inferred that Sm^{3+} occupies 9-coordinated Sr^{2+} in strontium silicate.

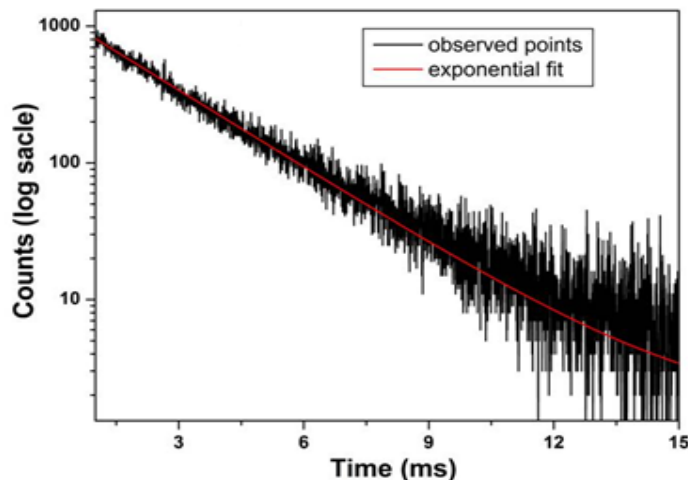


Figure 4.18: Luminescence decay time profile of $\text{Sr}_2\text{SiO}_4:\text{Sm}^{3+}$ at $\lambda_{\text{ex}}-407$ nm under $\lambda_{\text{em}}- 597$ nm

4.8. X-ray absorption spectroscopy: EXAFS

Sr_2SiO_4 doped with rare earths Eu and Dy were characterized by EXAFS technique at Sr K- edge to probe the local structure surrounding the strontium sites. The EXAFS measurements were carried out at the dispersive EXAFS beamline (BL-8) in transmission mode at the INDUS-2 Synchrotron Source (2.5 GeV, 100 mA) at Raja Ramanna Centre for Advanced Technology (RRCAT), Indore, India [197-199]. The beamline uses a 460-mm long Si (111) crystal having 2d value equal to 6.2709Å mounted on an elliptical bender, which can bend the crystal to take the shape of an ellipse. The crystal is first set in such a fashion that the central portion makes the proper Bragg angle (θ_0) w.r.t. the incident beam and it selects the energy (E_0) corresponding to the absorption edge of interest. Due to the divergent nature of the synchrotron beam, the angle of incidence varies from ($\theta_0 - \Delta\theta$) at one end of the crystal to ($\theta_0 + \Delta\theta$) at the other end and hence a band of energy of $E_0 \pm \Delta E$ is selected by the crystal, which then falls on the sample due to the elliptical bending of the crystal. The elliptical optics offers minimum aberration. The radiation transmitted through the sample is detected by a position-sensitive CCD detector having

2048x2048 pixels. The plot of absorption versus photon energy is obtained by recording the intensities I_0 and I_T , as the CCD outputs, without and with the sample, respectively, and the absorption coefficient μ is obtained using the relation:

$$I_T = I_0 e^{-\mu x} \quad (4.5)$$

where, x is the thickness of the absorber. Thus using the above beamline, the full EXAFS spectrum of the sample at any specified absorption edge can be obtained as a single shot within a time frame of 300 msec.

For the present measurement at Sr edge, the Si (111) crystal was set at a proper Bragg angle to obtain a band of energy around 16105 eV and pellets of commercial Bi_2O_3 (for Bi LI-edge) and Y_2O_3 (for Y K edge) powders were used for calibration of the CCD channels. All samples of appropriate weight, estimated to obtain a reasonable edge jump were taken in powder form and mixed thoroughly with cellulose powder to obtain total weight of 100 mg. Homogenous pellets of 15 mm diameter were prepared using an electrically operated hydraulic press. Fig. 4.19 shows the normalized EXAFS spectra ($\mu(E)$ versus E) for undoped Sr_2SiO_4 along with Dy and Eu doped Sr_2SiO_4 .

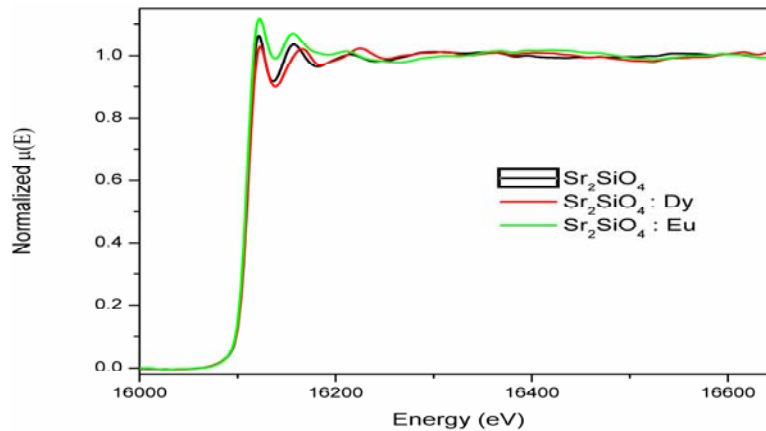


Figure 4.19: Normalized EXAFS spectra of blank Sr_2SiO_4 along with Dy and Eu doped Sr_2SiO_4 .

In order to take care of the oscillations in the absorption spectra $\mu(E)$ has been converted to absorption function $\chi(E)$ defined as follows [200]:

$$\chi(E) = \frac{\mu(E) - \mu_0(E)}{\Delta\mu_0(E_0)} \quad (4.5)$$

where E_0 absorption edge energy, $\mu_0(E_0)$ is the bare atom background and $\Delta\mu_0(E_0)$ is the step in $\mu(E)$ value at the absorption edge. The energy dependent absorption coefficient $\chi(E)$ has been converted to the wave number dependent absorption coefficient $\chi(k)$ using relation,

$$K = \sqrt{\frac{2m(E - E_0)}{\hbar^2}} \quad (4.6)$$

m is the electron mass. $\chi(k)$ is weighted by k^2 to amplify the oscillation at high k and the $\chi(k)k^2$ functions are Fourier transformed in R space to generate the $\chi(R)$ versus R spectra in terms of the real distances from the center of the absorbing atom. The set of EXAFS data analysis available in within IFEFFIT software package have been used for EXAFS data analysis [201]. This includes background reduction and Fourier transform to derive the $\chi(R)$ versus R spectra from the absorption spectra (using ATHENA software), generation of the theoretical EXAFS spectra starting from an assumed crystallographic structure and finally fitting of experimental data with the theoretical spectra using ARTEMIS software.

The $\chi(R)$ versus R spectra have been generated for all the samples from the $\mu(E)$ versus E spectra following the methodology described above and the best fit $\chi(R)$ versus R spectra of the samples have been shown in Fig. 4.20. The structural parameters (atomic coordination and lattice parameters) of Sr_2SiO_4 used for simulation of theoretical EXAFS spectra of the samples have been obtained from reported values in the literature [202, 157]. There are two crystallographic sites of Strontium in structure in which one is 10 coordinated and another is 9 coordinated. The scattering paths are generated using each Sr atom as central atom and have been used in the fitting of the experimental data with 50% weightage given to each crystallographic site [157]. The bond distances, co-ordination numbers (including scattering amplitudes) and disorder (Debye-Waller) factors (σ^2), which give the mean square fluctuations in the distances, have been used as fitting parameters. The best fit results are summarized in Table 4.4. There are two different crystallographic sites for Sr in Sr_2SiO_4 structure. One is 10 coordinated Sr (1) and another is 9-coordinated Sr (2). It can be seen from the Table 4.4 that on incorporation of Eu, average bond lengths are unchanged, which can be explained as the ionic radii of 10-coordinated Eu^{2+} (1.35 Å) and 9-coordinated Eu^{2+} (1.30 Å) are close to 10 coordinated

Sr^{2+} (1.36 Å) and 9-coordinated Sr^{2+} (1.31 Å) respectively [203]. There is an increase in σ^2 values for both Sr (1)-O and Sr (2)-O bonds, which manifests increase in disorder at both the Sr sites and thus corroborates the earlier results that Eu incorporates in both 10 and 9 coordination sites [157]. However, it has been observed that the change in σ^2 value is higher for 9-coordinated Sr site than for 10-coordinated Sr site. This may be due to higher Eu incorporation in 9-coordinated site than in 10-coordination sites. Nguyen et al. [204] have also reported preferentially higher Eu substitution in 9-coordinated Sr sites on the basis of enhanced intensity of the yellow luminescence. The EXAFS fitting results for Dy doped Sr_2SiO_4 are also given in Table 1. The average Sr(2)-O bond length is found to decrease in Dy doped samples compared to the undoped samples; however there is no change in Sr(1)-O average bond length. The decrease in Sr (2)-O bond length can be due the smaller ionic size of Dy^{3+} (1.083 Å for 9 coordination) than Sr^{2+} ion (1.31 Å for 9 coordination) [203]. It may be possible that Dy ions only occupy Sr (2) site and not Sr (1) site, since 10-coordinated Dy geometry does not exist [203]; however, EXAFS measurements at Dy edge is required to ascertain that.

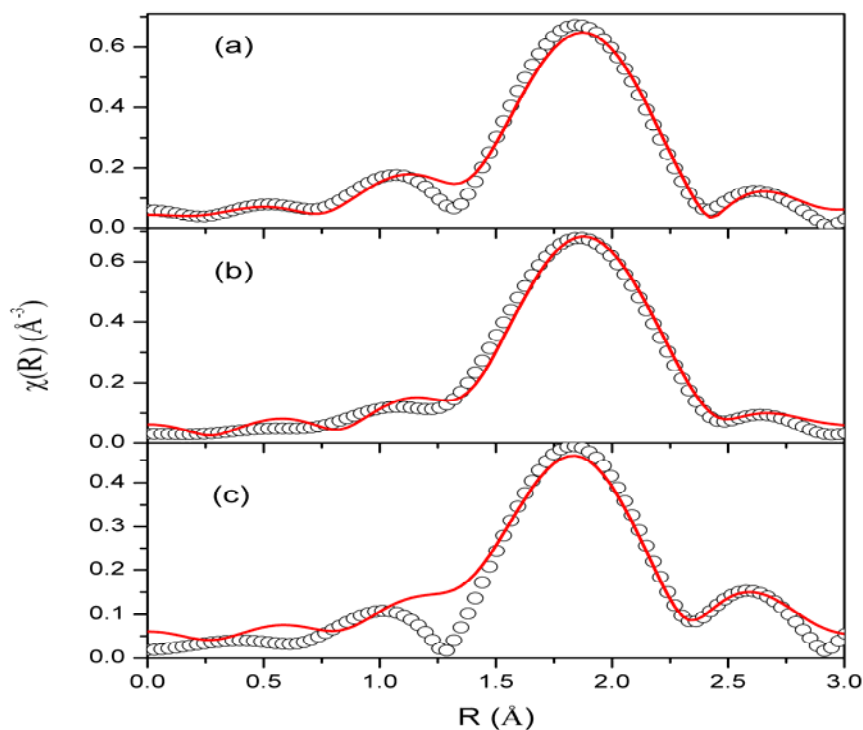


Figure 4.20: Fourier transformed EXAFS spectra at Sr K-edge (Scatter points) and theoretical fit (Solid line) for (a) Sr_2SiO_4 (b) Dy doped Sr_2SiO_4 and (c) Eu doped Sr_2SiO_4 .

Table 4.4: Structural parameters for undoped and Lanthanide ion doped strontium silicate as obtained by EXAFS fitting.

	Parameter	Sr ₂ SiO ₄	Sr ₂ SiO ₄ :Dy	Sr ₂ SiO ₄ :Eu
Sr(1)-O	R (Å) (2.38)	2.45	2.45	2.38
	N (1)	1*0.5	1*0.5	1*0.5
	σ^2	0.001	0.001	0.002
Sr(2)-O	R (Å) (2.51)	2.58	2.46	2.55
	N (2)	2*0.5	2*0.5	2*0.5
	σ^2	0.001	0.001	0.002
Sr(2)-O	R (Å) (2.60)	2.58	2.56	2.57
	N (5)	5*0.5	5*0.5	5*0.5
	σ^2	0.001	0.001	0.007
Sr(1)-O	R (Å) (2.85)	2.85	2.86	2.84
	N (5)	5*0.5	5*0.5	5*0.5
	σ^2	0.001	0.001	0.004
Sr(1)-O	R (Å) (3.07)	3.07	3.08	3.07
	N (4)	4*0.5	4*0.5	4*0.5
	σ^2	0.001	0.001	0.0044
Sr(2)-O	R (Å) (3.11)	3.07	3.08	3.07
	N (2)	2*0.5	2*0.5	2*0.5
	σ^2	0.001	0.001	0.006
Sr-Si	R (Å) (3.33)	3.14	3.14	3.15
	N (4)	4*0.689	4*0.8	4*0.76
	σ^2	0.01	0.017	0.013
Average Sr(1)-O (10 Coordinated)		2.90	2.91	2.90
Average Sr(2)-O (9 Coordinated)		2.69	2.65	2.68

4.9. Positron annihilation spectroscopy: Probing defects

In order to probe the electronic environment of positron trapping centres in the doped strontium silicate, CDB (expand) studies were carried out on pure Sr₂SiO₄ as well as Eu / Dy / Sm doped samples. The ratio spectrum of Dy/Eu doped samples with respect to pure sample is shown in Fig. 2.21. The low momentum part of the Doppler spectrum arises mainly from the annihilation with the valence electrons; the core electrons that can be taken as signature of an element, contribute to the high

momentum part of the spectrum. While profiles of both undoped and doped samples are identical, there is considerable increase in area under high momentum region for Dy doped sample. This indicates different chemical surrounding of defects in Dy sample. To get further insight into nature of defects, positron annihilation lifetime spectroscopic studies were carried out. The results are tabulated in Table 4.5.

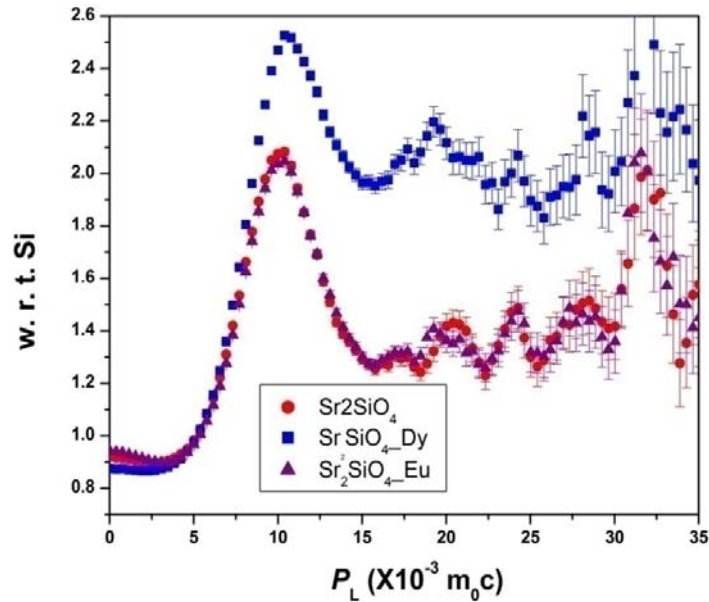


Figure 4.21: Ratio curves with respect to Si single crystal from coincidence Doppler broadening measurements on different Sr_2SiO_4 samples

Table 4.5: Positron life time values with their intensity

Sample	τ_1 (ps)	τ_2 (ps)	I_1 (%)	τ_{ave} (ps)
Sr_2SiO_4	183.6 \pm 2.2	343.8 \pm 3.8	48.3 \pm 1.0	266.5 \pm 7.0
Eu- doped	212.5 \pm 1.9	395.0 \pm 7.1	67.0 \pm 1.0	272.7 \pm 6.8
Dy- doped	235.9 \pm 1.9	399.6 \pm 8.6	70.9 \pm 1.1	283.6 \pm 7.9
Sm - doped	223.2 \pm 2.2	383.5 \pm 5.9	60.9 \pm 1.1	286.0 \pm 7.3

As seen from Table 2.21, on doping with Eu, Dy or Sm, τ_1 increases from 184 ps to 212-236ps – indicating that electron density has decreased. The increase in τ_1 is higher than seen due to oxygen vacancies. In general, life time of oxygen vacancies are 10 ps, oxygen clusters 10-20 ps and cation vacancies 30-50 ps [205]; so the most

likely defect/vacancy in this case is - cation vacancies (V''_{Sr}). The 2nd lifetime value is in the range 340-400 ps, which is attributed to vacancies clusters. Average lifetime for Dy or Sm doped samples is almost similar, while it is higher than Eu doped samples. This may be because of different site occupancy of Dy/Sm ions compared to Eu as evident from other studies.

4.10. Theoretical calculations to probe the difference in behavior of lanthanide ion in same host

All calculations were carried out using the spin-polarized DFT with a plane wave basis set, implemented in the Vienna Ab-initio Simulation Package (VASP). The electron-ion interactions were described by the projector augmented wave (PAW) method. The spin polarized generalized gradient approximation using the Perdew-Burke-Ernzerhof (PBE) functional has been used to calculate the exchange-correlation energy. The cut off energy for the plane wave basis set was fixed at 400 eV. The geometry optimization was performed by ionic relaxation, using a conjugate gradient minimization. The geometries are considered to be converged when the force on each ion becomes 0.01eV/Å or less. The total energy convergence was tested with respect to the plane-wave basis set size and simulation cell size, and the total energy was found to be accurate to within 1 meV. Three-dimensional periodic boundary conditions were applied to approximate a bulk solid (i.e. orthorhombic phase of Sr₂SiO₄). Conventional cubic unit ($\alpha=\beta=\gamma=90^\circ$) cell containing 28 atoms (8 Sr, 4 Si, 16 O) were used for calculations. Structural optimization was performed with respect to atomic coordinates and unit-cell parameters. A Monkhorst-Pack k-point grid of 3 x 3 x 3 was employed to map the first Brillouin zone. For the orthorhombic unit cell, the lattice parameters were found to be $a=5.673$ Å $b=7.073$ Å and $c=9.766$ Å. These values are excellent in comparison to the experimental lattice constants ($a=5.682$ Å $b=7.091$ Å and $c=9.772$ Å). In case of Eu-doped Sr₂SiO₄, out of 8 Sr atoms of unit cell, one atom was replaced with Eu/Sm/Dy atom.

It has been explained previously that in the structure of Sr₂SiO₄, there are two different Sr sites: one having coordination number 9 and the other with coordination number 10. The ten coordinated Sr(1) sites form linear three-membered rows of (Si-O-Sr(1)-O-Sr(2)) whereas the nine coordinated Sr(2) sites form zig-zag chains of (Sr(1)-O-Sr(2)-O-Sr(1)) along the b-axis [178]. A schematic of the crystal structure

for the strontium silicate showing the difference in coordination of strontium atom presented in Figure 4.22.

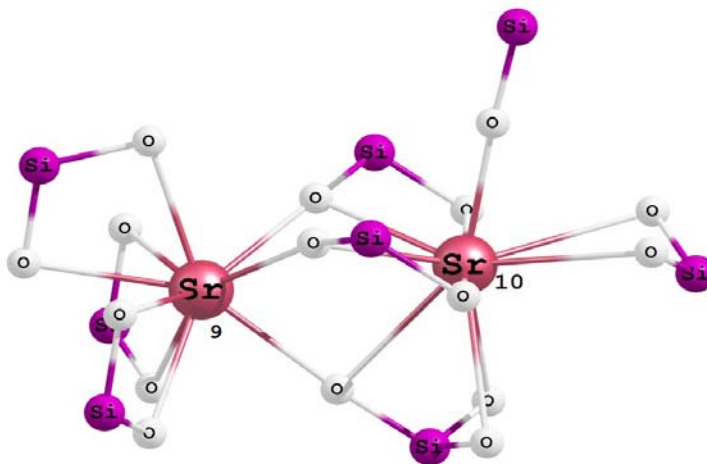


Figure 4.22: Structure of Sr_2SiO_4 showing 9 and 10-coordinated Sr-sites

Theoretical calculation showed that in SrO_9 polyhedra, shortest Sr-O bond length is 2.50 Å, largest one is 3.04 Å, Average Sr-O bond length is 2.68 Å. Experimentally obtained value is 2.70 Å. In case of SrO_{10} polyhedra, shortest Sr-O bond length is 2.38 Å, largest one is 3.10 Å, Average Sr-O bond length is 2.84 Å. Experimentally obtained value is 2.85 Å. So there is close proximity in experimental and theoretical values. All the Sr-O bond lengths in SrO_9 and SrO_{10} in Sr_2SiO_4 are depicted pictorially in Figures 4.23 and 4.24 respectively. One interesting observation in case of SrO_{10} polyhedra is the very low value of shortest Sr-O bond length compared to SrO_9 polyhedra. This is because of single coordination with nearby SiO_4 tetrahedron. Table 4.6 indicates the energetic calculations for relative stability of metal ion at 9- and 10- coordinated Sr^{2+} sites.

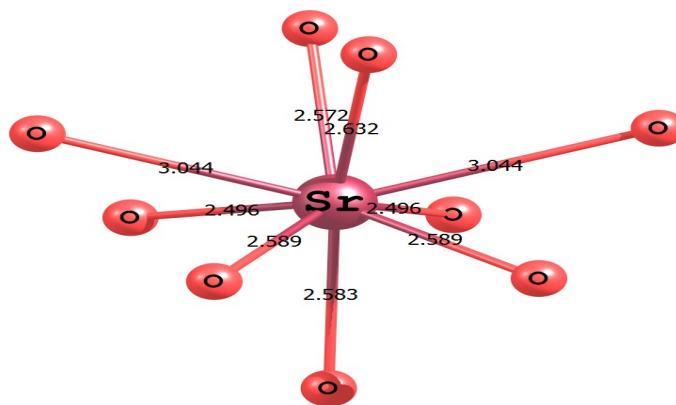


Figure 4.23: Pictorial representation of various Sr-O bond lengths in SrO_9 polyhedra in Sr_2SiO_4 .

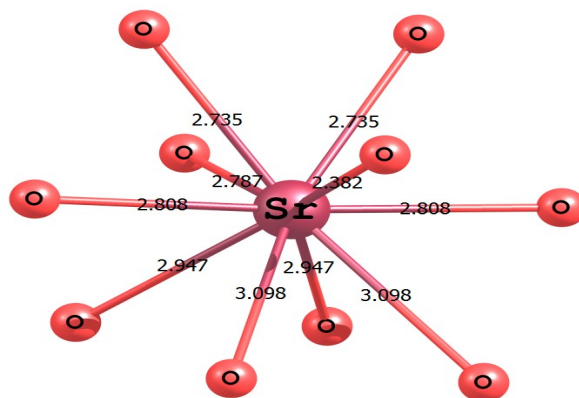


Figure 4.24: Pictorial representation of various Sr-O bond lengths in SrO₁₀ polyhedra in Sr₂SiO₄.

Table 4.6: Energetics for various lanthanides in Sr₂SiO₄ for two different sites of Sr.

M = Sm/Dy/Eu	Total Energy (eV)		
	Sm	Dy	Eu
M at 9-Sr	-200.64246	-200.65750	-207.56386
M at 10-Sr	-200.06394	-199.93754	-207.53293
Relative stability (10-9)	0.57852	0.72005	0.03093

It can be seen from the table that occupancy of 9-coordinated site is more favorable than 10-coordinated site. For Eu, the difference in stability for substitution of 9 and 10-coordination is only 0.03 eV (Comparable with room temperature thermal energy 0.025eV). For Sm and Dy, the relative stability values for substitution of 9 and 10-coordination are almost 20 times higher than that observed in case of Eu and well above the room temperature thermal energy 0.025eV. This analogy can be explained on the basis of bond energy value for various M-O bonds. The trend in bond energy for M-O bond (eV/atom) is Sr-O (2.86) < Eu-O (2.95) < Sm-O (3.58) < Dy-O (3.84). This indicates those Dy-O/Sm-O bonds are much stronger than the Eu-O bond, whereas Eu-O has comparable strength as that of Sr-O. As a result, inclusion of Sm/Dy results in shortening of few M-O, which lead to distortion in MO₁₀ polyhedra, whereas relatively inclusion of Eu has weaker effect on the M-O bond lengths of

SrO₁₀ polyhedra. Such a distortion leads to destabilization of the conformer having Dy/Sm at 10-coordinated sites.

4.10. Evaluation of color coordinates:

To evaluate the material performance on colour luminescent emission, CIE chromaticity coordinates were evaluated adopting standard procedures. The values of x and y coordinates of the system were calculated and represented on CIE diagram as shown in Figure 4.25. It is clear from the values that, Sr₂SiO₄:Eu³⁺ gives a ‘Red’ emission, Sr₂SiO₄:Eu²⁺/Dy³⁺ emits near white colour light and Sr₂SiO₄:Sm³⁺ gives a ‘Red-orange’ emission.

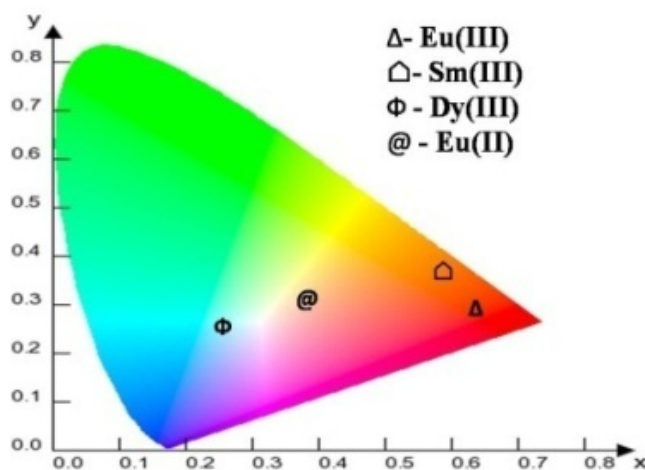


Figure 4.25: CIE index diagram of Sr₂SiO₄ doped with various lanthanides

4.11. Summary

Luminescence life time studies showed the presence of two different types of europium ions- 1.2 ms (short lived) and 4.7 ms (long lived). Long lived Eu³⁺ species was occupying more symmetric 10-coordinated Sr(1) sites, whereas the short lived Eu³⁺ was present at relatively less symmetric 9-coordinated Sr(2) sites. Eu²⁺ also substitutes at both the Sr²⁺ sites- leading to two emission bands. When Eu occupies Sr(1) site with weak crystal field, the emission band is about 470–490 nm, while the Sr(2) site has a more compact environment and stronger crystal field effect, leading to a longer emission wavelength of 590–610 nm. PL decay time confirms the presence of two types of Dy³⁺ species, which are responsible for bi-exponential decays. TRES does not reveal any change in the spectral feature of short and long lived species except in intensity. Both these species are present in asymmetric 9-coordinated

environment; but short lived species is nearer to charge compensating defects and long lived species is far off from charge compensating defects. EXAFS measurement also corroborated these studies. Fluorescence life time measurement has shown monoexponential behavior for Sm^{3+} in strontium silicate with lifetime value of 2.23 ms. Based on lifetime and emission spectra, it can be inferred that Sm^{3+} occupies 9-coordinated Sr^{2+} in strontium silicate. Theoretical modelling suggested that substitution of Sr in α' - Sr_2SiO_4 at 9-coordinated site is more favourable than at 10-coordinated site. Due to relatively higher bond strength of Dy-O and Sm-O bonds, the inclusion of these ions at 10-coordinated site results in shortening of few M-O, which leads to distortion in MO_{10} polyhedra. Such a distortion leads to destabilization of the conformer having Dy/Sm at 10-coordinated sites.

Chapter 5

Luminescent properties of various lanthanide ions (Sm, Eu, Gd and Dy) in SrZrO₃: A distorted perovskite

CHAPTER 5

5.1. General Introduction

Amongst the plethora of inorganic structures, there is one that stands out through its versatility in derived structures and physical properties: the perovskite structure. Along with their related structures, perovskites have been widely studied for their interesting properties and have found many applications within an abundance of fields. As quoted by Stolen et al. [206] these structures have been termed inorganic chameleons due to their large flexibility, since the cubic mother structure easily distorts and adapts to the relative sizes of the ions forming the compound. The source of fascination is the diversity of the properties and their high sensitivity to crystal chemical tuning; *i.e.*, a tiny change in chemical the composition or/and the crystal structure may induce huge changes in chemical and physical properties.

In particular, materials, which represent the ABO_3 perovskite structure, have constituted a central theme in the area of materials science and technology owing to their wide variety potential technological applications as fuel-cells, proton conduction [207], magnetoresistance [208], pigments [209], ferroelectricity [210-212], dielectricity [213], photocatalytic [214], photoluminescence [215,216] and others. Recently, the $4d^0$ band insulator perovskite $SrZrO_3$ (SZ) have attracted much attention as novel electronic materials. Because these materials have high melting points (over 2600°C) [217], they can be used for high temperature devices, such as electrochemical devices, due to their proton conductivity at fairly high temperatures [218].

Light emission from lanthanide ions plays an important role in solid state lighting (phosphor-converted light emitting diodes), display (plasma and field emission displays), and bioimaging (fluorescent markers) technologies. Owing to their high thermal and chemical stabilities and low environmental toxicity, lanthanide-doped alkaline-earth perovskite oxides of formula ABO_3 and their corresponding solid solutions $(A,A')(B,B')O_3$ ($A, A' = \text{Ca, Sr, Ba}$; $B, B' = \text{Ti, Zr, Hf}$) are attractive candidates for nanostructured phosphors for display and bioimaging technologies. Specifically, they have shown potential as phosphors for field emission [219] and electroluminescent [220] displays and as fluorescent markers for bioimaging [221]. Recently, much attention is focused on the photoluminescent (PL) properties of titanates and zirconates with disordered perovskite structures, the main reason being

their distinct potential for electro-optic applications [222, 223]. The optical properties of disordered semiconductors are characterized by the presence of a broad PL band. This phenomenon is attributed to the electronic states inside the band gap, which are the main defects for an intense PL response. According to Longo et al., the displacement of Zr or Sr atoms in disordered perovskite SrZrO₃ may induce some vacancy defects at the axial and planar oxygen sites of the [ZrO₆] octahedral [224]. It is well known that the vacancies play important roles as luminescence centers and thus it is expected that the perovskite SrZrO₃ may show host emission. Defect induced violet blue emission from strontium zirconate host has been observed by many workers [224, 225-227].

The perovskite material of ABO₃ types having various crystalline structures shows interesting physiochemical properties, which offer a potential host for the chemical substitution. Substitution at both A and B site can lead to change in symmetry and composition and thus create various defects viz. cation or oxygen vacancies, which can drastically influence the band structures and this is the main factor in determining the electronic structures. In particular, these materials can accommodate lanthanide ions at the A-site or B-site. These doped oxides are not only used as probes to investigate local centers and energy, but also to provoke changes in their optical behavior. Moreover, doping foreign elements into a semiconductor with a wide band gap to create a new optical absorption edge, is known to be one of the primary strategies for developing materials with optically driven properties. However, the role of the rare earth ions in the perovskite structure is not really clear and is still being discussed.

In recent years, the lanthanide ion doped SrZrO₃ materials have been widely investigated due to their significance to fundamental research and their high potential for application in optical materials [154, 180, 226-233]. The luminescence efficiency of trivalent rare earth ions doped into inorganic matrices depends on the energy transfer from the host to the ion. It has been shown that the quantum efficiency of rare earth ion emission doped in nanocrystals increases as crystal size decreases [234].

SrZrO₃ has been prepared by several synthetic routes including solid-state reaction [235], sol-gel [236], co-precipitation [237] and hydrothermal methods [238]. The conventional solid state reaction route requiring temperatures in excess of 1400 K suffers from inhomogeneous and coarse sample formation with non uniform size distribution. Large and non-uniform phosphor particles are more likely to be prone to

poor adhesion to the substrate and loss of coating. For good luminescence characteristics, phosphors should have fine size, narrow size distribution, non-aggregation and spherical morphology. Similarly, several disadvantages have also been noted with the other synthetic techniques such as the evaporation of solvents resulting in phase segregation, alteration of the stoichiometry due to incomplete precipitation, expensive chemicals and time consuming processes. To overcome these limitations, a facile combustion synthesis route was suggested by Zhang et al., where the combustion reaction takes place at a lower temperature of 300⁰C [230]. Through this method, a single phase compound could be synthesized without intermediate grinding or annealing steps.

Gel combustion is a novel method that uses a unique combination of the chemical gel process and combustion. The Gel synthesis of ceramic oxides offers advantages such as high purity, good homogeneity, and low processing temperature. Combustion synthesis offers advantages such as low energy requirements, simple equipment, and a short operation time because it uses a sustainable exothermic solid-solid reaction among the raw materials. The Gel combustion method is based on the gelling and subsequent combustion of an aqueous solution containing salts of the desired metals and an inorganic fuel such as acetylene black, and it yields a voluminous and fluffy product with a large surface area. This process has the advantages of inexpensive precursors, a simple preparation method, and the ability to yield nanosized powders. Most of the earlier luminescence reports on this ceramic host have been obtained with Eu, Ce or Dy as the activator ion.

However, when an active dopant is introduced into these perovskite, their optical and magnetic properties are dramatically changed depending on its distribution in the perovskite ceramic. Studies of dopant ion distribution in perovskite have attracted much attention, because they may allow better understanding of the correlations between structure and properties such as color, magnetic behavior, catalytic activity, and optical properties, *etc.*, which are strongly dependent on the occupation of these two sites by metal ions. None of the literature available explains the site symmetry of Ln³⁺ in SrZrO₃ nanocrystals. Considering the relatively wide band gaps, high refractive indices and lower phonon energy, SZ is a good candidate to be used as the host material for RE ions in order to excite them efficiently and to yield intense luminescence. Metal ions could be conveniently substituted into the SZ lattice, if their ionic radii are comparable to that of the Sr²⁺/Zr⁴⁺ cations. It is thought that

these “magic” dopants can choose their site occupancy as a result of the local Sr/Zr ratio and oxygen partial pressure during firing. Such dopants are also termed “amphoteric”, because the site change of a well defined valence dopant causes a change of the relative charge. We have used PL to investigate a series of lanthanide-doped strontium zirconate, with the main aim of determining the site occupancy of the lanthanide ions.

5.2. Synthesis and characterization of $\text{SrZrO}_3:\text{Ln}^{3+}$ (Ln=Sm, Eu, Dy and Gd)

5.2.1. *Synthesis of $\text{SrZrO}_3:\text{Ln}^{3+}$ (Ln=Sm, Eu, Dy and Gd)*

All the chemicals used in the sample preparation were of ‘Analytical Reagent’ grade and procured from Sigma Aldrich. Zirconyl oxychloride (ZrOCl_2), strontium nitrate $\text{Sr}(\text{NO}_3)_2$, ammonium nitrate (NH_4NO_3) and citric acid ($\text{C}_6\text{H}_8\text{O}_7\cdot\text{H}_2\text{O}$) were used as starting materials for the synthesis in the molar ratio 1:1:10:1.25. First, $\text{Sr}(\text{NO}_3)_2$ and NH_4NO_3 were dissolved in quartz double distilled (QDD) water with stirring and then ZrOCl_2 solution was added to it. Under vigorous stirring, citric acid solution (2 M) prepared initially was poured into the mixed solution resulting an opal gel. This gel was dried at 100°C for 10 h under IR lamp, and then transferred to a quartz beaker in a muffle furnace and kept at 300°C for 10 min. so as to form an ash-colored fluffy substance. In this step, the actual combustion reaction takes place using citric acid as the fuel. The ash-like product was then calcined at 600°C for 1 h. resulting in a white powder. The obtained white powders were ground and calcined at different temperatures. For preparation of Ln^{3+} doped sample (1.0 mol %), appropriate quantity of lanthanide nitrate were added at the initial stage prior to addition of ZrOCl_2 so that the final rare earth concentration was 1.0 mol %.

5.2.2. *Characterization of SrZrO_3*

5.2.2.1. Phase purity and Structure: XRD

Figure 5.1 indicates the XRD patterns of SrZrO_3 samples obtained after different annealing temperatures. The patterns matched with orthorhombic phase of SrZrO_3 (ICDD file no 44-0161). Smaller peaks due to minor impurities of SrCO_3 , observed in the pattern (around $2\theta = 25^\circ$), are hardly avoided at such a low calcination temperature and a short time. However, their existence seems to have little influence

on the luminescence of SrZrO₃, comparing the emission spectra of the present sample and SrZrO₃ synthesized by another method [239]. Pure SrZrO₃ could be obtained on annealing the samples above 800°C. The XRD data was indexed on an orthorhombic system with space group *Pnma* having cell parameters $a = 5.817 \text{ \AA}$, $b = 8.204 \text{ \AA}$ and $c = 5.797 \text{ \AA}$ as represented in Table 5.1. EDXRF pattern shown in Figure 5.2 further confirms the formation of pure SrZrO₃ at 600°C.

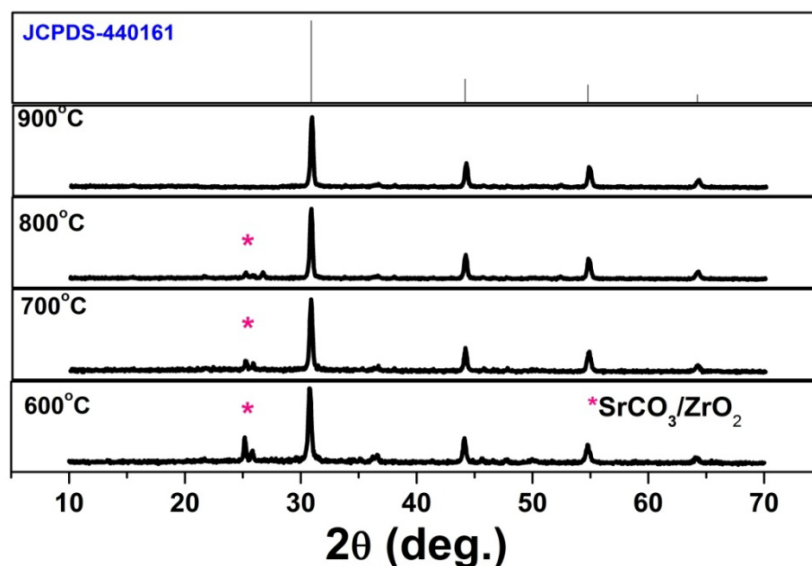


Figure 5.1: XRD patterns of the SrZrO₃ samples annealed at different temperatures and the standard JCPDS pattern for file no 44-0161. The peaks corresponding to minor impurity phases are identified by asterisk.

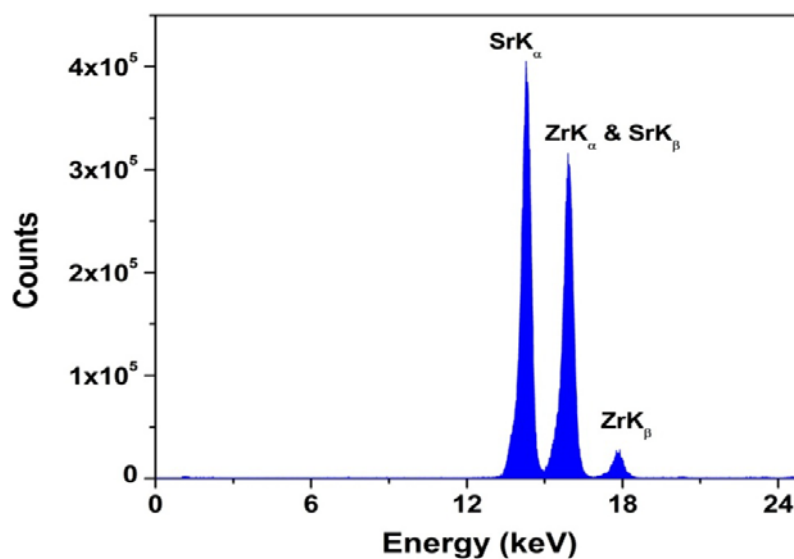


Figure 5.2: EDXRF pattern for SrZrO₃

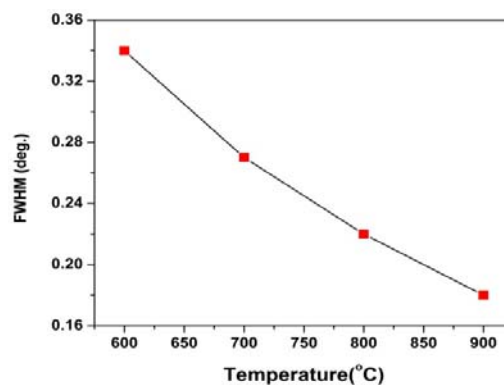
Table 5.1: XRD data of strontium zirconate ($\lambda= 0.15406$ nm) annealed at 600°C

2 θ values	d value (Å)	I/I ₀	h k l	Lattice parameter
25.181	3.5327	22	1 1 1	Due to SrCO₃ (minor impurity)
25.837	3.4455	9	0 2 1	
30.796	2.9610	100	0 0 2	Due to SrZrO₃ a = 5.817 Å, b=8.204 Å and c=5.797 Å
44.073	2.0530	29	0 4 0	
54.676	1.6773	22	2 4 0	
64.122	1.4511	10	2 4 2	

X-ray line broadening takes place because of various reason like instrumental artefacts (Non-monochromaticity of the source, imperfect focusing) crystallite size , and residual strain arising from dislocations, coherent precipitates etc. Grain size from X-ray line broadening is obtained from Scherer's formula.

$$B(2\theta) = \frac{0.94\lambda}{L \cos \theta} \quad (5.1)$$

where L is the crystallite size, λ is the wavelength (for Cu-K α , $\lambda=1.5418$ Å) and $B = \sqrt{(B_M^2 - B_S^2)}$ (B_M is the full width at half maximum of the sample and B_S is that of a standard grain size of around 2 μ m). From the Scherer formula, it can be noted that peak width (B) is inversely proportional to crystallite size (L). As the crystallite size gets smaller, the peak gets broader. With increase in temperature; size of crystallite increases and so B decreases. A smaller particle gives a broader Bragg peak. Effect of temperature on the broadness of strong diffraction peak (30 degree) is shown in Figure 5.3.

**Figure 5.3: Effect of temperature on broadness of strong diffraction peak (30 degree)**

Ideal ABO_3 perovskite structure has a cubic unit cell with $Pm-3m$ space group having A atom at corner position (0, 0, 0), B atom at body centre position (1/2, 1/2, 1/2) and oxygen atoms at face centered position (1/2, 1/2, 0). The relative ionic size requirements for the stability of cubic structure are quite stringent; hence slight buckling and distortion can produce several low symmetric distorted compounds. The structure is commonly visualized as a three-dimensional network of regular corner-linked BO_6 octahedra, the A-cation being centrally located in the spaces between them. The most commonly occurring distortion in perovskites is octahedral tilting. This means that the tilting of the BO_6 octahedra about one or more of their symmetry axes, maintaining both regularity of the octahedral (approximately) and their corner connectivity (strictly). Such tilting allows greater flexibility in the coordination of A-cation, while leaving the environment of B-cation essentially unchanged. Crystal system adopted for a particular A and B cations can be predicted from the Goldschmidt's tolerance factor (τ) [240], which is an indicator for the stability and distortion of crystal structures.

$$\tau = \frac{r_a + r_o}{\sqrt{2}(r_b + r_o)} \quad (5.2)$$

where r_a is the radius of the A-cation, r_b is the radius of the B-cation and r_o is the radius of the anion (usually oxygen). When τ is near to unity, it has a cubic structure and whereas deviation from 1 leads to triclinic, orthorhombic, rhombohedral etc. $SrZrO_3$ perovskite structure is built up from ZrO_6 octahedra that form a network by sharing corners, in combination with the Sr^{2+} ion, which fills the hole in between the octahedra. The coordination number of Sr and Zr ions is 8 and 6 respectively. In $SrZrO_3$, the size of Sr ion is smaller than the hole in an undistorted structure. The incorporation of a smaller ion in the perovskite structure is accompanied by rotation of the octahedra leading to the lowering of the symmetry with respect to an ideal perovskite. For this reason, $SrZrO_3$ is considered to be pseudo cubic or orthorhombic at room temperature. A schematic of the crystal structure for the $SrZrO_3$ and Gd^{3+} doped $SrZrO_3$ is presented in Figure 5.4

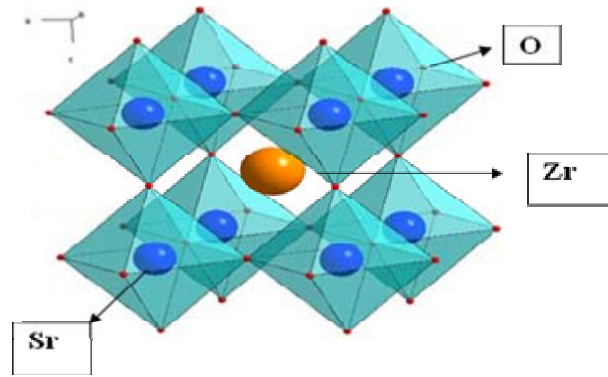


Figure 5.4: Schematic crystal structure of SrZrO_3

5.2.2.2. Morphological studies: SEM

SEM studies showed that, the particles are uniformly distributed and mostly of spherical morphology as can be seen from Figure 5.5. Furthermore, the particle size is in a narrow range, the average grain size of them is about 150 nm in diameter. The particle sizes increase with the increase in the temperature, because higher temperature can significantly promote the growth of particles and lead to excessive sintering and aggregation of particles. It is remarkable that all the samples have same morphology. These images exhibited homogeneous aggregates with a sphere-like aspect, which are composed of large number of small grains. Numbers on SEM micrograph at different temperatures indicate size of phosphor particle at that particular temperature. It can be seen that with increase in temperature, extent of agglomeration increases and therefore size increases.

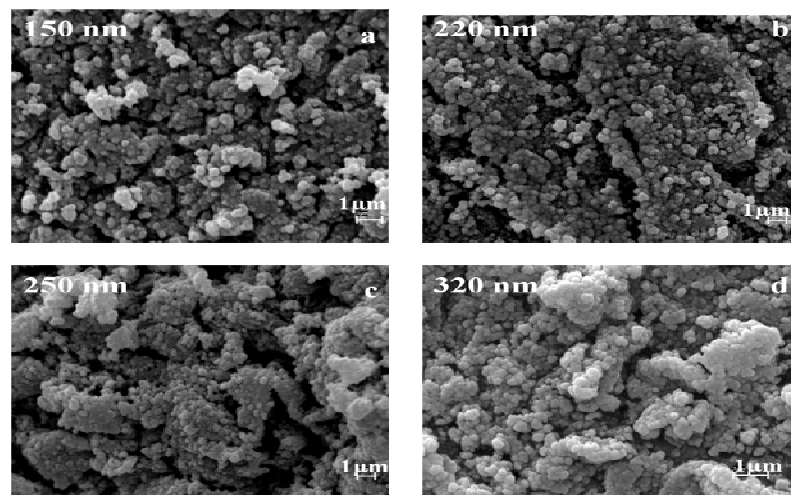


Figure 5.5: SEM micrographs of SrZrO_3 sample annealed at (a) 600 (b) 700 (c) 800 and (d) 900°C at similar magnification.

5.2.2.3. Size distribution: DLS

The average grain size of 0.5 mol% Eu doped strontium zirconate phosphor has also been obtained from the DLS studies, which show a narrow size distribution of particles centered at 100 nm (Figure 5.6). It was found that average particles size increases with increase in temperature.

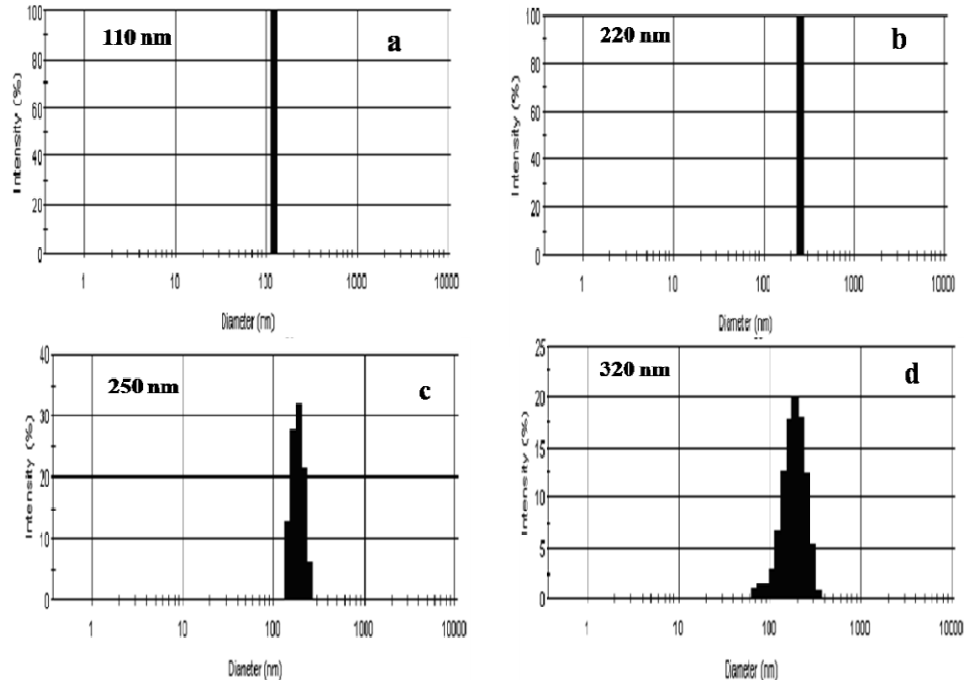


Figure 5.6: Size distribution plot obtained by dynamic light scattering studies strontium SrZrO_3 sample annealed at (a) 600 (b) 700 (c) 800 and (d) 900°C.

5.3. Unique properties of undoped SrZrO_3 : Luminescence and EPR

5.3.1. Emission spectroscopy

As well-known, nanomaterials were abundant in defects. Fig. 5.7 showed the room temperature photoluminescence spectra of SrZrO_3 nanoparticles. When exposed to 243 nm Xenon flash lamp, the sample exhibited visible light emission in a broad range of 400–635 nm. The most intensive photoluminescence peaks centered at 425 nm, implying violet-blue light emission.

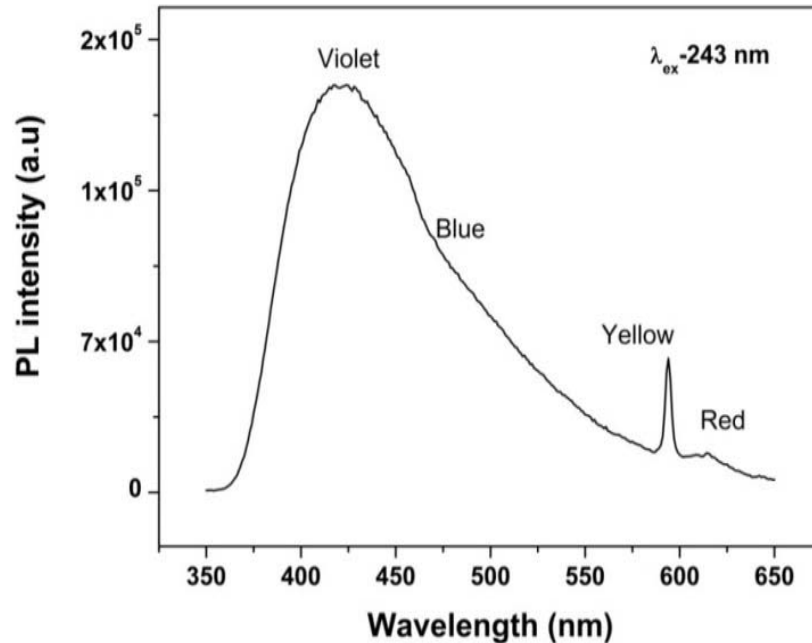


Figure 5.7: Emission spectra of air sintered SrZrO₃

The PL profile is typical of a multiphonon process, i.e., emission that occurs by several paths and involves numerous states within the forbidden band gap. Considerable studies had verified that the photoluminescence properties of perovskite oxides arise because of oxygen vacancies and structural defects. Kan et al. reported that the photoluminescence intensity was directly related to the defects in the perovskite SrTiO₃ crystals and films [241]. Further Longo et al. confirmed the defects related photoluminescence intensities through controlling the annealing temperature for perovskite SrZrO₃ and BaZrO₃ nanocrystals that were prepared by combustion method [242-244]. The higher the calcining temperature, the more frequent the ZrO₆ conformation and the more ordered the structure. The yellow and red peaks decrease and the violet-blue peaks increase with heat treatment, since yellow-red emission is linked to the disordered structure and violet-blue to the ordered structure. The visible spectrum wavelengths are usually between 400 nm and 700 nm. The energy carried by each visible photon is between 3.1 eV and 1.8 eV. Violet/blue color is more energetic than yellow/red/orange component. In our experiments, the intense violet and blue emission was therefore attributed to shallow defects in the band-gap and a more ordered structure, while the weak yellow and red emission was linked to defects deeply inserted in the band-gap and disorders in the lattice. Therefore it can be concluded that in SrZrO₃, each colour has a different origin and is linked to a specific

structural arrangement. When the sample was exposed to UV light, deep and shallow defects generated localized states in the band gap and non-homogeneous charge distribution formed traps for electrons. Due to the energy dependant localized levels, exciting the trapped electrons requires various energies. After excited, the blue luminescence originated from the recombination process in which an excited electron of the conductive band (CB) lost its energy and re-occupied the energy levels of an electron hole in the valence band (VB) through the localized defect levels.

5.3.2 Theoretical calculations

The calculated lattice parameters for SZ are $a = 5.845 \text{ \AA}$, $b = 8.295 \text{ \AA}$ and $c = 5.909 \text{ \AA}$ using GGA-PBE, which agree well with our XRD data of $a = 5.797 \text{ \AA}$, $b = 8.204 \text{ \AA}$ and $c = 5.817 \text{ \AA}$ and other experimentally determined values [245] within less than 1.5% deviations. Therefore, the GGA approximation is able to provide reliable results for the equilibrium lattice constants of the present system. The GGA-PBE calculated band gap for SZ is 3.7 eV which is not in agreement with the experimental value of 5.6 eV by optical conductivity analysis of the polycrystalline sample at room temperature [246]. But our calculated band-gap energy matches very well with previous GGA-PBE calculation of Z. Guo et al. [247]. The underestimation of band gap energy is a typical problem of DFT calculations in the GGA approximation. Nevertheless, the present calculations properly reproduce the good insulating character of ideal SZ.

Three structural models were built based on the ideal/ordered SZ structure (o-SZ) (Fig. 5.8) in order to simulate the disordered types and structural complex vacancies associated with them: (i) by displacement of the Zr (f-SZ); (ii) by displacement of Sr (m-SZ); and (iii) by simultaneous displacement Zr/Sr (fm-SZ) as described by V.M. Longo et al. [242]. The DOS were calculated with the total 0.5 \AA vector displacement of the Zr and Sr network in all the dislocated models.

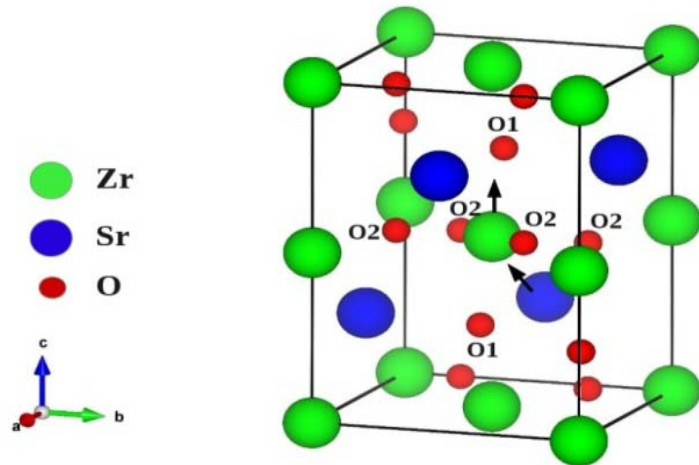


Figure 5.8: Schematic of SrZrO₃ unitcell. Arrows indicate direction of atomic displacement for the Zr and Sr network. O₁ and O₂ are the axial and planar oxygen atoms, respectively.

The calculated total and orbital angular momentum resolved DOS for o-SZ, f-SZ, m-SZ and fm-SZ are shown in **Fig. 5.9**, ranging from -4 eV below the top of the VB to 6 eV above and presenting the principal orbital states, which influence the gap states. As seen in Fig. 5(a), the upper valence bands (VB) consist of O 2p states taking equivalent contributions from axial and planar oxygen atoms (shown in Fig. 4) with some additional contributions from Zr 4d states. The lower conduction bands (CB) are mainly Zr 4d states with some additional contributions from O 2p states. This clearly indicates covalent nature of Zr-O bonds and these DOS characters of SZ are consistent with the previous GGA results of Guo et al. [247]. In the case of f-SZ (Fig. 5(b)), the VB is composed of O 2p states and the upper part of VB, i.e. the new states, is composed mainly of axial oxygen 2p states. In the m-SZ case (Fig. 5(c)), the upper part of VB is composed mainly of planar O 2p states. The fm-SZ structure shows a strong axial oxygen contribution in the new DOS present in the upper part of VB which is analogous to the f-SZ model. Moreover, the band gap energies of o-SZ, f-SZ, m-SZ and fm-SZ are 3.7, 2.96, 3.10 and 2.76 eV, respectively. The displacement in network former causes increased disorder in the lattice compared to the network modifier. The greater disorder occurs when both network modifier and former are displaced. This disorder is characterized by the reduction in band-gap energy in the disordered model [242]. Even though the numerical values of the GGA-PBE calculated band-gap energies of dislocation model structures are not correct but it follow the same sequence in which degree of disorder is present in these model

structures. Therefore, the DOS features of o-SZ, f-SZ, m-SZ and fm-SZ are essentially similar to the DOS calculated by Longo et. al. [242] using DFT based calculations combined with the B3LYP hybrid functional. So the GGA-PBE methodology captures the essential features of structural defects and degree of disorder in SZ resulting from network former and modifier displacements.

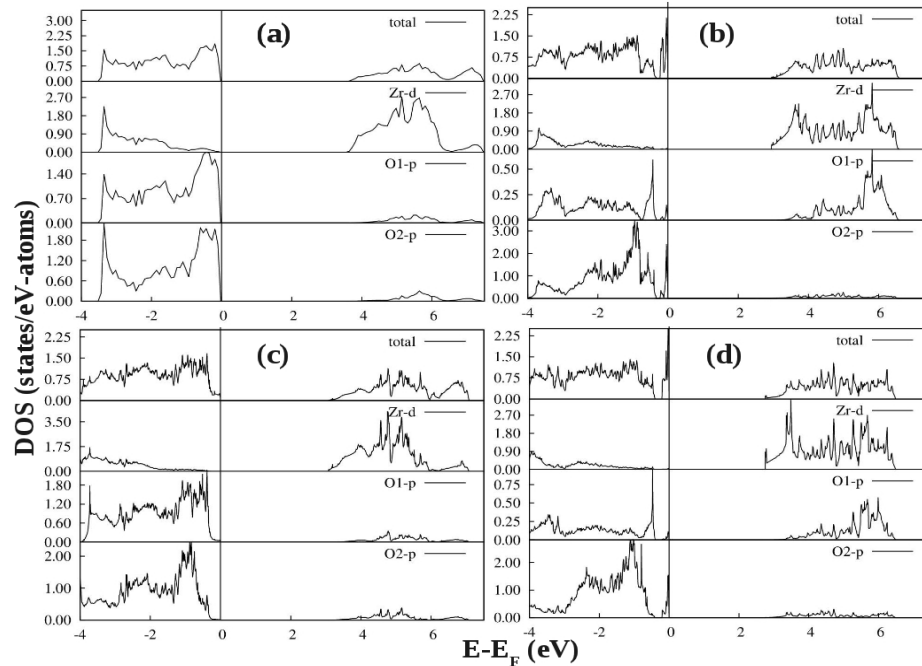


Figure 5.9: Total and orbital angular momentum projected DOS for: (a) o-SZ, (b) f-SZ, (c) m-SZ and (d) fm-SZ models. The vertical lines represent Fermi level.

The displacement in Zr (former) network promotes an increased disorder in the lattice when compared to the Sr (modifier) network. The greater disorder occurs when both the atoms are displaced. This disorder is characterized by the reduction in band-gap energy in the disordered model. The decrease in band gap in structurally disordered powder can be attributed to defects and/or local bond distortion, which yield local electronic levels in the band gap of this material. Increased disorder is linked to deep defects inserted in the band-gap and increased order is associated with shallow defects, which disappear when total order is reached. Increased disorder is due to presence of $[\text{ZrO}_5 \cdot \text{V}_\text{O}^{\bullet\bullet}]$ and $[\text{ZrO}_5 \cdot \text{V}_\text{O}^{\bullet}]$ complex clusters and are deeply inserted in the band-gap, leading to orange-red PL emission. $[\text{SrO}_{11} \cdot \text{V}_\text{O}^{\bullet\bullet}]$ and $[\text{SrO}_{11} \cdot \text{V}_\text{O}^{\bullet}]$ complex clusters are linked to shallow defects in the band-gap and lead to a more energetic PL emission (violet-blue light) [242]. The deep defects linked to the Sr/Zr disorder are associated with the 2p states of axial oxygens and evidently shown in

Figure 5.9 (d). The shallow defects can be ascribed to the 2p states of planar oxygens in the VB as described in our DOS analysis. Increasing the lattice order causes these complex vacancies and the PL emission to disappear. The presence of oxygen vacancy is also confirmed by EPR studies as discussed in section 5.3.4

5.3.3. Excitation spectroscopy

To confirm that emission in SrZrO₃ is mediated by defect and is responsible for origin multicolour, we have recorded excitation spectra (Figure 5.10) corresponding to violet, blue, yellow and red emission. It was observed that excitation spectral feature remains same at entire wavelength range, dominated by a wide band center at about 246 nm (5.04eV), which indicates that the UV irradiation energy can be efficiently absorbed by SrZrO₃ host lattices and then is transferred to the emission centers. This band belongs to the host absorption band (HAB) and is generally ascribed to the charge transfer from the oxygen ligands to the central zirconium atom.

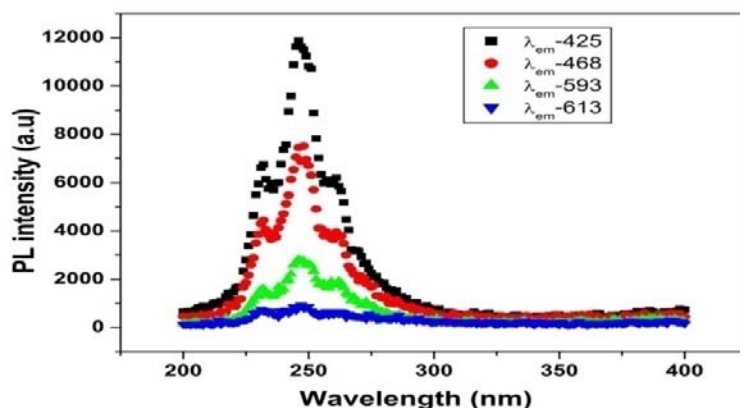


Figure 5.10: Excitation spectra of air sintered SrZrO₃ under different excitation wavelength

5.3.4. EPR spectroscopy for probing defect

Electron paramagnetic resonance (EPR) shows a great potential for studying the local structure and properties of nanoparticles. It has to be noted that the influence of external factors on the radio-spectroscopic characteristics of nanosized and large (microns) particles is not identical since the charge state and other characteristics of intrinsic and impurity defects in nanoparticles depend on particle size and surface conditions. The EPR spectrum of bare SrZrO₃ (Fig. 5.11), recorded after the final calcinations in air, is not a flat line (as one should expect in the case of the perfect stoichiometry) and shows an intense and asymmetric signal of the spin

Hamiltonian at room temperature indicating the presence of some intrinsic defects in the as prepared material. In the literature, this signal is related with singly ionized oxygen vacancies V_O^\bullet and vacancy-related defects, [248-250] where the single asymmetrical peak g presents some variations of 1.9560–2.0030. We believe that the changes in g values are related to differences in the preparation method, chemical environment, and heat treatment conditions. The broad line width of signal indicates a certain degree of heterogeneity (several species differ slightly in spectral parameters) typical of disordered environments, such as those found at the surface of nanostructured crystals. Even broader signals are found, for instance, for species formed at the surface of TiO_2 [251]. Matta *et al.* [252] used EPR measurements to verify the phase transformation from tetragonal to monoclinic zirconia and observed a signal $g = 2.0018$, which was attributed to trapped single electrons located in oxygen vacancies of ZrO_2 . Lin *et al.* [253] reported that the EPR band at $g=1.9800$ is oxygen vacancy related. Thus, in the disordered structure, these V_O^\bullet are linked to ZrO_5 clusters, called $[ZrO_5 \cdot V_O^\bullet]$ oxygen complex clusters [244].

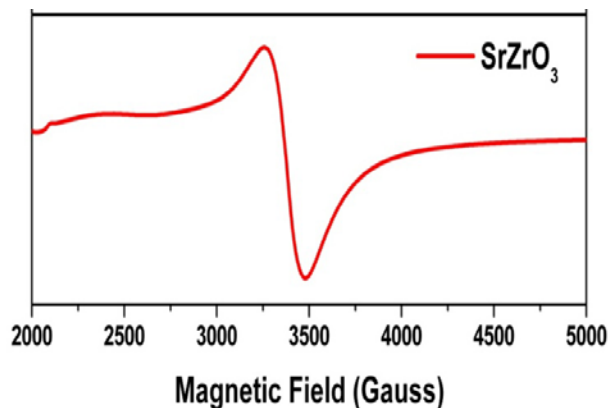


Figure 5.11: X-band EPR spectra of $SrZrO_3$ sample recorded at RT

5.3.5. Luminescence decay

Emission lifetimes were recorded using the time-correlated single-photon-counting (TCSPC) technique. The new experimental setup is described as follows: samples were excited with 243 nm laser pulses provided by the frequency-doubled output of Nd: YAG pumped OPO laser regenerative amplifier operating at a 10 Hz repetition rate. The decay curves of $SrZrO_3$ annealed at 600°C (as prepared sample) are shown in Figure 5.12 at excitation wavelengths of 243 nm monitoring emission at various wavelength on a 100 μs scale and fitted using biexponential decay as mentioned in equation 3.4. The decays measured here were all found to be multi-

exponential in all the cases and could be adequately fit to a sum of two exponentials. The life-time values and % occupancy of each species obtained under different emission are given in Table 5.2. Broadly life time values obtained were ~ 2.00 and ~ 12.0 μs which are attributed to different types of defects present in bare SrZrO_3 nanocrystals. Slower decaying species was attributed to shallow defects in the band-gap and a more ordered structure whereas the faster decaying component is linked to defects deeply inserted in the band-gap and disorders in the lattice.

Table 5.2: Life time and % occupancy for the life time of SrZrO_3 host with different emission wavelength

λ_{em} (nm)	τ_1 in μs and (% occupancy for short lived species)	τ_2 in μs and (% occupancy for short lived species)
425 violet)	1.85 (50)	13.9 (50)
468 (blue)	1.99 (49)	12.2 (51)
593 (yellow)	2.00 (48)	11.7 (52)
615(red)	2.14 (44)	10.4 (50)

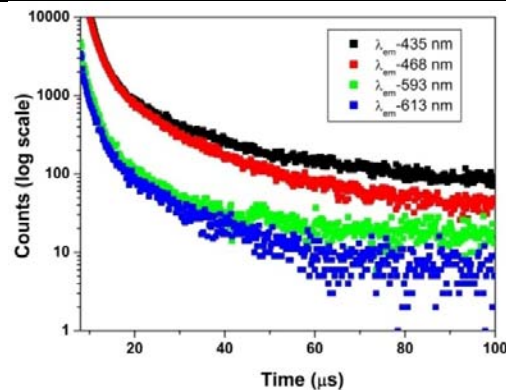


Figure 5.12: Decay curves of SrZrO_3 sample. Samples were excited at 243 nm and the emission was monitored at different wavelength.

5.4. Luminescence properties of $\text{SrZrO}_3:\text{Sm}^{3+}$

5.4.1. Excitation and Emission spectroscopy of Sm^{3+} doped SrZrO_3

Trivalent samarium ions emit a considerably bright luminescence in the visible and near infrared region in various kinds of host materials. The luminescence bands observed in this ion emission are due to transitions between the energy levels in the $4f^5$ electron configuration. The excitation spectrum of the system at 597 nm emission is shown in figure 5.13. Broad band in the range of 200–275 nm and was assigned to the charge transfer band $\text{O}^{2-} \rightarrow \text{Sm}^{3+}$ (CTB) peaking at 243 nm. In the wavelength region 320–550 nm, several excitation peaks are observed and are located at 346 nm

(${}^6\text{H}_{5/2}$ - ${}^6\text{H}_{13/2}$), 365 nm (${}^6\text{H}_{5/2}$ - ${}^4\text{D}_{3/2}$), 379 nm (${}^6\text{H}_{5/2}$ - ${}^6\text{P}_{7/2}$), 407 nm (${}^6\text{H}_{5/2}$ - ${}^4\text{F}_{7/2}$), 417 nm (${}^6\text{H}_{5/2}$ - ${}^6\text{P}_{5/2}$), 438 nm (${}^6\text{H}_{5/2}$ - ${}^4\text{G}_{9/2}$), 462 nm (${}^6\text{H}_{5/2}$ - ${}^4\text{I}_{9/2}$), 469 nm (${}^6\text{H}_{5/2}$ - ${}^4\text{I}_{11/2}$), 473 nm (${}^6\text{H}_{5/2}$ - ${}^4\text{I}_{13/2}$) and 485 nm (${}^6\text{H}_{5/2}$ - ${}^4\text{I}_{15/2}$) which are attributed to f-f transitions of Sm^{3+} . From the excitations spectrum, it was found that the intensity of f-f transition at 407 nm is high compared with the other transitions and has been chosen for the measurement of emission spectra of $\text{SrZrO}_3:\text{Sm}^{3+}$ phosphors. The most intense peak at 407 nm clearly indicates that these phosphors are effectively excited by near ultraviolet light emitting diodes.

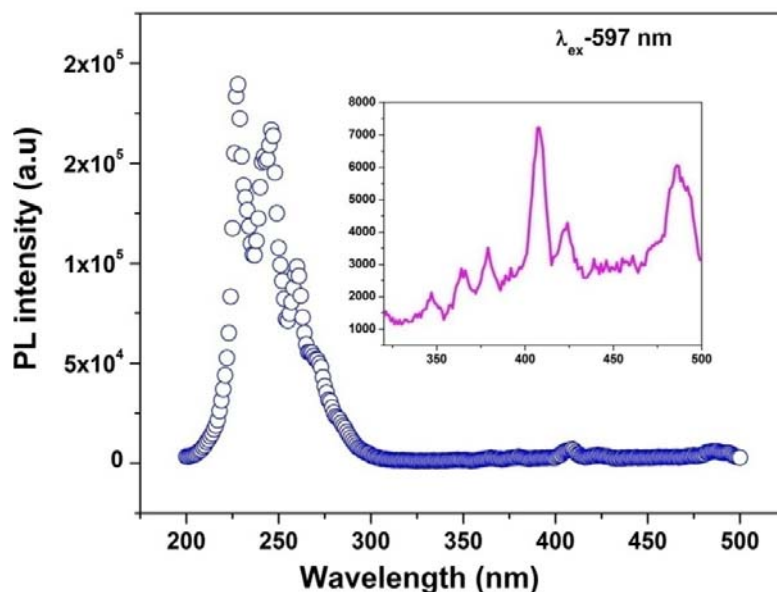


Figure 5.13: Excitation spectra $\text{SrZrO}_3:\text{Sm}^{3+}$. Inset shows the f-f lines of Sm^{3+}

Fig. 5.14 reveals that the emission spectra of Sm^{3+} ions doped SrZrO_3 with an excitation wavelength of 243 nm (CTB)/ 407 nm (f-f band). Spectral features remain same on excitation with 250 nm (charge transfer) and 406 nm (f-f band). It is also noticed that, the intensities of emission bands are found to be low, when excited with the characteristic absorption band at 407 nm of Sm^{3+} ions, compared to that of emission intensities obtained with LMCT excitation band (250 nm). This may be due to the fact that the Sm^{3+} absorption bands corresponding to the f-f transitions are forbidden and exhibit poor absorptivities in UV region. The high intensities of emission bands when excited with LMCT are due to the intramolecular energy transfer (IMET) process, which occurs in the UV region. The emission spectra consist of two parts: one is due to host in the region of 400-550 nm, another region comprising three sharp emission lines from 550 to 700 nm are the characteristic of the samarium ions. Three peaks are ascribed to the ${}^4\text{G}_{5/2}$ - ${}^6\text{H}_{5/2}$, ${}^4\text{G}_{5/2}$ - ${}^6\text{H}_{7/2}$ and ${}^4\text{G}_{5/2}$ - ${}^6\text{H}_{9/2}$

transitions at 565, 597 and 643 nm of the Sm^{3+} ions, respectively. The peak at 703 nm is due to ${}^4\text{G}_{5/2}$ - ${}^6\text{H}_{11/2}$ transition. Among these, the transition at 597 nm (${}^4\text{G}_{5/2}$ - ${}^6\text{H}_{7/2}$) is having the maximum intensity, which corresponds to the red emission of $\text{SrZrO}_3:\text{Sm}^{3+}$ phosphors. It can be stated that the strong red emitting transition ${}^4\text{G}_{5/2}$ - ${}^6\text{H}_{7/2}$ at 597 nm ($\Delta J = \pm 1$) is a partly magnetic dipole (MD) and partly electric dipole (ED) nature emission band. The other transition at 565 nm (${}^4\text{G}_{5/2}$ - ${}^6\text{H}_{5/2}$) is purely MD natured and at 643 nm (${}^4\text{G}_{5/2}$ - ${}^6\text{H}_{9/2}$) is purely ED natured, which is sensitive to crystal field. Generally, the intensity ratio of ED and MD transition has been used to measure the symmetry of the local environment of the trivalent 4f ions. The greater the intensity of the ED transition, the more the asymmetry nature. In our present study, the ${}^4\text{G}_{5/2}$ - ${}^6\text{H}_{5/2}$ (MD) transition of Sm^{3+} ions is less intense than ${}^4\text{G}_{5/2}$ - ${}^6\text{H}_{9/2}$ (ED) transition, indicating Sm^{3+} occupied asymmetric site in SrZrO_3 .

We know that coordination number of Sr and Zr ions is 8 and 6 respectively. Since ionic size difference between 8-coordinated Sr^{2+} (126 pm) and 8-coordinated Sm^{3+} (108 pm) is less, Sm^{3+} ions occupying the Sr^{2+} sites will not lead to a large distortion in the lattice and if the associated defect due to charge difference is at a large distance, the local site symmetry will be having an inversion symmetry. On the other hand 6-coordinated Sm^{3+} with ionic size 96 pm while occupying 6-coordinated Zr^{4+} (ionic size 72 pm) has a larger size difference and can lead to distortion in the octahedra and the resulting in local site without inversion symmetry. On the other hand 6-coordinated Sm^{3+} with ionic size 96 pm while occupying 6-coordinated Zr^{4+} (ionic size 72 pm) has a larger size difference and can lead to distortion in the octahedra and the resulting in local site without inversion symmetry. Thus observed spectra where ${}^4\text{G}_{5/2}$ - ${}^6\text{H}_{5/2}$ (MD) transition of Sm^{3+} ions is less intense than ${}^4\text{G}_{5/2}$ - ${}^6\text{H}_{9/2}$ (ED) transition can be attributed to majority of Sm^{3+} ions occupying Zr^{4+} site without inversion symmetry though oxygen vacancies are introduced in vicinity to ensure local charge compensation. In SrZrO_3 the Zr^{4+} ion has the local symmetry D_{2h} within the ZrO_6 octahedron. However, the ionic radius of Sm^{3+} exceeds that of Zr^{4+} by about 24 pm (96 vs. 72 pm) and therefore induces a significant lattice distortion. From symmetry considerations it is known that in a noncubic environment a ${}^{2S+1}L_J$ manifold of RE^{3+} ion containing an odd number of electrons is split to $J + 1/2$ Stark levels with each level maintaining two-fold Kramers degeneracy [254]. Indeed, in the case of ${}^6\text{H}_{5/2}$ and ${}^6\text{H}_{7/2}$ the corresponding number of spectral lines can be counted. For ${}^6\text{H}_{9/2}$ and ${}^6\text{H}_{11/2}$ some of the transitions are probably too weak to be resolved. Splitting

in the spectral line of Sm^{3+} further supports the fact that majority of samarium ion occupy low symmetric Zr^{4+} site.

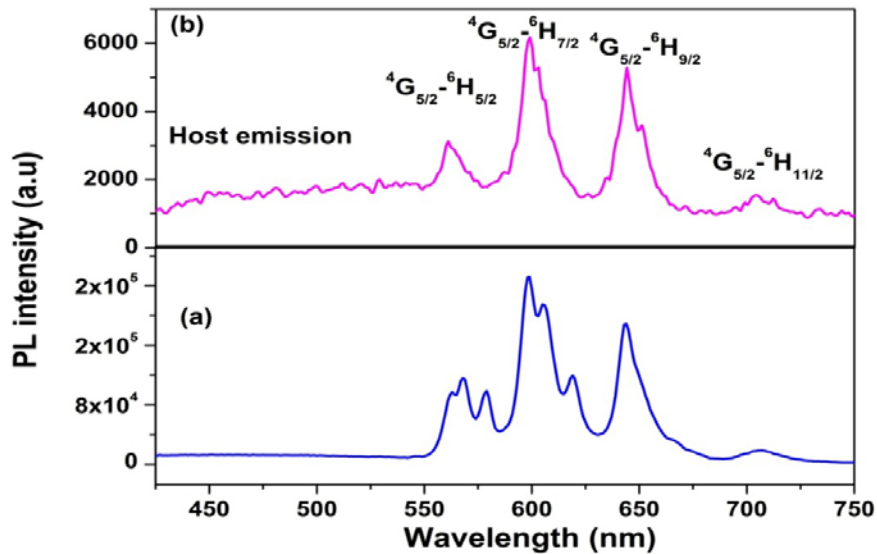


Figure 5.14: Emission spectra of air sintered $\text{SrZrO}_3:\text{Sm}^{3+}$ at excitation wavelength (a) 243 nm (CTB) (b) 407 nm (f-f band)

5.4.2. Decay Time and TRES studies:

In SrZrO_3 perovskite structure the coordination numbers of Sr and Zr ions are 8 and 6 respectively as already discussed that can be occupied by the Sm^{3+} ions. To get an idea about the nature of the dopant ion occupancy in these lattice sites, PL decay time (life time) studies were conducted. The decay curves corresponding to the ${}^4G_{5/2}$ level of Sm^{3+} ions in the 1.0 mol % samarium doped SrZrO_3 shown in Figure 5.15 at excitation wavelength of 407 nm, monitoring emission at various wavelength viz. 565, 597 and 643 nm. For $\text{SrZrO}_3:\text{Sm}^{3+}$, a good fit was found to a biexponential decay using the similar equation as mentioned in equation (3.4). Broadly, the analysis showed the presence of two components; one short lived and one long lived. In all the cases roughly the life time values were $\sim 500 \mu\text{s}$ (short component, T_1 , 75 %) and 1.6 ms (long component, T_2 , 25 %), which can be indicative of the presence of two emitting species or states.

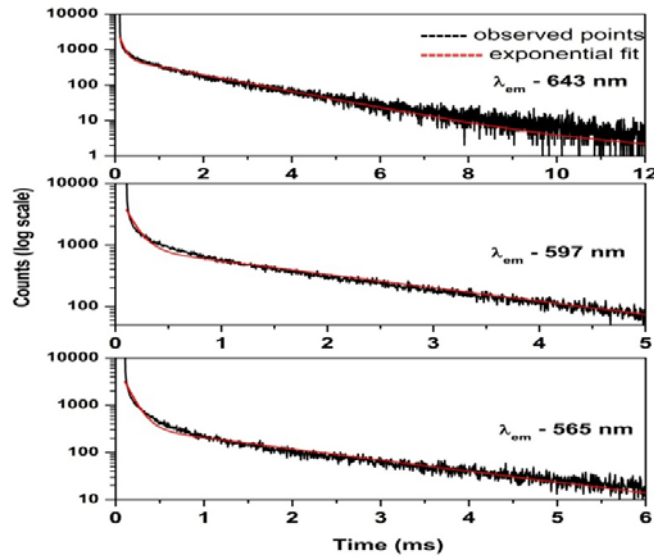


Figure 5.15: Luminescence decay time profile of SrZrO₃:Sm³⁺ at λ_{ex} -407 nm under λ_{em} -565, 597 and 643.

Makishima et al. [255] previously investigated the luminescence of Sm³⁺ in BaTiO₃ host lattice and found that the spectra consist of the two different series with various properties. They also found that some foreign ions can change the relative strength of the emissions of the two series owing to a charge compensation mechanism. On the basis of their results, they concluded that one series of the emissions is attributed to Sm³⁺ at the Ti⁴⁺ site, while the other series of emissions is related to the presence of Sm³⁺ in the Ba²⁺ site.

Assuming a given phonon energy (same host for the lanthanide ions), a relatively longer PL decay time should be attributed to a more symmetric site, as the f-f transition becomes more forbidden, whereas a shorter decay time is often associated with an asymmetric site due to relaxation in the selection rules. In SrZrO₃ perovskite structure the coordination numbers of Sr and Zr ions are 8 and 6. Species T₁ (500 μ s) which is the major one arises because of Sm³⁺ ions occupying 6-coordinated Zr⁴⁺ site without inversion symmetry whereas minor species T₂ (1.6 ms) can be ascribed to Sm³⁺ ions occupying 6-coordinated Sr²⁺ with inversion symmetry. These results also corroborates our emission studies where we have observed that majority of Sm³⁺ ions occupying Zr⁴⁺ site without inversion symmetry.

In order to identify the environment associated with the species exhibiting different life-times, time resolved emission spectra (TRES) were recorded at different time-delays with constant integration time. Figure 5.16 shows the spectra recorded

with time delays of 600 μs , and 3.0 ms respectively with integration time of 50 μs . As seen from the Figure 16 after and giving a delay time of 600 μs ; characteristic emission predominated by Sm^{3+} ions in asymmetric environment ($\text{Intensity}_{(643)} > \text{Intensity}_{(597)}$) was observed. After delay time of 3.0 ms, the emission characteristics were overall similar to those observed after 600 μs delay with difference in intensity which is usually expected.

The spectra observed after 3.0 ms delay is expected from long-lived species (1.6 ms) as the other species would have reduced in intensity by a factor of e^{-6} . The spectra obtained after 600 μs delay time has contributions from both short-lived and long-lived species. The spectral characteristics of short lived species were obtained by subtracting the contribution of long-lived species (obtained mathematically using the spectra observed after 3.0 ms delay) from the observed spectra of 600 μs delay. Spectra for short lived and long lived species obtained after mathematical calculations are shown in the Figure 5.17. The ${}^4\text{G}_{5/2} \rightarrow {}^6\text{H}_{5/2}$ line is observed at 565, which originates from the magnetic dipole (MD) transition, and does not depend on chemical surroundings of the luminescent centre and its symmetry. However, the hypersensitive ${}^4\text{G}_{5/2} \rightarrow {}^6\text{H}_{9/2}$ transition at 643 nm is magnetic-dipole forbidden and electric-dipole allowed and its intensity increases as the environmental symmetry become lower. The asymmetry ratio was found to be 0.28 and 0.128 for short lived ($\mu = 500 \mu\text{s}$) and long lived ($\tau = 1.6 \text{ ms}$) species respectively. This is in correspondence with phonon energy concept where short lived species will have more asymmetric component than long lived species.

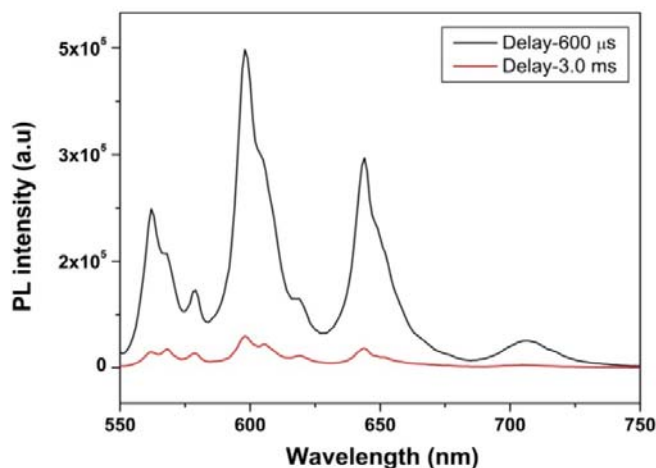


Figure 5.16: Time-resolved emission spectra of $\text{SrZrO}_3:\text{Sm}^{3+}$ nanophosphor under the excitation at 243 nm after giving suitable delay time

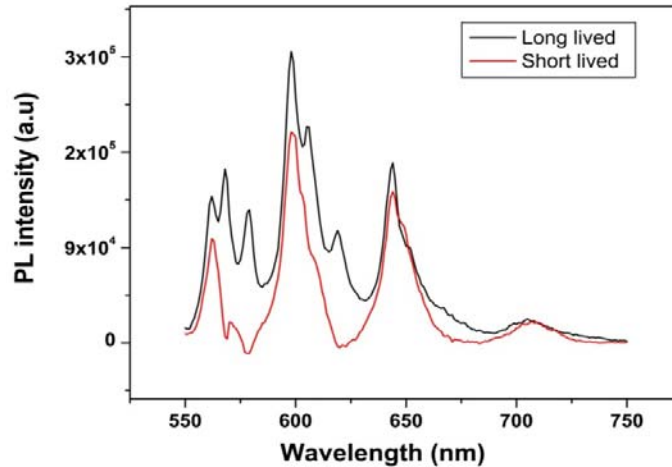


Figure 5.17: Time-resolved emission spectra of for short and long lived Sm^{3+} ion in SrZrO_3

5.4.3. Energy Transfer from Host to Rare-Earth Ions in $\text{SrZrO}_3:\text{Sm}^{3+}$

5.4.3.1. Luminescence Experiment

An obvious spectral overlap between the emission of host (oxygen-vacancy) and the excitation of Sm^{3+} can be observed, which is shown in Fig. 5.18. According to Dexter theory [256] an effective energy transfer (ET) requires a spectral overlap between the donor emission and the acceptor excitation. Consequently, the effective ET from the host to Sm^{3+} ions is expected. Therefore, the samples SrZrO_3 and $\text{SrZrO}_3:\text{Sm}^{3+}$ were subjected into oxygen-deficient atmosphere (vacuum) to sinter with an attempt to observe the influence of the oxygen vacancies on the PL of the powders. We adopted vacuum atmosphere rather than reduction atmosphere sintering for preventing the reduction of Zr^{4+} in SrZrO_3 and $\text{SrZrO}_3:\text{Sm}^{3+}$. The results presented in Fig. 5.19 indicate that the sintering in vacuum is quite effective to improve the violet-blue emission of SrZrO_3 compared to emission intensity of air sintered sample as mentioned in earlier Figure 5.14. It is safe to say that the vacuum-sintering in this study can create oxygen vacancies effectively. Comparing with the air-sintered $\text{SrZrO}_3:\text{Sm}^{3+}$ phosphor (Figure 5.14), the red emission intensity increased about 150% when the sample is sintered in vacuum. Based on the above results, we can suggest that the PL intensity enhancement in the vacuum-sintered $\text{SrZrO}_3:\text{Sm}^{3+}$ phosphor is related to the creation of the oxygen vacancies. To clarify the relation between the red emission and oxygen vacancies in the vacuum-sintered $\text{SrZrO}_3:\text{Sm}^{3+}$, the emission (435 nm) of SrZrO_3 and $\text{SrZrO}_3:\text{Sm}^{3+}$ were examined. The results are shown in Fig.

15; the ET process from host (oxygen-vacancy) to Sm^{3+} can be confirmed, as the violet-blue emission is largely decreased after Sm^{3+} doping into SrZrO_3 . Consequently, in vacuum, the ET between the host and luminescence center (Sm^{3+}) becomes more effective, leading to higher red emission intensity.

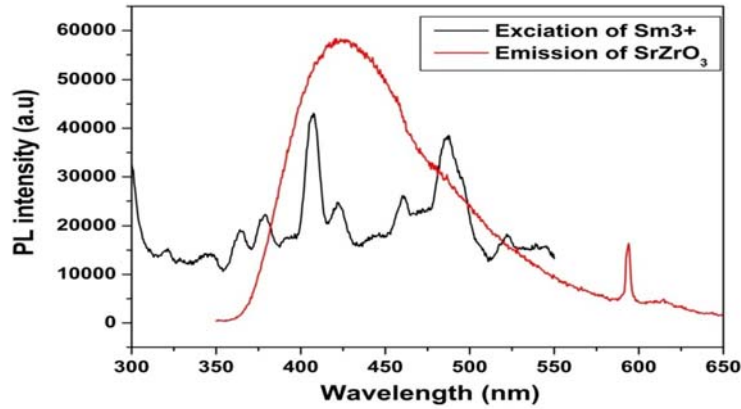


Figure 5.18: Emission spectra SrZrO_3 ($\lambda_{\text{ex}}=243$ nm) and excitation spectra of $\text{SrZrO}_3:\text{Sm}^{3+}$ ($\lambda_{\text{em}}=597$ nm)

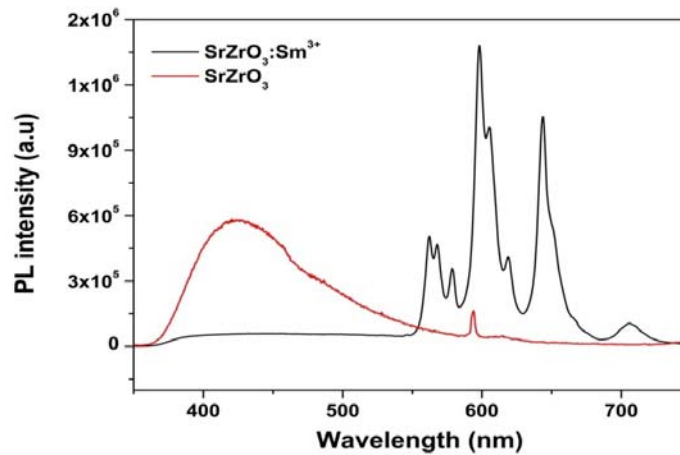


Figure 5.19 Energy transfer from host to Sm^{3+} ion (Vacuum sintered sample).

5.4.3.2. Electronic structure

To obtain a clear picture of the effect of samarium doping in ideal/ordered SZ, a $2 \times 2 \times 1$ supercell (with 80 atoms) of o-SZ was made and one Sm atom is placed in Sr position (Sr-SZ), which corresponds to doping level of 6.25 atom%. Another $2 \times 2 \times 1$ supercell with one Sm atom placed in place of Zr atom was also made (Zr-SZ). Then these two structures were optimized with respect to volume, b/a , c/a ratio and atomic positions. Our GGA-PBE optimized equilibrium volume shows a reduction of 0.827 \AA^3 and increase of 3.0 \AA^3 for the Sr-SZ and Zr-SZ compared to o-SZ unitcell,

respectively. In whichever position Sm goes, parent host structure remains orthorhombic and our XRD data for Sm doped SZ signifies this theoretical prediction.

To identify the localization of Sm ion in the distorted SZ (fm-SZ), two 2x2x1 supercell (80 atoms) of fm-SZ was made. In one case, one Sm atom was placed in position of a Sr atom (Sr-fm-SZ) and in another case one Sm atom was placed in position of a Zr atom (Zr-fm-SZ), which corresponds to 6.25 atom% doping. Total DOS calculated with these Sm doped supercells are shown in Figure 5.20 (a) and (b). In both the cases, the calculated band gaps, 2.69 eV for Sr-fm-SZ and 2.77 eV for Zr-fm-SZ (Fig. 5.20(a) and (b)), are comparable to the 2.76 eV for fm-SZ. Small change in the calculated band gap usually signifies small change in degree of order/disorder prevails in fm-SZ.

PL spectra of vacuum sintered $\text{SrZrO}_3:\text{Sm}^{3+}$ sample (Fig. 5.19) shows an energy transfer from host to Sm^{3+} at a higher wavelength compared to undoped SrZrO_3 . In other words, Sm doping increases the disordering prevails in the host SrZrO_3 . Therefore, localization of Sm atoms solely in the Sr position or in the Zr position does not justify the increase of disorder in the host SrZrO_3 . In order to further reveal possible localization of Sm ions, a 2x2x2 supercell (160 atoms) of fm-SZ was made and two Sm atoms were placed each in the Sr position and Zr position. Total DOS calculated with this Sm doped supercell is shown in Figure 5.20 (c) and the band gap of 2.2 eV can be evaluated from the same. The reduced band gap compared to fm-SZ is manifestation of increase in disorder and it is justifying energy transfer from undoped SrZrO_3 to vacuum sintered $\text{SrZrO}_3:\text{Sm}^{3+}$ sample at higher wavelength. Thus, localization of Sm ions is most probable in both Sr as well as Zr positions. These theoretical results are in complete agreement with our luminescence lifetime measurements described in section 3.5. Further the lifetime studies have shown the presence of Sm^{3+} in SZ nanocrystal having life time value of 500 μs and 1.6 ms corresponding to Sm^{3+} at Zr and Sr sites respectively.

The information about bonding mechanism could be provided by the partial DOS. Fig. 5.20 (c) shows partial DOS of Sm^{3+} doped both in Sr and Zr position of fm-SZ. Overall DOS for CB and VB of Sm^{3+} doped fm-SZ is similar to that of fm-SZ (as described in Fig. 5.9 (d)). But the presence of some additional states in the band gap of Sm doped fm-SZ makes it different in the band gap region. The additional states in the upper part of VB (in the energy range -0.3 to 0 eV, scaled by Fermi energy (E_F)) are mainly contributed by the 4f-nonbonding states of Sm^{3+} placed in the

position of Zr atoms of fm-SZ. Moreover, the additional states in the lower part of CB (in the energy range 2 to 2.25 eV, scaled by E_F) arise mainly from 4f-nondonding states of Sm^{3+} localized in the Sr position of fm-SZ. So the reduction in band gap of Sm^{3+} doped fm-SZ can be manifested from the presence of 4f-impurity states of Sm^{3+} in the band gap. Apart from the impurity states, the 4f-states of Sm^{3+} (localized at Zr position) are hybridized with O 2p-states in the energy range -4.2 eV to -0.25 eV. Importantly, the 4f-states of Sm^{3+} are concentrated in the energy range of -4.2 to -0.25 eV and 2.5 to 5 eV (scaled by E_F) and these energy ranges are also the lower VB portion and upper CB portion of the fm-SZ, respectively. Therefore, distribution of 4f-states of dopant Sm^{3+} are matching well with the Zr(d)-O(p) bonding states, Zr non-bonding d-states as well as defect states of host fm-SZ. Thus, the overlap of electronic DOS between host fm-SZ and Sm^{3+} doped fm-SZ makes the energy transfer process from host fm-SZ to Sm^{3+} doped fm-SZ feasible.

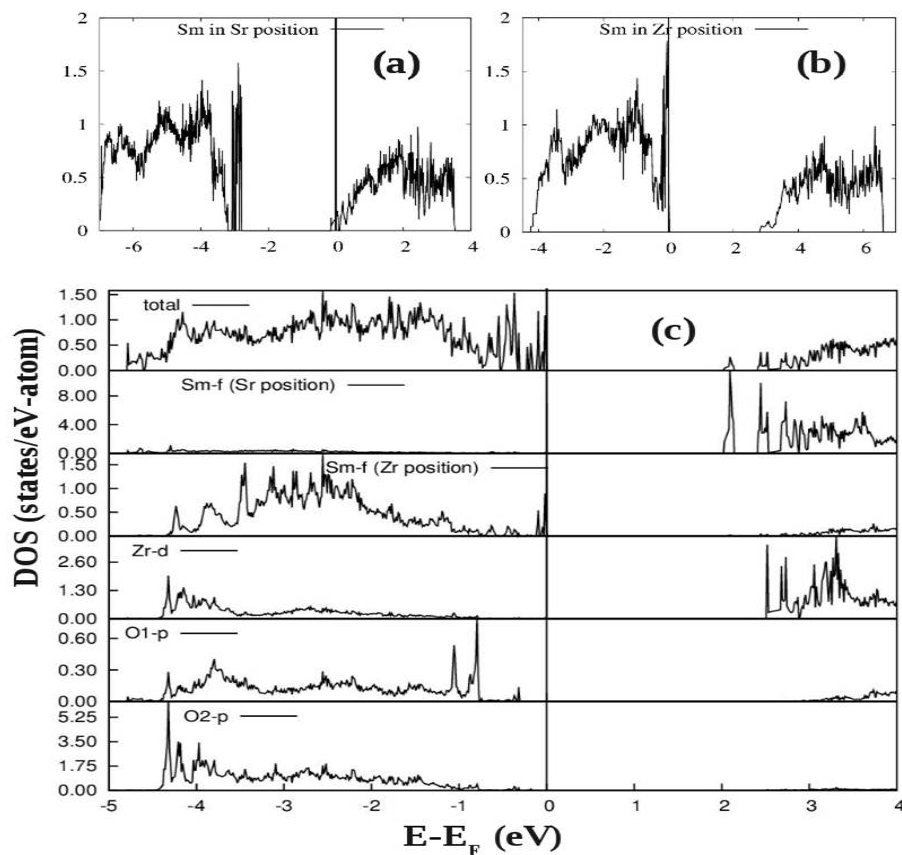


Figure 5.20: Total DOS for Sm doped fm-SZ in (a) Sr position and (b) Zr position. Total and partial DOS of Sm doped fm-SZ in both Sr and Zr position (c). The vertical lines represent Fermi level (E_F).

5.4.4. Photoluminescence mechanism in Sm^{3+} doped SZ

A combination of experimental study and theoretical calculations enable us to derive further insight into the energy transfer and transition mechanism (shown in Figure 5.21). In Sm^{3+} doped fm-SZ, the absorption band is associated with excitation of oxygen-vacancy-trapped electrons from shallow and/or deep defect states (present in the top of the VB) to defect states present in the lower part of the CB. Subsequently, the photo excited electrons in the defect states of CB may migrate to the Sm^{3+} related multiple excited states through the process of energy transfer, due to the energy match between the electronic states of fm-SZ and the energy states of Sm^{3+} (as shown in Figure 5.20 (c)). Finally, the excited photo-electrons at the excited f-states of Sm^{3+} could transfer to the long lived $^4\text{G}_{5/2}$ of Sm^{3+} via non-radiative relaxation, and then produce strong orange-red emission (combined by the emission of 565, 579, 643 and 703 nm) via radiative relaxation.

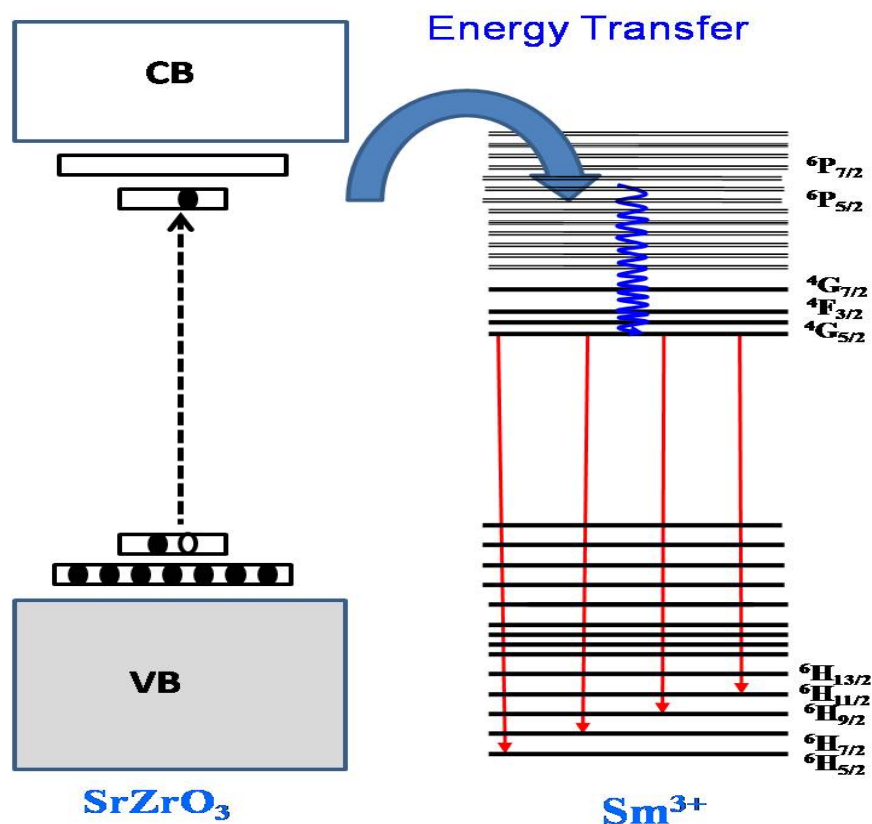


Figure 5.21: Schematic of energy transfer mechanism from SrZrO₃ host to Sm³⁺ ions.

5.4.5. Materials Performance: Color coordinates

To evaluate the material performance on color luminescent emission, CIE chromaticity coordinates were evaluated for undoped and 1.0 mol% doped sample adopting standard procedures. The values of x and y coordinates of the system were calculated to be 0.202 and 0.166 respectively. This is represented as the point ‘*’ in the CIE diagram shown in Figure 5.22 (a). It is clear from the values that, strontium zirconate, give a ‘violet-blue’ emission. The color can be tuned to orangish-red emission ($x = 0.550$ and $y = 0.375$) on doping 1.0 mol% Sm^{3+} as shown in Fig. 5.22 (b).

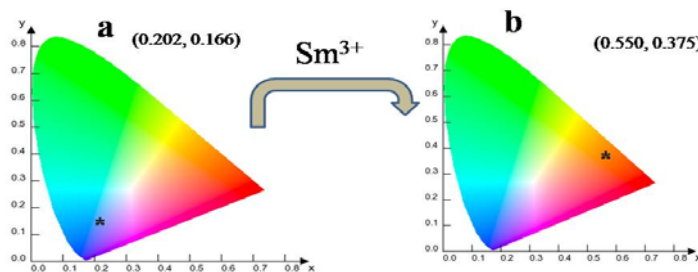


Figure 5.22: (a) CIE index diagram of (a) SrZrO_3 and (b) $\text{SrZrO}_3:\text{Sm}^{3+}$ system showing violet blue white and red emission (point *) respectively.

5.4.6 Radiative and non-radiative transition in $\text{SrZrO}_3:\text{Sm}^{3+}$ compared to pure Sm_2O_3 powder- Photoacoustic spectroscopy

When a periodically chopped light falls on a sample enclosed in an air tight enclosure, called PA cell the molecules of the sample become excited from the ground state to the higher energy state after the absorption of radiation. These excited molecules may relax to the ground state either through emission of photon, called radiative transition or by energy transfer through non-radiative process. As a result of this non-radiative de-excitation process a small amount of heat is generated within the sample. The heat, thus generated within the sample diffuses across the sample boundary, gives rise to temperature variation in the coupling gas (air) adjacent to the sample, which result in the periodic pressure fluctuations and is finally detected in the form of the acoustic signal by a sensitive microphone. The technique is especially sensitive whenever non-radiative relaxation pathways are more predominant compared to radiative transition. It is known that a compound in the excited state will relax by two processes: radiative and non-radiative processes. PA spectrum only responds to the non-radiative relaxation process, whereas the PA signal of

fluorescence energy levels, which relax by radiative process, will be very weak or vanished. The PA spectra of pure Sm_2O_3 and Sm^{3+} doped SrZrO_3 are shown in Fig.5.23. As compared to pure powder the PA spectra of $\text{SrZrO}_3:\text{Sm}^{3+}$ is very weak and broad and moreover most of the transitions are not well resolved. Pure samarium oxide shows very sharp PA spectra with lot of features. The PA spectra of Sm_2O_3 samples can reveal the absorption and relaxation processes of Sm^{3+} . The PA intensity spectrum of Sm_2O_3 at room temperature is shown in Figure 5.23. It is distinguished by sharply defined and almost line like absorption band. Compared with the absorption spectra in solution, the PA spectrum is more complex and more intense.

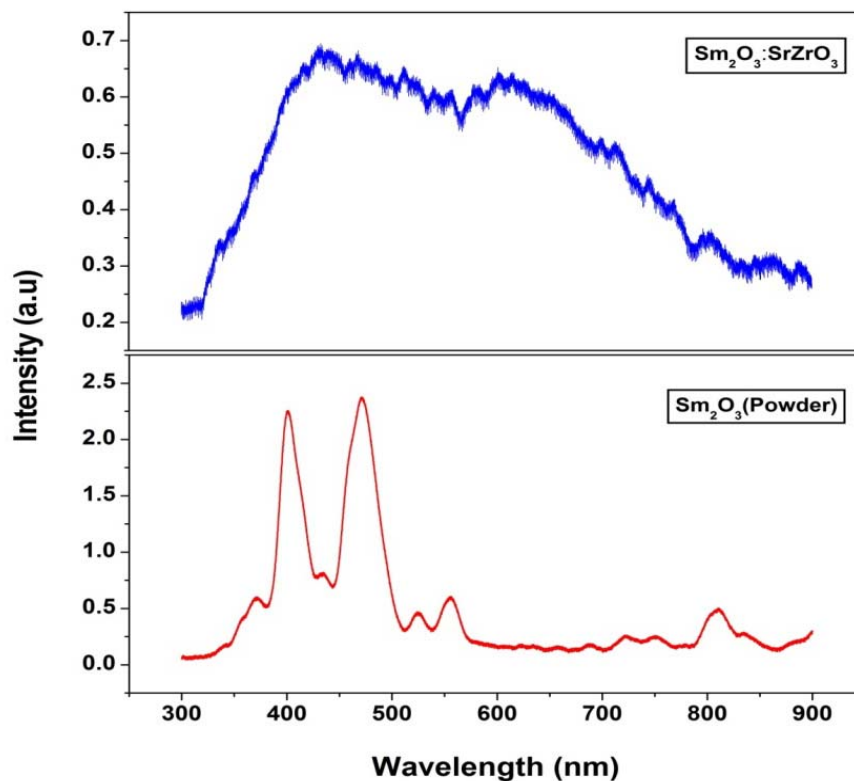


Fig.5.23. PA spectra of $\text{SrZrO}_3:\text{Sm}^{3+}$

In Fig. 5.23, the strongest PA band appears in the region of 400 and 471 nm which is attributed to the transition from the ground state to excited state $^4\text{P}_{3/2}$ and $^4\text{I}_{3/2}$ [257, 258]. This indicates that the superior relaxation process of $^4\text{P}_{3/2}$ and $^4\text{I}_{3/2}$ is non-radiative relaxation. The weaker PA bands in the region of 556 and 525 nm are attributed to the transitions from ground state to the excited state $^4\text{G}_{5/2}$ and $^4\text{F}_{3/2}$ respectively. The $^4\text{G}_{5/2}$ level is the first excited state of Sm^{3+} , which means the radiative relaxation of $^4\text{G}_{5/2}$ is its prominent process. Since the $^4\text{F}_{3/2}$ level have many

similarities with the $^4G_{5/2}$ level, the energy transferred to this level is easy to be transferred to the $^4G_{5/2}$ level. So $^4G_{5/2}$ and $^4F_{3/2}$ are two radiative levels of Sm^{3+} . As indicated in Fig. 5.23, the PA intensity corresponding to these two levels is fairly weak. Among the energy levels of Sm^{3+} , the longest-lived energy level is $^4G_{5/2}$ (about 6.26 ms) and it is also a strong fluorescence energy level [259]. The electron in the excited level $^4G_{5/2}$ has a high probability to take a radiative relaxation process. When the electrons are excited to higher energy levels such as $^4G_{7/2}$, $^4F_{3/2}$, usually they will relax to $^4G_{5/2}$ by a non-radiative process, and then relax by radiative process (fluorescence), which can be interpreted according to the model discussed by Yang et.al. [260]. In Fig. 5.23, PA signals of the energy levels $^4G_{7/2}$, $^4F_{3/2}$, $^4G_{5/2}$ are so weak that we could just detect them, whereas excitation spectra shows all such transitions. In doped sample, PA intensity is very weak compared to pure powder. This study confirms that non-radiative component is negligible small in $SrZrO_3:Sm^{3+}$ and this might be a good candidate for near ultraviolet (~ 400 nm) light emitting diodes.

5.5. Luminescence properties of $SrZrO_3:Eu^{3+}$

5.5.1. Effect of annealing temperature on PL properties:

To investigate the effect of annealing temperature on the PL properties of the 0.5 mol% Eu doped zirconate phosphors, the as-formed sample (finally heated at $600^{\circ}C$) was further annealed at 700, 800 and $900^{\circ}C$ and the changes in PL intensity and decay profile ($\lambda_{ex}=229$ nm and $\lambda_{em}=594$ nm) were measured. Decay curves obtained for samples annealed at different temperatures could be fitted as a bi-exponential decay indicating that Eu^{3+} ions in two different environments are present in the host. Two life-times obtained by bi-exponential fitting showed similar variation due to annealing sample at different temperatures. The PL emission and decay time obtained for long-lived species are presented in Figure 5.24. It was observed that, the PL intensity and decay time increased with increase in temperature up to $800^{\circ}C$ while above $800^{\circ}C$, a decrease in intensity and nearly constant decay time were observed. Initial increase in decay time and finally attaining saturation can be attributed to reduction in non-radiative transitions as a result of reducing surface defects with increasing annealing temperature up to $800^{\circ}C$ and beyond this there is no change in number of surface defects. This also resulted in increase in the intensity with increasing annealing temperature up to $800^{\circ}C$, however, on annealing the sample at $900^{\circ}C$ though decay time remained constant (suggesting no change in surface defects)

the sample intensity decreased. The decrease in intensity therefore cannot be attributed to non-radiative decay resulting from surface defects. SEM studies have shown that the 900 °C annealed samples is highly agglomerated and can lead to reduced intensity because of scattering effects on incident and emitted light.

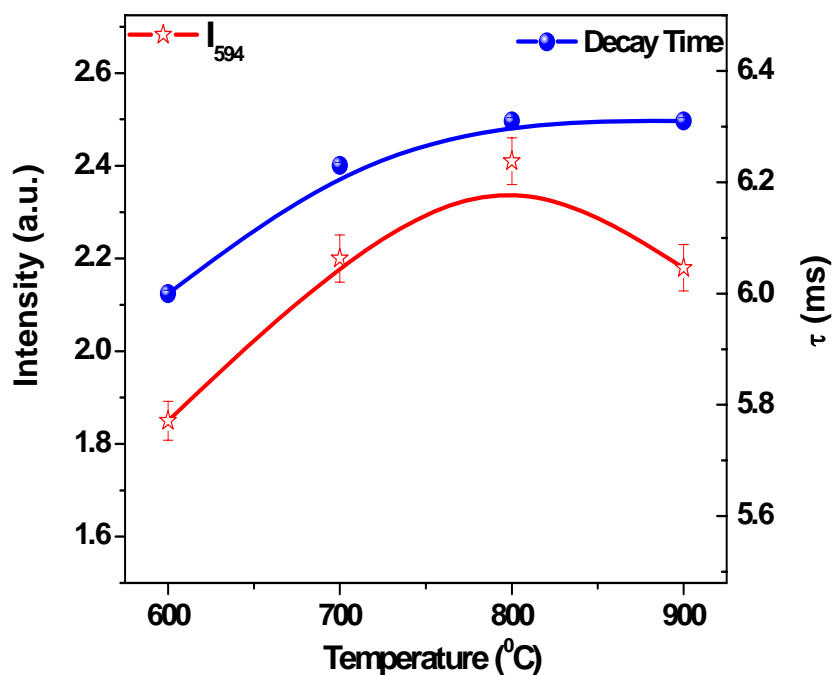


Figure 5.24: Variations in PL emission and decay time with annealing temperature.

Based on these observations, further investigations on the system were carried out on the sample which was giving the best emission output (0.5 mol% sample annealed at 800°C).

5.5.2. Excitation and Emission characteristics:

Figure 5.25 shows the excitation spectra ($\lambda_{em} = 594$ nm) of the 0.5 mol% Eu doped strontium zirconate sample annealed at 800°C. The sharp peak at 229 nm belonged to host absorption band (HAB) and is ascribed to charge transfer from the oxygen to central Zr atom of ZrO_3^{2-} [261]. A broadband in the region of 240–300 nm has been attributed to the $O^{2-} \rightarrow Eu^{3+}$ charge transfer band (CTB), which is caused by the electron transfer from 2p orbits of O^{2-} ions to 4f shells of Eu^{3+} ions. The sharp lines in 300–500 nm are attributed to intra-configurational 4f–4f transition of Eu^{3+} in host lattice. The peaks seen at 320, 360, 380, 393, 420, 460 and 480 nm were assigned to electronic transitions of ${}^7F_0 \rightarrow {}^5H_3$, 5L_9 , 5L_7 , 5L_6 , 5D_4 , 5D_3 and 5D_2 respectively. 430–

500 nm region excitation spectra were recorded by keeping yellow filter on excitation side.

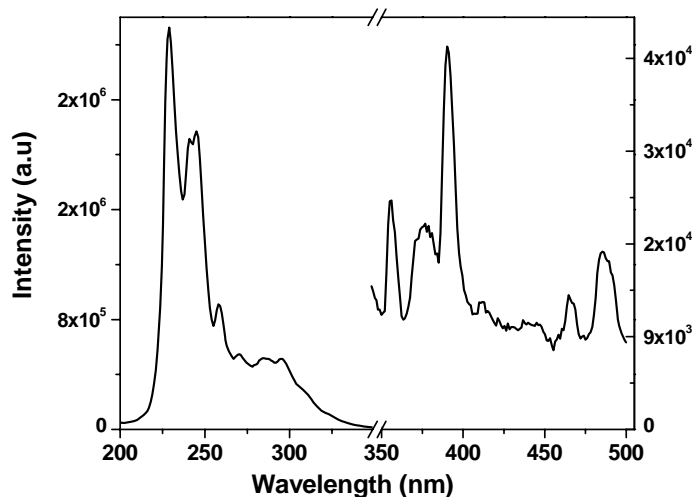


Figure 5.25: Excitation spectra of the powder sample of SrZrO₃:Eu³⁺ 0.5 mol% annealed at 800°C.

Figures 5.26 (a) (b) and (c) show the emission spectra for SrZrO₃:Eu³⁺ annealed at 800°C at $\lambda_{\text{ex}} = 229$ nm (Host absorption band), 296 nm (Charge transfer band) and 393 nm (f-f band) respectively. The spectra consists of series of peaks in the range of 560-730 nm corresponding to the characteristic transition of Eu³⁺, from the excited ⁵D₀ state to ⁷F_J (J= 1-4) levels. However emission characteristics were observed to be different in relative intensities with the different excitations. This also confirmed the presence of Eu³⁺ ions at more than one site having different environments. The orange emission (590–600 nm) of Eu³⁺ due to the magnetic dipole transition (MDT) ⁵D₀→⁷F₁ is not affected much by the site symmetry because they are parity-allowed; while the red emission (~610–630 nm) due to the electric dipole transition (EDT) of ⁵D₀→⁷F₂ being hypersensitive is affected by the site symmetry of Eu³⁺ ion.

Upon excitation at 229 nm (Host absorption band), the emission spectrum exclusively contains the strong bands of ⁵D₀→⁷F₁ (594 nm), ⁵D₀→⁷F₂ (614) and the very weak lines of ⁵D₀→⁷F₃ (653 nm) and ⁵D₀→⁷F₄ (704 nm). Moreover ⁵D₀→⁷F₁ line at 594 nm (MD) is very strong in comparison to ⁵D₀→⁷F₂ line at 614 nm (ED). Very weak emission from the ZrO₃²⁻ group is observed indicating efficient energy transfer from the host to the rare earth ions. On the other hand, upon excitation by 296 nm (charge transfer band), emissions due to the rare earth and the host both could be seen in the emission spectrum. Moreover ⁵D₀→⁷F₂ line at 614 nm (ED) is very strong

in comparison to ${}^5D_0 \rightarrow {}^7F_1$ line at 594 nm (MD). Also with 296 nm excitation, the ${}^5D_0 \rightarrow {}^7F_4$ transition, which is also electronic dipole transition, is stronger, whereas it appears very weak on excitation with 229 nm excitation. Upon excitation with 393 nm, corresponding to the ${}^7F_0 \rightarrow {}^5L_6$ band, emission properties similar to that of CTB excitation were observed. The observed differences in the spectra on different excitation wavelength suggested the possibility of Eu^{3+} ions occupying minimum two types of sites in the host.

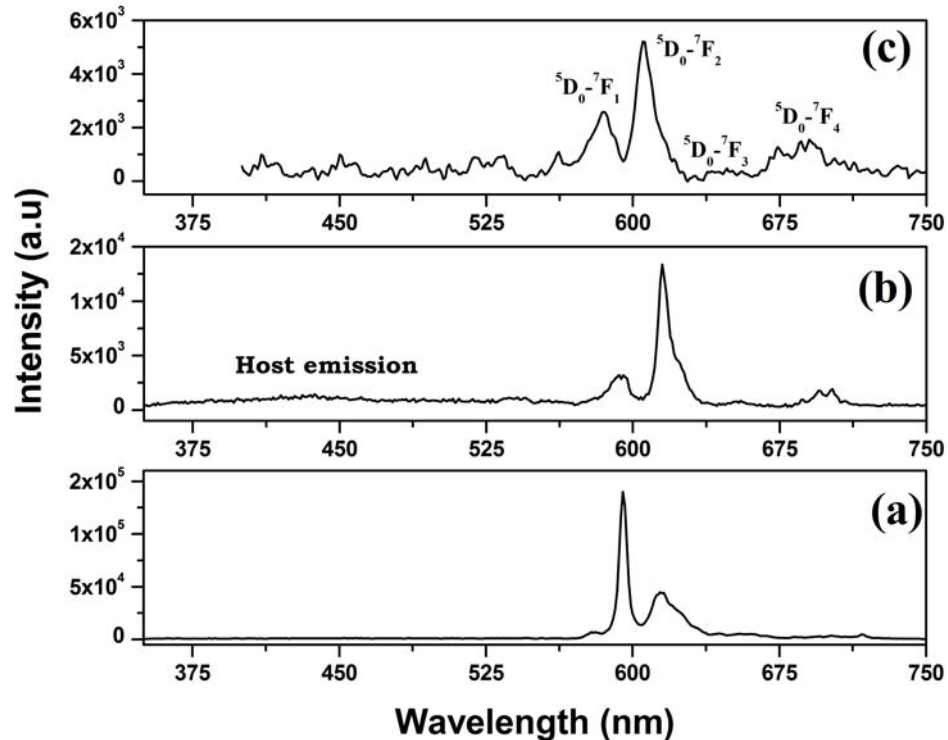


Figure 5.26 (a): Emission spectra at (a) 229 nm excitation (b) 296 nm excitation and (c) 393 nm excitation of the powder sample of $\text{SrZrO}_3:\text{Eu}^{3+}$ 0.5 mol% annealed at 800°C .

Huang et al [261] has ascribed such differences in strontium zirconate matrix to presence of europium at different sites. Since ionic size difference between 8-coordinated Sr^{2+} (126 pm) and 8-coordinated Eu^{3+} (107 pm) is less, Eu^{3+} ions occupying the Sr^{2+} sites will not lead to a large distortion in the lattice and if the associated defect due to charge difference is at a large distance, the local site symmetry will be having an inversion symmetry. On the other hand 6-coordinated Eu^{3+} with ionic size 95 pm while occupying 6-coordinated Zr^{4+} (ionic size 72 pm) has a larger size difference and can lead to distortion in the octahedra, resulting in local site without inversion symmetry. Thus different spectra observed with different

excitations can be attributed to (i) Eu^{3+} ions occupying Sr^{2+} site with inversion symmetry and (ii) Eu^{3+} ions occupying Zr^{4+} site without inversion symmetry. The charge balance after substitution of ions with differing charges can be achieved either by (i) simultaneous substitution of 2 Eu^{3+} ions one at Sr site and another at Zr^{4+} site or (ii) With adequate Sr vacancy and presence of O related defects.

5.5.3. Decay Time and TRES studies:

In order to understand the Eu^{3+} substitution at the two sites detailed investigations were carried out for the three excitations involving life-time and time resolved emission characteristics. The decay curves corresponding to the ${}^5\text{D}_0$ level of Eu^{3+} ions in 0.5 mol % europium doped SrZrO_3 annealed at 800°C are shown in Figure 5.27 at excitation wavelengths of 229, 296 and 393 nm monitoring emission at 594 nm. Decay curves could not be fitted with single exponential decay and it was observed that the curves could be fitted with as bi-exponential decay using same equation as 3.4. The life-time values and % occupancy of each species obtained under different excitations are given in Table 5.3.

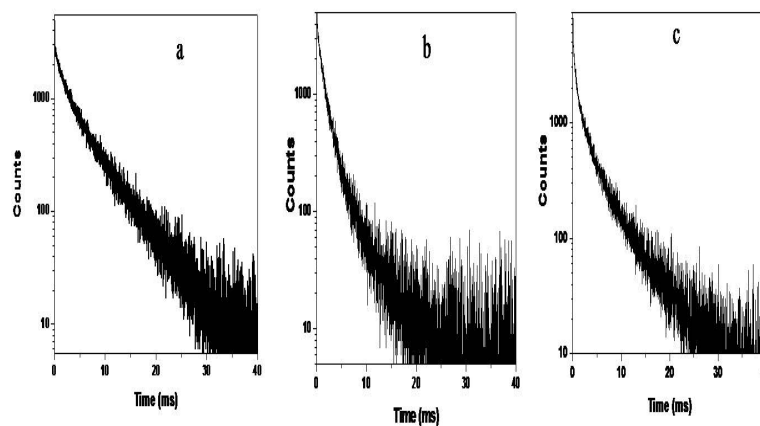


Figure 5.27: Luminescence decay time profile of the Eu doped strontium zirconate annealed at 800°C (a) λ_{ex} -229 nm (b) λ_{ex} -296 nm and (c) 393 nm under $\lambda_{\text{em}} - 594$ nm

Table 5.3: Life time and % occupancy for the Eu^{3+} species in 800°C annealed sample with different excitation wavelength

λ_{ex} (nm)	τ_1 in ms and (% occupancy for short lived species)	τ_2 in ms and (% occupancy for short lived species)
229 (HAB)	1.0 (14%)	6.0 (86%)
296 (CTB)	1.0 (65%)	4.0 (35%)

393 (f-f band)	1.0 (49%)	6.0 (51%)
----------------	-----------	-----------

As seen from Figure 5.27 and Table 5.3, for all the three excitations, decay curves displayed two major life-times indicating the presence of Eu^{3+} ions in two different environments; however the % occupancy was different with each excitation. Further, 296 nm excitation showed a presence of separate species with life-time of the order of 4 ms. In order to identify the environment associated with the species exhibiting different life-times, time resolved emission spectra were recorded for the three excitations (viz. 229, 296 and 393 nm) at different time-delays with constant integration time.

Figure 5.28(a) shows the spectra recorded with time delays of 10 μs , 1 ms and 7 ms respectively with integration time of 50 μs . As seen from Figure 5.28 (a), on excitation with host absorption band after and giving a delay time of 10 μs , ZrO_3^{2-} emission (host) in 350-550 nm region peaking around 450 nm (host emission) along with weaker europium emission from $^5\text{D}_0$ as well as from higher excited levels $^5\text{D}_1$, $^5\text{D}_2$ etc., was observed. It is interesting to note that the broad band emission due to the transition within the zirconate group appeared only at the very early time of 10 μs (Figure 5.28a). This suggested that the zirconate emission is too weak to be observed (relative to Eu^{3+} emission) in the long time resolved emission spectrum. The rapid energy transfer is responsible for the quenching of zirconate emission in Eu^{3+} -doped SrZrO_3 . The broad zirconate emission band of Eu^{3+} -doped SrZrO_3 peaked at around 440 nm and extended from 375 nm to 525 nm. In comparison with zirconate emission band observed for the non-doped SrZrO_3 crystal [262], the band is shifted about 30 nm to longer wavelengths.

Further as delay time was increased to 1 ms, broad emission from host reduced in intensity and characteristic emission predominated by Eu^{3+} ions in symmetric environment ($\text{Intensity}_{(594)} > \text{Intensity}_{(614)}$) was observed. After delay time of 7 ms, the emission characteristics were overall similar to those observed after 1 ms delay, with a small reduction in intensity ratio I_{614}/I_{594} suggesting that the two species ($\tau=1$ ms & $\tau = 6\text{ms}$) have differences in local site symmetry. The spectra observed after 7 ms delay is expected from long-lived species (6 ms) as the other species would have reduced in intensity by a factor of e^{-6} . The spectra showed stronger emission from $^5\text{D}_0 \rightarrow ^7\text{F}_1$ transition indicating that the long-lived species can be ascribed to Eu^{3+} ions

having symmetric environment with inversion symmetry. The spectra obtained after 1 ms delay time had contributions from both short-lived and long-lived species. The spectral characteristics of short lived species were obtained by subtracting the contribution of long-lived species (obtained mathematically using the spectra observed after 7 ms delay) from the observed spectra of 1 ms delay. Spectra for short lived and long lived species obtained are shown in Figure 5.28(b) below. As seen from the figure, short lived species showed stronger emission from ${}^5D_0 \rightarrow {}^7F_2$ transition indicating that the Eu^{3+} ions exhibiting short life-time are in asymmetric environment without inversion symmetry.

Similar exercise was carried out for 296 nm excitation and spectra with different delay times are shown in Figure 5.29(a) and the spectra obtained for short-lived (1 ms) and long-lived (4 ms) species by following similar approach as mentioned earlier are shown in Figure 5.29(b). As seen from Figure 5.29, on excitation with charge transfer band after delay time of 10 μs , ZrO_3^{2-} emission in 350-550 nm region peaking around 450 nm (host emission) along with weaker europium emissions from excited states 5D_0 , 5D_1 , 5D_2 etc. were observed. Further as the delay time was increased to 1 ms, broad emission from host reduced in the intensity and characteristic emission predominated by Eu^{3+} ions in asymmetric environment ($\text{Intensity}_{(614)} > \text{Intensity}_{(594)}$) was observed. After delay time of 7 ms, the emission characteristics were overall similar to those observed after 1 ms delay. This suggested the presence of Eu^{3+} ions at asymmetric environment for both the species. Spectra obtained after appropriate treatment for 1 and 4 ms life-time species confirmed the findings with marginal difference in spectra.

Since no host emission was noticed, while recording emission spectra on excitation with 393 nm, time resolved emission studies were carried out only in 550-750 nm range and displayed in Figure 5.30 for the short lived and long-lived species. As seen from the figure, emission observed for short-lived species is predominated by Eu^{3+} ions in asymmetric environment without inversion symmetry and emission spectra obtained for long-lived species corresponds to that of Eu^{3+} in symmetric environment. The spectra obtained for all excitations with short life-time (1 ms) are almost similar and can be attributed to Eu^{3+} ions in asymmetric environment without inversion symmetry. Similarly the Eu^{3+} ions exhibiting 6 ms life-time under 229 and 393 nm excitation are similar and arise due to Eu^{3+} ions having symmetric environment with

inversion symmetry. The spectra obtained on excitation with 296 nm having life-time 4 ms is due to Eu^{3+} ions in asymmetric environment; the ions in symmetric environment are not getting excited by this excitation. In general, Eu^{3+} ions are present in three different environments in the host matrix.

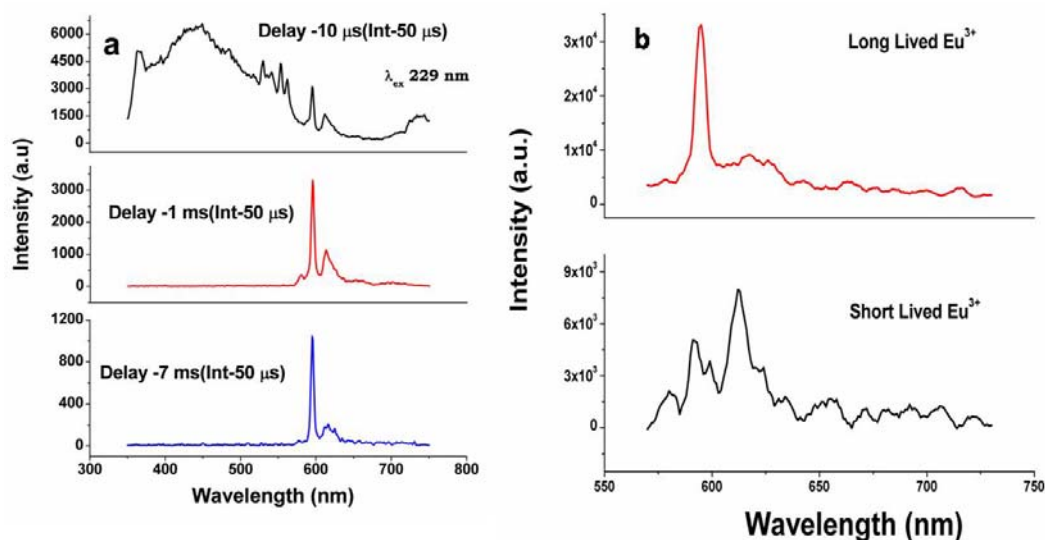


Figure 5.28: Time-resolved emission spectra of $\text{SrZrO}_3:\text{Eu}^{3+}$ nanophosphors annealed at 800°C under the excitation at 229 nm (a) after giving suitable delay time (b) for short and long lived species

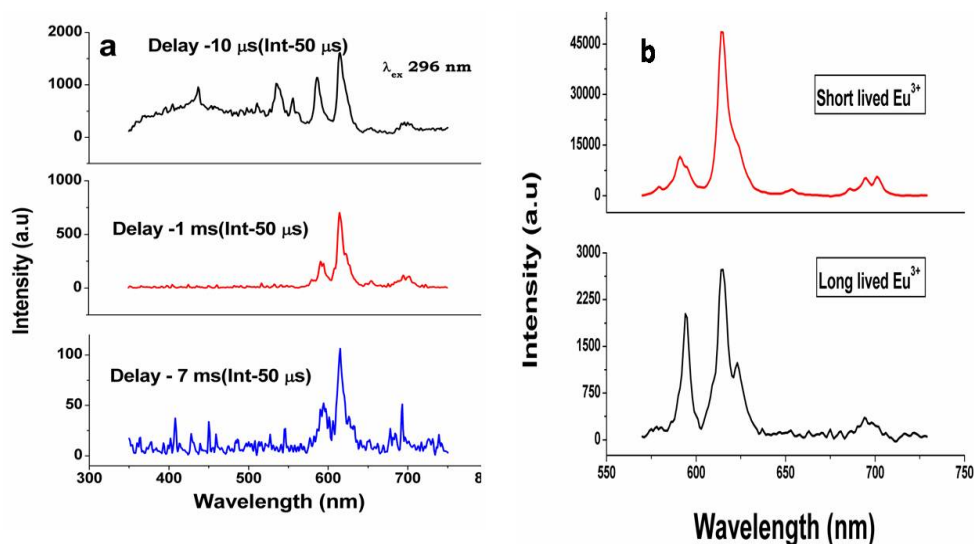


Figure 5.29: Time-resolved emission spectra of $\text{SrZrO}_3:\text{Eu}^{3+}$ nanophosphors annealed at 800°C under the excitation at 296 nm (a) after giving suitable delay time (b) for short and long lived species

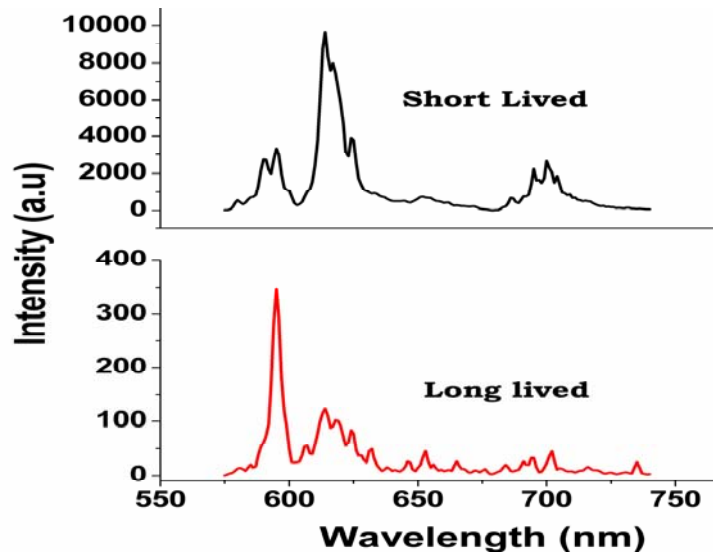


Figure 5.30: Time-resolved emission spectra of $\text{SrZrO}_3:\text{Eu}^{3+}$ nanophosphor annealed at 800°C under the excitation at 393 nm for short and long-lived species.

The symmetric environment observed for long lived species (6 ms) can be because of Eu^{3+} ions occupying Sr^{2+} site with inversion symmetry and short lived species (1 ms and 4 ms) can be ascribed to Eu^{3+} ions occupying Zr^{4+} site without inversion symmetry. The difference in life-time observed for Eu^{3+} ions at Zr^{4+} site suggests a differences in their non-radiative pathways probably due to minor difference in environment such as presence of charge compensating defect being in near vicinity or residing far off.

393 nm excitation corresponds to f-f absorption due to ${}^7\text{F}_0 \rightarrow {}^5\text{L}_6$ transition is expected to occur at nearly same position for both species of Eu^{3+} ions and % occupancy of Eu^{3+} ions is observed to be nearly same with this excitation. The deviation in % occupancy observed with host band and charge transfer band excitation can be the result of differences in energy transfer to the Eu^{3+} ions at specific sites. In particular charge transfer band selectively excite Eu^{3+} ions sitting at Zr^{4+} site and is not at all exciting the ions present in symmetric environment. Host absorption band excites both the Eu^{3+} (i) Eu_{Sr} and (ii) Eu_{Zr} ; transfers most of its energy to Eu^{3+} sitting at Sr^{2+} .

The ratio of intensity of red line (${}^5\text{D}_0 \rightarrow {}^7\text{F}_2$) to orange line (${}^5\text{D}_0 \rightarrow {}^7\text{F}_1$) in Eu^{3+} is shown to be related to degree of covalency between Eu^{3+} and O^{2-} [263]. The larger the difference in the intensities of these two lines, larger is the asymmetry and covalency effects. In case of short lived species, ${}^5\text{D}_0 \rightarrow {}^7\text{F}_2$ is markedly more intense as

compared with those of ${}^5D_0 \rightarrow {}^7F_1$ line i.e. R/O shows marked increase, so larger is the asymmetry and covalency effect around the Eu^{3+} ion site. Emission spectrum of the long lived species ($\tau \sim 6.0$ ms) shows that intensity of ${}^5D_0 \rightarrow {}^7F_1$ transition is more than that of ${}^5D_0 \rightarrow {}^7F_2$ transition. This shows R/O decreases and so are the asymmetry and covalency around Eu^{3+} ion.

5.5.4. Evaluation of J-O parameters of the Eu^{3+} sample:

The J-O analysis of the emission spectrum is a powerful tool for calculating the parity-forbidden electric-dipole radiative transition rates between the various levels of a rare earth ion such as Eu^{3+} [264, 265]. Through these analyses, the local environment around the metal ion can be interpreted. It is possible to determine the J-O intensity parameters Ω_λ (where $\lambda = 2, 4$ and 6 etc.) from the emission spectral data. For these analyses, the corrected emission spectra with respect to the source and detector response were taken into consideration. The details of these analyses of the emission spectra for calculating the J-O parameters of Eu^{3+} ion in various matrices are discussed elsewhere [266]. Since JO parameter is calculated based on the emission spectra of the Eu^{3+} ion, normal emission spectra gives J-O parameter of composite system (both long lived and short lived species), whereas the time resolved spectra gives the J-O parameters of individual species based on their different spectra. Since in this case different excitation wavelength produces different emission spectra, JO parameter in case of 229, 296 and 393 nm excitation wavelengths will be different. The J-O parameters for the two types of Eu^{3+} species (obtained from the TRES spectra after suitable delay time) for all excitation is mentioned in Table-4.4. The J-O parameter, Ω_2 exhibits dependence on the covalence between rare-earth ions and ligands and gives information about the asymmetry of the local environment of Eu^{3+} site.

Table 4.4: J-O intensity parameters of the Eu^{3+} doped SrZrO_3 annealed at 800°C

Eu^{3+} Species	<i>Long lived</i>		<i>Short lived</i>	
	$\Omega_2 (10^{-20} \text{ cm}^2)$	$\Omega_4 (10^{-20} \text{ cm}^2)$	$\Omega_2 (10^{-20} \text{ cm}^2)$	$\Omega_4 (10^{-20} \text{ cm}^2)$
$\lambda_{\text{ex}}\text{-}229 \text{ nm}$	4.93	4.04	1.11	1.37
$\lambda_{\text{ex}}\text{-}296 \text{ nm}$	1.17	1.56	1.15	1.49
$\lambda_{\text{ex}}\text{-}393 \text{ nm}$	4.89	3.94	1.19	1.56

For 229 nm and 393 nm, the trend observed in the parameters ($\Omega_2 < \Omega_4$) for short lived component proves that the particular species is present in an asymmetric environment. On the other hand, for the long-lived species the trend observed in the J-

O parameter was $\Omega_2 > \Omega_4$ which confirms our observation that long-lived species sits at more symmetric Sr site, whereas short-lived species sits at relatively less symmetric Zr sites. For 296 nm, for both species ($\Omega_2 < \Omega_4$) which ascertain their presence in asymmetric environment. This is in confirmation with our spectral findings as obtained from TRES which says on excitation with 296 nm, two types of Eu^{3+} ($\tau \sim 1\text{ms}$ and 4ms) gets excited but both are presence in asymmetric environment. The ${}^5\text{D}_0 \rightarrow {}^7\text{F}_3$ transition could not be accounted for by either the magnetic or electric dipole mechanisms. Table 5.5 shows spectral features of three types of Eu^{3+} .

Table 5.5: Spectral characteristics of three different types of Eu^{3+}

Species	Life time	Environments
Short -Lived	1.0 ms	Eu^{3+} sitting at Zr^{4+}
296 nm selectively excited short-lived species	4.0 ms	Eu^{3+} sitting at Zr^{4+} . The two Zr^{4+} sites differs in their non-radiative pathways due to presence of charge compensating defects
Long lived	6.0 ms	Eu^{3+} sitting at Sr^{2+}

5.5.5. Evaluation of colour coordinates:

To evaluate the material performance on colour luminescent emission, CIE chromaticity coordinates were evaluated adopting standard procedures. The values of x and y coordinates of the system were calculated to be 0.66 and 0.29 respectively. This is represented as the point 'x' in the CIE diagram shown in Figure 5.31. It is clear from the values that, $\text{SrZrO}_3:\text{Eu}^{3+}$ system, gives a 'Red' emission. Table 5.6 represents chromaticity coordinates for sample annealed at different temperature and at different excitation wavelength. Since 800°C annealed sample was showing the maximum emission intensity, chromaticity coordinates at 296nm and 393 nm excitation is determined for that particular sample only.

Table 5.6: Chromaticity coordinates for sample annealed at different temperature and at different excitation wavelength.

Sample annealing Temp	λ_{ex} (nm)	X coordinate of CIE	Y coordinate of CIE
800 °C (Showing maximum intensity)	229	0.632	0.366
	296	0.570	0.342
	393	0.582	0.416
600 °C	229	0.594	0.356
700 °C	229	0.605	0.327
900 °C	229	0.626	0.333

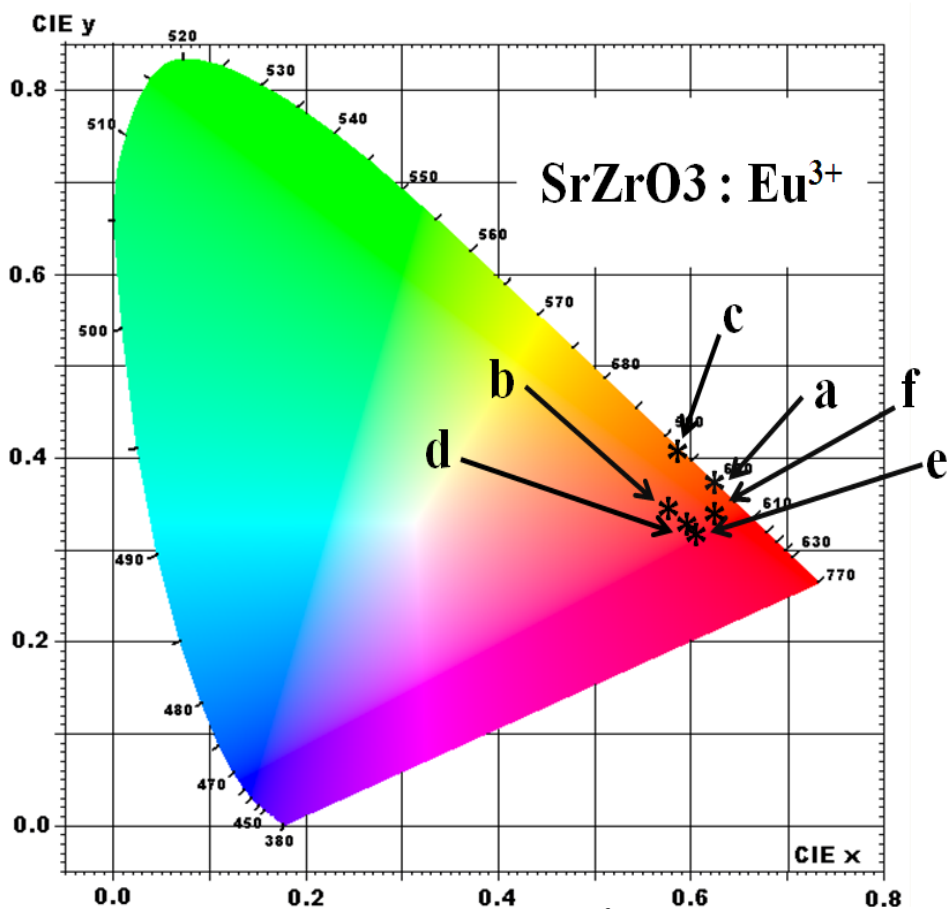


Figure 5.31: CIE index diagram of $\text{SrZrO}_3:\text{Eu}^{3+}$ system annealed at various temperatures and at different excitation wavelength.

Point a, b and c indicates CIE co-ordinates for samples annealed at 800°C at excitation wavelength of 229 nm, 296 nm and 393 nm respectively. Point d, e and f indicate CIE co-ordinates for samples annealed at 600°C, 700°C and 900°C at 229 nm excitation wavelength respectively.

5.6. Luminescence and EPR properties of $\text{SrZrO}_3:\text{Gd}^{3+}$

It is well known that phosphor materials which emit visible light are mostly formed by doping the oxide materials with rare earth ions. Thus, it is clear that the wavelength of the emitted spectrum depends on the energy states of the dopant ions. It

is also known that Gd^{3+} ion has a very wide space between energy states. Therefore, an oxide material that is doped with Gd ions would be expected to emit an ultraviolet spectrum. In this work, Gd^{3+} doped $SrZrO_3$ nanoparticles were synthesized and their luminescence properties were investigated.

Gadolinium is an excellent probe to investigate distinct varieties of environment in a particular host using EPR spectroscopy. The ground state (GS) of Gd^{3+} (4f_7 , ground state $^8S_{7/2}$) is essentially an S-state. The crystal field induced by the surrounding ligands does not split an S-state to first order. Nevertheless, although the GS is slightly admixed with higher energy states (the first excited level $^6P_{7/2}$ lies at 31000 cm^{-1} above the GS), relatively large crystal field (CF) splitting are observed. As Gd^{3+} is paramagnetic in nature, electron paramagnetic resonance (EPR) technique can be very effectively used to find out its environment. This is the first report on EPR and luminescence investigations of Gd^{3+} doped $SrZrO_3$.

5.6.1. Emission and Life time

Figure 5.32a shows the excitation spectrum of Gd^{3+} doped $SrZrO_3$ observed at room temperature. The spectrum exhibits an intense band at 274 nm and weaker bands at around 246 nm, 253 nm, and 280 nm. These bands can be ascribed to the 4f–4f intra configurational transitions of Gd^{3+} ions between 8S ground state and 6I_J and 6D_J multiplets [267]. The observed band positions and their assignments are given in Table 5.7. The observed band positions are in good agreement with the optical absorption band positions reported for Gd^{3+} ions by Binnemans et al. [268]. Figure 5.32b shows the emission spectrum observed in the ultra violet region with excitation wavelength fixed at 274 nm. The emission spectrum exhibits an intense band centered at 313 nm and two weak bands on either side of the intense band at 306 and 319 nm. Gd^{3+} is unique among triply ionized rare-earth ions having an energy difference between the $^8S_{7/2}$ ground state and the first excited state $^6P_{7/2}$ which is the largest in the series. According to the mean free-ion parameters of Gd^{3+} , the excited state is predicted to be 32,200 cm^{-1} , above the ground state [269]. The intense peak observed at 313 nm has been attributed to $^6P_{7/2} \rightarrow ^8S_{7/2}$ of Gd^{3+} ions. A weak photoluminescence band observed at 306 nm has been assigned to $^6P_{5/2} \rightarrow ^8S_{7/2}$ transition. Vetter et al. [270] and Shishonok et al. [269] observed a similar peak for Gd^{3+} ions in aluminium nitride (AlN) and boron nitride (BN), respectively.

Table 5.7: The observed band positions Gd³⁺ doped SrZrO₃ along with their assignments

Observed Band Position(nm)	Transition
246	$^8S_{7/2} \rightarrow ^6D_{7/2}$
253	$^8S_{7/2} \rightarrow ^6D_{9/2}$
272	$^8S_{7/2} \rightarrow ^6I_{13/2}$
279	$^8S_{7/2} \rightarrow ^6I_{9/2}, ^6I_{11/2}$
280	$^8S_{7/2} \rightarrow ^6I_{7/2}$

The decay curves of Gd³⁺ doped SrZrO₃ annealed at 600°C (as prepared sample) are shown in Figure 5.33 at excitation wavelengths of 274 nm monitoring emission at 313 nm on a 2 ms scale and fitted using the equation mentioned in 3.4. Inset in Figure 5.33 shows plot of residuals with life time and is indicative of closeness of fit value with real life time. This is indicated with chi-square value (2.14). Decay curves are displaying two life-times indicating the presence of Gd³⁺ ions in two different environments (56 μs and 345 μs). It is reported that in nano-sized phosphors rare earth ion exhibit two lifetimes one arising out of conventional emission and other is the lifetime of the same level of rare earth ions near and/or on the surface [271-273].

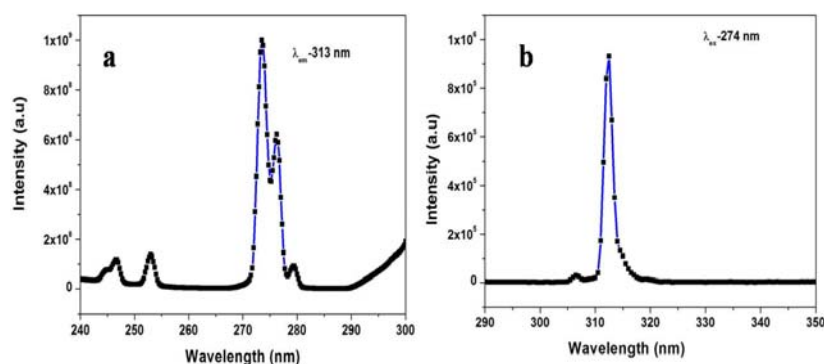


Figure 5.32: Photoluminescence spectra of the Gd³⁺ doped SrZrO₃ calcined at 600°C (a) Excitation spectrum of SrZrO₃:Gd³⁺ (λ_{em}= 313 nm) and (b) Emission spectrum of SrZrO₃:Gd³⁺ (λ_{ex}= 274 nm)

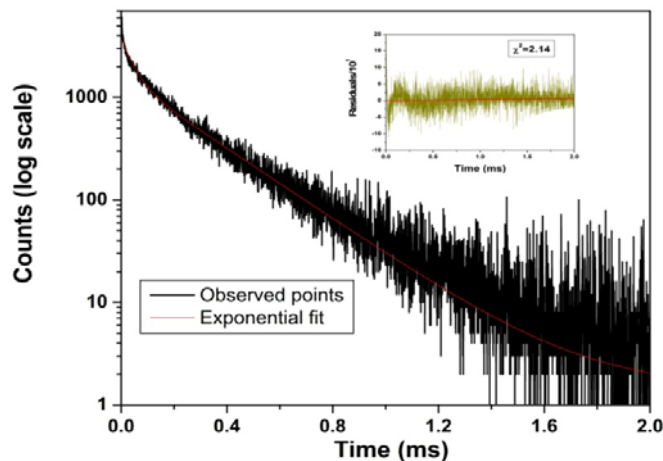


Figure 5.33: Luminescence decay time profile of the Gd^{3+} doped $SrZrO_3$ annealed at $600^\circ C$ (as prepared sample) at λ_{ex} -274 nm under λ_{em} – 313 nm

5.6.2. EPR studies

Gd^{3+} has $4f^7$ electronic configuration with a free-ion ground state of $^8S_{7/2}$. For a pure $^8S_{7/2}$ state, the only nonzero interaction in a magnetic resonance experiment is the Zeeman splitting. S-state ions are much less sensitive to the crystal field than other ions, being only affected by second-order interactions [274]. Unlike the other Kramers (i.e., odd number of electrons) rare-earth ions, Gd^{3+} has a relatively long relaxation time, making it observable at higher temperatures, including room temperature. It was reported that the EPR signal of Gd^{3+} in disordered hosts (when present at concentration less than 2 mol %) exhibits a broad complex structure at g ca 6.0, 2.8 and 2.0 referred in text as the “Ubiquitous” spectrum or U-spectrum [275–277]. Figure 5.34 shows the representative X-band EPR spectrum of Gd^{3+} doped $SrZrO_3$ measured at room temperature. EPR spectrum recorded at room temperature (RT) consisted of broad U - type spectrum having at g ca 6.0, 2.8, and 2.0. Apart from this, a weak shoulder at g ca 4.8 was also observed. There is lot of controversy on the origin of these signals in Gd doped glasses or in disordered systems [278]. The g signals observed at 6.0 and 2.8 are attributed to tetrahedral, octahedral or cubic sites of weak crystal field [279]. In these cases, Gd ions situated in an environment having coordination number greater than six were responsible for this signal, whereas the weak shoulder at 4.8 was attributed to Gd ions situated at sites of strong crystal field having low coordination number. Brodbeck and Iton [280] have offered more meaningful explanation for occurrence of U-type spectrum. They have shown that the observed U-spectrum could be deconvoluted into two contributions (a) a broad

distribution of crystal field parameter b^0 for Gd^{3+} ions with a maxima in the range $0.051 < b^0 < 0.056 \text{ cm}^{-1}$ and (b) a broad distribution of asymmetry parameter $\lambda = b^2/b^0$ in the range $0.0 < \lambda < 1.0$. They have offered an explanation that U-spectrum will be observed in case of S-state ion like Gd^{3+} ion, when they are situated in environment having high coordination number within the lattice due to irregular occupancy of sites by chemically inequivalent ion. In the present investigation, the U-type spectrum may be arising due to the presence of Gd^{3+} ion at Sr^{2+} site having high coordination number (C.N=8) or it might be associated with presence of Gd^{3+} ions on surface of the nanocrystalline region leading to the asymmetry in the coordination sphere (due to incomplete coordination sphere of Gd^{3+} situated on the surface of nanocrystals), whereas the relatively sharp signal at $g = 2.0$ is associated with isolated Gd^{3+} ion in polycrystalline region. The Gd^{3+} present on the surface of nanocrystals can be treated as those ions which are not going to lattice site.

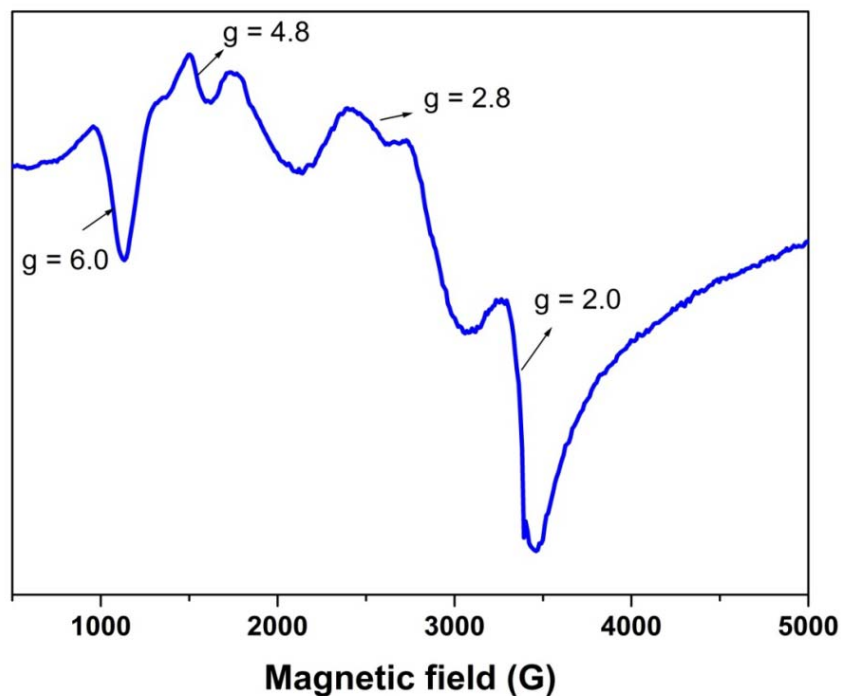


Figure 5.34: X-band EPR spectra of Gd^{3+} doped $SrZrO_3$ at room temperature

5.7. Luminescence properties of $SrZrO_3:Dy^{3+}$

Figure 5.35 shows excitation spectra ($\lambda_{em} = 576 \text{ nm}$) of the 0.5 mol% Dy doped strontium zirconate (as prepared sample) respectively. In the excitation spectrum, the

sharp peak observed at 229 nm was assigned as the host absorption band (HAB) occurring due to the charge transfer from the oxygen ion to the central Zr atom of ZrO_3^{2-} [261]. A broad hump observed in the region of 240–255 nm has been attributed to the $\text{O}^{2-} \rightarrow \text{Dy}^{3+}$ charge transfer band (CTB), which is caused by the electron transfer from 2p orbits of O^{2-} ions to 4f shells of Dy^{3+} ions [281]. The excitation lines of Dy^{3+} ion can hardly be detected, because the absorption intensity of the f–f transitions of the Dy^{3+} ions in the longer wavelength region is very weak with respect to that of the ZrO_3^{2-} groups, suggesting that the excitation of the Dy^{3+} ions is mainly through the energy transfer from the ZrO_3^{2-} groups to Dy^{3+} ions. The sharp lines observed in the wavelength range 300–450 nm, are attributed to the 4f–4f transition of Dy^{3+} . The peaks seen at 326, 351, 366, 387, 427 and 450 nm were assigned to electronic transitions of ${}^6\text{H}_{15/2} \rightarrow {}^6\text{P}_{3/2}$, ${}^6\text{P}_{7/2}$, ${}^6\text{P}_{5/2}$, ${}^4\text{I}_{13/2}$, ${}^4\text{G}_{11/2}$ and ${}^4\text{I}_{15/2}$ respectively. Figures 5.36 (a) (b) and (c) show the emission spectra for $\text{SrZrO}_3:\text{Dy}^{3+}$ annealed at 600°C at $\lambda_{\text{ex}} = 229$ nm (Host absorption band), 243 nm (Charge transfer band) and 351 nm (f–f band) respectively.

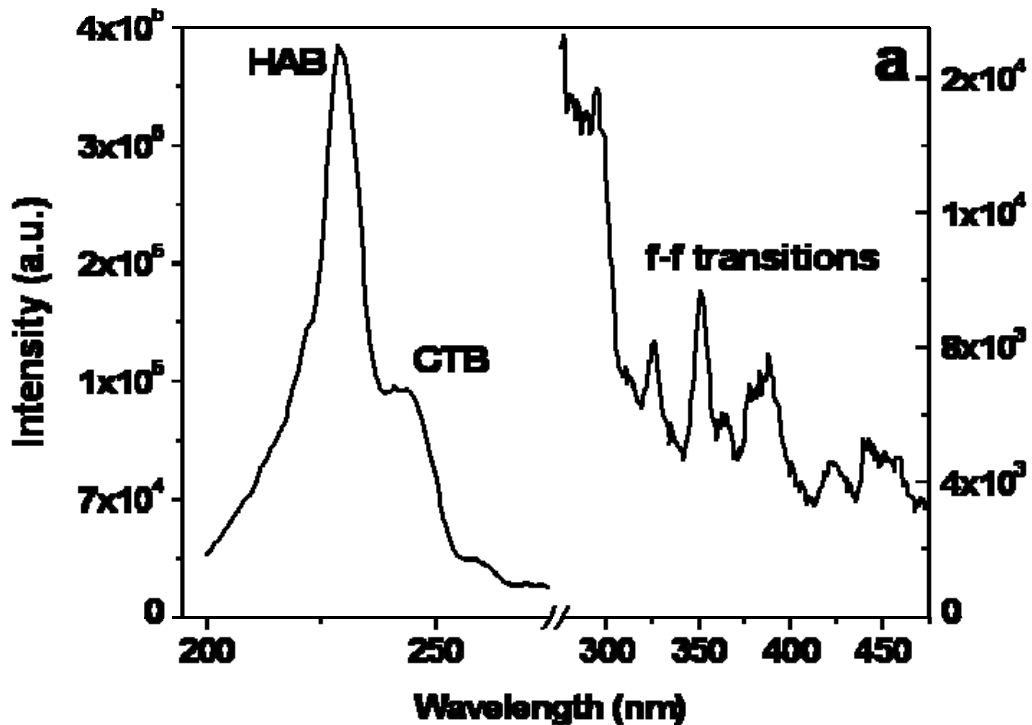


Figure 5.35: Excitation spectra of the powder sample of $\text{SrZrO}_3:\text{Dy}^{3+}$ annealed at 600°C (as prepared sample).

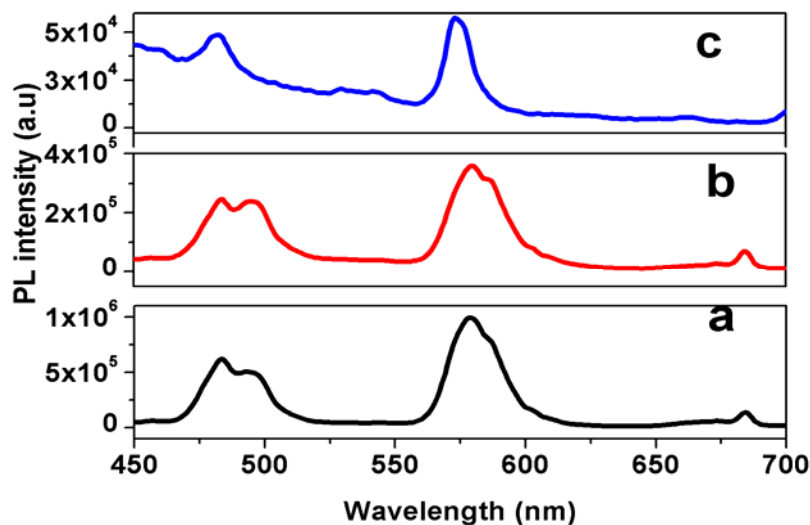


Figure 5.36: Emission spectra of the powder sample of $\text{SrZrO}_3:\text{Dy}^{3+}$ (as prepared sample) on excitation with (a) 229 nm (host absorption band) b) 243 nm (charge transfer band) and (c) 351 nm (f-f band)

Upon excitation into the zirconate group at 229 nm, the emission spectrum is characterized by three bands located at 482, 577 and 677 nm corresponding to the transitions ${}^4\text{F}_{9/2} \rightarrow {}^6\text{H}_{15/2}$ (blue), ${}^4\text{F}_{9/2} \rightarrow {}^6\text{H}_{13/2}$ (yellow) and ${}^4\text{F}_{9/2} \rightarrow {}^6\text{H}_{9/2}$ (red) respectively. Spectral features remain same on excitation with 243 nm (charge transfer) and (f-f band). No emission from the ZrO_3^{2-} group is observed, indicating the efficient energy transfer from the ZrO_3^{2-} group to Dy^{3+} ions. However emission characteristics were observed to be different in relative intensities with the different excitations as shown in Figure 5.37.

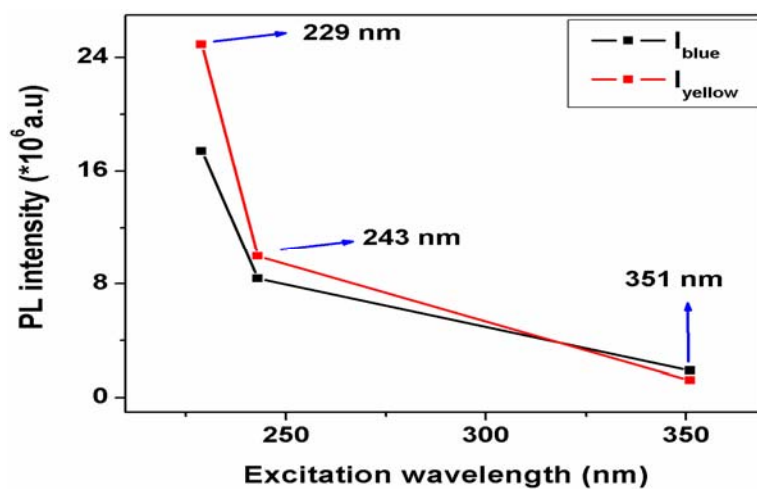


Figure 5.37: Effect of excitation wavelength on emission intensity of blue and yellow line

Emission intensity of both blue and yellow lines is found to be highest on excitation with 229 nm (Host absorption band), decreases with 243 nm (Charge transfer band) and least for 351 nm (f-f band). PL intensity is found to be least with f-f band because f-f transitions are La-Porte forbidden transition and energy transfer by f-f band to Dy^{3+} will be less as compared to CTB and HAB, which are allowed transitions. The energy pumped to dysprosium ion by HAB, which is due charge transfer from the oxygen ion to the central Zr atom of ZrO_3^{2-} ($\text{O}^{2-} \rightarrow \text{Zr}^{4+}$) is more than that by charge transfer band, which is due charge transfer from filled 2p orbital of oxygen to vacant f-orbital of Dy^{3+} ($\text{O}^{2-} \rightarrow \text{Dy}^{3+}$). It is also known that the Dy^{3+} emission around 482 nm is of magnetic dipole and 577 nm is of electric dipole (ED) origin. Generally, when Dy^{3+} is located at a low symmetry (without an inversion center), the yellow emission is dominant, whereas the blue emission is stronger, when Dy^{3+} is located at a high symmetry (with an inversion center). However yellow emission at 577 nm (${}^4\text{F}_{9/2} \rightarrow {}^6\text{H}_{13/2}$) is predominant in Dy^{3+} ion-doped SrZrO_3 suggesting that the ligand field deviates from inversion symmetry. This indicates that the luminescence centers Dy^{3+} are situated at low-symmetry local sites with no inversion centre. In perovskite structure, strontium is 8-coordinated and its ionic radii is 126 pm, whereas zirconium is 6-coordinated, whose ionic radii is 72pm. Since the radius difference between 8-coordinated Sr^{2+} (126 pm) and 8-coordinated Dy^{3+} (103 pm) is larger than that between 6-coordinated Dy^{3+} (91 pm) and 6-coordinated Zr^{4+} (72 pm), most of the Dy^{3+} ions may occupy the Zr^{4+} sites and partly occupy the Sr^{2+} sites in SrZrO_3 lattice. Ions size and charge differences between Dy^{3+} and Zr^{4+} sites disturb the local field, where such disturbance is evidenced by the more intense emission of ${}^4\text{F}_{9/2} \rightarrow {}^6\text{H}_{13/2}$. It can be concluded that the DyO_6 octahedra in the $\text{SrZr}_{1-x}\text{Dy}_x\text{O}_3$ host lattice are distorted and there is lack of inversion symmetry at Dy^{3+} site. As evidence, the particular charge transfer band structure (shown in Fig. 5.35) consisting of peaks at 239 nm and low shoulders at around 255 nm, is presumably associated with two kinds of Dy–O bonds, with different bond lengths in the slightly distorted DyO_6 octahedra. In the case of $\text{SrZr}_{1-x}\text{Dy}_x\text{O}_3$, the incorporation of Dy^{3+} on an octahedral Zr^{4+} site will inevitably result in distortion of the ZrO_6 octahedra. The distortion is due to the radius difference between Dy^{3+} and Zr^{4+} ions as well as the generation of defects and oxygen vacancies. It is well known that positive ion is coordinated with more negative ions as possible, when they contact each other. The polyhedron form of the structure would

be determined by radius ratio of positive ion to negative ion. When the value of r^+/r^- (radius_{cation}/radius_{anion}) is more than 0.414, but less than 0.732, the selected coordination number of the positive ion is 6 and the octahedron structure come into play. However, when the value of r^+/r^- is beyond 0.732, the selected coordination number is 8. In strontium zirconate perovskite crystal lattice, the ion radii of O^{2-} are 0.1365 and 0.1535 nm corresponding to six-coordinate and eight-coordinate and the value of $r_{Dy^{3+}}/r_{O^{2-}}$ are 0.668 and 0.669, respectively. Since the value of $r_{Dy^{3+}}/r_{O^{2-}}$ is less than 0.732; Dy^{3+} prefers to be six coordinated. Furthermore, the ions radii of six-coordinated Dy^{3+} (91 pm) is much closer to that of 6-coordinated Zr^{4+} (72 pm). Therefore, it is Zr^{4+} site that is the preferentially occupied site.

The decay curves corresponding to the ${}^6H_{15/2}$ level of Dy^{3+} ions in 0.5 mol % dysprosium doped $SrZrO_3$ annealed at $600^\circ C$ (as prepared sample) are shown in Figure 5.38 at excitation wavelengths of 229, 243 and 351 nm monitoring emission at 576 nm. The life-time values and % occupancy of each species obtained under different excitations are given in Table 5.8. As seen from Figure 5.38 and Table 5.8, for all the three excitations, decay curves display two life-times indicating the presence of Dy^{3+} ions in two different environments.

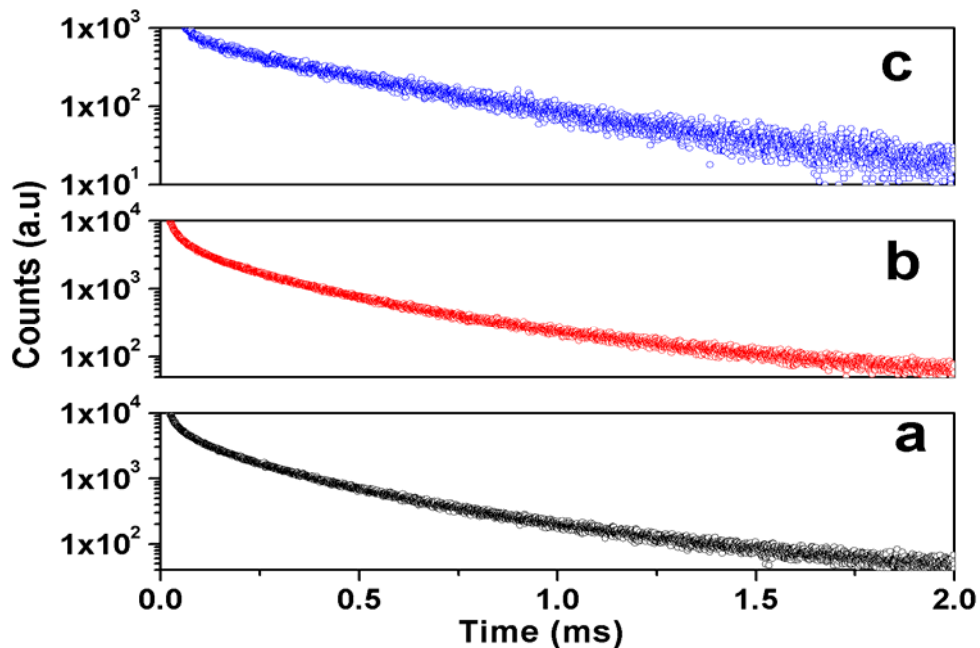


Figure 5.38: Luminescence decay time profile of the Dy doped strontium zirconate annealed at $600^\circ C$ (as prepared sample) (a) λ_{ex} -229 nm (host absorption band) (b) λ_{ex} -243 nm (charge transfer band) and (c) 351 nm (f-f band) under λ_{em} – 576 nm

Table-5.8: Life time and % occupancy for the Dy³⁺ species in as-prepared sample with different excitation wavelength

λ_{ex} (nm)	τ_1 in μs and (% occupancy for short lived species)	τ_2 in μs and (% occupancy for short lived species)
229 (HAB)	40 (18%)	320 (82%)
243 (CTB)	70 (20%)	338 (80%)
351 (f-f band)	23 (20%)	408 (80%)

In order to evaluate the colorimetric performance of the phosphor, the color coordinates for the sample SrZrO₃:Dy³⁺ (0.5mol %) annealed at different temperature were calculated using the intensity-corrected emission spectra excited by 229 nm. The calculated CIE coordinates for SrZrO₃:Dy³⁺ (0.5mol %) nanophosphors are found to be 0.38 and 0.41, which are indicated in the CIE chromaticity coordinate diagram and confirm the yellowish white color (on the boundary line of CIE white domain), as shown in Fig. 5.41. The brightness of the phosphor increases with temperature due to pure phase, high crystallinity, and good dispersion of doping components inside the host material, which are easily obtained in the solution combustion method. Moreover, Yellow-to-blue (Y/B) intensity ratio (I_{577}/I_{482}) falls in the region 1.14-1.36 for all samples. It is expected that pure white light emission can be achieved by controlling suitable Y/B intensity ratio. To bring the color indices closer to the white light region, the as prepared samples were annealed at different temperatures.

The influence of annealing temperature on the emission intensity of SrZrO₃:Dy³⁺ was also investigated. The emission spectra of the as-synthesized sample with different annealing temperatures on 229 nm excitation are shown in Figure 5.39. With increasing annealing temperature, both the yellow emission at 574nm and the blue emission at 485nm are enhanced as result of the better crystallinity, which can be ascribed to the decrease in surface area, presumably due to the reduction of the concentration of inherent defects states which are source of non-radiative transitions. Figure 5.40 presents the temperature-dependent characteristic of Y/B value. The Y/B value decreased with increasing annealing temperature, indicating a lower annealing temperature is favorable to achieve superior chromaticity. The annealing temperature affected the Y/B value by controlling the particle size and crystallization, both of which had a great impact on the chromaticity. When the SrZrO₃:Dy³⁺ samples are annealed at high temperature, the particle size increased and the number of surface

sites was reduced, resulting in poor chromaticity. At the same time, the particles were better crystallized, which could cause a lower level of disorder, further lowering the Y/B value. Larger Y/B value also reflects higher degree of covalency between Dy^{3+} and O^{2-} [282]. With increase in temperature Y/B decreases and so is covalency between Dy^{3+} and O^{2-} .

The (x, y) color coordinates and the correlated color temperatures (CCT) of the all the annealed samples are given in Table-5.9. It can be seen from the table that all the samples show near white light emission, which improves on annealing at higher temperatures. This is pictorially shown in the CIE index diagram given in Figure 5.41. From this discussion, it is clear that, the simple perovskite ceramic $SrZrO_3$, when doped with Dy ions, is capable of emitting near white light with 229 nm excitation and thus has enough potential to be a white light emitting phosphor.

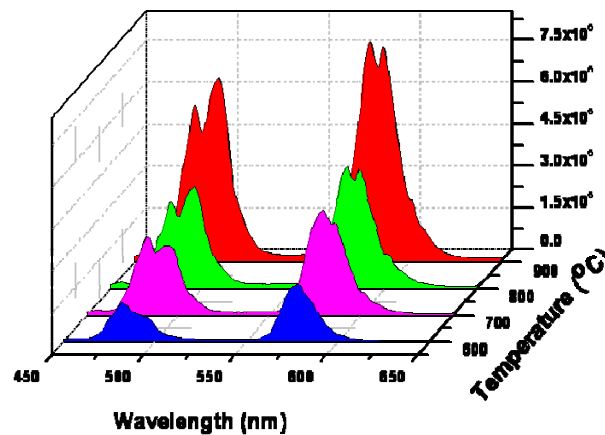


Figure 5.39: Emission intensity of the $SrZrO_3:Dy^{3+}$ as a function of annealing temperature.

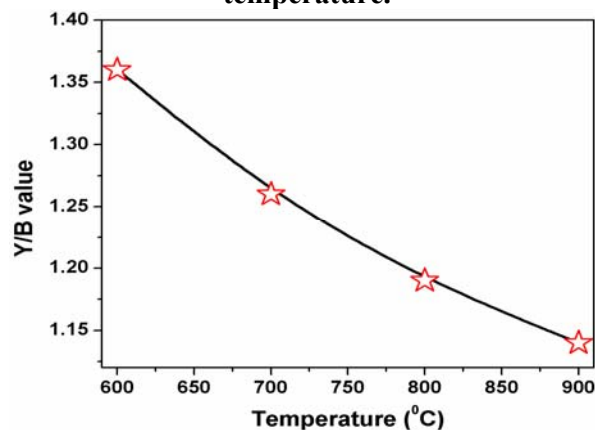


Figure 5.40: Influence of annealing temperature on the Y/B value of the as-prepared $SrZrO_3:Dy^{3+}$.

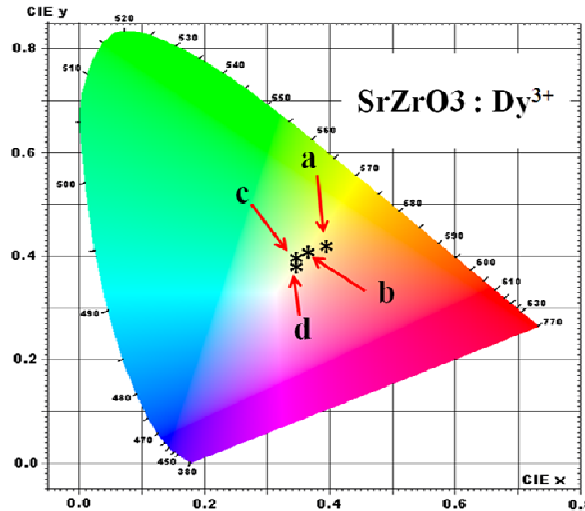


Figure 5.41: CIE index diagram of the $\text{SrZrO}_3:\text{Dy}^{3+}$ annealed at different temperatures, a-(as prepared sample), b- 700°C , c- 800°C and d- 900°C .

Table 5.9: CIE indices and the CCT of the Dy^{3+} doped SrZrO_3 samples annealed at different temperatures.

Annealing Temperature ($^\circ\text{C}$)	(x, y) coordinates	Correlated color temperatures (CCT in K)
600	(0.38, 0.41)	4217
700	(0.36, 0.40)	4631
800	(0.35, 0.39)	4941
900	(0.35, 0.36)	4835

5.8. Summary

Nanocrystalline SZ sample showed defect induced intense violet blue and weak orange red emissions. Based on EPR and theoretical studies, these defects were attributed to the presence of shallow and deep defects respectively. Their corresponding lifetimes were calculated using PL decay measurements. On doping Sm^{3+} in SZ, an efficient energy transfer takes place and Sm^{3+} ions are localized both at Sr and Zr positions of SZ. Theoretical calculation has shown that incorporating Sm at individual site does not change the band gap at all; but incorporating Sm simultaneously at Sr and Zr site decreases the band gap by 0.7 eV. PL decay time showed the presence of two life times in case of nanocrystalline $\text{SrZrO}_3:\text{Sm}^{3+}$: (i) Sm^{3+} at Zr^{4+} site ($\tau=500 \mu\text{s}$) and (ii) Sm^{3+} at Sr^{2+} site ($\tau=1.2 \text{ ms}$) in the ratio of 3:1. In europium doped SZ sample also, europium is distributed between two sites, Sr and Zr;

HAB (host absorption band) excites mostly Eu ion at Sr site, CTB (charge transfer band) excites mostly Eu ion at Zr site, where as f-f band excites both Eu ions at Sr and Zr sites equally. However Gd ion prefers Sr²⁺ sites and Dy ion prefers Zr⁴⁺ site only in SZ. Moreover SrZrO₃:Dy³⁺ showed near white light emission due to presence of blue, yellow and red emission.

CHAPTER 6

Luminescent properties of Eu^{3+}
ion in Sr_2CeO_4 : A low phonon
energy host

CHAPTER 6

6.1. General Introduction

Danielson et al. [283] have reported a novel blue luminescent material Sr_2CeO_4 prepared by combinatorial material synthesis technique, which exhibits the emission peak at 485 nm. The luminescence was believed to originate from a ligand-to-metal Ce^{4+} charge transfer mechanism. Sr_2CeO_4 phosphor has been confirmed to have an orthorhombic crystal structure with one-dimensional chains of edge-sharing CeO_6 octahedrons linked by strontium ions [284], and was considered to be a potential candidate for blue phosphors [285]. Thus, Sr_2CeO_4 belongs to a small group of crystals whose luminescence properties are governed by regularly located luminescent elements. The main feature of such luminescent systems is the interaction of its regular optical centers, which promote spatial delocalization of excitation energy. Such an interaction will facilitate the effective excitation energy transfer from the host to doped centers emitting in another spectral range. In addition, Sr_2CeO_4 was found to emit efficiently under ultraviolet, cathode ray and X-ray excitation [283, 286]. The reported thermal stability study suggests that $\text{Sr}_2\text{CeO}_4(\text{s})$ is unstable at higher temperatures and decomposes peritectically to $\text{SrCeO}_3(\text{s})$ and $\text{SrO}(\text{s})$ [287]. Sahu et al [288] have measured the thermal expansion and heat capacity of $\text{Sr}_2\text{CeO}_4(\text{s})$ as function of temperature and arrived at a second order phase transition at ~ 750 K.

Luminescent properties of materials were found to greatly depend on particle size, size distribution and particle morphology. Therefore, it will be interesting to develop different process parameters and synthetic routes to yield high quality Sr_2CeO_4 . Various chemical methods have been developed for the synthesis of pure, single-phase powders with controlled powder characteristics of Sr_2CeO_4 phosphor. Based on the literature survey, it is clear that the preparation method and the precursors play an important role in the formation of pure Sr_2CeO_4 luminescent phase. High heating temperature is usually required for the preparation of Sr_2CeO_4 via conventional solid state reaction technique [283], [284], [289] and [290]. Relatively lower heating temperature is required for the synthesis of Sr_2CeO_4 via poly ethylene glycol sol-gel process [291], citrate-gel process [292], co-precipitation method [286], ultrasonic spray pyrolysis [293] and combustion reaction [294]. Other methods like

microwave-hydrothermal [295], microwave-solvothermal methods [296] and Pechini method [297-298] have also been adopted for the synthesis of Sr_2CeO_4 . Serra et al [297] has used pechini method for the synthesis of pure Sr_2CeO_4 at 1373 K and arrived at mixture of monoclinic Sr_2CeO_4 and CeO_2 . However they have not mentioned about the quantity of citric acid and PEG. The morphology and particle size has also not been described by the authors. Viagin et al [298] has also synthesized pure and Eu-doped Sr_2CeO_4 following the same procedure as Serra et al [297]. A systematic study has been carried out to optimize the synthesis conditions of $\text{Sr}_2\text{CeO}_4:\text{Eu}^{3+}$ (mol % of Eu=0, 0.5, 0.8, 1.0, 3.0, 5.0, and 13.0) by complex polymerization method. Very few reports are available on europium doped strontium cerate [298, 299-301]. None of them discuss the systematic effect of europium concentration on the emission and lifetime properties.

In this study, the formation temperature, morphology and photoluminescence of Sr_2CeO_4 phosphor doped with different amount of Eu^{3+} were investigated. We have extensively studied the effect of Eu^{3+} concentration on its PL properties in cerate host. Concentration is optimized for maximum luminance. Judd-Ofelt (J-O) parameter for Eu^{3+} in the cerate host was evaluated by adopting standard Judd-Ofelt (J-O) analysis procedures. These J-O parameters reflect the local structure around the metal ion in the host and provide information regarding nature of the metal-ligand bonding in the matrix. CIE chromaticity coordinates were evaluated both for undoped and doped system.

6.2. Synthesis and characterization of $\text{Sr}_2\text{CeO}_4:\text{Eu}^{3+}$

6.2.1. Synthesis of $\text{Sr}_2\text{CeO}_4:\text{Eu}^{3+}$

$\text{Sr}_2\text{CeO}_4:\text{Eu}^{3+}$ (mol % of Eu=0, 0.5, 0.8, 1.0, 3.0, 5.0, and 13.0) was synthesized by complex polymerization method. The starting materials were strontium carbonate (99.99%, M/s Alfa Aesar, Lancaster), Eu_2O_3 (99.95% purity supplied by Rare Earth Development Section, BARC, Mumbai), and CeO_2 (99.9% purity supplied by Rare Earth Development Section, BARC, Mumbai). Citric acid (99.7%, M/s Chemco fine chemicals, Mumbai) was used as a complexing agent. Ethylene glycol (99.0%, M/s Thomas Baker, Mumbai) was used for polyesterification to stabilize the complex. Strontium carbonate was heated at 1273 K to remove all the moisture before taking for the synthesis. Strontium carbonate was dissolved in minimum amount of nitric

acid. Similarly both Eu_2O_3 and CeO_2 were dissolved in minimum amount of suprapure nitric acid and analyzed for Eu and Ce content by ICP-MS. Appropriate amounts of these solutions were used for synthesis. All the metal solutions were mixed and citric acid was added to maintain fuel to oxidant ratio as 1. The pH of the solution was maintained around 5-6. Ethylene glycol was added to the resulting solution. Citric acid and ethylene glycol were added in the mass ratio of 6:4. The solutions were stirred for 20-30 minutes at 353 K. Then upon evaporation, it formed a yellowish transparent polymeric gel. Then the gel was burnt at 673 K on a hot plate. The foamy precursor was ground and kept at 773 K in a furnace for 5h. Then the respective precursors were uniaxially pressed using hardened steel die applying a pressure of 500MPa. The green pellets were heated at 1273 K for 30h. The heating rate used was 2 K min^{-1} .

6.2.2. Characterization of undoped and $\text{Sr}_2\text{CeO}_4:\text{Eu}^{3+}$

6.2.2.1. Phase purity and Structure: XRD

The XRD patterns for $\text{Sr}_2\text{CeO}_4:\text{Eu}^{3+}$ (mol % of Eu= 0.5, 5.0, and 13.0) superfine particles as prepared at various temperatures are shown in Fig. 6.1, 6.2 and 6.3. JCPDF data files nos. 50-0115, 05-0418, 34-0394, 78-1830, and 47-1689 were used to identify Sr_2CeO_4 , SrCO_3 , CeO_2 , $\text{Sr}(\text{OH})_2\text{H}_2\text{O}$, and SrCeO_3 , respectively.

The precursor of $\text{Sr}_{1.995}\text{Eu}_{0.005}\text{CeO}_4$ was heated at 1073 K, 1223 K and 1273K to check the progress in the formation of product. The sample heated at 1073 K showed the presence of peaks due to SrCeO_3 , SrCO_3 and CeO_2 . When heated subsequently at 1223 K the peak intensity of CeO_2 reduced and the peak intensity of SrCeO_3 increased. When heated at 1273 K for 17 h, the peaks due to SrCO_3 , SrCeO_3 and CeO_2 disappeared and the peaks due to Sr_2CeO_4 started appearing.

The precursor of $\text{Sr}_{1.95}\text{Eu}_{0.05}\text{CeO}_4$ showed somewhat different behavior. At 1073 K, all the peaks were due to SrCO_3 and CeO_2 . When heated subsequently at 1223 K, the intensity of peak due to SrCO_3 reduced and the intensity of Sr_2CeO_4 and CeO_2 increased. At 1273 K, sample showed moisture sensitivity and a very few peaks were observed which were assigned to Sr_2CeO_4 , SrCeO_3 and CeO_2 . When heated at 1373 K, most of the peaks were found to be of Sr_2CeO_4 with a few peaks of SrCeO_3 . Again when heated at 1443 K, Sr_2CeO_4 decomposed to SrCeO_3 and SrO . While XRD

was recorded, SrO gets converted to $\text{Sr}(\text{OH})_2 \cdot (\text{H}_2\text{O})$ on reaction with atmospheric moisture.

The precursor of $\text{Sr}_{1.87} \text{Eu}_{0.13} \text{CeO}_4$ was found to show more moisture sensitivity than $\text{Sr}_{1.995} \text{Eu}_{0.005} \text{CeO}_4$ and $\text{Sr}_{1.95} \text{Eu}_{0.05} \text{CeO}_4$. When heated at 1073 K, it showed peaks due to SrCO_3 , CeO_2 and SrCeO_3 . Subsequently it was heated at 1223 K, which showed the appearance of Sr_2CeO_4 phase along with SrCO_3 and CeO_2 . At 1273 K, peaks were found to be of Sr_2CeO_4 with a single peak of SrCeO_3 . When heated at 1373 K and 1443 K, both the XRD patterns were similar, which showed the decomposition of Sr_2CeO_4 to SrCeO_3 .

From the above observations, it was concluded that the formation of Sr_2CeO_4 is possible from SrCeO_3 and SrO at 1273 K while heating for long time. Therefore the precursors were heated at 1273K for 30h. The X-ray diffraction pattern of the undoped and different Eu –doped Sr_2CeO_4 are given in Fig.6.4. There are no peaks due to any reactants or decomposed products. The crystallite size of powder samples were calculated from X-ray peak broadening of the diffraction using Scherer's equation. The calculated average crystallite size of $\text{Sr}_{2-x} \text{Eu}_x \text{CeO}_4$ ($x = 0, 0.005, 0.008, 0.01, 0.02, 0.05, \text{ and } 0.13$) phosphors is in the range of 38-52 nm. In these calculations corrections for instrumental broadening were taken care of.

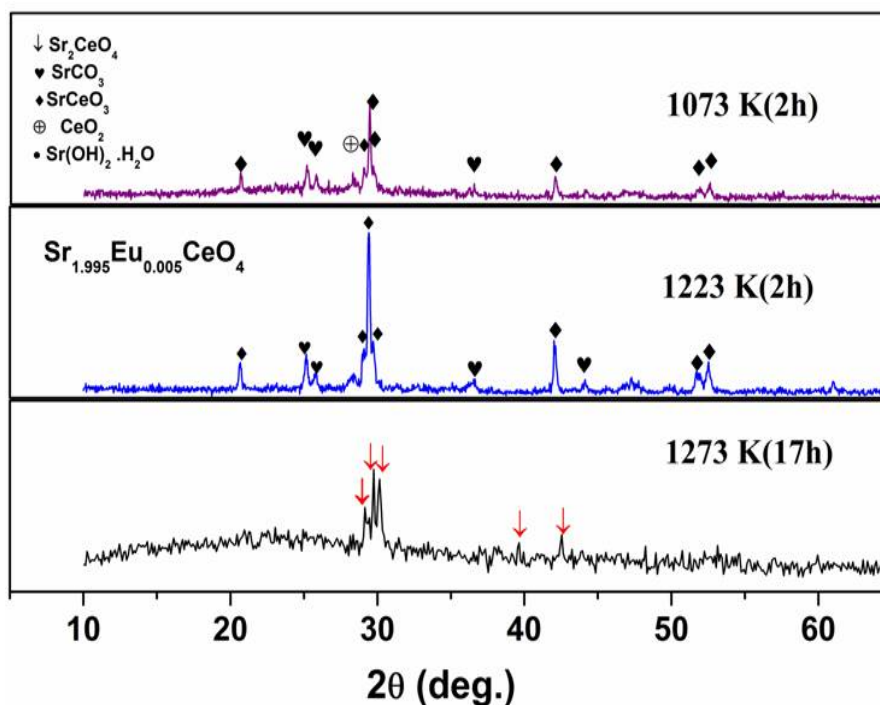
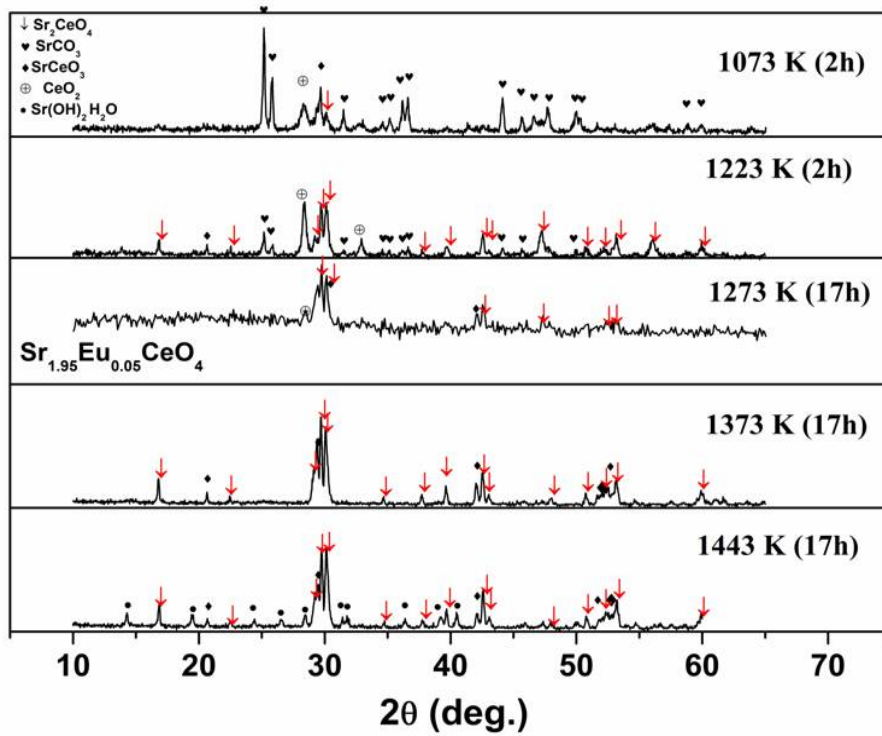
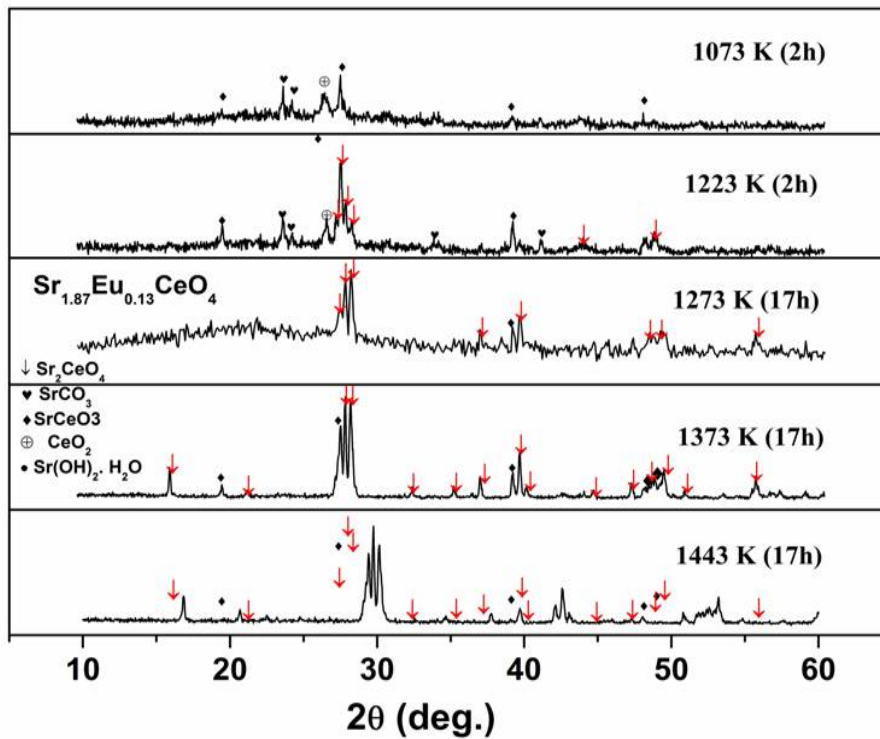


Figure 6.1: XRD pattern of $\text{Sr}_{1.995}\text{Eu}_{0.005}\text{CeO}_4$ at different temperature

Figure 6.2: XRD pattern of $\text{Sr}_{1.95}\text{Eu}_{0.05}\text{CeO}_4$ at different temperatureFigure 6.3: XRD pattern of $\text{Sr}_{1.97}\text{Eu}_{0.13}\text{CeO}_4$ at different temperature

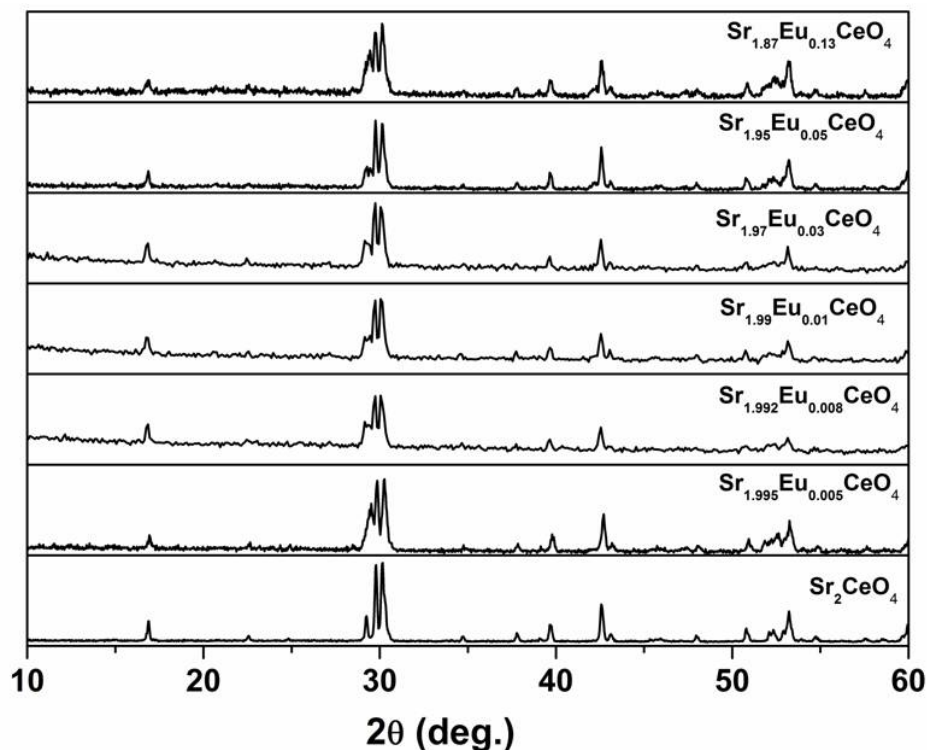


Figure 6.4: XRD pattern of undoped and doped strontium cerate at synthesized at 1323 K.

6.2.2.2. Thermal analysis: TGA/DTA

Fig.6.5 shows the TG-DTA curves for the precursor of $\text{Sr}_{1.995}\text{Eu}_{0.005}\text{CeO}_4$ and $\text{Sr}_{1.87}\text{Eu}_{0.13}\text{CeO}_4$ prepared by complex polymerization method. The TG curve showed three steps in this measurement. End of weight loss occurred around 1250 K. Endothermic peaks appeared at around 800 and 1150 K. Initially weight loss is continuous up to 790 K, which was due to continuous loss of absorbed moisture and dehydration of metal citrate. The first peak correspond to major weight loss at 800 K, is associated with the decomposition of polymeric network with possible formation of carbonates and burnout of most of the organic residues [302, 303]. The peak at 1150 K might correspond to the decomposition of SrCO_3 and formation of Sr_2CeO_4 .

In complex polymerization method, a stable metal–chelate complex between metal nitrates and citric acid was formed, which again formed a polymeric resin in the presence of ethylene glycol. The metal cations were homogeneously distributed in the polymeric resin and no combustion was observed. This can be confirmed by DTA analysis, since no exothermic peak due to combustion was observed. In case of involvement of volatile reactants and thermodynamically less stable desired product, complex polymerization method is more preferred than combustion synthesis.

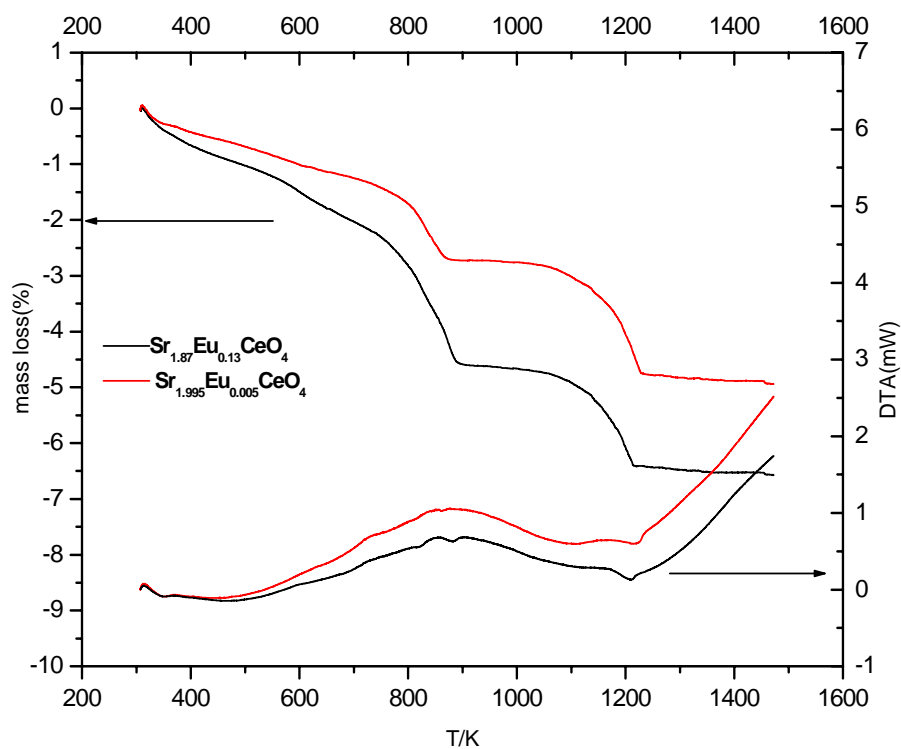


Figure 6.5: TG-DTA curves for the precursor of $\text{Sr}_{1.995}\text{Eu}_{0.005}\text{CeO}_4$ and $\text{Sr}_{1.97}\text{Eu}_{0.13}\text{CeO}_4$ prepared by complex polymerization method

6.2.2.3. Morphological studies: SEM

The SEM photograph of Sr_2CeO_4 synthesized by the polymeric precursor route is shown in Fig. 6.6. The phosphor consists of many crystalline nanoplates with irregular shapes mostly in the form of nanobeads, which are linked together in a crotch-like way as shown in Fig. 6.6 (d). The distribution of particle size is in the range of 50-100 nm. The crotch like morphology is ascribed to slight sintering as a result of relative ductile property of alkaline earth metals [304].

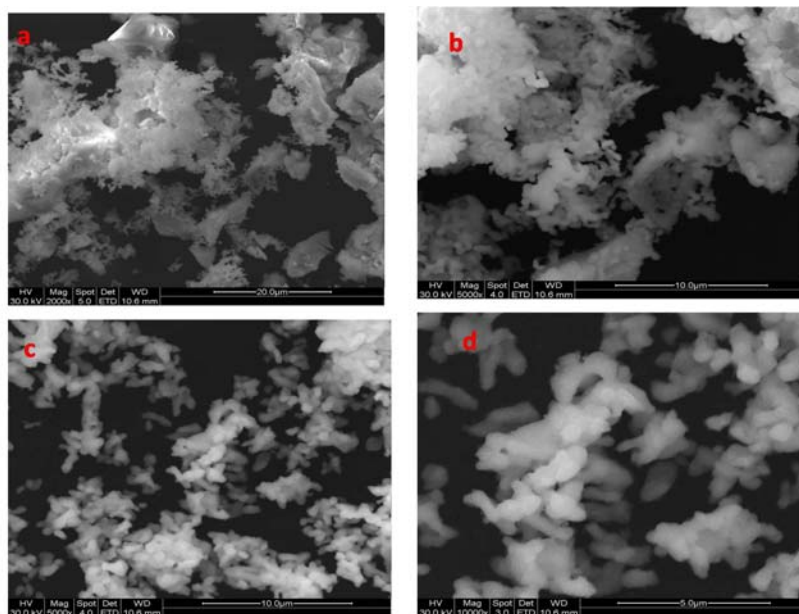


Figure 6.6: SEM micrograph of strontium cerate sample calcined at 1000 °C for 30 h in air at different magnifications (a) 2000X (b) & (c) 5000 X and (d) 10000 X

6.3. Luminescence properties of Sr_2CeO_4

Figure 6.7(a) shows excitation spectra ($\lambda_{\text{em}} = 485 \text{ nm}$) of the strontium cerate sample. The excitation spectrum consists of two peaks a broadband at 315 nm and a shoulder at 360 nm. In Sr_2CeO_4 , there are two different types of $\text{Ce}^{4+} - \text{O}^{2-}$ bonds in the lattice [283]. The two excitation peaks observed in the Figure are thus attributed to the different charge transfer transitions.

Considering the edge shared octahedral (CeO_6) structure [284], the strong excitation band at 315 nm is assigned to the charge transfer from the axial O^{2-} to the Ce^{4+} ions, whereas the shoulder at 360 nm is ascribed to charge transfer from the equatorial O^{2-} to the same energy level of the Ce^{4+} ion.

Figure 6.7(b) shows emission spectra ($\lambda_{\text{em}} = 315 \text{ nm}$) of the strontium cerate sample. The emission spectrum is a simple broad band which centre is located at 485 nm. This is attributed to Ce^{4+} charge transfer emission. In Ce^{4+} , the 4f shell is vacant. Therefore, the only possible transition is one, wherein an electron is excited from the oxygen ligand to the Ce^{4+} ion: a charge transfer transition.

The decay curves for Sr_2CeO_4 annealed at 1273 K (as prepared sample) are shown in Fig. 6.8 at excitation wavelengths of 315 nm monitoring emission at 485 nm on a 500 μs scale and fitted using the mono-exponential decay equation.

$$I(t) = A_1 \exp(-t/\tau_1) \quad (6.1)$$

As has been discussed, the emission band at 485 nm is associated with CT transition. For all known crystals, CT luminescence results from the allowed transitions with the decay constant of about 50 ns, while the decay time of Sr_2CeO_4 is 59 μs . Such a long lifetime is ascribed by the authors [290] to the transition of an excited electron from an oxygen ion to a cerium ion with an electron spin flip that results in the formation of an excited triplet state. The transition from the excited triplet state to the ground singlet state is forbidden.

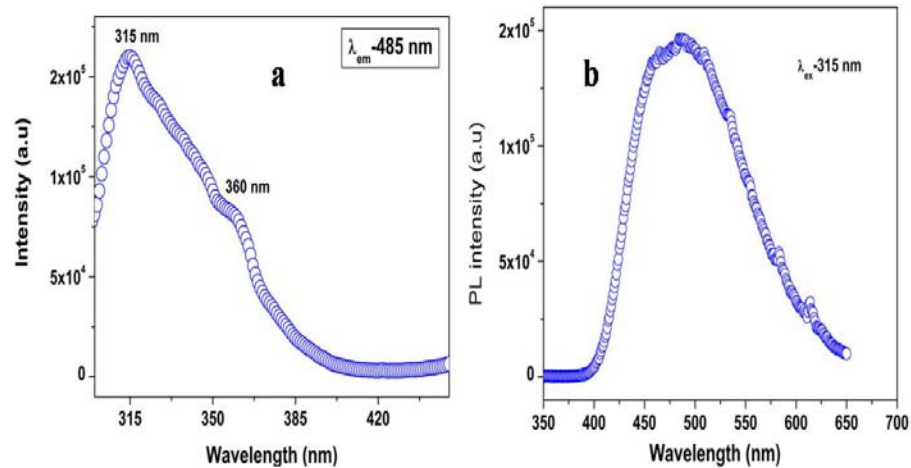


Figure 6.7: (a) Excitation and (b) emission spectra of Sr_2CeO_4 sample calcined at 1000 °C for 30 h in air

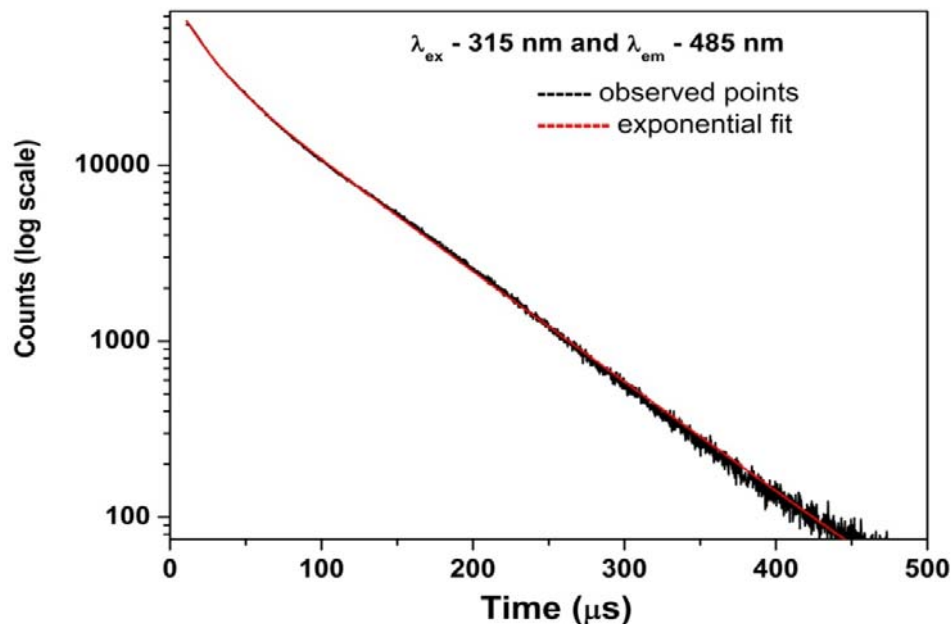


Figure 6.8: Luminescence decay time profile for Sr_2CeO_4 sample calcined at 1000 °C for 30 h in air

6.4. Luminescence properties of $\text{Sr}_2\text{CeO}_4:\text{Eu}^{3+}$

6.4.1 Emission, excitation and luminescence decay studies on $\text{Sr}_2\text{CeO}_4:\text{Eu}^{3+}$

The excitation spectra of $\text{Sr}_2\text{CeO}_4:\text{Eu}^{3+}$ powders with different europium ion concentration monitored at the emission wavelength of 614 nm is shown in Fig.6.9. It consists of a strong broad band and several weak lines in the range 220–450 nm.

The excitation spectra recorded by fixing the highest intensity Eu^{3+} emission as the monitoring wavelength show similar features for all the compositions. The spectra show a broad band in the range 220-300 nm and a broad and sharp shoulder at 315 nm, which are already assigned to the $\text{Ce}^{4+}-\text{O}^{2-}$ CT transition in undoped Sr_2CeO_4 .

The broad band peaking at 280 nm was ascribed to the overlap of charge transfer (CT) bands from oxygen to europium (O–Eu) and the host band (Ce–O). Weaker lines in 300-480 nm are attributed to intra-configurational 4f-4f transition of Eu^{3+} in host lattice. The peaks seen at 320, 360, 380, 395 and 420 nm were assigned to electronic transitions of ${}^7\text{F}_0 \rightarrow {}^5\text{H}_3, {}^5\text{L}_9, {}^5\text{L}_7, {}^5\text{L}_6$ and ${}^5\text{D}_4$ respectively .

Initially with increase in europium ion concentration, excitation intensity increases up to 5 mol % thereafter concentration quenching takes place.

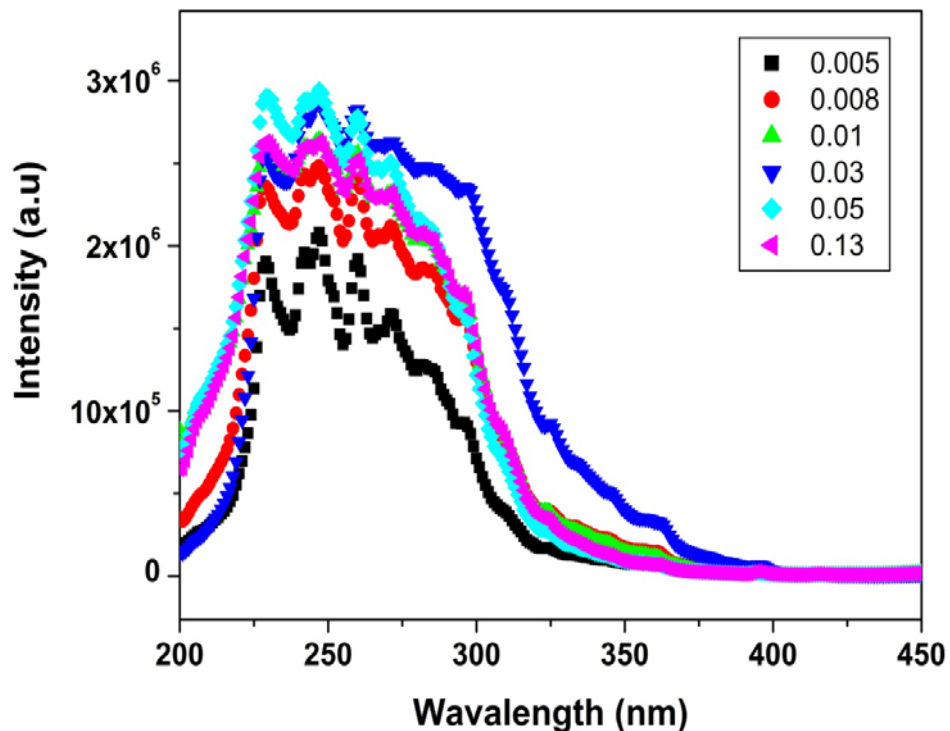


Figure 6.9: Excitation spectra of $\text{Sr}_{2-x}\text{Eu}_x\text{CeO}_4$ ($x=0.005, 0.008, 0.01, 0.03, 0.05,$ and 0.13) calcined at $1000\text{ }^\circ\text{C}$ for 30 h in air

Upon excitation at Charge transfer band, the emission spectrum (shown in Figure 6.10) exclusively contains very weak lines of ${}^5D_2 \rightarrow {}^7F_0$ (465 nm), ${}^5D_2 \rightarrow {}^7F_2$ (490 nm), ${}^5D_2 \rightarrow {}^7F_3$ (510 nm), ${}^5D_1 \rightarrow {}^7F_1$ (535 nm), and ${}^5D_1 \rightarrow {}^7F_2$ (555 nm) [302] embedded over broad host emission (420-530 nm) and the strong bands of ${}^5D_0 \rightarrow {}^7F_1$ (594 nm), ${}^5D_0 \rightarrow {}^7F_2$ (614 nm), ${}^5D_0 \rightarrow {}^7F_3$ (653 nm) and ${}^5D_0 \rightarrow {}^7F_4$ (704 nm). ${}^5D_{1, 2, 3} \rightarrow {}^7F_J$ lines usually appear in a compound with low-lattice phonon energy which leads to multiphonon relaxation. They are usually difficult to occur among the levels of Eu^{3+} . As shown in Fig. 6.10, the emission spectra of $\text{Sr}_2\text{CeO}_4: \text{Eu}^{3+}$ phosphors consist of emissions from the higher energy levels (5D_1 and 5D_2) also. The presence of emission lines from higher excited states of Eu^{3+} is attributed to the low vibration energy of CeO_4^{4-} groups. Multiphonon relaxation by CeO_4^{4-} is not able to bridge the gaps between the higher energy levels and the 5D_0 level of Eu^{3+} completely, resulting in weak emissions from these levels [305].

The orange emission at 592 nm belongs to the magnetic dipole ${}^5D_0 \rightarrow {}^7F_1$ transitions of Eu^{3+} , and the transition hardly varies with the crystal field strength. The red emission at about 615 nm ascribes to the electric dipole ${}^5D_0 \rightarrow {}^7F_2$ transitions of Eu^{3+} , which is very sensitive to the local environment around the Eu^{3+} and depends on the symmetry of the crystal field.

On excitation by 280 nm (charge transfer band), emissions due to the rare earth and the host both could be seen in the emission spectrum. Moreover ${}^5D_0 \rightarrow {}^7F_2$ line at 615 nm (ED) is very strong in comparison to ${}^5D_0 \rightarrow {}^7F_1$ line at 594 nm (MD). This can be attributed to Eu^{3+} ions in asymmetric environment without inversion symmetry. Upon excitation with 393 nm, corresponding to the ${}^7F_0 \rightarrow {}^5L_6$ band, emission properties similar to that of CTB excitation were observed.

It was also noticed that, the intensities of emission bands are low, when excited with the characteristic absorption band at 395 nm of Eu^{3+} ions, compared to the emission intensities obtained with LMCT excitation band (245 nm). This may be due to the fact that the Eu^{3+} absorption bands corresponding to the f-f transitions are forbidden and exhibit poor absorptivities in UV region. The high intensities of emission bands, when excited with LMCT are due to the intra-molecular energy transfer (IMET) process, which occurs in the UV region.

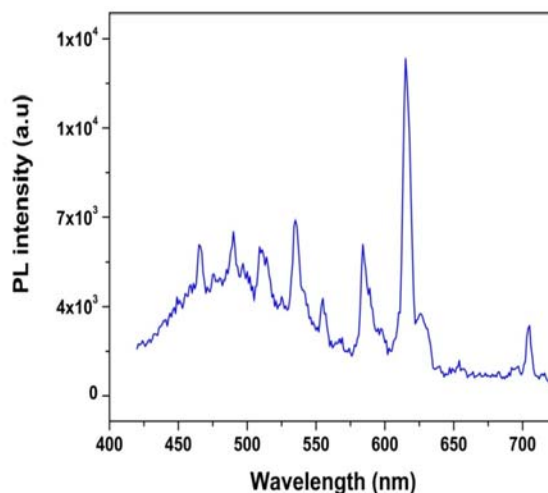


Figure 6.10: Emission spectra of the powder sample of Sr_2CeO_4 : 0.5 mol % Eu^{3+} on excitation with 280 nm (charge transfer band) calcined at 1000 °C for 30 h in air

The decay curve corresponding to the $^5\text{D}_0$ level of Eu^{3+} ions in 0.5 mol % europium doped Sr_2CeO_4 are shown in Fig. 6.11. These decay time studies were carried out at excitation wavelength of 280 nm with $\lambda_{\text{em}} = 614$ nm and fitted using equation mentioned in 3.4. For 0.5 mol % Eu^{3+} doped sample (280 nm, excitation), the decay has found to be bi-exponential with a short lifetime component of 60 μs and a long lifetime component of 800 μs . Longer lifetime component arises due to the Eu^{3+} ions sitting at regular centrosymmetric Ce^{4+} sites and the short lifetime component arises due to the Eu^{3+} ion at non-centrosymmetric Sr^{2+} sites.

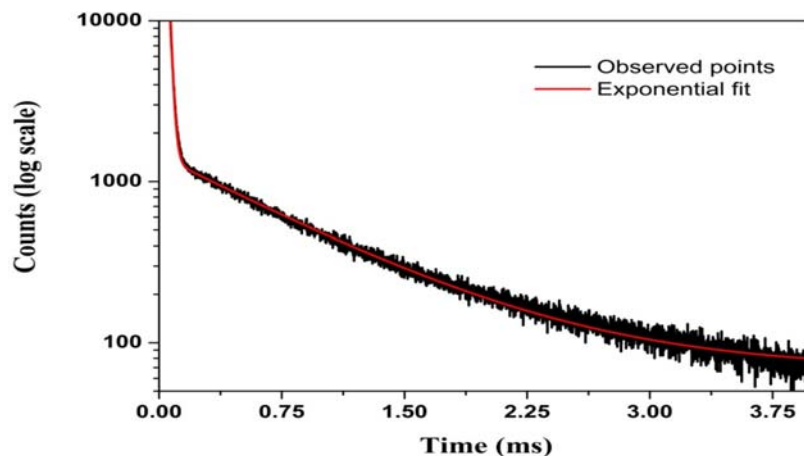


Figure 6.11: Luminescence decay time profile of the Sr_2CeO_4 : 0.5 mol % Eu^{3+} , $\lambda_{\text{ex}}=280$ nm $\lambda_{\text{em}}=614$ nm. The black line gives the observed points and the red line gives its exponential fitting.

6.4.2. Concentration variation effect on Eu^{3+} photoluminescence:

To evaluate the emission characteristics of the cerate host with the trivalent europium ion as dopant, its concentration was varied from 0.5 to 13 mol%. For these studies, the average lifetime was taken into account. The average lifetime for the present system was calculated using the following equation.

$$\tau_{av} = \frac{(A_1 \tau_f^2 + A_2 \tau_s^2)}{(A_1 \tau_f + A_2 \tau_s)} \quad (6.2)$$

Here the τ_f represents the lifetime of the fast decaying component (S_1) and τ_s represents the lifetime of the slow decaying component (S_2).

Figure 6.12 shows the dependence of the PL emission intensity (obtained with λ_{ex} 280 nm) of the rare earth ion with varying doping concentration.

It was observed that, the emission intensity of Eu^{3+} increases with the increase in concentration initially, reaching maxima at 5.0 mol % and then decreases with the increasing concentration due to concentration quenching. Thus the optimum concentration for Eu^{3+} is somewhere between 0.05 and 0.13. The concentration quenching might be due to non-radiative energy transfer from one Eu^{3+} ion to another Eu^{3+} ion. Non-radiative energy transfer can take place via two different mechanisms (i) Forster resonance energy transfer (multipole– multipole interaction) and (ii) Dexter mechanism (exchange interaction).

A rough estimation of the critical transfer distance (R_c) for energy transfer can be obtained using the relation given by Blasse [306].

$$R_c = 2 \left(\frac{3V}{4\pi N X_c} \right)^{\frac{1}{3}} \quad (6.3)$$

Here V is the volume of the unit cell, X_c the critical concentration and N the number of available crystallographic sites occupied by the activator ions in the unit cell. Values of V and N for the crystalline Sr_2CeO_4 (orthorhombic system with primitive lattice, One unit cell of Sr_2CeO_4 comprises of 2 formula units) are 227.79 \AA^3 and 4, respectively (ICDD card 50-0115). Considering $X_c = 5\%$ (0.05), critical energy transfer distance R_c in $\text{Sr}_2\text{CeO}_4: \text{Eu}^{3+}$ phosphor was calculated to be 13 \AA . In this case, the Eu^{3+} - Eu^{3+} distance is larger than 10 \AA . Thus the exchange interactions are ruled out. Therefore, the electric multipolar interaction is believed to be the only mode for the energy transfer among the Eu^{3+} ions in Sr_2CeO_4 phosphor.

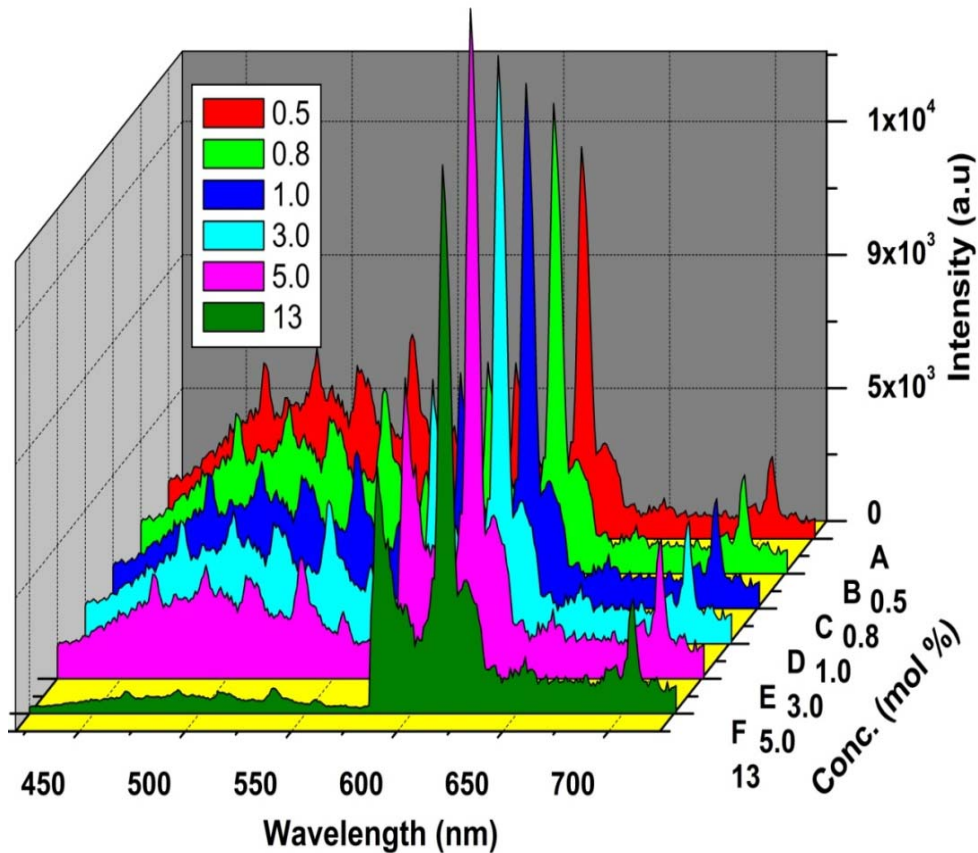


Figure 6.12: The emission spectra at $\lambda_{\text{ex}} = 280$ nm for Sr_2CeO_4 doped with different concentration of Eu^{3+} ions calcined at 1000°C for 30 h in air

Fig. 6.13 shows the average lifetime dependence of Sr_2CeO_4 doped with different Eu^{3+} ion concentrations under an excitation of 280 nm with signals detected at 614 nm. Different concentrations of Eu^{3+} ion doping did not obviously change the decay behavior; all the decay curves were attributed to a bi-exponential behavior. The concentration quenching effect occurred, when Eu^{3+} concentrations were above 5 mol%, and the average decay time obviously decreased with increasing Eu^{3+} concentration above 5.0 mol% (0.5 mol%:0.535 ms, 0.8 mol%:0.606 ms, 1.0 mol%:0.728 ms, 3.0 mol%:0.817 ms, 5.0 mol%:0.893 ms, 13 mol%:0.574 ms). This was due to the effect of energy exchange between the Eu^{3+} ions as the distance between them decreased with increasing Eu^{3+} ion concentrations, enhancing the energy depletion rate and causing the decay time to decrease.

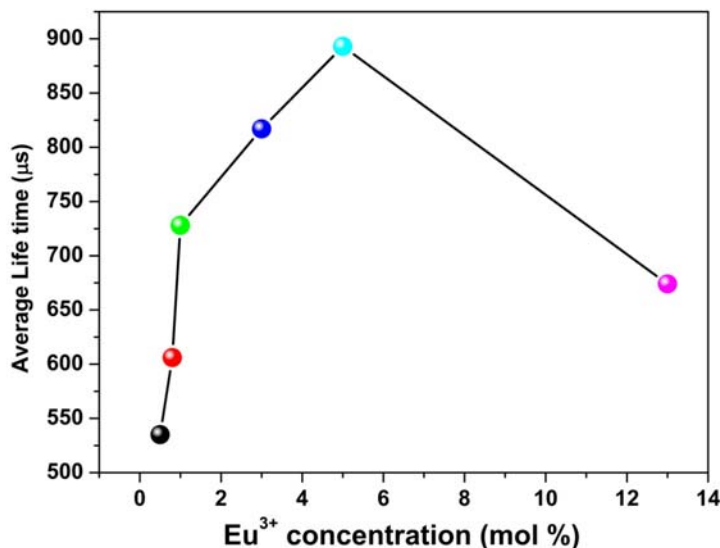


Figure 6.13: The relationship between the average life time of 5D_0 state and Eu^{3+} ion concentrations.

6.4.3. Energy transfer mechanism in $\text{Sr}_2\text{CeO}_4:\text{Eu}^{3+}$:

In luminescent materials, energy transfer mechanism is a well known phenomenon. This process is either due to resonance or exchange interactions or multipolar interactions between the ions of the same or different types and depends on the critical energy transfer distance (R_c) between the absorbing groups in the crystal lattice.

In the excitation spectra of Eu^{3+} in Sr_2CeO_4 (Figure 6.9) we observed that at all Eu concentrations, the Ce^{4+} emission band (overlapped with O-Eu CTB) is present. In emission spectra also (Figure 6.12), Ce^{4+} emission band is observed together with the Eu lines at all the concentrations. The broad Ce^{4+} emission band is found to cover all the Eu lines up to 550 nm (mainly the dominant 485 nm) indicating that Ce transfers some of its energy to the Eu ion. Increase in Eu concentration increases the intensity of Eu lines with a corresponding decrease in the intensity of the Ce emission band. Thus, the energy transfer is incomplete and it is highly probable that both radiative and nonradiative energy transfers occur in $\text{Sr}_2\text{CeO}_4:\text{Eu}$ with Ce acting as the sensitizer and Eu ion as the activator in the host matrix [299].

It was observed that at higher europium concentration (> 0.05) only Eu^{3+} emission lines are observed and Ce^{4+} ion emission is almost totally quenched. Thus, for $x > 0.05$, the energy transfer from Ce^{4+} ion to Eu^{3+} ion in Sr_2CeO_4 is complete and nonradiative. It is well known that the energy transfer from a broad band emitter to a line emitter is only possible for nearest neighbours in the lattice [307]. In the

compound Sr_2CeO_4 , the crystal structure is one-dimensional with a fairly short interchain distance of 3.597 \AA (c -lattice parameter). The lifetime of Ce^{4+} in the undoped Sr_2CeO_4 has been measured to be unusually long ($59 \mu\text{s}$). Hence, there is a high probability of energy transfer due to exchange interactions [since $3.6 \text{ \AA} < Rc$ for exchange interaction (5 \AA)], which can occur between Ce^{4+} and Eu^{3+} ions in different chains in addition to that within the chains.

Since the highest intensity was observed for 5 mol% doped sample, further investigations were carried out on this particular sample only.

6.4.4. Materials Performance: Color coordinates

To evaluate the material performance on color luminescent emission, CIE chromaticity coordinates were evaluated for undoped and 5 mol% doped sample adopting standard procedures. The values of x and y coordinates of the system were calculated to be 0.27 and 0.32 respectively. This is represented as the point ‘*’ in the CIE diagram shown in Figure 6.14 (a). It is clear from the values that, strontium cerate, gives a ‘bluish white’ emission. Fig. 6.14(b) shows the CIE chromaticity diagram for $\text{Sr}_2\text{CeO}_4:5 \text{ mol\% Eu}^{3+}$ phosphors. The color coordinates of the emission was $x = 0.631$ and $y = 0.285$, which is located in the red light region.

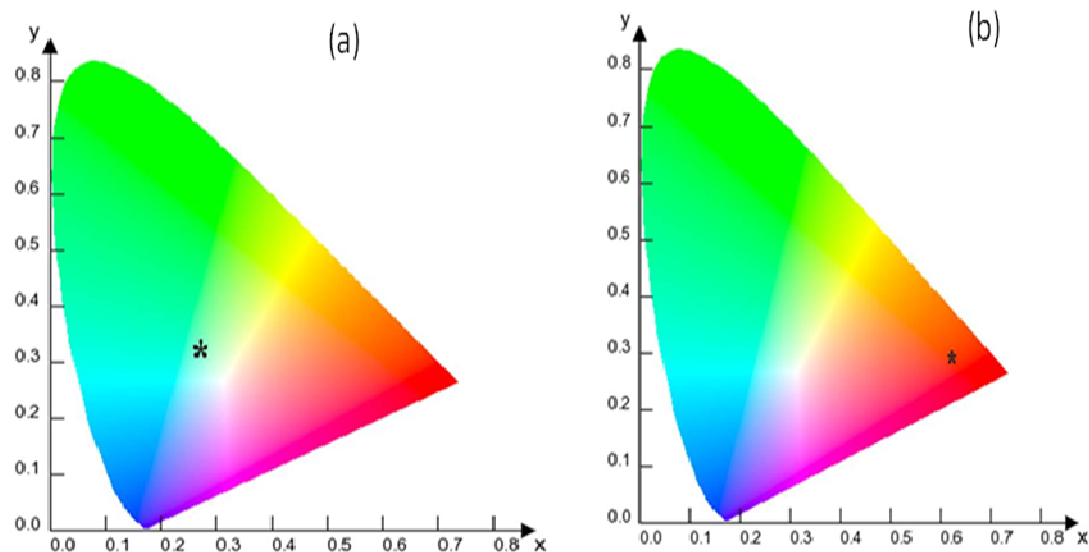


Figure 6.14: (a) CIE index diagram of (a) Sr_2CeO_4 and (b) $\text{Sr}_2\text{CeO}_4:5 \text{ mol\% Eu}^{3+}$ system calcined at $1000 \text{ }^\circ\text{C}$ for 30 h in air showing bluish white and red emission (point *) respectively.

6.4.5. Judd-Ofelt Analysis:

The intensity parameter (Ω_λ) where $\lambda = 2$ and 4 , quantum yields of luminescence along with the radiative (A_{rad}) and non-radiative (A_{nrad}) rates for Eu^{3+} ions in different europium doped Sr_2CeO_4 , were calculated from the emission spectra and decay curves based on the reported literature [264-266]. The values are shown in **Table 6.1** and detailed discussion is given in the following section. The value of refractive index used in J-O calculation for Sr_2CeO_4 is 1.93.

It is well known that the parameter Ω_2 , is an indication of the dominant covalent nature and/or structural changes in the vicinity of the Eu^{3+} ion (short range effects), while Ω_4 intensity parameters are long range parameters that can be related to the bulk properties such as viscosity and rigidity of the inorganic matrices. The Ω_2 parameter is related to the degree of covalence and polarizability of the chemical environment experienced by the Eu^{3+} ion; higher Ω_2 values point to more covalent and polarisable environments. High values of the Ω_2 parameters can also be related to high asymmetry of the Eu^{3+} surrounding environment.

Form table 6.1 it is clear that, with increase in europium concentration up to 5 mol % radiative transition rate increases and non-radiative rate decreases. This can be corroborated with our earlier studies, wherein concentration quenching was observed beyond 5.0 mol % due to non-radiative energy transfer between europium ions. This is also getting reflected in quantum efficiency which is highest for 5 mol % sample. Moreover trend in J-O parameter for all the samples shows that Ω_2 value is greater than Ω_4 , which is related to high asymmetry of the Eu^{3+} surrounding environment. This can also be seen from asymmetry ratio values wherein for all sample $I_{02} > I_{01}$. The spectral features obtained for all samples are almost similar and can be attributed to Eu^{3+} ions in asymmetric environment without inversion symmetry. Since ionic size difference between Sr^{2+} (132 pm) and Eu^{3+} (109 pm) is more, Eu^{3+} ions occupying the Sr^{2+} sites will lead to a large distortion in the lattice and if the associated defect due to charge/size difference is at a smaller distance, the local site symmetry will have a non-inversion symmetry. On the other hand, Eu^{3+} with ionic size 109 pm while occupying Ce^{4+} (ionic size 101 pm), has a smaller size difference and will not lead to a large distortion in the lattice and if the associated defect due to charge/size difference is at a large distance, the local site symmetry will have an inversion symmetry.

The ratio of intensity of red line (${}^5D_0 \rightarrow {}^7F_2$) to orange line (${}^5D_0 \rightarrow {}^7F_1$) in Eu^{3+} is shown to be related to degree of covalency between Eu^{3+} and O^{2-} [263]. The larger the difference in the intensities of these two lines, larger is the asymmetry and covalency effects. For all the samples ${}^5D_0 \rightarrow {}^7F_2$ is markedly more intense as compared with those of ${}^5D_0 \rightarrow {}^7F_1$ line i.e. R/O shows marked increase, so larger is the asymmetry and covalency effect around the Eu^{3+} ion site. These can also be seen in trend of J-O parameter.

Table 6.1: Luminescence lifetimes, radiative and non-radiative decay rates, quantum efficiencies (5D_0 level), intensity ratio between the ${}^5D_0 \rightarrow {}^7F_2$ and ${}^5D_0 \rightarrow {}^7F_1$ transitions, Judd–Ofelt intensity parameters, and chromaticity coordinates of the Eu^{3+} doped strontium cerate

Conc.	τ_{av} (μs)	A_{RAD} (s^{-1})	A_{NRAD} (s^{-1})	$\eta(\%)$	I_{02}/I_{01}	Ω_2 (* 10^{-20} cm^2)	Ω_4 (* 10^{-20} cm^2)	Chromaticity	
								x	y
0.5	535	343	1527	18.4	1.66	2.6	0.745	0.49	0.40
0.8	606	364	1287	22.0	1.76	2.75	0.958	0.51	0.40
1.0	728	359	1015	26.1	1.69	2.64	1.06	0.52	0.40
3.0	817	380	847	31.0	1.85	2.89	1.25	0.57	0.38
5.0	893	472	746	33.2	1.80	2.82	1.20	0.63	0.38
13.0	674	415	1068	28.0	2.08	3.26	1.5	0.58	0.41

6.5. Summary:

In summary, the polymeric precursors method has been successfully applied for the obtainment of nanosized cerate red phosphors with different europium ion concentrations. Detailed X-ray investigations were done to optimize the parameters such as calcination temperature and time to get pure phase. Detailed photoluminescence investigations of undoped Sr_2CeO_4 showed bluish white emission with single lifetime of 59 μs . The emission spectra of europium doped cerate sample showed characteristic peaks corresponding to the ${}^5D_0 \rightarrow {}^7F_j$ ($j=1, 2$) transitions of Eu^{3+} ion as well as host emission under CTB. The PL decay time studies showed a bi-exponential decay, which was attributed to presence of europium ion at both Sr^{2+} as well as Ce^{4+} sites. Concentration quenching of the PL signal intensity was observed for Eu^{3+} ion concentration of more than 5 mol%. From this, the critical energy transfer distance of Eu^{3+} was calculated to be 13 Å and the mechanism of concentration quenching was determined to be the multipole – multipole interaction. It was

observed that with increase in Eu^{3+} concentration, PL intensity of europium emission peaks increase, whereas that of host emission decreases. This is assigned to energy transfer between host and europium ion. The J-O parameters and other radiative properties were evaluated for each sample adopting standard procedure and was related with spectral features of europium ion.

CHAPTER 7

**Synthesis, structural
characterization and
spectroscopic investigations on a
new host for lanthanide doping:**



CHAPTER 7

7.1. General Introduction

Luminescence properties of hosts like $Zn_2P_2O_7$ (both undoped and doped) with lanthanide ions (Eu and Sm) were investigated for the first time with a view to develop new and robust phosphor materials having multifunctional applications. Zinc pyrophosphate is known to undergo structural phase transition at 132°C . We have doped 2.0 mol % Mn^{2+} in zinc pyrophosphate and used EPR as a probe to understand the mechanism for phase transition. This aspect was also supported by HTXRD and DSC. Among the various hosts used as phosphor systems, phosphate based matrices offer a range of compositional and structural possibilities that facilitate the tailoring of chemical and physical properties of interest for specific technological applications. These hosts offer better homogeneity, chemical and thermal stability with lower sintering temperatures [308-311]. Pyrophosphates having general formula $M_2P_2O_7$ (M=Ca, Sr, Ba, Mg, Zn, Mn etc.) are one of the phosphate systems, which are reported to be excellent host materials [312, 313]. Special interest in pyrophosphate arises from the unique spectroscopic behavior of the metal cation polyhedra with well-defined and low symmetry coordination [314, 315]. Among these, the thortveitite-type pyrophosphate $\alpha\text{-Zn}_2\text{P}_2\text{O}_7$ is a promising low temperature co-fired ceramic (LTCC) material [316]. In zinc pyrophosphate, there are two cationic sites in lattice, i.e., five-coordinated Zn^{2+} sites (square pyramidal coordination) and six-coordinated Zn^{2+} sites (octahedral coordination). Europium was used as a structural probe to understand the local environment.

Since effect of crystal field can be more prominently seen in transition metal than lanthanide ion; 2.0 mol% $MnCO_3$ was doped in $Zn_2P_2O_7$. It is very interesting to know that in $Zn_2P_2O_7$, manganese was stabilized as both Mn (II) and Mn (IV). This has been validated using EPR and PL spectroscopy. Photoluminescence properties of Eu, Sm and Mn doped zinc pyrophosphate are also studied.

7.2. Synthesis and characterization of $Zn_2P_2O_7$

7.2.1. Synthesis of $Zn_2P_2O_7$

The $Zn_2P_2O_7$ was synthesized by complex polymerization method. The starting materials were $(NH_4)_2HPO_4$ (99.99%, M/s Alfa Aesar, Lancaster) and ZnO (Spectrographically standardized substance supplied by M/s Johnson mathey &Co Ltd, UK). Citric acid (99.7%, M/s Chemco fine chemicals, Mumbai) was used as the complexing agent while Ethylene glycol (99.0%, M/s Thomas Baker, Mumbai) was used for polyestification to stabilize the complex. At first the reactants $(NH_4)_2HPO_4$ and ZnO were preheated to remove moisture. Thereafter ZnO was dissolved in concentrated HNO_3 followed by addition of $(NH_4)_2HPO_4$ to this zinc solution. All the solutes were dissolved completely to result in a clear solution. The pH of the solutions was maintained around at 5.2. The citric acid and ethylene glycol were added in the mass ratio of 6:4 to the resulting solutions. Citric acid was added to maintain the fuel to oxidant ratio as 1. The solutions were stirred for 20-30 minutes at $80^\circ C$. Upon evaporation of this solution, a transparent polymeric gel was obtained. The gel was then burned at $500^\circ C$ on a hot plate. The obtained foamy carbonaceous precursor was then ground and kept at $900^\circ C$ in a furnace for 6h for complete formation of the pure product. The heating rate used was $3 K min^{-1}$. Citric acid was used as the complexing agent while Ethylene glycol was used for polyestification to stabilize the complex.

7.2.2. Characterization of $Zn_2P_2O_7$

7.2.2.1. Phase purity and Structure: XRD

The XRD patterns of the zinc pyrophosphate sample are shown in Fig.7.1, from which it can be seen that all the diffraction peaks could be indexed to the monoclinic phase of α - $Zn_2P_2O_7$ (JCPDS card No. 08-0238). The XRD data of the relatively intense peak ($I/I_0 > 10$) was indexed on a monoclinic system with space group C2/m having cell parameters $a = 19.59 \text{ \AA}$, $b=8.282 \text{ \AA}$ and $c=9.103$. Crystal structure of α - $Zn_2P_2O_7$ is shown in Fig. 7.2. On Rietveld refinement using C2/m space group, XRD pattern for zinc pyrophosphate was fitted perfectly. Rietveld fitted XRD pattern is shown in Figure 7.1. $Zn_2P_2O_7$ is having thortveitite structure, in which $[P_2O_7]^{4-}$ groups are in stagger configuration and belong to monoclinic with space group I2/c as shown in

figure 1b. The coordination number of the cations to oxygen atoms is either 5 (for 2 Zn) or 6 (for 1 Zn) [317]. In the structure of α - $\text{Zn}_2\text{P}_2\text{O}_7$, 5-coordinated Zn (S_1 site) is surrounded by five nearest neighbour oxygen ions in the form of square pyramidal (C_{4v}), which is a more heavily distorted structure than that of the 6-coordinated Zn (S_2) site with regular octahedra.

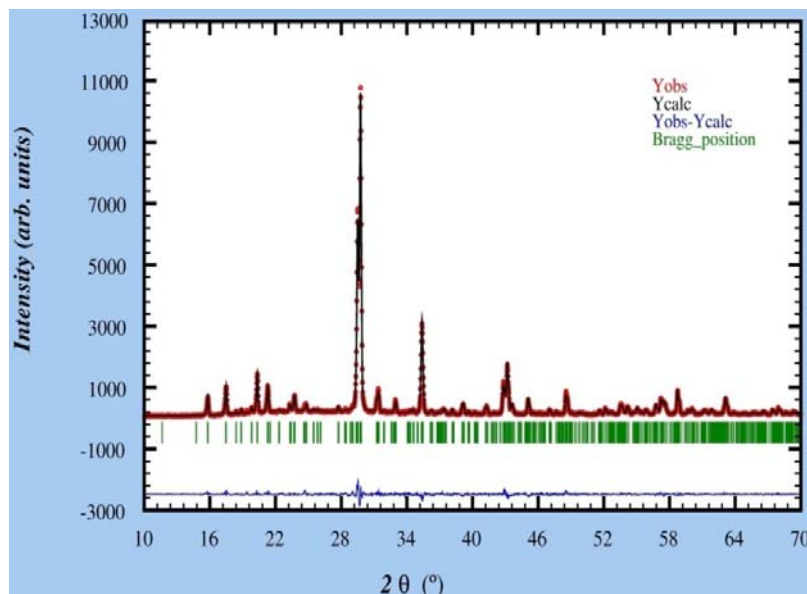


Figure 7.1: Rietveld- refined X-ray diffraction pattern of α - $\text{Zn}_2\text{P}_2\text{O}_7$

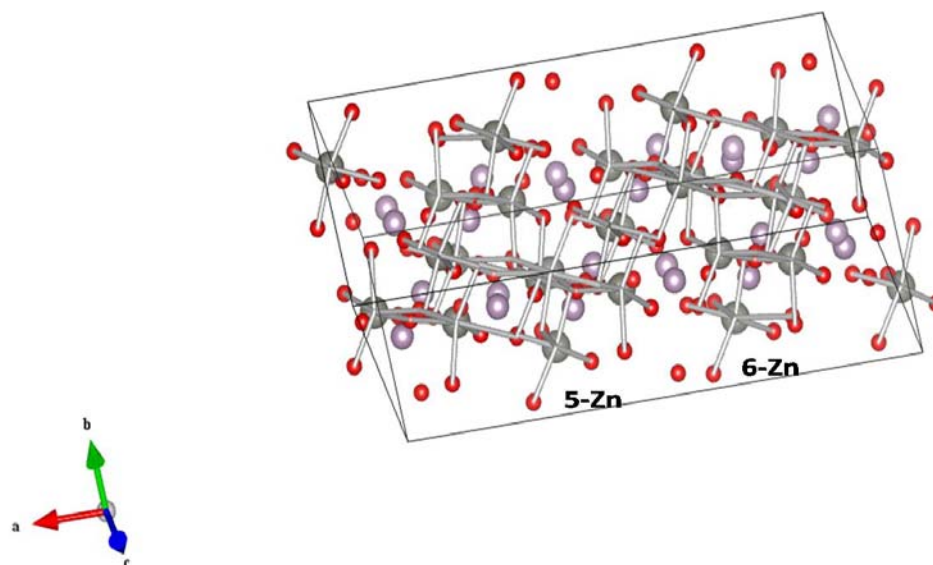


Figure 7.2: Crystal structure of α - $\text{Zn}_2\text{P}_2\text{O}_7$

7.2.2.2. Compositional characterization- FTIR

The FTIR investigation was carried out to confirm the bonds present in the samples. Figure 7.3 shows the FT-IR spectra of zinc pyrophosphate. The peaks at 3417.5 cm^{-1}

and 1645.3 cm^{-1} correspond to the stretching vibration of -OH group and the bending vibration of adsorbed molecular water, respectively. As the strength of P-O bond in the P-O-P Bridge is weaker than in the $(\text{PO}_2)^{2-}$ radical, the stretching frequencies of the P-O-P Bridge are expected to be lower than those in the $(\text{PO}_2)^{2-}$ radical [318]. The asymmetric and symmetric stretching frequencies of the $(\text{PO}_2)^{2-}$ radical are generally observed in the frequency areas $1100\text{--}1000\text{ cm}^{-1}$, $1000\text{--}900\text{ cm}^{-1}$, respectively [319] in the present investigation, it was observed around 1062 cm^{-1} and 962 cm^{-1} , respectively, for pure zinc pyrophosphate. Asymmetric P-O-P bridge vibration was observed at 570 cm^{-1} . Metal-oxygen stretching vibration was observed in the region $400\text{--}520\text{ cm}^{-1}$. The multiplication and fineness of the absorption bands of phosphates lie in the lower range, which indicate complexity of the internal crystalline structure of the $[\text{PO}_4]$ tetrahedron. The degree of condensation of the anion, $[\text{PO}_4]^{3-}$ to $[\text{P}_2\text{O}_7]^{4-}$ is directly related to its multiplicity of absorption bands [320]. Table 7.1 represents the assignments of different absorption bands in FT-IR spectrum of pyrophosphate crystals.

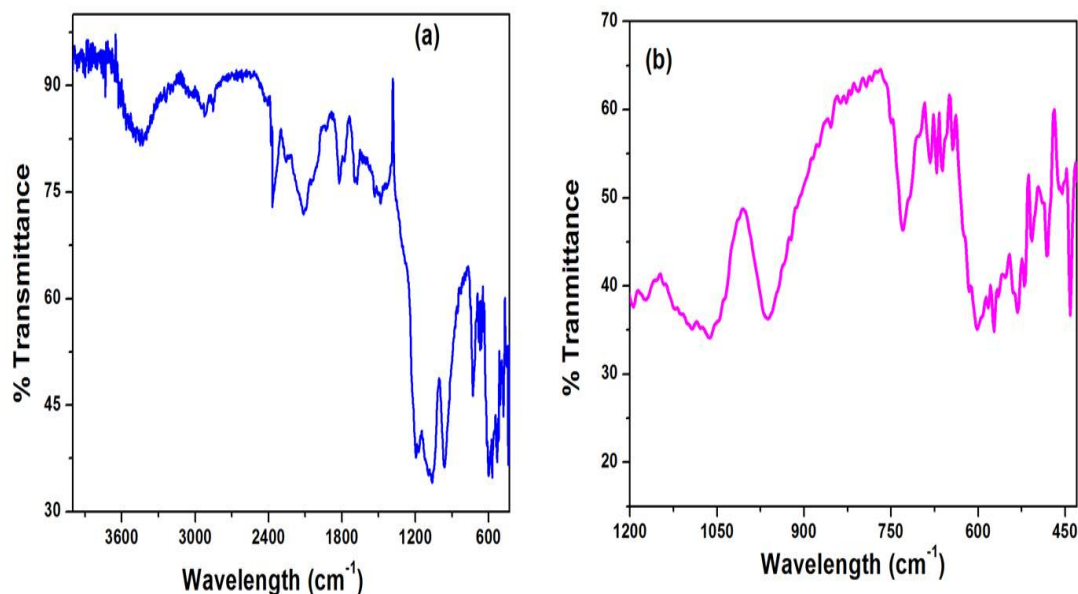


Figure 7.3: FTIR spectrum of zinc pyrophosphate crystals. (a) Full range 4000-400 (extended range) and (b) $1200\text{--}430\text{ cm}^{-1}$ (absorption band of phosphate)

Table 7.1: Assignments of different absorption bands in the FT-IR spectrum of zinc pyrophosphate crystals

<i>Assignments</i>	Observed frequencies (cm⁻¹)
<i>O-P-O bending</i>	550.6, 505.3
<i>P-O Symmetric stretching bonds</i>	909.4, 990.4
<i>P-O Asymmetric stretching bonds</i>	1027.0, 1088.7
<i>Metal-Oxygen bands</i>	400 to 520

7.2.2.3. Phase transition: HTXRD, EPR and DSC

Two polymorphic transformations of zinc pyrophosphate have been known to exist. These are α and β modifications connected with each other by reversible transformation at 405 K. The high temperature β -modification exists to the temperature of congruent melting 1288 K [321]. Mn^{2+} being EPR sensitive are chosen as a probe ion to investigate structural phase transformation in powder zinc pyrophosphate because the isostructural relationship of the high-temperature forms permits a definite assignment of the Mn^{2+} site in the structure, and more importantly because the relatively high sensitivity of the ESR spectra to the Mn^{2+} environment might permit a detailed study of the various phase transitions. Same was corroborated with high temperature XRD (HTXRD) and Differential scanning Calorimetry (DSC). HTXRD pattern is shown in Figure 7.4a. There is pure α -phase at 120°C; phase transformation takes place at 405 K, which is having mixed features of α and β , but at 473 K pure β -phase is seen. Individual XRD pattern of α and β phase and their standard pattern is shown in Figure 7.4(b). Crystallographic data of zinc pyrophosphate is mentioned in Table 7.2. Lattice parameter obtained for β phase is $a = 6.61 \pm 0.01 \text{ \AA}$, $b = 8.29 \pm 0.01 \text{ \AA}$ and $c = 4.51 \pm 0.01 \text{ \AA}$ and $\beta = 105.4 \pm 0.2^\circ$

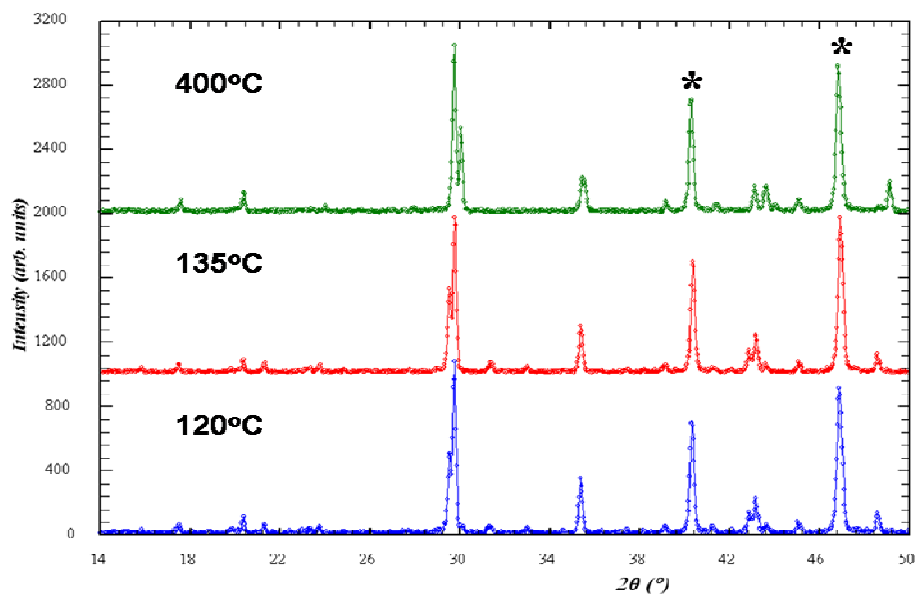


Figure 7.4a: XRD pattern of 2 mol% Mn²⁺ in Zn₂P₂O₇ at various temperatures. Asterisk indicates the pattern of Pt which arises due to usage of Pt-Rh as a sample holder in HTXRD

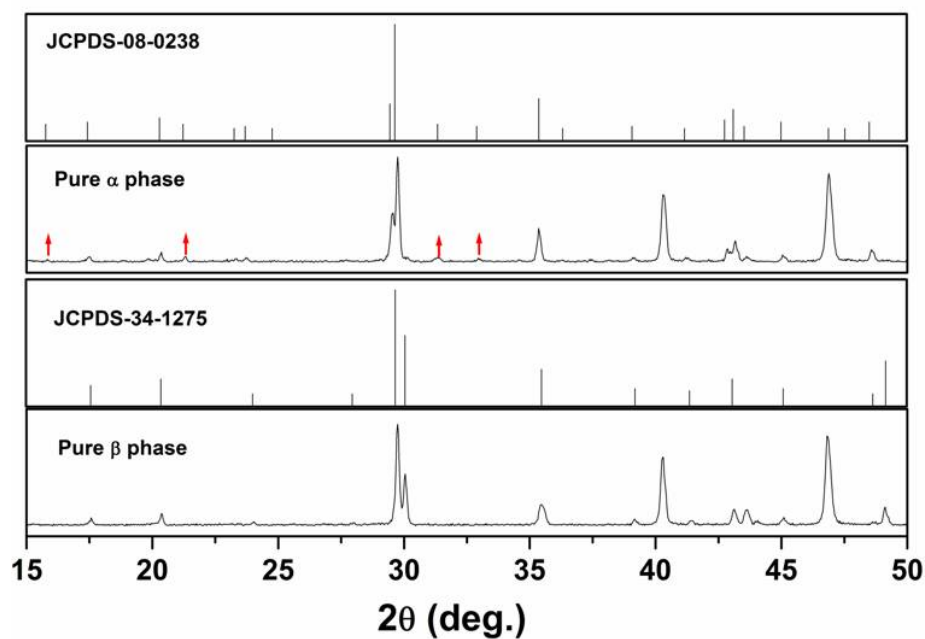


Figure 7.4b: XRD pattern α and β phase and their standard pattern of 2 mol% Mn²⁺ in Zn₂P₂O₇. Arrows indicate missing reflections in β-phase.

Table 7.2: Allotropic forms and crystallographic data of $\text{Zn}_2\text{P}_2\text{O}_7$

Allotropic Form	Space Group	Coordination Group	P-O-P angle (deg)	P-O bond length (Å)
α	I2/c	5,6	139 and 148	Mean P-O= 1.557
β	C2/m	Only 5	180 (linear)	P-O _{br} = 1.569 P-O _{nbr} = 1.553

Although structurally both α and β phases are same i.e. monoclinic, they crystallize in different space group. α -phase has lower symmetry I2/c space group where as β is having more symmetric C2/m space group. From XRD pattern, it can be seen that reflections at 2θ values of 16.414, 21.344, 30.0487 and 31.972 completely disappears in more symmetric β -phase. In the β -phase, the four cations in the unit cell lie on the twofold axes and are symmetry related by the centering operation (1/2, 1/2, 0) and by the mirror plane. The variation in unit cell volume from 298K to 1023 K is shown in Figure 7.5. On going from α to β phase, length of a- and c-axis are reduced by a factor of 1/3 and 1/2 as is observed using HTXRD. This is the reason for volume reduction unit cell while going from alpha to beta phase. There is sudden discontinuity in volume at 405 K, which shows that transition is of first order.

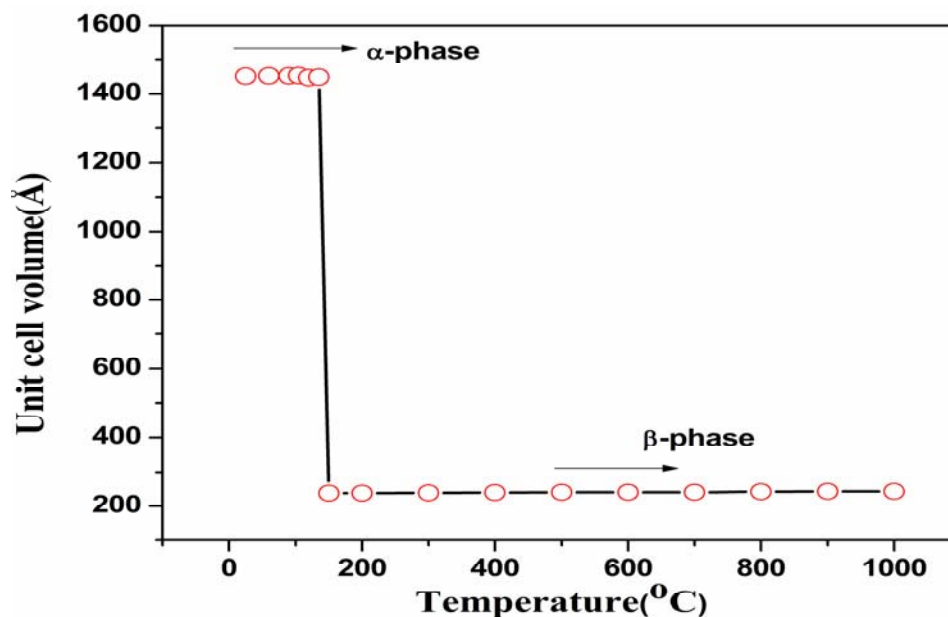


Figure 7.5: The temperature variation of unit cell volume of 2 mol% Mn^{2+} in $\text{Zn}_2\text{P}_2\text{O}_7$. Error bars are smaller than symbols.

This result has also been corroborated with dynamic scanning calorimetry (DSC). Around 405 K, zinc pyrophosphate undergoes a reversible, first order isostructural

transition, the phenomenon being supported by the differential scanning calorimetry data (Figure 7.6).

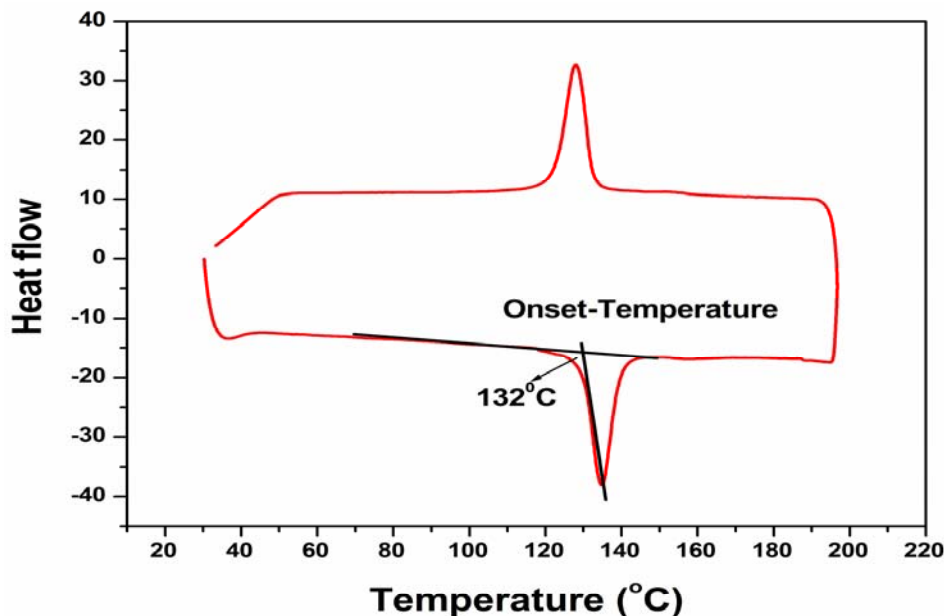


Figure 7.6: DSC studies of Mn doped $\text{Zn}_2\text{P}_2\text{O}_7$

The structure of α -phase is characterized by sequence of layers. A layer like that found in $\alpha\text{-Cu}_2\text{P}_2\text{O}_7$ is followed by two layers like those found in $\alpha\text{-Mg}_2\text{P}_2\text{O}_7$ [322]. The former layers have anions lying on twofold axes, and the cations are coordinated to five oxygen atoms; in the next two layers, half of the cations are five coordinates and another half is six coordinated, and the anions in these layers show only approximate twofold axes. All the anions show nonlinear P–O–P bonds.

The crystal structure of β -phase is identical with that of $\text{Mn}_2\text{P}_2\text{O}_7$ [323]. In β -phase, the structure is described by alternate anion and cation layers stacked along c direction and observed at $z=0$ and $z=1/2$, respectively. The asymmetric unit contains a unique Zn^{2+} cation. The short distance between cations along the c direction is about 4.51 Å. In the cationic layers, Zn^{2+} is found on twofold axes in irregular 6-fold coordination [324], i.e. they are not at the centre of the oxygen atom environment and displaced by about 0.3 Å from a line joining O3 to its mate generated by the twofold axis. The major component of these distortions arises from a rotation of the O3–O3 edge from its ideal position by 30° about the twofold axis. Such a distortion arises from the constraints placed upon the positions of the oxygen atoms by the requirement of its bonding to the phosphorus atom. Detailed Crystallographic data of both these two phases are mentioned in Table 7.2.

Temperature dependent EPR investigation of Mn in $\text{Zn}_2\text{P}_2\text{O}_7$ is shown in Figure 7.7. Chambers et al. [323] have reported EPR evidence for phase transition in single crystal of $\text{Zn}_2\text{P}_2\text{O}_7$ using Mn^{2+} as EPR probe. Their studies have showed that α - $\text{Zn}_2\text{P}_2\text{O}_7$, the stable phase at room temperature, undergoes a first order phase transition at 405 K and an inhomogeneous second order transformation between 405 K and 428 K. We could identify the phase transitions at 132°C in our powder sample; but second order phase transition is difficult to identify in powder sample, although small kink at 428 K was obtained in DSC studies (Figure 7.6), discussed earlier.

It can be seen from the EPR pattern (Fig. 7.7) that spectra changed drastically in going from 390 to 400 K. Highly resolved hyperfine sextet of Mn^{2+} could be seen till 390 K whereas at 400 K, the hyperfine splitting completely disappears and the spectrum merges to broad signal. Zero field splitting parameter (D) was evaluated for Mn^{2+} from room temperature to 500 K (Figure 7.8). It was observed that there is a sudden jump (discontinuity) in the value at 400 K (Phase transition temperature) confirming the transition to be of first order.

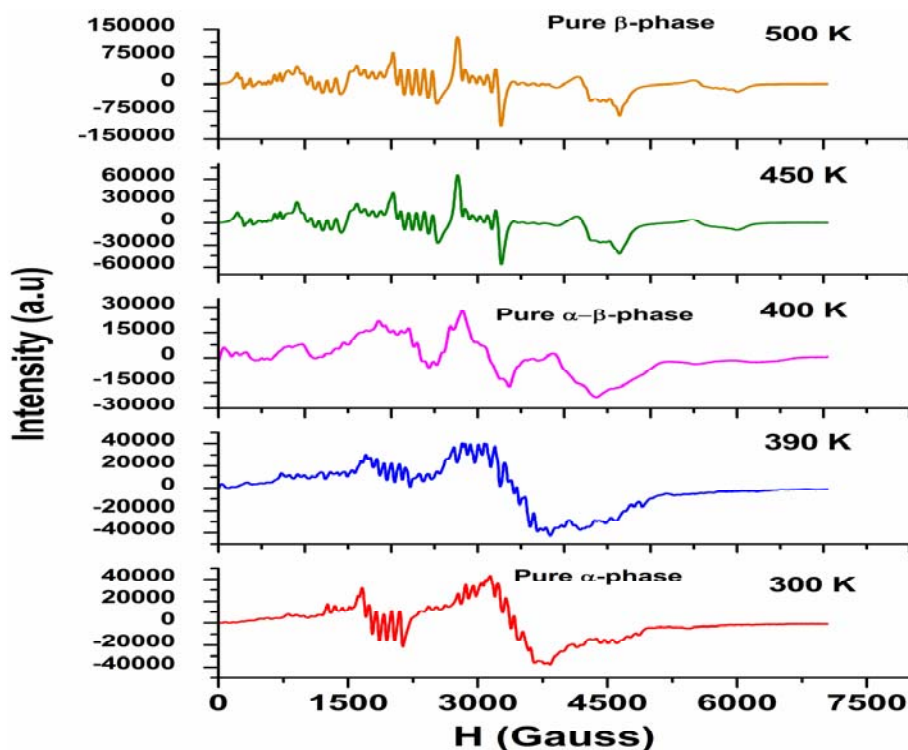


Figure 7.7: EPR spectra of 2 mol% Mn^{2+} in $\text{Zn}_2\text{P}_2\text{O}_7$ at various temperatures

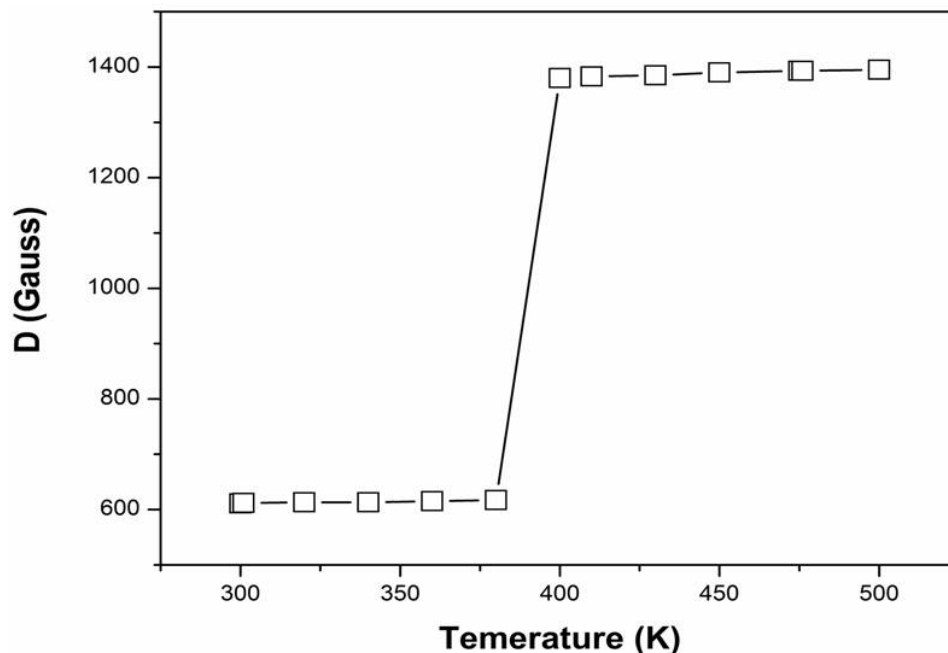


Figure 7.8: The temperature variation of the zero field splitting parameter for $\text{Zn}_2\text{P}_2\text{O}_7: \text{Mn}^{2+}$

The D value for Mn^{2+} in the β phase (1380 G) is unusually large. It is tempting to suggest that this large D value is related to the highly irregular cation environment. The D values in the intermediate temperature region however, show very large changes from their high-temperature value despite an apparently small change in the electron density distribution of the crystal. These observations could be consistent only if D depends on a higher power of a component of the crystalline field. The enhanced line broadening in β -phase could result from a residual short range ordering near the transition temperature, which yields a small spread in crystalline field. The fact that orthorhombic distortion term (E) is small in β -phase and large change in D across transition temperature suggests that the structural change involves primarily distortions along Zn-O3 bond. Since the bond between the central oxygen atom and adjacent phosphorous atom of the $[\text{P}_2\text{O}_7]^{4-}$ lies along the z -direction in the β -phase, it might be suggested that the mechanism for the change in structure involves primarily either a small change in length of these P-O bonds or a contraction of the P-O-P bond angle.

As evident by HTXRD and structural studies (Figure 7.4a), in α -phase there are two types of zinc ion; asymmetric 5 coordinated Zn^{2+} and relatively symmetric 6

coordinated Zn^{2+} (Zn1 and Zn2). In case of β -phase, only asymmetric 5-coordinated zinc exists (Zn1) as discussed earlier.

Main changes in EPR pattern from α to β phase is enhanced line broadening and unusual large zero field splitting parameter. This can be correlated to presence of distorted octahedra of oxygen around Zn^{2+} ion in β -phase. The phase transformation then requires that the five-fold coordinated sites of α phase form a sixth bond with oxygen atoms. This requires that oxygen atoms move from an average cation-oxygen distance of 3.2\AA to the "normal" bond distance of 2.15\AA found in $\beta \text{Zn}_2\text{P}_2\text{O}_7$.

7.3. Photoluminescence properties of europium doped $\text{Zn}_2\text{P}_2\text{O}_7$

7.3.1. Excitation and emission spectroscopy properties of $\text{Zn}_2\text{P}_2\text{O}_7:\text{Eu}^{3+}$

Figure 7.9 shows excitation spectra ($\lambda_{\text{em}} = 592 \text{ nm}$) of Eu doped zinc pyrophosphate sample. A broadband in the region of 220–280 nm has been attributed to the $\text{O}^{2-} \rightarrow \text{Eu}^{3+}$ charge transfer band (CTB), which is caused by the electron transfer from 2p orbits of O^{2-} ions to 4f shells of Eu^{3+} ions. The sharp lines in 300–500 nm are attributed to intra-configurational 4f–4f transition of Eu^{3+} in host lattice. The peaks seen at 320, 360, 380, 395, 420, 460 and 480 nm were assigned to electronic transitions of ${}^7\text{F}_0 \rightarrow {}^5\text{H}_3, {}^5\text{L}_9, {}^5\text{L}_7, {}^5\text{L}_6, {}^5\text{D}_4, {}^5\text{D}_3$ and ${}^5\text{D}_2$ respectively.

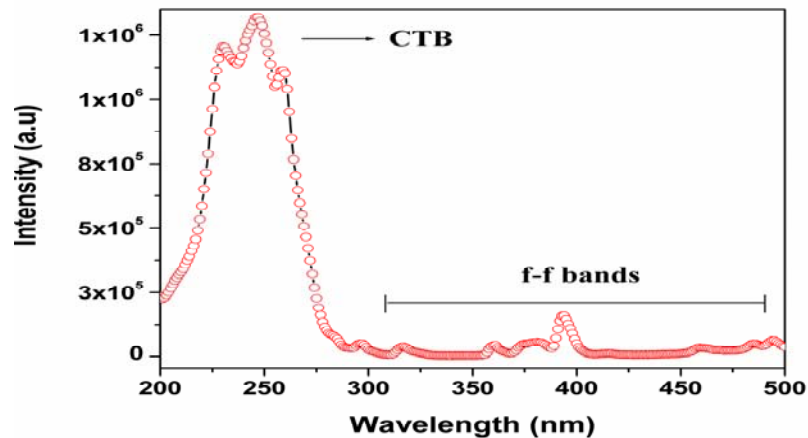


Figure 7.9: Excitation spectra of $\text{Zn}_2\text{P}_2\text{O}_7:\text{Eu}^{3+}$ powder sample ($\lambda_{\text{em}}=592 \text{ nm}$)

Emission spectra was recorded for weighed amount of undoped and doped sample at $\lambda_{\text{ex}} = 230 \text{ nm}$ (charge transfer band, CTB) under similar condition and is shown in figure 7.10. It was observed that there is a broad band ranging 400–560 peaking at 440

nm. This emission was assigned to oxygen related defects in the lattice of zinc pyrophosphate. No emission from the host was observed in europium doped sample, indicating the efficient energy transfer from the host to Eu^{3+} ions.

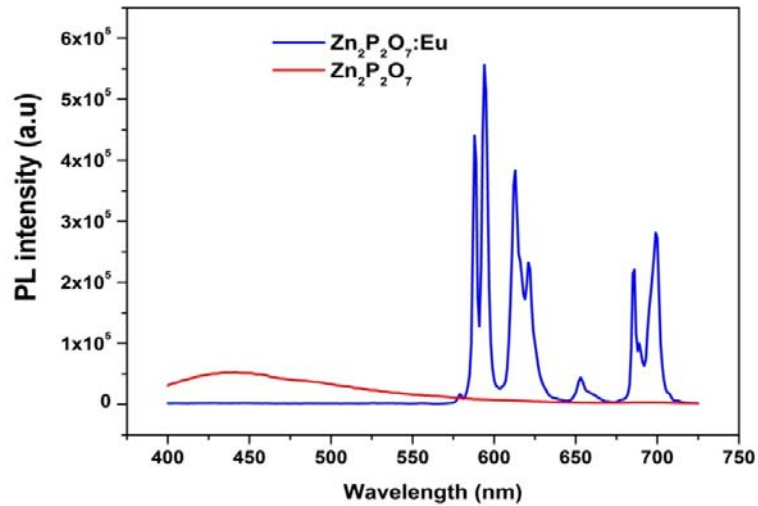


Figure 7.10: Emission spectra at 230 nm excitation wavelength of undoped and doped zinc pyrophosphate

Figure 7.11 shows the emission spectra for $\text{Zn}_2\text{P}_2\text{O}_7:\text{Eu}^{3+}$ at $\lambda_{\text{ex}} = 230$ nm (charge transfer band, CTB), $\lambda_{\text{ex}} = 254$ nm corresponding to Hg excitation used in Hg based fluorescent lamps and $\lambda_{\text{ex}} = 395$ nm (f-f band) respectively. The spectra consists of series of peaks in the range of 560-720 nm corresponding to the characteristic transition of Eu^{3+} , from the excited $^5\text{D}_0$ state to $^7\text{F}_J$ ($J=0-4$) levels. Upon excitation at 230 nm (CTB), the emission spectrum exclusively contains the strong bands of $^5\text{D}_0 \rightarrow ^7\text{F}_1$ (592 nm), $^5\text{D}_0 \rightarrow ^7\text{F}_2$ (613), $^5\text{D}_0 \rightarrow ^7\text{F}_3$ (653 nm) and $^5\text{D}_0 \rightarrow ^7\text{F}_4$ (704 nm). Upon excitation with 395 nm and 254 nm, emission properties similar to that of 230 nm excitation were observed. Excitation wavelength does not drastically change the spectral features for $^5\text{D}_0 \rightarrow ^7\text{F}_J$ emission of Eu^{3+} . The orange emission (590–600 nm) of Eu^{3+} due to the magnetic dipole transition (MDT) $^5\text{D}_0 \rightarrow ^7\text{F}_1$ was not affected much by the site symmetry, because they are parity-allowed, while the red emission (~610–630 nm) due to the electric dipole transition (EDT) of $^5\text{D}_0 \rightarrow ^7\text{F}_2$, being hypersensitive, was affected by the site symmetry of Eu^{3+} ion. Moreover $^5\text{D}_0 \rightarrow ^7\text{F}_1$ line at 592 nm (MD) was stronger in comparison to $^5\text{D}_0 \rightarrow ^7\text{F}_2$ line at 613 nm (ED) on excitation with all the three wavelengths (but I_{613}/I_{592} is different), which indicated that predominant spectral features are due to Eu^{3+} having Centro-symmetric environment.

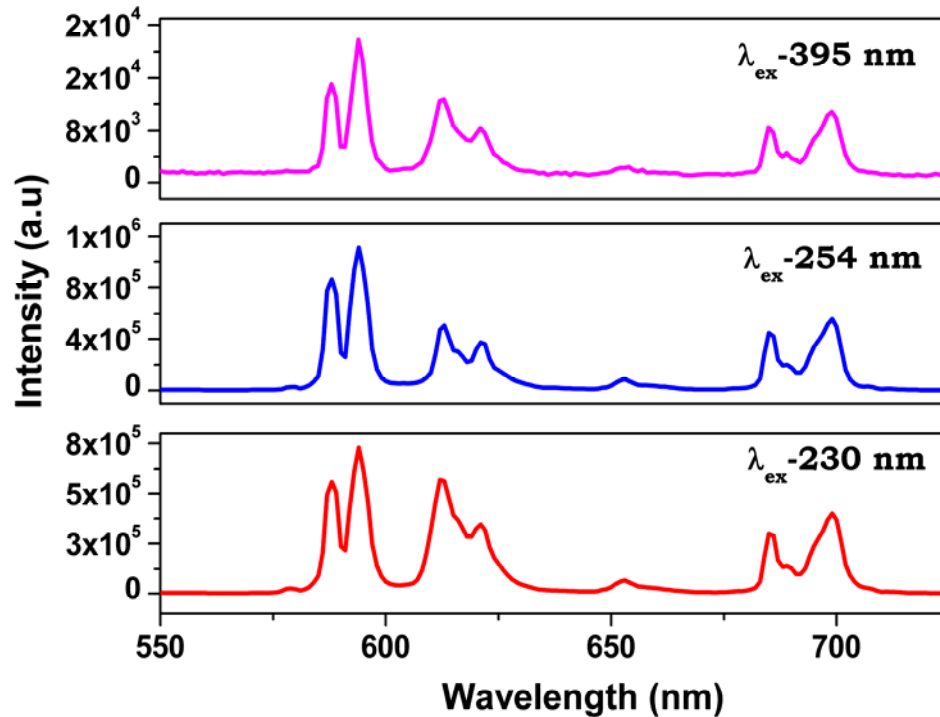


Figure 711: Emission spectra at different excitation wavelength of $\text{Zn}_2\text{P}_2\text{O}_7:\text{Eu}^{3+}$

7.3.2. Life-Time and time resolved fluorescence spectroscopy (TRES):

Zn has two lattice sites (5 and 6-coordinated Zn) in zinc pyrophosphate structure, namely S_1 and S_2 as already discussed, that can be occupied by the Eu^{3+} ions. To get an idea about the nature of the dopant ion occupancy in these lattice sites, PL decay time (life time) studies were conducted. The decay curves corresponding to the $^5\text{D}_0$ level of Eu^{3+} ions in the 2 mol % europium doped $\text{Zn}_2\text{P}_2\text{O}_7$ shown in Figure 7.12 at excitation wavelength of 395 nm, monitoring emission at 592 nm. For $\text{Zn}_2\text{P}_2\text{O}_7:\text{Eu}^{3+}$, a good fit was found to a biexponential decay using the following equation:

$$I(t) = A_0 + A_1 \exp\left(\frac{-t}{\tau_1}\right) + A_2 \exp\left(\frac{-t}{\tau_2}\right) \quad (7.1)$$

where A_0 , A_1 , A_2 and A_3 are scalar quantities obtained from the curve fitting, t is the time and τ_1 , and τ_2 are decay time values for exponential components, respectively. The percentage occupancy of Eu^{3+} ions exhibiting a specific life-time is obtained in such case using the formula

$$\% \text{ of species (n)} = \left[\frac{(A_n \times \tau_n)}{\sum_{n=1,2} A_n \times \tau_n} \right] \times 100 \quad (7.2)$$

Broadly, the analysis showed the presence of two components; one short lived and one long lived. The life time values were 620 μs (short component, T_1 , 50 %) and 1.77 ms (long component, T_2 , 50 %), which can be indicative of the presence of two emitting species or states.

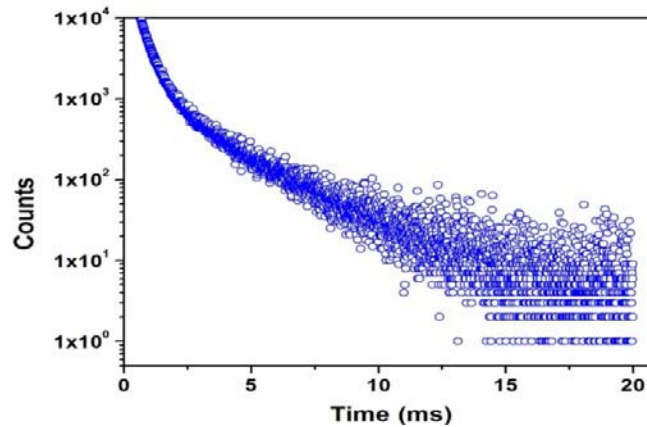


Figure 7.12: Luminescence decay time profile of Eu doped zinc pyrophosphate at λ_{ex} -395 nm under λ_{em} -592 nm

In order to identify the environment associated with the species exhibiting different life-times, time resolved emission spectra were recorded with 395 nm excitation at different time-delays with constant integration time. Figure 7.13 shows the spectra recorded with time delays of 100 μs , 1.1 ms and 3.1 ms respectively with constant integration time of 400 μs . As seen from the Figure 7.13, on excitation with f-f band of Eu^{3+} and after giving a delay time of 100 μs ; characteristic emission predominated by Eu^{3+} ions in symmetric environment (Intensity₍₅₉₄₎ > Intensity₍₆₁₄₎) was observed; here T_1 is the predominant species since we have integrated for very short duration.

With longer delay T_1 species completely decayed and the spectrum corresponding to only T_2 species was observed. Thus the spectra observed after 3.1 ms delay is expected only due to T_2 (1.77 ms). The spectra shows stronger emission from ${}^5\text{D}_0 \rightarrow {}^7\text{F}_2$ transition indicating that the T_2 can be ascribed to Eu^{3+} ions having asymmetric environment .

The spectra obtained after 1.1 ms delay time had contributions from both T_1 and T_2 species. The respective spectra for the T_1 and T_2 species obtained after applying suitable correction factors are given in Figure 7.14 below.

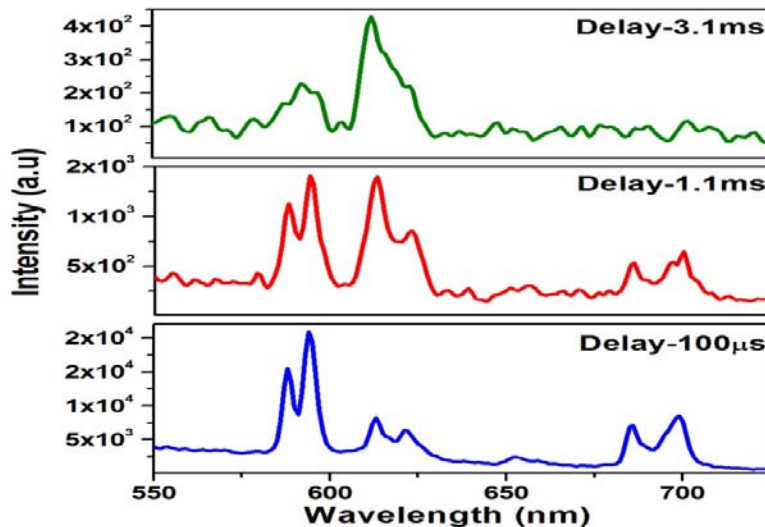


Figure 7.13: Time-resolved emission spectra of $Zn_2P_2O_7:Eu^{3+}$ under the excitation at 395 nm after giving suitable delay

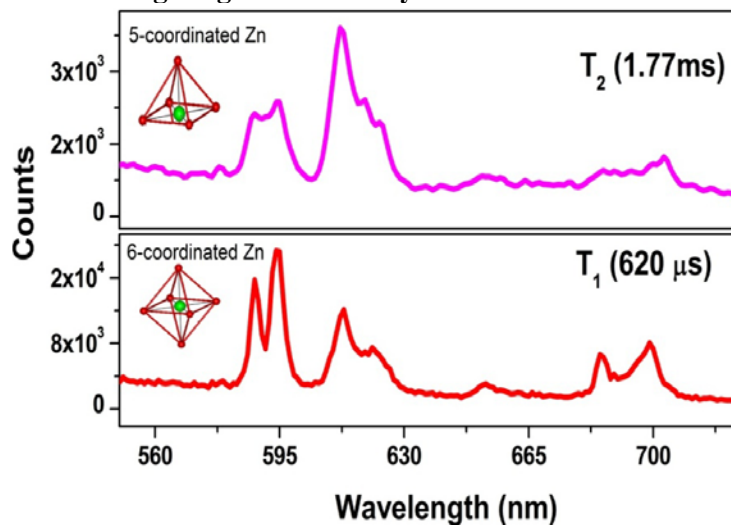


Figure 7.14: Time-resolved emission spectra of $Zn_2P_2O_7:Eu^{3+}$ under the excitation at 395 nm for short and long lived species

In the structure of α - $Zn_2P_2O_7$, 5-coordinated Zn (S_1 site) is surrounded by five nearest neighbour oxygen ions in the form of trigonal-bipyramid, which is a more distorted structure than that of the 6-coordinated Zn (S_2) site with regular octahedra. The symmetric environments observed for T_1 (620 μ s) can be because of Eu^{3+} ions occupying S_2 with inversion symmetry and asymmetric scenario for T_2 (1.77 ms) can

be ascribed to Eu^{3+} ions occupying S_1 without inversion symmetry. This Site selectivity of Eu^{3+} in $\text{Zn}_2\text{P}_2\text{O}_7$ is pictorially represented in Figure 7.15.

As seen from the figure, emission observed for T_1 (620 μs) is predominated by Eu^{3+} ions in symmetric environment with inversion symmetry and emission spectra obtained for T_2 (1.77 ms) corresponds to that of Eu^{3+} in asymmetric environment. This is unusual from the normal trend which suggests longer lived species occupy more symmetric sites and shorter one occupies more asymmetric sites. This anomalous behavior is explained in section 7.3.3.

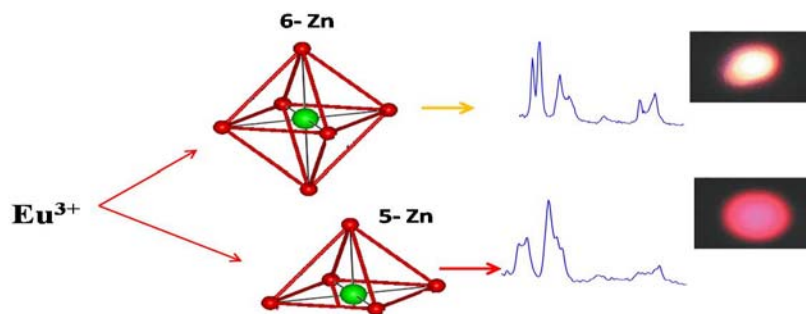


Figure 7.16: Site selective emission of Eu^{3+} in $\text{Zn}_2\text{P}_2\text{O}_7$

7.3.3. Judd-Ofelt Analysis:

The J-O parameters and radiative properties for the two types of Eu^{3+} species were calculated and mentioned in Table-7.3. It can be seen from the table that, the radiative life times for symmetric species (T_1) is higher than the asymmetric species. That is for the RE ion in symmetric environment, the transition is less probable and the reverse is true for the species in asymmetric environment (5 coordinated). Thus with the help of τ_R values it is possible to correlate the symmetry and the decay times exactly. Moreover, the J-O intensity parameters (Ω_i) of Eu^{3+} ion in this matrix reveal information regarding the covalence and surrounding of the metal ion. The parameter Ω_2 is related to the covalency and structural changes in the vicinity of the Eu^{3+} ion (short range effect) and Ω_4 are related to the long-range effects. For the short lived species T_1 , the trend observed in the J-O parameters ($\Omega_2 < \Omega_4$) proves that the particular species is present in a more symmetric 6 coordinated Zn site (S_2) with a low degree of covalence of the metal-ligand bonds. On the other hand, for the long-lived species (T_2) the reverse trend is observed in the J-O parameter ($\Omega_2 > \Omega_4$), which

confirms that the long-lived species sits at more asymmetric 5 coordinated Zn site (S_1).

Table 7.3: Comparison of J-O intensity parameters and radiative properties for two different species Eu^{3+} in $\text{Zn}_2\text{P}_2\text{O}_7$

species	Ω_2 (10^{-20} cm^2)	Ω_4 (10^{-20} cm^2)	η (%)	A_{total} (s^{-1})	τ_R (ms)	τ_{NR} (ms)
T_1 (0.62 ms)	1.16	2.33	9.13	392	2.55	0.819
T_2 (1.77 ms)	3.16	2.83	41.2	530	1.89	27.8

7.4: Effect of crystal field: Mn doped $\alpha\text{-Zn}_2\text{P}_2\text{O}_7$

To see the effect of octahedral and square pyramidal crystal field: Transition metal will be a better candidate than lanthanide ion in which crystal field effect is more dominant; so 2.0 mol % Mn is doped as can be seen from figure 7.17.

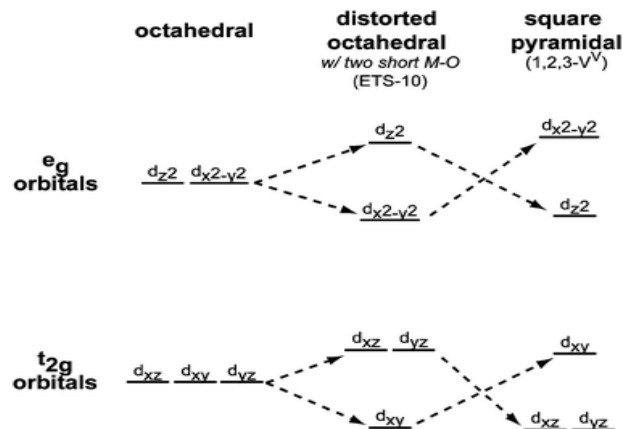


Figure 7.17: Crystal field splitting in octahedral and square pyramidal coordination.

7.4.1. EPR spectroscopy:

In the present study, EPR experiments have been used to get information about the oxidation state, the site occupancy and coordination sphere around the transition metal ions doped in different inorganic matrices [324, 325]. It is also useful in getting information about the local site symmetry around the paramagnetic ion and to quantify the number of unpaired spins of different paramagnetic ions present in different oxidation states. In addition, EPR is one of the most powerful tool used for studying structural phase transitions and magnetic phase transition in solids. This technique can differentiate between Mn^{2+} and Mn^{4+} due to the difference in number of fine transitions and the g values (Mn^{4+} , $S=3/2$, three fine transitions and $g < 2.00$; Mn^{2+} $S=5/2$, five fine transitions and $g=2.00$). However, Mn^{3+} (non Kramer ion with $S=2$) though paramagnetic, may not be detected due to the possibility of its ground

state being a singlet and a large zero field splitting. The ground state of Mn^{2+} with d^5 configuration is a most unique feature among d^n configurations in that there is only one state with maximum spin multiplicity (${}^6S_{5/2}$). In case of d^5 transition metal ions, the axial distortion of octahedral symmetry gives rise to three Kramer's doublets $\pm 5/2$, $\pm 3/2$ and $\pm 1/2$ [326]. Application of a Zeeman field lifts the spin degeneracy of the Kramer's doublets. In the present system, since the magnitude of crystal field splitting is greater than the microwave energy, the resonance observed is most likely to be due to transition within the lowermost Kramer's doublets ($\pm 1/2$). However, in cases where crystal field splitting is less than the microwave energy one can get all five fine transitions which further split to sextet because of the hyperfine interaction with ${}^{55}Mn$ (100% abundance, $I=5/2$).

The EPR spectra recorded for the polycrystalline sample of Mn doped zinc pyrophosphate is shown in Figure 7.18. The spectrum at room temperature and at 100 K consisted of signals arising due to manganese situated in two different oxidation states. An intense EPR signal with partially resolved hyperfine structure was observed at $g \sim 2.00$ (attributed to Mn^{2+} in octahedral co-ordination). On either side of this intense transition, two weak fine structures separated by $2D$ and $4D$ were observed ($D \sim 590$ G, $E \sim 12$ G) where D is the zero field splitting parameter and E is orthorhombic distortion term. Each fine transition showed an unresolved sextet hyperfine structure due to ${}^{55}Mn$ ($I=5/2$, 100% abundance, ${}^{55}A=80$ Gauss). It may be noted here that part of the Mn^{4+} signal overlaps with that of Mn^{2+} . The EPR spectrum due to Mn^{4+} showed a complex hyperfine pattern consisting of several differently resolved sextets. In polycrystalline samples, such complex EPR pattern of isolated Mn^{4+} ($3d^3$, $S=3/2$) and isolated Mn^{2+} ($3d^5$, $S=5/2$) ions essentially arise from the different fine structure terms (zero field splitting and orthorhombic distortion term), the g-factor for both the species (1.99 for Mn^{4+} and 2.00 for Mn^{2+}) being isotropic and close to that of free electron g-value. Table 7.4 lists the EPR parameters for isolated Mn^{4+} species. The spin Hamiltonian for Mn^{2+} ($S=5/2$) and Mn^{4+} ($S=3/2$) is given below:

$$\mathbf{H} = \beta \mathbf{B}_0 \cdot \mathbf{g} \cdot \mathbf{S} + D[\mathbf{S}_z^2 - (1/3)\mathbf{S}(\mathbf{S}+1)] + \mathbf{E}(\mathbf{S}_x^2 - \mathbf{S}_y^2) + \mathbf{I} \cdot \mathbf{A} \cdot \mathbf{S} \quad (3.3)$$

where B_0 is the external magnetic field, β is Bohr magneton, g is a g tensor, D is zero field splitting (ZFS) parameter, E is the orthorhombic distortion term, $I=5/2$ is the nuclear spin of ${}^{55}Mn$ and \mathbf{A} is the hyperfine interaction tensor. In the present study, the field positions of the Mn^{4+} resonance in $Zn_2P_2O_7$ are given in Table 7.5. The EPR

spectra of polycrystalline samples of Fe³⁺ (S=5/2) and Mn⁴⁺ (S=3/2) has been treated theoretically by Aasa and Van Reijen [327, 328]. The EPR of Mn⁴⁺ in zinc pyrophosphate gave four sextets at 103 mT, 149mT, 188.3 mT, 365 mT and a weak spectral line at 546.5 mT as seen from the second derivative spectrum shown in Fig.7.19.

These resonances are not part of Mn²⁺ in Zn₂P₂O₇. The plots of hv/D Vs. gβB₀/hv, reported by Van Reijen for Mn⁴⁺ ions were used for assignment of resonance lines and evaluation of spin Hamiltonian parameters E/D~0.20 and hv/D~0.3; D~1 cm⁻¹ (zero field splitting D>>hv). The large value of E/D indicates that Mn⁴⁺ is situated in a lower symmetry site, which probably arises due to the substitution of Mn⁴⁺ at Zn²⁺ site thereby invoking charge compensation by the presence of interstitial oxygen ions around Mn⁴⁺ ion (0.46 Å) or due to substitution of Mn at 5-coordinated zinc site (0.68 Å). EPR parameters for Mn²⁺ were evaluated using Bruker Simfonia simulation program (as zero field splitting in case of Mn²⁺ is moderate D << hv). The lower value of E/D for Mn²⁺ indicates that Mn²⁺ is situated in a higher symmetry site, which can arise due to the substitution of Mn²⁺ (0.69 Å) at 6-coordinated zinc site (0.74 Å).

The absolute concentration of the Mn²⁺ and Mn⁴⁺ species were deduced from the intensities of the integrated spectra with respect to CuSO₄ .5H₂O as standards. Weighed amounts of the standard and the sample were placed in EPR quartz tubes and kept in the resonant cavity for full length geometry. Under these conditions, the number of spins, N, for the sample ‘‘a’’ and ‘‘b’’ for the standard are related by equation [329],

$$N_a = \frac{N_b g_b S_b (S_b + 1) A_a}{g_a S_a (S_a + 1) A_b} \quad (7.4)$$

Where A is the integrated area normalized for the instrument condition, g the average g-value and S the electronic spin of the sample. The estimated concentration of Mn²⁺ and Mn⁴⁺ were found out to be 60 and 40% respectively. This is in close agreement with our findings which says that there are 65% 5-coordinated Zn²⁺ site and 35 % 6-coordinated Zn²⁺ site.

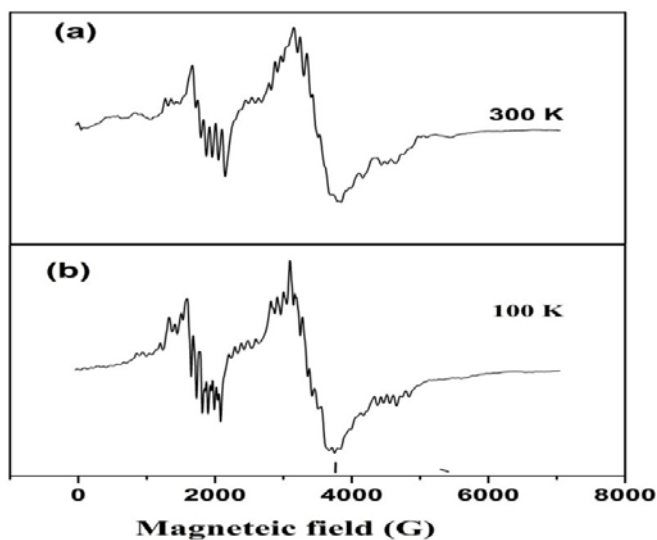


Figure 7.18: EPR spectra of monoclinic 2 mol% Mn doped $\text{Zn}_2\text{P}_2\text{O}_7$ (a) at 300 K and (b) 100 K.

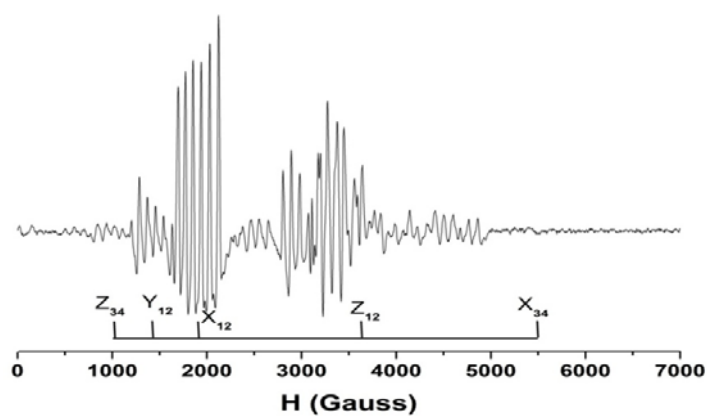


Figure 7.19: Second derivative EPR spectra of Mn in $\text{Zn}_2\text{P}_2\text{O}_7$.

Table 7.4: EPR parameters of isolated Mn^{4+} in monoclinic zincpyrophosphate matrix

Sextet	g	A/Gauss
1	6.626	87
2	4.5989	85
3	3.6390	85.5
4	1.8774	80
5	1.2539	Not resolved

Table 7.5: Peak assignments of isolated Mn⁴⁺ species in monoclinic Zinc pyrophosphate matrix

Sextet	Shape	g ₀ /g	Assignments	Resonance field(G)
1	a	0.2991	Z ₃₄	1035
2	a	0.4305	Y ₁₂	1490
3	d	0.5441	X ₁₂	1883
4	e	1.0547	Z ₁₂	3650
5	e	1.5791	X ₃₄	5465

a. absorption; d, derivative; e, emission. The value of $g_0 = 1.980$ has been assumed. X,Y,Z are the canonical orientations and 1-4 the spin labels in order of increasing energy. The operating frequency of the spectrometer is 9.60 GHz.

7.4.2. PL spectroscopy:

Photoluminescence studies show the presence of both Mn²⁺ as well as Mn⁴⁺ in zinc pyrophosphate. In the emission spectra shown in Figure 7.20 two bands were observed: one is centered at 500 nm (green emission) and the other one is centered at 686 nm (red emission) but with different intensity. The wide emission bands in red with a maximum at 686 nm are attributed to the electronic transition between ²E and ⁴A₂ of Mn⁴⁺ accompanied with vibronic transitions. The green emission observed at 500 nm is attributed to the ⁴T_{1g} (⁴G)–⁶A_{1g} (⁶S) transition of Mn²⁺. The excitation spectrum shown in Figure 7.21 monitored at 686 nm and 500 nm consists of broad features at 230 nm and 250 nm respectively which are assigned to Mn²⁺-O²⁻ and Mn⁴⁺-O²⁻ charge transfer band (CTB) respectively. Mn (IV) is more electropositive than Mn (II). Therefore, it could be easier for the electronic transition from the 2p orbital of O²⁻ to the 3d orbital of Mn⁴⁺ than that in Mn²⁺ and thus the CTB energy of

Mn^{4+} is less than that for Mn^{2+} compound. Therefore Mn (IV)-O CTB is red shifted w.r.t Mn (II)-O CTB. It was also evident from the emission spectra that on excitation with 250 nm PL intensity of Mn (II) is more than that of Mn (IV) whereas as reverse is true in case of 230 nm (Fig. 7.20). Crystal field of square pyramidal is more than octahedral as is observed in figure 7.17. Generally green emission -arise from weak crystal field and the red one from stronger crystal field. Based on above two points we can tell that Mn(II) -occupy Octahedral Zn(II) site and Mn(IV) occupy square pyramidal Zn(II) site

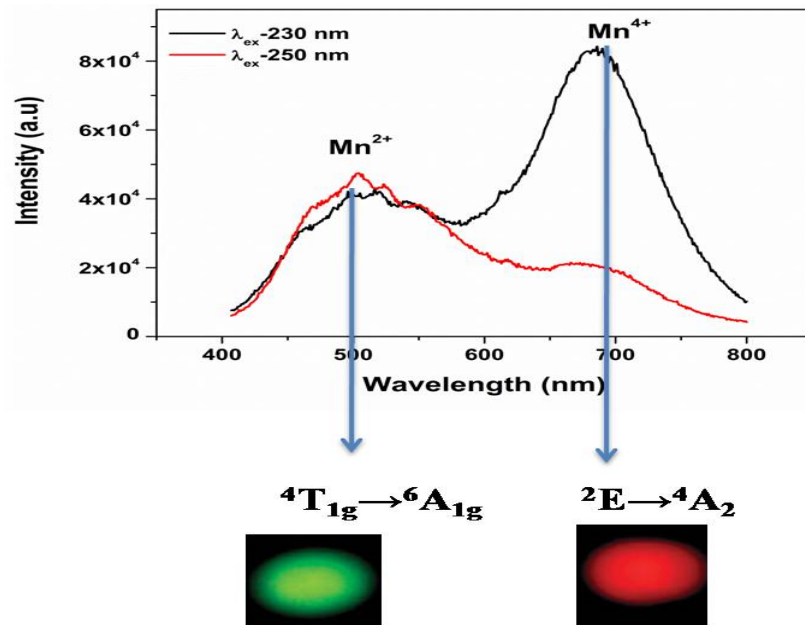


Figure 7.20: Emission spectra of Mn doped zinc pyrophosphate

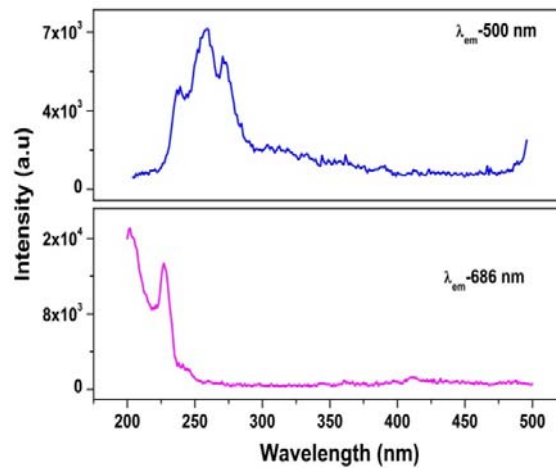


Figure 7.21: Excitation spectra of Mn doped zinc pyrophosphate

To confirm the presence of manganese as divalent and tetravalent state, the as prepared samples were heated in both oxidizing and reducing environments. It was observed from the emission spectra shown in figure 7.22 that the intensity of Mn^{4+} is higher in oxidizing atmosphere while that of Mn^{2+} is higher in a reducing atmosphere.

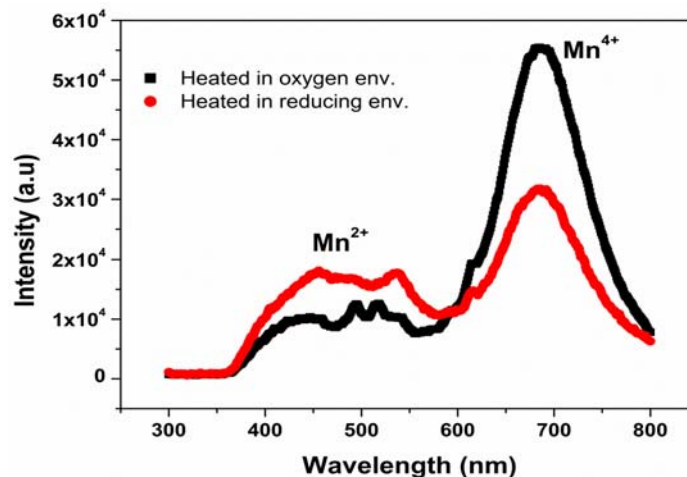


Figure 7.22: Emission spectra of Mn doped zinc pyrophosphate heated in oxidizing and reducing atmosphere

To evaluate the material performance on color luminescent emission, CIE chromaticity coordinates were evaluated adopting standard procedures. The values of x and y coordinates of the system were calculated to be 0.37 and 0.37 on excitation with 230 nm and 0.30 and 0.38 on excitation with 250 nm respectively. This is represented as the point ‘*’ in the CIE diagram shown in Figure 7.23. It is clear from the values that, $\text{Zn}_2\text{P}_2\text{O}_7:\text{Mn}$, gives a ‘near white’ emission.

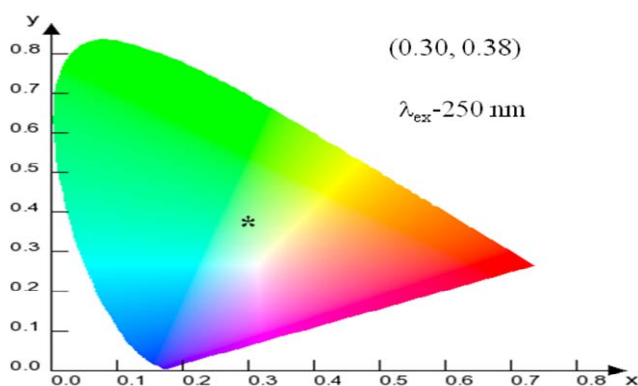


Figure 7.23: CIE index diagram of 2 mol% Mn doped $\text{Zn}_2\text{P}_2\text{O}_7$ in air showing the white emission (point *).

7.5: Exploring α - $\text{Zn}_2\text{P}_2\text{O}_7$ for synthesis of lanthanide ion based White LEDs:

7.5.1. Effect of synthesis condition (rare earth concentration and annealing temperature) on luminescence properties:

To evaluate the emission characteristics of the pyrophosphate host with the trivalent samarium ion as dopant, the RE ion concentration was varied from 0.1 mol% to 2 mol%. Figure 7.24a shows the dependence of the PL emission intensity (obtained with $\lambda_{\text{ex}} = 403$ nm) of the rare earth ion with varying doping concentration. Integral intensity of 597 nm ($^4\text{G}_{5/2}$ - $^6\text{H}_{7/2}$) is considered. It was observed that, the emission intensity of Sm^{3+} increases with the increase in concentration initially, reaching maxima at 1.0 mol % and then decreases with the increasing concentration due to concentration quenching. Thus the optimum concentration for Sm^{3+} is 1.0 mol %. The concentration quenching might be due to non-radiative energy transfer from one Sm^{3+} ion to another Sm^{3+} ion. Considering $X_c = 1\%$ (0.01), critical energy transfer distance R_c in $\text{Zn}_2\text{P}_2\text{O}_7:\text{Sm}^{3+}$ phosphor was calculated to be 29 Å. In this case, the Sm^{3+} - Sm^{3+} distance is larger than 10 Å. Thus the exchange interactions are ruled out. Therefore, the electric multipolar interaction is believed to be the only mode for the energy transfer among the Sm^{3+} ions in $\text{Zn}_2\text{P}_2\text{O}_7$. Since the highest intensity was observed for the 1 mol% doped sample, all further investigations were carried out on this particular sample only.

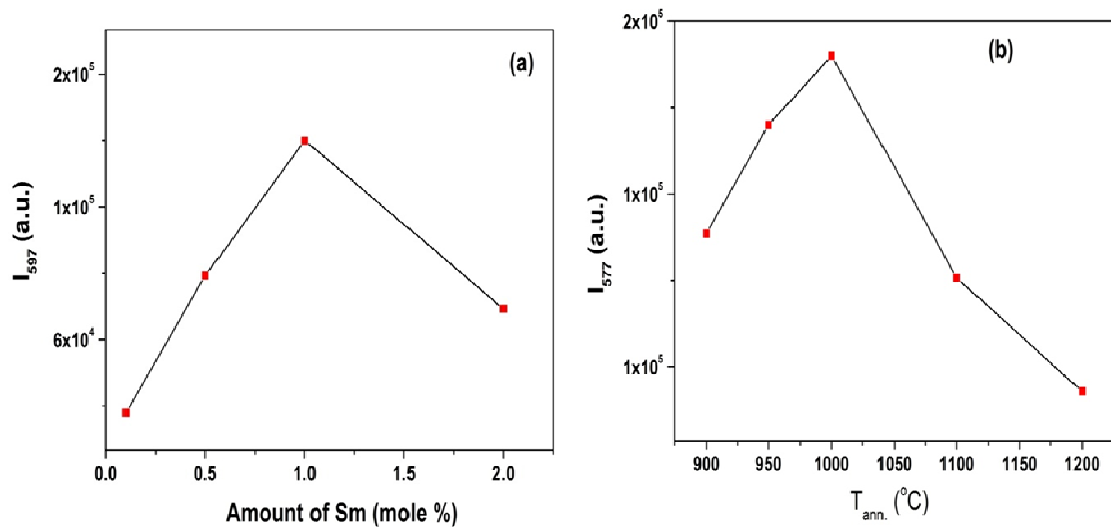


Figure 7.24: The PL emission intensity of Sm^{3+} as a function of its (a) concentration (b) annealing temperature in crystalline $\text{Zn}_2\text{P}_2\text{O}_7$.

To investigate the effect of annealing temperature on the PL properties of the 1 mol% Sm doped zinc pyrophosphate, the as-formed sample (finally heated at 900^oC) was further annealed at 950, 1000, 1100 and 1200 ^oC and the changes in PL intensity were measured and shown in figure 7.24 b. It was observed that, the PL intensity increased with increase in temperature up to 1000^oC; above this temperature, a decrease in intensity is observed. Initial increase in PL intensity is attributed to reduction in non-radiative transitions as a result of reducing surface defects with increasing annealing temperature up to 1000^oC. At 1100 ^oC and beyond, the annealed samples were highly agglomerated and can lead to reduced intensity because of scattering effects on incident and emitted light.

7.5.2. Excitation and emission spectroscopy of Zn₂P₂O₇: Sm³⁺

Figure 7.25a shows the excitation spectra of undoped and samarium doped zinc pyrophosphate. Broad band at around 240 nm in undoped sample is due O to P charge transfer. In case of doped sample there us a broad peak ranging from 220 to 280 nm which is due to overlap of O to P and O to Sm charger transfer process. Inset in spectra of doped sample is expanded f-f region of Sm³⁺. In the wavelength region 320–550 nm, several excitation peaks are observed and are located at 345nm (⁶H_{5/2}-⁶H_{13/2}), 362 nm (⁶H_{5/2}-⁴D_{3/2}), 376 nm (⁶H_{5/2}-⁶P_{7/2}), 403 nm (⁶H_{5/2}-⁴F_{7/2}), 417 nm (⁶H_{5/2}-⁶P_{5/2}), 438 nm (⁶H_{5/2}-⁴G_{9/2}), 462 nm (⁶H_{5/2}-⁴I_{9/2}), 469 nm (⁶H_{5/2}-⁴I_{11/2}), 473 nm (⁶H_{5/2}-⁴I_{13/2}) and 485 nm (⁶H_{5/2}-⁴I_{15/2}), which are attributed to f–f transitions of Sm³⁺. From the excitation spectrum, it was found that the intensity of f–f transition at 403 nm is high compared to the other transitions and thereby 403 nm has been chosen as an excitation wavelength for the measurement of emission spectra of Zn₂P₂O₇: Sm³⁺ phosphors. The most intense peak at 403 nm clearly indicates that these phosphors are effectively excited by near ultraviolet light emitting diodes.

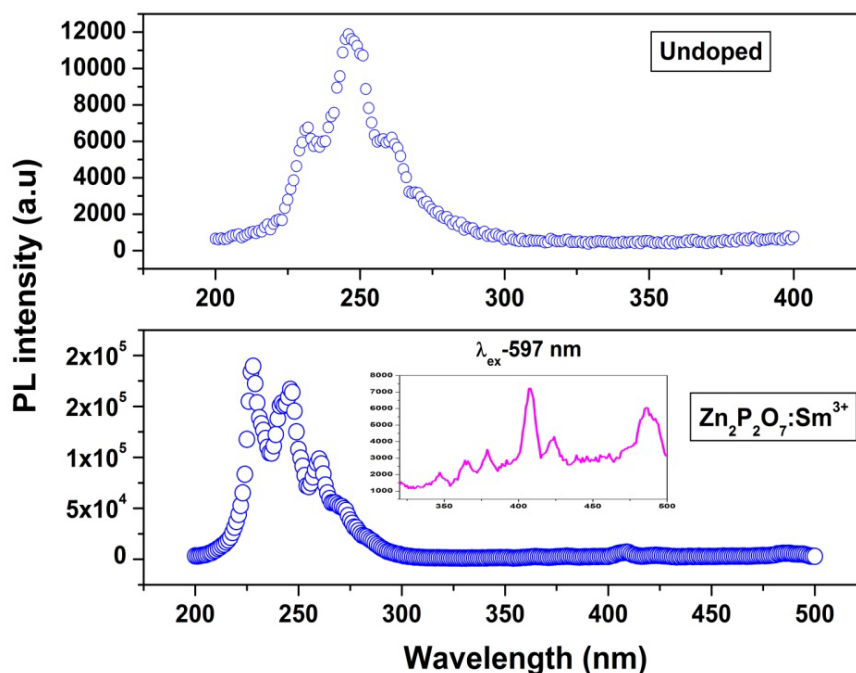


Figure 7.25: Excitation spectra of $\text{Zn}_2\text{P}_2\text{O}_7$ and $\text{Zn}_2\text{P}_2\text{O}_7: \text{Sm}^{3+}$. Inset in spectra of doped sample shows the expanded f-f region of Sm^{3+} .

Emission spectrum is recorded for weighed amount of undoped and doped sample under similar condition and is shown in Figure 7.26. It was observed that there is a broad band ranging 400-560 nm peaking at 475 nm for undoped sample. This emission is assigned to oxygen related defects in the lattice of zinc pyrophosphate. In doped sample there is some shift in host broad band in higher wavelength region; this may be because of decrease in band gap of zinc pyrophosphate on Sm^{3+} doping. The emission spectra of Sm^{3+} ions doped $\text{Zn}_2\text{P}_2\text{O}_7$ consist of two parts: one is due to host in the region of 400-550 nm and the other region is comprising of three sharp emission lines from 550 to 700 nm, which are the characteristic lines of the samarium ions. Three peaks at 565, 597 and 643 nm are ascribed to the ${}^4\text{G}_{5/2} - {}^6\text{H}_{5/2}$, ${}^4\text{G}_{5/2} - {}^6\text{H}_{7/2}$ and ${}^4\text{G}_{5/2} - {}^6\text{H}_{9/2}$ transitions of the Sm^{3+} ions respectively. Among these, the transition at 597 nm (${}^4\text{G}_{5/2} - {}^6\text{H}_{7/2}$) is having the maximum intensity, which corresponds to the red emission of $\text{Sm}^{3+}: \text{Zn}_2\text{P}_2\text{O}_7$ phosphors. It can be stated that the strong red emitting transition ${}^4\text{G}_{5/2} - {}^6\text{H}_{7/2}$ at 597 nm ($\Delta J = \pm 1$) is a partly magnetic dipole (MD) and partly electric dipole (ED) nature emission band. The other transition at 565 nm (${}^4\text{G}_{5/2} - {}^6\text{H}_{5/2}$) is purely MD natured and at 643 nm (${}^4\text{G}_{5/2} - {}^6\text{H}_{9/2}$) is purely ED natured, which is sensitive to crystal field. Generally the intensity ratio of ED and MD transition has been used to measure the symmetry of the local environment of the trivalent 4f ions.

The greater the intensity of the ED transition, the more the asymmetry nature. In our present study, the $^4G_{5/2}-^6H_{5/2}$ (MD) transition of Sm^{3+} ions is less intense than $^4G_{5/2}-^6H_{9/2}$ (ED) transition, which indicates Sm^{3+} ions preferentially occupy asymmetric site in $Zn_2P_2O_7$.

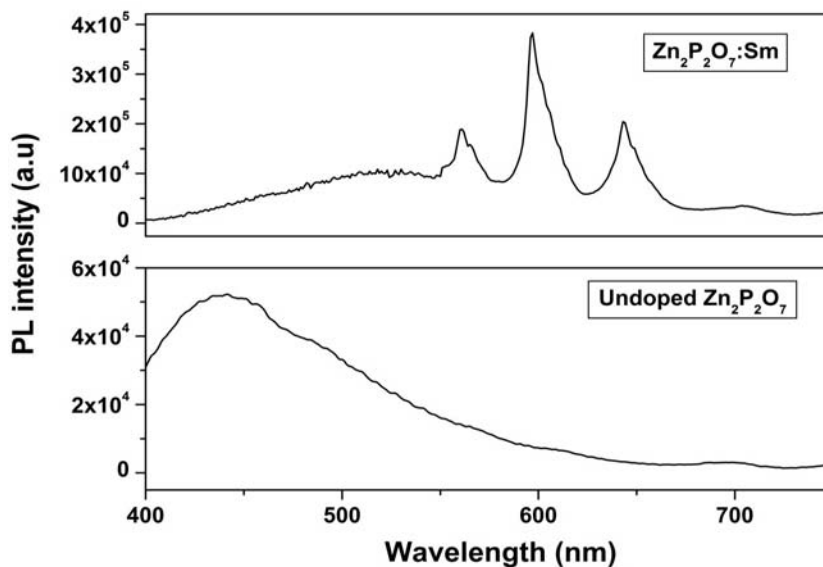


Figure 7.26: Emission spectra $Zn_2P_2O_7$ and $Zn_2P_2O_7: Sm^{3+}$

In order to evaluate the colorimetric performance of the phosphor, the color coordinates for the sample $Zn_2P_2O_7:Sm^{3+}$ (1mol %) were calculated using the intensity-corrected emission spectra excited by 403 nm. The calculated CIE coordinates for $Zn_2P_2O_7:Sm^{3+}$ (1mol %) are found to be 0.37 and 0.36 as indicated in the CIE chromaticity coordinate diagram and thereby confirms the near white color emission (on the boundary line of CIE white domain) as shown in Fig. 7.27.

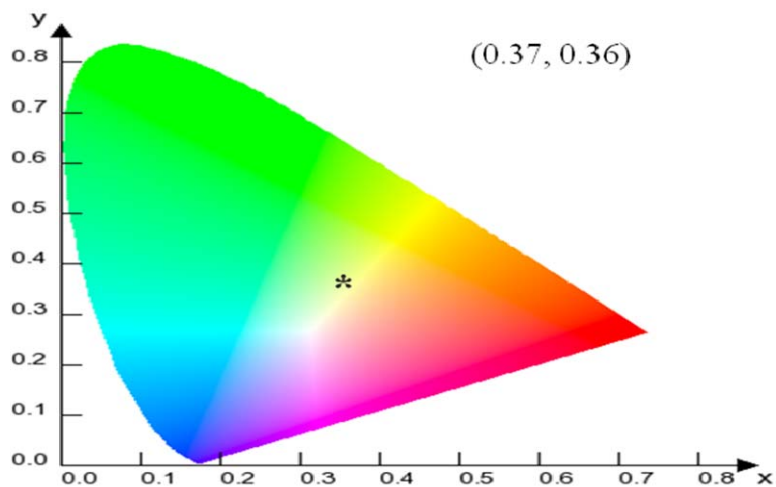


Figure 7.27: CIE index diagram of the $Zn_2P_2O_7: Sm^{3+}$

The correlated color temperatures (CCT) is also calculated using same equation as mentioned in 3.2. The value of CCT ($x= 0.37$ and $y= 0.36$) for $\text{Zn}_2\text{P}_2\text{O}_7:\text{Sm}^{3+}$ (1 mol %) is 4195 K. Since Zn has two lattice sites (5 and 6-coordinated Zn) in $\text{Zn}_2\text{P}_2\text{O}_7$, namely S_1 and S_2 as already discussed which can be occupied by the Sm^{3+} ions, PL decay time (life time) studies were also conducted and the obtained lifetimes value were tabulated in 5.6 . Broadly, the analysis showed the presence of two components; one short lived and one long lived. The life time values were $\sim 100 \mu\text{s}$ (short component, T_1) and 1.9 ms (long component, T_2) which can be indicative of the presence of two emitting species or states.

Table 5.6: Life time data for $\text{Zn}_2\text{P}_2\text{O}_7:\text{Sm}^{3+}$ at $\lambda_{\text{ex}}=403 \text{ nm}$ under different λ_{em}

Emission wavelength	$\tau_1(\mu\text{s})$	$\tau_2(\text{ms})$
565	102	1.92
597	107	1.93
643	104	1.97

Assuming a given phonon energy (same host for the lanthanide ions), a relatively longer PL decay time should be attributed to a more symmetric site, as the f-f transition becomes more forbidden, whereas a shorter decay time is often associated with an asymmetric site due to relaxation in the selection rules. In the structure of $\alpha\text{-Zn}_2\text{P}_2\text{O}_7$, 5-coordinated Zn (S_1 site) is surrounded by five nearest neighbour oxygen ions in the form of square pyramidal, which is a more heavily distorted structure than that of the 6-coordinated Zn (S_2) site with regular octahedra. Species T_1 (100 μs) arises because of Sm^{3+} ions occupying S_1 without inversion symmetry whereas T_2 (1.77 ms) can be ascribed to Sm^{3+} ions occupying S_2 with inversion symmetry.

In the $\text{Zn}_2\text{P}_2\text{O}_7:\text{Sm}^{3+}$ phosphor, Sm^{3+} ion is incorporated into a host lattice and substitutes for Zn^{2+} ion, in which the substitution is imbalanced. To maintain the electrical neutrality, two Sm^{3+} ions should substitute for three Zn^{2+} ions. So the defects that affect the luminescent intensity exist in the $\text{Zn}_2\text{P}_2\text{O}_7:\text{Sm}^{3+}$. One vacancy

defect of V''_{Zn} with two negative charges, and two positive defects of Sm_{Zn}^{\cdot} would be created by each substitution of every two Sm^{3+} ions in $Zn_2P_2O_7$.

7.6. Summary:

In summary, the polymeric precursor method has been successfully applied for the synthesis of α - $Zn_2P_2O_7$. We could identify the phase transitions between 390 and 400 K in our powder sample by EPR and HTXRD. DSC confirmed that the transition is reversible and is of 1st order. In case of $Zn_2P_2O_7: Eu^{3+}$, PL Emission and decay time data of the sample suggested the stabilization of the rare earth ion at two different sites. The first type was a long lived species ($\sim\tau= 1.77$ ms) present at asymmetric '5-coordinated Zn (square pyramidal, S_1)' sites and the second was a short lived component ($\tau= 620$ μ s) present at relatively symmetric '6-coordinated Zn (octahedral, S_2) sites. Low temperature PL experiment did not give any light on this except the enhancement in emission intensity and decay time. This unusual phenomenon was explained by calculating theoretical value of radiative lifetime- J-O calculations. Radiative life time of Eu^{3+} species present in symmetric environment was higher than that of the species present in asymmetric environment, which is consistent with the selection rules governing the transition. To see the effect of octahedral and square pyramidal crystal field, Transition metal ion will be a better candidate than lanthanide ion, for which crystal field effect is more dominant; Hence Manganese ion was doped in the host lattice. Based on EPR and PL investigations, it was inferred that Mn is getting stabilized as both Mn (II) and Mn (IV). Crystal field of square pyramidal is more than octahedral and generally green emission - arises from weak crystal field and the red one from stronger crystal field. Based on above two points, we can conclude that Mn (II) –occupies octahedral Zn(II) site and Mn(IV) occupies square pyramidal Zn(II) site. For exploring zinc pyrophosphate as a luminescent host, Sm^{3+} doped $Zn_2P_2O_7$ was synthesised. Upon near UV light excitation (403 nm), $Zn_2P_2O_7:Sm^{3+}$ exhibits host emission at 450 nm along with characteristic emission lines of Sm^{3+} . Based on PL decay measurement, it was inferred that two different types of Sm^{3+} ions were present in the zinc pyrophosphate. The first type was a short lived species ($\sim\tau= 100$ μ s) present at less symmetric '5-coordinated Zn' sites, while the second was a long lived species ($\sim\tau= 1.9$ ms) present at symmetric '6-coordinated Zn' sites. The colour coordinates of the system were evaluated using CIE index

diagram to be 0.36 and 0.37, which suggested that the prepared material is a potential near white light emitting phosphor. As a luminescent material $\text{Zn}_2\text{P}_2\text{O}_7$: Eu^{3+} gives red/orange emission depending on the site occupancy of europium ion, while $\text{Zn}_2\text{P}_2\text{O}_7$ doped with Mn and Sm gives near white emission.

Conclusions and future scope

Conclusions

The work presented in this thesis deals with the synthesis and characterization of a variety of inorganic luminescent materials based on oxides viz. silicate, zirconate, cerate and phosphate. Luminescent and structural properties of these materials before and after doping with lanthanide ions have been investigated using XRD, SEM, TEM, FT-IR, EXAFS, PAS, TSL and photoluminescence techniques. A brief introduction to nanomaterials, their luminescence properties and different types of luminescent materials are discussed. Basic principles of different experimental techniques used for the characterization of the prepared nanomaterials are discussed along with details of the instruments used in chapter 2. Subsequent chapters (chapters 3-7) deal with the synthesis of lanthanide doped nanomaterials and investigation of their structural and luminescent properties.

Sm^{3+} and Eu^{3+} behave differently in nanocrystalline ThO_2 . Emission spectroscopy shows warm white light emission in $\text{ThO}_2:\text{Sm}^{3+}$, whereas intense red emission is observed in case of $\text{ThO}_2:\text{Eu}^{3+}$. Biexponential decay is observed for Sm^{3+} as well as for Eu^{3+} in ThO_2 . In both cases, longer lived species is due to the presence of $\text{Sm}^{3+}/\text{Eu}^{3+}$ ion in cubic (O_h) site with inversion symmetry. In case of Sm^{3+} doped thoria, shorter lived species is due to its presence on the surface of nanocrystals, whereas europium behaves distinctly in nano ThO_2 ; short lived species T_1 (~1.3-3.4 ms) arises because of Eu^{3+} ions occupying non-cubic ($<C_{2v}$) sites without inversion symmetry. It was also observed in case of $\text{ThO}_2:\text{Eu}^{3+}$ that extent of asymmetry around Eu^{3+} at 700/900°C is very high as compared to as prepared or 500°C annealed sample. Short lived species T_1 (~1.3-3.4 ms), which predominates at higher annealing temperature, arises because of Eu^{3+} ions occupying non-cubic ($<C_{2v}$) site without inversion symmetry, whereas long-lived species T_2 (~4.6-6.6 ms) can be ascribed to Eu^{3+} ions occupying cubic (O_h) with inversion symmetry. Eu behaves entirely different in zirconia and thoria in terms of local site symmetry.

Different lanthanide ions viz. Eu, Sm and Dy ions have been used as structural probes to understand their site occupancy in Sr_2SiO_4 and SrZrO_3 . These ions were found to behave differently in terms of their local site occupancy in these matrices. This aspect has been investigated in detail in the present work. Theoretical modeling and EXAFS

Conclusions and future scope

studies were carried out to explain such anomaly. Effect of replacing Si (IV) by Ce (IV) in Sr_2SiO_4 is investigated in Sr_2CeO_4 system. Ionic size of silicon 0.40 Å; not ideal for Eu^{3+} substitution- entire Eu is distributed to Sr^{2+} site. Si (IV) is replaced by Ce (IV) whose ionic radius is very close to Eu (III). Also synthesizing Sr_2CeO_4 is a challenge, because it decomposes peritectically to SrO and SrCeO_3 at higher temperatures.

TRFS has been extensively used; combined with EXAFS and theoretical calculations to understand the local site symmetry of Eu, Dy and Sm in sol-gel derived Sr_2SiO_4 .

Based on these studies, it was inferred that $\text{Eu}^{3+}/\text{Eu}^{2+}$ occupies both 9- and 10-coordinated Sr^{2+} sites in strontium silicate whereas $\text{Dy}^{3+}/\text{Sm}^{3+}$ ions occupy only 9-coordinated sites. Long lived Eu^{3+} species was occupying a more symmetric 10-coordinated Sr(1) sites, whereas the short lived Eu^{3+} was present at relatively less symmetric 9-coordinated Sr(2) . Eu^{2+} also substitutes both the Sr^{2+} - leading to two emission bands. When Eu occupies Sr(1) site with weak crystal field, the emission band is about 470–490 nm, while Sr(2) site has a more compact environment and stronger crystal field effect, leading to a longer emission wavelength of 590–610 nm.

Theoretical modelling suggested that substitution of Sr in α' - Sr_2SiO_4 at 9-coordinated site is more favourable than 10-coordinated site. Due to relatively higher bond strength of Dy-O and Sm-O bond, the inclusion of these ions at 10-coordinate site result in shortening of few M-O, which leads to distortion in MO_{10} polyhedra. Such a distortion leads to destabilization of the conformer having Dy/Sm at 10-coordinated sites.

In Sr_2SiO_4 , all the lanthanides occupy Sr sites only but with different coordination. To see a similar effect, we wanted to synthesize a compound, where two different types of site (A and B) for lanthanide occupancy was present.

Keeping this in mind, SrZrO_3 and Sr_2CeO_4 were synthesized using gel-combustion and polymeric precursor route respectively. Nanocrystalline SZ sample showed defect induced intense violet blue and weak orange red emissions. Based on EPR and theoretical studies, these defects were attributed to presence of shallow and deep defects, respectively. Their corresponding lifetimes were calculated using PL decay measurements. On doping Sm^{3+} in SZ, an efficient energy transfer takes place and Sm^{3+} ions are localized both at Sr and Zr positions of SZ. Theoretical calculation has also shown that incorporating Sm at individual site does not change the band gap at all; but incorporating Sm simultaneously at Sr and Zr site decreases the band gap by

Conclusions and future scope

0.7 eV. PL decay time showed the presence of two life times in case of nanocrystalline $\text{SrZrO}_3:\text{Sm}^{3+}$: (i) Sm^{3+} at Zr^{4+} site ($\tau=500 \mu\text{s}$) and (ii) Sm^{3+} at Sr^{2+} site ($\tau=1.2 \text{ ms}$) in the ratio of 3:1. In europium doped sample also, europium is distributed between two sites Sr and Zr; HAB (host absorption band) excites mostly Eu at Sr site, CTB (charge transfer band) excites mostly Eu at Zr site, whereas f-f band excites both types of europium equally. In case of Gd/Sm doped SZ samples, Gd prefers Sr^{2+} site and Dy prefers Zr^{4+} site only. Moreover $\text{SrZrO}_3:\text{Dy}^{3+}$ shows near white light emission: due to presence of blue, yellow and red emissions.

Detailed photoluminescence investigations of undoped Sr_2CeO_4 showed bluish white emission with single lifetime of 59 ns. The emission spectra of the europium doped cerate sample showed characteristic peaks corresponding to the $^5\text{D}_0 \rightarrow ^7\text{F}_j$ ($j=1, 2$) transitions of Eu^{3+} ion as well as host emission under CTB. The PL decay time studies showed a bi-exponential decay, which was attributed to presence of europium ion at both Sr^{2+} as well as Ce^{4+} sites. Concentration quenching of the PL signal intensity was observed for Eu ion concentration of more than 5 mol%. From this, the critical energy transfer distance of Eu^{3+} was calculated to be 13 Å and the mechanism of concentration quenching was determined to be the multipole–multipole interaction. It was observed that with increase in Eu^{3+} concentration, PL intensity of europium emission lines increases, whereas that of host emission decreases. This is assigned to energy transfer between host and europium ions.

Luminescence properties of hosts like $\text{Zn}_2\text{P}_2\text{O}_7$ (both undoped and doped) with lanthanide ions have been investigated for the first time with a view to develop new and robust phosphor materials with multifunctional applications. Zinc pyrophosphate is known to undergo structural phase transition at 132°C. We doped 2.0 mol % Mn^{2+} in zinc pyrophosphate and used electron paramagnetic resonance (EPR) as a probe to understand the mechanism for phase transition. This aspect was also supported by high temperature x-ray diffraction (HTXRD) and differential scanning calorimetry (DSC). In case of $\text{Zn}_2\text{P}_2\text{O}_7:\text{Eu}^{3+}$, PL emission and decay time data of the sample suggested the stabilization of the rare earth ion at two different sites. The first type was a long lived species ($\sim\tau= 1.77 \text{ ms}$) present at asymmetric ‘5-coordinated Zn (square pyramidal, S_1)’ sites and the second was a short lived component ($\tau= 620 \text{ ns}$) present at relatively symmetric ‘6-coordinated Zn (octahedral, S_2)’ sites. Low temperature PL experiment did not give any light on this, except the enhancement in

Conclusions and future scope

emission intensity and decay time. This unusual phenomenon was explained by calculating theoretical value of radiative lifetime- J-O calculations. Radiative life time of the Eu^{3+} species present in symmetric environment was higher than that of the species present in asymmetric environment, which is consistent with the selection rules governing the transition. To see the effect of octahedral and square pyramidal crystal fields (on what?), transition metal will be better candidate than lanthanide ion, wherein crystal field effect is more dominant, Manganese ion was doped in $\text{Zn}_2\text{P}_2\text{O}_7$. Based on EPR and PL investigations, it was inferred that Mn is getting stabilized as both Mn (II) and Mn (IV). Crystal field of square pyramidal is more than octahedral and generally green emission arises from weak crystal field and the red one from strong crystal field. Based on above two points, it can be inferred that that Mn (II) ions occupy octahedral Zn(II) sites and Mn(IV) ions occupy square pyramidal Zn(II) sites. For exploring zinc pyrophosphate as a luminescent host, $\text{Zn}_2\text{P}_2\text{O}_7: \text{Sm}^{3+}$ was synthesized. Upon near UV light excitation (403 nm), $\text{Zn}_2\text{P}_2\text{O}_7: \text{Sm}^{3+}$ exhibited host emission at 450 nm along with characteristic emission lines of Sm^{3+} . Based on PL decay measurements, it was inferred that two different types of Sm^{3+} ions were present in zinc pyrophosphate. The first type was a short lived species ($\sim\tau= 100 \mu\text{s}$) present at less symmetric '5-coordinated Zn' sites, while the second was a long lived species ($\sim\tau= 1.9 \text{ ms}$) present at symmetric '6-coordinated Zn' sites. The colour coordinates of the system were evaluated using CIE index diagram to be 0.36 and 0.37, which suggested that the prepared material is a potential near white light emitting phosphor.

Future scope

- (1) Theoretical and EXAFS measurements to understand the local structure of Eu, Dy Gd and Sm in SrZrO_3 .
- (2) Comparing the PL properties of CaZrO_3 , SrZrO_3 and BaZrO_3 and their origin.
- (3) Exploring thorium oxide for synthesizing pure white light materials
- (4) EPR and SQUID measurement on SrZrO_3 to understand the mechanism for defect induced magnetic properties

REFERENCES

1. K.A. Gschneider, L. Eyring, *Handbook on the Physics and Chemistry of Rare earths*, North Holland Publishing Company, Amsterdam, (1979).
2. I.K. Hemmilä, *Applications of Fluorescence in Immunoassays*, Wiley and Sons, New York, (1991).
3. (a) F.J. Steemers, W. Verboom, D.N. Reinhoudt, E.B. van der Tol, J. Verhoeven, *J. Am. Chem. Soc.* **117** (1995) 9408. (b) F.J. Steemers, H.G. Meuris, W. Verboom, D.N. Reinhoudt, *J. Org. Chem.* **62** (1997) 4229.
4. R. Moncorge, L.D. Merkle, B. Zandi, *MRS Bull*, **24** (1999) 21, and references cited therein.
5. E. Desurvire, *Phys. Today*, **97** (1994) 20.
6. M. Karplus, R.N. Porter, *Atoms and Molecules*, The Benjamin-Cummings Publishing Company, Amsterdam, (1970).
7. W.T. Carnall, G.L. Goodman, K. Rajnak, R.S. Rana, *J. Phys. Chem.* **90** (1989) 3443.
8. S.V. Eliseeva, J.C.G. Bunzli, *Chem. Soc. Rev.*, **39** (2010) 189. |
9. F. Auzel. *Chem. Rev.*, **104** (2004) 139.
10. (a) B. R. Judd, *Phys. Rev.* **127** (1962) 750. (b) G. S. Ofelt, *J. Chem. Phys.* **37** (1962) 511.
11. M.H.V. Werts, R.T.F. Jukes, J.W. Verhoeven, *Phys. Chem. Chem. Phys.* **4** (2002) 1542.
12. R.T. Wegh, H. Donker, K.D. Oskam, A. Meijerink, *Science*, **283** (1999) 663.
13. M.J. Weber, *Phys. Rev. B*, **8** (1973) 54.
14. Y. Haas, Y. G. Stein, *J. Phys. Chem.*, **76** (1972) 1093.
15. W.D. Horrocks Jr., and D.R. Sudnick, *Acc. Chem. Res.*, **14** (1981) 384.
16. A. Beeby, I.M. Clarkson, R.S. Dickins, S. Faulkner, D. Parker, L. Royle, A.S. Sousa, J.A.G Williams, and M. Woods, *J. Chem. Soc., Perkin Trans.*, **2** (1999) 493.
17. (a) Y. Haas, Y. G. Stein, *J. Phys. Chem.*, **75** (1971) 3668 (b) (a) Y. Haas, Y. G. Stein, *J. Phys. Chem.*, **75** (1971) 3677.
18. V.L. Ermolaev, E.B. Sveshnikova, *Russ. Chem. Rev.*, **63** (1994) 905.

19. M.P.O. Wolbers, F.C.J.M. Van Veggel, B.H.M. Snellink-Ruël, J.W. Hofstratt, F.A.J. Geurts, D.N. Reinhoudt, *J. Am. Chem. Soc.* **119** (1997) 138.
20. I. Hemmilä, V.M. Mukkala, H. Takolo, *J. Fluorescence*, **5** (1995) 159.
21. I. Hemmilä, V.M. Mukkala, *Crit. Rev. Clin. Lab. Sci.*, **38** (2001) 441.
22. I. Hemmilä, T. Stahlberg and P. Mottram, *Bioanalytical applications of labeling technologies*, Wallac Oy, Turku, (1995).
23. A.I. Voloshin, N.M. Shavaleev and V.P. Kazakov, *J. Lumin*, **39** (2001) 199.
24. J. Kido and Y. Okamoto, *Chem. Rev.*, **102** (2002) 2357.
25. J.W. Stouwdam, G.A. Hebbink, J. Huskens and F.C.J.M. Van Veggel, *Chem. Mater.*, **15** (2003) 4604.
26. A. Shalav, B. S. Richards and M. A. Green, *Sol. Energy Mater. Sol. Cells*, **91** (2007) 829.
27. G. J. Ding, F. Gao, G. H. Wu and D. H. Bao, *J. Appl. Phys.*, **109** (2011) 123101.
28. Y. Zhang, J. H. Hao, C. L. Mak and X. H. Wei, *Opt. Express*, **19** (2011) 1824.
29. H. T. Wong, H. L. W. Chan and J. H. Hao, *Appl. Phys. Lett.*, **95** (2009) 022512.
30. Y. Zhang, G. Y. Gao, H. L. W. Chan, J. Y. Dai, Y. Wang and J. H. Hao, *Adv. Mater.*, **24** (2012) 1729.
31. H. X. Zhang, C. H. Kam, Y. Zhou, X. Q. Han, S. Buddhudu, Q. Xiang, Y. L. Lam and Y. C. Chan, *Appl. Phys. Lett.* **77** (2000) 609.
32. C.G. Walrand, K. Binnemans, *Spectral intensities of f-f transitions*. In: Gschneidner KA Jr, Eyring L (eds) *Handbook on the physics and chemistry of rare earths*, vol **25**. Elsevier BV, Amsterdam, Ch. 167.
33. B.M. Walsh (2006) *Judd–Ofelt theory: principles and practices*. In: Di Bartolo B, Forte O (Eds) *Advances in spectroscopy for lasers and sensing*. Springer Verlag, Berlin, pp 403–433.
34. W.T. Carnall *The absorption and fluorescence spectra of rare earth ions in solution*. In: Gschneidner KA Jr, Eyring L (eds) *Handbook on the physics and chemistry of rare earths*, vol **3**. Elsevier BV, Amsterdam, Ch. 24. (1979)
35. P. Dorenbos, *J Lumin.* **91** (2000) 91.
36. S. Shionoya, W.M. Yen, *Principal phosphor materials and their optical properties*. In: Shionoya S, Yen WM (eds) *Phosphor handbook*. CRC, Boca Raton, Ch. 235 (1999).
37. M. Bredol, U. Kynast, C. Ronda, *Adv. Mater.*, **3** (1991) 361.

38. E. Brunet, O. Juanes, R. Sedano, J.C. Rodriguez-Ubis, *Photochem. Photobiol. Sci.*, **1** (2002) 613.
39. M. Kleinerman, S.I. Choi, *J Chem. Phys.*, **49** (1968) 3901.
40. J.C.G. Bunzli, S. Petoud, E. Moret, *Spectrosc. Lett.* **32** (1999) 155.
41. S. Hufner, *Optical spectra of transparent rare earth compounds*. Academic, New York (1978).
42. A. Aebischer, F. Gumy, J.C.G Bunzli, *Chem. Phys. Phys. Chem*, **11** (2009) 1346.
43. J.C.G Bunzli, P. D. Morand and J. M. Pfefferle, *J. Physique*, **48** (1987) C7/625.
44. G. Muller, S. D. Kean, D. Parker and J. P. Riehl, *J. Phys. Chem. A*, **106** (2002) 12349.
45. S. T. Frey and W. D. Horrocks, Jr, *Inorg. Chim. Acta*, **229** (1995) 383.
46. J.C.G Bunzli, in *Lanthanide Probes in Life, Chemical and Earth Sciences. Theory and Practice*, ed. J.C.G Bunzli and G. R. Choppin, Elsevier Science Publ. B.V., Amsterdam, Ch. 7, pp. 219–93 (1989).
47. J.C.G Bunzli, G.O. Pradervand, *J Phys Chem Phys*, **85** (1986) 2489.
48. C.G. Walrand, K. Binnemans *Rationalization of crystal field parameters*. In: Gschneidner KA Jr, Eyring L (eds) *Handbook on the physics and chemistry of rare earths*, vol **23**. Elsevier BV, Amsterdam, Ch. 155 (1996).
49. J.C.G Bunzli, A.S. Chauvin, C.D.B. Vandevyver B. Song, S. Comby, *Ann NY Acad Sci* **1130** (2008) 97.
50. N. Puntus, K. A. Lyssenko, M. Y. Antipin and J.C.G Bunzli, *Inorg. Chem.*, **47** (2008) 11095.
51. <https://www.physics.umn.edu/research/workshops/fluorescence/Fluoro6.pdf>
52. <http://photochemistryportal.net/home/index.php/2009/10/30/quenching-mechanisms/>
53. A. Gilbert, J. Baggot, *Essentials of molecular photochemistry*; Blakwell Scientific Publications: London, (1991).
54. Th. Forster, *Ann. Physik*, **2** (1948) 55.
55. D.L. Dexter, *J. Chem. Phys.* **21** (1953) 836.
56. M. Inokuti, F. Hirayama, *J. Chem. Phys.* **43** (1965) 1978.
57. N.T. Melamed, D.E. Harrison, 1962 *Westinghouse Research Laboratories* [online]. [http:// www.dtic.mil/cgi-bin/GetTRDoc?AD=AD0406473](http://www.dtic.mil/cgi-bin/GetTRDoc?AD=AD0406473)
58. S. Saini. H. Singh H and B. Bagchi, *J. Chem. Sci.* **118** (2006) **23**.

59. <http://en.wikipedia.org/wiki/Quenching> (fluorescence).
60. Dexter energy transfer [online]. Available from http://chemwiki.ucdavis.edu/Theoretical_Chemistry/Fundamentals/Dexter_Energy_Transfer.
61. C. Strohhofer, A. Polman, *Opt. Mater.*, **21** (2003) 705.
62. (a) C. Strohhofer, A. Polman, *J. Appl. Phys.* **90** (2003) 4314; (b) J.E. Townsend, W.L. Barnes, K.P. Jdrzejewski, *Electro. Lett.* **27** (1991) 1958.
63. (a) B.M. Walsh, N.P. Barnes, B. D. Bartolo, *J. Lumin.*, **75** (1997) 89 (b) B.M. Walsh, N.P. Barnes, B. D. Bartolo, *J. Lumin.*, **90** (2000) 39.
64. J.H. Song, J. Heo, S.H. Park, *J. Appl. Phys.* **93** (2003) 9441.
65. W. Chen, *J. Nanosci. Nanotech.* **8** (2008) 1017.
66. G. Wang, Q. Peng, and Y. Li, *Acc. Chem. Res.* **44** (2011) 322.
67. D. Dosev, M. Nichkova, M. Liu, G. Guo, B. Hammock, I. Kennedy, *J. Biomed. Opt.* **10** (2005) No. 064006.
68. (a) D.K. Williams, B. Bihari, B.M. Tissue, J.M. McHale, *J. Phys. Chem. B*, **102** (1998) 916; (b) H. Eilers, B.M. Tissue, *Chem. Phys. Lett.*, **251** (1996) 74.
69. G. Wakefield, E. Holland, P.J. Dobson, J.L. Hutchison, *Adv. Mater.* **13** (2001) 1557.
70. Q. Li, L. Gao, D. Yan, *Nanostruct. Mater.* **8** (1997) 825.
71. G.K. Liu, H.Z. Zhuang, X.Y. Chen, *Nano Lett.* **2** (2002) 535.
72. H.S. Yang, K.S. Hong, S.P. Feofilov, B.M. Tissue, R.S. Meltzer, W.M. Dennis, *J. Lumin.* **83-84** (1999) 139; (b) B.M. Tissue, *Chem. Mater.* **10** (1998) 2837.
73. X.Y. Chen, H.Z. Zhuang, G.K. Liu, S. Li, R.S. Niedbala, *J. Appl. Phys.* **94** (2003) 5559.
74. (a) Z. Wei, L. Sun, C. Liao, C. Yan, S. Huang, *Appl. Phys. Lett.* **80** (2002) 1447; (b) Z. Wei, L. Sun, C. Liao, X. Jiang, C. Yan, *J. Mater. Chem.* **12** (2002) 3665; (c) Z. Wei, L. Sun, C. Liao, X. Jiang, C. Yan, *J. Appl. Phys.* **93** (2003) 9783.
75. C.H. Yan, L.D. Sun, C.S. Liao, Y.X. Zhang, Y.Q. Lu, S.H. Huang, S.Z. Lü, S. Z. *Appl. Phys. Lett.* **82** (2003) 3511.
76. (a) F.J.P. Schuurmans, A. Lagendijk, *J. Appl. Phys.* **113** (2000) 8; (b) F.J.P. Schuurmans, D.T.N. de Lang, G.H. Wegdam, R. Sprik, A. Lagendijk, *Phys. Rev. Lett.* **80** (1998) 5077.

77. R.S. Meltzer, S.P. Feofilov, B. Tissue, H.B. Yuan, *Phys. Rev. B* **60** (1999) 14012; (b) R.S. Meltzer, W.M. Yen, H. Zheng, S.P. Feofilov, M.J. Dejneka, B. Tissue, H.B. Yuan, *J. Lumin.* **94-95** (2001) 217.
78. (a) M. Fujii, M. Yoshida, Y. Kanzawa, S. Hayashi, K. Yamamoto, *Appl. Phys. Lett.* **71** (1997) 1198; (b) P.G. Kik, A. Polman, *Mat. Sci Eng. B* **81** (2001) 3; (c) H.S. Han, S.Y. Seo, J.H. Shin, *Appl. Phys. Lett.* **79** (2001) 4568.
79. (a) S.T. Selvan, T. Hayakawa, M. Nogami, M. Möller, *J. Non-Cryst. Solids*, **291** (2001) 137; (b) T. Hayakawa, S.T. Selvan, M. Nogami, *J. Sol-Gel Sci. Technol.* **19** (2000) 779.
80. M. Nogami, T. Enomoto, T. Hayakawa, *J. Lumin.* **97** (2002) 147.
81. (a) R.N. Bhargava, *J. Lumin.* **70** (1996) 85; (b) E.T. Goldburt, R.N. Bhargava, *J. Soc. Inf. Display*, **4** (1996) 365; (c) R.S. Kane, R.E. Cohen, R. Silbey, *Chem. Mater.* **11** (1999) 90; (d) M. Ihara, T. Igarashi, T. Kusonoki, K. Ohno, *J. Electrochem. Soc.* **147** (2000) 2355.
82. S. Okamoto, M. Kobayashi, Y. Kanemitsu, T. Kushida, *Phys. Stat. Sol. B* **229** (2002) 481.
83. S.C. Qu, W.H. Zhou, F.Q. Liu, N.F. Chen, Z.G. Wang, H.Y. Pan, D.P. Yu, *Appl. Phys. Lett.* **80** (2002) 3605.
84. A.A. Bol, R. van Beek, A. Meijerink, *Chem. Mater.* **14** (2002) 1121.
85. B.L. Cushing, V.L. Kolesnichenko, C.J. O'Connor, *Chem. Rev.* **104** (2004) 3893.
86. J. Livage, M. Henry, C. Sanchez, C, *Prog. Solid State Chem.* **18** (1988) 259.
87. L.L. Hench, J.K. West, *Chem. Rev.* **90** (1990) 33.
88. R.C. Mehrotra, A. Singh, *Prog. Inorg. Chem.* **46** (1997) 239.
89. R. D. Purohit and A. K. Tyagi, *J. Mater. Chem.* **2** (2002) 312.
90. S. V. Chavan and A. K. Tyagi, *J. Mater. Res.*, **19** (2004) 3181.
91. M P Pechini, US Patent No. 330697 (1967).
92. N.H. Chan, R.K. Sharma, and D.M. Smyth, *J. Electrochem. Soc.* **128** (1981) 1762.
93. M. Kakihana, *J. Sol Gel Sci. Tech.* **6** (1996) 7.
94. M. Kakihana, M. Arima, Y. Nakamura, M. Yashima and M. Yoshimura, *Chem. Mater.* **11**(1998) 438.
95. M. Boutonnet, J. Kizling, P. Stenius, G. Maire. *Colloids Surf.* **5** (1982) 209
96. M. P. Pileni, L. Motte, C. Petit. *Chem. Mater.* **4** (1992) 338.

97. T. Ahmad, G. Kavitha, C. Narayana, A. K. Ganguli. *J. Mater. Res.* **20** (2005) 1415
98. T. Ahmad, A. K. Ganguli. *J. Mater. Res.* **19** (2004) 2905.
99. I. Lisiecki, M. P. Pileni. *J. Am. Chem. Soc.* **115** (1993) 3887.
100. J. P. Wilcoxon, R. L. Williamson, R. Baughman. *J. Chem. Phys.* **98**, (1993) 9933.
101. K. Osseo-Asare, F. J. Arriagada. *Colloids Surf.* **50**, (1990) 321.
102. H. Herrig, R. Hempelmann. *Nanostruct. Mater.* **9** (1997) 241.
103. A. R. Koran, R. Hull, R. L. Opila, M. G. Bawendi, M. L. Steigerwald, P. J. Carroll, L. E. Brus. *J. Am. Chem. Soc.* **112** (1990) 1327.
104. X-Ray Generation, Available from: <http://xrayweb.chem.ou.edu/notes/xray.html>
105. B.D. Cullity, *Elements of x-ray diffraction* (Reading: Addison Wesley) (1956) p. 16.
106. Powder X-ray Diffraction, [online]. Available from http://chemwiki.ucdavis.edu/Analytical_chemistry/instrumental_Analysis/Diffraction/Powder_X-ray_Diffraction.
107. R.W. Seigel, *Ann. Rev. Mater. Sci.* **10** (1980) 393.
108. R.N. West, *Adv. Phys.* **22** (1974) 263.
109. V.I. Grafutin, E.P. Prokop'ev, *Phys. Usp.* **45** (2002) 59.
110. B. A. Dumasquier, *Positron Solid State Physics*, North-Holland, Amsterdam, (1984).
111. M. J. Puska, R.M. Nieminen, *Rev. Mod. Phys.* **66** (1994) 841.
112. P. Asoka-Kumar, M. Alatalo, V.J. Ghosh, A.C. Kruseman, B. Nielsen, K.G. Lynn, *Phys. Rev. Lett.* **10** (1996) 2097.
113. J.R. Lakowicz, *Principles of fluorescence spectroscopy*, Springer Science Business Media LLC, New York, USA (2006).
114. Edinburgh Photonics, Technical note, TN/2012/02.
115. C.J. Sun, Z. Xu, B. Hu, G.S. Yi, G.M. Chow, J. Shen, *Appl. Phys. Lett.* **91** (2007) 191113.
116. G.Y. Chen, Y. Liu, Y.G. Zhang, G. Somesfalean, Z.G. Zhang, Q. Sun, *Appl. Phys. Lett.* **91** (2007) 1333103.
117. W.X. Li, J. Hagen, R. Jones, J. Heikenfeld, A.J. Steckl, *J. Solid State Electrochem.* **51** (2007) 500.

118. J. Shen, L.D. Sun, J.D. Zhu, L.H. Wei, H.F. Sun, C.H. Yan, *Adv. Funct. Mater.* **20** (2010) 3708.
119. N. Claussen, M. Ruhle and A.H. Heuer Science and Technology of Zirconia II (Series in Advances in Ceramics vol 12) (Columbus, OH: *American ceramic society* (1984).
120. N.G. Petrik, D.P. Taylor, T.M. Orlando, *J. Appl. Phys.*, **85** (1999) 6670.
121. C. Urlacher, C.M. De Lucas, J. Mugnier, *Synth. Met.*, **90** (1997) 199.
122. A. Emeline, G.V. Kataeva, A.S. Litke, A.V. Rudakvo, V.K. Ryabchuk, N. Serpone, *Langmuir* , **14** (1998) 5011 .
123. A. Emeline, G.V. Kataeva, A.S. Litke, A.V. Panasuk, V.K. Ryabchuk, N.V. Sheremetyeva N. Serpone, *J. Phys. Chem. B.*, **109** (2005) 5175.
124. A. Patra, C.S. Friend, R. Kapoor, P.N. Prasad, *Appl. Phys. Lett.*, **83** (2003) 284.
125. Z. Assefa, R.G. Haire, P.E. Raison, *Spectrochim. Acta Part A*, **60** (2004) 89.
126. E. De la Rosa-Cruz, L.A. Diaz-Torres, P. Salas, R.A. Rodriguez, G.A. Kumar, M.A. Meneses, J.F. Mosino, J.M. Hernandez, O. Barbosa-Garcia, *J. Appl. Phys.*, **94** (2003) 3509.
127. P. Salas, C. Angeles, J.A. Montoya, E. De la Rosa, L.A. Diaz-Torres, A. Martinez, M.A. Romero-Romo, J. Morales, *Opt. Mater.*, **27** (2005) 1295.
128. R.C. Garvie, *J. Phys. Chem.* **82** (1978) 218.
129. S. Hubert, P. Thouvenot, *J. Alloys Compd.* **180** (1992) 193.
130. M. Breysse, L. Faure, *J. Lumin.* **180** (1992) 107.
131. S.V. Godbole, J.S. Nagpal, A.G. Page, *Radiat. Meas.* **32** (2000) 349.
132. S.V. Godbole, A.R. Dhobale, M.D. Sastry, C.H. Lu, A.G. Page, *J. Lumin.* **105** (2003) 89.
133. M. Breysse, L. Faure, H. Pralraud, *Chem. Phys. Lett.* **61** (1979) 132.
134. L.C. Porter, J.C. Wright, *J. Lumin.* **27** (1982) 237.
135. M. Yin, J.C. Krupa, E.A. Fidancev, A.L. Rubben, *Phys. Rev. B.* **61** (2000) 8073.
136. S. Hubert, P. Thouvenot, N. Edelstein, *Phys. Rev. B.* **48** (1993) 5751.
137. L. Chen, Y. Liu, Y. Li, *J. Alloys Compd.*, **381** (2004) 266.
138. B. Julion, R. Coberan, E. Cordoncillo, P. Escribano, B. Viana, C. Sanchez, *Nanotechnology*, **16** (2005) 2707.

139. G. Ehrhart, M. Bouazaoui, B. Capoen, V. Farreiro, R. Mahiou, O. Robbe, S. Turrell, *Opt. Mater.* **29** (2007) 1723.
140. B.N. Mahally, R.B. Pode, P.K. Gupta, *Phys. Status Solidi A*, **177** (1999) 293.
141. A. Parma, I. Freris, P. Riello, F. Enrichi, D. Cristofori, A. Benedetti, *J. Lumin.* **130** (2010) 2429.
142. K. Smits, L. Grigorjeva, D. Millers, A. Sarakovskis, A. Opalinska, J. D. Fidelus, W. Lojkowski, *Opt. Mater.* **32** (2010) 827.
143. P. Ghosh, A. Patra, *Langmuir*, **22** (2006) 321.
144. Z.W. Quan, L.S. Wang, *Mater. Res. Bull.*, **40** (2005) 810.
145. N. Rajee, A. V. R. Reddy, *Thermochimica Acta*, **505** (2010) 53.
146. I. L. Jenkins, F. H. Moore, M. J. Watermann, *J. Inorg. Nucl. Chem.* **27** (1965) 81.
147. F.S. Liu, Q.L. Liu, J.K. Liang, J. Luo, L.T. Yang, G.B. Song, Y. Zhang, L.X. Wang, J.N. Yao, G.H. Rao, *J. Lumin.* **111** (2005) 61.
148. R.J. Harvey, J.B. Hallett, *J. Solid State Chem.* **12** (1975) 219.
149. K.L. Kelly, *J. Opt. Soc. Am.*, **53** (1963) 999.
150. C.S. McCamy, *Color Res. Appl.* **17** (1992) 142.
151. J.J. Moore and H.J. Feng, *Prog. Mater. Sci.* **39** (1995) 243.
152. T. Mimani and K.C. Patil, *Mater. Phys. Mech.* **4** (2001) 13.
153. R. C. Linares, *J. Opt. Soc. Am.* **56** (1966) 1700.
154. S. K. Gupta, M. Mohapatra, V. Natarajan and S.V.Godbole, *J. Mater. Sci.*, **47** (2012) 3504.
155. S.P. Sinha, E. Butter, *Mol. Phys.* **16** (1969) 285.
156. N. Mercier, E. Antic-Fidancev, M. Lemaitre- Blaise and M. Leblanc, *J. Solid State Chem.* **132** (1997) 33.
157. S. K. Gupta, M. Mohapatra, S. Kaity, V. Natarajan and S.V.Godbole, *J. Lumin.* **132** (2012) 1329.
158. S. K. Gupta, M. Mohapatra, V. Natarajan and S.V.Godbole, *RSC Adv.* **3** (2013) 2004.
159. X.Y. Chen, W. Zhao, R.E. Cook, G.K. Liu, *Phys. Rev. B*, **70** (2004) 205122.
160. X.Y. Chen, G.K.J. Liu, *J. Solid State Chem.* **178** (2005) 419.
161. S. V. Eliseeva and J.C.G Buzli, *Chem. Soc. Rev.*, **39** (2010) 189.
162. M. Yin, J.C. Krupa, E.A. Fidancev, A.L. Rubben, *Phys. Rev. B.* **61** (2000) 8073.

163. C. Tiseanu, V.I. Parvulescu, M.S. Dominguez, M. Boutonnet, *J. Appl. Phys.* **110**, (2011) 103521.
164. W.H. Green, K.P. Le, J. Grey, T.T. Au, M.J. Sailor, *Science*, **276** (1997) 1826.
165. L.D Carlos, R.A. Ferreira, R.N. Pereira, M. Assuncao, V. Bermudez, Z. De, *J. Phys. Chem. B*, **108** (2007) 14924.
166. C. Zhang, C. Li, J. Yang, Z. Cheng, Z. Hou, Y. Fan, and J. Lin, *Langmuir*, **25** (2009) 7078.
167. G. Blasse, A. Bril, *Philips Tech. Rev.* **31** (1970) 314.
168. H. Guo, M. Yin, N. Dong, M. Xu, L. Lou, W. Zhang, *Appl. Surf. Sci.* **243** (2005) 245.
169. W.W. Zhang, W.P. Zhang, P.B. Xie, M. Yin, H.T. Chen, L. Jing, Y.S. Zhang, L.R. Lou, S.D. Xia, *J. Colloid Interf. Sci.*, **262** (2003) 588.
170. W.W. Zhang, M. Xu, W.P. Zhang, M. Yin, Z.M. Qi, S.D. Xia, C. Garapon, *Chem. Phys. Lett.* **376** (2003) 318.
171. G.H. Dieke, H.M. Crosswhite, H. Crosswhite, *Spectra and Energy levels of Rare-Earth Ions in Crystals*, Wiley, New York, (1968).
172. I. K. Hemmilä, *Applications of Fluorescence in Immunoassays*, Wiley and Sons, New York, (1991).
173. (a) F.J. Steemers, W. Verboom, D.N. Reinhoudt, E.B. Tol, J.W. Verhoeven. *J. Am. Chem. Soc.* **117** (1995) 9408 (b) F.J. Steemers, F.J. Meuris, D.N. Reinhoudt, W. Verboom, D.N. Reinhoudt. *J. Org. Chem.* **62** (1997) 4229.
174. R. Moncorge, L.D. Merkle, B. Zandi. *MRS Bull.* **24** (1999) 21, and references cited therein.
175. E. Desurvire. *Phys. Today*, **97** (1994) 20.
176. S.C. Prashantha, B.N. Lakshminarasappa, B.M. Nagabhushana *J. Alloys Compd.*, **509** (2011) 10185.
177. Y. P. Naik, M. Mohapatra, N. D. Dahale, T. K. Seshagiri, V. Natarajan, S.V. Godbole, *J. Lumin.* **129** (2009) 1225.
178. A. Nag, T. R. N. Kutty, *J. Mater. Chem.* **14** (2004) 1598.
179. S. K. Gupta, M. Sahu, K. Krishnan, M. Saxena, V. Natarajan and S.V. Godbole, *J. Mater. Chem. C*, **1** (2013) 7054.
180. S. K. Gupta, M. Mohapatra, V. Natarajan and S.V. Godbole, *Int. J. App. Ceram. Tech* **10** (2013) 593.

181. S. K. Gupta, M. Kumar, V. Natarajan and S.V. Godbole, *Opt. Mater.*, **35** (2013) 2320
182. S. K. Gupta, R. Gupta, V. Natarajan and S.V. Godbole, *Mater. Res. Bull.*, **49** (2014) 297.
183. S.H.M. Poort, G. Blasee, *J. Lumin.* **72-74** (1997) 247.
184. Takao Kobayasi, Stanley Mroczkowski and James F. Owen, *J. Lumin.* **21** (1980) 247
185. <http://www.cree.com>.
186. P Dorenbos, *J. Lumin.*, **104** (2003) 239.
187. S. Kamei, Y. Kojima, N. Nishimiya, *J. Lumin.* **130** (2010) 2247.
188. H.Y. Chen, M.H. Weng, S.J. Chang, R.Y. Yang, *Ceram. Int.* **38** (2012) 125.
189. W.H. Hsu, M.H. Sheng, M.S. Tsai, *J. Alloys Compd.* **467** (2009) 491.
190. C. Guo, Y. Xu, F. Lv, X. Ding, *J. Alloys Compd.* **497** (2010) L21-L24.
191. J. Yang , L. Yang, W. Liu, Y. Zhang, H. Fan, Y. Wang, H. Liu, J. Lang, D. Wang, *J. Alloys Compd.* **454** (2008) 506.
192. M. Catti, G. Gazzoni, G. Ivaldi, *Acta Crystallogr. Sect. C.* **39** (1983) 29.
193. J. S. Kim, J. Y. Kang, P. E. Jeon, J. C. Choi, H. L. Park, T. W. Kim, *Japanese J. Appl. Phy.* **43** (2004) 989.
194. Vijay Singh, R. P. S. Chakradhar, J.L. Rao, I. Ko, H.Y. Kwok, *J. Lumin.* **130** (2010) 703.
195. Y.J. Park, T.J. Kim, Y.H. Cho, Y. Jung, H. J. Im, K. Song, K.Y. Jee, *Bull. Korean Chem. Soc.* **29** (2008) 127.
196. C.H. Lu, C.H. Huang, C.T. Chen, S.M. Wang, S.J. Huang, D. Zhang, R. Kadam, *Key Engg. Mater.* **317-318** (2006) 93.
197. S. Basu, D. K. Patel, J. Nuwad, S. N. Jha, D. Bhattacharyya, V. Sudarsan, R. K. Vatsa and S. K. Kulshreshtha, *Chem. Phys. Lett.* , **561-562** (2013) 82.
198. S. Basu, S. Verma, A. N. Shirsat, B.N. Wani, S. R. Bharadwaj, A. Chakrabarti, S.N. Jha and D. Bhattacharria, *J. Appl. Phys.*, **113** (2013) 043508.
199. N. L. Misra, A. K. Yadav, Sangita Dhara, Rohan Phatak, S. K. Mishra, A. K. Poswal, S. N. Jha, A. K. Sinha and D. Bhattacharyya, *Anal. Sci.*, **29** (2013) 579.
200. *X-Ray Absorption: Principles, Applications, Techniques of EXAFS, SEXAFS and XANES*, edited by D.C. Konigsberger and R. Prince (Wiley, New York, 1988).

201. M. Newville, B. Ravel, D. Haskel, J.J. Rehr, E.A. Stern and Y. Yacoby, *Physica B* **154** (1995) 208.
202. M. Catti, G. Gazzoni, G. Ivaldi and G. Zanini, *Acta Cryst. B*, **39** (1983) 674.
203. <http://abulafia.mt.ic.ac.uk/shannon/ptable.php>
204. H. Nguyen, I. Yeo, S. Mho, *ECS Transaction*, **28** (2010) 167.
205. E. R. Vance, J. V. Hanna and J. H. Hadley, *Adv. Appl. Ceram.* **111** (2012) 94.
206. S. Stolen, E. Bakken and C.E. Mohn, *Phys. Chem. Chem. Phys.*, **8** (2006) 429.
207. H. Iwahara, T. Yajima, T. Hibino and H. Ushida, *J. Electrochem. Soc.*, **140** (1993) 1687.
208. A.P. Ramirez, *J. Phys. Condens. Matter*, **9** (1997) 8171.
209. M. Jansen and H.P. Letschert, *Nature*, **404** (2000) 980.
210. R. Ramesh and N.A. Spaldin, *Nat. Mater.*, **6** (2007) 21.
211. J.F. Scott and C.A.P. De Araujo, *Science*, **246** (1989) 1400.
212. S. Mathews, R. Ramesh, T. Venkatesan and J. Benedetto, *Science* **276** (1997) 238.
213. C.C. Homes, T. Vogt, S.M. Shapiro, S. Wakimoto and A.P. Ramirez, *Science* **293**, (2001) 673.
214. H. Iwakura, H. Einaga and Y. Teraoka, *Inorg. Chem.*, **49** (2010) 11362.
215. E. Longo et al., *Phys. Rev. B*, **69** (2004) 1251151.
216. V.M. Longo, L.S. Cavalcante, M.G.S. Costa, M.L. Moreira, A.T. de Figueiredo, J. Andres, J.A. Varela and E. Longo, *Theor. Chem. Acc.*, **124** (2009) 385.
217. E. A. Slonimskaya and A. V. Belyakov, *Glass Ceram.* **58** (2000) 54.
218. R. A. Davies, M. S. Islam and J. D. Gale, *Solid State Ionics*, **126** (1999) 323.
219. A. Vecht, D. Smith, S. S. Chadha, C. S. Gibbons, J. Koh and D. Morton, *J. Vac. Sci. Technol.*, **12** (1994) 781.
220. H. Takashima, K. Shimada, N. Miura, T. Katsumata, Y. Inaguma, K. Ueda and M. Itoh, *Adv. Mater.*, **21** (2009) 3699.
221. R. Pazik, R. Tekoriute, S. Hakansson, R. Wiglusz, W. Strek, G. Seisenbaeva, Y. K. Gun'ko and V. G. Kessler, *Chem. Eur. J.*, **15** (2009) 6820.
222. B. Bouma and G. Blasse, *J. Phys. Chem. Solids*, **56** (1995) 261.
223. P. S. Pizani, H. C. Basso, F. Lanciotti, T. M. Baschi, F. M. Pontes, E. Longo and E. R. Leite, *Appl. Phys. Lett.*, **81** (2002) 253.

224. V.M. Longo, L.S. Cavalcante, R. Erlo, V.R. Mastelaro, A.T. De Figueiredo, J. R. Sambrano, S. de Lazaro, A.Z. Freitas, L. Gomes, N.D. Vieira Jr., J.A. Varela and E. Longo, *Acta Mater.*, **56** (2008) 2191.
225. D. J. Lee, D. H. Kim, J. W. Park and Y.S. Lee, *J. Korean Phys. Soc.*, **59** (2011) 2797.
226. J. W. Park, D. J. Lee, D. H. Kim and Y.S. Lee, *J. Korean Phys. Soc.*, **58** (2011) 316.
227. V. M. Longo, L.S. Cavalcante, A.T. De Figueiredo, L. P. S. Santos, E. Longo, J.A. Varela, J.R. Sambrano, and A.C. Hernandez, *Appl. Phys. Lett.*, **90** (2007) 091906.
228. H. Zhang, X. Fu, S. Niu and Q. Xin, *J. Alloy Comd.*, **459** (2008) 103.
229. J. Huang, L. Zhou, Z. Wang, Y. Lan, Z. Tong, F. Gong, J. Sun and L. Li, *J. Alloys Compd.*, **487** (2009) L5.
230. A. Zhang, M. Lü, G. Zhou, Y. Zhou, Z. Qiu and Q. Ma, *J. Alloys Compd.* **468** (2009) L17.
231. B.-B. Wang and W.-D. Yang *Adv. Mater. Res.* **679** (2013) 3.
232. Y. Jin, Y. Hu, L. Chen, X. Wang, G. Ju and Z. Mou, *J. Am. Ceram. Soc.*, **96** (2013) 3821.
233. D.H. Kim, J.H. Kim, J.S. Chung and Y. Lee, *J. Nanosci. Nanotech.* **13** (2013) 7572.
234. R. Bazzi, M. A. Flores-Gonzalez, C. Louis, K. Lebbou, C. Dujardin, A. Brenier, W. Zhang, O. Tillement, E. Bernstein and P. Perriat, *J. Lumin.*, **102-103** (2003) 445.
235. B. Popescu, S. Enache, C. Ghica and M. Valeanu, *J. Alloys Compd.*, **509** (2011) 6395.
236. C.Y. Liu and T.Y. Tseng, *J. Phys. D: Appl. Phys.*, **40** (2007) 2157.
237. H.S. Potdar, S.B. Deshpande, A.J. Patil, A.S. Deshpande, Y.B. Kholam and S.K. Date, *Mater. Chem. Phys.* **65** (2000)178.
238. M.M. Lencka, E. Nielsen, A. Anderko and R.E. Riman, *Chem. Mater.*, **9** (1997) 1116.
239. A. Zhang, M. Lu, S. Wang, G. Zhou, S. Wang, Y. Zhou, *J. Alloy Compd.*, **433** (2007) L7-L11.
240. V. M. Goldschmidt, *Naturwissenschaften*, **14** (1926) 477.

241. D. Kan, T. Terashima, R. Kanda, A. Masuno, K. Tanaka, S. Chu, H. Kan, A. Ishizumi, Y. Kanemitsu, Y. Shimakawa and M. Takano, *Nat. Mater.*, **4** (2005) 816.
242. V.M. Longo, L.S. Cavalcante, R. Erlo, V.R. Mastelaro, A.T. De Figueiredo, J. R. Sambrano, S. de Lazaro, A.Z. Freitas, L. Gomes, N.D. Vieira Jr., J.A. Varela and E. Longo, *Acta Mater.*, **56** (2008) 2191.
243. V. M. Longo, L.S. Cavalcante, A.T. De Figueiredo, L. P. S. Santos, E. Longo, J.A. Varela, J.R. Sambrano, and A.C. Hernandez, *Appl. Phys. Lett.*, **90** (2007) 091906.
244. L. S. Cavalcante, V. M. Longo, M. Zampieri, J. W. M. Espinosa, P. S. Pizani, J. R. Sambrano, J. A. Varela, E. Longo, M. L. Simoes and C. A. Paskocimas, *J. Appl. Phys.*, **103** (2008) 063527.
245. B.J. Kennedy, C.J. Howard, B.C. Chakoumakos, *Phys Rev B*, **59** (1999) 4023.
246. Y.S. Lee, J.S. Lee, T.W. Noh, D.Y. Byun, K.S. Yoo, K. Yamaura, *Phys Rev B*, **67**(2003) 113101.
247. Z. Guo, B. Sa, J. Zhou, Z. Sun Z, *J. Alloys Compd.* **580** (2013) 148.
248. K. Vanheusden, W. L. Warren, C. H. Seager, D. R. Tallant, J. A. Voigt, and B. E. Gnade, *J. Appl. Phys.* **79** (1996) 7983.
249. P. H. Kasai, *Phys. Rev.* **130** (1963) 989.
250. M. Z. Z. Jin, J. Zhang, X. Guo, J. Yang, W. Li, X. Wang, and Z. Zhang, *J.Mol. Catal. A: Chem.* **217** (2004) 203.
251. S. Livraghi, M. Chiesa, M. C. Paganini, E. Giamello, *J. Phys. Chem. C*, **115** (2011) 25413.
252. J. Matta, J.-F. Lamonier, E. Abi-Aad, E. A. Zhilinskaya, and A. Aboukaïs, *Phys. Chem. Chem. Phys.* **1** (1999) 4975.
253. C. Lin, C. Zhang, and J. Lin, *J. Phys. Chem. C*, **111** (2007) 3300.
254. G.H. Dieke, *Spectra and Energy Levels of Rare Earth Ions in Crystals*, Interscience, New York, (1968).
255. S. Makishima, H. Yamamoto, T. Tomotsu, S. Shionoya, *J. Phys. Soc. Jpn* **20**.(1965) 2147.
256. D. Dexter, *J. Chem. Phys.*, **21** (1953) 836.
257. Y. Yuetao, Z. Shuyi, *J. Mol. Struct.* **646** (2003) 103.
258. S. Qingade, W. Qin, L. Jingci, N. Qida, *Spectrosc. Lett.* **29** (1996) 1285.
259. Y. Yang and S. Zhang, *Spectrochim. Acta, Part A*, **59** (2003) 1205.

260. Y. Yang, Q. Su, G. Zhao, *Spectrochim. Acta, Part A*, **54** (1998) 645.
261. J. Huang, L. Zhou, Z. Wang, Y. Lan, Z. Tong, F. Gong, J. Sun, L. Li, *J. Alloys Compds.* **487** (2009):L5-L7.
262. A. Zhang, M. Lu, S. Wang, G. Zhou, S. Wang, Y. Zhou, *J. Alloy Compd.* **433** (2007) L7–L11.
263. G.V. Prakash, R. Jagannathan, *Spectrochim. Acta, Part A*, **55** (1999) 179.
264. B. R. Judd, *Phys. Rev.* **127** (1962) 750.
265. G. S. Ofelt, *J. Chem. Phys.* **37** (1962) 511.
266. M. Mohapatra, R.K. Mishra, C.P. Kaushik, S.V. Godbole, *Physica B* **405** (2010) 4790.
267. F. Moretti, N. Chiodini, M. Fasoli, L. Vedda, *J. Lumin.*, **126** (2007) 759.
268. K. Binnemans, C.G. Walrand, J.L. Adam, *Chem. Phys. Lett.*, **280** (1997) 333.
269. E.M. Shishonok, S.V. Leonchik, J.W. Steeds, D. Wolverson, *Diam. Relat. Mater.*, **16** (2007) 1602.
270. H. Guo, M. Yin, N. Dong, M. Xu, L. Lou, W. Zhang, *Appl. Surf. Sci.* **243** (2005) 245.
271. W.W. Zhang, W.P. Zhang, P.B. Xie, M. Yin, H.T. Chen, L. Jing, Y.S. Zhang, L.R. Lou, S.D. Xia, *J. Colloid Interf. Sci.* **262** (2003) 588.
272. W.W. Zhang, M. Xu, W.P. Zhang, M. Yin, Z.M. Qi, S.D. Xia, C. Garapon, *Chem. Phys. Lett.* **376** (2003) 318.
273. U. Vetter, J. Zenneck, H. Hofsass, *Appl. Phys. Lett.*, **83** (2003) 2145.
274. A. Abragam, B. Bleaney, *Electron Paramagnetic Resonance of Transition Ions*; Clarendon Press: Oxford, U.K., 197.
275. L.E. Iton, J. Turkevich, *J. Phys. Chem.* **81** (1997) 435.
276. R.C. Nicklin, J.K. Johnstone, R.G. Barness, D.R. Wilder, *J. Chem. Phys.* **59** (1973) 1652.
277. L. Cugunov, J. Kliava, *J. Phys. C* **15** (1982) L933.
278. K.K. Rao, N. Anantharamulu, M. Salagram, M. Vithal, *Spectrochim. Acta. A* **66** (2007) 646.
279. E. Malchukova, B. Boizot, D. Ghaleb, G. Petite, *J. Non-Cryst. Solids*, **352** (2006) 297.
280. C.M. Brodbeck, L.E. Iton, *J. Chem. Phys.* **83** (1985) 4284.
281. I. Omkaran and S. Buddhudu, *Opt. Mater.* **32** (2009) 8.
282. J. Pisarska, L. Z'ur, W.A. Pisarski, *Spectrochim. Acta. A*, **79** (2011) 705.

283. E. Danielson, M. Devenney, D.M. Giaquinta, J.H. Golden, R.C. Haushalter, E.W. McFarland, D.M. Poojary, C.M. Reaves, W.H. Weinberg, X.D. Wu, *Science*, **279** (1998) 837.
284. E. Danielson, M. Devenney, D.M. Giaquinta, J.H. Golden, R.C. Haushalter, E.W. McFarland, D.M. Poojary, C.M. Reaves, W.H. Weinberg, X.D. Wu, *J. Mol. Struct.*, **470** (1998) 229.
285. M. Liu, Y. Luo, J. Lin, *J. Cryst. Growth*, **290** (2006) 266.
286. T. Masui, T. Chiga, N. Imanaka, G. Adachi, *Mater. Res. Bull.*, **38** (2003) 17.
287. A.N. Shirsat, K.N.G. Kaimal, S.R. Bharadwaj, D. Das, *Thermochim. Acta*, **447** (2006) 101.
288. M. Sahu, K. Krishnan, B.K. Nagar, M.K. Saxena, S. Dash, *Thermochim. Acta*, **525** (2011) 167.
289. C.H. Park, C.H. Kim, C.H. Pyun, J.H. Choy, *J. Lumin.*, **87–89** (2000) 1062.
290. L. Van Pieterse, S. Soverna, A. Meijerink, *J. Electrochem. Soc.*, **1477** (2000) 4688.
291. S.J. Chen, X.T. Chen, Z. Yu, J.M. Hong, Z. Xue, X.Z. You, *Solid State Commun.* **130** (2004) 281.
292. X. Yu, X. He, S. Yang, X. Xu, *Mater. Lett.* **58** (2004) 48.
293. S.K. Hong, S.H. Ju, H.Y. Koo, D.S. Jung, Y.C. Kang, *Mater. Lett.* **60** (2006) 334.
294. J. Junkasem, R. Rujiravanit, P. Supaphol, *Nanotechnology*, **17** (2006) 4519.
295. Y.B. Kholam, S.B. Deshpande, P.K. Khanna, P.A. Joy, H.S. Potdar, *Mater. Lett.* **58** (2004) 2521.
296. T.Y. Wu, C.H. Lu, C.H. Hsu, *J. Lumin.*, **130** (2010) 737.
297. O.A. Serra, V.P. Severino, P.S. Calefi, S.A. Cicillini, *J. Alloys Compd.*, **323–324** (2001) 667.
298. O. Viagin, A. Masalov, I. Ganina, Y. Malyukin, *Opt. Mater.*, **31** (2009) 1808.
299. R. Sankar and G. V. Subba Rao, *J. Electrochem. Soc.*, **147** (2000) 2773.
300. T. Hirai, Y. Kawamura, *J. Phys. Chem. B*, **108** (2004) 12763.
301. X. Xiao, B. Yan, *J. Phys. Chem. Sol.*, **69** (2008) 1665.
302. W.D. Yang, Y.H. Chang, S.H. Huang, *J. Eur. Ceram. Soc.*, **25** (2005) 3611.
303. A. Gaki, O. Anagnostaki, D. Kioupis, T. Perraki, D. Gakis, G. Kakali, *J. Alloys Compd.*, **451** (2008) 305.
304. T. Hirari, Y. Kawamura, *J. Phys. Chem. B*, **108** (2004) 12763

305. M. Yu, J. Lin, Z. Wang, J. Fu, S. Wang, H.J. Zhang, Y.C. Han, *Chem. Mater.*, 2002, **14** 2228.
306. G. Blasse, *J. Solid State. Chem.*, 1986, **62**, 207.
307. G. Blasse and E. C. Grabmaier, *Luminescent Materials*, Springer-Verlag, Berlin (1994).
308. M. Zhao, L. Li, J. Zheng, L. Yang, G. Li, *Inorg. Chem.*, **52** (2013) 807.
309. B.S. Naidu, B. Vishwanadh, V. Sudarsan, R. Vatsa, *Dalton Trans.*, **41** (2012) 3194.
310. E. Song, W. Zhao, G. Zhou, X. Dou, H. Ming, C. Yi, *Curr. Appl. Phys.*, 11 (2011)1374
311. D.E. Day, Z. Wu, C.S. Ray, P. Hrma, *J. Non-Cryst. Solids*, 241 (1998) 1.
312. G.K. Marasinghe, M. Karabulut, C.S. Ray, D.E. Day, D.K. Shuh, P.G. Allen, M.L. Saboungi, M. Grimsditch, D. Haefner, *J. Non-Cryst. Solids*, **263-264** (2000) 146.
313. M. Karabulut, G.K. Marasinghe, C.S. Ray, D.E. Day, G.D. Waddill, C.H. Booth, P.G. Allen, J.J. Bucher, D.L. Caulder, D.K. Shuh, *J. Non-Cryst. Solids*, **306** (2002) 182.
314. M. Weil, R. Glaum, *Eur. J. Solid State Inorg. Chem.*, L **35** (1998) 495.
315. J.J. Bian, D.W. Kim, K.S. Hong, *Jpn. J.Appl. Phys.*, **43** (2004) 3521.
316. J.J. Bian, K.S. Hong, *J Mater. Sci.*, **40** (2005)1801.
317. B. E. Robertson, C. Calvo, Crystal structure of α -Zn₂P₂O₇, *J.Solid State Chem.*,**1** (1970) 120.
318. S.R. Vasant and M.J. Joshi, *Eur. Phys. J. Appl. Phys*, **53** (2011) 10601.
319. K. Byrappa, I.I. Plyysnina and G.I. Dorohova, *J. Electroanalit. Chem.* **74** (1970) 125.
320. I.D. Brown and C. Calvo, *J. Solid state chem.* **1** (1970) **173**
321. C. Calvo, *Can. J. Chem.* **43**, (1965) 1147.
322. C. Calvo, J.P.V. Nest and W.R. Datars, *Mater. Res. Bull.* **2** (1967) 283.
323. J. G. Chambers, W.R. Datars and C. Calvo: ESR Study of the Crystallographic Phases in Zn₂P₂O₇:Mn and Zn₂P₂O₇:Cu *J. Chem. Phys.* **41**, 806 (1964)
324. R. Bottcher, H.T. Langhammer, T. Muller, H. P. Abicht, *J. Phys. Condens. Matter.* **17** (2005) 4925.

325. A. Sengupta, R.M.Kadam, Rajeswari B., A.R.Dhobale, Y Babu and S.V.Godbole; *Applied Clay Science*, **50** (2010) 305
326. V. Singh, R.P.S. Chakradhar, J.L. Rao, Dong-Kuk Kim, *J. Sol. State Chem.* **180** (2007) 2067
327. R. Aasa, *J. Chem. Phys.*, **52** (1970) 3919.
328. L. L. Van Reijen, PhD Thesis, Technische Hogeschool, Eindhoven, The Netherlands, **1964**
329. M. Occhiuzzi, D. Cordischi, R. Gragone, *Phys. Chem. Chem. Phys.* **5** (2003) 4938.